

DISSERTATION

**Kinetic and Spectroscopic Characterization of
N₂ and H₂ Activation by Tantalum Clusters
under Cryo Conditions**

vom Fachbereich Chemie der Rheinland-Pfälzischen Technischen Universität
Kaiserslautern-Landau zur Verleihung des akademischen Grades

“Doktor der Naturwissenschaften”

genehmigte Dissertation

DE 386

vorgelegt von

Daniela Veronika FRIES

geboren in Ludwigshafen am Rhein

Betreuer: Prof. Dr. Gereon NIEDNER-SCHATTEBURG

Kaiserslautern, 12.09.2023

Die vorliegende Dissertation wurde von Januar 2020 bis Juni 2023 im Fachbereich Chemie and der Technischen Universität Kaiserslautern bzw. ab 01.01.2023 an der Rheinland-Pfälzischen Technischen Universität Kaiserslautern-Landau unter Betreuung von Prof. Dr. Gereon NIEDNER-SCHATTEBURG angefertigt.

Datum des Antrags der Eröffnung des Promotionsverfahrens: 15.01.2020

Tag der wissenschaftlichen Aussprache: 12.09.2023

PROMOTIONSKOMMISSION:

Kommissionsvorsitzender Prof. Dr. Georg MANOLIKAKES

- | | |
|---------------------|--------------------------------------|
| 1. Berichterstatter | Prof. Dr. Gereon NIEDNER-SCHATTEBURG |
| 2. Berichterstatter | Jun.-Prof. Dr. Jennifer MEYER |
| 3. Prüfer | Prof. Dr. Werner THIEL |

IN THE BEGINNING WAS THE WORD...

Johannes 1, 1

ABSTRACT

Kinetic and Spectroscopic Characterization of N₂ and H₂ Activation by Tantalum Clusters under Cryo Conditions

The present thesis reports on studies of atomically precise, size-selected tantalum cluster ions Ta_n^\pm under cryogenic conditions in a FT-ICR mass spectrometer with respect to surface adsorbate interactions at the fundamental level, focusing on N₂ and H₂ adsorption and activation. The wealth of results presented here is the result of systematic studies that have revealed valuable kinetic, spectroscopic, and quantum chemical information, which together paint a comprehensive picture of the elementary adsorption steps and mechanisms in detail.

The N₂ and H₂ adsorption processes to Ta_n^+ clusters exhibit dependencies on cluster size n and on adsorbate load. In terms of N₂ adsorption, there is evidence for spontaneous N₂ activation and cleavage by Ta_{2-4}^+ , while it appears to be suppressed by Ta_{5-8}^+ . The activation and cleavage of N₂ molecules proceeds across surmountable barriers and along much-involved multidimensional reaction paths. Underlying reaction processes and involved intermediates are elucidated. Two different processes are characteristic of H₂ adsorption: There are fast adsorption processes without competing desorption reactions at low H₂ loadings, indicating dissociative adsorption processes, followed by slow adsorption reactions accompanied by multiple desorption reactions at high H₂ loadings, indicating molecular H₂ adsorption. The threshold is the completion of the first adsorbate shell.

The N₂ adsorption study of Ta_n^- clusters revealed that the N₂ adsorption ability of anionic tantalum clusters depends strongly on cluster size n . The cluster size $n=9$ is the minimum size for N₂ adsorption onto Ta_n^- clusters to yield stable and detectable cluster adsorbate species $[Ta_n(N_2)_m]^-$.

KURZZUSAMMENFASSUNG

Kinetic and Spectroscopic Characterization of N₂ and H₂ Activation by Tantalum Clusters under Cryo Conditions

In der vorliegenden Arbeit werden Untersuchungen an gröÙenselektierten Tantalclusterionen Ta_n[±] unter kryogenen Bedingungen in einem FT-ICR Massenspektrometer im Hinblick auf Wechselwirkungen mit Adsorbaten auf fundamentaler Ebene präsentiert. Der Schwerpunkt liegt auf der Adsorption und Aktivierung der Adsorbatmoleküle N₂ und H₂. Die Fülle der hier vorgestellten Ergebnisse stammt aus systematischen Untersuchungen, die in diesem Zusammenhang ausführliche kinetische, spektroskopische und quantenchemische Informationen lieferten. Es ergibt sich ein umfassendes und detailliertes Bild der elementaren Adsorptionsschritte und -mechanismen.

Die Adsorptionsprozesse von N₂ und H₂ an Ta_n⁺ Cluster zeigen eine Abhängigkeit von der Clustergröße n und der Anzahl angelagerter Adsorbate. Die dargestellten Ergebnisse weisen auf spontane Aktivierung und Spaltung von N₂ durch Ta₂₋₄⁺ hin, während dies durch Ta₅₋₈⁺ nicht möglich ist. Die N₂ Moleküle werden über überwindbare Barrieren und entlang mehrdimensionaler Reaktionswege aktiviert und gespalten. Die zugrundeliegenden Reaktionsprozesse und beteiligten Zwischenstufen werden aufgezeigt. Für die H₂ Adsorption sind zwei verschiedene Prozesse charakteristisch: Bei einer geringen Anzahl an H₂ Anlagerungen erfolgen schnelle Adsorptionsprozesse ohne konkurrierende Desorptionsreaktionen, was auf dissoziative Adsorptionsprozesse hinweist. Bei einer hohen Anzahl an H₂ Anlagerungen erfolgen langsame Adsorptionsreaktionen, welche von Desorptionsreaktionen begleitet werden, was auf molekulare N₂ Adsorption hinweist. Die Schwelle zwischen diesen beiden Prozessen ist die Vollendung der ersten Adsorbatschale.

Die Untersuchung der Adsorption von N₂ an Ta_n⁻ ergibt, dass die N₂ Adsorptionsfähigkeit der anionischen Tantalcluster stark von der Clustergröße n abhängt. Die Clustergröße n = 9 ist die Mindestgröße zur Bildung stabiler und nachweisbarer Clusteradsorbatspezies [Ta_n(N₂)_m]⁻.

CONTENTS

Abstract	v
Kurzzusammenfassung	vii
1 Introduction	1
2 Experimental and Computational Methods	11
2.1 Fourier Transform Ion Cyclotron Resonance Mass Spectrometry . . .	11
2.1.1 Experimental Setup	12
2.1.2 Laser Vaporization Source	15
2.1.3 Ion Cyclotron Resonance Cell	16
2.2 Cryo Kinetics	18
2.2.1 Relative Rate Constants	19
2.2.2 Absolute Rate Constants	19
2.2.3 Collision Rates	20
2.3 Cryo Infrared Spectroscopy	21
2.3.1 Infrared Photon Dissociation Spectroscopy	22
2.3.2 Optical Parametric Oscillator / Amplifier IR Laser System . .	23
2.4 Density Functional Theory	26
3 Observation and Mechanism of Cryo N₂ Cleavage by a Tantalum Cluster	33
3.1 Preamble	33
3.2 Reprint	34
3.3 Supplementary Information	45

4	Cryo IR Spectroscopy and Cryo Kinetics of Dinitrogen Activation and Cleavage by Small Tantalum Cluster Cations	73
4.1	Preamble	73
4.2	Reprint	74
4.3	Supplementary Information	92
5	Cryo-IR Spectroscopy and Cryo-Kinetics of Cluster N₂ Adsorbate Complexes of Tantalum Cluster Cations Ta₅₋₈⁺	173
5.1	Preamble	173
5.2	Reprint	174
5.3	Supplementary Information	189
6	Kinetics of H₂ Adsorption onto Ta₂₋₈⁺ Clusters under Cryogenic Conditions	247
6.1	Preamble	247
6.2	Paper draft	248
6.2.1	Abstract	248
6.2.2	Introduction	248
6.2.3	Experimental and Computational Methods	250
6.2.4	Results and Discussion	252
6.2.5	Conclusion	269
6.2.6	Acknowledgements	270
6.2.7	References	270
6.3	Supplementary Information	274
7	Cryo IR Spectroscopy of H₂ Adsorption to Ta₂₋₈⁺ Clusters	285
7.1	Preamble	285
7.2	Paper draft	286
7.2.1	Abstract	286
7.2.2	Introduction	286
7.2.3	Experimental and Computational Methods	289
7.2.4	Results and Discussion	290
7.2.5	Conclusion	309
7.2.6	Acknowledgements	310
7.2.7	References	310
7.3	Supplementary Information	316

8	Size Dependence of N₂ Adsorption onto Ta₄₋₁₀⁻ Cluster Anions	339
8.1	Preamble	339
8.2	Paper draft	340
8.2.1	Abstract	340
8.2.2	Introduction	340
8.2.3	Experimental and Computational Methods	342
8.2.4	Results and Discussion	343
8.2.5	Conclusion	350
8.2.6	Acknowledgements	350
8.2.7	References	351
8.3	Supplementary Information	354
9	Summary and Outlook	357
10	Zusammenfassung und Ausblick	363
	Appendix: Selected Joint Publications	371
A.1	Kinetics of Stepwise Nitrogen Adsorption by Size-Selected Iron Cluster Cations: Evidence for Size-Dependent Nitrogen Phobia	371
A.1.1	Preamble	371
A.1.2	Reprint	372
A.2	Cryo Spetroscopy of N ₂ on Cationic Iron Clusters	393
A.2.1	Preamble	393
A.2.2	Reprint	394
A.3	Cryo Infrared Spectroscopy of N ₂ Adsorption onto Bimetallic Rhodium-Iron Clusters in Isolation	407
A.3.1	Preamble	407
A.3.2	Reprint	408
	Curriculum Vitae	ix
	List of Publications	xi
	Contribution to Conferences	xv
	Danksagung	xix
	Eidesstattliche Erklärung	xxiii

1 INTRODUCTION

Transition metals (TM) and transition metal compounds find applications as catalysts in numerous disciplines and are thus essential for everyday life and ubiquitous in scientific research. In biological processes, TM are involved as co-factors or active sites for the catalytic conversion of numerous of substrates. [1–6] Likewise, chemical industry utilizes numerous processes that are based on the application of TM in heterogeneous catalysis. [7–12] Therefore, it is mandatory to describe and understand materials and elementary processes at the molecular level. Atomically precise TM clusters may serve in this regard. [13–19] All of this research elucidates cluster size effects on their structure, and on their reactivity.

Small tantalum clusters and their cluster adsorbates are subject of the present thesis. In particular, there are numerous studies which demonstrate the interaction and reactivity of tantalum clusters, and of their alloys, carbides and chalcogenides, with small molecules such as N_2 [20–28], CH_4 [22, 29–31], CO_2 [32], and O_2 [33]. Interaction, leading towards adsorption, is understood to yield cluster adsorbate complexes which may act as precursor states for activation and bond cleavage of the adsorbates. The activation and cleavage of the N_2 triple bond and H_2 single bond is of particular interest considering the overall picture of industrial ammonia formation [12, 34, 35] and is therefore part of ongoing research efforts to develop an energetically optimized protocol for this process. [36, 37] Experimental studies and theoretical modeling at the Density Functional Theory (DFT) level have shown that the interaction of H_2 with TM clusters, complexes, and with metal surfaces leads to the formation of activated and dissociated hydrogen [38–46]. In particular, DFT modeling predicts that Ta_2^+ is capable of mediating the formation of NH_3 from N_2 and H_2 . [26]

Mass spectrometry (MS) techniques [47] combined with a laser evaporation (LVAP) source [48] for ion and cluster generation allow characterization of TM cluster ions under isolated conditions, as experiments in the gas phase allow the study of ions free of solvent or packing effects. A mass spectrometer equipped with a mass filter and an ion trap, providing a region where clusters can react with molecules of interest, additionally enables the study of cluster adsorbate complexes. The development of cryogenically cooled ion traps makes it possible to coordinate weakly bound messengers - atoms or small molecules - to the clusters. This opens up the possibility of generating previously inaccessible reaction products. [49–52]

Furthermore, vibrational spectroscopic methods can be used to obtain additional information about the structures of clusters and cluster adsorbates. Historically, the inelastic electron scattering off technique has proved valuable for structural characterization. [53, 54] The technical advancement of infrared photon dissociation (IR-PD) spectroscopy by either free electron lasers (FEL) or optical parametric oscillator (OPO) technology has helped to record vibrational bands, in particular when applied to isolated clusters and their complexes, and thereby achieve sufficient spectral resolution. [55–58] This method is widely applicable and well established by now. [59–68] It provides insights into the coordination motifs of the respective adsorbates on the TM clusters and is able to reveal possible activation of the adsorbates. The so-called *tagging* or *messenger* technique yields messenger complexes with low binding energies that allow sensitive single photon dissociation, avoiding spectral artifacts caused by adsorption of multiple photons. [49, 69, 70] The strength of the interaction between the adsorbate and the cluster affects the shift in the vibrational frequency of the adsorbed molecule. [71] Cluster size and structure as well as charge and spin state of the cluster and furthermore coordination and binding motifs of the adsorbate on the cluster are possible influencing factors. Consequently, the characteristic IR-PD fingerprint corresponds to a very specific degree of attenuation of the binding strength of an adsorbent. From this, in turn, one can infer the binding motif and derive structural information about the cluster adsorbate complex. In any case, it is mandatory to augment recorded experimental data with quantum chemical modeling by DFT methods in order to enable sound structural and dynamic interpretation. [72–75]

By virtue of previous studies from our research group, it has been established to perform cryo kinetic measurements of isolated TM clusters complemented with cryo IR-PD spectroscopic studies and DFT modeling of the resulting cluster adsorbate complexes. These techniques serve as strong tool for the elucidation of elementary adsorption and reaction processes as well as of cluster (adsorbate) geometries and structures. [20, 76–87] A modified Fourier transform ion cyclotron resonance mass spectrometry (FT-ICR MS) instrument is used to deposit small molecules, such as N₂ or H₂, to be adsorbed onto size-selected TM clusters under well-defined cryogenic conditions and allows recording of adsorption kinetics and IR-PD spectra. [88]

All research studies that are part of the present thesis are based on the techniques mentioned above and combine cryo kinetics and IR-PD spectroscopy measurements with DFT modeling of tantalum cluster ions and their H₂ and N₂ adsorbates. Initial findings of N₂ adsorption to Ta_{2–5}⁺ clusters were achieved by myself (master thesis [89]) and M. P. Klein (doctoral thesis [90]). The present thesis is a comprehensive follow-up and extension of this prior work. It comprises seven research studies, each of which provides for individual introduction, experimental, discussion and conclusion parts. Beforehand, chapter 2 introduces the applied experimental setup and the experimental and computational methods. Chapters 3, 4 and 5 address the topic of stepwise N₂ adsorption on size-selected tantalum cluster cations Ta_n⁺, n = 2–8. Mass spectrometry studies reveal adsorption limits of each cluster size. The cryo adsorption kinetics, the evaluated kinetic fits, and rate constants of certain cluster sizes indicate dissociative adsorption and activation of N₂ with formation of tantalum nitrides and/or isomerization processes in the course of the N₂ adsorption chain. Cryo IR-PD spectroscopy of the cluster adsorbates [Ta_n(N₂)_m]⁺ and DFT modeling provide evidence for spontaneous N₂ activation and bond cleavage on small tantalum clusters Ta_{2–4}⁺ while this ability seems suppressed for Ta_{5–8}⁺. Chapters 6 and 7 focus on stepwise adsorption of H₂ to size-selected tantalum cluster cations Ta_n⁺, n = 2–8. Cryo kinetic studies show that the adsorption limits and processes depend on the cluster size n and the adsorbate load. Cryo IR-PD spectroscopy of the cluster adsorbates and DFT modeling demonstrate that all clusters n = 3–8 dissociatively adsorb H₂ until the formal first adsorbate shell is completed. Chapter 8 elucidates the ability of N₂ adsorption to tantalum cluster anions Ta_n[–], n = 4–10, under cryogenic conditions, and it opens the road towards subsequent studies beyond the current thesis work.

References

- [1] M. Frey, *ChemBioChem* **2002**, *3*, 153–160.
- [2] S. Shima, R. K. Thauer, *The Chemical Record* **2007**, *7*, 37–46.
- [3] M. Bruschi, M. Tiberti, A. Guerra, L. De Gioia, *Journal of the American Chemical Society* **2014**, *136*, 1803–1814.
- [4] D. Jantz, B. T. Amann, G. J. Gatto, J. M. Berg, *Chemical Reviews* **2004**, *104*, 789–800.
- [5] K. J. Waldron, J. C. Rutherford, D. Ford, N. J. Robinson, *Nature* **2009**, *460*, 823–830.
- [6] K. Kostenkova, G. Scalese, D. Gambino, D. C. Crans, *Current Opinion in Chemical Biology* **2022**, *69*, 102155.
- [7] F. Fischer, H. Tropsch, DE484337C, **1925**.
- [8] F. Fischer, H. Tropsch, DE524468C, **1931**.
- [9] Badische Anilin- und Soda-Fabrik, DE235421C, **1911**.
- [10] W. Ostwald, GB190200698A, **1902**.
- [11] H. Breil, E. Holzkamp, H. Martin, K. E. H. Ziegler, DE973626C, **1960**.
- [12] A. Mittasch, *Geschichte der Ammoniaksynthese*, Verlag Chemie, **1951**.
- [13] M. M. Kappes, *Chemical Reviews* **1988**, *88*, 369–389.
- [14] P. B. Armentrout, *Annual Reviews* **2001**, *52*, 423–461.
- [15] R. A. J. O’Hair, G. N. Khairallah, *Journal of Cluster Science* **2004**, *15*, 331–363.
- [16] D. K. Böhme, H. Schwarz, *Angewandte Chemie International Edition* **2005**, *44*, 2336–2354.
- [17] S. M. Lang, T. M. Bernhardt, *Physical Chemistry Chemical Physics* **2012**, *14*, 9255–9269.
- [18] P. B. Armentrout, *Catalysis Science & Technology* **2014**, *4*, 2741–2755.

-
- [19] M. D. Morse, M. E. Geusic, J. R. Heath, R. E. Smalley, *The Journal of Chemical Physics* **1985**, *83*, 2293–2304.
- [20] D. V. Fries, M. P. Klein, A. Steiner, M. H. Prosenc, G. Niedner-Schatteburg, *Physical Chemistry Chemical Physics* **2021**, *23*, 11345–11354.
- [21] L.-H. Mou, Y. Li, Z.-Y. Li, Q.-Y. Liu, H. Chen, S.-G. He, *Journal of the American Chemical Society* **2021**, *143*, 19224–19231.
- [22] L.-H. Mou, Y. Li, G.-P. Wei, Z.-Y. Li, Q.-Y. Liu, H. Chen, S.-G. He, *Chemical Science* **2022**, *13*, 9366–9372.
- [23] M. R. Zakin, D. M. Cox, A. Kaldor, *The Journal of Chemical Physics* **1987**, *87*, 5046–5048.
- [24] G.-D. Jiang, L.-H. Mou, J.-J. Chen, Z.-Y. Li, S.-G. He, *The Journal of Physical Chemistry A* **2020**, *124*, 7749–7755.
- [25] X. Sun, X. Huang, *ACS Omega* **2022**, *7*, 22682–22688.
- [26] C. Geng, J. Li, T. Weiske, H. Schwarz, *Proceedings of the National Academy of Sciences* **2018**, *115*, 11680–11687.
- [27] C. Geng, J. Li, T. Weiske, H. Schwarz, *Proceedings of the National Academy of Sciences* **2019**, *116*, 21416–21420.
- [28] M. Kumar Yadav, A. Mookerjee, *Physica B: Condensed Matter* **2010**, *405*, 3940–3942.
- [29] J. F. Eckhard, T. Masubuchi, M. Tschurl, R. N. Barnett, U. Landman, U. Heiz, *The Journal of Physical Chemistry C* **2018**, *122*, 25628–25637.
- [30] J. Lengyel, N. Levin, F. J. Wensink, O. V. Lushchikova, R. N. Barnett, U. Landman, U. Heiz, J. M. Bakker, M. Tschurl, *Angewandte Chemie International Edition* **2020**, *59*, 23631–23635.
- [31] J. F. Eckhard, T. Masubuchi, M. Tschurl, R. N. Barnett, U. Landman, U. Heiz, *The Journal of Physical Chemistry A* **2021**, *125*, 5289–5302.
- [32] N. Levin, J. T. Margraf, J. Lengyel, K. Reuter, M. Tschurl, U. Heiz, *Physical Chemistry Chemical Physics* **2022**, *24*, 2623–2629.

- [33] J. F. Eckhard, D. Neuwirth, C. Panosetti, H. Oberhofer, K. Reuter, M. Tschurl, U. Heiz, *Physical Chemistry Chemical Physics* **2017**, *19*, 5985–5993.
- [34] G. Ertl, *Catalysis Reviews* **1980**, *21*, 201–223.
- [35] G. Ertl, *Angewandte Chemie International Edition* **2008**, *47*, 3524–3535.
- [36] R. Schlögl, *Angewandte Chemie International Edition* **2003**, *42*, 2004–2008.
- [37] H. Liu, *Cuihua Xuebao/Chinese Journal of Catalysis* **2014**, *35*, 1619–1640.
- [38] M. E. Geusic, M. D. Morse, R. E. Smalley, *The Journal of Chemical Physics* **1985**, *82*, 590–591.
- [39] G. J. Kubas, *Accounts of Chemical Research* **1988**, *21*, 120–128.
- [40] K. Christmann, *Surface Science Reports* **1988**, *9*, 1–163.
- [41] D. A. Hite, K. S. McKay, S. Kotler, D. Leibfried, D. J. Wineland, D. P. Pappas, *MRS Advances* **2017**, *2*, 2189–2197.
- [42] K. García-Díez, J. Fernández-Fernández, J. A. Alonso, M. J. López, *Physical Chemistry Chemical Physics* **2018**, *20*, 21163–21176.
- [43] W. F. Hoffman, E. K. Parks, G. C. Nieman, L. G. Pobo, S. J. Riley, *Zeitschrift für Physik D Atoms Molecules and Clusters* **1987**, *7*, 83–89.
- [44] I. Swart, P. Gruene, A. Fielicke, G. Meijer, B. M. Weckhuysen, F. M. F. de Groot, *Physical Chemistry Chemical Physics* **2008**, *10*, 5743–5745.
- [45] O. V. Lushchikova, H. Tahmasbi, S. Reijmer, R. Platte, J. Meyer, J. M. Bakker, *The Journal of Physical Chemistry A* **2021**, *125*, 2836–2848.
- [46] C. Kerpál, D. J. Harding, D. M. Rayner, A. Fielicke, *The Journal of Physical Chemistry A* **2013**, *117*, 8230–8237.
- [47] J. Gross, P. Roepstorff, *Mass Spectrometry: A Textbook*, Springer Berlin Heidelberg, **2011**.
- [48] M. A. Duncan, *Review of Scientific Instruments* **2012**, *83*, 041101.
- [49] A. B. Wolk, C. M. Leavitt, E. Garand, M. A. Johnson, *Accounts of Chemical Research* **2014**, *47*, 202–210.

-
- [50] D. Gerlich, J. Jašík, E. Andris, R. Navrátil, J. Roithová **2016**, *17*, 3723–3739.
- [51] Z. Wu, A. Płucienik, Y. Liu, M. Naschitzki, W. Wachsmann, S. Gewinner, W. Schöllkopf, H. Kuhlenbeck, H.-J. Freund, *Review of Scientific Instruments* **89**, 083107.
- [52] L. Ferrand, S. Soorkia, G. Gregoire, M. Broquier, B. Soep, N. Shafizadeh, *Physical Chemistry Chemical Physics* **2015**, *17*, 25693–25699.
- [53] M. C. Tsai, U. Ship, I. C. Bassignana, J. Küppers, G. Ertl, *Surface Science* **1985**, *155*, 387–399.
- [54] H. J. Freund, B. Bartos, R. P. Messmer, H. Grunze, H. Kuhlenbeck, M. Neumann, *Surface Science* **1987**, *185*, 187–202.
- [55] A. Fielicke, A. Kirilyuk, C. Ratsch, J. Behler, M. Scheffler, G. Von Helden, G. Meijer, *Physical Review Letters* **2004**, *93*, 023401–1.
- [56] J. Oomens, B. G. Sartakov, G. Meijer, G. von Helden, *International Journal of Mass Spectrometry* **2006**, *254*, 1–19.
- [57] J. R. Eyler, *Mass Spectrom Rev* **2009**, *28*, 448–67.
- [58] P. Maitre, D. Scuderi, D. Corinti, B. Chiavarino, M. E. Crestoni, S. Fornarini, *Chemical Reviews* **2020**, *120*, 3261–3295.
- [59] J. Roithová, *Chemical Society Reviews* **2012**, *41*, 547–559.
- [60] G. Altinay, R. B. Metz, *International Journal of Mass Spectrometry* **2010**, *297*, 41–45.
- [61] B. Chiavarino, M. E. Crestoni, M. Schütz, A. Bouchet, S. Piccirillo, V. Steinmetz, O. Dopfer, S. Fornarini, *Journal of Physical Chemistry A* **2014**, *118*, 7130–7138.
- [62] O. Dopfer, *Journal of Physical Organic Chemistry* **2006**, *19*, 540–551.
- [63] N. I. Hammer, J. W. Shin, J. M. Headrick, E. C. Diken, J. R. Roscioli, G. H. Weddle, M. A. Johnson, *Science* **2004**, *306*, 675–679.
- [64] J. M. Headrick, E. G. Diken, R. S. Walters, N. I. Hammer, R. A. Christie, J. Cui, E. M. Myshakin, M. A. Duncan, M. A. Johnson, K. D. Jordan, *Science* **2005**, *308*, 1765–1769.
- [65] A. M. Rijs, J. Oomens, *Topics in Current Chemistry* **2015**, *364*, 1–42.

- [66] T. R. Rizzo, O. V. Boyarkin, *Topics in Current Chemistry* **2015**, 364, 43–98.
- [67] T. R. Rizzo, J. A. Stearns, O. V. Boyarkin, *International Reviews in Physical Chemistry* **2009**, 28, 481–515.
- [68] W. H. Robertson, M. A. Johnson, *Annual Review of Physical Chemistry* **2003**, 54, 173–213.
- [69] M. A. Duncan, *International Reviews in Physical Chemistry* **2003**, 22, 407–435.
- [70] L. MacAleese, P. Maître, *Mass Spectrometry Reviews* **2007**, 26, 583–605.
- [71] A. Crossley, D. A. King, *Surface Science* **1977**, 68, 528–538.
- [72] G. L. Gutsev, C. W. Weatherford, K. G. Belay, B. R. Ramachandran, P. Jena, *The Journal of Chemical Physics* **2013**, 138, 164303.
- [73] A. S. Chaves, M. J. Piotrowski, J. L. F. Da Silva, *Physical Chemistry Chemical Physics* **2017**, 19, 15484–15502.
- [74] F. Neese, *Coordination Chemistry Reviews* **2009**, 253, 526–563.
- [75] J. Du, X. Sun, G. Jiang, *The Journal of Chemical Physics* **2012**, 136, 094311.
- [76] J. Mohrbach, S. Dillinger, G. Niedner-Schatteburg, *The Journal of Physical Chemistry C* **2017**, 121, 10907–10918.
- [77] S. Dillinger, J. Mohrbach, G. Niedner-Schatteburg, *The Journal of Chemical Physics* **2017**, 147, 184305.
- [78] A. A. Ehrhard, M. P. Klein, J. Mohrbach, S. Dillinger, G. Niedner-Schatteburg, *Molecular Physics* **2021**, 119, e1953172.
- [79] A. A. Ehrhard, M. P. Klein, J. Mohrbach, S. Dillinger, G. Niedner-Schatteburg, *The Journal of Chemical Physics* **2022**, 0, 054308.
- [80] A. Straßner, M. P. Klein, D. V. Fries, C. Wiehn, M. E. Huber, J. Mohrbach, S. Dillinger, D. Spelsberg, P. B. Armentrout, G. Niedner-Schatteburg, *The Journal of Chemical Physics* **2021**, 155, 244306.
- [81] A. Straßner, C. Wiehn, M. P. Klein, D. V. Fries, S. Dillinger, J. Mohrbach, M. H. Prosenc, P. B. Armentrout, G. Niedner-Schatteburg, *The Journal of Chemical Physics* **2021**, 155, 244305.

-
- [82] S. Dillinger, J. Mohrbach, J. Hewer, M. Gaffga, G. Niedner-Schatteburg, *Physical Chemistry Chemical Physics* **2015**, *17*, 10358–10362.
- [83] C. Berg, T. Schindler, G. Niedner-Schatteburg, B. V. E., *The Journal of Chemical Physics* **1995**, *102*, 4870–4884.
- [84] S. Dillinger, M. P. Klein, A. Steiner, D. C. McDonald, M. A. Duncan, M. M. Kappes, G. Niedner-Schatteburg, *The Journal of Physical Chemistry Letters* **2018**, *9*, 914–918.
- [85] M. P. Klein, A. A. Ehrhard, J. Mohrbach, S. Dillinger, G. Niedner-Schatteburg, *Topics in Catalysis* **2018**, *61*, 106–118.
- [86] M. P. Klein, A. A. Ehrhard, M. E. Huber, A. Straßner, D. V. Fries, S. Dillinger, J. Mohrbach, G. Niedner-Schatteburg, *The Journal of Chemical Physics* **2022**, *156*, 014302.
- [87] J. Mohrbach, S. Dillinger, G. Niedner-Schatteburg, *The Journal of Chemical Physics* **2017**, *147*, 184304.
- [88] S. Dillinger, G. Niedner-Schatteburg in *Chapter 19 - Cryo trapping by FT-MS for kinetics and spectroscopy* (Eds.: B. Kanawati, P. Schmitt-Kopplin), Elsevier, **2019**, pp. 593–621.
- [89] D. V. Fries, *Master Thesis*, Technische Universität Kaiserslautern, **2019**.
- [90] M. P. Klein, *PhD Thesis*, Technische Universität Kaiserslautern, **2021**.

2 EXPERIMENTAL AND COMPUTATIONAL METHODS

2.1 Fourier Transform Ion Cyclotron Resonance Mass Spectrometry

As early as the 1930s, Lawrence described the principles of a cyclotron that could accelerate ions without requiring high voltages. [1–4] These findings formed the basis for the development of the first ion cyclotron resonance mass spectrometer (ICR MS) in the early 1950s. [5] About 20 years later, with the introduction of the Fourier transform mass spectrometry (FT MS), a Fourier transform ion cyclotron resonance mass spectrometer (FT-ICR MS) was constructed by Comisarow and Marshall. [6, 7] Combining these mass spectrometers with superconducting magnets has improved their performance. [8, 9] A so-called ion cyclotron resonance cell (ICR) is the heart of such a FT-ICR MS instrument and is located inside the superconducting magnet. A strong homogeneous magnetic field forces the ions of interest to follow a circular trajectory within the ICR cell. The radius r of this motion is determined by the Lorentz force F_L (2.1) and the centrifugal force F_{Cf} (2.2), which must be in equilibrium to ensure stable ion motion (2.3).

$$\text{Lorentz force:} \quad F_L = qv_{xy}B \quad (2.1)$$

$$\text{Centrifugal force:} \quad F_{Cf} = \frac{mv_{xy}^2}{r_I} \quad (2.2)$$

$$\Rightarrow \text{stable ion motion:} \quad qv_{xy}B = \frac{mv_{xy}^2}{r_I} \quad (2.3)$$

q	charge of the ion ($q = z \cdot e$)
z	number of charges
e	elementary charge (1.602×10^{-19} C)
v_{xy}	velocity of the ion in the xy plane
B	magnetic field
m	ion mass
r_I	radius of the ion orbit

This results in the following mathematical correlations for the radius of the ion orbit r_I (2.4), the angular velocity ω_c (2.5), and the cyclotron frequency ν_c (2.6):

$$\text{radius of the ion orbit:} \quad r_I = \frac{mv_{xy}}{qB} \quad (2.4)$$

$$\text{angular velocity:} \quad \omega_c = \frac{v_{xy}}{r_I} = \frac{qB}{m} \quad (2.5)$$

$$\text{cyclotron frequency:} \quad \nu_c = \frac{\omega_c}{2\pi} = \frac{qB}{2\pi m} \quad (2.6)$$

Accordingly, the cyclotron frequency ν_c depends only on the m/z ratio of the ions, but not on the velocity of the ions on the xy plane.

$$\frac{m}{z} = \frac{eB}{2\pi\nu_c} \quad (2.7)$$

2.1.1 Experimental Setup

All experiments in this thesis were performed on the experimental setup called “FRITZ” (Fourier transform reactive investigation test zoo, *cf.* Figure 1 and 2). This instrument is a heavily modified mass spectrometer based on a commercially available FT-ICR MS *Apex Ultra* from Bruker Daltonics. It is equipped with two ion sources: an electrospray ionization (ESI) source (*Apollo II*, Bruker Daltonics) and a laser vaporization (LVAP) source, both coupled to the quadrupole ion bender of the mass spectrometer by home built gate valves. The ESI source allows a smooth ion transfer from a solution into the gas phase and therefore was not used for the experiments in this work. The LVAP source serves for TM cluster generation (*cf.* chapter 2.1.2). Ion optics guide the ions into the quadrupole ion bender, where the ions of interest are bent 90° to the magnetic field axis. This ion beam bending removes neutral clusters and ions of opposite polarity from the beam. In the next step, the cluster ions are steered into a quadrupole mass filter by another stack of

home built ion optics. This quadrupole mass filter allows to select the ions by size. These mass selected ions are injected into the hexapole ion trap. There it is possible to store the respective cluster ions for various times (storage times or collision (cell) delays) from a few seconds up to 30 s. It is also possible to introduce reaction or collision gases continuously via two valves. For all experiments performed in the context of this thesis, helium served as the collision gas which ensures efficient trapping and cooling of the ions. The reaction gases nitrogen or hydrogen were added as required. For detection, the manipulated ions are steered into the ICR cell (*cf.* chapter 2.1.3) by a series of electrostatic lenses.

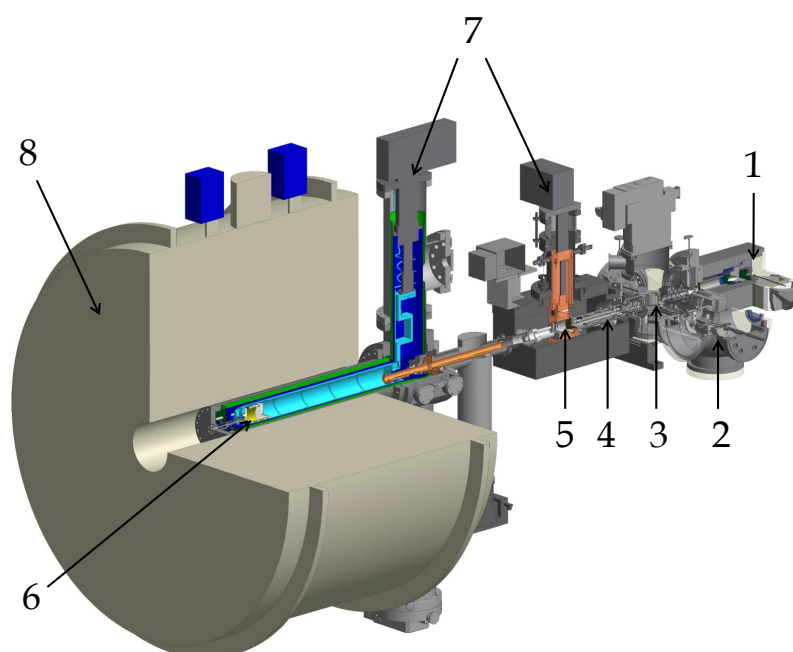


Figure 1: Schematic drawing of the “FRITZ” setup [10], a modified *Apex Ultra* (Bruker Daltonics) instrument. 1: electro-spray ionisation (ESI) source (here arranged on the magnetic field axis for easier representation, in the actual setup it is mounted perpendicular to the magnetic field axis and opposite to the LVAP source, *cf.* Figure 2), 2: laser vaporization (LVAP) source, 3: quadrupole ion bender, 4: quadrupole mass filter, 5: cryogenically cooled hexapole ion trap, 6: cryogenically cooled ICR cell, 7: two-stage closed-cycle He cryostats, 8: superconducting magnet ($B = 7$ T).

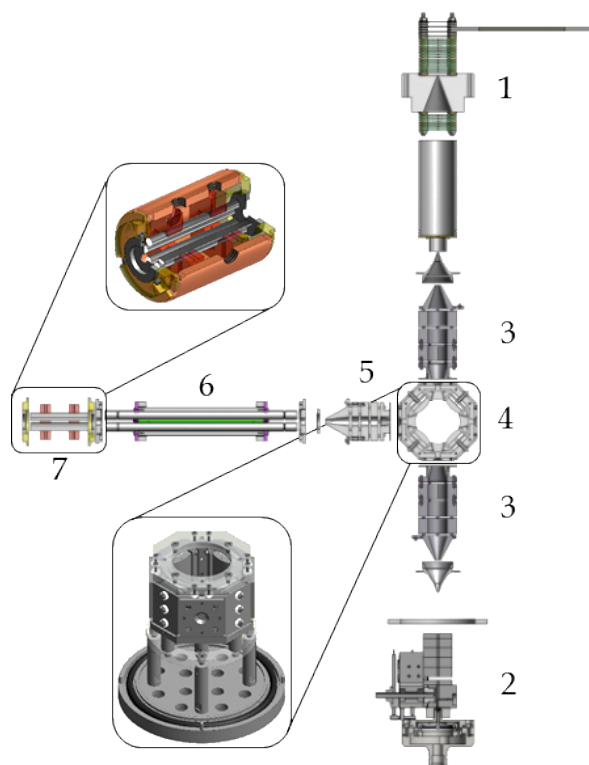


Figure 2: Schematic overview of the ion sources and ion optics in the “FRITZ” setup [10] generating the ions and guiding them to the hexapole ion trap. 1: ESI source, 2: LVAP source, 3: ion optics and gate valve, 4: quadrupole ion bender, 5: ion optics, 6: quadrupole mass filter, 7: cryogenically cooled hexapole ion trap.

The described setup of the “FRITZ” FT-ICR MS instrument allows measurements at room temperature as well as at cryogenic temperatures. In order to perform measurements at low temperatures down to below 20 K, the hexapole ion trap and the ICR cell can each be cooled with a closed-cycle two-stage cryostat. A 4 K cryostat (*Sumitomo* SRDK-101E, compressor HC-4E) is attached to the hexapole ion trap (*cf.* Figure 3). Two temperature sensors (*LakeShore*, Cernox™CX-1060-CO-HT-P-1.M, calibrated for a temperature range of 1.4 to 420 K), monitor both cooling stages of the cryostat. Heating resistors (*Cartridge Heater, Janis Research*, $R = 50 \Omega$), enable temperature adjustments via a corresponding temperature controller (*LakeShore*, model 336). Both gas injection lines run along the cooling stages of the cryostat to ensure that the collision and reaction gases are introduced into the hexapole ion trap pre-cooled. The ICR cell is cooled in a similar manner. A 10 K cryostat (*Sumitomo* SRDK-408R2, Kompressor W-71D), connected to three temperature sensors (*LakeShore*, Cernox™CX-1050-CO-HT-P, calibrated for a temperature

range of 4 to 325 K) and controlled by a temperature controller (*LakeShore*, Modell 340), is mounted in front of the ICR cell. When reaction gas is introduced into the ICR cell, it is pre-cooled via the cryostat.

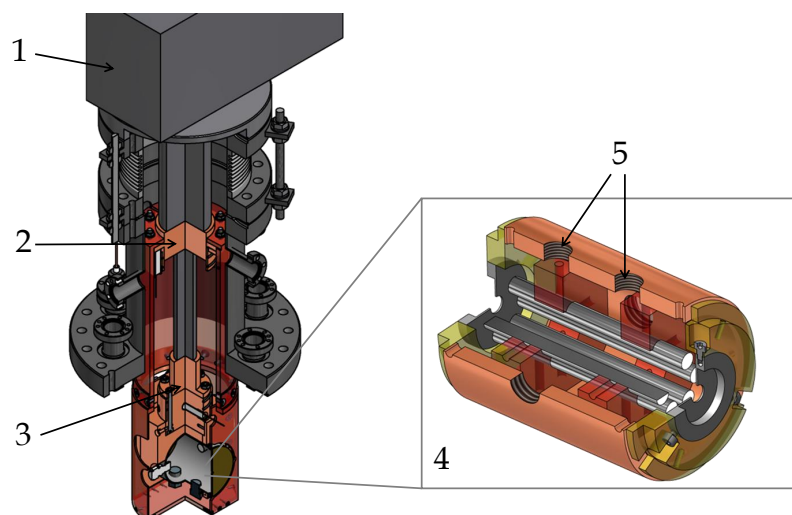


Figure 3: Schematic drawing of the cryogenically cooled hexapole ion trap [10] comprising 1: cryostat, 2: first cooling stage (3 W), 3: second cooling stage (0.15 W), 4: hexapole ion trap, 5: inlet for warm or pre-cooled gases.

2.1.2 Laser Vaporization Source

The cluster ions are generated by laser vaporization. [11] An ion source based on this technique was first described by Smalley [12, 13] as well as Bondybey and English [14, 15]. The LVAP source mounted to our FT-ICR MS instrument comprises three components, as shown in Figure 4: a home built piezoelectric valve [16], an expansion/interaction block and an expansion channel. The vaporization unit contains the metal target (0.5 mm thick) which rotates powered by a rotation motor. The second harmonic of a pulsed Nd:YAG (532 nm, Innolas Spitlight 300, 20 Hz) evaporates metal atoms from this rotating target. The hot plasma consisting of atoms and ions thus generated is captured by a He gas pulse (40 μ s, 15 bar) from a home-built piezoelectric valve [16]. This valve operates in synchronization with the laser. The expansion channel (length: 69 mm, diameter: 2 mm) guides the plasma into vacuum (10^{-7} mbar). During this expansion, the atoms and ions of the plasma are cooled by collisions with the He carrier gas and aggregate into metal clusters of up

to 40 atoms. Finally, a mesh (metal grid) focuses the resulting cluster size distribution onto a skimmer with an aperture of 1.45 mm. From there on, electrostatic lenses guide the cluster ions to the ion beam bender and into the mass spectrometer (*cf.* chapter 2.1.1).

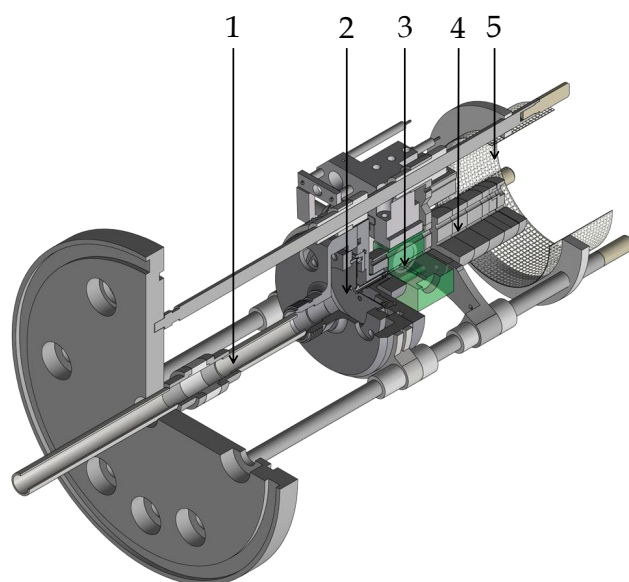


Figure 4: Schematic drawing of a laser vaporization (LVAP) source [10]. 1: gas inlet, 2: piezoelectric valve, 3: expansion / interaction block, 4: expansion channel, 5: mesh.

A variation of the source parameters, such as the backing pressure, the delay between the laser pulse and the opening of the piezoelectric valve, the opening time of the piezoelectric valve, or the source voltage, affects the intensity maximum of the generated cluster size distribution. Furthermore, it is possible to select the generated clusters by charge based on the polarity of the source voltage and the potentials applied to the ion optics.

2.1.3 Ion Cyclotron Resonance Cell

The ion cyclotron resonance (ICR) cell of the so-called *infinity cell* type [17] is the heart of the FT-ICR MS instrument. Such an ICR cell consists of six plates: a front and a back trapping plate, as well as two excitation and two detection plates (*cf.* Figure 5).

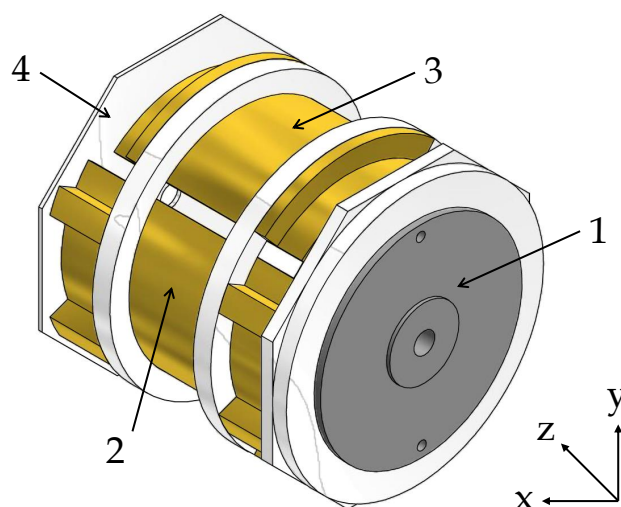


Figure 5: Schematic drawing of an ion cyclotron resonance (ICR) cell [10] of the so-called *infinity cell* type [17]. 1: front trapping plate, 2: excitation plate, 3: detection plate, 4: back trapping plate.

An electrostatic field applied to the front and back trapping plates traps the ions in the cell along the magnetic field axis (z-axis). It is possible to store the ions for several hours depending on the quality of the vacuum in the ICR cell. [8] This trapping results in an oscillatory motion of the ions between the two trapping plates along the z-axis - the trapping motion. An alternating electric field applied to the two opposing excitation plates excites the ions in the ICR cell over a wide frequency range. The trapped ions enter larger orbits due to the changing polarity of the plates. However, the ions retain their specific cyclotron frequency. As a consequence, the overall motion of trapped ions in the ICR cell is composed of three components: Trapping motion and cyclotron motion superimpose with the radial motion to form the total ion motion (*cf.* Figure 6). The oscillating ions induce an image current on the detector plates as soon as the excitation pulse is switched off. These image current can be recorded and evaluated as a function of time. Fourier transformation is used to determine frequency-dependent intensities, which in turn can be converted into a mass spectrum. Such a mass spectrum is the graphical representation of the detected intensity against the m/z ratio of the ions under investigation.

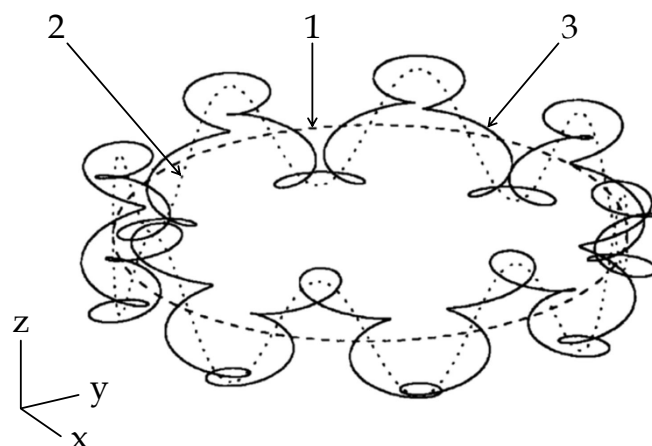


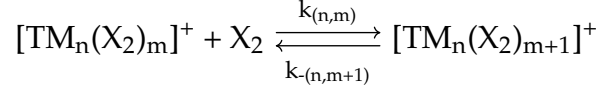
Figure 6: Schematic drawing of the ion motion within an ICR cell [18]. 1: magnetron motion (dashed line), 2: magnetron motion plus the trapping motion (dotted line), 3: overall motion including the cyclotron motion (solid line).

The ICR cell serves not only for mass detection but also for selection and storage of ions to be investigated. On the one hand, a specific ion species can be resonantly excited with a specific m/z ratio. As a result, these ions enter higher, more unstable orbits and are thus removed from the ICR cell. Only ions with the desired m/z ratio remain in the ICR cell for further investigation and analysis (*shot* mode). On the other hand, it is possible to isolate the m/z ratio of one ion species in the ICR cell by removing all other ion species from the cell by pulses with changing frequency (*sweep* mode).

2.2 Cryo Kinetics

Performing kinetic measurements allows to investigate the adsorption processes of reaction gas molecules X_2 on TM^\pm cluster ions at cryogenic temperatures. The mass-selected TM^\pm clusters are stored in the hexapole ion trap at a defined temperature and reaction gas pressure for various storage times (collision cell delays). The recorded mass spectrum for each reaction delay consists of an average of 40 scans. We receive a temporal evolution of mass spectra, in which the mass signals for the reaction products increase in intensity with increasing storage time, while at the same time the initial cluster ion intensities decrease.

The stepwise adsorption of X_2 to TM clusters, such as TM_n^+ , in an adsorption chain can be described as follows:

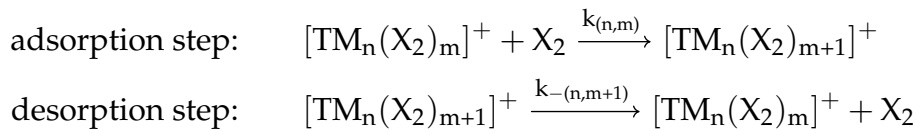


The reaction gas molecules X_2 are in excess compared to the cluster ions during the adsorption reaction. As a consequence, the concentration of the reaction gas can be considered constant during the course of the reaction. Therefore, the adsorption process of the reaction gas molecules onto the cluster species corresponds to a pseudo-first-order reaction with its rate law expression (2.8).

$$-\frac{d[[TM_i]^+]}{dt} = k_i \cdot [[TM_i]^+] \cdot [X_2] = k_i \cdot [[TM_i]^+] \quad (2.8)$$

2.2.1 Relative Rate Constants

The experimentally recorded mass spectra are evaluated using the program *Data Analysis 4.0* (Bruker Daltonics) to obtain signal intensities and assigned storage times for each adsorbate complex. These data serve as input for evaluation by *evofit* [19], which is the in-house genetic algorithm fitting routine. This program normalizes the ion intensities and performs pseudo-first-order kinetic fits which yield relative rate constants for all adsorption $k_{(n,m)}$ and desorption $k_{-(n,m+1)}$ steps along the adsorption chain.



2.2.2 Absolute Rate Constants

Fitting the experimental kinetic intensity data delivers relative rate constants $k_{(n,m)}$. By converting these into absolute rate constants $k_{(n,m)}^{\text{abs}}$ according to equation (2.9), the rate constants of all kinetic measurements can be compared. Absolute collision gas number densities $\rho_{H_2}(T)$ are the conversion factor.

$$k_{(n,m)}^{\text{abs}} = \frac{k_{(n,m)}}{\rho_{H_2}(T)} \quad (2.9)$$

2. Experimental and Computational Methods

The pressure in the surrounding chamber $p_c^{300\text{K}}$ and the effective geometry factor c_{app} give approximate values for the absolute collision gas number densities $\rho_{\text{H}_2}(T)$ according to (2.10).

$$\rho_{\text{H}_2}(T) = \frac{c_{\text{app}} \cdot p_c^{300\text{K}}}{k_B \cdot T_{300\text{K}}} \quad (2.10)$$

The geometry factor c_{app} is estimated as 1.8 at 26 K with an uncertainty of $\pm 50\%$ by a virtue of numerous kinetic studies. The quotient of the absolute rate constants k^{abs} and the collision rates k^{coll} give the absolute reaction efficiency $\gamma_{(n,m)}$ according to equation (2.11). It can be considered as a reaction probability, when a collision occurs between the TM cluster and the reaction gas molecule.

$$\gamma_{(n,m)} = \frac{k^{\text{abs}}}{k^{\text{coll}}} \quad (2.11)$$

2.2.3 Collision Rates

Three models serve for determination of collision rates:

- The average dipole orientation (ADO) theory by Su and Bowers [20, 21] gives the theoretical limit of the absolute rate constant (equation (2.12)). It is based on the concept of a classical trajectory of a linear dipole in the field of a point charge. It extends the classical Langevin collision rate [22].

$$k^{\text{ADO}} = \left(\frac{q}{2 \cdot \epsilon_0 \cdot \sqrt{\mu}} \right) \cdot \left(\sqrt{\alpha} + c \cdot \mu_D \cdot \sqrt{\frac{2}{\pi \cdot k_B \cdot T}} \right) \quad (2.12)$$

μ reduced mass of the cluster adsorbate complex

α polarizability

μ_D dipole moment

ϵ_0 vacuum permittivity

q charge of the ion

k_B Boltzmann constant

T temperature

The parameter c can take values between 0 and 1 and is expressed by the parameter for the polarizable volume α' and the dipole moment μ_D . [23] Note,

that a vanishing dipole moment, as of N_2 or H_2 , causes k^{ADO} to become identical to the Langevin rate constant. However, the collision rates output by ADO theory often underestimate the measured rate constants for charged metal clusters. [24, 25] Nevertheless, this model is often used to calculate reaction rates of charged clusters with small molecules.

- Kummerlöwe and Beyer [26] introduced two other models to approximate collision rates of ionic clusters reacting with neutral molecules.
 - The hard sphere average dipole orientation (HSA) model considers both the ion clusters and the neutral molecules as solid spheres. The charge is assumed to be localized as a point charge in the center of the cluster. The nature of attraction between this point charge and the neutral reactant is of the ADO type.
 - The surface charge capture (SSC) model also describes ionic clusters and their reactants (neutral molecules) as hard spheres. However, this model is based on the assumption of an ideally conducting cluster. The point charge is free to move throughout the cluster and migrates to the cluster surface by interaction with neutral molecules.

2.3 Cryo Infrared Spectroscopy

Infrared (IR) spectroscopy serves for structure elucidation and characterization of molecules. In the condensed phase, the sample resonantly absorbs IR radiation and the extinction is evaluated as a function of IR frequency. In the gas phase, studying isolated molecules excludes solvent and packing effects and the influence of counterions. However, these isolated molecules in the gas phase do not provide sufficient particle density to achieve measurable absorbance. Thus it is impossible to perform classical light adsorption spectroscopy of gaseous molecules. More sophisticated methods are required to overcome this sensitivity problem. The so-called *action spectroscopy* methods address this need. Instead of measuring adsorption intensity, IR-induced effects (fragmentation, ionization, etc.) are measured as a function of IR frequency. [27] The combination of action spectroscopy with mass spectrometry allows to detect both the precursors and the products of irradiation. This enables recording of IR (action) spectra.

2.3.1 Infrared Photon Dissociation Spectroscopy

One method for recording vibrational spectra of isolated gaseous ions is infrared (multi)photon dissociation (IR-(M)PD) spectroscopy. It is based on the fragmentation of ions by the successive absorption of several IR photons: A tunable IR laser irradiates the gaseous ions. When the laser frequency resonates with a vibrational mode of the ion, it absorbs a photon. The absorbed energy is immediately distributed to the internal vibrational degrees of freedom of the ion. This process of energy redistribution is called “internal vibrational redistribution” (IVR) and repeats until the dissociation threshold of the ion (the binding energy of the weakest bond) is exceeded (*cf.* Figure 7). [28–31]

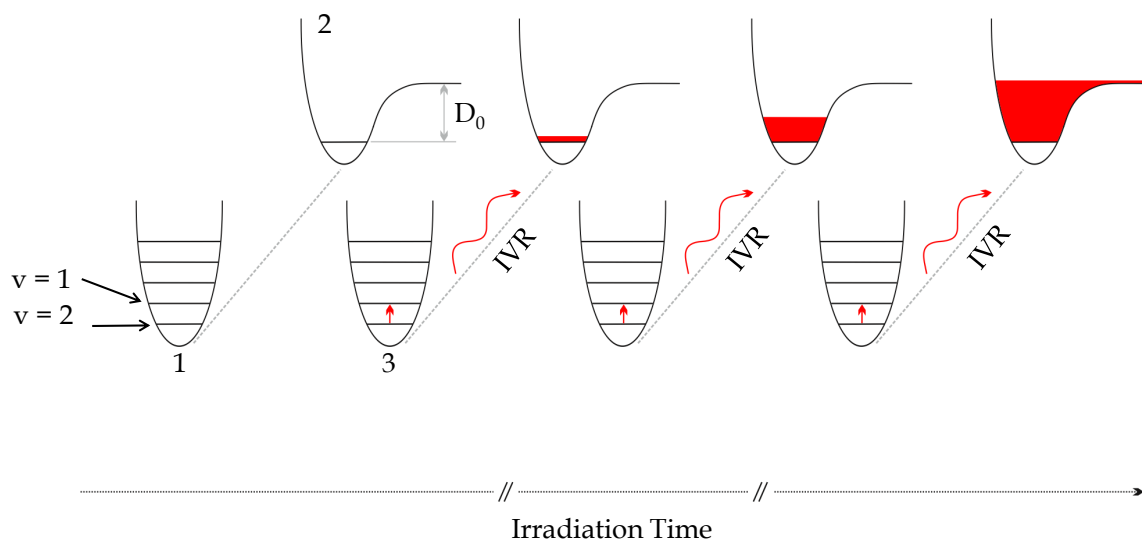


Figure 7: Schematic diagram of the IR-(M)PD Process according to Roithová [31]. The ion absorbs a resonant IR photon. The adsorbed energy is redistributed via IVR processes. This adsorption and redistribution process repeats until the dissociation threshold of the ion is exceeded. As a result, fragmentation of the ion occurs. 1: absorbing vibrational mode, 2: potential energy curve for ion dissociation, 3: adsorption of an IR photon.

The FT-ICR MS setup allows the detection of both the parent and fragment species of the IR-PD process. Plotting the fragmentation efficiency μ_f as a function of laser frequency yields the IR-PD spectrum of the investigated ion species.

$$\eta_f = \frac{\sum_i I_F(i)}{\sum_j I_M(j) + \sum_i I_F(i)} \quad (2.13)$$

$I_F(i)$ intensity of the fragment ions

$I_M(j)$ intensity of the parent ions

The energy of an IR photon generated by an OPO/OPA laser system (*cf.* chapter 2.3.2) is 800 to 8000 cm^{-1} . This corresponds to 10 to 50 kJ mol^{-1} which is far below the binding energies of e.g. C-C bonds (345 kJ mol^{-1}), C=O bonds (708 kJ mol^{-1}) or O-H bonds (463 kJ mol^{-1}). [32] Thus, the cleavage of a covalent bond requires multiple IR photons. Note, that the fragmentation efficiency is not linear correlated to laser intensity and the adsorption cross section in the case of a multi photon dissociation process. As a result, the adsorption intensities of an IR-(M)PD spectrum may differ from predicted linear adsorption spectra. [31, 33] However, so-called *messenger* or *tagging* techniques enable single-photon processes: An unreactive molecule such as argon (Ar), helium (He), nitrogen (N_2) or hydrogen (H_2) coordinates weakly to the ion species. Supersonic expansion jets or cryogenically cooled ion traps meet the low temperature requirements for this messenger attachment. The messenger molecules have a negligible effect on the vibrational spectra of the ion species, and the low binding energies lead to low dissociation thresholds which can be reached and exceeded by irradiation with single photon energy. [34–36]

2.3.2 Optical Parametric Oscillator / Amplifier IR Laser System

The infrared laser radiation generated by an optical parametric oscillator (OPO) [37] / optical parametric amplifier (OPA) [38] laser system meets the requirements of an intense and tunable IR radiation for recording IR-PD spectra over a wide frequency range. The laser system is calibrated using a wavelength meter (821B-NIR, *Bristol Instruments*).

2. Experimental and Computational Methods

The OPO/OPA laser system (*LaserVision*, cf. Figure 8) is pumped by a pulsed injection seeded Nd:YAG laser (Powerlite DLS 8000, *Continuum*, 10 Hz, 530 to 600 mJ/pulse) which provides an intense 1064 nm laser radiation. A beam profile camera (WinCamD, *DataRay Inc.*) serves to continuously monitor the beam profile of the pump laser. Non-linear optical processes and frequency conversions within the OPO/OPA laser system yield the required IR radiation (cf. Figure 9).

In a first step, the Fundamental beam (1064 nm) is divided by a beam splitter into two beams with one-third and two-thirds of the initial radiation intensity, respectively. The former is directed to the OPA stage and the latter is frequency-doubled by a potassium titanyl phosphate (KTP) crystal [39]. The resulting second harmonic (532 nm) is separated from remnants of the Fundamental beam and then guided to the OPO resonator which consists of two KTP crystals. Thereby, a nonlinear process splits the 532 nm radiation into two output radiations: Signal 1 ($14\,000$ to $11\,300\text{ cm}^{-1}$) and Idler 1 (7400 to 4700 cm^{-1}). The sum of the photon energy of these two radiations in turn equals 532 nm due to energy conservation and by definition the higher energy one is called Signal radiation. The wavelengths of Signal 1 and Idler 1 can be tuned by varying the crystal positions (rotation). [37].

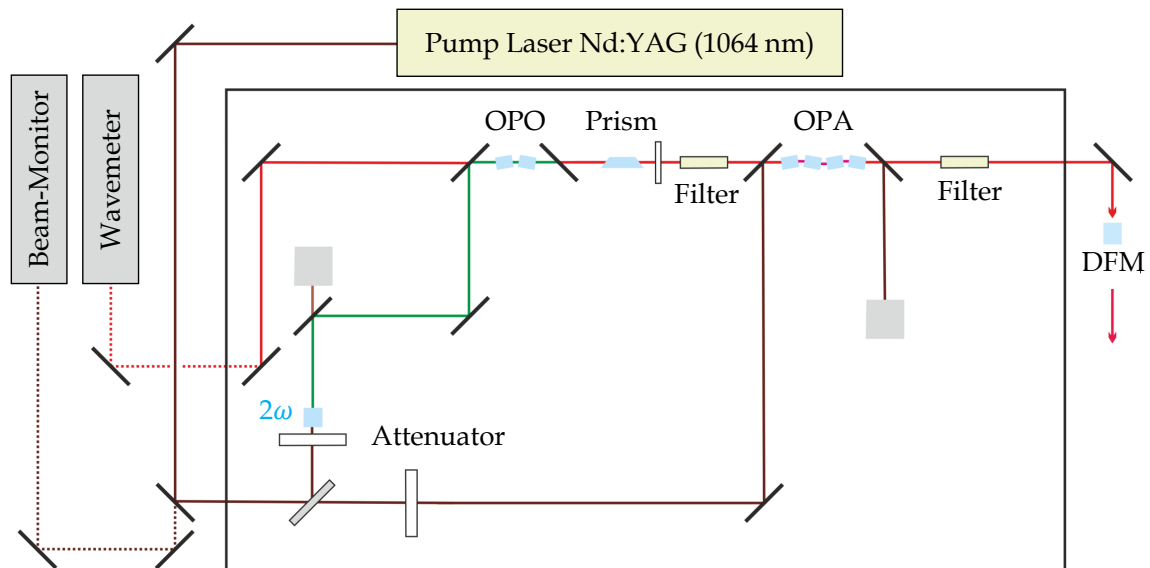


Figure 8: Optical setup of the *LaserVision* OPO/OPA laser system according to Dillinger [40]. Lines indicate beam paths.

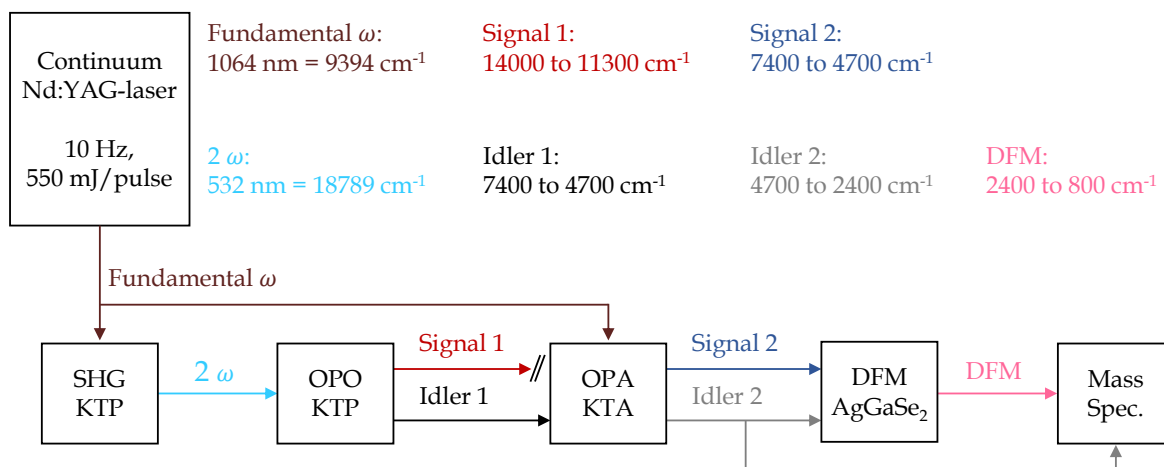


Figure 9: Schematic diagram of the non-linear optical processes and frequency conversions within the OPO/OPA laser system according to Dillinger [40].

However, a silicon filter dumps the Signal 1 radiation while the Idler 1 radiation is directed to the OPA stage. This stage consists of four potassium titanyl arsenate (KTA) crystals, and therein the Idler 1 beam mixes with the remaining two-thirds of the Fundamental beam from the pump laser. This process yields Signal 2 (7400 to 4700 cm^{-1}) and Idler 2 (4700 to 2400 cm^{-1}). Their linear polarization differ by 90° . Note, that the generated Signal 2 beam corresponds to the amplified Idler 1 beam. In the next step, a second silicon filter allows the separation of either Signal 2 or Idler 2, provided it is tuned to the corresponding Brewster angle. The remaining beam is guided to the mass spectrometer in order to be utilized for spectroscopy experiments. Alternatively, both beams (Signal 2 and Idler 2) combine by differential frequency mixing (DFM) on an AgGaSe₂ crystal [41]. The resulting DFM radiation is tunable within an energy range from 2400 to 800 cm^{-1} . A ZnSe filter dumps remnants of Signal 2 and Idler 2 radiation.

Overall, this OPO/OPA laser systems provides intense IR radiation in the energy range from 7400 to 800 cm^{-1} with a pulse energy of 0.1 to 20 mJ and a spectral resolution of 0.9 cm^{-1} . In detail, the generated Idler 2 beam provides IR radiation in the so-called *mid*-IR range (4700 to 2400 cm^{-1}) which serves to probe OH, NH or CH stretching modes. Signal 2 radiation (7400 to 4700 cm^{-1}) allows the spectroscopic investigation of low-lying electronic transitions. The difference frequency mixing of Signal 2 and Idler 2 extends the IR radiation range by the *far*-IR radiation which

covers an energy range from 2400 to 800 cm^{-1} . This enables IR spectroscopic investigation of C=O stretching vibrations and deformation vibrations in the so-called *fingerprint* range. Note that N₂ and Ta-H vibrations, which are relevant to this thesis, also fall within energy range of DFM radiation.

2.4 Density Functional Theory

To achieve a conclusive interpretation of the experimental data, the overall picture of the results benefits from additional insights from theoretic modelling. These quantum chemical calculations typically use Density Functional Theory (DFT), which has become an established approach for modeling molecular properties such as geometry optimization and frequency calculations. [42, 43] In the 1920s, Thomas and Fermi described the idea on which DFT is based: All properties of a quantum chemical system can be described as a function of the electron density distribution. [44, 45] The first theorem of Hohnberg and Kohn proves the correctness of this idea. [46, 47] In their second theorem it is shown that the variation principle is applicable to yield more accurate results. Kohn and Sham [47] achieved a substantial simplification of energy minimization by the variational principle and described the energy as a function of electron density as follows:

$$E(\rho) = T_0(\rho) + \int dr \rho(\vec{r}) \left(V_{\text{eff}}(\vec{r}) + \frac{1}{2}\varphi(\vec{r}) \right) + E_{\text{xc}}(\rho) \quad (2.14)$$

$T_0(\rho)$	kinetic energy
$V_{\text{eff}}(\vec{r})$	effective potential
$\rho(\vec{r})$	electron density
$\varphi(\vec{r})$	Coulomb potential
$E_{\text{xc}}(\rho)$	exchange-correlation energy

The Kohn-Sham wave function is a single Slater determinant which is constructed from a set of Kohn-Sham orbitals, which are lowest energy solutions of the Schrödinger equation (2.15).

$$\left(-\frac{\hbar^2}{2m}\nabla^2 + V_{\text{eff}}(\vec{r}) \right) \Phi_i(r) = \epsilon_i \Phi_i(r) \quad (2.15)$$

$\Phi_i(r)$ Kohn-Sham orbital i
 ϵ_i orbital energy

(2.16) describes the electron density of the entire system.

$$\rho(\vec{r}) = \sum_i^N |\Phi_i(r)|^2 \quad (2.16)$$

The exchange-correlation energy $E_{\text{xc}}(\rho)$ is of crucial importance since it contributes significantly to the total energy. However, since it is composed of all unknown factors, it is difficult to approximate and depends strongly on the functional used. There are two common approaches to estimate the exchange-correlation energy: the local density approximation (LDA) [42], which considers uniform density at a local point, and the generalized gradient approximation (GGA), which assumes a local charge of density. Hybrid functionals contain exchange terms from Hartree-Fock theory. The use of such functionals has been shown to give accurate results for atomic and molecular properties of many systems. [48, 49]

The process of finding geometries that correspond to the stationary points of the energy surface is called geometry optimization. These stationary points occur when the first derivative of energy as a function of spatial coordinates is zero, and exhibit geometries in energetic minima, called minimum structures, or geometries in energetic saddle points, called transition state structures. Distinguishing whether the point found is a minimum energy structure or a transition state structure requires an examination of the second derivatives of the potential energy surface. Positive second derivatives indicate minimum energetic structures. The stationary point found indicates a transition state structure if the second derivative has exactly one negative value (imaginary frequency) among the positive values. However, this method yields local minimum structures similar to the respective initial geometries. The global minimum can be determined by comparing the calculated relative energies of these local minimum structures. Minimum structures represent stable isomers of a molecule that could potentially exist in experimental environments. By comparing calculated molecular properties, such as predicted linear adsorption spectra,

with experimental data, the existence of such isomers can be confirmed or ruled out. Transition state structures separate adjacent energetic minima along the path of the minimum potential energy surface. Such transition state structures are of particular interest for the evaluation and characterization of reaction mechanisms and processes.

In the present thesis, the Gaussian09 and 16 program packages [50, 51] were used for all quantum chemical modeling by DFT to obtain optimized cluster (adsorbate) geometries and vibrational frequencies. Calculation details such as the functionals and basis sets used are addressed in detail in the respective chapters.

References

- [1] E. O. Lawrence, N. E. Edlefsen, *Science* **1930**, 72, 376–377.
- [2] E. O. Lawrence, M. S. Livingston, *Physical Review* **1932**, 40, 19–35.
- [3] E. O. Lawrence, D. H. Sloan, *Proceedings of the National Academy of Sciences* **1931**, 17, 64–70.
- [4] E. O. Lawrence, D. Cooksey, *Physical Review* **1936**, 50, 1131–1140.
- [5] H. Sommer, H. A. Thomas, J. A. Hipple, *Physical Review* **1951**, 82, 697–702.
- [6] M. B. Comisarow, A. G. Marshall, *Chemical Physics Letters* **1974**, 26, 489–490.
- [7] M. B. Comisarow, A. G. Marshall, *Chemical Physics Letters* **1974**, 25, 282–283.
- [8] A. G. Marshall, C. L. Hendrickson, G. S. Jackson, *Mass Spectrom Reviews* **1998**, 17, 1–35.
- [9] A. G. Marshall, *International Journal of Mass Spectrometry* **2000**, 200, 331–356.
- [10] T. Kolling, H. Kampschulte, *T. K. Autodesk Inventor*®.
- [11] M. A. Duncan, *Review of Scientific Instruments* **2012**, 83, 041101.
- [12] S. Maruyama, L. R. Anderson, R. E. Smalley, *Review of Scientific Instruments* **1990**, 61, 3686–3693.
- [13] T. G. Dietz, M. A. Duncan, D. E. Powers, R. E. Smalley, *The Journal of Chemical Physics* **1981**, 74, 6511–6512.

-
- [14] C. Berg, T. Schindler, G. Niedner-Schatteburg, B. V. E., *The Journal of Chemical Physics* **1995**, *102*, 4870–4884.
- [15] V. Bondybey, J. English, *The Journal of Chemical Physics* **1981**, *74*, 6978–6979.
- [16] D. Proch, T. Trickl, *Review of Scientific Instruments* **1989**, *60*, 713–716.
- [17] P. Caravatti, M. Allemann, *Organic Mass Spectrometry* **1991**, *26*, 514–518.
- [18] L. Schweikhard, J. Zeigler, H. Bopp, K. Lützenkirchen, *International Journal of Mass Spectrometry and Ion Processes* **1995**, *141*, 77–90.
- [19] M. Graf, *Diploma Thesis*, Technische Universität Kaiserslautern, **2006**.
- [20] T. Su, M. T. Bowers, *Journal of the American Chemical Society* **1973**, *95*, 7609–7610.
- [21] T. Su, M. T. Bowers, *The Journal of Chemical Physics* **1973**, *58*, 3027–3037.
- [22] M. Langevin, *Annales de chimie et de physique* **1905**, 245–288.
- [23] T. Su, M. T. Bowers, *International Journal of Mass Spectrometry and Ion Physics* **1973**, *12*, 347–356.
- [24] I. Balteanu, O. P. Balaj, B. S. Fox-Beyer, P. Rodrigues, M. T. Barros, A. M. C. Moutinho, M. L. Costa, B. M. K., V. E. Bondybey, *Organometallics* **2004**, *23*, 1978–1985.
- [25] M. L. Anderson, M. S. Ford, P. J. Derrick, T. Drewello, D. P. Woodruff, S. R. Mackenzie, *The Journal of Physical Chemistry A* **2006**, *110*, 10992–11000.
- [26] G. Kummerlöwe, M. K. Beyer, *International Journal of Mass Spectrometry* **2005**, *244*, 84–90.
- [27] N. C. Polfer, J. Oomens, *Mass Spectrom Reviews* **2009**, *28*, 468–494.
- [28] D. W. Lupo, M. Quack, *Chemical Reviews* **1987**, *87*, 181–216.
- [29] E. R. Grant, P. A. Schulz, A. S. Sudbo, Y. R. Shen, Y. T. Lee, *Physical Review Letters* **1978**, *40*, 115–118.
- [30] N. C. Polfer, *Chemical Society Reviews* **2011**, *40*, 2211–2221.
- [31] J. Roithová, *Chemical Society Reviews* **2012**, *41*, 547–559.

- [32] E. Riedel, C. Janiak, *Anorganische Chemie*, De Gruyter, Berlin, Boston, **2007**.
- [33] D. Schröder, H. Schwarz, P. Milko, J. Roithová, *The Journal of Physical Chemistry A* **2006**, *110*, 8346–8353.
- [34] A. B. Wolk, C. M. Leavitt, E. Garand, M. A. Johnson, *Accounts of Chemical Research* **2014**, *47*, 202–210.
- [35] N. R. Walker, R. S. Walters, M. K. Tsai, K. D. Jordan, M. A. Duncan, *The Journal of Physical Chemistry A* **2005**, *109*, 7057–7067.
- [36] M. Z. Kamrath, E. Garand, P. A. Jordan, C. M. Leavitt, A. B. Wolk, M. J. Van Stipdonk, S. J. Miller, M. A. Johnson, *Journal of the American Chemical Society* **2011**, *133*, 6440–6448.
- [37] R. C. Eckardt, C. D. Nabors, W. J. Kozlovsky, R. L. Byer, *Journal of the Optical Society of America B* **1991**, *8*, 646–667.
- [38] D. Brida, C. Manzoni, G. Cirimi, M. Marangoni, S. De Silvestri, G. Cerullo, *Optics Express* **2007**, *15*, 15035–15040.
- [39] P. A. Franken, A. E. Hill, C. W. Peters, G. Weinreich, *Physical Review Letters* **1961**, *7*, 118–119.
- [40] S. Dillinger, *PhD Thesis*, Technische Universität Kaiserslautern, **2017**.
- [41] M. Gerhards, *Optics Communications* **2004**, *241*, 493–497.
- [42] W. Kohn, A. D. Becke, R. G. Parr, *The Journal of Physical Chemistry* **1996**, *100*, 12974–12980.
- [43] R. G. Parr, W. Yang **1995**, *46*, 701–728.
- [44] L. H. Thomas, *Mathematical Proceedings of the Cambridge Philosophical Society* **1927**, *23*, 542–548.
- [45] E. Fermi, *Zeitschrift für Physik* **1928**, *48*, 73–79.
- [46] P. Hohenberg, W. Kohn, *Physical Review* **1964**, *136*, B864–B871.
- [47] W. Kohn, L. J. Sham, *Physical Review* **1965**, *140*, A1133–A1138.
- [48] A. D. Becke, *The Journal of Chemical Physics* **1993**, *98*, 5648–5652.

- [49] A. D. Becke, *The Journal of Chemical Physics* **1993**, *98*, 1372–1377.
- [50] M. J. Frisch, G. W. Trucks, H. B. Schlegel, G. E. Scuseria, M. A. Robb, J. R. Cheeseman, G. Scalmani, V. Barone, B. Mennucci, G. A. Petersson, H. Nakatsuji, M. Caricato, X. Li, H. P. Hratchian, A. F. Izmaylov, J. Bloino, G. Zheng, J. L. Sonnenberg, M. Hada, M. Ehara, K. Toyota, R. Fukuda, J. Hasegawa, M. Ishida, T. Nakajima, Y. Honda, O. Kitao, H. Nakai, T. Vreven, J. A. Montgomery, Jr., J. E. Peralta, F. Ogliaro, M. Bearpark, J. J. Heyd, E. Brothers, K. N. Kudin, V. N. Staroverov, R. Kobayashi, J. Normand, K. Raghavachari, A. Rendell, J. C. Burant, S. S. Iyengar, J. Tomasi, M. Cossi, N. Rega, J. M. Millam, M. Klene, J. E. Knox, J. B. Cross, V. Bakken, C. Adamo, J. Jaramillo, R. Gomperts, R. E. Stratmann, O. Yazyev, A. J. Austin, R. Cammi, C. Pomelli, J. W. Ochterski, R. L. Martin, K. Morokuma, V. G. Zakrzewski, G. A. Voth, P. Salvador, J. J. Dannenberg, S. Dapprich, A. D. Daniels, O. Farkas, J. B. Foresman, J. V. Ortiz, J. Cioslowski, D. J. Fox, *Wallingford CT* **2009**.
- [51] M. J. Frisch, G. W. Trucks, H. B. Schlegel, G. E. Scuseria, M. A. Robb, J. R. Cheeseman, G. Scalmani, V. Barone, G. A. Petersson, H. Nakatsuji, X. Li, M. Caricato, A. V. Marenich, J. Bloino, B. G. Janesko, R. Gomperts, B. Mennucci, H. P. Hratchian, J. V. Ortiz, A. F. Izmaylov, J. L. Sonnenberg, Williams, F. Ding, F. Lipparini, F. Egidi, J. Goings, B. Peng, A. Petrone, T. Henderson, D. Ranasinghe, V. G. Zakrzewski, J. Gao, N. Rega, G. Zheng, W. Liang, M. Hada, M. Ehara, K. Toyota, R. Fukuda, J. Hasegawa, M. Ishida, T. Nakajima, Y. Honda, O. Kitao, H. Nakai, T. Vreven, K. Throssell, J. A. Montgomery Jr., J. E. Peralta, F. Ogliaro, M. J. Bearpark, J. J. Heyd, E. N. Brothers, K. N. Kudin, V. N. Staroverov, T. A. Keith, R. Kobayashi, J. Normand, K. Raghavachari, A. P. Rendell, J. C. Burant, S. S. Iyengar, J. Tomasi, M. Cossi, J. M. Millam, M. Klene, C. Adamo, R. Cammi, J. W. Ochterski, R. L. Martin, K. Morokuma, O. Farkas, J. B. Foresman, D. J. Fox, *Wallingford CT* **2016**.

3 OBSERVATION AND MECHANISM OF CRYO N₂ CLEAVAGE BY A TANTALUM CLUSTER

3.1 Preamble

The following chapter is a reprint of a publication in the journal *Physical Chemistry Chemical Physics*

A. Steiner, M. P. Klein and myself performed the experiments. M. P. Klein and myself evaluated the data. M. P. Klein, M. H. Prosenc and myself performed the calculations. M. P. Klein, M. H. Prosenc, G. Niedner-Schatteburg and myself wrote and revised the manuscript. All authors evaluated and discussed the results.

I concerted all of the conducted efforts, and I took the lead in this project, under the guidance of my thesis supervisor.

Full Reference

Observation and Mechanism of Cryo N₂ Cleavage by a Tantalum Cluster

D. V. Fries, M. P. Klein, A. Steiner, M. H. Prosenc, G. Niedner-Schatteburg, *Physical Chemistry Chemical Physics* **2021**, 23, 11345–11354.

<https://doi.org/10.1039/D0CP06208A>

3.2 Reprint

Reprint permission

Reproduced with permission from the PCCP Owner Societies.

Observation and mechanism of cryo N₂ cleavage by a tantalum cluster

D. V. Fries, M. P. Klein, A. Steiner, M. H. Prosenc and G. Niedner-Schatteburg, *Phys. Chem. Chem. Phys.*, 2021, **23**, 11345 DOI: 10.1039/D0CP06208A

To request permission to reproduce material from this article, please go to the [Copyright Clearance Center request page](#).

If you are **an author contributing to an RSC publication**, you do not need to request **permission** provided correct acknowledgement is given.

If you are **the author of this article**, you do not need to request **permission to reproduce figures and diagrams** provided correct acknowledgement is given. If you want to reproduce the whole article in a third-party publication (excluding your thesis/dissertation for which permission is not required) please go to the [Copyright Clearance Center request page](#).

Read more about [how to correctly acknowledge RSC content](#).


 Cite this: *Phys. Chem. Chem. Phys.*,
2021, **23**, 11345

Observation and mechanism of cryo N₂ cleavage by a tantalum cluster†

 Daniela V. Fries,[†] Matthias P. Klein,[†] Annika Steiner,[†] Marc H. Prosenč[†] and Gereon Niedner-Schatteburg^{†*}

We explore the cryogenic kinetics of N₂ adsorption to Ta₄⁺ and the infrared signatures of [Ta₄(N₂)_m]⁺ complexes, *m* = 1–5. This is accomplished by N₂ exposure of isolated ions within a cryogenic ion trap. We find stepwise addition of numerous N₂ molecules to the Ta₄⁺ cluster. Interestingly, the infrared signatures of the [Ta₄(N₂)₁]⁺ and [Ta₄(N₂)₂]⁺ products are special: there are no NN stretching bands. This is consistent with cleavage of the first two adsorbed dinitrogen molecules. DFT calculations reveal intermediates and barriers along reaction paths of N₂ cleavage in support of these experimental findings. We indicate the identified multidimensional path of N₂ cleavage as an across edge-above surface (AEAS) mechanism: initially end-on coordinated N₂ bends towards a neighboring Ta-atom which yields a second intermediate, with a μ₂ bonded N₂ across an edge of the Ta₄⁺ tetrahedron core. Further rearrangement above a Ta–Ta–Ta surface of the Ta₄⁺ tetrahedron results in a μ₃ bonded N₂ ligand. This intermediate relaxes swiftly by ultimate NN cleavage unfolding into the final dinitrido motif. Submerged activation barriers below the entrance channel confirm spontaneous cleavage of the first two dinitrogen molecules (–59 and –33 kJ mol^{–1}, respectively), while cleavage of the third N₂ ligand is kinetically hindered (+55 kJ mol^{–1}). We recognize that substoichiometric N₂ exposure allows for spontaneous activation by Ta₄⁺, while higher N₂ exposure causes self-poisoning.

 Received 30th November 2020,
Accepted 5th April 2021

DOI: 10.1039/d0cp06208a

rsc.li/pccp

Introduction

Life on earth relies on the essential element nitrogen.¹ High temperature, high pressure Haber–Bosch synthesis managed to couple the ubiquitous reservoir of inert dinitrogen, N₂, from the biosphere on a large scale. Biotic low temperature N₂ hydration by metallo-enzymatic complexes^{2,3} – amazing as it is – takes place by an apparent waste of metabolic energy (16 ATP per N₂ molecule).⁴ Likewise inefficient, the Haber–Bosch process as well as other industrial processes take place only at the expense of high pressure and high temperature.^{5–7} An energetically optimized technical protocol of inert N≡N triple bond activation is still to be found^{8,9} – despite all of the high effort and award winning research as of now.^{10–12} This is the more so as heterogeneous N₂ activation at high temperatures is entropically disfavored and thus is often presumed to become rate limiting.

Obviously, there is a quest for an enhanced understanding at the molecular level of heterogeneous catalytic N₂ activation and functionalization. Such insight would allow for an able interpretation of the ground-breaking empirical survey of prospective

Haber–Bosch catalysts by Mittasch *et al.*¹³ It seems certain that multi metallic cooperativity is a prerequisite for N₂ activation prior to further cleavage and functionalization.¹⁴ For example, the DFT modeling of experimental ammonia synthesis by supported Ru catalyst¹⁵ managed to predict elementary steps along a feasible reaction path. Step sites are found much more reactive than terrace sites – and alkali adatoms act as promoters.¹⁶

The synthesis of seemingly appropriate mononuclear transition metal complexes received inspiration from enzymatic N₂ cleavage. It showed that N₂ may coordinate in an activating M–NN–M motif through aggregation of mononuclear W and Mo complexes.^{17–19} Dissociation kinetics of a Mo–NN–Mo complex reveal activation barriers as low as 100 kJ mol^{–1} and thereby confirm considerable N₂ activation within the complex.²⁰ Alkaline promotion in turn reached out towards synthesized TM complexes. In this regard, a synthetic Fe-phenoxide-K complex provides for a flexible di-iron core and rapid formation of di-iron-N₂ products. Modeling suggests N₂ preorientation by K and subsequent N≡N activation by Fe–Fe cooperativity which together creates a low-energy pathway towards N₂ reactions.²¹ Variation of alkali promoters (Na, K, Rb, Cs) suggests that it might take at least three Fe centers to cleave N≡N.^{22,23} Ti_{3,4}-imide and Ti_{3,4}-hydride frameworks enable N₂ activation and hydrogenation through a partly reversible interplay among hydride, imide, and nitride ligands. A precursor complex showed to encompass an N₂

Fachbereich Chemie and Forschungszentrum OPTIMAS, Technische Universität Kaiserslautern, 67663 Kaiserslautern, Germany. E-mail: gns@chemie.uni-kl.de
† Electronic supplementary information (ESI) available. See DOI: 10.1039/d0cp06208a

3. Observation and Mechanism of Cryo N₂ Cleavage by a Tantalum Cluster

Paper

PCCP

molecule bonded to three Ti atoms in a $\mu\text{-}\eta^1\text{:}\eta^2\text{:}\eta^2$ -end-on/side-on fashion to give a $\mu_2\text{-N}/\mu_3\text{-N}$ dinitrido species.^{24,25}

In the gas phase, further mechanistic insights at the molecular level were provided by studying well defined model systems and their characterization by advanced methods. In this regard TM clusters and complexes were recognized to unravel elementary processes of relevance to heterogeneous catalysis.^{26–31} Naked transition metal dimers of Gd,³² Sc,³³ and Ta³⁴ are known to activate N₂ spontaneously. Also, small Ta-nitride cations are able to activate NH₃.³⁵

Early surveys of larger transition metal (Fe, Co, Ni, Cu, Nb) clusters included some studies of N₂ adsorption and introduced the concept of cluster surface reactivity.³⁶ In another early study, size-selected clusters of Nb and Ta exhibited bi-exponential reaction kinetics for N₂ adsorption.³⁷ Larger clusters of Fe and Al revealed convincing, yet indirect, evidence for N₂ activation without explicit structural characterization.^{38,39} Larger Ta clusters received attention in the context of various oxidation reactions.^{40–44} Size-selected anion clusters of V and Ta-nitrides and of Co-hydrides showed N₂ adsorption kinetics, and concomitant *ab initio* modeling^{45–47} pointed to N₂ activation. More recently, the gas phase chemistry of metal clusters received renewed attention;⁴⁸ in part, this is motivated by advances in cryogenic ion trapping and IR vibrational spectroscopy.⁴⁹ Quantum chemical modeling proved extremely helpful towards a better understanding of N₂ activation at bare metal atoms, and the findings relate to corresponding processes at organometallic complexes, clusters and surfaces up to enzymatic nitrogenase catalysis.⁵⁰

Raman spectra of Ta₄⁺ clusters confirmed a tetrahedral geometry for the ground state.⁵¹ Infrared-induced multiple photon dissociation (IR-MPD) spectra of Ta_n⁺ clusters ($6 \leq n \leq 20$)⁵² received structural interpretation by DFT modeling⁵³ and were in line with previous studies.⁵⁴ Ta₄⁺ clusters were found to dehydrogenate CH₄ while Ta₅⁺ does not.⁵⁵

DFT modeling predicted dissociative adsorption of the very first N₂ molecule when reacted with small Ta_n⁺ clusters ($n \leq 4$).⁵⁶ Combined DFT and experimental studies of Ta₆⁺ confirmed single N₂ activation under slightly hyperthermal conditions.⁵⁷ Subsequent DFT studies focused on reverse catalysis modeling, namely on ammonia activation, by Ta_n⁺ ($n = 2\text{--}10$) cluster complexes.⁵⁸

In the present contribution we present a detailed mechanism of N₂ activation by the model system Ta₄⁺. This choice was motivated by an increase of the electron reservoir with respect to the well-studied Ta₂⁺.³⁴ We combine kinetic and IR-PD spectroscopic cryo ion trap investigations with DFT modeling; this is a continuation of a series of related studies on model systems.^{59–61} Here, we provide an elucidation of a detailed across edge-above surface (AEAS) mechanism for the cleavage of first and second N₂ adsorbates.

Experimental and computational methods

All experiments were performed by a customized Fourier transform ion cyclotron resonance (FT-ICR) mass spectrometer

(Apex Ultra, Bruker Daltonics). Using this instrument, we were able to produce the Ta_n⁺ clusters, to isolate the generated cluster ions and adsorb N₂ to them prior to examination by infrared multi photon dissociation (IR-PD) spectroscopy and mass spectrometry of the adsorbate complexes. A home built laser evaporation source (LVAP)^{62,63} was used for cluster generation from a rotating Ta-target (99.95%, 0.5 mm thick, Alfa Aesar). The respective cluster ions were mass isolated and stored in the cryogenic hexapole ion trap (26 K) where the reaction gas (N₂; 2.6×10^{-7} mbar) is introduced continuously. In addition, collision gas (He; up to 6.8×10^{-6} mbar) ensures efficient trapping and cooling of the ions in the hexapole. After trapping in the hexapole for various storage times (reaction delays: 0–20 s), the cluster complexes were guided by electrostatic lenses into the FT-ICR cell (~ 10 K).

In order to investigate adsorption kinetics, reaction delay scans were recorded. Subsequently, the obtained mass spectra were evaluated by the program *evofit*⁶⁴ yielding pseudo-first-order kinetics and relative rate constants for each N₂ adsorption and desorption step. Absolute rate constants originate from normalization of relative rate constants to the absolute N₂ number densities.

In the IR-PD experiments, the chosen complexes of interest are trapped in the ICR cell and irradiated by a tunable OPO IR-laser. Thus, every isolated ion packet was treated by 7–10 laser pulses with an energy of 0.3–4.0 mJ per pulse within a wavelength range of 1200 to 2400 cm⁻¹. The obtained IR-PD signals of the fragment F_I and the parent ion P_I are evaluated as $\sum_I F_I / \left(\sum_I F_I + \sum_I P_I \right)$. To obtain an IR-PD spectra, the determined fragmentation efficiency is plotted as a function of laser frequency.

All quantum chemical calculations are carried out by the Gaussian 09⁶⁵ and the Gaussian 16 suite of programs.⁶⁶ We employed the PBE0 functional^{67,68} and the def2-TZVP basis set.^{69,70} We did so in continuation of previous studies which have succeeded to model N₂ adsorption before, as *e.g.* in the cases of Rhodium clusters⁷¹ and Nickel clusters.^{60,61} Moreover, we verified our choice of method by employing a multitude of available exchange correlation functionals, and CC2 calculations on top (*cf.* Fig. S8, ESI[†]) along some part of the reaction path of initial N₂ activation along three local minima (**I**_{2(4,1)} and **I**_{3(4,1)} and **P**_{vic(4,1)}) and both intermediate transition states (**TS**_{23(4,1)} and **TS**_{3P_{vic(4,1)}}). It shows that the optimized minimum structures and transition states are robust (for a survey of some critical geometric parameters refer to Tables S15 and S16 in the ESI[†]), as well as the relative energies by less than 30 kJ mol⁻¹ (*cf.* Table S14, ESI[†]). We take this as a valid gauge of the chosen level of theory, PBE0/def2-TZVP. All stationary points were checked by second derivative calculations revealing no and one imaginary frequency in cases of minima and transition states, respectively. Reaction paths were searched for by QST2/3⁷² or linear transit methods⁷³ and after location and optimization of the transition states calculated along the IRC (Intrinsic Reaction Coordinate).⁷⁴ Orbital and charge analysis were performed using molecular orbitals as well as Natural Bonding Orbitals (NBO) as employed in the Gaussian 16 program.^{75,76}

Results and discussion

N₂ adsorption limits

We have facilitated the investigation of the N₂ adsorption kinetics to Ta₄⁺ clusters at a cryo temperature of 26 K. The recorded mass spectra (*cf.* Fig. S1 in the ESI†) show a series of N₂ adsorbates (+28 *m/z*) which increase at extended storage time. Ultimately, we find an apparent adsorption limit of 13 N₂ molecules onto Ta₄⁺ at storage times of up to 20 s where the further adsorbate growth ceases (*cf.* Fig. S1, ESI†).

Cryo kinetics and rate constants of N₂ adsorption to the Ta₄⁺ cluster

The measurement of the temporal evolution of the adsorbate intensities for each N₂ adsorption step onto Ta₄⁺ reveals their adsorption kinetics (Fig. 1, Fig. S2 and Table S1, ESI†). We opt for fitting the recorded intensities to pseudo-first-order kinetics by the genetic algorithm routine *evofit*.⁶⁴ The resulting fit confirms the model of consecutive adsorption/desorption steps.

The first and second N₂ molecules adsorb differently than subsequent ones, up to the 7th N₂ molecule: the first and second fitted relative rate constants ($k_0 = 9.58 \text{ s}^{-1}$ and $k_1 = 1.88 \text{ s}^{-1}$) deviate significantly from k_2 to k_6 of around 5 s^{-1} . We tentatively assign equivalent adsorption sites for [Ta₄(N₂)₂]⁺ through [Ta₄(N₂)₆]⁺, and different sites (or processes) in the cases of [Ta₄(N₂)₀]⁺ and [Ta₄(N₂)₁]⁺. The fitted intensities of [Ta₄(N₂)₇]⁺ to [Ta₄(N₂)₁₁]⁺ deviate somewhat from the recorded ones; this implies the occurrence of further species and/or processes beyond our simple stepwise adsorption model.

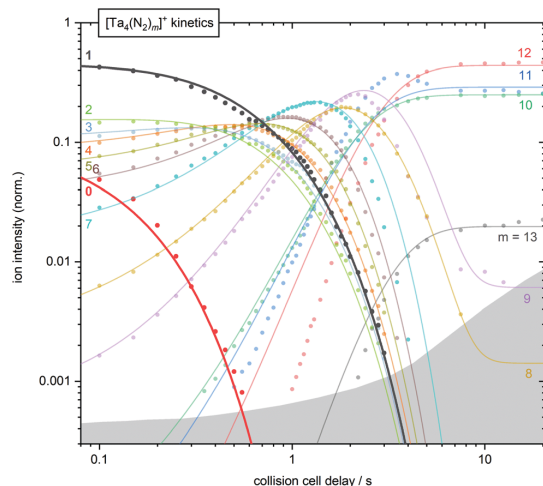


Fig. 1 Double logarithmic plot of isothermal kinetics of N₂ adsorption by mass-selected Ta₄⁺ clusters at 26 K, He buffer gas (6.8×10^{-6} mbar) and an exposure of 2.6×10^{-7} mbar N₂. The experimental data (solid dots) and the fits (solid lines) assume pseudo-first order kinetics for the N₂ adsorption in up to 13 consecutive steps. The kinetics of first and second N₂ adsorption are highlighted. The gray-shaded area indicates the background noise level. Corresponding rate constants of the pseudo-first order fits for each adsorption/desorption is shown in the ESI† (*cf.* Fig. S2).

Such processes might involve adsorbate shell reorganization and/or adsorbate induced cluster relaxation both of which may induce some N₂ ligand desorption. While such desorption is taken into account in the form of a “backwards reaction” it is the conceivable – and likely – isomerism of multiple participating structures which hampers a more effective fitting. Further elucidation is subject of ongoing studies and beyond the scope of the current study.

The kinetic curves at storage times beyond 8 s reveal horizontal and parallel curves for the generation of the ultimate products [Ta₄(N₂)_{*m*}]⁺, $m = 9-13$. This clearly indicates that these five adsorbate complexes are in a dynamic equilibrium. Our fitting supports this conclusion by non-vanishing rate constants for the desorption.

Cryogenic IR-PD spectra

We recorded infrared-photo dissociation (IR-PD) spectra of [Ta₄(N₂)_{*m*}]⁺ adsorbate complexes, $m = 1-5$, under adiabatic conditions in the ICR ion trap (Fig. 2), and we annotate these complexes in a short notation as (*m*). For the first two N₂ adsorptions onto Ta₄⁺, *i.e.* for the product complexes (4,1) and (4,2), we observe no resonant IR induced fragmentation. However, for (4,3) to (4,5) one notes multiple IR bands in two spectral regions. We observe broad vibrational bands in the range of 2200 cm⁻¹ to 2300 cm⁻¹ for (4,4) and (4,5). We tentatively assign all of these bands to N–N stretching vibrations of N₂ adsorbates which bind end-on to single Ta centers – in line with previously reported cases of Co, Ni, Rh and Ru.^{59-61,71} Starting with (4,3), vibrational bands in the range of 1400 cm⁻¹ to 1500 cm⁻¹ shift to the red by 21 cm⁻¹ and 11 cm⁻¹ per additionally adsorbed N₂ molecule.

The absence of vibrational bands in the cases of (4,1) and (4,2), and the deviating adsorption rate constants k_0 and k_1 raised our interest. The following DFT calculations shall gain further insights into these processes and the species involved.

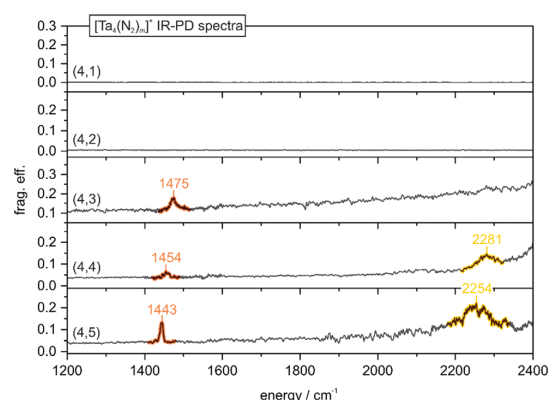


Fig. 2 IR-PD spectra of [Ta₄(N₂)_{*m*}]⁺ (simplified nomenclature: (*m*)), $m = 1-5$ in the range of 1200 cm⁻¹ to 2400 cm⁻¹. Note the absence of vibrational bands in the cases of (4,1) and (4,2). The gradual rise of baseline in cases (4,3) to (4,5) may originate either from auto-dissociation or from multi-photon absorptions into low lying electronic states.

3. Observation and Mechanism of Cryo N₂ Cleavage by a Tantalum Cluster

Paper

PCCC

DFT modeling of consecutive N₂ activations by Ta₄⁺ clusters

Recalling the lack of any vibrational bands in the recorded IR-PD spectra of [Ta₄(N₂)₁]⁺ and [Ta₄(N₂)₂]⁺, it seems possible that the bare Ta₄⁺ cluster activates and cleaves the first and second N₂ adsorbates. This would be analogous to the dinitride formation by Ta₂⁺, as described by Geng *et al.*,³⁴ and for Ta₆⁺ by Mafuné *et al.*⁵⁷ In order to verify this suggestion, we undertook DFT modeling for conceivable N₂ adsorption, activation and nitride formation pathways. We chose as a starting point Jahn Teller distorted, near tetrahedral geometries of the Ta₄⁺ bare cluster in doublet and quartet states (Fig. 3, in blue for doublet state and in red for quartet state). It showed that the excited quartet state pathway runs in parallel to the ground doublet state with an energy gap of about 50 kJ mol⁻¹ without intersecting each other. In the following, we therefore focus on the doublet ground state.

The initial N₂ adsorption to Ta₄⁺ leads to the cation **I1**_(4,1). The optimized structure reveals distances of *d*(Ta1–N1) = 2.13 Å and *d*(N1–N2) = 1.11 Å. This indicates a σ-bonded N₂ molecule that coordinates to a single Ta center (Fig. 3). Adopting the

notation scheme of IUPAC and Salzer,⁷⁷ this coordination is denoted as μ₁:κN1 with the N₂ molecule almost perpendicular to the (Ta1–Ta2–Ta3) plane.

A facile tilting of the N₂ ligand in **I1**_(4,1) leads to **TS12**_(4,1) with *d*(Ta2–N1) = 2.51 Å (–0.61 Å with respect to **I1**_(4,1)) and requires merely an activation of +5 kJ mol⁻¹. The adjacent intermediate **I2**_(4,1) is significantly more stable than **I1**_(4,1), by 52 kJ mol⁻¹. Note, that this μ₂:κN1:κN1,N₂ coordination motif corresponds to a tantalum complex with a bridging N₂ unit that is coordinated both side-on and end-on.^{78,79} Related complexes with **I2** type bonding motifs were reported for Gd,³² Sc,³³ and V.⁴⁵

A transformation from μ₂ to μ₃ coordination takes some activation, and it takes place by further decrease the Ta2–N1 and Ta2–N2 distances while bending the N₂ unit sideways towards the Ta3 center. This torsional reorganization of initially in-plane μ₂:κN:κN,N coordination across an intact Ta–Ta edge in **I2**_(4,1) towards a perpendicular μ₃:κN:κN,N:κN,N coordination above a Ta–Ta–Ta surface in **I3**_(4,1) will prove to be crucial for N₂ cleavage. It is this transition from a structural motif **I2** via a transition state **TS23** to a structural motif **I3**

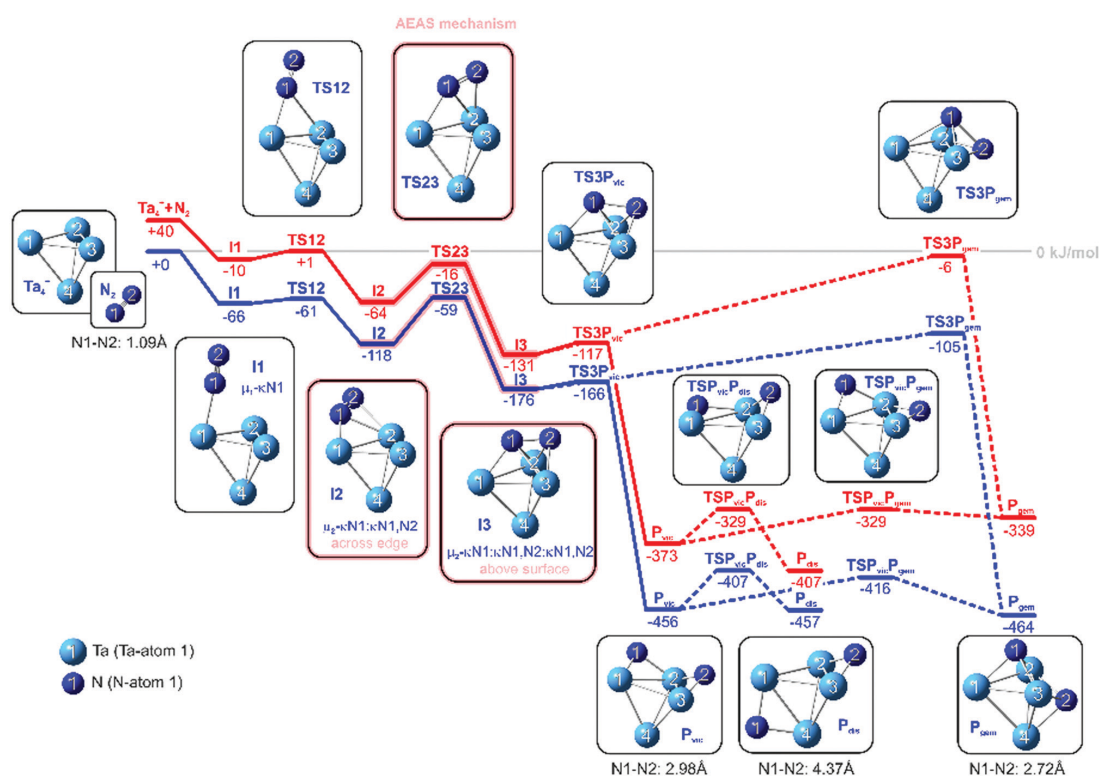


Fig. 3 Reaction pathway of N₂ activation by Ta₄⁺ (blue: doublet, red: quartet). Three submerged transition states allow for facile stepwise activation, which ultimately leads to the μ₂ or μ₃ bridging nitrido product structures **P**_{vic} or **P**_{gem}. Transition state **TSP**_{vic}**P**_{dis(4,1)} gives rise to a third isomer **P**_{dis(4,1)}. The subscript abbreviations gem, vic, and dis indicate geminal, vicinal, and distal, respectively, and they are more explicitly described in the supplement. Relative Energies are in kJ mol⁻¹. The torsional reorganization of the AEAS mechanism from an initial in-plane μ₂:κN:κN,N coordination across an intact Ta–Ta edge towards perpendicular μ₃:κN:κN,N:κN,N coordination above a Ta–Ta–Ta surface is highlighted. For reasons of clarity, the nomenclature is presented in an abbreviated form (e.g. **I1** stands for **I1**_(4,1)).

which we shall label as an across edge-above surface (AEAS) mechanism. The transition state $\text{TS23}_{(4,1)}$ is located merely 59 kJ mol^{-1} above $\text{I2}_{(4,1)}$, it is thus almost isoenergetic to $\text{TS12}_{(4,1)}$. The subsequent intermediate $\text{I3}_{(4,1)}$ engages a stabilization of 58 kJ mol^{-1} below $\text{I2}_{(4,1)}$. Note, that an AEAS mechanism requires four atomic centers at minimum. It operates significantly more likely on small clusters, and on highly corrugated and open surfaces.

$\text{I3}_{(4,1)}$ proves metastable against further activation. We find facile N–N bond cleavage which requires a shallow barrier of mere $+10 \text{ kJ mol}^{-1}$. The concomitant increase of the N–N bond length from 1.43 \AA , $\text{I3}_{(4,1)}$, to 1.67 \AA in the transition state $\text{TS3P}_{\text{vic}(4,1)}$ is decisive for product formation.

There is a steep decline of the computed energy surface along the reaction coordinate towards the conceivable product $\text{P}_{\text{vic}(4,1)}$ of as much as -280 kJ mol^{-1} below intermediate $\text{I3}_{(4,1)}$. This vicinal (vic) di-nitride structure comprises a Ta_4 -tetrahedron with two vicinal μ_2 -bridged nitrido ligands. The total decline of -456 kJ mol^{-1} is along the line of the previously published value of -550 kJ mol^{-1} in the case of Ta_6^+ .⁵⁷ Most of this energy decline is due to the final N_2 cleavage from $\text{I3}_{(4,1)}$ to $\text{P}_{\text{vic}(4,1)}$ and to an actual transfer of electron density from Ta to N atoms as evidenced by NPA charges from the DFT calculations (*cf.* Table S4, ESI[†]).

We found an alternative, second pathway for the N–N bond cleavage starting at the intermediate $\text{I3}_{(4,1)}$. There is a transition state $\text{TS3P}_{\text{gem}(4,1)}$, which lies 71 kJ mol^{-1} above $\text{I3}_{(4,1)}$, and 61 kJ mol^{-1} above $\text{TS3P}_{\text{vic}(4,1)}$. In $\text{TS3P}_{\text{gem}(4,1)}$, the pre-activated N_2 ligand, $d(\text{N1–N2}) = 1.83 \text{ \AA}$, coordinates perpendicular to the Ta2–Ta3 bond, as found before for the N_2 activation by Ta_2^+ .³⁴ This reaction path from $\text{I3}_{(4,1)}$ to $\text{TS3P}_{\text{gem}(4,1)}$ continues to an alternative product $\text{P}_{\text{gem}(4,1)}$, which comprises of two μ_3 -bridging geminal nitrido ligands with $d(\text{N1–N2}) = 2.72 \text{ \AA}$. It is almost isoenergetic to $\text{P}_{\text{vic}(4,1)}$ (-8 kJ mol^{-1}) and connected by a transition state $\text{TSP}_{\text{vic}^{\text{P}}_{\text{gem}(4,1)}}$ *via* a barrier of 40 kJ mol^{-1} above $\text{P}_{\text{vic}(4,1)}$. There is a third isomer, the dinitrido Ta_4^+ cation with a distal configuration of the two nitrido ligands ($\text{P}_{\text{dis}(4,1)}$) and it is almost isoenergetic with $\text{P}_{\text{vic}(4,1)}$ by -1 kJ mol^{-1} and connected by a barrier of 49 kJ mol^{-1} *via* transition state $\text{TSP}_{\text{vic}^{\text{P}}_{\text{dis}(4,1)}}$. Product $\text{P}_{\text{vic}(4,1)}$ forms directly from $\text{I3}_{(4,1)}$ whereas $\text{P}_{\text{dis}(4,1)}$ and $\text{P}_{\text{gem}(4,1)}$ would form only *via* slow isomerization from $\text{P}_{\text{vic}(4,1)}$.

In summary, the DFT modeling suggests a considerably exothermic cleavage along an allover declining reaction path (-456 kJ mol^{-1}). Cleavage of the dinitrogen molecule by the bare Ta_4^+ takes place across three subsequent transition states, and it leads either to μ_2 or μ_3 bridging nitrido structures. The highest barrier of 59 kJ mol^{-1} ($\text{I2}_{(4,1)}$ to $\text{I3}_{(4,1)}$) is surmountable as it is submerged with respect to the entrance channel. Thus, N_2 cleavage by Ta_4^+ is a fast thermal process. These findings nicely agree with the observation of a fast initial N_2 adsorption process (*cf.* Fig. 1), and with the lack of vibrational N_2 fingerprints in the IR-PD spectra of (4,1), (*cf.* Fig. 2).

Obviously, one wonders if a second N_2 cleavage is feasible, subsequent to the thermal cleavage of the first N_2 molecule. The IR-PD spectra revealed no fingerprint of a coordinated and

intact N_2 molecule in the readily formed $[\text{Ta}_4(\text{N}_2)_2]^+$ complex (*cf.* Fig. 2). This observation provides strong evidence for the cleavage of a second N_2 molecule.

Indeed, the DFT modeling revealed energetically accessible pathways for second N≡N cleavage (Fig. 4, Fig. S5 and Fig. S6, ESI[†]). Starting from the likely product complex $\text{P}_{\text{vic}(4,1)}$ (Fig. 3), all four Ta centers may act as coordination sites for a second N_2 adsorbate. This results in four conceivable intermediates $\text{I1}^{\text{Ta1}}_{(4,2)}$, $\text{I1}^{\text{Ta2}}_{(4,2)}$, $\text{I1}^{\text{Ta3}}_{(4,2)}$, or $\text{I1}^{\text{Ta4}}_{(4,2)}$. Initial N_2 coordination through $\text{I1}^{\text{Ta2}}_{(4,2)}$ proves not suitable for the second N_2 activation due to steric congestion (*cf.* Fig. S6, ESI[†]). Two of the other initial intermediates are equivalent, $\text{I1}^{\text{Ta1}}_{(4,2)}$, $\text{I1}^{\text{Ta3}}_{(4,2)}$ and $\text{I1}^{\text{Ta4}}_{(4,2)}$ is slightly less stable. Both subsequent reaction pathways towards full N_2 cleavage evolve in a mechanistically related manner, and the corresponding energetics of stationary points and minima are likewise. We refer to the ESI[†] (Fig. S5 and Table S6) for the pathway of second N_2 activation, which starts at $\text{I1}^{\text{Ta3}}_{(4,2)}$.

In the following, we discuss in more detail the pathway which starts at $\text{I1}^{\text{Ta4}}_{(4,2)}$. In analogy to the path for the first N_2 cleavage (Fig. 3) the second N_2 ligand at the complex $\text{I1}_{(4,2)}$ (-41 kJ mol^{-1}) bends *via* transition state $\text{TS12}_{(4,2)}$ (-25 kJ mol^{-1}) into $\text{I2}_{(4,2)}$ (-100 kJ mol^{-1}) and subsequently *via* $\text{TS23}_{(4,2)}$ (-33 kJ mol^{-1}) towards $\text{I3}_{(4,2)}$ (-157 kJ mol^{-1} , Fig. 4). Note the remarkable similarity of the coordination motif of N_2 in $\text{I3}_{(4,1)}$ (Fig. 3). This implies the capability of the Ta_4^+ cluster to achieve N_2 cleavage twice *via* comparable intermediate geometries. In particular, there is considerable similarity of the N3–N4 distances of stationary points along the reaction path of the second activation and the respective values of N1–N2 distances along the reaction path of first activation (*cf.* Table S2 and S7, ESI[†]). Note that similar to the first N_2 activation path, the path of the 2nd activation also follows an AEAS mechanism at this point: torsional reorganization of initial in plane μ_2 -κN:κN,N coordination across an intact Ta–Ta edge towards μ_3 -κN:κN,N:κN,N coordination above a Ta–Ta–Ta surface. Ultimately, a transition state $\text{TS3P}_{(4,2)}$, located 37 kJ mol^{-1} above $\text{I3}_{(4,2)}$ leads to the product $\text{P}_{(4,2)}$, -222 kJ mol^{-1} below $\text{I3}_{(4,2)}$.

All activation barriers along the second N_2 cleavage path are submerged with respect to the entrance channel $[\text{Ta}_4\text{NN}]^+ + \text{N}_2$. The decisive step for the activation of the second N_2 , which proceeds from $\text{I3}_{(4,2)}$ across $\text{TS3P}_{(4,2)}$ to $\text{P}_{(4,2)}$, takes $+37 \text{ kJ mol}^{-1}$ activation, while the cleavage of the first N_2 molecule from $\text{I3}_{(4,1)}$ across $\text{TS3P}_{\text{vic}(4,1)}$ to $\text{P}_{\text{vic}(4,1)}$ requires less activation, namely $+10 \text{ kJ mol}^{-1}$. Nevertheless, both processes are facile. Thus, the modeling is in line with our spectroscopic findings.

Note, that $\text{P}_{\text{dis}(4,1)}$ cannot serve as a starting point for a second N_2 activation *via* an AEAS mechanism. A second N_2 activation which starts at $\text{P}_{\text{gem}(4,1)}$ leads to some $\text{P}_{(4,2)}$ like isomer in as much as starting from $\text{P}_{\text{vic}(4,1)}$ would do.

The facile activation of two N_2 molecules raises the question whether the cleavage of a third N_2 molecule is also accessible. We calculated the initial coordination and reaction paths of a third N_2 reactant to possible Ta sites of the $\text{P}_{(4,2)}$ structure of Fig. 4. Other starting points, namely $\text{P}_{(4,2)}$ of Fig. S5 and S6 (ESI[†]), are less likely. They would inevitably run into steric

3. Observation and Mechanism of Cryo N₂ Cleavage by a Tantalum Cluster

Paper

PCCP

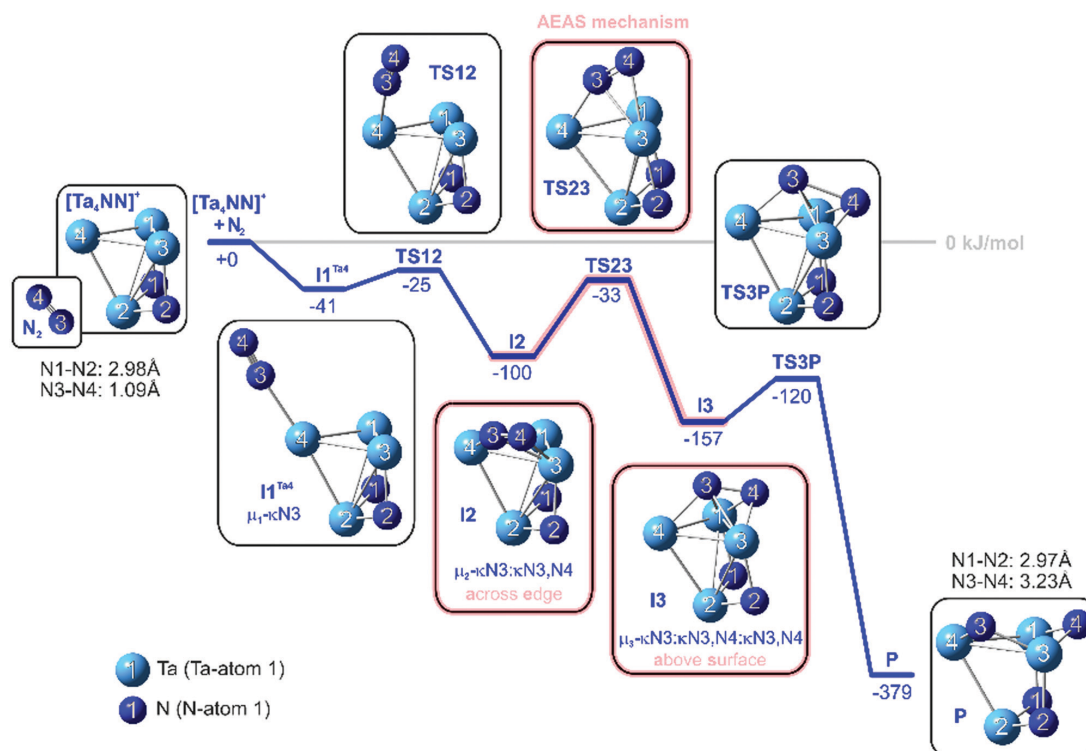


Fig. 4 A reaction pathway of second N₂ cleavage on a [Ta₄NN]⁺ cluster complex. There is a striking similarity to the first cleavage pathway, *cf.* Fig. 3, including the highlighted AEAS mechanism. Note, that the prior dissociated N1–N2 couple remains activated (at least 2.97 Å apart) in the course of the second activation, as compared to the free N₂ bond length of 1.09 Å.

congestion by the unavoidable proximity of the third N₂ ligand and the adjacent μ₂ nitrido ligands.

Thus, a conceivable AEAS mechanism might start by coordination of a third N₂ molecule to Ta1 of P_(4,2) (Fig. 5). This leads to the [Ta₄NNNN(N₂)]⁺ complex **I1**^{Ta1}_(4,3) with a stabilization of –64 kJ mol^{–1}. As revealed in the previous two cases of N₂ reorganization this third N₂ molecule bends over *via* transition state **TS12**_(4,3), +42 kJ mol^{–1}, into the intermediate **I2**_(4,3), –23 kJ mol^{–1} below **I1**_(4,3), which exhibit a μ₂-κN5:κN5,N6 coordination as in both previous cases. Further reorganization would take place *via* a transition state **TS23**_(4,2) which turns out to hamper such a process by virtue of its remarkable barrier of +142 kJ mol^{–1}, and towards the intermediate **I3**_(4,3); the latter is by +11 kJ mol^{–1} higher in energy than intermediate **I2**_(4,3). Note, that this barrier locates +55 kJ mol^{–1} above the starting point which prevents any thermal reaction process at this point. While the corresponding **I3**_(4,1) and **I3**_(4,2) states of the first and second N₂ activation stabilize with respect to the according **I2**_(4,1) and **I2**_(4,2) states, the **I3**_(4,3) state for the third N₂ activation is destabilized with respect to **I2**_(4,3). Further rearrangements from **I3**_(4,3) towards a product **P**_(4,3) would lead *via* a transition state **TS3P**_(4,3), +82 kJ mol^{–1}, to the product complex cation **P**_(4,3); the latter is stabilized by –176 kJ mol^{–1} with respect to **I3**_(4,3).

In the third N₂ activation, there are striking similarities of mechanisms at work with respect to those of first and second N₂ activation. The energetics, however, are quite unfavorable for the third N₂ activation step. Initial coordination of a third N₂ molecule to sites other than the structurally equivalent sites Ta1 and Ta2, namely Ta3 and Ta4, would lead to highly congested transition states which come along with even higher barriers.

The conclusions for the 3rd N₂ activation, based on the modeling, are twofold: firstly, we note, that the reaction path reveals a chain of rearranging steps which invoke the AEAS mechanisms in salient analogy to the reaction paths for activation of the prior two N₂ molecules. We take this sturdiness of N₂ activation by Ta₄⁺ as strong indication for a more general concept that might operate on highly corrugated surfaces at sub stoichiometric N₂ load under moderate operation conditions.

While the first two N₂ cleavages are facile, there are two subsequent activation barriers, which work against thermal cleavage of a 3rd N₂ adsorbate. We find evidence for this lack of 3rd N₂ activation in the IR-PD spectra: there is an undisputable presence of N₂ vibrations in the case of the cluster cations (4,*m*), *m* ≥ 3. The obtained frequencies clearly indicate the

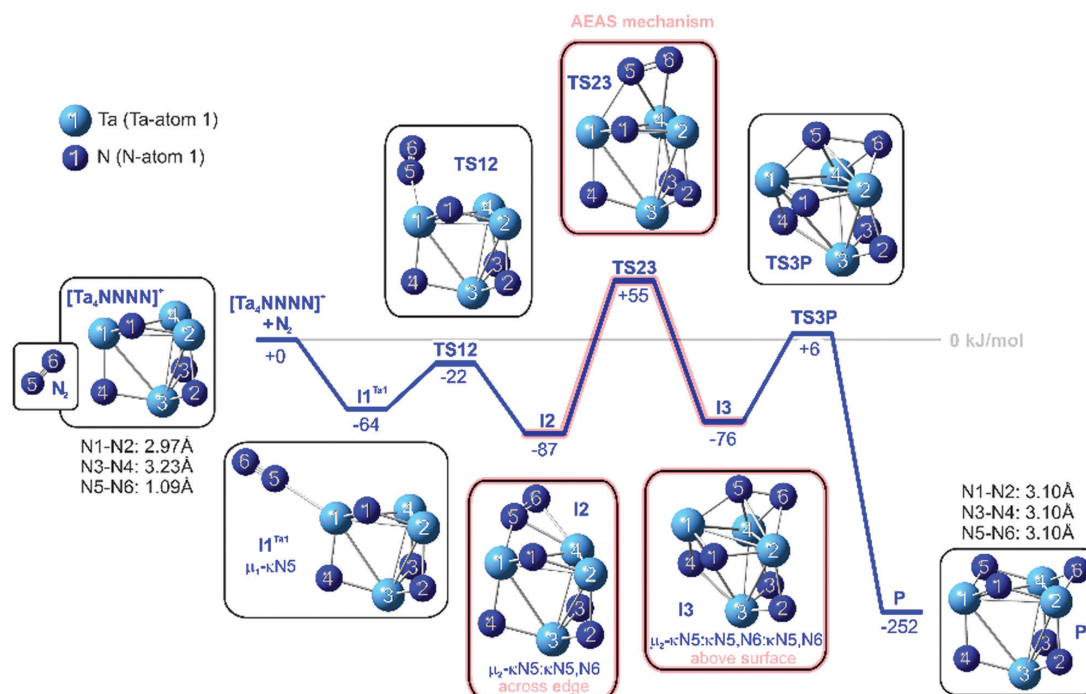


Fig. 5 A reaction pathway of 3rd N_2 cleavage on a $[\text{Ta}_4\text{NNNN}]^+$ cluster complex. The facile and highlighted AEAS mechanism across **TS23** of first and second N_2 activation becomes demanding in this case.

presence of at least one polarized but otherwise intact N_2 ligand. We will assign these vibrational bands in the following to structures in analogy to $\text{I}_{2(4,3)}$, and we will assume unsurmountable activation barriers for any further activation.

In the course of the discussion of the reaction paths, a multitude of model structures were presented, and they possess vibrational frequencies within the regions of 2200 cm^{-1} to 2310 cm^{-1} (cf. Fig. S7, ESI[†]). They serve to interpret the experimental IR-PD spectra of $[\text{Ta}_4(\text{N}_2)_m]^+$ labeled as $(4,m)$, $m = 1-5$, (Fig. 2) in some more detail. In addition we identified conceivable $[\text{Ta}_4(\text{N})_j(\text{N}_2)]^+$ species, with $j = 1-3$ starting from $\text{I}_{2(4,3)}$ (cf. Tables S11–S13, ESI[†]). The optimized structures reveal some noticeable findings:

(a) Numerous isomers (cf. Fig. S7, ESI[†]) suggest a likely coexistence of species which feature IR-PD absorptions within ranges of the observed broad bands of $(4,4)$ and $(4,5)$ (Fig. 2, 2200 cm^{-1} to 2300 cm^{-1}).

(b) Calculated IR-PD bands of $\text{I}_{2(4,3)}$ type core structures without or with additional end-on coordinated N_2 ligands (cf. Table S11, ESI[†]) nicely correspond to IR-PD band(s) around 1475 cm^{-1} , $(4,3)$, up to 1443 cm^{-1} , $(4,5)$. This spectral evidence of $\text{I}_{2(4,3)}$ indicates the absence of a third AEAS type N_2 cleavage in $(4,3)$. The flow of reaction stops at $\text{I}_{2(4,3)}$ in front of the unsurmountable **TS23** barrier – subsequent N_2 uptake prevailing.

(c) Addition of end-on N_2 ligands to **I2** type structures shifts the calculated vibration of the $\mu_2\text{-}\kappa\text{N}:\kappa\text{N},\text{N}$ N_2 ligand up to

40 cm^{-1} to the red depending on the coordination site. This agrees with the observed shifts per additional N_2 ligand of 21 cm^{-1} , $(4,3)$ to $(4,4)$, and 11 cm^{-1} , $(4,4)$ to $(4,5)$. NPA-calculations revealed an increase of the positive charge at the π -coordinated Ta4 atom by *ca.* $+0.02\text{ e}$ and an increase of the corresponding N–N bond distance by *ca.* 0.01 \AA upon coordination of an end-on coordinated N_2 molecule to an adjacent Ta atom (Ta1, Ta2, Ta3). Similar effects are reported in the correlation of charge density shifts with IR-PD vibration band shifts in transition metal π -coordinated benzene complexes.⁸⁰ It has also been reported that the decrease of IR-PD stretching frequencies of $\mu\text{-N}_2$ ligands correlates with the N_2 bond length activation.²⁰ By further addition of a second end-on coordinated N_2 molecule the positive charge at Ta4 increases along with a slight increase of the N–N bond distance. Thus, stepwise addition of N_2 molecules to the Ta_4^+ cluster result in a softening of the $\mu_2\text{-}\kappa\text{N}:\kappa\text{N},\text{N}$ N_2 coordinated ligand and manifests in a redshift of the corresponding IR-PD band.

Conclusions

The cryogenic kinetics of N_2 adsorption to Ta_4^+ reveal stepwise addition of numerous N_2 molecules, with peculiar details for the first and second adsorptions. The infrared signatures of $[\text{Ta}_4(\text{N}_2)_1]^+$ and $[\text{Ta}_4(\text{N}_2)_2]^+$ are special: there are no NN

3. Observation and Mechanism of Cryo N₂ Cleavage by a Tantalum Cluster

Paper

PCCP

stretching bands. This is consistent with cleavage of the first two adsorbed dinitrogen molecules. The cleavage of N₂ molecules proceeds *via* a novel across edge-above surface (AEAS) mechanism: the reaction path proceeds *via* an initial end-on coordination of N₂. Bending of the N₂ ligand towards a neighboring Ta atom yields a second intermediate, with a μ_2 N₂ bonding motif across an edge of the Ta₄⁺ tetrahedron core. Further rearrangement above a Ta-Ta-Ta surface of the Ta₄⁺ tetrahedron results in a μ_3 bonded N₂ ligand that relaxes swiftly by ultimate NN bond cleavage, and it unfolds into the final dinitrido species. Calculated activation barriers confirm spontaneous cleavage of the first two dinitrogen molecules. Cleavage of the third N₂ ligand is kinetically hindered. Substoichiometric N₂ exposure allows for spontaneous activation, whereas higher exposure imposes self-poisoning.

The found AEAS mechanism provides for a mechanistic understanding of facile N₂ cleavage by a sub nano structure with a highly curved surface. It shall serve as an inspiration for the knowledge inspired design of future tailor made catalyst materials that might invoke highly corrugated surfaces and operate under moderate conditions.

Author contributions

D. V. F., M. P. K. and A. S. performed the experiments. D. V. F. and M. P. K. evaluated the data. D. V. F., M. P. K. and M. H. P. performed the calculations. D. V. F., M. P. K., M. H. P. and G. N. S. wrote and revised the manuscript. All authors evaluated and discussed the results.

Conflicts of interest

There are no conflicts to declare.

Acknowledgements

This work was supported by the German research foundation DFG within the transregional collaborative research center SFB/TRR 88 "Cooperative effects in homo and heterometallic complexes" (3MET.de) and by the state research center OPTIMAS. We thank Helmut Schwarz for valuable and critical comments and for his ongoing support. We thank Thomas Kolling for technical assistance and valuable discussions. Quantum chemical modeling took place at the "Regionales Hochschulrechenzentrum Kaiserslautern (RHRK)".

References

- 1 D. E. Canfield, A. N. Glazer and P. G. Falkowski, *Science*, 2010, **330**, 192–196.
- 2 B. K. Burgess and D. J. Lowe, *Chem. Rev.*, 1996, **96**, 2983–3012.
- 3 D. Sippel and O. Einsle, *Nat. Chem. Biol.*, 2017, **13**, 956–960.
- 4 B. M. Hoffman, D. Lukoyanov, Z.-Y. Yang, D. R. Dean and L. C. Seefeldt, *Chem. Rev.*, 2014, **114**, 4041–4062.
- 5 M. Appl, *Ammonia: Principles and Industrial Practice*, Wiley-VCH, 2007.
- 6 R. Schlögl, *Ammonia Synthesis in Handbook of Heterogeneous Catalysis*, Wiley-VCH, 2008, pp. 2501–2575.
- 7 H. Liu, *Ammonia Synthesis Catalysts*, World Scientific, Singapore, 2013.
- 8 R. Schlögl, *Angew. Chem., Int. Ed.*, 2003, **42**, 2004–2008.
- 9 H. Liu and Cuihua Xuebao, *Chin. J. Catal.*, 2014, **35**, 1619–1640.
- 10 G. Ertl, *Catal. Rev.*, 1980, **21**, 201–223.
- 11 G. Ertl, S. B. Lee and M. Weiss, *Surf. Sci.*, 1982, **114**, 515–526.
- 12 G. Ertl, *Angew. Chem., Int. Ed.*, 2008, **47**, 3524–3535.
- 13 A. Mittasch, *Geschichte der Ammoniaksynthese*, Verlag Chemie, Berlin-Weinheim, 1951.
- 14 S. Gambarotta and J. Scott, *Angew. Chem., Int. Ed.*, 2004, **43**, 5298–5308.
- 15 K. Honkala, A. Hellman, I. N. Remediakis, A. Logadottir, A. Carlsson, S. Dahl, C. H. Christensen and J. K. Nørskov, *Science*, 2005, **307**, 555–558.
- 16 Á. Logadottir and J. K. Nørskov, *J. Catal.*, 2003, **220**, 273–279.
- 17 C. E. Laplaza and C. C. Cummins, *Science*, 1995, **268**, 861–863.
- 18 C. E. Laplaza, A. R. Johnson and C. C. Cummins, *J. Am. Chem. Soc.*, 1996, **118**, 709–710.
- 19 B. Schluschaß, J. Abbeneth, S. Demeshko, M. Finger, A. Franke, C. Herwig, C. Würtele, I. Ivanovic-Burmazovic, C. Limberg, J. Telsner and S. Schneider, *Chem. Sci.*, 2019, **10**, 10275–10282.
- 20 C. E. Laplaza, M. J. A. Johnson, J. C. Peters, A. L. Odom, E. Kim, C. C. Cummins, G. N. George and I. J. Pickering, *J. Am. Chem. Soc.*, 1996, **118**, 8623–8638.
- 21 K. P. Chiang, S. M. Bellows, W. W. Brennessel and P. L. Holland, *Chem. Sci.*, 2014, **5**, 267–274.
- 22 K. Grubel, W. W. Brennessel, B. Q. Mercado and P. L. Holland, *J. Am. Chem. Soc.*, 2014, **136**, 16807–16816.
- 23 S. F. McWilliams and P. L. Holland, *Acc. Chem. Res.*, 2015, **48**, 2059–2065.
- 24 T. Shima, S. Hu, G. Luo, X. Kang, Y. Luo and Z. Hou, *Science*, 2013, **340**, 1549–1552.
- 25 T. Shima, G. Luo, S. Hu, Y. Luo and Z. Hou, *J. Am. Chem. Soc.*, 2019, **141**, 2713–2720.
- 26 E. L. Muetterties, *Bull. Soc. Chim. Belg.*, 1975, **84**, 959–986.
- 27 D. K. Böhme and H. Schwarz, *Angew. Chem., Int. Ed.*, 2005, **44**, 2336–2354.
- 28 A. W. Castleman and P. Jena, *Proc. Natl. Acad. Sci. U. S. A.*, 2006, **103**, 10552–10553.
- 29 Z. Luo, A. W. Castleman and S. N. Khanna, *Chem. Rev.*, 2016, **116**, 14456–14492.
- 30 S. M. Lang and T. M. Bernhardt, *Phys. Chem. Chem. Phys.*, 2012, **14**, 9255–9269.
- 31 O. Hübner and H.-J. Himmel, *Chem. – Eur. J.*, 2018, **24**, 8941–8961.
- 32 M. Zhou, X. Jin, Y. Gong and J. Li, *Angew. Chem., Int. Ed.*, 2007, **46**, 2911–2914.
- 33 Y. Gong Zhao and M. Zhou, *J. Phys. Chem. A*, 2007, **111**, 6204–6207.

- 34 C. Geng, J. Li, T. Weiske and H. Schwarz, *Proc. Natl. Acad. Sci. U. S. A.*, 2018, **115**, 11680–11687.
- 35 C. Geng, J. Li, T. Weiske and H. Schwarz, *Proc. Natl. Acad. Sci. U. S. A.*, 2019, **116**, 21416–21420.
- 36 M. D. Morse, M. E. Geusic, J. R. Heath and R. E. Smalley, *J. Chem. Phys.*, 1985, **83**, 2293–2304.
- 37 Y. M. Hamrick and M. D. Morse, *J. Phys. Chem.*, 1989, **93**, 6494–6501.
- 38 B. Cao, A. K. Starace, O. H. Judd, I. Bhattacharyya and M. F. Jarrold, *J. Chem. Phys.*, 2014, **141**, 204304.
- 39 P. B. Armentrout, *Catal. Sci. Technol.*, 2014, **4**, 2741–2755.
- 40 K. Lange, B. Visser, D. Neuwirth, J. F. Eckhard, U. Boesl, M. Tschurl, K. H. Bowen and U. Heiz, *Int. J. Mass Spectrom.*, 2015, **375**, 9–13.
- 41 D. Neuwirth, J. F. Eckhard, B. R. Visser, M. Tschurl and U. Heiz, *Phys. Chem. Chem. Phys.*, 2016, **18**, 8115–8119.
- 42 J. F. Eckhard, D. Neuwirth, C. Panosetti, H. Oberhofer, K. Reuter, M. Tschurl and U. Heiz, *Phys. Chem. Chem. Phys.*, 2017, **19**, 5985–5993.
- 43 J. F. Eckhard, D. Neuwirth, M. Tschurl and U. Heiz, *Phys. Chem. Chem. Phys.*, 2017, **19**, 10863–10869.
- 44 T. Masubuchi, J. F. Eckhard, G. Goddard, M. Tschurl and U. Heiz, *Phys. Chem. Chem. Phys.*, 2019, **21**, 20743–20749.
- 45 X. Cheng, Z.-Y. Li, L.-H. Mou, Y. Ren, Q.-Y. Liu, X.-L. Ding and S.-G. He, *Chem. – Eur. J.*, 2019, **25**, 16523–16527.
- 46 Y. Zhao, J.-T. Cui, M. Wang, D. Y. Valdivielso, A. Fielicke, L.-R. Hu, X. Cheng, Q.-Y. Liu, Z.-Y. Li, S.-G. He and J.-B. Ma, *J. Am. Chem. Soc.*, 2019, **141**, 12592–12600.
- 47 L.-H. Mou, Z.-Y. Li, Q.-Y. Liu and S.-G. He, *J. Am. Soc. Mass Spectrom.*, 2019, **30**, 1956–1963.
- 48 R. A. J. O’Hair and G. N. Khairallah, *J. Cluster Sci.*, 2004, **15**, 331–363.
- 49 H. Schwarz and K. R. Asmis, *Chem. – Eur. J.*, 2019, **25**, 2112–2126.
- 50 H.-J. Himmel and M. Reiher, *Angew. Chem., Int. Ed.*, 2006, **45**, 6264–6288.
- 51 H. Wang, R. Craig, H. Haouari, J.-G. Dong, Z. Hu, A. Vivoni, J. R. Lombardi and D. M. Lindsay, *J. Chem. Phys.*, 1995, **103**, 3289–3292.
- 52 P. Gruene, A. Fielicke and G. Meijer, *J. Chem. Phys.*, 2007, **127**, 234307.
- 53 J. Du, X. Sun and G. Jiang, *J. Chem. Phys.*, 2012, **136**, 094311.
- 54 F. Wei, C. Luo and J. Dong, *J. Chem. Phys.*, 2006, **125**, 114305.
- 55 J. F. Eckhard, T. Masubuchi, M. Tschurl, R. N. Barnett, U. Landman and U. Heiz, *J. Phys. Chem. C*, 2018, **122**, 25628–25637.
- 56 M. Kumar Yadav and A. Mookerjee, *Phys. B*, 2010, **405**, 3940–3942.
- 57 F. Mafuné, Y. Tawarayama and S. Kudoh, *J. Phys. Chem. A*, 2016, **120**, 4089–4095.
- 58 M. Arakawa, K. Ando, S. Fujimoto, S. Mishra, G. N. Patwari and A. Terasaki, *Phys. Chem. Chem. Phys.*, 2018, **20**, 13974–13982.
- 59 S. Dillinger, J. Mohrbach, J. Hewer, M. Gaffga and G. Niedner-Schatteburg, *Phys. Chem. Chem. Phys.*, 2015, **17**, 10358–10362.
- 60 J. Mohrbach, S. Dillinger and G. Niedner-Schatteburg, *J. Phys. Chem. C*, 2017, **121**, 10907–10918.
- 61 S. Dillinger, M. P. Klein, A. Steiner, D. C. McDonald, M. A. Duncan, M. M. Kappes and G. Niedner-Schatteburg, *J. Phys. Chem. Lett.*, 2018, **9**, 914–918.
- 62 C. Berg, T. Schindler, G. Niedner-Schatteburg and V. E. Bondybey, *J. Chem. Phys.*, 1995, **102**, 4870–4884.
- 63 V. E. Bondybey and J. H. English, *J. Chem. Phys.*, 1981, **74**, 6978–6979.
- 64 M. Graf, Diploma thesis, TU Kaiserslautern, 2006.
- 65 M. J. Frisch, G. W. Trucks, H. B. Schlegel, G. E. Scuseria, M. A. Robb, J. R. Cheeseman, G. Scalmani, V. Barone, B. Mennucci, G. A. Petersson, H. Nakatsuji, M. Caricato, X. Li, H. P. Hratchian, A. F. Izmaylov, J. Bloino, G. Zheng, J. L. Sonnenberg, M. Hada, M. Ehara, K. Toyota, R. Fukuda, J. Hasegawa, M. Ishida, T. Nakajima, Y. Honda, O. Kitao, H. Nakai, T. Vreven, J. A. Montgomery Jr., J. E. Peralta, F. Ogliaro, M. J. Bearpark, J. Heyd, E. N. Brothers, K. N. Kudin, V. N. Staroverov, R. Kobayashi, J. Normand, K. Raghavachari, A. P. Rendell, J. C. Burant, S. S. Iyengar, J. Tomasi, M. Cossi, N. Rega, N. J. Millam, M. Klene, J. E. Knox, J. B. Cross, V. Bakken, C. Adamo, J. Jaramillo, R. Gomperts, R. E. Stratmann, O. Yazyev, A. J. Austin, R. Cammi, C. Pomelli, J. W. Ochterski, R. L. Martin, K. Morokuma, V. G. Zakrzewski, G. A. Voth, P. Salvador, J. J. Dannenberg, S. Dapprich, A. D. Daniels, Ö. Farkas, J. B. Foresman, J. V. Ortiz, J. Cioslowski and D. J. Fox, *Gaussian 09, Revision D.01*, Gaussian, Inc., Wallingford, CT, USA, 2009.
- 66 M. J. Frisch, G. W. Trucks, H. B. Schlegel, G. E. Scuseria, M. A. Robb, J. R. Cheeseman, G. Scalmani, V. Barone, G. A. Petersson, H. Nakatsuji, X. Li, M. Caricato, A. V. Marenich, J. Bloino, B. G. Janesko, R. Gomperts, B. Mennucci, H. P. Hratchian, J. V. Ortiz, A. F. Izmaylov, J. L. Sonnenberg, F. Ding Williams, F. Lipparini, F. Egidi, J. Goings, B. Peng, A. Petrone, T. Henderson, D. Ranasinghe, V. G. Zakrzewski, J. Gao, N. Rega, G. Zheng, W. Liang, M. Hada, M. Ehara, K. Toyota, R. Fukuda, J. Hasegawa, M. Ishida, T. Nakajima, Y. Honda, O. Kitao, H. Nakai, T. Vreven, K. Throssell, J. A. Montgomery Jr., J. E. Peralta, F. Ogliaro, M. J. Bearpark, J. J. Heyd, E. N. Brothers, K. N. Kudin, V. N. Staroverov, T. A. Keith, R. Kobayashi, J. Normand, K. Raghavachari, A. P. Rendell, J. C. Burant, S. S. Iyengar, J. Tomasi, M. Cossi, J. M. Millam, M. Klene, C. Adamo, R. Cammi, J. W. Ochterski, R. L. Martin, K. Morokuma, O. Farkas, J. B. Foresman and D. J. Fox, *Gaussian 16, Revision C.01*, Gaussian, Inc., Wallingford, CT, USA, 2016.
- 67 C. Adamo and V. Barone, *J. Chem. Phys.*, 1999, **110**, 6158–6170.
- 68 J. P. Perdew, K. Burke and M. Ernzerhof, *Phys. Rev. Lett.*, 1996, **77**, 3865.
- 69 D. Andrae, U. Häußermann, M. Dolg, H. Stoll and H. Preuß, *Theor. Chim. Acta*, 1990, **77**, 123–141.
- 70 F. Weigend and R. Ahlrichs, *Phys. Chem. Chem. Phys.*, 2005, **7**, 3297–3305.

3. Observation and Mechanism of Cryo N₂ Cleavage by a Tantalum Cluster

Paper

PCCP

- 71 M. P. Klein, A. A. Ehrhard, J. Mohrbach, S. Dillinger and G. Niedner-Schatteburg, *Top. Catal.*, 2018, **61**, 106–118.
- 72 C. Peng and H. Bernhard Schlegel, *Isr. J. Chem.*, 1993, **33**, 449–454.
- 73 L. Fan, D. Harrison, L. Deng, T. K. Woo, D. Swerhone and T. Ziegler, *Can. J. Chem.*, 1995, **73**, 989–998.
- 74 K. Fukui, *Acc. Chem. Res.*, 1981, **14**, 363–368.
- 75 F. Weinhold and J. E. Carpenter, in *The Structure of Small Molecules and Ions*, ed. R. Naaman and Z. Vager, Springer US, Boston, MA, 1988, DOI: 10.1007/978-1-4684-7424-4_24, pp. 227–236.
- 76 E. D. Glendening, C. R. Landis and F. Weinhold, *J. Comput. Chem.*, 2013, **34**, 1429–1437.
- 77 A. Salzer, *J. Pure Appl. Chem.*, 1999, **71**, 1557.
- 78 M. D. Fryzuk, S. A. Johnson and S. J. Rettig, *J. Am. Chem. Soc.*, 1998, **120**, 11024–11025.
- 79 M. D. Fryzuk, S. A. Johnson, B. O. Patrick, A. Albinati, S. A. Mason and T. F. Koetzle, *J. Am. Chem. Soc.*, 2001, **123**, 3960–3973.
- 80 T. D. Jaeger, D. van Heijnsbergen, S. J. Klippenstein, G. von Helden, G. Meijer and M. A. Duncan, *J. Am. Chem. Soc.*, 2004, **126**, 10981–10991.

3.3 Supplementary Information

Electronic Supplementary Information

Observation and mechanism of cryo N₂ cleavage by a tantalum cluster

Daniela V. Fries, Matthias P. Klein, Annika Steiner, Marc H. Prosenc and Gereon Niedner-Schatteburg

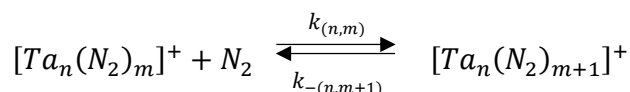
*Fachbereich Chemie and Forschungszentrum OPTIMAS,
Technische Universität Kaiserslautern, 67663 Kaiserslautern, Germany*

Text 1: Detailed Experimental and Computational Methods

The experiments were performed with a customized Fourier transform ion cyclotron resonance (FT-ICR) mass spectrometer (Apex Ultra, Bruker Daltonics). This specific apparatus configuration allows us to generate cluster ions and isolate required mass complexes. Furthermore, we are able to adsorb reaction gases while trapping the ions in the hexapole cell and record mass spectra of the adsorbate complexes. Finally, we can examine the ions in the ICR cell by adsorption kinetics and infrared (multi) photon dissociation (IR-PD) spectroscopy.

First, we generate required cluster ions using a home-built laser vaporization (LVAP) source as described before.^{1,2} The second harmonic of a pulsed Nd:YAG laser (Spitlight300, Innolas, 20 Hz) was used to evaporate tantalum atoms from a rotating tantalum foil (0.5 mm thick, 99.95 %, Alfa Aesar). Next, a gas pulse created from a piezoelectric valve³ captures the hot plasma. While guided subsequently through the expansion channel (69 mm long, 2 mm diameter) the atoms and ions cool down and aggregate. Passing electrostatic lenses, the resulting cluster size distribution reaches the 90° ion beam bender. The bare clusters can be mass selected by a quadrupole mass filter and reach the cryogenic hexapole cell (10 K) subsequently. Therein, we are able to trap required mass complexes and introduce buffer or reaction gases. This can be done continuously or in pulses. For our investigations on tantalum clusters we only used continuously injection of up to $2.6 \cdot 10^{-7}$ mbar N₂. To achieve sufficient cluster signal and thermalization, additional collision gas (He; up to $6.8 \cdot 10^{-6}$ mbar) was introduced into the hexapole. After trapping the clusters and cluster adsorbates for various storage times (0 - 20 s), the ions are guided by electrostatic lenses into the FT-ICR cell for detection. If required, it is possible to isolate ion complexes within and introduce further reaction gas into this infinity cell.⁴

Reaction delay scans were recorded in order to investigate adsorption kinetics of nitrogen molecules to tantalum clusters. From this, we obtain a temporal evolution of mass spectra, which is evaluated by the program DataAnalysis 4.0 (Bruker Daltonics). The outcoming signal intensities and assigned storage times of each adsorbate complexes are input data for evaluation by evofit⁵. This program performs pseudo-first-order fits, from which we receive relative rate constants for adsorption ($k_{(n,m)}$) and desorption steps ($k_{-(n,m+1)}$), respectively.



The relative rate constants ($k_{(n,m)}$, $k_{-(n,m+1)}$) determine the absolute rate constants ($k_{(n,m)}^{abs}$, $k_{-(n,m+1)}^{abs}$), the absolute collision gas number densities $\rho_{N_2}(T)$ serving as the conversion factor.

$$k_{(n,m)}^{abs} = \frac{k_{(n,m)}}{\rho_{N_2}(T)} \quad k_{-(n,m+1)}^{abs} = \frac{k_{-(n,m+1)}}{\rho_{N_2}(T)}$$

Approximate values for $\rho_{N_2}(T)$ are indirectly given by the pressure in the surrounding chamber p_c^{300K} and an effective geometry factor c_{app} .

$$\rho_{N_2}(T) = \frac{c_{app} \cdot p_c^{300K}}{k_B \cdot T_{300K}}$$

This geometry factor c_{app} shows a significant dependency on the temperature of the hexapole ion trap. We evaluated this factor to 1.8 at 26 K (uncertainty of $\pm 50\%$) by numerous of previous kinetic studies of transition metal cluster cations with neutral reactants at cryo temperatures. Three models are used for determination of collision rates. The average dipole orientation (ADO) theory is based on a concept of a classical trajectory of a linear dipole in the field of a point charge.

$$k_{coll} = \frac{q}{2\epsilon_0\sqrt{\mu}} \cdot \left(\sqrt{\alpha} + c\mu_D \sqrt{\frac{2}{\pi k_B T}} \right)$$

Whereby μ is the reduced mass of the cluster adsorbate complex, μ_D stands for the dipole moment and α is the polarizability. The parameter c can take values from 0 to 1 and can be expressed by the polarizability of the neutral reactant, here N_2 . The volume α' and μ_D .⁶ It simplifies to the Langevin rate in the case of a negligible dipole moment. The ADO theory often underestimates the reaction rates for charged clusters with small molecules. Nevertheless, it is frequently used to calculate reaction rates for charged clusters with small molecules.⁷ Therefore, Kummerlöwe and Beyer⁸ devised two new models to determine collision rates of ionic clusters with neutral molecules. While the hard sphere average dipole orientation (HSA) model assumes a point charge in the center of the ionic cluster, the charge in the surface charge capture (SSC) theory is able to migrate to the cluster surface by its attractive interaction with the neutral collision partner.

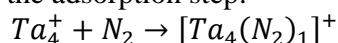
For performing IR-PD experiments, a tuneable IR laser ($\delta t = 7$ ns) is coupled into the ICR cell. This laser is comprised of a KTP/KTA optical parametric oscillator/amplifier (OPO/OPA, LaserVision) system pumped by a pulsed injection seeded Nd:YAG laser (10 Hz, PL8000, Continuum). To obtain IR radiation ($1100 - 2400$ cm^{-1}), an AgGaSe₂ crystal is used to generate the difference frequency (DF) between the OPA signal and idler waves. During irradiation with the IR laser, the ions are isolated and trapped in the ICR cell. Subsequently, every ion package is treated by 7 – 10 laser pulses (0.3 – 4.0 mJ/pulse) to yield sufficient fragment ions. A series of fragmentation mass spectra is recorded while continuously scanning the IR wavelength. The measured IR-PD signal is evaluated as $\sum_I F_I / (\sum_I F_I + \sum_I P_I)$, where F_I and P_I represent fragment and parent ion signal, respectively. Finally, the determined fragmentation efficiency is plotted as a function of laser frequency in order to obtain an IR-PD spectrum.

All quantum chemical calculations are carried out by the program package Gaussian 09⁹ and the Gaussian 16 suite¹⁰. We employed the PBE0 functional^{11, 12} for nonlocal corrections and the DEF2TZVP basis set^{13, 14} for all atoms. All stationary states were checked by second derivative calculations revealing no (minima) and only one (transition state) imaginary frequency. Reaction paths were searched by QST2/3¹⁵ or linear transit methods¹⁶ and after location and optimization of the transition states scanned by IRC calculations.¹⁷ Orbital analyses were performed using Molecular Orbitals as well as Natural Bonding Orbitals as employed in the Gaussian 16 program.^{18, 19}

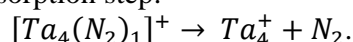
Text 2: Nomenclature for the Ta₄⁺ cluster and its adsorbates

There are 14 complexes of the form [Ta₄(N₂)_m]⁺, where *m* stands for the number of N₂ molecules attached to the cluster. The index *m* ranges from 0 to 13. For ease of reference, we use the notation (4,*m*). The 14 complexes are interlinked by 13 processes, respectively, in the form of adsorption and desorption reactions. The rate constants for these adsorption and desorption processes are labelled as *k_m* and *k_{-(m+1)}*. Therefore, *m* can assume values from 0 to 12.

We use e.g. *k₀* := *k_{0→1}* for the adsorption step:



and *k₋₁* := *k_{1→0}* for the desorption step:



Text 3: Detailed discussion of the intermediate I_{1(4,1)}

According to an NBO analysis, there are minor contributions from 6s and 6p orbitals which we omit in further discussion. The Ta1 atom provides for five 5d electrons. It utilizes three of these to form three σ-bonds to the remaining three Ta atoms of the cluster. The Ta1 atom thereby experiences a local weak ML3 ligand field splitting of the 5d orbitals which destabilizes the thus empty d_{z²} orbital.²⁰ The remaining two d electrons fill the d_{xz} orbital. This d_{xz} orbital is a lone pair orbital at the Ta1 atom within the NBO framework. The N₂ ligand's lone pair donates towards the empty d_{z²} orbital which locates perpendicular to the (Ta1-Ta2-Ta3) plane. The bonding of the N₂ ligand to the Ta1 atom seems to increase the Ta1-Ta4 bond length from 2.52 Å in Ta₄⁺ to 2.72 Å in I_{1(4,1)}, and the N₂ binding energy amounts to 66 kJ mol⁻¹ (in the doublet state).

Text 4: Detailed discussion of the intermediate I_{2(4,1)}

The stabilization of I_{2(4,1)} with respect to I_{1(4,1)} is accompanied by a reduction of d(Ta1-N1) to 2.02 Å (-0.11 Å with respect to I_{1(4,1)}), an elongation of d(N1-N2) to 1.19 Å (+0.08 Å), and a tilting of the N₂ ligand towards Ta2. The result is a bridged μ₂-κN1:κN1κN2 structure with d(Ta2-N1) = 2.12 Å (-1.00 Å with respect to I_{1(4,1)}) and d(Ta2-N2) = 2.18 Å (-1.80 Å). Note, that this coordination motif corresponds to a tantalum complex with a bridging N₂ unit that is coordinated both side-on and end-on^{20, 21}. Related complexes with I2 type bonding motifs were reported for Gd²², Sc²³, and V²⁴. By the tilting, the distance d(Ta1-Ta4) in I_{2(4,1)} decreases to 2.56 Å (-0.16 Å with respect to I_{1(4,1)}) due to the diminished donation of the coordinating nitrogen lone pair electron density into the Ta1-Ta4 σ*-antibonding orbital. In effect, the Ta1-Ta4 bond strengthens and the distance between the Ta atoms shrinks. Note, that at this point there are no Ta3-N1 and Ta3-N2 interactions.

Text 5: Detailed discussion of the intermediate I3_(4,1)

The structure of I3_(4,1) reveals the bridged $\mu_3\text{-}\kappa\text{N1}:\kappa\text{N1,N2}:\kappa\text{N1,N2}$ bonded nitrogen ligand which comprises an elongated N1-N2 bond of 1.43 Å (+0.24 Å with respect to I2_(4,1)). The Ta1-N1 distance has decreased to 1.92 Å (-0.10 Å), as well as the Ta2-N2 distances of 2.00 Å (-0.17 Å) and Ta3-N2 distance of 1.96 Å (-2.29 Å). The Ta2-Ta3 bond has elongated from 2.57 Å, I2_(4,1), to 2.87 Å, I3_(4,1), (+0.30 Å), and the Ta1-Ta3 bond from 2.56 Å, I2_(4,1), to 2.92 Å, I3_(4,1), (+0.36 Å); the charge density of both bonds dilutes significantly. In parallel, the N1-N2 bond elongates from 1.19 Å, I2_(4,1), to 1.43 Å, I3_(4,1), (+0.24 Å). Note, that this points to a mere N-N single bond distance as e.g. found in hydrazine²⁵ and related complexes (1.45 Å). Thus, the adaptive Ta₄⁺ cluster enables a bridged μ_3 coordination of N₂ (cf. I3 in Figure 3). The concomitant cleavage of the N₂ triple bond is accompanied by a relaxation of the Ta₄⁺ scaffold.

Text 6: Detailed discussion of the product P_{vic(4,1)}

The four Ta N bonds in P_{vic(4,1)} possess almost equal bond length on the order of 1.84 - 1.90 Å. Minor variations might originate from partial double and single bond characters. Accordingly, the two N bridged Ta1-Ta2 and Ta2-Ta3 bonds are equally elongated to 2.81 Å as compared to the non bridged Ta-Ta bonds, e.g. d(Ta1 Ta3) = 2.69 Å.

3. Observation and Mechanism of Cryo N₂ Cleavage by a Tantalum Cluster

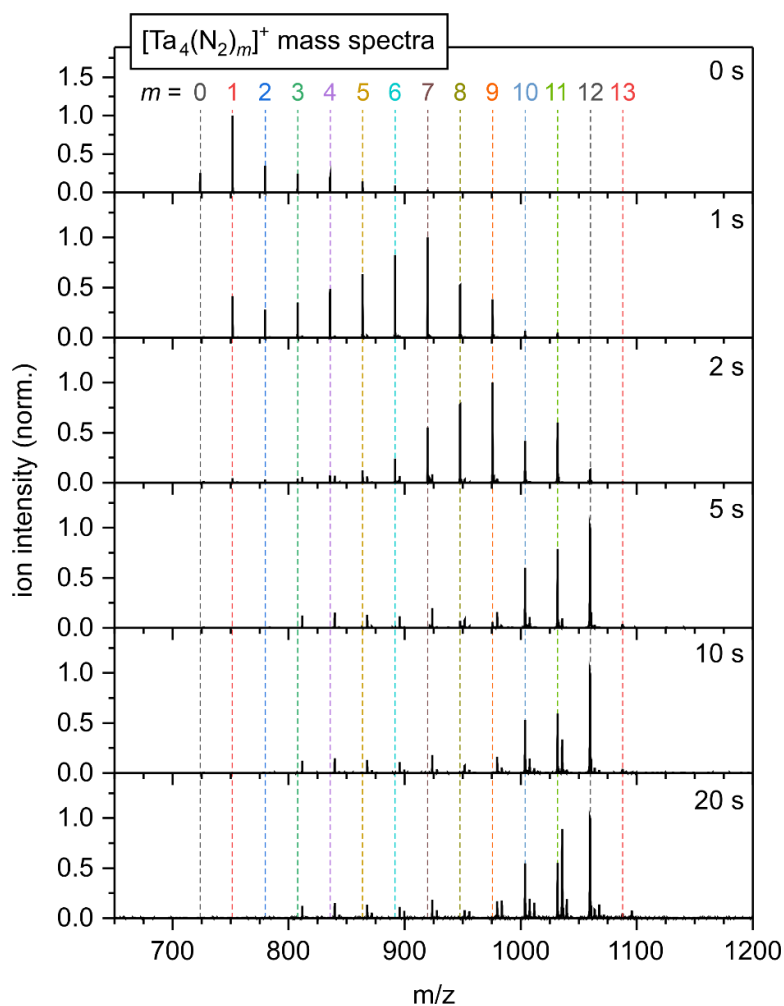


Fig. S1. Temporal evolution of the FT-ICR mass spectra of Ta₄⁺ cluster complexes at 26 K and various storage times in the cryogenic hexapole ion trap exposed to an N₂ pressure of 2.6x10⁻⁷ mbar. The least quantifiable maximum of N₂ adsorption to Ta₄⁺ clusters from the carried-out measurement is 13 N₂.

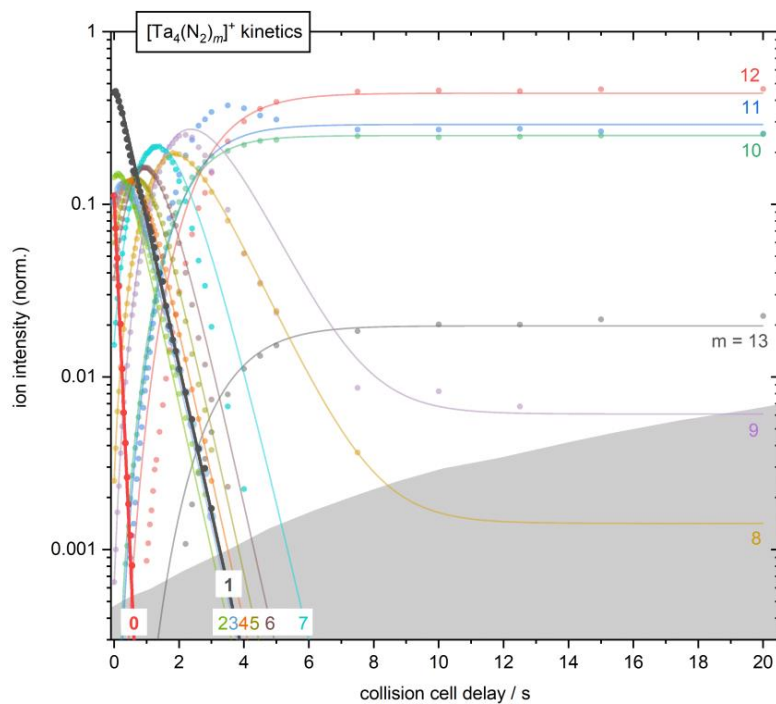


Fig. S2. Isothermal kinetics of N_2 adsorption by mass-selected Ta_4^+ clusters at 26 K, He buffer gas (6.8×10^{-6} mbar) and an exposure of 2.6×10^{-7} mbar N_2 . The experimental data (solid dots) and the fits (solid lines) assume pseudo-first order kinetics for the N_2 adsorption in up to 13 consecutive steps. The kinetics of first and second N_2 adsorption are highlighted. The grey-shaded area indicates the background noise level. Corresponding rate constants of the pseudo-first order fits for each adsorption/desorption is shown in the Supporting Information (cf. Fig. S3).

3. Observation and Mechanism of Cryo N₂ Cleavage by a Tantalum Cluster

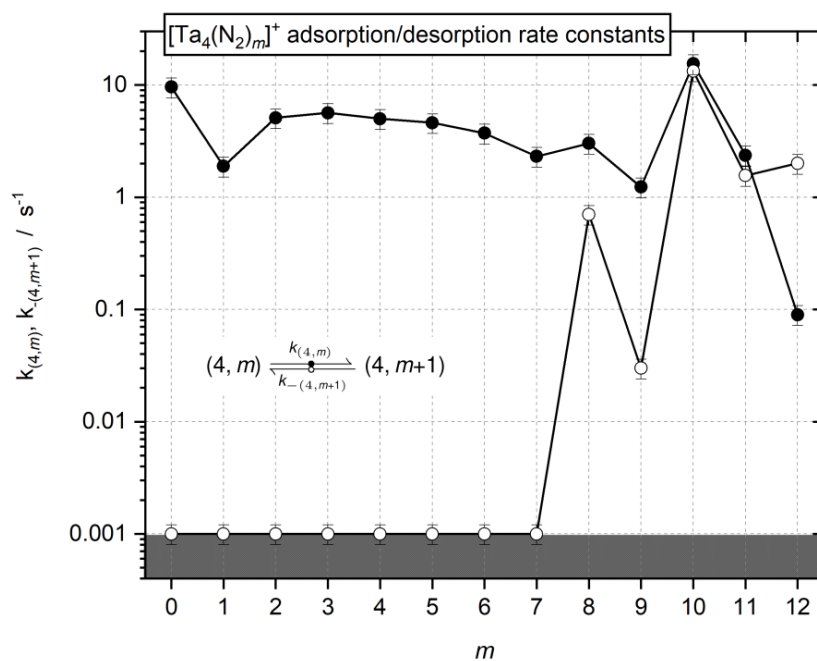


Fig. S3. Observed rate constants resulting from pseudo-first-order fits of measured kinetic data of the Ta₄⁺ cluster complex as a function of stepwise N₂ adsorption. Filled circles show the rate of adsorption ($k_{(4,m)}$). Desorption rates ($k_{-(4,m+1)}$) are represented by open circles. The gray shaded area indicates the background noise level.

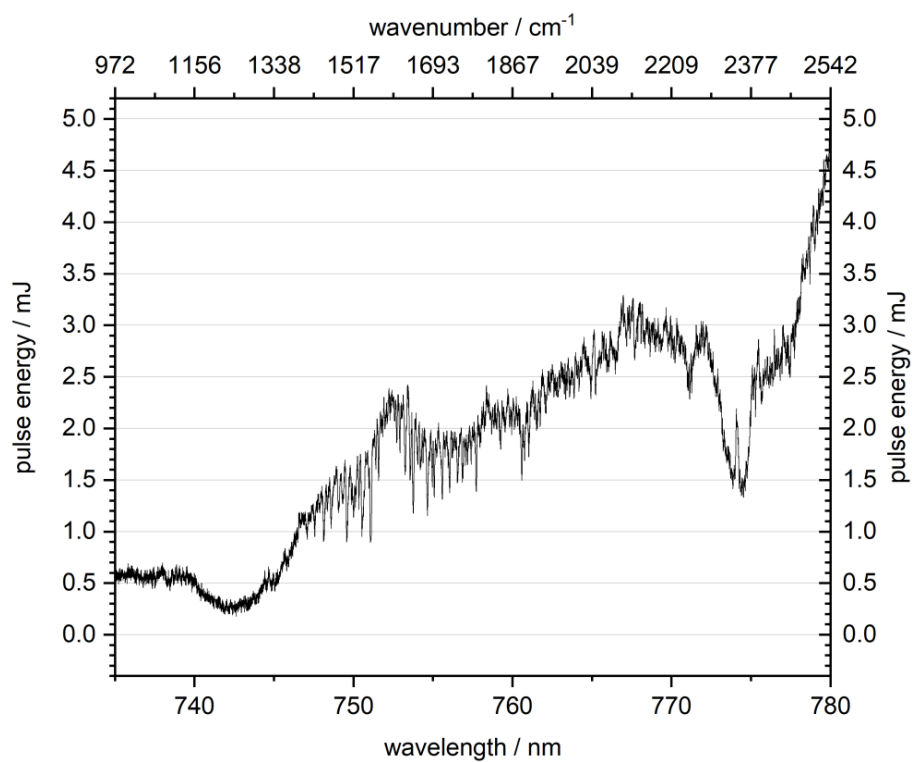


Fig. S4. Laser pulse energy in dependence of wavelength and wavenumber.

3. Observation and Mechanism of Cryo N₂ Cleavage by a Tantalum Cluster

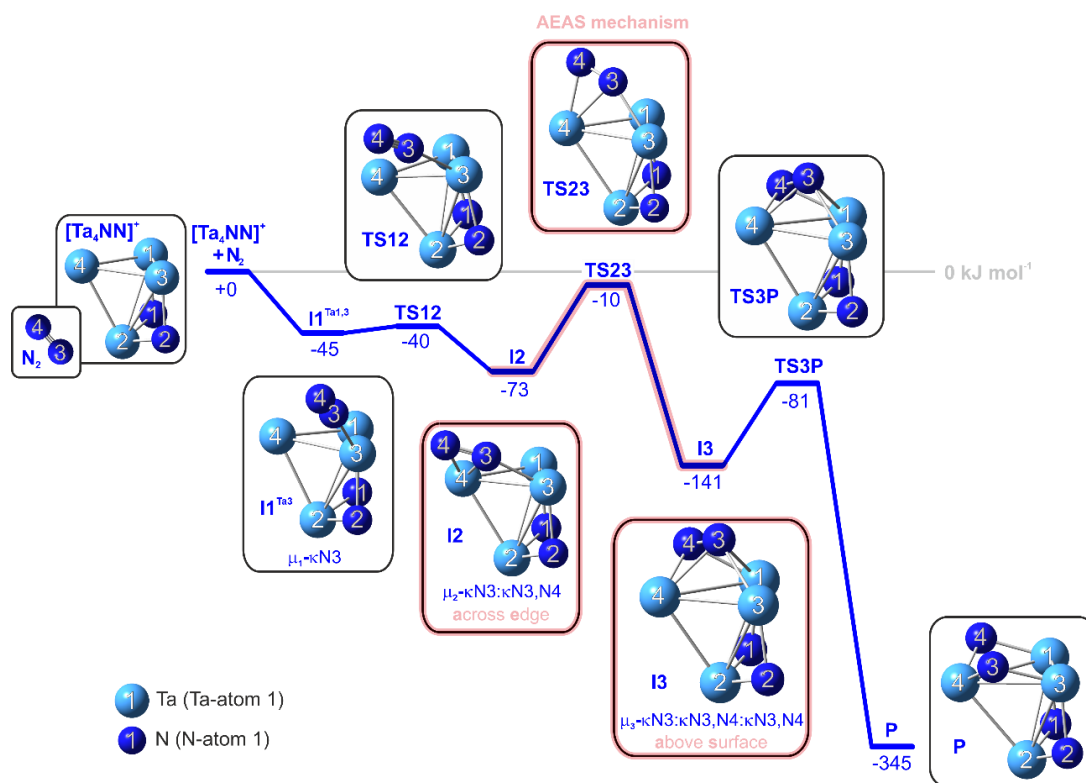


Fig. S5. A reaction pathway of second N₂ cleavage on a [Ta₄NN]⁺ cluster complex (adsorption site: Ta3). The torsional reorganization of the AEAS mechanism is highlighted. For reasons of clarity, the nomenclature is presented in a shortened form (e.g. here I1 stands for I1_(4,2) or rather I1^{Ta3}_(4,2)).

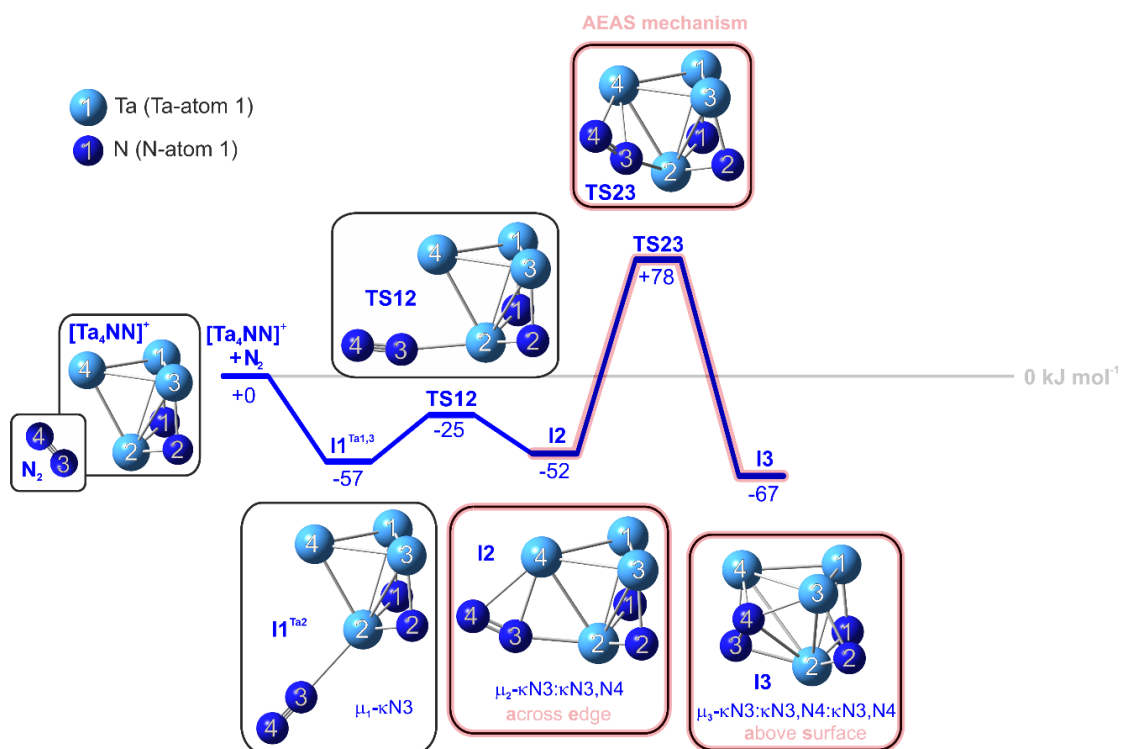


Fig. S6. A reaction pathway of second N_2 cleavage on a $[\text{Ta}_4\text{NN}]^+$ cluster complex (adsorption site: Ta2). The torsional reorganization of the AEAS mechanism is highlighted. For reasons of clarity, the nomenclature is presented in a shortened form (e.g. here I1 stands for I1_(4,2) or rather I1^{Ta2}_(4,2)).

3. Observation and Mechanism of Cryo N₂ Cleavage by a Tantalum Cluster

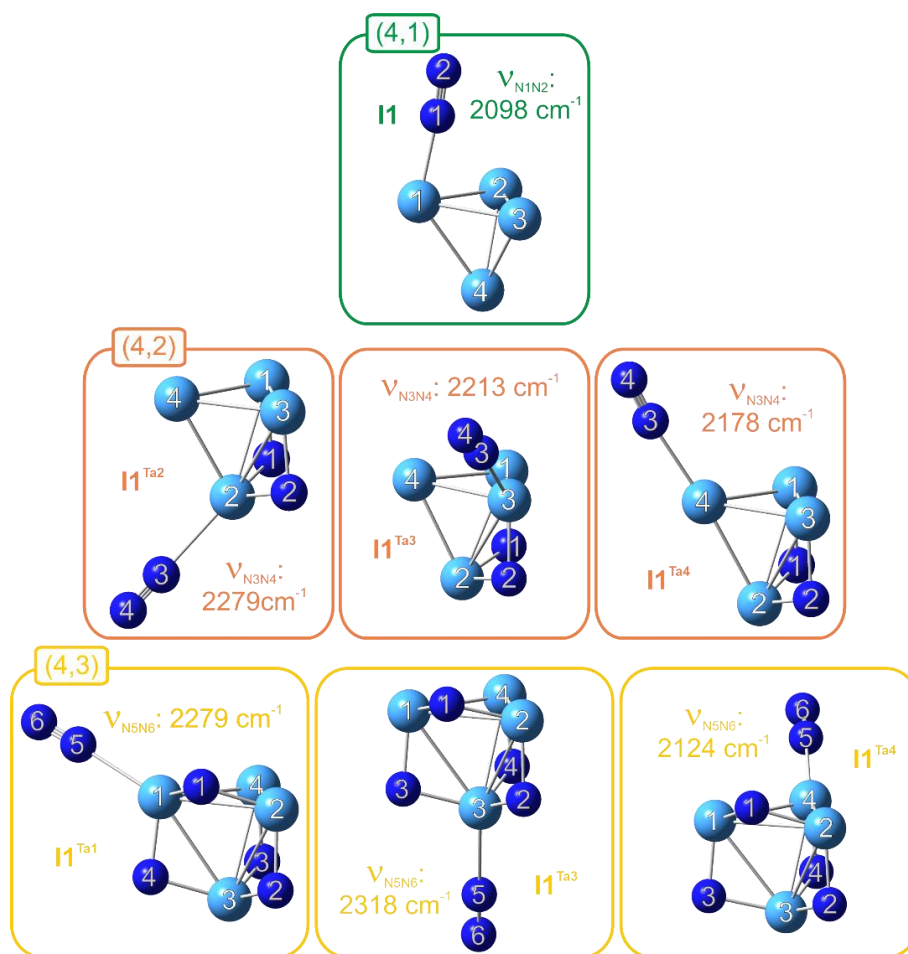


Fig. S7. Model structures with an end-on bound N₂ molecule ($\mu_1\text{-}\kappa\text{N}1$ coordination) obtained from DFT calculations on the first, second and third N₂ activation pathway. Their scaled vibrational frequencies are within the range of 2100 cm^{-1} to 2300 cm^{-1} (scale factor: 0.9376).

Table S1. Relative pseudo-first-order rate constants, absolute rate constants, collision rates and sticking probabilities for the N₂ adsorption on (4,*m*) clusters at a N₂ pressure of 2.6x 10⁻⁷ mbar. Gray shaded elements highlight sticking probabilities $\gamma > 1$. Orange highlighted values are likely to be questionable as the limits of *evofit* (5) (fit program) have been exceeded.

2.6x10 ⁻⁷ mbar N ₂				
<i>m</i>	$k_{\text{coll}}(4,m) / 10^{-16} \text{ m}^3/\text{s}$	$k_{(4,m)} / \text{s}^{-1}$	$k_{\text{abs}}(4,m) / 10^{-16} \text{ m}^3/\text{s}$	γ
0	6.00	9.58	8.48	1.41
1	6.00	1.88	1.67	0.28
2	5.99	5.10	4.51	0.75
3	5.99	5.65	5.00	0.84
4	5.99	5.01	4.43	0.74
5	5.98	4.60	4.07	0.68
6	5.98	3.72	3.29	0.55
7	5.98	2.31	2.05	0.34
8	5.97	3.02	2.67	0.45
9	5.97	1.23	1.09	0.18
10	5.97	15.43	13.7	2.29
11	5.97	2.37	2.09	0.35
12	5.96	0.09	0.08	0.01

3. Observation and Mechanism of Cryo N₂ Cleavage by a Tantalum Cluster

Table S2. Calculated distances in Å of atoms within Ta₄⁺, N₂ and [Ta₄(N₂)₁]⁺ in the doublet state along the activation pathway of the first N₂ molecule on a Ta₄⁺ cluster complex.


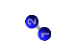












	[Ta ₄] ⁺	N ₂	I1 _(4,4)	TS12 _(4,4)	I2 _(4,4)	TS23 _(4,4)	I3 _(4,4)	TS3P _{(4,1)vic}	TS3P _{(4,1)gem}	P _{(4,1)vic}	TSP _{vic} P _{gem}	P _{(4,1)gem}	TSP _{vic} P _{dfs}	P _{(4,1)dfs}
														
Ta1-Ta2	2.64281		2.53029	2.53803	2.63597	2.58405	2.51053	2.9816	2.58642	2.80981	2.81177	2.54861	2.9854	2.65808
Ta2-Ta3	2.52474		2.54831	2.54441	2.57044	2.4606	2.87221	2.80459	2.9635	2.80852	3.05656	2.84528	2.80194	2.77209
Ta3-Ta4	2.55383		2.52596	2.54142	2.60882	2.51033	2.46294	2.55785	2.61668	2.58246	2.57717	2.5485	2.55304	2.65861
Ta1-Ta4	2.52494		2.72035	2.71223	2.55912	2.58949	2.5635	2.57129	2.46981	2.57679	2.55691	2.67861	2.60097	2.66287
Ta2-Ta4	2.52393		2.52619	2.51859	2.57036	2.77776	2.54261	2.44979	2.61663	2.61516	2.55519	2.54854	2.54783	2.65895
Ta1-Ta3	2.5242		2.53039	2.52825	2.55924	2.59023	2.91928	2.51185	2.58647	2.69019	2.66673	2.54863	2.67202	2.65872
Ta1-N1			2.12606	2.08579	2.0197	2.02836	1.91925	1.91264	2.43664	1.83777	1.85736	1.99248	1.8178	1.85619
Ta1-N2														
Ta2-N1			3.1238	2.51358	2.12104	2.16581	2.19976	2.10592	1.94684	1.89471	1.87219	2.00009	1.94786	
Ta2-N2			3.9722		2.17607	2.10638	2.00254	1.92269	1.96373	1.89543	1.95083	1.99998	1.87395	1.85724
Ta3-N1					3.61223		2.2019	2.29594	1.94692			2.00003		
Ta3-N2					4.24793		1.95998	1.9417	1.96381	1.83664	1.84741	1.99997	1.85766	1.85718
Ta4-N1														1.85593
Ta4-N2												1.99291		
N1-N2		1.08948	1.10833	1.12038	1.18967	1.22901	1.43062	1.66522	1.83186			2.71973		

Table S3. Calculated energies of the cluster adsorbate complex $[\text{Ta}_4(\text{N}_2)_1]^+$ in the doublet and quartet state along the activation pathway of the first N_2 molecule on a Ta_4^+ cluster complex.

	doublet state		quartet state	
	energy E / Ha	ΔE / kJ/mol	energy E / Ha	ΔE / kJ/mol
$\text{Ta}_4^+, \text{N}_2$	-337.05023	0	-337.035182	40
$\text{I1}_{(4,1)}$	-337.07549	-66	-337.054152	-10
$\text{TS12}_{(4,1)}$	-337.07342	-61	-337.050021	1
$\text{I2}_{(4,1)}$	-337.09514	-118	-337.074784	-64
$\text{TS23}_{(4,1)}$	-337.07269	-59	-337.056313	-16
$\text{I3}_{(4,1)}$	-337.11716	-176	-337.10029	-131
$\text{TS3P}_{\text{vic}(4,1)}$	-337.1135	-166	-337.094742	-117
$\text{P}_{\text{vic}(4,1)}$	-337.22397	-456	-337.192304	-373
$\text{TSP}_{\text{vic}} \text{P}_{\text{dis}(4,1)}$	-337.20507	-407	-337.175449	-329
$\text{P}_{\text{dis}(4,1)}$	-337.22438	-457	-337.205372	-407
$\text{TSP}_{\text{gem}} \text{P}_{\text{vic}(4,1)}$	-337.20852	-416	-337.17545	-329
$\text{TS3P}_{\text{gem}(4,1)}$	-337.09007	-105	-337.05264	-6
$\text{P}_{\text{gem}(4,1)}$	-337.22681	-464	-337.179527	-339

3. Observation and Mechanism of Cryo N₂ Cleavage by a Tantalum Cluster

Table S4. Calculated NPA charges in electrons (e) of atoms within I3_(4,1), TS3P_{(4,1)vic} and P_{(4,1)vic} in the doublet state.




	I3 _(4,1)	TS3P _{(4,1)vic}	P _{(4,1)vic}
			
Ta1	0.61512	0.60802	0.68992
Dif. *I3		-0.0071	0.0748
Dif. *TS3P_{(4,1)vic}			0.0819
Ta2	0.76117	0.85803	1.01663
Dif. *I3		0.09686	0.25546
Dif. *TS3P_{(4,1)vic}			0.1586
Ta3	0.67714	0.68491	0.69468
Dif. *I3		0.00777	0.01754
Dif. *TS3P_{(4,1)vic}			0.00977
Ta4	0.05111	0.04651	0.1791
Dif. *I3		-0.0046	0.12799
Dif. *TS3P_{(4,1)vic}			0.13259
N1	-0.57428	-0.64387	-0.78987
Dif. *I3		-0.06959	-0.21559
Dif. *TS3P_{(4,1)vic}			-0.146
N2	-0.53027	-0.5536	-0.79046

Table S5. Calculated energies of the cluster adsorbate complex $[\text{Ta}_4(\text{N}_2)_2]^+$ in the doublet state along the activation pathway of the second N_2 molecule depending on the adsorption site (Ta2, Ta3 or Ta4) to the $[\text{Ta}_4\text{NN}]^+$ cluster complex.

	N₂ adsorption on Ta3		N₂ adsorption on Ta4		N₂ adsorption on Ta2	
	energy E / Ha	ΔE / kJ/mol	energy E / Ha	ΔE / kJ/mol	energy E / Ha	ΔE / kJ/mol
$[\text{Ta}_4\text{NN}]^+, \text{N}_2$	-446.67025	0	-446.67025	0	-446.67025	0
I1_(4,2)	-446.68723	-45	-446.68591	-41	-446.69202	-57
TS12_(4,2)	-446.68534	-40	-446.67966	-25	-446.68012	-26
I2_(4,2)	-446.69788	-73	-446.70842	-100	-446.68996	-52
TS23_(4,2)	-446.67392	-10	-446.68283	-33	-446.64057	78
I3_(4,2)	-446.72388	-141	-446.73011	-157	-446.69561	-67
TS3P_(4,2)	-446.70106	-81	-446.71585	-120		
P_(4,2)	-446.80153	-345	-446.81452	-379		

3. Observation and Mechanism of Cryo N₂ Cleavage by a Tantalum Cluster

Table S6. Calculated distances in Å of atoms within [Ta₄NN]⁺ (P_{vic(4,1)}), N₂ and [Ta₄(N₂)₂]⁺ in the doublet state along the activation pathway of the second N₂ molecule on a [Ta₄NN]⁺ cluster complex at the adsorption site Ta3.


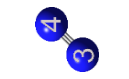

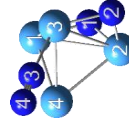
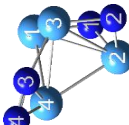





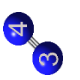






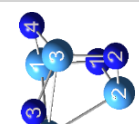
	P _{vic(4,1)}	N ₂	I1 _(4,2)	TS12 _(4,2)	I2 _(4,2)	TS23 _(4,2)	I3 _(4,2)	TS3P _(4,2)	P _(4,2)
									
Ta1-Ta2	2.80981		2.82055	2.81846	2.81562	2.79044	2.84153	2.83419	2.86942
Ta2-Ta3	2.80852		2.81321	2.8097	2.83041	2.77281	2.7486	2.74203	2.86981
Ta3-Ta4	2.58246		2.58503	2.57503	2.62351	2.72479	2.61416	2.6479	2.86977
Ta1-Ta4	2.57679		2.56888	2.55941	2.61602	2.61317	2.9945	2.9591	2.86938
Ta2-Ta4	2.61516		2.63087	2.62885	2.66096	2.79316	2.7182	2.75419	2.75944
Ta1-Ta3	2.69019		2.71185	2.72558	2.73453	2.66141	2.65038	2.6742	2.75968
Ta1-N1	1.83777		1.83769	1.83437	1.83017	1.81963	1.86045	1.86293	1.87286
Ta1-N3							2.14574	2.31351	
Ta1-N4							1.98228	1.89827	1.87311
Ta2-N1	1.89471		1.89627	1.89915	1.90254	1.92068	1.90306	1.89545	1.87305
Ta2-N2	1.89543		1.88368	1.87654	1.88278	1.837	1.8778	1.87783	1.87285
Ta3-N2	1.83664		1.85651	1.86706	1.85636	1.92233	1.87172	1.87342	1.87306
Ta3-N3			2.30132	2.15797	2.06218	2.00033	2.1264	2.10443	1.87283
Ta4-N3					2.13317	2.1527	2.0368	1.88939	1.87309
Ta4-N4				3.37324	2.24011	1.96456	1.98694	2.02749	1.87284
N3-N4		1.08948	1.09618	1.11553	1.17958	1.26022	1.44534	1.86585	

Table S7. Calculated distances in Å of atoms within $[\text{Ta}_4\text{NN}]^+$ ($P_{vic(4,1)}$), N_2 and $[\text{Ta}_4(\text{N}_2)_2]^+$ in the doublet state along the activation pathway of the second N_2 molecule on a $[\text{Ta}_4\text{NN}]^+$ cluster complex at the adsorption site Ta_4 .

	$P_{vic(4,1)}$	N_2	$\text{I1}_{(4,2)}$	$\text{TS12}_{(4,2)}$	$\text{I2}_{(4,2)}$	$\text{TS23}_{(4,2)}$	$\text{I3}_{(4,2)}$	$\text{TS3P}_{(4,2)}$	$P_{(4,2)}$
									
Ta1-Ta2	2.80981		2.83727	2.81923	2.84027	2.79306	2.82791	2.83734	2.89667
Ta2-Ta3	2.80852		2.83709	2.81664	2.81509	2.77074	2.82787	2.81818	2.89051
Ta3-Ta4	2.58246		2.58158	2.58516	2.65604	2.66614	2.61228	2.62146	2.80618
Ta1-Ta4	2.57679		2.58141	2.5747	2.60394	2.57583	2.61193	2.67172	2.73099
Ta2-Ta4	2.61516		2.72586	2.69287	2.68509	2.71478	2.6901	2.7219	2.73246
Ta1-Ta3	2.69019		2.67366	2.68907	2.72829	2.73086	3.13204	3.03091	2.88981
Ta1-N1	1.83777		1.84822	1.84722	1.83673	1.821	1.86045	1.87169	1.87684
Ta1-N3							2.00934	2.26048	
Ta1-N4							2.16871	1.91141	1.85197
Ta2-N1	1.89471		1.88124	1.88215	1.8974	1.91623	1.88128	1.87141	1.87634
Ta2-N2	1.89543		1.88112	1.90161	1.86633	1.86	1.88118	1.86907	1.85192
Ta3-N2	1.83664		1.84818	1.83024	1.87476	1.89818	1.86052	1.87643	1.90732
Ta3-N3				2.78782	2.13583	2.16181	2.16863	2.17606	1.93905
Ta3-N4					2.13585	2.18539	2.00921	1.9844	1.90715
Ta4-N3			2.28513	2.14424	2.01852	1.94927	1.94453	1.85692	1.82058
N3-N4		1.08948	1.09805	1.1171	1.19908	1.22114	1.45082	1.88124	3.22509

3. Observation and Mechanism of Cryo N₂ Cleavage by a Tantalum Cluster

Table S8. Calculated distances in Å of atoms within [Ta₄NN]⁺ (P_{vic(4,1)}), N₂ and [Ta₄(N₂)⁺] in the doublet state along the activation pathway of the second N₂ molecule on a [Ta₄NN]⁺ cluster complex at the adsorption site Ta2.

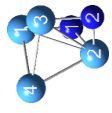





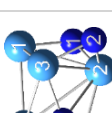
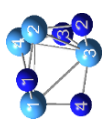
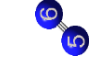

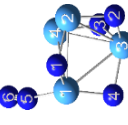
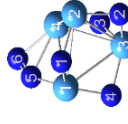
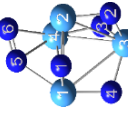

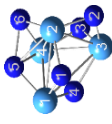
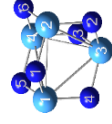
	P _{vic(4,1)}	N ₂	I1 _(4,2)	TS1 _{2(4,2)}	I2 _(4,2)	TS2 _{3(4,2)}	I3 _(4,2)
							
Ta1-Ta2	2.80981		2.81513	2.78882	2.79645	2.79156	2.80208
Ta2-Ta3	2.80852		2.81529	2.78883	2.79699	2.77467	2.6197
Ta3-Ta4	2.58246		2.58552	2.58659	2.63276	2.52906	2.95895
Ta1-Ta4	2.57679		2.58532	2.58658	2.63207	2.64573	2.582
Ta2-Ta4	2.61516		2.62512	2.62782	2.68194	2.65112	3.06341
Ta1-Ta3	2.69019		2.70673	2.70501	2.68166	2.7193	2.71683
Ta1-N1	1.83777		1.83311	1.83438	1.84518	1.8294	1.861
Ta2-N1	1.89471		1.90516	1.91897	1.9048	1.91194	1.88476
Ta2-N2	1.89543		1.90542	1.91897	1.90526	1.89714	1.9482
Ta2-N3			2.36296	2.14761	2.07339	2.19879	2.01995
Ta2-N4							2.39541
Ta3-N2	1.83664		1.83295	1.83437	1.84477	1.83515	1.83541
Ta3-N4							1.97752
Ta4-N3				2.60943	2.13529	2.13624	1.97593
Ta4-N4					2.2617	2.25311	2.01989
N3-N4		1.08948	1.09143	1.12419	1.18514	1.17595	1.43254

Table S9. Calculated distances in Å of atoms within $[\text{Ta}_4\text{NNNN}]^+$ ($\text{P}_{(4,2)}$), N_2 and $[\text{Ta}_4(\text{N}_2)_3]^+$ in the doublet state along the activation pathway of the third N_2 molecule on a $[\text{Ta}_4\text{NNNN}]^+$ cluster complex.

	$\text{P}_{(4,2)}$	N_2	$\text{I1}_{(4,3)}$	$\text{TS12}_{(4,3)}$	$\text{I2}_{(4,3)}$	$\text{TS23}_{(4,3)}$	$\text{I3}_{(4,3)}$	$\text{TS3P}_{(4,3)}$	$\text{P}_{(4,3)}$
									
Ta1-Ta2	2.89667		2.90994	2.87769	2.93005	2.85026	2.72582	2.76575	3.0643
Ta2-Ta3	2.89051		2.90311	2.92722	2.98695	3.01501	2.88929	2.86835	3.06265
Ta3-Ta4	2.80618		2.8047	2.82866	2.83734	2.94419	2.54255	2.57789	3.06413
Ta1-Ta4	2.73099		2.72676	2.71213	2.75695	2.67934	2.85667	2.9236	3.06575
Ta2-Ta4	2.73246		2.75834	2.76559	2.8308	2.75024	2.93891	2.89893	3.06486
Ta1-Ta3	2.88981		2.88935	2.83791	2.85544	3.05579	3.37458	3.38825	3.06333
Ta1-N1	1.87684		1.90147	1.906	1.90697	1.90828	1.83387	1.83147	1.88945
Ta1-N4	1.85197		1.85296	1.88849	1.87502	1.88057	1.97257	1.9503	1.8892
Ta1-N5			2.35714	2.18602	2.0513	2.18602	1.91426	1.89104	1.88959
Ta2-N1	1.87634		1.86135	1.86241	1.85264	1.85229	1.95201	1.96964	1.88959
Ta2-N2	1.85192		1.85731	1.85202	1.84419	1.85237	1.8486	1.85811	1.88944
Ta2-N5							2.34129	2.37533	
Ta2-N6							2.1297	2.04184	1.88967
Ta3-N2	1.90732		1.90617	1.9099	1.91809	1.89812	1.92122	1.91462	1.88953
Ta3-N3	1.93905		1.94295	1.94474	1.91172	1.87877	1.86091	1.85886	1.8894
Ta3-N4	1.90715		1.90975	1.89442	1.90933	1.88815	2.08733	2.04167	1.8898
Ta4-N3	1.82058		1.81801	1.81703	1.85547	1.88415	1.91334	1.91923	1.88949
Ta4-N5					2.1355	2.20318	2.16854	2.13948	1.88935
Ta4-N6					2.12976	2.20298	2.02923	1.94534	1.88927
N5-N6		1.08948	1.09095	1.11783	1.20694	1.2035	1.38899	1.86645	

3. Observation and Mechanism of Cryo N₂ Cleavage by a Tantalum Cluster

Table S10. Calculated energies of the cluster adsorbate complex [Ta₄(N₂)₃]⁺ in the doublet state along the activation pathway of the third N₂ molecule to the [Ta₄NNNN]⁺ cluster complex.

	energy E / Ha	ΔE in kJ/mol
[Ta ₄ NNNN] ⁺ , N ₂	-556.2608	0
I1 _(4,3)	-556.28521	-64
TS12 _(4,3)	-556.26904	-22
I2 _(4,3)	-556.29382	-87
TS23 _(4,3)	-556.23984	55
I3 _(4,3)	-556.28957	-76
TS3P _(4,3)	-556.25859	6
P _(4,3)	-556.35682	-252

Table S11. Calculated energies and vibrational frequencies of model systems (scaling factor: 0.9376).

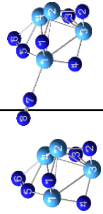
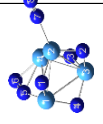
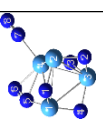
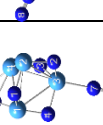
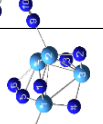
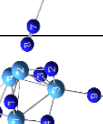
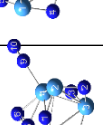
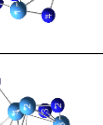
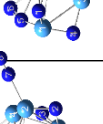
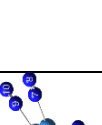
	$Ta_4(N_2)_2^+$			$[Ta_4(N_2)]^+$			$[Ta_4(N_2)]^+$						
	$I_{2(4,3)}$	$(4,4)_{top}$ *Ta1	$(4,4)_{top}$ *Ta2	$(4,4)_{top}$ *Ta3	$(4,4)_{top}$ *Ta4	$(4,4)_{top}$ *Ta5	$(4,5)_{top}$ *Ta1 *Ta3	$(4,5)_{top}$ *Ta1 *Ta2	$(4,5)_{top}$ *Ta1 *Ta3	$(4,5)_{top}$ *Ta1 *Ta4	$(4,5)_{top}$ *Ta2 *Ta3	$(4,5)_{top}$ *Ta2 *Ta4	$(4,5)_{top}$ *Ta3 *Ta4
energy E / Ha	-556.29382	-665.76333	-665.76489	-665.76485	-665.76475	-665.76485	-775.23182	-775.2347	-775.23182	-775.23465	-775.23609	-775.23499	-775.23499
energy E / kJ/mol		-1747961.382	-1747965.478	-1747964.848	-1747965.11	-1747964.848	-2035378.863	-2035378.424	-2035378.871	-2035378.293	-2035382.074	-2035379.186	-2035379.186
ΔE / kJ/mol		-1747961.382	-1747965.478	-1747964.848	-1747965.11	-1747964.848	-775.23182	-775.2347	-775.23182	-775.23465	-775.23609	-775.23499	-775.23499
$\nu_{(NNS)} / \text{cm}^{-1}$	1516.31	1473.52	1517.75	1475.3	1490.68	1475.3	1458.64	1474.1	1458.64	1423.29	1478.16	1475.63	1475.63
$\nu_{(NNS)}^{\text{scaled}} / \text{cm}^{-1}$	1422	1382	1423	1383	1388	1383	1368	1382	1368	1327	1386	1384	1384
$\nu_{(NNS)} / \text{cm}^{-1}$		2481.53	2461.79	2492.59	2403.02	2492.59	2480.81	2481.4	2480.81	2476.65	2415	2476.27	2476.27
$\nu_{(NNS)}^{\text{scaled}} / \text{cm}^{-1}$		2326.615362	2308.107672	2336.984918	2253.006511	2336.984918	2325.940309	2326.493477	2325.940309	2322.040006	2264.238634	2321.683728	2321.683728
$\nu_{(NNS)} / \text{cm}^{-1}$								2423.01	2491.86	2405.77	2488.26	2399.66	2399.66
$\nu_{(NNS)}^{\text{scaled}} / \text{cm}^{-1}$								2271.748594	2336.30049	2255.584836	2332.925228	2337.219312	2249.856266

3. Observation and Mechanism of Cryo N₂ Cleavage by a Tantalum Cluster

Table S12. Calculated distances in Å of atoms within model systems in the doublet state.

	Ta ₄ (N ₂) ₂ ⁺ I ₂ (c _{2v})	(4 ₄) _{top} -Ta1	(4 ₄) _{bot} -Ta2	[Ta ₄ (N ₂) ₂] ⁺	(4 ₄) _{top} -Ta3	(4 ₄) _{bot} -Ta4	(4 ₄) _{top} -Ta3	(4 ₄) _{bot} -Ta4	(4 ₅) _{top} -Ta1-Ta2	(4 ₅) _{top} -Ta1-Ta3	(4 ₅) _{bot} -Ta1-Ta4	[Ta ₄ (N ₂) ₂] ⁺	(4 ₅) _{top} -Ta4-Ta3	(4 ₅) _{bot} -Ta2-Ta3	(4 ₅) _{top} -Ta4-Ta3	(4 ₅) _{bot} -Ta2-Ta3	(4 ₅) _{top} -Ta2-Ta3	(4 ₅) _{bot} -Ta2-Ta4
Ta1-Ta2	2.93005	2.96352	2.92226	2.93769	2.91401	2.94426	2.92393	2.97832	2.92393	2.92393	2.97832	2.92393	2.92776	2.88943	2.92776	2.88943	2.92776	2.88943
Ta2-Ta3	2.98695	2.8486	2.97279	2.92539	3.02814	2.97279	2.98623	2.93948	2.92539	2.98623	2.93948	2.98623	3.02048	3.00167	3.02048	3.00167	3.02048	2.96424
Ta3-Ta4	2.83734	2.80566	2.84709	2.87449	2.88121	2.83583	2.87087	2.83913	2.84709	2.83583	2.87087	2.83913	2.91576	2.90965	2.91576	2.90965	2.91576	2.88324
Ta1-Ta4	2.75695	2.80731	2.77777	2.81097	2.73511	2.82968	2.77981	2.83961	2.80731	2.77981	2.83961	2.77981	2.76023	2.76349	2.76023	2.76349	2.76023	2.8256
Ta2-Ta4	2.8308	2.81436	2.83143	2.85005	2.82047	2.80704	2.81742	2.81862	2.81436	2.81742	2.81862	2.81742	2.82694	2.81037	2.82694	2.81037	2.82694	2.85432
Ta1-Ta3	2.85544	2.89859	2.86735	2.84297	2.89649	2.93278	2.95135	2.92159	2.86735	2.93278	2.95135	2.92159	2.9092	2.93339	2.9092	2.93339	2.9092	2.85337
Ta1-N1	1.90697	1.91016	1.9046	1.90687	1.91042	1.90379	1.91529	1.90849	1.91016	1.90379	1.90849	1.91529	1.91203	1.90209	1.91203	1.90209	1.91203	1.90645
Ta1-N4	1.87502	1.87323	1.87602	1.87156	1.88034	1.87655	1.87698	1.87425	1.87323	1.87655	1.87698	1.87425	1.88098	1.88406	1.88098	1.88406	1.88098	1.87392
Ta1-N5	2.0513	2.03829	2.05057	2.05122	2.04029	2.0344	2.031	2.03136	2.05122	2.0344	2.031	2.03136	2.02038	2.03561	2.02038	2.03561	2.02038	2.04693
Ta1-N7		2.3757				2.37482	2.39362	2.36477			2.37482	2.39362						
Ta2-N1	1.85264	1.85783	1.86394	1.85622	1.85238	1.87465	1.85735	1.86201	1.85264	1.85735	1.86201	1.85735	1.85336	1.87002	1.85336	1.87002	1.85336	1.8647
Ta2-N2	1.84419	1.84845	1.8562	1.84425	1.8521	1.86459	1.86124	1.84785	1.84419	1.86459	1.86124	1.84785	1.85194	1.87132	1.85194	1.87132	1.85194	1.8522
Ta2-N7			2.37603														2.32757	2.35998
Ta2-N9						2.35444												
Ta3-N2	1.91809	1.91638	1.91333	1.91866	1.91584	1.90728	1.90737	1.91846	1.91809	1.90728	1.90737	1.91846	1.91658	1.90478	1.91658	1.90478	1.91658	1.9166
Ta3-N3	1.91172	1.91774	1.91408	1.91217	1.90912	1.91659	1.91035	1.91568	1.91172	1.91659	1.91035	1.91568	1.9078	1.91285	1.9078	1.91285	1.9078	1.91335
Ta3-N4	1.90933	1.91615	1.91261	1.91253	1.91061	1.9165	1.91806	1.91141	1.90933	1.9165	1.91806	1.91141	1.90751	1.90943	1.90751	1.90943	1.90751	1.91301
Ta3-N7					2.38548													
Ta3-N9							2.39766						2.38438		2.38438		2.3876	
Ta4-N3	1.85547	1.8532	1.85431	1.85345	1.86258	1.85038	1.86262	1.8541	1.85547	1.85038	1.86262	1.8541	1.86273	1.85856	1.86273	1.85856	1.86273	1.85403
Ta4-N5	2.1355	2.12958	2.13941	2.1306	2.11912	2.13757	2.1166	2.122	2.1355	2.13757	2.1166	2.122	2.10771	2.12673	2.10771	2.12673	2.10771	2.13181
Ta4-N6	2.12976	2.12091	2.1243	2.17063	2.10878	2.11489	2.10592	2.16231	2.12976	2.11489	2.10592	2.16231	2.143	2.10529	2.143	2.10529	2.143	2.16701
Ta4-N7				2.2843				2.28743										
Ta4-N9													2.28335		2.28335		2.28658	
N5-N6	1.20694	1.21471	1.20768	1.20564	1.21669	1.21592	1.22442	1.21875	1.20694	1.21592	1.21875	1.22442	1.22772	1.21933	1.22772	1.21933	1.22772	1.20793
N7-N8	1.08882	1.08882	1.8956	1.09506	1.08629	1.08882	1.08881	1.08908	1.08882	1.08882	1.08881	1.08908	1.09308	1.09223	1.09308	1.09223	1.09308	1.08903
N9-N10						1.09173	1.08817	1.09311			1.09173	1.08817	1.08834	1.08818	1.08834	1.08818	1.08834	1.08919

Table S13. Calculated NPA charges in electrons (e) of atoms within model systems in the doublet state.

	$\Gamma_{2g}(N_2)_d^+$		$\Gamma_{2g}(N_2)_d^+$		$\Gamma_{2g}(N_2)_d^+$		$\Gamma_{2g}(N_2)_d^+$		$\Gamma_{2g}(N_2)_d^+$		$\Gamma_{2g}(N_2)_d^+$	
	$(4,4)_{000}$ *Ta1	$(4,4)_{401}$ *Ta2	$(4,4)_{402}$ *Ta4	$(4,4)_{403}$ *Ta3	$(4,5)_{000}$ *Ta2	$(4,5)_{002}$ *Ta1 *Ta3	$(4,5)_{401}$ *Ta1 *Ta4	$(4,5)_{402}$ *Ta4 *Ta3	$(4,5)_{411}$ *Ta2 *Ta3	$(4,5)_{410}$ *Ta2 *Ta4	npa	npa
												
Ta1	npa	npa	npa	npa	npa	npa	npa	npa	npa	npa		
	1.516	1.527	1.532	1.507	1.458	1.445	1.468	1.544	1.534	1.538		
Ta2	1.336	1.209	1.34	1.324	1.182	1.295	1.328	1.33	1.19	1.221		
Ta4	1.069	1.093	0.963	1.086	1.133	1.092	0.978	0.989	1.123	0.986		
Ta3	1.757	1.757	1.735	1.677	1.738	1.668	1.726	1.676	1.686	1.732		
N4	-1.022	-1.028	-1.017	-1.022	-1.027	-1.024	-1.017	-1.021	-1.031	-1.023		
N3	-1.003	-1.007	-0.988	-1.001	-1.003	-0.998	-0.985	-0.988	-1.004	-0.991		
N2	-1.014	-1.019	-1.013	-1.021	-1.021	-1.022	-1.016	-1.02	-1.026	-1.017		
N1	-0.988	-0.996	-0.996	-0.991	-1.001	-0.994	-1.002	-0.999	-0.999	-1.002		
N5	-0.426	-0.435	-0.433	-0.451	-0.438	-0.455	-0.455	-0.486	-0.454	-0.437		
N6	-0.224	-0.247	-0.207	-0.251	-0.256	-0.267	-0.241	-0.257	-0.256	-0.218		
N7	-0.105	-0.118	-0.123	-0.103	-0.102	-0.098	-0.101	-0.114	-0.125	-0.11		
N8	0.235	0.242	0.204	0.244	0.233	0.222	0.232	0.196	0.222	0.24		
N9					-0.121	-0.1	-0.114	-0.1	-0.103	-0.117		
N10					0.225	0.237	0.199	0.241	0.244	0.198		

References

1. C. Berg, T. Schindler, G. Niedner-Schatteburg and V. E. Bondybey, *The Journal of Chemical Physics*, 1995, **102**, 4870-4884.
2. V. E. Bondybey and J. H. English, *The Journal of Chemical Physics*, 1981, **74**, 6978-6979.
3. D. Proch and T. Trickl, *Review of Scientific Instruments*, 1989, **60**, 713-716.
4. P. Caravatti and M. Allemann, *Organic Mass Spectrometry*, 1991, **26**, 514-518.
5. M. Graf, Diploma Technische Universität Kaiserslautern, 2006.
6. T. Su and M. T. Bowers, *International Journal of Mass Spectrometry and Ion Physics*, 1973, **12**, 347-356.
7. I. Balteanu, O. P. Balaj, B. S. Fox-Beyer, P. Rodrigues, M. T. Barros, A. M. C. Moutinho, M. L. Costa, M. K. Beyer and V. E. Bondybey, *Organometallics*, 2004, **23**, 1978-1985.
8. G. Kummerlöwe and M. K. Beyer, *International Journal of Mass Spectrometry*, 2005, **244**, 84-90.
9. G. W. T. M. J. Frisch, H. B. Schlegel, G. E. Scuseria, M. A. Robb, J. R. Cheeseman, G. Scalmani, V. Barone, B. Mennucci, G. A. Petersson, H. Nakatsuji, M. Caricato, X. Li, H. P. Hratchian, A. F. Izmaylov, J. Bloino, G. Zheng, J. L. Sonnenberg, M. Hada, M. Ehara, K. Toyota, R. Fukuda, J. Hasegawa, M. Ishida, T. Nakajima, Y. Honda, O. Kitao, H. Nakai, T. Vreven, J. A. Montgomery, Jr., J. E. Peralta, F. Ogliaro, M. Bearpark, J. J. Heyd, E. Brothers, K. N. Kudin, V. N. Staroverov, T. Keith, R. Kobayashi, J. Normand, K. Raghavachari, A. Rendell, J. C. Burant, S. S. Iyengar, J. Tomasi, M. Cossi, N. Rega, J. M. Millam, M. Klene, J. E. Knox, J. B. Cross, V. Bakken, C. Adamo, J. Jaramillo, R. Gomperts, R. E. Stratmann, O. Yazyev, A. J. Austin, R. Cammi, C. Pomelli, J. W. Ochterski, R. L. Martin, K. Morokuma, V. G. Zakrzewski, G. A. Voth, P. Salvador, J. J. Dannenberg, S. Dapprich, A. D. Daniels, O. Farkas, J. B. Foresman, J. V. Ortiz, J. Cioslowski, and D. J. Fox, *Journal*, 2013.
10. M. J. Frisch, G. W. Trucks, H. B. Schlegel, G. E. Scuseria, M. A. Robb, J. R. Cheeseman, G. Scalmani, V. Barone, G. A. Petersson, H. Nakatsuji, X. Li, M. Caricato, A. V. Marenich, J. Bloino, B. G. Janesko, R. Gomperts, B. Mennucci, H. P. Hratchian, J. V. Ortiz, A. F. Izmaylov, J. L. Sonnenberg, Williams, F. Ding, F. Lipparini, F. Egidi, J. Goings, B. Peng, A. Petrone, T. Henderson, D. Ranasinghe, V. G. Zakrzewski, J. Gao, N. Rega, G. Zheng, W. Liang, M. Hada, M. Ehara, K. Toyota, R. Fukuda, J. Hasegawa, M. Ishida, T. Nakajima, Y. Honda, O. Kitao, H. Nakai, T. Vreven, K. Throssell, J. A. Montgomery Jr., J. E. Peralta, F. Ogliaro, M. J. Bearpark, J. J. Heyd, E. N. Brothers, K. N. Kudin, V. N. Staroverov, T. A. Keith, R. Kobayashi, J. Normand, K. Raghavachari, A. P. Rendell, J. C. Burant, S. S.

- Iyengar, J. Tomasi, M. Cossi, J. M. Millam, M. Klene, C. Adamo, R. Cammi, J. W. Ochterski, R. L. Martin, K. Morokuma, O. Farkas, J. B. Foresman and D. J. Fox, *Journal*, 2016.
11. J. P. Perdew, K. Burke and M. Ernzerhof, *Physical Review Letters*, 1996, **77**, 3865-3868.
 12. C. Adamo and V. Barone, *The Journal of Chemical Physics*, 1999, **110**, 6158-6170.
 13. F. Weigend and R. Ahlrichs, *Physical Chemistry Chemical Physics*, 2005, **7**, 3297-3305.
 14. D. Andrae, U. Häußermann, M. Dolg, H. Stoll and H. Preuß, *Theoretica Chimica Acta*, 1990, **77**, 123-141.
 15. C. Peng and H. Bernhard Schlegel, 1993, **33**, 449-454.
 16. L. Fan, D. Harrison, L. Deng, T. K. Woo, D. Swerhone and T. Ziegler, *Canadian Journal of Chemistry*, 1995, **73**, 989-998.
 17. K. Fukui, *Accounts of Chemical Research*, 1981, **14**, 363-368.
 18. F. Weinhold and J. E. Carpenter, in *The Structure of Small Molecules and Ions*, eds. R. Naaman and Z. Vager, Springer US, Boston, MA, 1988, DOI: 10.1007/978-1-4684-7424-4_24, pp. 227-236.
 19. E. D. Glendening, C. R. Landis and F. Weinhold, 2013, **34**, 1429-1437.
 20. T. A. Albright, J. K. Burdett and M. H. Whangbo, in *Orbital Interactions in Chemistry*, eds. T. A. Albright, J. K. Burdett and M. H. Whangbo, John Wiley & Sons, 2013, DOI: 10.1002/9781118558409.ch18, ch. 18, pp. 503-526.
 21. M. D. Fryzuk, S. A. Johnson and S. J. Rettig, *Journal of the American Chemical Society*, 1998, **120**, 11024-11025.
 22. M. Zhou, X. Jin, Y. Gong and J. Li, *Angewandte Chemie International Edition*, 2007, **46**, 2911-2914.
 23. Y. Gong, Zhao and M. Zhou, *The Journal of Physical Chemistry A*, 2007, **111**, 6204-6207.
 24. X. Cheng, Z.-Y. Li, L.-H. Mou, Y. Ren, Q.-Y. Liu, X.-L. Ding and S.-G. He, *Chemistry - A European Journal*, 2019, **25**, 16523-16527.
 25. M. D. Fryzuk, S. A. Johnson, B. O. Patrick, A. Albinati, S. A. Mason and T. F. Koetzle, *Journal of the American Chemical Society*, 2001, **123**, 3960-3973.

4 CRYO IR SPECTROSCOPY AND CRYO KINETICS OF DINITROGEN ACTIVATION AND CLEAVAGE BY SMALL TANTALUM CLUSTER CATIONS

4.1 Preamble

The following chapter is a reprint of a publication in the journal *“The Journal of Chemical Physics”*

The experiments were performed by M. P. Klein, A. Straßner, M. E. Huber and myself. I performed the calculations. M. Luczak and C. Wiehn assisted partially with experiments and calculations. The evaluation of the measured data was carried out by myself and it was accompanied by discussions with A. Straßner, M. P. Klein and G. Niedner-Schatteburg. I wrote the first full paper draft of the manuscript plus supplementary information, and G. Niedner-Schatteburg and I revised it together. Subsequently, it was revised and approved by all other authors.

Full Reference

Cryo IR Spectroscopy and Cryo Kinetics of Dinitrogen Activation and Cleavage by Small Tantalum Cluster Cations

D. V. Fries, M. P. Klein, A. Straßner, M. E. Huber, M. Luczak, C. Wiehn, G. Niedner-Schatteburg, *The Journal of Chemical Physics* **2023**, 159, 164303.

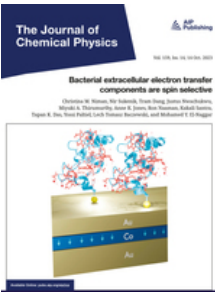
<https://doi.org/10.1063/5.0157217>

4. Cryo IR Spectroscopy and Cryo Kinetics of Dinitrogen Activation and Cleavage by Small Tantalum Cluster Cations

4.2 Reprint

Reprint permission

Reproduced with permission of AIP Publishing.



Cryo IR spectroscopy and cryo kinetics of dinitrogen activation and cleavage by small tantalum cluster cations

Author: Fries, Daniela V.; Klein, Matthias P.

Publication: Journal of Chemical Physics

Publisher: AIP Publishing

Date: Oct 24, 2023

Rights managed by AIP Publishing.

Creative Commons

This is an open access article distributed under the terms of the [Creative Commons CC BY](https://creativecommons.org/licenses/by/4.0/) license, which permits unrestricted use, distribution, and reproduction in any medium, provided the original work is properly cited.

You are not required to obtain permission to reuse this article.

Cryo IR spectroscopy and cryo kinetics of dinitrogen activation and cleavage by small tantalum cluster cations

Cite as: *J. Chem. Phys.* **159**, 164303 (2023); doi: [10.1063/5.0157217](https://doi.org/10.1063/5.0157217)

Submitted: 5 May 2023 • Accepted: 18 September 2023 •

Published Online: 24 October 2023



Daniela V. Fries, Matthias P. Klein, Annika Straßner, Maximilian E. Huber, Maximilian Luczak, Christopher Wiehn, and Gereon Niedner-Schatteburg

AFFILIATIONS

Department of Chemistry and State Research Center OPTIMAS, Rheinland-Pfälzische Technische Universität (RPTU) Kaiserslautern-Landau, 67663 Kaiserslautern, Germany

^{a)} Author to whom correspondence should be addressed: gns@rptu.de

ABSTRACT

We investigate small tantalum clusters Ta_n^+ , $n = 2-4$, for their capability to cleave N_2 adsorption spontaneously. We utilize infrared photon dissociation (IR-PD) spectroscopy of isolated and size selected clusters under cryogenic conditions within a buffer gas filled ion trap, and we augment our experiments by quantum chemical simulations (at DFT level). All Ta_n^+ clusters, $n = 2-4$, seem to cleave N_2 efficiently. We confirm and extend a previous study under ambient conditions on Ta_2^+ cluster [Geng *et al.*, *Proc. Natl. Acad. Sci. U. S. A.* **115**, 11680–11687 (2018)]. Our cryo studies and the concomitant DFT simulations of the tantalum trimer Ta_3^+ suggest cleavage of the first and activation of the second and third N_2 molecule across surmountable barriers and along much-involved multidimensional reaction paths. We unravel the underlying reaction processes and the intermediates involved. The study of the N_2 adsorbate complexes of Ta_4^+ presented here extends our earlier study and previously published spectra from (4,m), $m = 1-5$ [Fries *et al.*, *Phys. Chem. Chem. Phys.* **23**(19), 11345–11354 (2021)], up to $m = 12$. We confirm the priory published double activation and nitride formation, succeeded by single side-on N_2 coordination. Significant red shifts of IR-PD bands from these side-on coordinated μ_2 -κN:κN₂ N_2 ligands correlate with the degree of tilting towards the second coordinating Ta center. All subsequently attaching N_2 adsorbates onto Ta_4^+ coordinate in an end-on fashion, and we find clear evidence for co-existence of end-on coordination isomers. The study of stepwise N_2 adsorption revealed adsorption limits $m_{(max)}$ of $[Ta_n(N_2)_m]^+$ which increase with n , and kinetic fits revealed significant N_2 desorption rates upon higher N_2 loads. The enhanced absolute rate constants of the very first adsorbate steps $k_{(n,0)}^{abs}$ of the small Ta_3^+ and Ta_4^+ clusters independently suggest dissociative N_2 adsorption and likely N_2 cleavage into Ta nitrides.

© 2023 Author(s). All article content, except where otherwise noted, is licensed under a Creative Commons Attribution (CC BY) license (<http://creativecommons.org/licenses/by/4.0/>). <https://doi.org/10.1063/5.0157217>

INTRODUCTION

The natural nitrogen cycle consists of constant transformation of nitrogen between the earth's atmosphere, water, soils and biomass, and it is subject of anthropogenic interference that requires careful management strategies of the nitrogen budget.³⁻⁵ The industrial ammonia production from N_2 and H_2 is expensive in terms of energy consumption,⁶⁻⁸ yet irreplaceable, and at present it requires high amounts of fossil fuels as feedstocks. There are various protocols of NH_3 synthesis, and among them the Haber-Bosch process is most prominent.

It warrants to undertake knowledge driven research on the underlying processes which comprise the catalytic N_2 conversion, and much of the previous efforts in this regard have led to an award winning picture.⁹⁻¹¹ It is subject of ongoing research, and further optimization is mandatory.^{12,13} There are some comprehensive reviews that provide an overview of the current state of N_2 splitting reactions and follow-up nitrogen transfer reactivity proofs for a variety of transition metal (TM) and lanthanoid complexes.¹⁴⁻¹⁶ It was recognized that the N_2 coordination mode correlates with the propensity of N_2 functionalization, which in turn requires prior N_2 cleavage.¹⁷ An auspicious site for N_2 activation seem to originate

4. Cryo IR Spectroscopy and Cryo Kinetics of Dinitrogen Activation and Cleavage by Small Tantalum Cluster Cations

from isolated tantalum atoms on silica surfaces,¹⁸ and an N₂ side-on coordination seems critical.¹⁹

TM clusters receive ongoing attention as model systems for the study of elementary processes of catalytic relevance.^{20–22} Bare transition metal clusters of V, Gd and Sc are known to cleave N₂ spontaneously.^{23–25} Some homo- and hetero-metallic carbides were found to cleave N₂ and achieve C–N bond formation.^{26–29} Lithium doped TM complexes were also found to activate N₂.³⁰

Tantalum clusters are susceptible to oxide formation by O₂ and CO₂,^{31,32} and the stoichiometry of their oxides is known to affect N₂ uptake.³³ Similar effects and size dependencies arise in reactions with methane.^{34,35} Some prior studies on small tantalum clusters provide for evidence of dissociative N₂ adsorption. Geng *et al.* described the dinitride formation by Ta₂⁺ and Ta₂NN⁺ and elaborated crucial steps of the N₂ activation process by the tantalum dimer clusters.^{1,36} DFT modelling predicted N₂ cleavage by neutral and anionic trinuclear tantalum clusters,^{37,38} and there is further DFT modelling and some N₂ desorption experiments on small tantalum clusters, which supported conceivable N₂ cleavage.^{39,40}

While all of the above gained insights stem either from mass spectrometric experiments and/or quantum chemical modelling, it is an obvious need to provide additional spectroscopic characterization. A focus on cluster vibrations seems fertile. Inelastic electron scattering off N₂ layered Fe surfaces has proved valuable in this regard, and it helped to identify a characteristic 1555(30) cm⁻¹ feature as fingerprint of a likely precursor to N₂ dissociation while definite structural information remained sparse due to the limited spectral resolution.^{41,42} Infrared photon dissociation (IR-PD) spectroscopy may serve to complement, in particular when applied to isolated clusters and their complexes. Several studies utilized free electron lasers (FEL) and achieved similar or slightly better resolution.^{43–46} It is the table top sized Optical Parametric Oscillator (OPO) technology which augments FEL based research, and it enables the recording of sometimes better resolved spectra (±5 cm⁻¹) of e.g. isolated cluster adsorbate complexes, and this method is widely applicable and well established much beyond TM cluster research by now.^{47–56} In any case it is the quantum mechanical modelling – appropriately conducted by DFT base methods – which takes the quest for explicit reaction path modelling of such gas phase reactions of isolated species, and for identification of participating intermediates, electronic states, barriers and crucial transition state geometries.^{21,57,58}

Experimental results from such IR-PD vibrational spectra of Ta_n⁺ clusters, n = 6–20, complemented by theoretical modelling provide for the geometries of these clusters, their relative stabilities and electronic properties.^{59,60} A 2022 perspective summarizes recent progress in the field of nitrogen activation by metal species in the gas phase, but also shows that a systematic understanding of cluster reactivity and N₂ activation and functionalization is lacking to date.⁶¹

Our current studies pick up this prevailing deficiency. We complement our prior study on Ta₄⁺ and thereby clarify the overall picture by a systematic study of N₂ on small tantalum clusters Ta_n⁺, n = 2–8. We have reacted these clusters with N₂ at 26 K and recorded IR-PD spectra of the adsorption species [Ta_n(N₂)_m]⁺, similar to our earlier studies on Ni, Rh, RhFe and Fe clusters.^{62–67}

In the present study [IRS1] we discuss the N₂ adsorption onto the three smallest cluster Ta_{2–4}⁺. In the adjoined IR-PD study [IRS2] we present findings for the N₂ adsorption onto the larger clusters Ta_{5–8}⁺. The findings of both studies, which we refer in the following as [IRS1] and [IRS2], respectively, find strong support through our complementary cryogenic kinetic study (cf. supplementary material). The combination of IR-PD measurements and DFT modeling with kinetic studies provides insights into the processes and structures involved in the adsorption, activation, and subsequent cleavage of the first few adsorbed N₂ molecules by Ta_{2–4}⁺. Furthermore, we gain insight into the coordination motifs and structures of the clusters with additional N₂ molecules, adsorbed on the small clusters after nitride formation.

EXPERIMENTAL AND COMPUTATIONAL METHODS

All experimental results presented were recorded using a customized Fourier transform ion cyclotron resonance (FT-ICR) mass spectrometer. (Apex Ultra, Bruker Daltonics). This FT-ICR instrument is used to generate cluster ions, select them by size, and coordinate them with N₂. The investigation of the respective cluster adsorption species is performed by mass spectrometry and infrared photon dissociation (IR-PD) spectroscopy. We refer to some of our previous publications for a detailed description of ion generation and N₂ adsorption process on TM clusters.^{2,62,63,67–70} Text S3 in the supplementary material also provides a comprehensive description, especially for Ta_n⁺ clusters. According to the routine described there, the ions are trapped in a RF hexapole ion trap and detected in the cryogenic (~10 K) FT-ICR trapping cell. In this ICR cell, the respective cluster adsorbates are irradiated with a tunable IR laser system (1200–2400 cm⁻¹, cf. Fig. S1 for a laser power curve). Absolute values of the DFM frequencies were derived from the online monitored OPO signal frequencies (continuous online wavemeter monitoring, Bristol Instruments, 8721B-NIR) and the pre-recorded value of the Nd:YAG frequency. A full description of the details of the laser system and its parameters can be found in the attached infrared spectroscopy study of Ta_{5–8}⁺ cluster [IRS2]. We record a series of fragmentation mass spectra during continuous scanning of the IR wavelength and evaluate the fragmentation efficiency of the measured IR-PD signals: frag. eff. = $\frac{\sum_i F_i}{\sum_i F_i + \sum_i P_i}$, F_i and P_i as fragment and parent ion signals. Finally, we obtain the IR-PD spectra for each species by plotting the fragmentation efficiencies as functions of the laser frequencies. For all irradiated species, N₂ loss was the only fragmentation channel observed.

We performed density functional modelling, geometry optimization and vibrational analysis using the program packages Gaussian 09⁷¹ and Gaussian 16 suite.⁷² The functional PBE0^{73,74} along with the Def2-TZVP basis set^{75,76} were applied for all atoms in (4,m) cases, and the Def2-TZVP basis set⁷⁵ for N atoms and cc-pVTZ-pp basis set⁷⁷ for Ta atoms in all (2,m) and (3,m) cases. We justify our choice of theory level by continuity with previous studies that have succeeded in predicting N₂ adsorption before.^{64,67,69,70,78} – particularly for the adsorption, activation, and cleavage of N₂ on Ta₄⁺ clusters.² In all cases, we tolerated a relaxed SCF convergence criteria of 10⁻⁶ (as compared to 10⁻⁸ in “standard” DFT calculations) in order to achieve SCF convergence. All stationary points were checked for no and one imaginary frequency in cases of minima

and transition states, respectively. All conceivable isomers were optimized to stable minimum structures, and the most stable one was regarded as global minimum. Reaction paths were searched for by QST2/3^{79–81} and after location and optimization of the transition states calculated along the Intrinsic Reaction Coordinate (IRC).^{81,82} To better compare our results for the cleavage of N₂ on Ta₂⁺ with the results of Geng *et al.*¹ we also performed DFT modeling for the activation pathway with B3LYP hybrid functional,^{83,84} cf. Fig. S4. We applied a scaling factor of 0.9736 to the recorded IR-PD spectra of the cluster species (4,m), in order to account for the pre-weighing anharmonicities. Tables of unscaled IR-PD frequencies for all cases are documented in the supplementary material. Predicted and scaled IR frequencies were convoluted with gaussian profiles of fwhm = 5 cm⁻¹ in order to compare to the experimental IR-PD spectra.

DISCUSSION AND RESULTS

In addition to kinetic measurements [provided and discussed in the supplementary material (cf. Text S2 ff., Fig. S14 ff. and Table S26 ff.)], we extended our studies of N₂ adsorption on Ta_n⁺ clusters, n = 2–4, by IR-PD spectroscopy measurements of the N₂ adsorbates of these clusters under adiabatic conditions in the ion trap. Further IR-PD spectroscopy investigations of N₂ adsorption on Ta_n⁺ clusters, n = 5–8, can be found in our adjoined infrared study [IRS2].

We found a concise variation of recorded IR-PD features as a function of the Tantalum cluster size and of Nitrogen adsorbate loading. It is straightforward to assign these features to vibrational bands of the adsorbed N₂ chromophore. Frequent IR-PD features, in the majority of cases, locate in the range of 2000–2350 cm⁻¹. These features are fingerprinting N₂ moieties that correspond most likely to end-on adsorbates to single Tantalum centers with little to no interaction to other centers. This interpretation is in line with previously reported cases for Fe_n⁺,⁶⁷ Co_n⁺,⁶⁸ Ni_n⁺,^{62,63} Ru_n⁺,⁶⁹ Rh_n⁺⁷⁰ and even Ta₄⁺.² In several cases, we obtained IR-PD bands in the range of 1300–1700 cm⁻¹. In all cases but (4,3) these bands occur in addition to the afore mentioned ones.

The recorded IR-PD patterns distinguish by n, the Ta_n⁺ cluster size, in a remarkable way, and for a given n, they vary by m, the amount of N₂ adsorbate loading. We choose to organize the (n,m) matrix of IR-PD spectra in discussing these by given n per chapter one after the other.

[Ta₂(N₂)_m]⁺

First, we consider in detail the IR-PD spectrum of the smallest tantalum cluster adsorbate of the (n,m) matrix - the tantalum dimer species [Ta₂(N₂)₁]⁺: (2,1). In the range of 1900–2400 cm⁻¹ we observe no structured IR-PD signal (Fig. S2). This was to expect in view of previous DFT results which suggest swift activation of N₂ upon encounter to Ta₂⁺.¹ The resulting Ta–N stretching mode falls outside the available photon range of our current study. Nevertheless, we can confirm the claim that Ta₂⁺ adsorbs an N₂ molecule that is not terminally bound to the Ta₂⁺ dimer in an end-on coordination^{1,39} by noting the absence of experimental vibrational bands for (2,1) in the corresponding wavenumber range.

The work of Geng *et al.*¹ describes the initial formation of a “side-on/end-on binding mode” of the Ta₂⁺ N₂ complex as a

barrier-free process. Our own DFT modelling confirms an equivalent μ₂-κN:κN₂ coordination for the cases of Ta₃⁺ (see later in this work) and Ta₄⁺ (previous work²). However, in all three cases of Ta₂⁺, Ta₃⁺ and Ta₄⁺, we find an initial N₂ end-on coordination and an additional barrier towards the μ₂-κN:κN₂ motif (side-on/end-on binding mode). In the supplementary material (cf. Fig. S4) the reader finds a direct comparison of our results and those of Geng *et al.*, both conducted with the same DFT functional (B3LYP).

Both employed DFT functionals, PBE0 and B3LYP, predict a bare Ta₂⁺ dimer in a doubled state and somewhat less favorably in a quartet state. Both multiplicities provide for reaction pathways that run largely in parallel when computed by PBE0 (cf. Fig. 1), and with energy gaps of up to 30 kJ/mol at I2_(2,1) at the most. Some enhanced barriers at TS23_(2,1) and beyond in quartet states when computed at B3LYP level of theory (cf. Fig. S3). The predicted geometries (cf. Tables S2 and S4) of intermediates and barriers along the reaction path are comparable to those of Geng *et al.*¹ but for the missing entrance channel complex. In summary, a feasible and spontaneous N₂ bond cleavage by Ta₂⁺ seems well confirmed.

[Ta₃(N₂)_m]⁺

We recorded the IR-PD spectra of the tantalum trimer Ta₃⁺ with up to five N₂ adsorbate species, (3,m), throughout a wavenumber range of 1200–2400 cm⁻¹ (Fig. 2). The low yields of higher loaded adsorbate species (m > 5, cf. Fig. S21 in the supplementary material) hampered recording IR spectra of these.

The absence of any vibrational bands for the first three adsorbate complexes (3,1), (3,2) and (3,3) is striking. We have observed such behavior before, e.g. for the cases of (2,1), cf. above, and for (4,1) and (4,2).² It was explained by swift N₂ activation and cleavage after initial adsorption to the cluster surface. The case of (4,3) revealed a different behavior, and it seems to constitute a peculiar case: The third N₂ molecule initially adsorbs end-on to the tantalum tetramer and subsequently tilts into a coordination motif which is end-on and side-on across an edge of the tetramer (μ₂-κN1:κN1,N2). N₂ pre-activation gets stuck at this point and thereby provides for an IR fingerprint of this frozen intermediate, namely a highly red shifted NN stretching band at 1475 cm⁻¹. Thus, it seemed imperative to check for end-on and also for side-on coordination motifs in the cases of (3,m) species, and we chose the wavenumber range of our IR spectroscopic investigations accordingly. We found no evidence of a NN stretching vibrational band in the recorded IR spectra. This absence of NN stretching fingerprints hints towards a likely NN activation and a possible NN bond cleavage.

In contrast, the IR spectra of the species (3,4) and (3,5) reveal some broad vibrational bands in the range of 2100–2200 cm⁻¹ (Fig. 2). Nevertheless, it is obvious that the broad band of (3,4) comprises of several partially overlapping bands, likely three of them, peaking at about 2137, 2180, and 2204 cm⁻¹. When the above statement speculation of triple N₂ activation by Ta₃⁺ holds, it would be a single N₂ oscillator that causes the three observable bands in the recorded spectrum of (3,4). This finding might be taken as a strong indication for co-existing isomers, that might result from distinguishable Ta sites and their N nitrido load. Similarly, the IR spectrum of (3,5) reveals a clearly recognizable band pattern with a partially resolved sub structure. Besides the broad main band at 2146 cm⁻¹ there are two narrower side bands at 2173 and 2189 cm⁻¹.

4. Cryo IR Spectroscopy and Cryo Kinetics of Dinitrogen Activation and Cleavage by Small Tantalum Cluster Cations

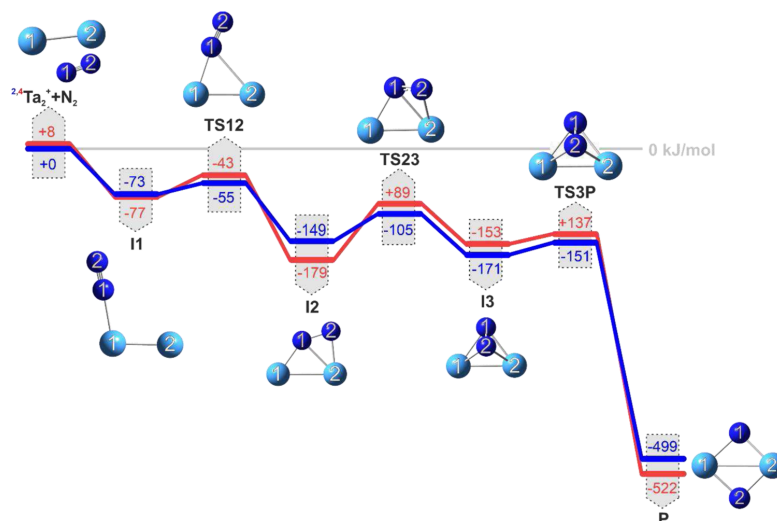


FIG. 1. Reaction pathway of N₂ cleavage by Ta₂⁺ (blue: doublet state, red: quartet state). Three submerged transition states allow for facile stepwise N₂ activation which ultimately leads to the dinitro product P_(2,1). Relative energies are in kJ/mol and displayed structures are those of doublet states with those of quartet states being very much comparable. For reason of clarity, the nomenclature is presented in an abbreviated form [e.g., I1 stands for I_{1(2,1)}].

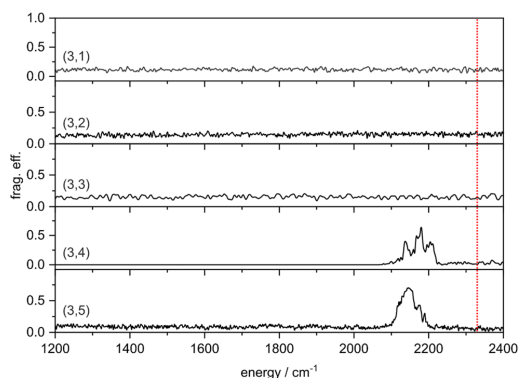


FIG. 2. IR spectra of Ta₃(N₂)_m⁺ [simplified nomenclature: (3,m)], m = 1–5 in the range of 1200–2400 cm⁻¹. Note the absence of vibrational bands in the cases of (3,1), (3,2) and (3,3). The bands in the cases (3,4) and (3,5) are significantly red shifted with respect to the free N₂ stretching vibrational frequency (2330 cm⁻¹,⁸⁵ red dotted line).

These three bands might indicate co-existing isomers as well. Due to the frequencies of the (3,4) and (3,5) bands, we assign them to N–N stretching vibrations of N₂ adsorbates which likely bind end-on to single tantalum centers – in line with previously reported cases of Fe_n⁺,⁶⁷ Co_n⁺,⁶⁸ Ni_n⁺,^{62,63} Rh_n⁺⁷⁰ and Ru_n⁺.⁶⁹ Furthermore, one

notices at first glance that the N₂ adsorbate bands for (3,4) and (3,5) are significantly redshifted with respect to the free N₂ stretching vibration frequency – –119.4 cm⁻¹ and –140.6 cm⁻¹, respectively – which would occur at 2330 cm⁻¹.⁸⁵ (Fig. 2 red line). This shift is much in line with a sigma donor – pi acceptor synergistic model as stated before for CO adsorption to TM surfaces – the Blyholder model,⁸⁶ and as stated before for CO coordination in TM complexes – the Dewar Chatt Duncanson model.⁸⁷ We have adopted like explanations before, in the course of our previous investigations of N₂ adsorption to other transition metal clusters, e.g. of Fe_n⁺,⁶⁷ Co_n⁺,⁶⁸ Ni_n⁺,^{62,63} Rh_n⁺⁷⁰ and Ru_n⁺.⁶⁹

DFT modelling (3,0) → (3,1)

In order to obtain mechanistic insights into the N–N bond cleavage by the tantalum triangle we undertook systematic DFT modelling and obtained activation pathways in singlet, triplet and quintet state (Fig. 3, blue for quintet state, red for triplet state and green for singlet state). The naked Ta₃⁺ is high spin, quintet or triplet, and less stable by 59 kJ/mol in singlet. Molecular N₂ adsorption reduces this gap but keeps relative stabilities and yields 82–112 kJ/mol adsorption enthalpy by μ₁-κN1 end-on coordination of N₂, intermediate I_{1(3,1)} and perpendicular to the Ta₃⁺ triangle. The ²I_{1(3,1)} intermediate on Ta₄²⁺ assumes same angles but a longer Ta–N distance, d(Ta1–N1) = 2.13 in ²I_{1(4,1)} as compared to d(Ta1–N1) = 2.05/2.07/2.09 Å in ¹I_{1(3,1)}/³I_{1(3,1)}/²I_{1(3,1)}. The interaction of molecularly adsorbed N₂ with Ta₃⁺ is thus somewhat more intimate than with Ta₄⁺, while spin state effects (such as high spin Pauli repulsion) are minor but discernible. In keeping with the prior

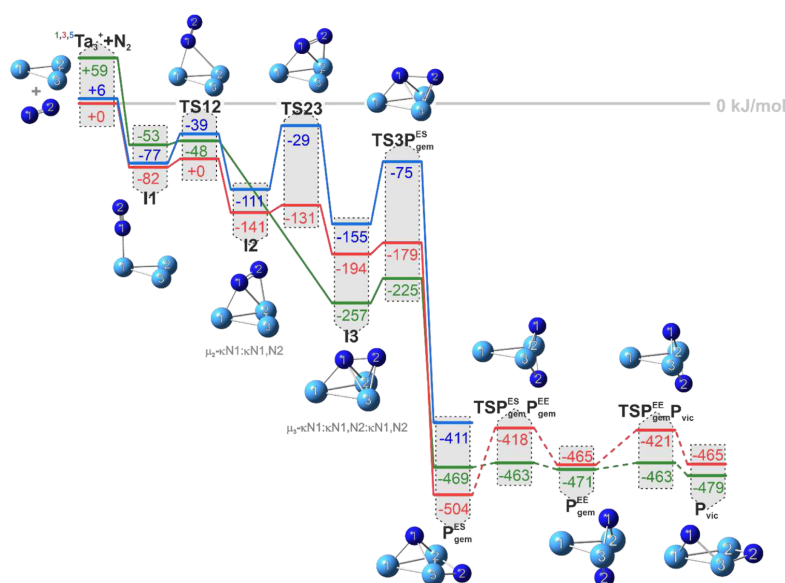


FIG. 3. Reaction pathways of N₂ cleavage by Ta₃⁺ (green: singlet state, red: triplet state, blue: quintet state). Three submerged transition states allow for facile stepwise activation which ultimately leads to the dinitro product P^{ES}_{gem(3,1)}. Conversion via barriers into two more stable dinitro isomers P^{EE}_{gem(3,1)} and P^{EE}_{vic(3,1)} is possible. The subscript abbreviations *gem* and *vic* as well as ES and EE indicate geminal and vicinal as well as edge/surface and edge/edge coordination, respectively. Further details and the naming of these coordination motifs are more explicitly described in the supplementary material. Relative energies are in kJ/mol and geometry structures are triplet states. Note the torsional reorganization of the AEAS mechanism from an initial in-plane μ_2 -κN1:κN1,N2 coordination across an intact Ta–Ta edge towards perpendicular μ_3 -κN1:κN1,N2:κN1,N2 coordination above the Ta–Ta–Ta surface. For reason of clarity, the nomenclature is presented in an abbreviated form [e.g. I1 stands for I1(3,1)].

notation of Ta₄⁺ N₂ adsorbate complexes we denote the I1(3,1) geometry of a sigma-bonded N₂ to a single Ta center as μ_1 -κN1.

As soon as N₂ switches towards end-on μ_2 -κN1:κN1 coordination bridging two Ta centers, the high spin quintet state becomes less favorable, which is much in line with our previous observation of spin quenching by N₂ adsorption.^{64,67} For all of the remaining pathway of N₂ cleavage the high spin quintet state runs above and in parallel to the singlet and triplet state pathways which are more stable, and we omit it in further discussion. The switching step occurs through the nitrogen ligand tilting slightly towards the neighboring Ta2 atom across the transition state TS12(3,1). The low barrier towards ³TS12(3,1) is +11 kJ/mol, and the low barrier towards ¹TS12(3,1) is +5 kJ/mol.

The singlet transition state ¹TS12(3,1) invokes no reorganization of the Ta₃⁺ triangle. The triplet transition state ³TS12(3,1) achieves its low barrier by significant elongation of the Ta1–Ta3 bond and concomitant shortening of the Ta2–Ta3 bond. As N1 moves in towards Ta2, Ta3 moves away from Ta1. In order to achieve the N₂ bridging configuration, the seeming “spectator” center Ta3 gives way and adopts. This works best in triplet configuration and it nicely illustrates the concept of induced fit among catalyst and substrate.

Beyond these transition states the further reaction pathways divert by spin state effects: The singlet state stabilizes directly towards the “above surface” intermediate ¹I3(3,1), and there is no stable “across edge” intermediate by our DFT modelling. In contrast, the triplet state does stabilize into an “above surface” coordinated intermediate ³I2(3,1) by −70 kJ/mol, which is −59 kJ/mol below ³I1(3,1). This energetics come close to the corresponding ones of the Ta₄⁺ case.² The bonding rearrangements are noteworthy: N₂ reorients from end-on coordination into a μ_2 -κN1:κN1,N2 asymmetric side-on coordination across a single edge of the Ta₃⁺ triangle. This comes with an additional N2–Ta2 interaction that occurs while Ta3 comes back towards Ta1 by −0.05 Å. Thus, Ta3 acts almost like a directing gatekeeper, swinging forth (cf. above) and back.

The ³I2(3,1) intermediate manages to continue a reaction pathway with a reorganization from its μ_2 coordination (across edge) to a μ_3 coordination (above surface), which is labelled μ_3 -κN1:κN1,N2:κN1,N2. This reorganization is the crucial step of the AEAS mechanism as observed in the case of Ta₄⁺ before.² The barrier across ³TS23(3,1) is noticeably shallow (10 kJ/mol), in contrast to the according ²TS23(4,1) barrier (+58 kJ/mol). Above surface coordination in the ³I3(3,1) structure is favorable by −53 kJ/mol with respect to ³I2(3,1).

4. Cryo IR Spectroscopy and Cryo Kinetics of Dinitrogen Activation and Cleavage by Small Tantalum Cluster Cations

While spin coupling in naked Ta_3^+ favored high spin, the above surface coordination of the pre-activated N_2 adsorbate enforces spin quenching: $^1\text{I}_{3(3,1)}$ is more stable than $^3\text{I}_{3(3,1)}$ by -63 kJ/mol. Both N_2 bond lengths in $^1\text{I}_{3(3,1)}$ and $^3\text{I}_{3(3,1)}$, $d(\text{N1-N2}) = 1.36$ and 1.43 Å, respectively, exemplify another case of progressive N_2 activation, similar to $^2\text{I}_{3(4,1)}$, where N_2 has elongated to 1.43 Å as well.³ The μ_3 coordinated N1 atom still experiences a C_3 symmetry breaking influence of its N_2 neighbor, which makes the opposite Ta1–N1 bond [$d(\text{Ta1-N2}) = 1.91$ Å] shorter by -0.24 Å than the Ta2–N1 and Ta3–N1 bonds [$d(\text{Ta2-N2}) = 2.15$ Å and $d(\text{Ta3-N2}) = 2.15$ Å].

Both $^1\text{I}_{3(3,1)}$ and $^3\text{I}_{3(3,1)}$ intermediates proceeds towards ultimate N_2 bond cleavage via $^1/3\text{TS3P}^{\text{ES}}_{\text{gem}(3,1)}$ across a barrier of $+32$ and $+15$ kJ/mol, respectively. At the transition states the N–N bond is further elongated by $+0.25$ to $+0.4$ Å with respect to the $\text{I}_{3(3,1)}$ states, and the N–N bond gets eventually lost towards the $\text{P}^{\text{ES}}_{\text{gem}(3,1)}$ product states, which is a remarkably exothermic process in all cases of spin states, -212 to -310 kJ/mol.

The nitride geometry of the favored $^3\text{P}^{\text{ES}}_{\text{gem}(3,1)}$ product state as displayed (Fig. 3) exemplifies singlet and quintet structures closely with some minor differences (cf. Tables S8–S11). It possesses a nitride atom each above the Ta triangle and across an edge (index ES for edge/surface). The μ_3 coordinated N1 atom shrinks its bond lengths towards all three Ta centers slightly by mere -0.05 Å with respect to $^3\text{I}_{3(3,1)}$. It however conserves its μ_3 coordination asymmetry of about -0.25 Å difference in Ta–N bond lengths as observed in $^3\text{I}_{3(3,1)}$. Thus, the C_3 symmetry breaking influence of N_2 is conserved even while it migrates around the Ta2–Ta3 axis, and while the pre-activated N1–N2 bond is cleaved.

In addition to the dinitro product $\text{P}^{\text{ES}}_{\text{gem}(3,1)}$ described above, we managed to identify two more stable $[\text{Ta}_3(\text{NN})]^+$ dinitro isomers: $\text{P}^{\text{EE}}_{\text{gem}(3,1)}$ and $\text{P}^{\text{EE}}_{\text{vic}(3,1)}$. The former, $\text{P}^{\text{EE}}_{\text{gem}(3,1)}$, is characterized by the fact that the two N atoms locate across the same edge of the Ta3 triangle, the slightly elongated Ta2–Ta3 bond. Therefore, we denote this isomer with the indices *gem* (geminal, over the same edge) and *EE* (edge/edge). In the latter isomer, $\text{P}^{\text{EE}}_{\text{vic}(3,1)}$, the two N atoms locate across two adjacent edges, denoted vicinal (*vic*). All three isomers have achieved full N–N bond cleavage. Each of the three product isomers, $\text{P}^{\text{ES}}_{\text{gem}(3,1)}$, $\text{P}^{\text{EE}}_{\text{gem}(3,1)}$ and $\text{P}^{\text{EE}}_{\text{vic}(3,1)}$, provides for singlet and triplet states which are significantly lower than I_3 , but vary in relative stabilities: The singlet states of the three isomers are almost degenerate (± 10 kJ/mol) and they may easily convert into each other via low barriers ($+6$ to $+16$ kJ/mol). The triplet states behave differently: $^3\text{P}^{\text{EE}}_{\text{gem}(3,1)}$ and $^3\text{P}^{\text{EE}}_{\text{vic}(3,1)}$ are less stable than $^3\text{P}^{\text{ES}}_{\text{gem}(3,1)}$, by about 39 kJ/mol, and the transition states come along with significant barriers of up to $+86$ kJ/mol. We therefore consider the most stable $^3\text{P}^{\text{ES}}_{\text{gem}(3,1)}$ as most likely product of the N_2 activation pathway.

In summary, the identified reaction path by our DFT modelling is overall declining (-504 kJ/mol) with all submerged barriers. Initial triplet and quintet states of Ta_3^+ seem to quench into the singlet $^1\text{I}_{3(3,1)}$ intermediate by N_2 coordination and exoergic activation, and the reaction proceeds towards ultimate N_2 cleavage via another spin flip, likely into most stable triplet state of geminal edge-surface N–N coordination. Most noteworthy, this Ta_3^+ activation pathway proceeds much in line with our previously identified across edge above surface (AEAS) mechanism of Ta_4^{2+} and shows similarities to the predicted N_2 cleavage at neutral an anionic $\text{Ta}_3^{0/+}$ clusters.^{37,38}

DFT modelling (3,1) → (3,2)

Previously, we found that Ta_4^+ manages to cleave subsequently two N_2 molecules as evidenced by the absence of IR fingerprint of coordinated and intact N_2 molecules for the first and the second Ta_4^+ adsorption species.² Here, we checked for a second NN triple bond cleavage by Ta_3^+ . The recorded IR spectra of $[\text{Ta}_3(\text{N}_2)_2]^+$ revealed no NN stretching bands between 1200 and 2400 cm^{-1} . This provides strong indication for a facile activation of a second N_2 molecule. In order to substantiate these findings we undertook DFT modelling, and we worked to find conceivable adsorption and activation pathways for a second N_2 molecule starting with the dinitro $\text{P}^{\text{ES}}_{\text{gem}(3,1)}$ as identified above (cf. Fig. 4). We consider singlet and triplet states and thus start with $^1\text{P}^{\text{ES}}_{\text{gem}(3,1)} + \text{N}_2$ and $^3\text{P}^{\text{ES}}_{\text{gem}(3,1)} + \text{N}_2$. All three Ta centers may act as coordination sites for a second N_2 adsorbate, Ta2 and Ta3 being equivalent due to C_s symmetry of $\text{P}^{\text{ES}}_{\text{gem}(3,1)}$. Thus, the DFT modelling yields four conceivable pathways for a second N_2 adsorption and activation: two singlet pathways, 1a and 1b, and two triplet pathways, 3a and 3b, each starting either through N_2 adsorption to Ta1 (pathways a) or to Ta3 (pathways b) (Fig. 4, dark green, light green, red, orange). Initial adsorption of the N_2 molecule yields intermediates $^1\text{I}_{1(3,2)}$, $^1\text{I}_{1(3,2)}$, $^3\text{I}_{1(3,2)}$, or $^3\text{I}_{1(3,2)}$ all of which possess the well-known end-on coordination of the N_2 either to Ta1 or to Ta3. The N_2 orients perpendicular to the Ta–Ta–Ta triangular facet at both sites. Among these four intermediates the triplet state of N_2 coordination to the Ta3 atom is most stable [$^3\text{I}_{1(3,2)}$: -91 kJ/mol with respect to the triplet entrance channel].

As observed before in the cases first and second N_2 activation by Ta_4^+ , and in the present case of first N_2 activation by Ta_3^+ , the end-on bound N_2 ligand of the four $\text{I}_{1(3,2)}$ intermediate states bend towards the neighboring Ta atom via four transition states $\text{TSI}_{2(3,2)}$ that comprise for barriers of $+27$ to $+73$ kJ/mol. These reorganizations eventually yield the $\text{I}_{2(3,2)}$ intermediates with the N_2 ligand coordinated in a μ_2 -κN3:κN3,N4 fashion, which is side-on across an edge of the Ta_3^+ cluster core, the Ta1–Ta3 bond. Note, that the two a pathways and the two b pathways encompass same kinetic motifs – the N_2 bending towards an across edge coordination – but in opposing directions: from Ta1 towards Ta3, pathways a, and vice versa from Ta3 towards Ta1, pathways b. Note furthermore, that singlet spin states become more stable than triplet states in $\text{I}_{2(3,2)}$, no matter which structure, a and b alike.

The next step of N_2 activation by the AEAS mechanism would involve a reorganization of the N_2 ligand from the μ_2 -κN3:κN3,N4 side-on coordination across an Ta–Ta edge in $\text{I}_{2(3,2)}$ towards an μ_3 -κN3:κN3,N4:κN3,N4 above surface coordination. By and large, this is what our DFT modeling yields in the present case, once more.

Along the b pathways, the reorganizations from $^1\text{I}_{2(3,2)}$ and $^3\text{I}_{2(3,2)}$ proceed via unfavorable $^1\text{bTS23}_{(3,2)}$ ($+122$ kJ/mol) and $^3\text{bTS23}_{(3,2)}$ ($+70$ kJ/mol) directly into $^1\text{I}_{3(3,2)}$ and $^3\text{I}_{3(3,2)}$. The high barriers seem to originate from N–N repulsion among N3 (of second N_2) and N2 (of first N_2). Subsequent N4 movement into final μ_2 coordination in I_3 seems facile, and it proceeds directly. N4 is not hindered by N1, and there is no further intermediate involved.

Instead, the pathways involve additional intermediates $^1\text{aI}_{23(3,2)}$ and $^3\text{aI}_{23(3,2)}$ connecting the respectively $^1\text{I}_{2(3,2)}$ and $^3\text{I}_{2(3,2)}$ states via consecutive transition states $^1\text{aTS223}_{(3,2)}$ and $^3\text{aTS223}_{(3,2)}$. The

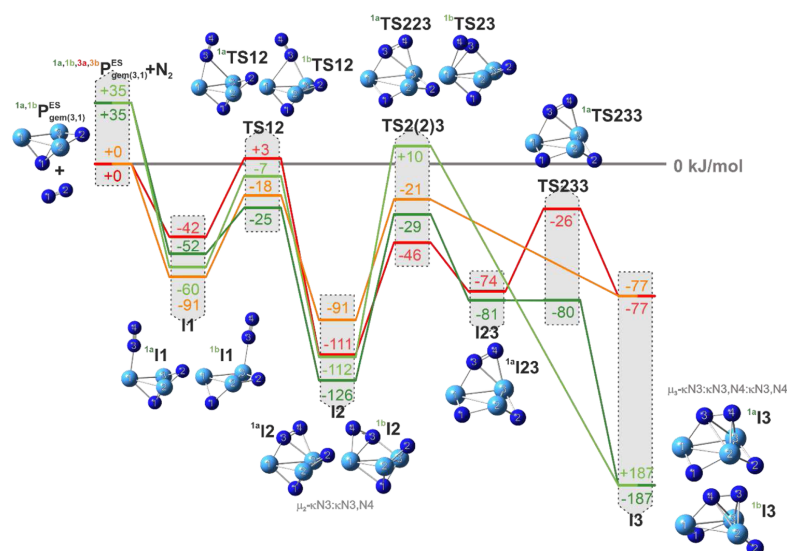


FIG. 4. Reaction pathways of a second N_2 activation by the dinitro species $P_{gem(3,1)}^{ES}$: two singlet pathways, 1a (dark green) and 1b (light green), and two triplet pathways, 3a (red) and 3b (orange), each of them starting either through N_2 adsorption to Ta1 (pathways a) or to Ta3 (pathways b). There is a striking similarity to the first cleavage pathway cf. Fig. 3: reorganization of the in-plane μ_2 - $\kappa N3:\kappa N3,N4$ coordination across an intact Ta–Ta edge towards perpendicular μ_3 - $\kappa N3:\kappa N3,N4:\kappa N3,N4$ coordination above the Ta–Ta–Ta surface. Starting from the most likely product complex $P_{gem(3,1)}^{ES}$ of the activation pathway of the first N_2 molecule by Ta_3^+ the pathway for a second N_2 molecule activation yields in the intermediate $I_{3(3,2)}$ which is independent of initial N_2 coordination to the Ta1 (paths a) or Ta3 (paths b) atom and gets stuck in front of unsurmountable barriers that hamper any further or ultimate NN bond cleavage (cf. Fig S5). For reason of clarity, the nomenclature is presented in an abbreviated form [e.g. I1 stands for $I_{1(3,2)}$].

${}^aTS_{223(3,2)}$ transition states are more stable than the ${}^bTS_{23(3,2)}$ of b pathways. ${}^aTS_{223(3,2)}$ does not suffer N–N repulsion, as both nitrido atoms N1 and N2 (originating from the first N_2 adsorbate) locate below the Ta₃ plane. However, N₂ needs to wag around the Ta₂–Ta₃ bond and further below the Ta₃ plane in order to allow for N₄ to locate above the Ta₁–Ta₂ edge. This N₂ downwards wagging becomes possible through concerted N1 upwards wagging around the Ta₁–Ta₂ bond, and it brings the cluster complex into ${}^{1a}I_{23}$ or ${}^{3a}I_{23}$. Spin state seems of little importance up to here. In contrast, the barriers towards ${}^{1a}I_{3(3,2)}$ or ${}^{3a}I_{3(3,2)}$ vary by spin states, with some uncertainty remaining. The influence of spin coupling increases significantly towards the next intermediate $I_{3(3,2)}$.

The reorganization from $I_{2(3,2)}$ to $I_{3(3,2)}$ occurs in concerted manner way via the b pathway (a single TS) or in a consecutive manner via the a pathway (two TSs).

At this point, the modelled activation pathways yield in the intermediate $I_{3(3,2)}$ which is independent of initial N_2 coordination to the Ta1 (paths a) or Ta3 (paths b) atom. $I_{3(3,2)}$ comprises of an μ_3 - $\kappa N3:\kappa N3,N4:\kappa N3,N4$ above surface coordination of the second N_2 adsorbate with an enlarged N₃–N₄ bond length of $d(N_3-N_4) = 1.36 \text{ \AA}$.

Note, that the two N atoms of the fully activated first N_2 adsorbate, N1 and N2, underwent reorganization from prior edge/surface

(ES) coordination in $P_{gem(3,1)}^{ES}$ into an edge/edge (EE) motif in $I_{3(3,2)}$. It seems as if the N atom which was coordinated above the Ta–Ta–Ta triangle surface had to finally give way for the I₃ above surface coordination of the second N_2 ligand.

Most notably, the singlet triplet splitting becomes of importance in $I_{3(3,2)}$. It rises up to 110 kJ/mol in favor of singlet ${}^1I_{3(3,2)}$, which is three times higher than at the starting point $P_{gem(3,1)}^{ES} + N_2$. N_2 adsorbate induced spin quenching sets in at this point, much in line with what was observed by us in some cases before.^{64,67}

At this point further activation of the second N_2 molecule in $[Ta_3(NN)(N_2)_1]^+$ would proceed in principle from singlet ${}^1I_{3(3,2)}$, -187 kJ/mol beneath the entrance channel, while the triplet ${}^3I_{3(3,2)}$ is not populated. However, any found pathway towards ultimate N_2 bond cleavage would imply to surmount significant barriers [$+154 \text{ kJ/mol}$, $+190 \text{ kJ/mol}$ or $+221 \text{ kJ/mol}$ above ${}^1I_{3(3,2)}$, cf. Fig S5 in the supplementary material, which we consider unlikely. The adsorption and activation pathways seem to get stuck at ${}^1I_{3(3,2)}$ in front of these barriers which have unsurmountable under isothermal conditions.

Reviving the absence of N_2 fingerprints between 1200 and 2400 cm^{-1} in the experimental IR spectrum of the $[Ta_3(N_2)_2]^+$ adsorbate species, for which we therefore expect a complete cleaved NN bond even for the second N_2 molecule by Ta_3^+ , it is a urgent

4. Cryo IR Spectroscopy and Cryo Kinetics of Dinitrogen Activation and Cleavage by Small Tantalum Cluster Cations

need to check the calculated IR frequency of the $I_{3(3,2)}$ above surface coordination of the second N_2 ligand. And indeed, DFT calculations revealed a frequency at 1093 cm^{-1} for the respective NN stretching mode. Thus, the enlargement of the NN bond to 1.36 \AA is sufficient to shift the NN stretching mode outside our currently accessible spectral range of measurements.

In summary we can conclude at this point that successful and facile cleavage of a first N_2 molecule by Ta_3^+ is followed by the second N_2 molecule proceeding via similar activation steps: from initial end-on coordination through a second intermediate, with a $\mu_2\text{-}\kappa N_3:\kappa N_3, N_4$ bonded N_2 across an edge of the Ta_3^+ triangle core towards a $\mu_3\text{-}\kappa N_3:\kappa N_3, N_4:\kappa N_3, N_4$ bonded N_2 ligand at intermediate $I_{3(3,2)}$. The cluster complex seem to get stuck in $I_{3(3,2)}$ in front of barriers that hamper further activation (N3–N4 bond enlargement beyond 1.36 \AA) under isothermal conditions. Whether ultimate NN bond cleavage into P_{gem} products (Fig. S5) does take place, depends on the experimental conditions. Verification would be subject of further spectroscopic verification, e.g. by the recording of TaN nitride fingerprint patterns through far IR radiation exposure by a free electron laser.

DFT modelling (3,2) \rightarrow (3,3)

We checked for feasible adsorption pathways of a third N_2 molecule to the Ta_3^+ cluster, and we started with singlet $^1I_{3(3,2)}$, a likely product of the second N_2 adsorption (cf. Fig. 5). The $I_{3(3,2)}$ structure provides for two preferential N_2 coordination sites, Ta1 and Ta3, the Ta2 suffering from steric hindrance. Thus, we conceive two distinguishable coordination motifs for initial end-on N_2 adsorption: $^1aI_{3(3,3)}$ for N_2 adsorption to Ta1 (Fig. 5, dark green pathway) and $^1bI_{3(3,3)}$ for N_2 adsorption to Ta3 (Fig. 5, light green pathway), both intermediates being almost degenerate.

Subsequent tilting towards the neighboring Ta cluster core atom proceeds via $^1aTS_{12(3,3)}$ and $^1bTS_{12(3,3)}$ with barriers just below the entrance channel (-3 and -4 kJ/mol) and yield $^1aI_{2(3,3)}$ and $^1bI_{2(3,3)}$, respectively. As coordination motif of the $I_{2(3,3)}$ intermediates we found the N_2 ligand to be coordinated in a $\mu_2\text{-}\kappa N_5:\kappa N_5, N_6$ fashion, which is side-on across an edge of the Ta_3^+ cluster core, the Ta1–Ta3 bond. Note, that the a pathway and the b pathway encompass same kinetic motifs – the N_2 bending towards an across edge coordination – but in opposing directions: from Ta1 towards Ta3, pathways a, and vice versa from Ta3 towards Ta1, pathways b. Although both $I_{2(3,3)}$ intermediates are $+19\text{ kJ/mol}$ or rather $+13\text{ kJ/mol}$ less stable than the respective $I_{1(3,3)}$ intermediates both are [$^1aI_{2(3,3)}$: -35 kJ/mol , $^1bI_{2(3,3)}$: -42 kJ/mol] significantly more stable than the entrance channel.

A consecutive step of N_2 activation by the AEAS mechanism would involve a reorganization of the N_2 ligand from the $\mu_2\text{-}\kappa N_5:\kappa N_5, N_6$ side-on coordination across an Ta–Ta edge in $I_{2(3,2)}$ towards a $\mu_3\text{-}\kappa N_5:\kappa N_5, N_6:\kappa N_5, N_6$ above surface coordination. However, the Ta_3^+ cluster core is quiet highly loaded from the two prior N_2 adsorptions at this point, and another μ_3 above surface coordination seems unlikely. Instead we managed to find a feasible reorganization, via transition states $^1aTS_{2III(3,3)}$ and $^1bTS_{2III(3,3)}$, from the $I_{2(3,2)}$ $\mu_2\text{-}\kappa N_5:\kappa N_5, N_6$ single side-on N_2 motif into a $\mu_2\text{-}\kappa N_5, N_6:\kappa N_5, N_6$ double side-on “butterfly” N_2 motif across the Ta1–Ta3 edge, yielding a single $^1a, ^1bIII_{3(3,3)}$ intermediate, as identified in (2,1) before.¹

In the present (3,3) case, the intermediate $^1a, ^1bIII_{3(3,3)}$ is $+38\text{ kJ/mol}$ less stable than the entrance channel. Further reorganization into an about -18 kJ/mol more stable cluster adsorbate species $IV_{3(3,3)}$ would require to surmount a barrier of $+180\text{ kJ/mol}$ ($TS_{III\ IV_{3(3,3)}}$), which seems unlikely.

At this point we like to correlate this predicted reaction path to our experimental IR spectroscopic findings. We aim to identify the actually populated product, and we take the intermediates $^1aI_{1(3,3)}$ and $^1bI_{1(3,3)}$ or $^1aI_{2(3,3)}$ and $^1bI_{2(3,3)}$ as well as $^1a, ^1bIII_{3(3,3)}$ into account. The $^1aI_{1(3,3)}$ and $^1bI_{1(3,3)}$ intermediates should provide for recordable IR fingerprints of end-on NN stretching vibration in the range of $2000\text{--}2400\text{ cm}^{-1}$.^{2,62,63,67–70} The absence of such fingerprints in our recorded (3,3) IR spectrum discards these intermediates. Predicted IR frequencies of tilted N_2 stretching vibration in $^1aI_{2(3,3)}$ and $^1bI_{2(3,3)}$ are 1816 and 1764 cm^{-1} , respectively (unscaled values). No according IR signals recorded we abandon these intermediates as well. The remaining $III_{3(3,3)}$ intermediate provides for predicted NN stretching frequencies below 1144 cm^{-1} (unscaled), which is in line with our observations.

So far DFT calculations are in line with our IR measurements. However, we have to address explicitly the fact that the intermediate $III_{3(3,3)}$ is $+38\text{ kJ/mol}$ less stable than the entrance channel. At this point it seems helpful to consider the big picture of consecutive N_2 adsorption to Ta_3^+ (cf. Fig. 6): The tantalum trimer manages to cleave the first adsorbed N_2 molecule (cf. Fig. 3, reaction path by DFT) and the subsequent adsorption of a second N_2 likely starts at $^3P_{gem}^{ES(3,1)}$, and it yields $^1I_{3(3,2)}$ (see Fig. 4, reaction path by DFT). By these two highly exothermic adsorption events, this $^1I_{3(3,2)}$ adsorption complex has stabilized by more than 600 kJ/mol . While the He buffer gas is certainly able to thermalize the stored ionic complex on the long run, it certainly takes a multitude of He collisions to achieve full thermalization. Thus, it is likely that $^1I_{3(3,2)}$ possess some internal energy when subsequently encountering a further N_2 partner. Thereby it becomes possible to explore the (3,3) potential hypersurface along a direct reaction up to $^1III_{3(3,3)}$ (cf. Fig. 5, reaction path by DFT) where it might get stuck in front of a seemingly unsurmountable barrier. Of course, it is conceivable to invoke the alternative possibility of a third N_2 addition and reaction to a fully activated $Ta_3N_4^+$ moiety in P_{gem} configuration (Fig. S5). DFT modelling and far IR spectral verification would be subject of future works.

Our further DFT modelling suggests swift adsorption of the fourth N_2 partner without further barriers and into some stable N_2 end-on coordination. It seems likely that $^1a, ^1bIII_{3(3,3)}$ sustains its priorly achieved structural motifs: an I_3 above surface coordination motif, one double-bridged triangular edge and two one single-bridged triangular edge. In effect, the additional end-on coordinating N_2 ligand may assume any of three available adsorption sites, Ta1, Ta2 or Ta3. These differ in the number of nearest neighbors. Geometry optimization of the singlet states of these resulting three isomers yield almost degenerate states $^1(3,4)^{Ta1}$, $+8\text{ kJ/mol}$, $^1(3,4)^{Ta2}$, and $^1(3,4)^{Ta3}$, $+6\text{ kJ/mol}$. Accordingly we expect all three isomers likely populated, and three slightly different IR active NN stretching frequencies. Indeed, the (3,4) IR-PD spectrum comprises of three partially resolved bands which strongly support the likely presence of end-on coordinated N_2 ligands in any of three different coordination sites. The DFT modelling provides for predictions on the harmonic frequencies of the N_2 stretching vibrations at

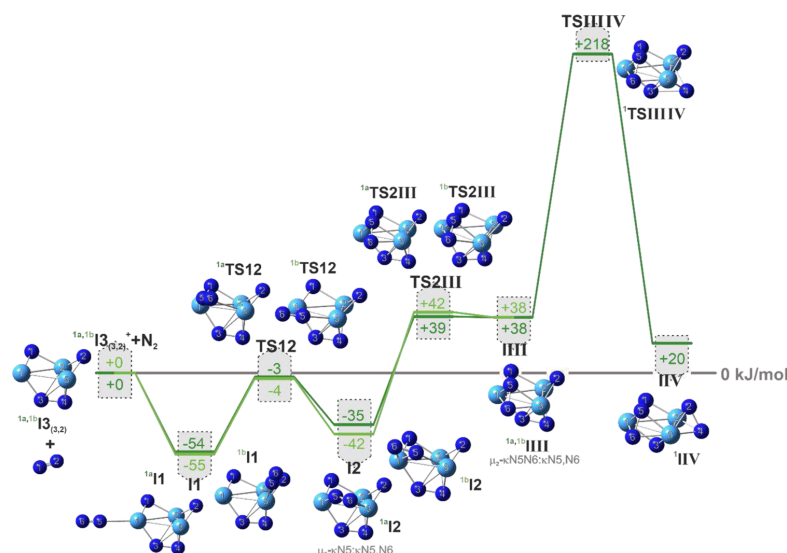


FIG. 5. Reaction pathways of a third N_2 adsorption by the dinitro species $I3_{(3,2)}$; two singlet pathways, 1a (dark green) and 1b (light green) starting either through N_2 adsorption to Ta1 (pathway a) or to Ta3 (pathway b). For the first steps of the pathway there is a striking similarity to the first and second N_2 activation pathways cf. Figs. 3 and 4: initial end-on adsorption of the N_2 ligand and subsequent tilting of the N_2 towards a neighboring Ta atom, eventually yielding an in-plane $\mu_2\text{-}\kappa\text{N3:}\kappa\text{N3,N4}$ coordination across an intact Ta-Ta edge. Starting from the most likely product complex $I3_{(3,2)}$ of the activation pathway of the second N_2 molecule by Ta_3^+ the adsorption pathway for a third N_2 molecule yields the intermediate $III_{(3,2)}$ which is independent of initial N_2 coordination to the Ta1 (path a) or Ta3 (path b) atom and gets stuck in front of unsurmountable barriers that hamper any further or ultimate NN bond cleavage. For reason of clarity, the nomenclature is presented in an abbreviated form [e.g. I1 stands for $I1_{(3,3)}$].

these three sites, and they agree qualitatively. Due to large ambiguities in the applicable anharmonic scaling factors, it is not possible to achieve a quantitative comparison, however (cf. Table S19 and Fig. S6 in the supplementary material).

Accordingly, we recorded an experimental IR spectrum of the (3,5) cluster adsorbate complex. Besides the main band at 2146 cm^{-1} it reveals two side bands at 2173 and 2189 cm^{-1} . These hint towards distinguishable isomers once more. We managed to determine at least two likely structures by DFT calculations, $I_{(3,5)}^{Ta_2,Ta_3}$ and $I_{(3,5)}^{Ta_1,Ta_2}$ (see Table S20 and Fig. S6). Both structures reveal a strong IR active vibration, and a weak one, which are split by $40\text{--}50\text{ cm}^{-1}$. While absolute frequencies suffer from the before mentioned ambiguity of scaling factors, the predicted splitting are much less affected, and they agree well with the observed ones. We therefore consider a mixture of the two singlet minimum structures as a likely explanation for the observed IR bands of (3,5).

As the fourth and fifth N_2 molecule adsorb to merely two out of three possible coordination sites there is one coordination site vacant for adsorption of a sixth N_2 molecule filling up the second adsorption shell of N_2 on the Ta_3^+ cluster for (3,6). We failed to obtain an IR spectrum of (3,6) due to its low abundance.

At this point, we want to address the question, whether the DFT predictions and the recorded IR-PD spectra are in line with the recorded adsorption kinetics (cf. Text S8, Fig. S21–S23 and Tables S29 and S30 in the supplementary material). These kinetics reveal

equally fast adsorption of first, second, fourth, and fifth N_2 molecule. The adsorption of the third and sixth N_2 molecule occur discernably slower, and the desorption is facile as evidenced by high values of $k_{(3,3)^*}$ and $k_{(3,6)^*}$. This indicates a likely meta stability of the formed $(3,3)^*$ and $(3,6)^*$ complexes. While the interpretation of the latter case would be much involved, the prior case of three N_2 adsorbates is well in line with the DFT predictions: It swiftly forms from a “hot” precursor $I3_{(3,2)}$, and it likely converts much of its stabilization into internal excitation. Note, that the larger the complexes, which involves increasing amounts of N_2 adsorbates, the swifter thermal relaxation and collisional cooling proceeds, and the larger the density of states becomes. Thus, the subsequent formation of larger complexes seems much less hampered by internal excitation.

$[Ta_4(N_2)_m]^+$

We extended the published spectra of (4,m), $m = 1\text{--}5$,² by the present work up to $m = 12$ (Fig. 7). In short, the published spectra have revealed the following: The first two adsorbed N_2 molecules undergo unconditional cleavage and yield TaN motifs. A single IR-PD band at 1475 cm^{-1} of the (4,3) spectrum was assigned to a side-on (above edge, $\mu_2\text{-}\kappa\text{N:}\kappa\text{N,N}$) activated N_2 intermediate.² In addition, there is a very broad unstructured IR-PD signal above 1500 cm^{-1} , up to 2400 cm^{-1} , and likely further beyond, which might originate from a low lying electronic absorption of (4,3) to (4,5)

4. Cryo IR Spectroscopy and Cryo Kinetics of Dinitrogen Activation and Cleavage by Small Tantalum Cluster Cations

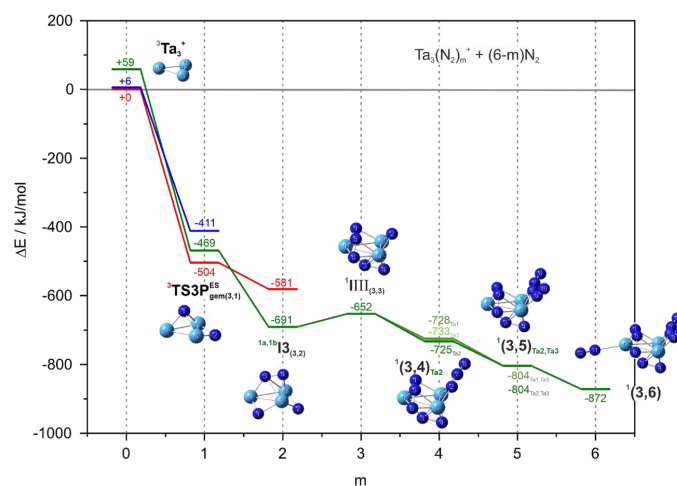


FIG. 6. The big picture of consecutive N_2 adsorption to Ta_3^+ . Ta_3^+ manages to cleave the first adsorbed N_2 molecule (cf. Fig. 3), and the subsequent adsorption of a second N_2 likely starts at ${}^3P_{gem(3,1)}^{ES}$, and it yields ${}^1I_{3(3,2)}$ (see Fig. 4). By these two highly exothermic adsorption events, this ${}^1I_{3(3,2)}$ adsorption complex has stabilized by more than 600 kJ/mol. It is likely that ${}^1I_{3(3,2)}$ possess some residual internal energy when subsequently encountering a further N_2 partner. Thereby it becomes possible to explore the (3,3) potential hypersurface along a direct reaction up to ${}^1III_{(3,3)}$ (cf. Fig. 5) where it finally gets stuck in front of a seemingly unsurmountable barrier.

complexes. The additional absorption around 2200–2300 cm^{-1} may arise from an end-on loosely bound N_2 molecule, which populates several isomers.

The newly recorded IR-PD spectra of the present work reveal the following: The IR-PD spectrum of the (4,6) cluster adsorbate complex displays a strong band at 1424 cm^{-1} , together with a medium strong sideband at 1435 cm^{-1} . Both likely indicate side-on μ_2 - $\kappa N:\kappa N,N$ N_2 adsorption. Two very weak absorptions occur at 1489 and 1580 cm^{-1} . In general, we assign all bands below 2000 cm^{-1} to side-on μ_2 - $\kappa N:\kappa N,N$ adsorbed N_2 molecules, and we take a variation of band position as indicators for varying motifs in the particular adsorption geometries. In the range of end-on coordinated N_2 adsorbates, above 2000 cm^{-1} , we find a strong band at 2252 cm^{-1} and four medium strong, sharp bands at 2209, 2224, and 2294 cm^{-1} . Note, that these bands are red shifted with respect to the free N_2 stretching vibration at 2330 cm^{-1} ⁸⁵ which is understood in terms of a σ -donor π -acceptor synergism that softens the N–N bond. This concept has been utilized for CO adsorbates in the Blyholder model⁸⁶ and for N_2 adsorbates in our earlier studies on Co_n^+ , Ni_n^+ , Fe_n^+ , Ru_n^+ , Rh_n^+ , and Rh_1Fe_1 alloy clusters.^{62,63,67–70,88,89} In the light of these findings, it is most noteworthy that we find another sharp IR-PD band at 2334 cm^{-1} which almost coincides with the free N_2 stretching vibration. This indicates that the corresponding N_2 molecule is very weakly bound to the cluster and therefore resemble an almost free, likely roaming N_2 molecule. Note, that any minute symmetry breaking of side-on N_2 coordination suffices to induce a non-vanishing dipole moment derivative. Thus, a “roaming” or second shell N_2 adsorbate may well acquire some IR transition moment.

The IR-PD spectrum of (4,7) resembles largely that one of (4,6), but with less bands in both regions of the spectrum: In the side-on N_2 range of the IR-PD spectrum, there is one strong (below 2000 cm^{-1}), sharp band at 1422 cm^{-1} and two weak bands at 1478 and 1535 cm^{-1} . In the end-on N_2 range above 2000 cm^{-1} , a sharp band at 2284 cm^{-1} appears, accompanied by a weak band at 2249 cm^{-1} . Finally, the 2333 cm^{-1} band much resembles an almost free N_2 as in (4,6). Such a band appears in all following (4,m) IR-PD spectra up to the largest observable cluster adsorbate complex (4,m_(max)) $\hat{=}$ (4,12). It is most remarkable that a high loading of an odd number of N_2 molecules – namely seven – on a cluster of merely four Ta atoms provides for solely two sharp main bands – one in the side-on and one in the end-on N_2 range. Such a low amount of IR-PD bands from a high number of ligands indicates a very high symmetrical arrangement of the N_2 ligands within the cluster adsorption complex (4,7). Considering the findings from our prior study on the adsorption, activation and cleavage of the first few N_2 molecules on the Ta_4^+ cluster, it seems most likely that the species (4,7) possesses two cleaved and at least one activated N_2 ligand. This looks highly asymmetric.² The four subsequent N_2 molecules which yield (4,7) are most likely end-on bound N_2 ligands. It is somewhat surprising that the resulting quite simple IR-PD spectrum indicates high symmetry.

In noticeable contrast to the merely two sharp main bands for species (4,7) we observe a larger total amount of bands in the IR-PD spectrum of (4,8). There are three sharp and intensive bands in the side-on range: at 1413, 1468, and 1564 cm^{-1} . The former is accompanied by two weak sidebands, one to the right (1431 cm^{-1}) and one on the left (1394 cm^{-1}). In the end-on range of the spectrum,

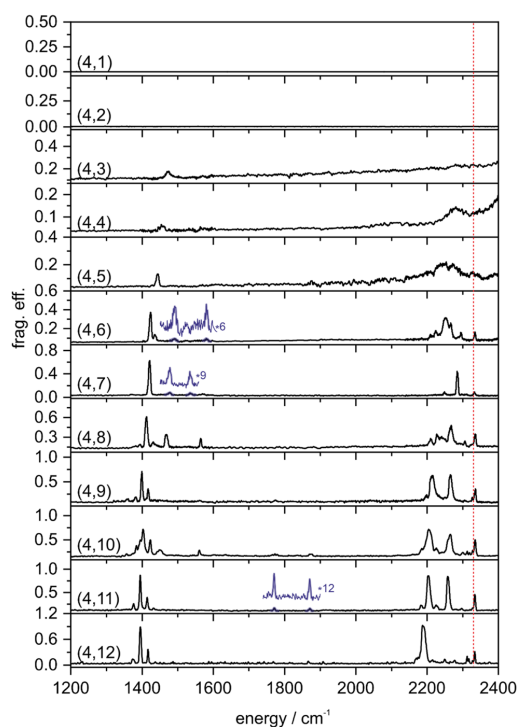


FIG. 7. IR-PD spectra of sequential N_2 adsorption steps onto Ta_4^+ cluster cations $[Ta_4(N_2)_m]^+$, $m = 1-12$, as recorded after 26 K He buffer gas cooling. The (4,1) to (4,5) spectra have been published before (Ref. 2, Fig. 2 therein). Note the significant red-shift of the IR-PD bands with respect to the free N_2 stretching vibrational frequency (2330 cm^{-1} ,⁸⁵ red dotted line).

we observe a broad absorption pattern with maxima at 2210, 2227, 2241, 2268, 2292, 2306, and 2335 cm^{-1} . The amount of 11 absorption maxima exceeds the number of eight N_2 oscillators and likely arises from co-existing isomers. A formal double N_2 occupation of some Ta atoms may combine with reorganization and isomerization. Note, that the enhanced width ($\sim 15\text{ cm}^{-1}$) of the strongest end-on band (2268 cm^{-1}) points towards a lack of high symmetry.

Some of the (4,9) bands coincide with those of (4,8). One notices the sharp and intense band at 1399 cm^{-1} with its both sidebands on the right (1383 cm^{-1}) and left side (1417 cm^{-1}). Very weak absorptions appear at 1361 and 1561 cm^{-1} . The three remaining main bands in the end-on range shift only slightly with respect to matching ones in (4,8): they appear at 2216 , 2265 , and 2336 cm^{-1} . The latter one shows a weak sideband to the left at 2327 cm^{-1} both of which match the free N_2 vibration quite well. This indicates that in species (4,9) likely two N_2 ligands are very weakly bound to the cluster core.

The general band pattern of (4,9) continues upon addition of further N_2 molecules up to (4,11). Total IR-PD yields of (4,10) are

high, and most of the numerous recorded bands are quite strong, yet still sharp, in part. We recognize absorption maxima at 1384 , 1403 cm^{-1} (with an indication of a sideband at 1395 cm^{-1} to the left), 1423 , and 1449 cm^{-1} . A band at 1561 cm^{-1} is also strikingly clear and intense. A similar band was already evident in the IR-PD spectrum of the species (4,8). All in all, the IR-PD band in the lower range appear somewhat broader than those of the (4,9) complex. In the end-on N_2 range we observe three intensive IR-PD bands at 2204 , 2265 , and 2335 cm^{-1} . The former is accompanied by two weak sidebands, one to the right (2226 cm^{-1}) and one to the left (2185 cm^{-1}), and the latter by a weak sideband at 2328 cm^{-1} . We also recognize three weak IR-PD adsorption bands at 2300 , 2313 and 2319 cm^{-1} .

It may be worthwhile to mention in passing that at this point the recorded IR-PD spectrum of (4,11) “simplifies” in terms of the total number of observed bands (ten) as compared to the IR-PD spectrum of (4,10) which provides for significantly larger number of IR-PD bands in total, namely 16. The bands of (4,11) resemble the (4,9) spectrum almost perfectly. The bands at 1376 , 1395 , 1414 , 2183 , 2202 , 2225 , 2258 , 2283 , 2297 , and 2334 cm^{-1} are only slightly red shifted with respect to those of (4,9), by up to 14 cm^{-1} and somewhat better separated. The good quality of the spectrum allows identifying of some very weak bands and thus two assumed combination bands at 1771 and 1871 cm^{-1} appear.

The side-on range of the (4,12) spectrum resembles the one of the (4,9) and the (4,11) spectra. In the end-on range, we observe a single strong band at 2187 cm^{-1} with a sideband at 2170 cm^{-1} to the left. There are additional weaker bands at 2215 , 2249 , 2277 , 2312 , and 2334 cm^{-1} . The latter two are accompanied by sidebands at 2317 and 2327 cm^{-1} .

The IR-PD spectra of the (4,m) cluster comprise of a multitude of bands that indicate a co-existence of side-on and end-on N_2 adsorbate molecules. Except for the IR-PD bands, which nearly match the free N_2 stretching vibration in frequency, the IR-PD adsorption bands in the end-on region show the typical red shift with respect to the free N_2 stretching vibration,⁸⁵ as also observed in our previous studies of other transition metal clusters.^{62,67-70,88,90} The total amount of IR-PD bands as compared to the total number of N_2 ligands reveals evidence for highly symmetric structures in some cases, and evidence for structural isomers in others. For the IR-PD bands in the side-on region, we observe a significant red shift of the most intense band from 1475 cm^{-1} in (4,3) to 1395 cm^{-1} in (4,12). Regarding this shift we remind the reader of our previous and detailed study on the adsorption of the initial N_2 molecules to the Ta_4^+ cluster.² There we have described and discussed an increase in the corresponding N- $N_{(\text{side-on})}$ bond distance upon coordination of a terminally coordinated N_2 molecule to an adjacent Ta atom. These previous findings up to $m = 4$ are extended up to $m = 12$ by the current experiment.

Next, we consult quantum chemical modelling results in order to enhance our understanding of the experimental IR-PD spectra of (4,m), $m = 1-12$. There are two new findings which deserve special attention.

Firstly, we address the question of why some experimental IR-PD bands in the end-on region ($2100-2400\text{ cm}^{-1}$) do not exhibit the typical and expected redshift, but most closely correspond to the frequency of free N_2 . This is remarkable, and it warrants further interpretation efforts. With the in detail discussed reaction paths of the first second and third N_2 activation from our prior publication on

4. Cryo IR Spectroscopy and Cryo Kinetics of Dinitrogen Activation and Cleavage by Small Tantalum Cluster Cations

the cationic Ta_4^+ cluster² at hand, we obtained a multitude of model structures with IR-PD features within the end-on region. In this context, the I1 type structures and geometry and their simulated IR-PD frequencies are of particular interest (Fig. 8, Fig. S7, Table S21). The N_2 coordinating Ta atom is crucial, and in particular its involvement into nitrido bonds (none, one, two or up to three). In consequence the red shift of IR-PD frequency diminishes with respect to free N_2 . In the Ta_4^+ cluster without any nitride ligands $I1^{Ta1}_{(4,1)}$ the bond lengths $Ta-N_{(end-on)}$ and $N-N_{(end-on)}$ are 2.126 02 Å and 1.108 33 Å, respectively. The simulated and unscaled IR-PD frequency for the NN stretching vibration is 2238 cm^{-1} . In comparison to this, DFT modelling revealed for $I1^{Ta4}_{(4,2)}$ a significantly longer bond $Ta-N_{(end-on)}$ of 2.285 13 Å, a correspondingly shorter bond $N-N_{(end-on)}$ of 1.098 05 Å and a higher IR-PD frequency at 2323 cm^{-1} . In this I1 type structure, the tetrahedral framework of the Ta_4^+ cluster is loaded by two nitrides on the edges opposite the Ta atom, which binds the N_2 ligands in an end-on motif. Even though the N_2 molecule adsorbs to a Ta center of the cluster which is not yet involved in a nitride bridge, the nitride ligands reveal an elongated $Ta-N_{(end-on)}$ bond, a correspondingly shorter $N-N_{(end-on)}$ bond, and an increased NN stretching frequency with respect to the cluster without nitride ligands, $I1^{Ta1}_{(4,1)}$. In the case of $I1^{Ta3}_{(4,2)}$, the N_2 ligand is adsorbed onto a Ta center (Ta3) that participates in a nitride bridge, correspondingly the $Ta-N_{(end-on)}$ bond is lengthened to 2.301 32 Å while the $N-N_{(end-on)}$ bond is simultaneously shortened to 1.096 18 Å. The simulated and unscaled IR-PD frequency of the NN stretching vibration accordingly blue-shifts to 2360 cm^{-1} . The N_2 adsorption to the Ta center which participates in two nitride bridges [$I1^{Ta2}_{(4,2)}$] yields an even longer $Ta-N_{(end-on)}$ bond (2.362 96 Å), an even shorter $N-N_{(end-on)}$ bond (1.091 43 Å) and even higher IR-PD frequency for the NN stretching (2431 cm^{-1}). This trend also results for I1 type structures for a Ta_4^+ cluster loaded by four nitride ligands: $I1_{(4,3)}$. The IR-PD frequency of the NN stretching vibration increases from 2266 cm^{-1} via 2431 to 2472 cm^{-1} by coordination of the end-on N_2 ligand to a tantalum atom participating in only a single nitride bridge [$I1^{Ta4}_{(4,3)}$], via coordination to a tantalum atom participating in two nitride bridges [$I1^{Ta1}_{(4,3)}$], and finally to N_2 ligand coordination to a tantalum atom that is part of three nitride bridges [$I1^{Ta3}_{(4,3)}$]. Also, there is the trend of increasing bond lengths $Ta-N_{(end-on)}$ and decreasing bond lengths $N-N_{(end-on)}$ with increasing number of nitride ligands in close proximity to the Ta atom, which is the adsorption center for the end-on N_2 ligand, from 2.239 15 and 1.099 63 Å [$I1^{Ta4}_{(4,3)}$ $Ta-N_{(end-on)}$ and $N-N_{(end-on)}$, respectively] to 2.357 14 and 1.090 95 Å [$I1^{Ta1}_{(4,3)}$ $Ta-N_{(end-on)}$ and $N-N_{(end-on)}$, respectively] to 2.399 13 and 1.088 99 Å [$I1^{Ta3}_{(4,3)}$ $Ta-N_{(end-on)}$ and $N-N_{(end-on)}$, respectively].

The above discussed trends show a correlation of N_2 bond length and N_2 coordination site with the DFT predicted NN IR-PD stretching frequency. The coordinating Ta center proves crucial: Its involvement into none, one, two or three $Ta^{(\delta+)}-N^{(\delta-)}$ bonds tunes its total partial charge and thereby its donor-acceptor capabilities. Accordingly, the coordinating intact N_2 adsorbate probes this partial charge and tells via its observable N_2 stretching mode frequency. Note, that many of the recorded IR-PD spectra reveal three sharp spectral features in the N_2 end-on stretching range.

Next, we want to address the conceivable existence of structural isomers for the various cluster adsorbate complexes. This seems nec-

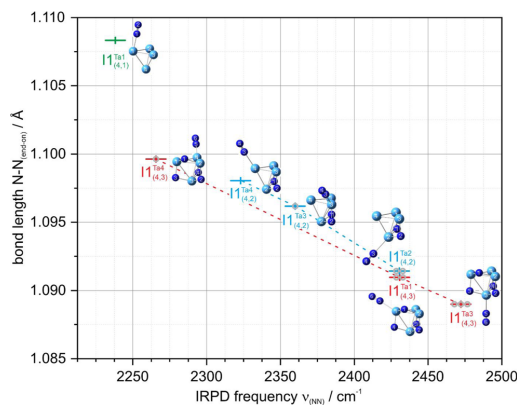


FIG. 8. Multitude of I1 type model structures and their simulated IR frequencies of the first second and third N_2 activation from our prior publication on the cationic Ta_4^+ cluster.² The N_2 coordinating Ta atom is crucial, and in particular its involvement into nitride bonds (none, one, two or up to three). In consequence the red shift of IR frequency diminishes with respect to free N_2 (2330 cm^{-1}).⁸⁵ The dotted lines serve to guide the eye. None, one, two or three open black circles at the computed data points indicate an according number of nitride bonds of the N_2 end-on coordinating Ta atom. An according trend in the $Ta-N$ bond length is found in Fig. S7 in the supplementary material.

essary in view of the many IR-PD bands that in some cases exceed the amount of adsorbed N_2 molecules. Our DFT modeling revealed such conceivable N_2 adsorption isomers, starting with the species (4,3) as dealt with in our previous study.² This species resulted from the three subsequent nitrogen adsorption, activation, and cleavage pathways in front of an unsurmountable barrier as the final product species $I2_{(4,3)}$. It comprises of two fully cleaved N_2 molecules and a side-on μ_2 - $\kappa N1:\kappa N1,N2$ N_2 ligand (cf. Fig. S8, Tables S22a and S23a). The vibrational frequency for the side-on μ_2 - $\kappa N1:\kappa N1,N2$ N_2 ligand obtained from the DFT calculations was scaled to the experimentally measured IR-PD band by a scaling factor of 0.9736. This scaling factor is applied to the determined IR-PD frequencies for all further modelled species (4,m). Predicted doublet states are more stable than quartet states, and we therefore focus on the doublet ground states throughout. In order to label conceivable isomers we augment the already known nomenclature (n,m) by alphabetic indices from a – w.

There are four distinguishable Ta centers which may act as coordination sites for the adsorption of the fourth N_2 molecule to the presumed $I2_{(4,3)}$ isomer. Accordingly, four structural isomers (4,4)a, (4,4)b, (4,4)c and (4,4)d result, within a total energy span of mere 4.3 kJ/mol (cf. Fig. S8, Tables S22b and S23b). From an energetic point of view, all four isomers may be populated. The scaled frequency and (4,4)c match the experimental range of observed band at 1454 cm^{-1} . Likewise, the predicted IR band of the end-on bound N_2 stretching vibration falls very well within the range of the broad experimental adsorption band around 2300 cm^{-1} .

If we take these isomers (4,4)a, (4,4)b (4,4)c and (4,4)d as starting points for the adsorption of a fifth N_2 molecule, we obtain eight isomers of the type (4,5), cf. supplementary material Fig. S9,

Tables S22c and S23c). The modelled IR spectra of (4,5)a, (4,5)d, and (4,5)f reflect quite well the experimentally measured IR-PD band at 1443 cm^{-1} and also provide three distinguishable bands in the end-on region that might well correspond to the broad experimental IR-PD adsorption band. The less stable isomer (4,5)c, $+11.0\text{ kJ/mol}$, may reflect the weak experimental sideband at 1428 cm^{-1} . This results in four isomers for species (4,5), which in turn are the starting point for the adsorption of the next (sixth) N_2 molecule.

Within an energy span of 92 kJ/mol we found in total 21 stable adsorption isomers (4,6) all of which are based on the $\text{I}_{2(4,3)}$ core structure (cf. Fig. S9, Tables S22d and S23d). We chose for further discussion seven stable isomers: (4,6)a, (4,6)c, (4,6)f, (4,6)g, (4,6)k, (4,6)l and (4,6)o. All of them derive from above discussed isomers of (4,5)a, (4,5)c, (4,5)d and (4,5)f, by addition of a single end-on coordinated N_2 . They provide for predicted IR bands that might match the observed IR-PD bands in the N_2 end-on stretching region. In total, they make up for a possible assignment of the observed experimental IR-PD pattern, cf. Fig. S9. Note, that the predicted 1663 cm^{-1} band finds no obvious counterpart in the IR-PD spectra. There are two bands close by at 1491 and 1580 cm^{-1} , but they deviate significantly. A closer look at the bond distances $d(\text{Ta4-N6})$ and angles $\angle(\text{Ta4-Ta1-N6})$ of the eight computed isomers (4,6)a, (4,6)c, (4,6)f, (4,6)g, (4,6)k, (4,6)l, (4,6)o and (4,6)r indicates increase an increasing tilt of the side-on $\mu_2\text{-}\kappa\text{N}:\kappa\text{N},\text{N}$ N_2 ligand with the observed red shift of its IR-PD vibrational frequency (cf. Table S24). We speculate that the observed IR-PD bands at 1491 and 1580 cm^{-1} might stem from some isomers similar to (4,6)r but with slightly shorter Ta4-N6 bonds and smaller angles $\angle(\text{Ta4-Ta1-N6})$, possibly enabled by mere re-orientation of some N_2 spectator ligand, while keeping hapticity as investigated.

For species (4,7) the recorded IR-PD spectrum is particularly interesting as it shows merely two intensive bands, one in the side-on and one in the end-on range, with four very weak IR-PD bands, two in the side-on and end-on range, respectively. Speculating about a single (4,7) isomer of high symmetry, we conducted our DFT survey of conceivable structures (cf. Tables S22e and S23e) and found numerous ones, although over a wide range of relative stabilities. A mixture of seven favorable isomers – (4,7)c, (4,7)g, (4,7)l, (4,7)k, (4,7)q, (4,7)s and (4,7)t – might reproduce the measured IR-PD spectrum (cf. Fig. S10). While for species (4,6) the assignment of the calculated IR bands to the weak adsorption bands in the side-on region was difficult, for species (4,7) the isomers (4,7)l and (4,7)k reproduce the weak bands at 1478 and 1535 cm^{-1} very well. It seems, that in this case we managed to identify N_2 spectator ligand orientations that modulate the tilted N_2 stretching frequency close to observation. As a matter of fact, it is a range of computed variations in the tilting angle $\angle(\text{Ta4-Ta1-N6})$ of mere two degrees (40° – 42°) and a variation of coordination distance $d(\text{Ta4-N6})$ of 0.1 \AA (2.1 – 2.2 \AA) which suffices to induce side-on N_2 stretching frequency shifts of up 145 cm^{-1} (1404 – 1549 cm^{-1} , cf. Table S24), in close correspondence to the experimental span of 113 cm^{-1} in the range of IR-PD bands (1422 – 1535 cm^{-1}). The obvious mismatch in predicted IR and observed IR-PD intensities of these bands may signify reduced rates of formation and thus reduced populations. Other than fingerprinting co-existing isomers, there is some alternative explanation for the two weak bands at 1478 and 1535 cm^{-1} in terms of combination bands. The most favorable isomer (4,7)c reveals a

bending vibration of the side-on $\mu_2\text{-}\kappa\text{N}:\kappa\text{N},\text{N}$ N_2 ligand at 111 cm^{-1} , which simultaneously represents bond compression and elongation of the Ta4-Ta2 bond, and a wagging mode of the $\text{N}_{2(\text{end-on})}$ ligand on Ta2 at 51 cm^{-1} (cf. Table S25). These two might couple to the side-on N_2 stretching mode at 1406 cm^{-1} (calc.)/ 1422 cm^{-1} (IR-PD) and thereby explain the observed side bands.

It shows, that the according computations finds likewise numerous conceivable isomers of (4,8) (Tables S22f and S23f) as anticipated from the many observed bands, which exceed the amount of available N_2 ligands, that may act as chromophores. A selection of six isomers, (4,8)c, (4,8)e, (4,8)f, (4,8)g, (4,8)l and (4,8)q, comes close to interpret the experimental IR-PD spectrum of (4,8) (cf. Fig. S10). It seems unlikely that the significantly strong IR-PD bands at 1468 and 1564 cm^{-1} would originate from combination bands. We may note in passing that the chosen isomers derive from likely (4,7) isomers by single N_2 end-on addition to varying adsorption sites, but without further isomerization amongst the previous N_2 ligands.

Furthermore, these seven chosen (4,8) isomers serve well to generate accordingly those five favorable (4,9) isomers ((4,9)b, (4,9)d, (4,9)f, (4,9)g, (4,9)h) which might interpret major parts of the observed IR-PD spectrum (cf. Fig. S11, Tables S22g and S23g). It takes, however, some additional isomer, as e.g. (4,9)j to interpret the IR-PD band at 1399 cm^{-1} . If indeed present, it cannot originate directly from any of the six considered (4,8) isomers by mere N_2 attachment. Thus, it either stems from another, yet unknown (4,8) isomer, or it forms by N_2 attachment to some of the above listed (4,8) isomers with concomitant or subsequent but swift isomerization. The IR-PD spectrum reveals a weak adsorption at 1561 cm^{-1} indicating a side-on $\mu_2\text{-}\kappa\text{N}:\kappa\text{N},\text{N}$ N_2 ligand with a slightly larger Ta4-N6 bond and a larger angle $\angle(\text{Ta4-Ta1-N6})$. No suitable calculated isomer has yet been found for this. It warrants to deliberate the significant splitting of the intensive end-on N_2 stretching doublet at 2215 and 2265 cm^{-1} ($\Delta\nu = 50\text{ cm}^{-1}$) and the meager splitting of the considerably strong doublet at 2327 and 2336 cm^{-1} ($\Delta\nu = 9\text{ cm}^{-1}$). The 50 cm^{-1} splitting finds interpretation through the computed (4,9)g and (4,9)h isomers, which reveal computed splittings of $\Delta\nu = 38$ and 36 cm^{-1} , respectively. These originate from symmetrically and asymmetrically coupled pairs of end-on bound N_2 oscillators that locate on neighboring Ta centers with a direct metal-to-metal bond, and without bridging nitrides or side-on coordinated N_2 in between. This situation allows for both a considerable coupling strength and high IR intensities. The latter arise from electron density shuffling across the metallic Ta-Ta bond, in phase with the N_2 stretching motion (cf. Fig. S13). The vibrational analysis of isomers (4,9)d and (4,9)j predicts symmetrically and asymmetrically coupled pairs of terminal N_2 ligands with a small splitting of $\Delta\nu = 13\text{ cm}^{-1}$, which might resemble the observed 9 cm^{-1} splitting of the two 2327 – 2336 cm^{-1} IR-PD bands. Here, the active oscillators locate on adjacent Ta centers with a direct metal-metal bond and without bridging nitrides or bridging side on coordinated N_2 ligands. Note, that two of the chosen favored isomers, (4,8)b and (4,8)f, reveal some pairs of end-on coordinated N_2 ligands with asymmetric/symmetric N_2 stretching modes that experience particularly high splittings of $\Delta\nu = 62$ and 63 cm^{-1} , respectively. The coordinating, neighboring Ta centers are bound to each other directly by a metal-to-metal bond and without bridging nitrides in between. The computed frequencies of these N_2 stretching doublet

4. Cryo IR Spectroscopy and Cryo Kinetics of Dinitrogen Activation and Cleavage by Small Tantalum Cluster Cations

coincide well with observed IR-PD bands in the 2200 and 2340 cm^{-1} range.

The isomer cascade of successive, stepwise N_2 adsorptions to the Ta_4^+ cluster predicts seven favorable isomers (4,10)g, (4,10)h, (4,10)i, (4,10)l, (4,10)o, (4,10)q and (4,10)r (cf. Fig. S11, Tables 22h and 23h) which altogether succeed to reproduce the observed IR-PD spectrum conclusively, but for some detail. In the side-on N_2 stretching range the following assignment can be made: isomer (4,10)q, (4,10)l and (4,10)o provides stretching modes that match the experimental IR-PD bands at 1484, 1395 and 1403 cm^{-1} . For the single band at 1423 cm^{-1} , isomer (4,10)r is found to deliver a match. Contributions from the three isomers (4,10)g, (4,10)h and (4,10)i manage to provide for a match to the broad experimental IR-PD band at 1443 and 1449 cm^{-1} . In the end-on range above 2000 cm^{-1} suitable modes of the seven selected isomers represent the recorded IR-PD bands quite well. A particular highlight is the stunning agreement of the predicted end on N_2 stretching bands of the isomers (4,10)l, (4,10)o, (4,10)q and (4,10)r with the measured IR-PD band pattern at 2300, 2313, 2319, 2328 and 2335 cm^{-1} . The observed intense N_2 stretching doublet at 2204 and 2265 cm^{-1} of (4,10) closely resembles a similar pattern in (4,9). These arise from symmetrically and asymmetrically coupled pairs of terminally bound N_2 oscillators located at neighboring Ta centers, Ta2 and Ta4, with a direct metal-metal bond and no bridging nitrides or side-on coordinated $\mu_2\text{-}\kappa\text{N}:\kappa\text{N}:\text{N}$ N_2 in between. With the adsorption cascade progressing, the number of adsorbed N_2 ligands increases stepwise, and with it the number of N_2 oscillators at the centers Ta2 and Ta4. As a consequence, the symmetric/asymmetric coupling of neighboring N_2 oscillators seems to diminish in favor of either globally coupled many oscillators or of few locally isolated N_2 stretching modes, maybe single ones. However, the adsorption band at 1561 cm^{-1} finds no counterpart in any predicted mode of any of the computed isomers. At least, our computed results for some adsorption isomers with less N_2 ligands, such as (4,7), did reveal some IR frequencies in this range with a side-on $\mu_2\text{-}\kappa\text{N}:\kappa\text{N}:\text{N}$ N_2 ligand with a slightly larger Ta4–N6 bond and a larger angle \angle (Ta4–Ta1–N6). It is well possible that our thorough survey of favorable isomers failed to achieve completeness, and we may have missed such a structural motif that likely contributes.

The recorded IR-PD bands of species (4,11) find, once more, a valid assignment by the computed predictions (cf. Fig. S12, Tables 22i and 23i): A mixture of isomers (4,11)s and (4,11)t provide for side-on coordinated N_2 oscillators that match very well the observed band at 1376 cm^{-1} , and according oscillators in isomers (4,11)a and (4,11)p resemble the intensive IR-PD band at 1395 cm^{-1} . The moderate IR-PD band at 1414 cm^{-1} and the weak IR-PD band at 1432 cm^{-1} may arise from side-on coordinated oscillators at isomers (4,11)f and (4,11)l. In the frequency range of end-on coordinated N_2 oscillators there are three intensive IR-PD bands at 2203, 2258 and 2334 cm^{-1} , which find an interpretation in terms of N_2 ligands at isomers (4,11)a, (4,11)l and (4,11)t. Further weak IR-PD bands in this range, at 2183, 2225 and 2297 cm^{-1} , may arise from isomers (4,11)f, (4,11)p and (4,11)s.

From our kinetic studies presented and discussed in the supplementary material (cf. Text S9, Fig. S24 and Table S31) we know that (4,12) is the most abundant complex at long reaction times, accompanied by a very minor (4,13) product and the smaller species (4,8), (4,9), (4,10) and (4,11) in equilibrium. Thus, (4,12)

became the largest N_2 adsorbate complex of our current IR-PD study. It finds interpretation in terms of a mixture of five favorable isomers (cf. Fig. S12, Tables 22j and 23j): (4,12)a, (4,12)d, (4,12)l, (4,12)o and (4,12)s. Two predicted IR bands from a side-on and end-on coordinated N_2 ligand each of isomer (4,12)a provide for an assignment of the intensive IR-PD bands at 1395 and 2187 cm^{-1} . Isomers (4,12)d and (4,12)o suit very well to interpret the weak IR-PD band at 1374 cm^{-1} and the IR-PD bands in the 2300 to 2340 cm^{-1} range. The moderate IR-PD band at 1417 cm^{-1} may result from isomer (4,12)i. In the five favored isomers, at least four or five of the end-on coordinated N_2 ligands are located at Ta centers Ta2 and Ta4 with a direct metal-metal bond, and no bridging nitrides or side-on coordinated N_2 in between. In the previous discussed, smaller cluster adsorbate complexes, the N_2 oscillators at these very two Ta centers provide for intense IR-PD doublets. With an increasing amount of N_2 ligands, both the IR-PD experiment and the DFT modelling of the complex (4,12) diminish the prior doublet to a single intense band at 2200 cm^{-1} , with some weak bands to the blue side, mostly beyond 2280 cm^{-1} . Upon saturation many N_2 ligands seem to experience a reduced/weak coordination to their Ta coordination sites, and accordingly a small or even vanishing redshift with respect to the stretching mode of a free N_2 molecule. In remarkable contrast, some isomers provide for a single end-on coordinated N_2 ligand that experiences a redshifted and intensively IR active stretching mode that indicates much stronger Ta– N_2 interaction.

IR-PD experiments and DFT modelling of (4,m) tantalum cluster N_2 adsorbate complexes confirms double activation and nitride formation, succeeded by single side-on N_2 coordination. Significant red shifts of IR-PD bands from these side-on coordinated $\mu_2\text{-}\kappa\text{N}:\kappa\text{N}:\text{N}$ N_2 ligands correlate with the degree of tilting towards the second coordinating Ta center. All subsequently attaching N_2 adsorbates coordinate in an end-on fashion, and we find clear evidence for co-existence of end-on coordination isomers. A large fraction, maybe the majority, of end-on coordinated N_2 ligands experience weak interaction with their coordination centers and reveal little to no red shift of their stretching frequencies, some of them even a slight blue shift. The tetrahedral Ta_4^+ framework persists but for some minor bond length relaxations.

CONCLUSION

We present an IR-PD study of selected tantalum cluster adsorbate complexes $[\text{Ta}_n(\text{N}_2)_m]^+$, abbreviated (n,m), $n = 2\text{--}4$, [IRS1]. In the adjoined IR-PD study [IRS2] we present our corresponding findings on larger complexes $[\text{Ta}_{5-8}(\text{N}_2)_m]^+$. The overall picture of N_2 adsorption onto the smallest Ta_n^+ clusters, $n = 2\text{--}4$, provides clear evidence for activation and cleavage of the initially adsorbing N_2 molecules.

We observe no structured IR-PD signal of the tantalum dimer species $[\text{Ta}_2(\text{N}_2)_1]^+$: (2,1). This primarily proves that Ta_2^+ adsorbs an N_2 molecule that is not terminally bound to the Ta_2^+ dimer in end-on coordination. Indeed, our IR-PD experiments and DFT modeling confirm and extend a previous study of Ta_2^+ clusters under ambient conditions,¹ and we identify an additional submerged entry channel barrier, such that spontaneous N_2 bond cleavage by Ta_2^+ is well confirmed.

We also present a detailed study of the N_2 adsorbate complexes of the Ta_3^+ cluster from IR-PD experiments and DFT modeling.

There is a striking absence of any vibrational bands in the IR-PD spectra of the first three adsorbate complexes (3,1), (3,2) and (3,3). In contrast, the IR-PD spectra of the species (3,4) and (3,5) do reveal some broad vibrational bands. Our DFT modelling revealed an overall exoergic reaction pathway with all submerged barriers. Initial triplet and quintet states of Ta_3^+ seem to spin quench into the singlet $^1I_{3(3,1)}$ intermediate by N_2 coordination and exoergic activation, and the reaction proceeds towards ultimate N_2 cleavage via another spin flip, likely into most stable triplet state of geminal edge-surface N–N coordination. Most noteworthy, this Ta_3^+ activation pathway proceeds much in line with our previously identified across edge above surface (AEAS) mechanism of Ta_4^+ .² This successful and simple cleavage of a first N_2 molecule by Ta_3^+ is followed by the second N_2 molecule undergoing similar activation steps until the cluster complex in $I_{3(3,2)}$ might get stuck in front of an unsurmountable barrier that hinders isothermal activation. An ultimate NN bond cleavage would be possible under adiabatic conditions. We identify an N_2 activation reaction pathway similar to the one of (2,1) for the adsorption of the third N_2 molecule on the Ta_3^+ cluster via a μ_2 -κN5,N6:κN5,N6 double side-on “butterfly” N_2 motif across the Ta1–Ta3 edge, yielding a single $^{1a,1b}III_{(3,3)}$ intermediate. From (3,4) on, the sequential adsorption of further N_2 molecules proceeds towards an end-on majority. The cluster adsorbate complex $^{1a,1b}III_{(3,3)}$ offers three distinguishable adsorption sites for further N_2 adsorption. The fourth, fifth and sixth N_2 molecules then coordinate on each of these free adsorption sites.

The study of the N_2 adsorbate complexes of Ta_4^+ presented here extends our earlier study and previously published spectra from (4,m), $m = 1-5$,² up to $m = 12$. In the past study, we have investigated N_2 cleavage on the Ta_4^+ cluster surface and we discussed the underlying reaction processes. The AEAS mechanism found provided a mechanistic understanding of the light N_2 cleavage which is the basis of this current work. The present IR-PD experiments and DFT modelling of the higher loaded N_2 adsorbate species (4,m), $m > 5$, confirm the published double activation and nitride formation, succeeded by single side-on N_2 coordination. Significant red shifts of IR-PD bands from these side-on coordinated μ_2 -κN:κN,N N_2 ligands correlate with the degree of tilting towards the second coordinating Ta center. All subsequently attaching N_2 adsorbates coordinate in an end-on fashion, and we find clear evidence for co-existence of end-on coordination isomers.

DFT predictions and IR fingerprints agree well in the case of Ta_4^+ , and there are no indications for dark IR bands of intact N_2 adsorbates in this case. This likely seems to hold for Ta_5^+ as well: Intact N_2 ligands yield some IR-PD bands, albeit sometimes weak ones (cf. our adjoined IR-PD study [IRS2]). A strict experimental proof would arise from future tagging experiments, or from future two color pump-probe experiments. The above findings find strong support through our complementary cryogenic kinetic studies, as documented in the supplementary material. The N_2 adsorption reaches a limit $m_{(max)}$, which depends on cluster size n . We observe a final equilibrium among those adsorbate complexes which possess up to three to five N_2 adsorbates less than $m_{(max)}$, in all cases but $n = 2$. In the cases of $n = 2$ and 3 the largest observable cluster adsorbate complex ($2, m_{(max)}$) and ($3, m_{(max)}$), respectively, are the most abundant complexes in equilibrium m^* , as well. Kinetic fits revealed significant N_2 desorption rates upon higher N_2 loads, and the vari-

ations of absolute rates find reasonable interpretation in terms of simple thermodynamic arguments. The kinetic findings provide for independent support of N_2 activation and likely cleavage.

The Ta_3^+ cluster experiences stepwise N_2 adsorption close to collision rate. There are either two dips in N_2 adsorption, at $k_{(3,2)}$ and $k_{(3,5)}$, or two spikes in N_2 desorption, at $k_{-(3,3)}$ and $k_{-(3,6)}$. Both variants find support by the IR-PD findings, and from the DFT modelling. We obtained new insights from the confirmation and extension of our prior study of N_2 activation by Ta_4^+ .² At high N_2 loads, $k_{(4,7)}$ to $k_{(4,11)}$, kinetic fits necessitate mechanisms beyond stepwise N_2 adsorption/desorption, such as e.g. adsorption isomers - and/or adsorbate shell reordering. Such a hypothesis is also well in line with the IR-PD findings and the DFT modelling.

We strongly encourage future experiments on a direct spectral identification and characterization of tantalum nitride bonds through their IR fingerprints, e.g. by application of far IR radiation from a free electron laser source.

SUPPLEMENTARY MATERIAL

Supplementary material comprises of comprehensive listings of energetics, structures and IR frequencies of computed structures, of plots energetics of reaction pathways by other multiplicities, of further computed IR spectra, and of multiple text blocks and viewgraphs on the conducted kinetic experiments, kinetic fits and their interpretation in detail.

ACKNOWLEDGMENTS

This work was supported by the German research foundation DFG within the trans-regional collaborative research center SFB/TRR 88 (Cooperative effects in homo and heterometallic complexes, 3met.de) and by the research center OPTIMAS. We thank Thomas Kolling for technical assistance and valuable discussion. Quantum chemical modelling took place at the “Regionales Hochschulrechenzentrum Kaiserslautern” (RHRK).

AUTHOR DECLARATIONS

Conflict of Interest

The authors have no conflicts to disclose.

Author Contributions

The experiments were performed by DVF with MPK, AS and MEH, and DVF performed the quantum chemical calculations. ML and CW assisted on experiments and calculations. The evaluation of the measured data was carried out by DVF, and it was accompanied by discussions with AS, MPK and GNS. DVF and GNS wrote the manuscript, which all of the authors revised and agreed to.

Daniela V. Fries: Data curation (lead); Formal analysis (equal); Investigation (lead); Project administration (equal); Validation (equal); Writing – original draft (equal); Writing – review & editing (equal). **Matthias P. Klein:** Conceptualization (supporting);

4. Cryo IR Spectroscopy and Cryo Kinetics of Dinitrogen Activation and Cleavage by Small Tantalum Cluster Cations

Data curation (supporting); Formal analysis (supporting); Investigation (supporting); Methodology (equal); Validation (supporting); Writing – review & editing (supporting). **Annika Straßner**: Data curation (supporting); Formal analysis (supporting); Investigation (supporting); Methodology (supporting); Validation (supporting); Writing – review & editing (supporting). **Maximilian E. Huber**: Data curation (supporting); Formal analysis (supporting); Investigation (supporting); Project administration (supporting); Validation (supporting); Writing – review & editing (supporting). **Maximilian Luczak**: Data curation (supporting); Formal analysis (supporting); Investigation (supporting); Methodology (supporting); Software (supporting); Validation (supporting); Writing – review & editing (supporting). **Christopher Wiehn**: Data curation (supporting); Formal analysis (supporting); Investigation (supporting); Methodology (supporting); Resources (supporting); Software (supporting); Validation (supporting); Writing – review & editing (supporting). **Gereon Niedner-Schatteburg**: Conceptualization (lead); Funding acquisition (lead); Methodology (lead); Project administration (lead); Resources (lead); Supervision (lead); Writing – original draft (equal); Writing – review & editing (equal).

DATA AVAILABILITY

The data that support the findings of this study are available from the corresponding author upon reasonable request.

REFERENCES

- C. Geng, J. Li, T. Weiske, and H. Schwarz, *Proc. Natl. Acad. Sci. U. S. A.* **115**(46), 11680–11687 (2018).
- D. V. Fries, M. P. Klein, A. Steiner, M. H. Prosenc, and G. Niedner-Schatteburg, *Phys. Chem. Chem. Phys.* **23**(19), 11345–11354 (2021).
- X. Zhang, B. B. Ward, and D. M. Sigman, *Chem. Rev.* **120**(17), 9834 (2020).
- X. Zhang, B. B. Ward, and D. M. Sigman, *Chem. Rev.* **120**(12), 5308–5351 (2020).
- D. E. Canfield, A. N. Glazer, and P. G. Falkowski, *Science* **330**(6001), 192–196 (2010).
- H. Liu, *Ammonia Synthesis Catalysts* (World Scientific, Singapore, 2013).
- R. Schlögl, *Ammonia Synthesis in Handbook of Heterogeneous Catalysis* (Wiley VCH, 2008).
- M. Appl, *Ammonia: Principles and Industrial Practice* (Wiley VCH, 2007).
- G. Ertl, *Angew. Chem., Int. Ed.* **47**(19), 3524–3535 (2008).
- G. Ertl, S. B. Lee, and M. Weiss, *Surf. Sci.* **114**(2-3), 515–526 (1982).
- G. Ertl, *Catal. Rev.* **21**(2), 201–223 (1980).
- R. Schlögl, *Angew. Chem., Int. Ed.* **42**(18), 2004–2008 (2003).
- H. Liu, *Chin. J. Catal.* **35**(10), 1619–1640 (2014).
- H.-P. Jia and E. A. Quadrelli, *Chem. Soc. Rev.* **43**(2), 547–564 (2014).
- S. J. K. Forrest, B. Schluschaß, E. Y. Yuzik-Klimova, and S. Schneider, *Chem. Rev.* **121**(11), 6522–6587 (2021).
- S. Kim, F. Loose, and P. J. Chirik, *Chem. Rev.* **120**(12), 5637–5681 (2020).
- R. J. Burford and M. D. Fryzuk, *Nat. Rev. Chem.* **1**(4), 0026 (2017).
- P. Avenier, M. Taoufik, A. Lesage, X. Solans-Monfort, A. Baudouin, A. de Mallmann, L. Veyre, J.-M. Basset, O. Eisenstein, L. Emsley, and E. A. Quadrelli, *Science* **317**(5841), 1056–1060 (2007).
- J. Li and S. Li, *Angew. Chem., Int. Ed.* **47**(42), 8040–8043 (2008).
- R. A. J. O’Hair and G. N. Khairallah, *J. Cluster Sci.* **15**(3), 331–363 (2004).
- D. K. Böhme and H. Schwarz, *Angew. Chem., Int. Ed.* **44**(16), 2336–2354 (2005).
- P. B. Armentrout, *Catal. Sci. Technol.* **4**(9), 2741–2755 (2014).
- M. Zhou, X. Jin, Y. Gong, and J. Li, *Angew. Chem., Int. Ed.* **46**(16), 2911–2914 (2007).
- X. Cheng, Z.-Y. Li, L.-H. Mou, Y. Ren, Q.-Y. Liu, X.-L. Ding, and S.-G. He, *Chem. - Eur. J.* **25**(72), 16523–16527 (2019).
- Y. Gong, Zhao, and M. Zhou, *J. Phys. Chem. A* **111**(28), 6204–6207 (2007).
- L.-H. Mou, Y. Li, G.-P. Wei, Z.-Y. Li, Q.-Y. Liu, H. Chen, and S.-G. He, *Chem. Sci.* **13**(32), 9366–9372 (2022).
- Z.-Y. Li, Y. Li, L.-H. Mou, J.-J. Chen, Q.-Y. Liu, S.-G. He, and H. Chen, *J. Am. Chem. Soc.* **142**(24), 10747–10754 (2020).
- L.-H. Mou, Y. Li, Z.-Y. Li, Q.-Y. Liu, H. Chen, and S.-G. He, *J. Am. Chem. Soc.* **143**(45), 19224–19231 (2021).
- Z.-Y. Li, F. Horn, Y. Li, L.-H. Mou, W. Schöllkopf, H. Chen, S.-G. He, and K. R. Asmis, *Chem. - Eur. J.* **29**(14), e202203384 (2022).
- Y.-Q. Ding, Z.-Y. Chen, Z.-Y. Li, X. Cheng, M. Wang, and J.-B. Ma, *J. Phys. Chem. A* **126**(9), 1511–1517 (2022).
- J. F. Eckhard, D. Neuwirth, C. Panosetti, H. Oberhofer, K. Reuter, M. Tschurl, and U. Heiz, *Phys. Chem. Chem. Phys.* **19**(8), 5985–5993 (2017).
- N. Levin, J. T. Margraf, J. Lengyel, K. Reuter, M. Tschurl, and U. Heiz, *Phys. Chem. Chem. Phys.* **24**(4), 2623–2629 (2022).
- M. R. Zakin, D. M. Cox, and A. Kaldor, *J. Chem. Phys.* **87**(8), 5046–5048 (1987).
- J. F. Eckhard, T. Masubuchi, M. Tschurl, R. N. Barnett, U. Landman, and U. Heiz, *J. Phys. Chem. A* **125**(24), 5289–5302 (2021).
- J. F. Eckhard, T. Masubuchi, M. Tschurl, R. N. Barnett, U. Landman, and U. Heiz, *J. Phys. Chem. C* **122**(44), 25628–25637 (2018).
- C. Geng, J. Li, T. Weiske, and H. Schwarz, *Proc. Natl. Acad. Sci. U. S. A.* **116**(43), 21416–21420 (2019).
- X. Sun and X. Huang, *ACS Omega* **7**(26), 22682–22688 (2022).
- G.-D. Jiang, L.-H. Mou, J.-J. Chen, Z.-Y. Li, and S.-G. He, *J. Phys. Chem. A* **124**(38), 7749–7755 (2020).
- M. Kumar Yadav and A. Mookerjee, *Physica B* **405**(18), 3940–3942 (2010).
- F. Mafuné, Y. Tawaray, and S. Kudoh, *J. Phys. Chem. A* **120**(24), 4089–4095 (2016).
- M. C. Tsai, U. Ship, I. C. Bassignana, J. Küppers, and G. Ertl, *Surf. Sci.* **155**(2-3), 387–399 (1985).
- H. J. Freund, B. Bartos, R. P. Messmer, H. Grunze, H. Kühlenbeck, and M. Neumann, *Surf. Sci.* **185**(1-2), 187–202 (1987).
- P. Maitre, D. Scuderi, D. Corinti, B. Chiavarino, M. E. Crestoni, and S. Fornarini, *Chem. Rev.* **120**(7), 3261–3295 (2020).
- J. R. Eyler, *Mass Spectrom. Rev.* **28**(3), 448–467 (2009).
- J. Oomens, B. G. Sartakov, G. Meijer, and G. von Helden, *Int. J. Mass Spectrom.* **254**(1-2), 1–19 (2006).
- A. Fielicke, A. Kirilyuk, C. Ratsch, J. Behler, M. Scheffler, G. Von Helden, and G. Meijer, *Phys. Rev. Lett.* **93**(2), 023401 (2004).
- J. Rothová, *Chem. Soc. Rev.* **41**(2), 547–559 (2012).
- G. Altinay and R. B. Metz, *Int. J. Mass Spectrom.* **297**(1-3), 41–45 (2010).
- B. Chiavarino, M. E. Crestoni, M. Schütz, A. Bouchet, S. Piccirillo, V. Steinmetz, O. Dopfer, and S. Fornarini, *J. Phys. Chem. A* **118**(34), 7130–7138 (2014).
- O. Dopfer, *J. Phys. Org. Chem.* **19**(8-9), 540–551 (2006).
- N. I. Hammer, J. W. Shin, J. M. Headrick, E. G. Diken, J. R. Roscioli, G. H. Weddle, and M. A. Johnson, *Science* **306**(5696), 675–679 (2004).
- J. M. Headrick, E. G. Diken, R. S. Walters, N. I. Hammer, R. A. Christie, J. Cui, E. M. Myshakin, M. A. Duncan, M. A. Johnson, and K. D. Jordan, *Science* **308**(5729), 1765–1769 (2005).
- A. M. Rijs and J. Oomens, *Top. Curr. Chem.* **364**, 1–42 (2015).
- T. R. Rizzo and O. V. Boyarkin, *Top. Curr. Chem.* **364**, 43–98 (2015).
- T. R. Rizzo, J. A. Stearns, and O. V. Boyarkin, *Int. Rev. Phys. Chem.* **28**(3), 481–515 (2009).
- W. H. Robertson and M. A. Johnson, *Annu. Rev. Phys. Chem.* **54**, 173–213 (2003).
- D. Schröder, S. Shaik, and H. Schwarz, *Acc. Chem. Res.* **33**(3), 139–145 (2000).
- H. Schwarz, *Catal. Sci. Technol.* **7**(19), 4302–4314 (2017).
- P. Gruene, A. Fielicke, and G. Meijer, *J. Chem. Phys.* **127**(23), 234307 (2007).
- J. Du, X. Sun, and G. Jiang, *J. Chem. Phys.* **136**(9), 094311 (2012).
- L.-H. Mou, Z.-Y. Li, and S.-G. He, *J. Phys. Chem. Lett.* **13**(18), 4159–4169 (2022).

- ⁶²J. Mohrbach, S. Dillinger, and G. Niedner-Schatteburg, *J. Phys. Chem. C* **121**(20), 10907–10918 (2017).
- ⁶³S. Dillinger, J. Mohrbach, and G. Niedner-Schatteburg, *J. Chem. Phys.* **147**(18), 184305 (2017).
- ⁶⁴A. A. Ehrhard, M. P. Klein, J. Mohrbach, S. Dillinger, and G. Niedner-Schatteburg, *Mol. Phys.* **119**(17-18), e1953172 (2021).
- ⁶⁵A. A. Ehrhard, M. P. Klein, J. Mohrbach, S. Dillinger, and G. Niedner-Schatteburg, *J. Chem. Phys.* **156**(5), 054308 (2022).
- ⁶⁶A. Straßner, M. P. Klein, D. V. Fries, C. Wiehn, M. E. Huber, J. Mohrbach, S. Dillinger, D. Spelsberg, P. B. Armentrout, and G. Niedner-Schatteburg, *J. Chem. Phys.* **155**(24), 244306 (2021).
- ⁶⁷A. Straßner, C. Wiehn, M. P. Klein, D. V. Fries, S. Dillinger, J. Mohrbach, M. H. Proscenc, P. B. Armentrout, and G. Niedner-Schatteburg, *J. Chem. Phys.* **155**(24), 244305 (2021).
- ⁶⁸S. Dillinger, J. Mohrbach, J. Hewer, M. Gaffga, and G. Niedner-Schatteburg, *Phys. Chem. Chem. Phys.* **17**(16), 10358–10362 (2015).
- ⁶⁹S. Dillinger, M. P. Klein, A. Steiner, D. C. McDonald, M. A. Duncan, M. M. Kappes, and G. Niedner-Schatteburg, *J. Phys. Chem. Lett.* **9**(4), 914–918 (2018).
- ⁷⁰M. P. Klein, A. A. Ehrhard, J. Mohrbach, S. Dillinger, and G. Niedner-Schatteburg, *Top. Catal.* **61**(1-2), 106–118 (2018).
- ⁷¹M. J. Frisch, G. W. Trucks, H. B. Schlegel, G. E. Scuseria, M. A. Robb, J. R. Cheeseman, G. Scalmani, V. Barone, B. Mennucci, G. A. Petersson, H. Nakatsuji, M. Caricato, X. Li, H. P. Hratchian, A. F. Izmaylov, J. Bloino, G. Zheng, J. L. Sonnenberg, M. Hada, M. Ehara, K. Toyota, R. Fukuda, J. Hasegawa, M. Ishida, T. Nakajima, Y. Honda, O. Kitao, H. Nakai, T. Vreven, J. A. Montgomery, Jr., J. E. Peralta, F. Ogliaro, M. Bearpark, J. J. Heyd, E. Brothers, K. N. Kudin, V. N. Staroverov, R. Kobayashi, J. Normand, K. Raghavachari, A. Rendell, J. C. Burant, S. S. Iyengar, J. Tomasi, M. Cossi, N. Rega, J. M. Millam, M. Klene, J. E. Knox, J. B. Cross, V. Bakken, C. Adamo, J. Jaramillo, R. Gomperts, R. E. Stratmann, O. Yazyev, A. J. Austin, R. Cammi, C. Pomelli, J. W. Ochterski, R. L. Martin, K. Morokuma, V. G. Zakrzewski, G. A. Voth, P. Salvador, J. J. Dannenberg, S. Dapprich, A. D. Daniels, Ö. Farkas, J. B. Foresman, J. V. Ortiz, J. Cioslowski, and D. J. Fox, *GAUSSIAN 09, Revision E.01*, Gaussian, Inc., Wallingford, CT, 2009.
- ⁷²M. J. Frisch, G. W. Trucks, H. B. Schlegel, G. E. Scuseria, M. A. Robb, J. R. Cheeseman, G. Scalmani, V. Barone, G. A. Petersson, H. Nakatsuji, X. Li, M. Caricato, A. V. Marenich, J. Bloino, B. G. Janesko, R. Gomperts, B. Mennucci, H. Hratchian, J. V. Ortiz, A. F. Izmaylov, J. L. Sonnenberg, D. Williams-Young, F. Ding, F. Lipparini, F. Egidi, J. Goings, B. Peng, A. Petrone, T. Henderson, D. Ranasinghe, V. G. Zakrzewski, J. Gao, N. Rega, G. Zheng, W. Liang, M. Hada, M. Ehara, K. Toyota, R. Fukuda, J. Hasegawa, M. Ishida, T. Nakajima, Y. Honda, O. Kitao, H. Nakai, T. Vreven, K. Throssell, J. A. Montgomery, Jr., J. E. Peralta, F. Ogliaro, M. J. Bearpark, J. J. Heyd, E. N. Brothers, K. N. Kudin, V. N. Staroverov, T. A. Keith, R. Kobayashi, J. Normand, K. Raghavachari, A. P. Rendell, J. C. Burant, S. S. Iyengar, J. Tomasi, M. Cossi, J. M. Millam, M. Klene, C. Adamo, R. Cammi, J. W. Ochterski, R. L. Martin, K. Morokuma, O. Farkas, J. B. Foresman, and D. J. Fox, *GAUSSIAN 16, Revision C.01*, Gaussian, Inc., Wallingford, CT, 2016.
- ⁷³J. P. Perdew, K. Burke, and M. Ernzerhof, *Phys. Rev. Lett.* **78**(7), 1396 (1997).
- ⁷⁴C. Adamo and V. Barone, *J. Chem. Phys.* **110**(13), 6158–6170 (1999).
- ⁷⁵F. Weigend and R. Ahlrichs, *Phys. Chem. Chem. Phys.* **7**(18), 3297–3305 (2005).
- ⁷⁶D. Andrae, U. Häußermann, M. Dolg, H. Stoll, and H. Preuß, *Theor. Chim. Acta* **77**(2), 123–141 (1990).
- ⁷⁷D. Figgen, K. A. Peterson, M. Dolg, and H. Stoll, *J. Chem. Phys.* **130**(16), 164108 (2009).
- ⁷⁸J. Mohrbach, S. Dillinger, and G. Niedner-Schatteburg, *J. Chem. Phys.* **147**(18), 184304 (2017).
- ⁷⁹H. B. Schlegel, *J. Comput. Chem.* **3**(2), 214–218 (1982).
- ⁸⁰C. Peng and H. Bernhard Schlegel, *Isr. J. Chem.* **33**(4), 449–454 (1993).
- ⁸¹H. P. Hratchian and H. B. Schlegel, *Theory and Applications of Computational Chemistry*, edited by C. E. Dykstra, G. Frenking, K. S. Kim, and G. E. Scuseria (Elsevier, Amsterdam, 2005), pp. 195–249.
- ⁸²K. Fukui, *Acc. Chem. Res.* **14**(12), 363–368 (1981).
- ⁸³C. Lee, W. Yang, and R. G. Parr, *Phys. Rev. B* **37**(2), 785–789 (1988).
- ⁸⁴A. D. Becke, *J. Chem. Phys.* **98**(7), 5648–5652 (1993).
- ⁸⁵W. M. Haynes, *CRC Handbook of Chemistry and Physics* (CRC Press Taylor & Francis Group, 2014).
- ⁸⁶G. Blyholder, *J. Phys. Chem.* **68**(10), 2772–2777 (1964).
- ⁸⁷J. Chatt and L. A. Duncanson, *J. Chem. Soc.* **1953**, 2939–2947.
- ⁸⁸M. P. Klein, A. A. Ehrhard, M. E. Huber, A. Straßner, D. V. Fries, S. Dillinger, J. Mohrbach, and G. Niedner-Schatteburg, *J. Chem. Phys.* **156**(1), 014302 (2022).
- ⁸⁹M. P. Klein, Doctoral thesis, Technische Universität Kaiserslautern, 2021.
- ⁹⁰S. Dillinger, Doctoral thesis, Technische Universität Kaiserslautern, 2017.

4.3 Supplementary Information

Supplementary material to

**Cryo IR Spectroscopy and Cryo Kinetics
of Dinitrogen Activation and Cleavage
by Small Tantalum Cluster Cations**

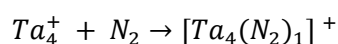
Daniela V. Fries, Matthias P. Klein, Annika Straßner, Maximilian E. Huber,
Maximilian Luczak, Christopher Wiehn, and Gereon Niedner-Schatteburg^{a)}

Department of Chemistry and
State Research Center OPTIMAS,
Rheinland-Pfälzische Technische Universität (RPTU) Kaiserslautern-Landau,
67663 Kaiserslautern, Germany

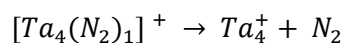
a) Author to whom correspondence should be addressed: gns@rptu.de

Text 1: Nomenclature for the Ta_n^+ clusters and their adsorbates

Nitrogen adsorption on the tantalum clusters yields cluster adsorbate complexes, which are referred to as $[Ta_n(N_2)_m]^+$ in typical chemical complex nomenclature. Continuing the series studies on transition metal clusters¹⁻⁷ and for better reference, we have again chosen an abridged (n,m) nomenclature for these Tantalum clusters $[Ta_n(N_2)_m]^+$. In this nomenclature, n represents the size of the cluster; e. g., n = 4 represents a cluster of four tantalum atoms. This cluster size consequently corresponds to the shortened notation (4,m). According to our investigations there are 14 complexes of the form (4,m), where m stands for the number of N_2 molecules attached to the cluster. Hence, for the cluster size n = 4 the index m ranges from 0 to 13. The 14 (4,m) complexes are interlinked by 13 processes, respectively, in the form of adsorption and desorption reactions. The rate constants for these adsorption and desorption processes are labelled as k_m and $k_{-(m+1)}$. Therefore, m can assume values from 0 to 12. We use e.g. $k_0 := k_{0 \rightarrow 1}$ for the adsorption step:



and $k_{-1} := k_{1 \rightarrow 0}$ for the desorption step:



To disambiguate the relative positions of the resulting nitride ligands on Ta_n^+ , n = 2 – 4, we additionally use the following subscript abbreviations: *gem* (geminal, on the same Ta-Ta edge), and *vic* (vicinal, on neighbored Ta-Ta edges), as well as ES (edge/surface, across the Ta-Ta-edge and above the Ta-Ta-Ta surface) and EE (edge/edge, twice across the same Ta-Ta-edge).

4. Cryo IR Spectroscopy and Cryo Kinetics of Dinitrogen Activation and Cleavage by Small Tantalum Cluster Cations

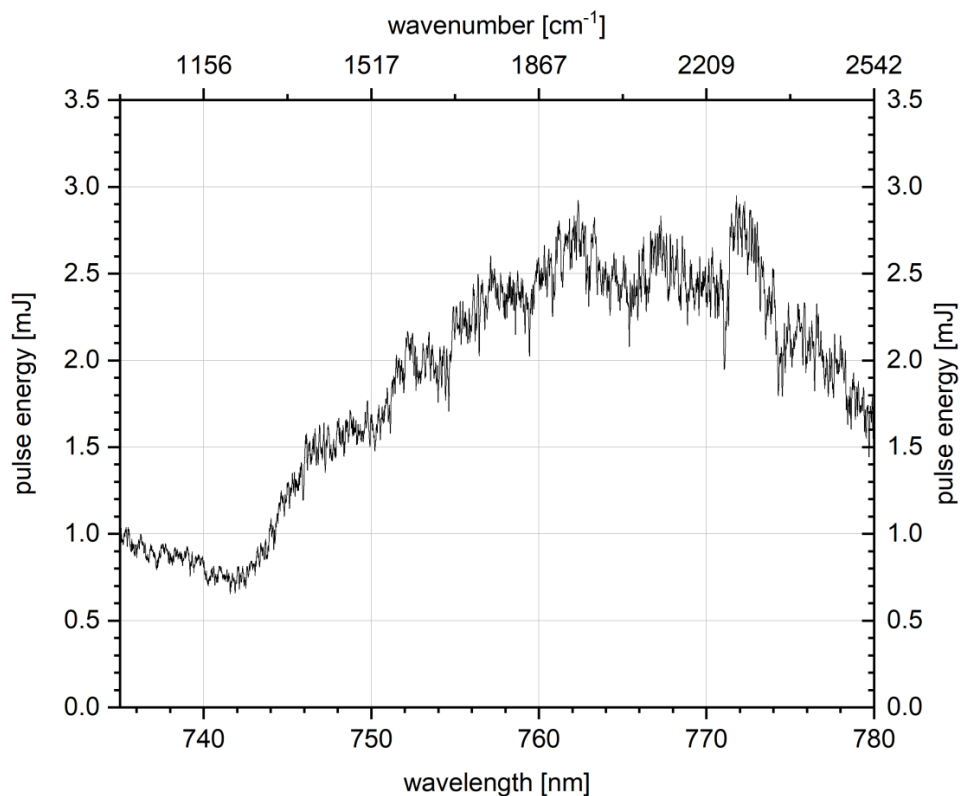


Figure S1: Laser pulse energy in dependence of wavelength and wavenumber.

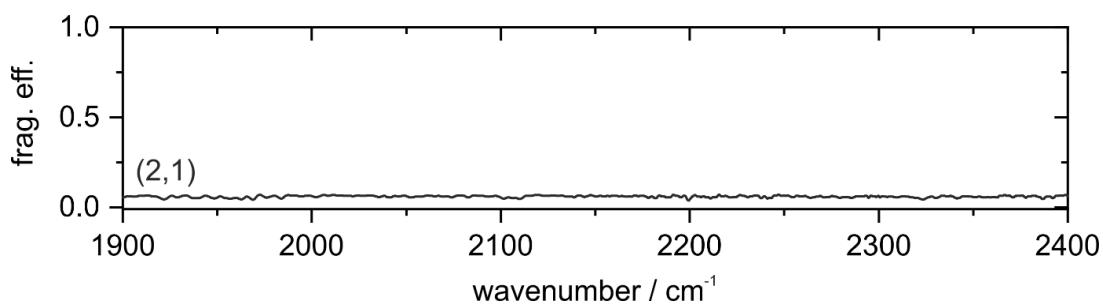


Figure S2: IR spectrum of $\text{Ta}_2(\text{N}_2)_1^+$ (simplified nomenclature: (2,1)) in the range of 1900 cm^{-1} to 2400 cm^{-1} . Note the absence of vibrational bands for this cluster species which reinforces the assertion from Geng et al. ⁸ of an activated N_2 molecule by Ta_2^+ .

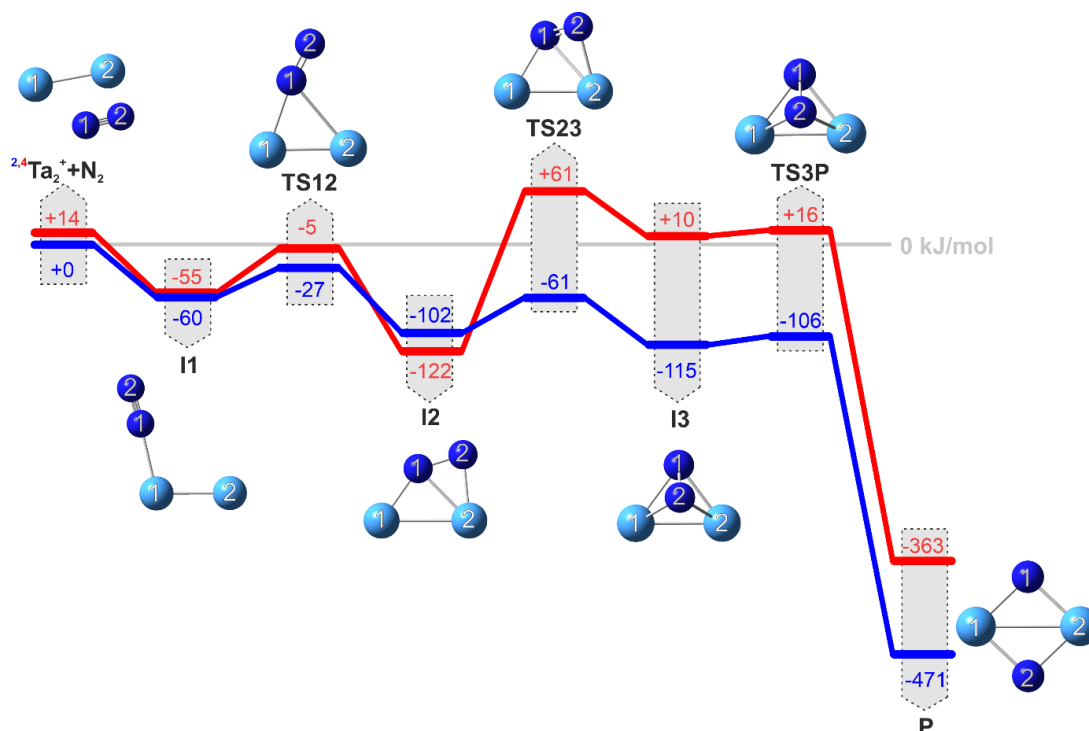


Figure S3: Reaction pathway of N_2 cleavage by Ta_2^+ (blue: doublet state, red: quartet state). Three submerged transition states allow for facile stepwise activation which ultimately lead to the dinitro product $\text{P}_{(2,1)}$. Relative energies are in kJ/mol and geometry structures are triplet states. Note the overlooked entrance channel barrier $\text{TS12}_{(2,1)}$ and the additional intermediate $\text{I1}_{(2,1)}$ in comparison to the previous study on Ta_2^+ cluster under ambient conditions⁸. For reason of clarity, the nomenclature is presented in an abbreviated form (e. g. I1 stands for $\text{I1}_{(3,1)}$).

4. Cryo IR Spectroscopy and Cryo Kinetics of Dinitrogen Activation and Cleavage by Small Tantalum Cluster Cations

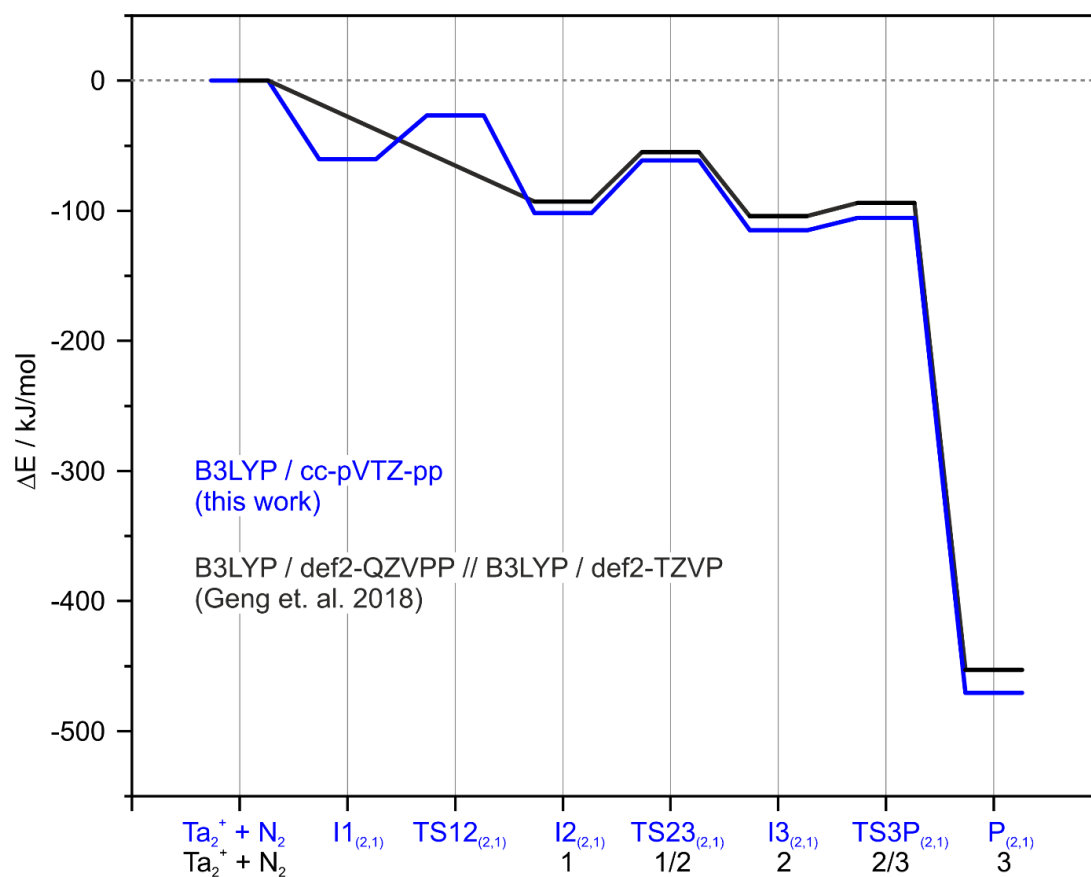


Figure S4: Reaction pathways of N₂ cleavage by Ta₂⁺ (blue: this work, B3LYP/cc-def2TZVP(N),PVTZ-pp(Ta); black: Geng et. al. ⁸, B3LYP/def2QZVPP//B3LYP/def2-TZVP). Note the overlooked entrance channel barrier TS12_(2,1) and the additional intermediate I1_(2,1) (blue) in comparison to the previous study on Ta₂⁺ cluster under ambient conditions (black).

Table S1: Calculated energies of the cluster adsorbate complex $[\text{Ta}_2(\text{N}_2)_4]^+$ in the doubled and quartet state along the activation pathway of the first N_2 molecule on a Ta_2^+ cluster complex. For both cases, the ΔE values are determined with respect to the initial doublet state (Ta_2^+ , N_2). For graphical representations, see Fig. 1 and Fig. S2.

	PBE0/cc-pVTZ-pp				B3LYP/cc-pVTZ-pp			
	doublet state		quartet state		doublet state		quartet state	
	energy E / Ha	ΔE / kJ/mol	energy E / Ha	ΔE / kJ/mol	energy E / Ha	ΔE / kJ/mol	energy E / Ha	ΔE / kJ/mol
Ta_2^+ , N_2	-223.894648	0	-223.891775	8	-224.095797	0	-224.090588	14
$\text{I1}_{(2,1)}$	-223.922430	-73	-223.924083	-77	-224.118790	-60	-224.116748	-55
$\text{TS12}_{(2,1)}$	-223.915659	-55	-223.910882	-43	-224.106040	-27	-224.097525	-5
$\text{I2}_{(2,1)}$	-223.951290	-149	-223.962751	-179	-224.134524	-102	-224.142448	-122
$\text{TS23}_{(2,1)}$	-223.934462	-105	-223.928369	-89	-224.119115	-61	-224.111191	61
$\text{I3}_{(2,1)}$	-223.959704	-171	-223.952947	-153	-224.139584	-115	-224.130760	10
$\text{TS3P}_{(2,1)}$	-223.952208	-151	-223.946917	-137	-224.135985	-106	-224.128330	16
$\text{P}_{(2,1)}$	-224.084558	-499	-224.093602	-522	-224.275079	-471	-224.272937	-363

Table S2: Calculated distances in Å of atoms within Ta_2^+ , N_2 and $[Ta_2(N_2)]^+$ in the doublet state along the activation pathway of N_2 on Ta_2^+ .

	$^2[Ta_2]^+$	1N_2	$^2^1[2,1]$	$^2TS12[2,1]$	$^2^1[2,1]$	$^2TS23[2,1]$	$^2^1[2,1]$	$^2TS3P[2,1]$	$^2P[2,1]$
Ta1-Ta2	2.15135	-	2.19501	2.24534	2.46833	2.32662	2.32365	2.33567	2.64616
Ta1-N1	-	-	2.11500	1.99905	1.78924	1.88122	1.96056	1.96305	1.85348
Ta1-N2	-	-	-	-	-	-	1.95943	1.90483	1.85330
Ta2-N1	-	-	-	2.47510	2.04418	2.13546	1.96072	1.96308	1.81361
Ta2-N2	-	-	-	-	1.86146	1.93177	1.95982	1.90481	1.81364
N1-N2	-	1.08948	1.10224	1.12800	1.32036	1.28810	1.52737	1.85602	-

Table S3: Calculated distances in Å of atoms within Ta_2^+ , N_2 and $[Ta_2(N_2)]^+$ in the quartet state along the activation pathway of N_2 on Ta_2^+ .

	$^4[Ta_2]^+$	1N_2	$^4^1[2,1]$	$^4TS12[2,1]$	$^4^1[2,1]$	$^4TS23[2,1]$	$^4^1[2,1]$	$^4TS3P[2,1]$	$^4P[2,1]$
Ta1-Ta2	2.16789	-	2.25730	2.29727	2.55569	2.55470	2.49863	2.48555	2.70328
Ta1-N1	-	-	2.06540	1.96580	1.84181	1.82866	1.93594	1.87377	1.84308
Ta1-N2	-	-	-	-	-	-	1.93600	2.06428	1.84314
Ta2-N1	-	-	-	2.35038	1.98476	2.18354	1.93574	1.96781	1.84267
Ta2-N2	-	-	-	-	1.86834	1.81956	1.93581	1.92172	1.84288
N1-N2	-	1.08948	1.10678	1.14103	1.30737	1.39166	1.54625	1.84334	-

Table S4: Calculated distances in Å of atoms within Ta_2^+ , N_2 and $[Ta_2(N_2)_1]^+$ in the doublet state along the activation pathway of N_2 on Ta_2^+ .

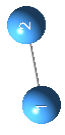
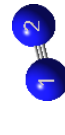
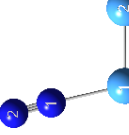
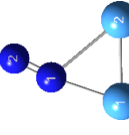

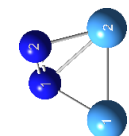
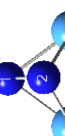
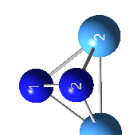
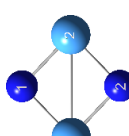


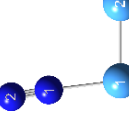
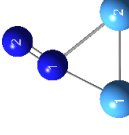
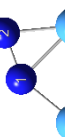
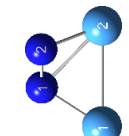
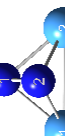
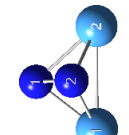
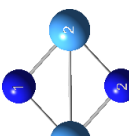
	$^2[Ta_2]^+$	1N_2	$^211_{(2,1)}$	$^2TS12_{(2,1)}$	$^212_{(2,1)}$	$^2TS23_{(2,1)}$	$^213_{(2,1)}$	$^2TS3P_{(2,1)}$	$^2P_{(2,1)}$
									
Ta1-Ta2	2.17084	-	2.20780	2.22881	2.484900	2.33756	2.35064	2.35695	2.66928
Ta1-N1	-	-	2.14731	2.02336	1.80263	1.88648	1.97305	1.93011	1.84174
Ta1-N2	-	-	-	-	-	-	1.97294	1.98107	1.84178
Ta2-N1	-	-	-	2.46216	2.06625	2.16350	1.97297	1.93000	1.84169
Ta2-N2	-	-	-	-	1.87300	1.92564	1.97290	1.98103	1.84168
N1-N2	-	1.09090	1.10329	1.13172	1.32793	1.31266	1.58809	1.87265	-

Table S5: Calculated distances in Å of atoms within Ta_2^+ , N_2 and $[Ta_2(N_2)_1]^+$ in the quartet state along the activation pathway of N_2 on Ta_2^+ .


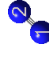
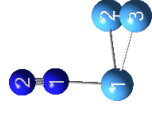
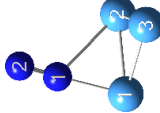
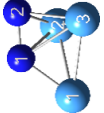
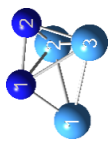

	$^4[Ta_2]^+$	1N_2	$^411_{(2,1)}$	$^4TS12_{(2,1)}$	$^412_{(2,1)}$	$^4TS23_{(2,1)}$	$^413_{(2,1)}$	$^4TS3P_{(2,1)}$	$^4P_{(2,1)}$
									
Ta1-Ta2	2.18472	-	2.27197	2.34318	2.58140	2.58227	2.52994	2.52012	2.72976
Ta1-N1	-	-	2.09733	2.00834	1.85361	1.84064	1.94954	1.86217	1.85657
Ta1-N2	-	-	-	-	-	-	1.94940	2.03360	1.85666
Ta2-N1	-	-	-	2.30017	2.01032	2.22359	1.95007	2.03409	1.85648
Ta2-N2	-	-	-	-	1.88488	1.83307	1.95019	1.86245	1.85651
N1-N2	-	1.09090	1.10753	1.14152	1.31136	1.40039	1.58501	1.81743	-

4. Cryo IR Spectroscopy and Cryo Kinetics of Dinitrogen Activation and Cleavage by Small Tantalum Cluster Cations

Table S6: Calculated energies of the cluster adsorbate complex $[\text{Ta}_3(\text{N}_2)]^+$ in the singlet, triplet and quintet state along the activation pathway of the first N_2 molecule on a Ta_3^+ cluster complex. The ΔE values are determined with respect to the initial triplet state (Ta_3^+ , N_2). For a graphical representation, see Fig. 3.

	singlet state		triplet state		quintet state	
	energy E / Ha	energy E / Ha	energy E / Ha	ΔE / kJ/mol	energy E / Ha	ΔE / kJ/mol
Ta_3^+ , N_2	-281.343447	59	-281.365799	0	-281.363447	6
$\text{I1}_{(3,1)}$	-281.385995	-53	-281.397049	-82	-281.395008	-77
$\text{TS12}_{(3,1)}$	-281.384100	-48	-281.393018	-71	-281.380739	-39
$\text{I2}_{(3,1)}$	-	-	-281.419327	-141	-281.407938	-111
$\text{TS23}_{(3,1)}$	-	-	-281.415778	-131	-281.376671	-29
$\text{I3}_{(3,1)}$	-281.463663	-257	-281.439709	-194	-281.424901	-155
$\text{TS3P}_{\text{gem}(3,1)}^{\text{ES}}$	-281.451599	-225	-281.434097	-179	-281.394390	-75
$\text{P}_{\text{gem}(3,1)}^{\text{ES}}$	-281.544245	-469	-281.557739	-504	-281.522403	-411
$\text{TSP}_{\text{gem}}^{\text{ES}}\text{P}_{\text{gem}(3,1)}^{\text{EE}}$	-281.542107	-463	-281.524983	-418		
$\text{P}_{\text{gem}(3,1)}^{\text{EE}}$	-281.545372	-471	-281.542995	-465		
$\text{TSP}_{\text{gem}}^{\text{EE}}\text{P}_{\text{vic}(3,1)}$	-281.542103	-463	-281.526037	-421		
$\text{P}_{\text{vic}(3,1)}$	-281.548386	-479	-281.542731	-465		

Table S7: Calculated distances in Å of atoms within Ta_3^+ , N_2 and $[\text{Ta}_3(\text{N}_2)]^+$ in the singlet state along the activation pathway of N_2 on Ta_3^+ from the initial state to $\text{P}^{\text{ES}}_{\text{gem}}$.

	$^1[\text{Ta}_3]^+$	$^1\text{N}_2$	$^1\text{I1}_{(3,1)}$	$^1\text{TS12}_{(1,1)}$	$^1\text{I2}_{(3,1)}$	$^1\text{TS23}_{(3,1)}$	$^1\text{I3}_{(3,1)}$	$^1\text{TS3P}^{\text{ES}}_{\text{gem}(3,1)}$	$^1\text{P}^{\text{ES}}_{\text{gem}(3,1)}$
									
Ta1-Ta2	2.30475	-	2.45859	2.45762	-	-	2.46374	2.48040	2.35659
Ta2-Ta3	2.46803	-	2.41215	2.39536	-	-	2.39035	2.44468	2.67570
Ta1-Ta3	2.46854	-	2.45860	2.45076	-	-	2.46369	2.48047	2.59123
Ta1-N1	-	-	2.04648	2.01838	-	-	1.90490	1.85955	1.92889
Ta1-N2	-	-	-	-	-	-	-	-	-
Ta2-N1	-	-	-	2.70148	-	-	2.20943	2.27596	1.88216
Ta2-N2	-	-	-	-	-	-	2.02660	1.91285	2.37736
Ta3-N1	-	-	-	-	-	-	2.20931	2.27603	1.81628
Ta3-N2	-	-	-	-	-	-	2.02649	1.91290	1.88450
N1-N2	-	1.08948	1.11174	1.12211	-	-	1.35905	1.72801	-

4. Cryo IR Spectroscopy and Cryo Kinetics of Dinitrogen Activation and Cleavage by Small Tantalum Cluster Cations

Table S8: Calculated distances in Å of atoms within Ta_3^+ , N_2 and $[Ta_3(N_2)]^+$ in the singlet state along the activation pathway of N_2 on Ta_3^+ from P_{gem}^{ES} to P_{vic}^{1} .


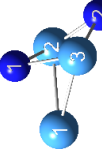

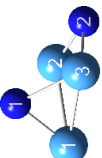
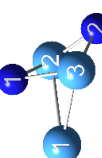

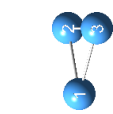
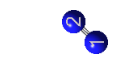
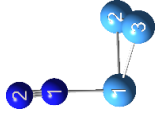
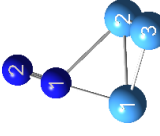
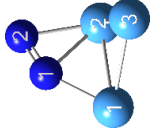
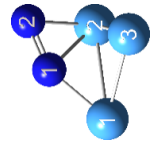
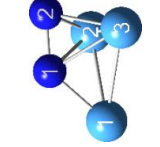
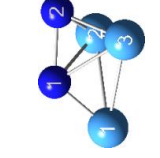
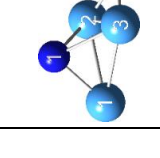
	$^1P_{gem}^{ES}$	$^1TS3P_{gem}^{ES}$	$^1P_{gem}^{EE}$	$^1TS3P_{gem}^{ES}$	$^1TS3P_{gem}^{EE}$	$^1P_{vic}^{1}$
						
Ta1-Ta2	2.35659	2.36137	2.43246	2.46840	2.58740	2.45784
Ta2-Ta3	2.67570	2.64619	2.68207	2.61660	2.64620	2.77423
Ta1-Ta3	2.59123	2.58743	2.43250	2.46848	2.36136	2.47270
Ta1-N1	1.92889	-	-	1.84790	-	1.88524
Ta1-N2	-	-	-	-	-	-
Ta2-N1	1.88216	2.01159	1.87872	2.17233	1.87348	-
Ta2-N2	2.37736	1.90198	1.87879	1.83471	1.81905	1.80537
Ta3-N1	1.81628	1.87346	1.87871	2.17227	2.01159	1.86283
Ta3-N2	1.88450	1.81904	1.87866	1.83477	1.90199	1.88967
N1-N2	-	-	-	-	-	-

Table S9: Calculated distances in Å of atoms within Ta_3^+ , N_2 and $[Ta_3(N_2)]^+$ in the triplet state along the activation pathway of N_2 on Ta_3^+ from the initial state to P_{gem}^{ES} .

	$^3[Ta_3]^+$	1N_2	$^3I1_{(3,1)}$	$^3TS12_{(1,1)}$	$^3I2_{(3,1)}$	$^3TS23_{(3,1)}$	$^3I3_{(3,1)}$	$^3TS3P_{gem(3,1)}^{ES}$	$^3P_{gem(3,1)}^{ES}$
									
Ta1-Ta2	2.40503	-	2.44641	2.42384	2.50454	2.55522	2.53755	2.57308	2.47986
Ta2-Ta3	2.40505	-	2.46010	2.41964	2.56192	2.51756	2.39642	2.39260	2.68493
Ta1-Ta3	2.40514	-	2.44630	2.52297	2.47538	2.46605	2.53953	2.57317	2.47993
Ta1-N1	-	-	2.07210	2.02970	1.91959	1.86831	1.90752	1.83090	1.84976
Ta1-N2	-	-	-	-	-	-	-	-	-
Ta2-N1	-	-	-	2.52946	2.05786	2.07330	2.15352	2.19072	2.10539
Ta2-N2	-	-	-	-	2.01668	1.91827	2.00898	1.94711	1.84797
Ta3-N1	-	-	-	-	-	-	2.15333	2.19063	2.10566
Ta3-N2	-	-	-	-	-	-	2.00872	1.94715	1.84797
N1-N2	-	1.08948	1.10816	1.12520	1.23180	1.32753	1.42803	1.76546	-

4. Cryo IR Spectroscopy and Cryo Kinetics of Dinitrogen Activation and Cleavage by Small Tantalum Cluster Cations

Table S10: Calculated distances in Å of atoms within Ta_3^+ , N_2 and $[Ta_3(N_2)]^+$ in the triplet state along the activation pathway of N_2 on Ta_3^+ from P_{gem}^{ES} to $P_{vic}^{(3,1)}$.

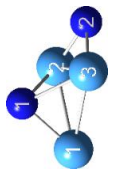

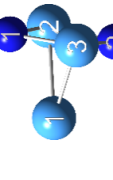
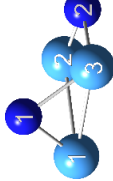


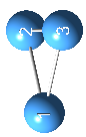

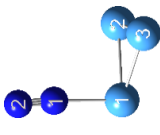
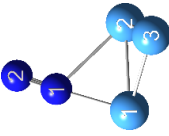

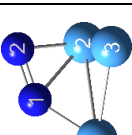

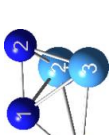

	${}^3P_{gem}^{ES}(3,1)$	${}^3TS3P_{gem}^{ES}$	${}^3P_{gem}^{EE}(3,1)$	${}^3TS3P_{gem}^{ES}$	${}^3TS3P_{gem}^{EE}$	${}^3P_{vic}^{(3,1)}$
						
Ta1-Ta2	2.47986	2.58756	2.40582	2.55835	2.60629	2.56412
Ta2-Ta3	2.68493	2.58008	2.85789	2.79995	2.76418	2.82931
Ta1-Ta3	2.47993	2.58657	2.40589	2.4837	2.41789	2.50616
Ta1-N1	1.84976	-	-	1.83388	-	1.85699
Ta1-N2	-	-	-	-	-	-
Ta2-N1	2.10539	1.86976	1.89995	2.85852	1.87961	-
Ta2-N2	1.84797	1.86928	1.90009	1.81909	1.81651	1.81805
Ta3-N1	2.10566	1.86969	1.90012	1.92516	1.9008	1.86315
Ta3-N2	1.84797	1.87011	1.90001	1.87278	1.92108	1.87754
N1-N2	-	-	-	-	-	-

Table S11: Calculated distances in Å of atoms within Ta_3^+ , N_2 and $[Ta_3(N_2)]^+$ in the quintet state along the activation pathway of N_2 on Ta_3^+ from the initial state to P_{gem}^{ES} .

	$^5[Ta_3]^+$	1N_2	$^5I1_{(3,1)}$	$^5TS12_{(1,1)}$	$^5I2_{(3,1)}$	$^5TS23_{(3,1)}$	$^5I3_{(3,1)}$	$^5TS3P_{gem(3,1)}^{ES}$	$^5P_{gem(3,1)}^{ES}$
									
Ta1-Ta2	2.42758	-	2.47306	2.49857	2.5475	2.0006	2.46979	2.9237	2.55529
Ta2-Ta3	2.52471	-	2.50638	2.49717	2.53358	2.50234	2.94051	2.42038	2.72319
Ta1-Ta3	2.42767	-	2.47317	2.48231	2.55113	2.49989	2.46976	2.53621	2.55533
Ta1-N1	-	-	2.09393	2.01304	1.93769	1.86344	2.03949	1.91643	2.15566
Ta1-N2	-	-	-	-	-	-	-	-	-
Ta2-N1	-	-	-	2.34498	2.06111	2.11941	2.06243	1.99611	1.91784
Ta2-N2	-	-	-	-	1.99186	1.88143	1.9261	1.96333	1.85692
Ta3-N1	-	-	-	-	-	-	2.06256	2.22725	1.91776
Ta3-N2	-	-	-	-	-	-	1.92619	1.9227	1.85701
N1-N2	-	1.08948	1.10496	1.13687	1.23633	1.32551	1.55042	1.74553	-

4. Cryo IR Spectroscopy and Cryo Kinetics of Dinitrogen Activation and Cleavage by Small Tantalum Cluster Cations

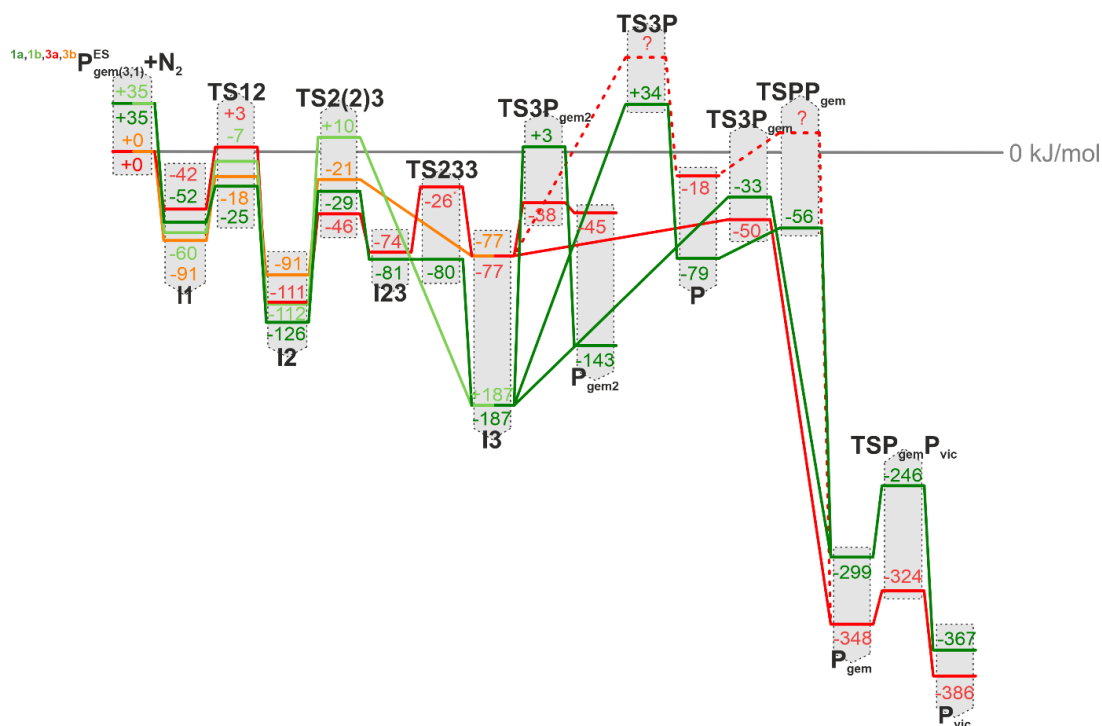


Figure S5: Reaction pathways of a second N_2 activation by the dinitro species $P_{gem(3,1)}^{ES}$ two singlet pathways, 1a (dark green) and 1b (light green), and two triplet pathways, 3a (red) and 3b (orange), each starting either through N_2 adsorption to Ta1 (pathways a) or to Ta3 (pathways b). There is a striking similarity to the first cleavage pathway cf. Fig. 3.: reorganization of the in-plane $\mu_2\text{-}\kappa N_3:\kappa N_3,N_4$ coordination across an intact Ta-Ta edge towards perpendicular $\mu_3\text{-}\kappa N_3:\kappa N_3,N_4:\kappa N_3,N_4$ coordination above the Ta-Ta-Ta surface. Starting from the most likely product complex $P_{gem(3,1)}^{ES}$ of the activation pathway of the first N_2 molecule by Ta_3^+ the pathway for a second N_2 molecule activation yields in the intermediate $I_{3(3,2)}$ which is independent of initial N_2 coordination to the Ta1 (paths a) or Ta3 (paths b) atom and gets stuck in front of unsurmountable barriers that hamper any further or ultimate NN bond cleavage. For reason of clarity, the nomenclature is presented in an abbreviated form (e. g. I1 stands for $I_{1(3,2)}$).

Table S12: Calculated energies of the cluster adsorbate complex $[\text{Ta}_3(\text{N}_2)_2]^+$ in the singlet state along the activation pathways a and b of the second N_2 molecule on a Ta_3^+ cluster complex. The ΔE values are determined with respect to the initial triplet state (${}^3\text{P}_{\text{gem}}^{\text{ES}}, \text{N}_2$). For graphical representation, see Fig. 4 and Fig. S4.

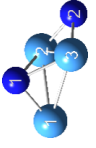

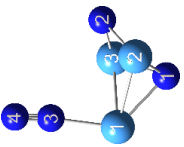
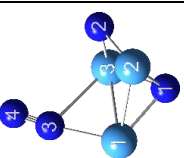
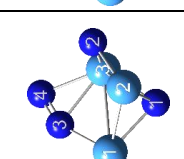
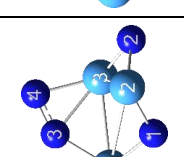
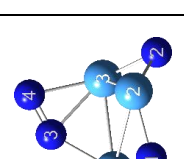
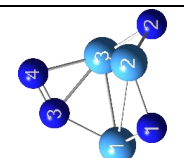
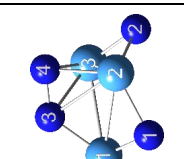
	pathway a		pathway b	
	energy E / Ha	energy E / Ha	energy E / Ha	ΔE / kJ/mol
$\text{P}_{\text{gem}}^{\text{ES}(3,1)}, \text{N}_2$	-390.984864	35	-390.984864	35
$\text{I1}_{(3,2)}$	-391.018245	-52	-391.021178	-60
$\text{TS12}_{(3,2)}$	-391.008110	-26	-391.001114	-7
$\text{I2}_{(3,2)}$	-391.046286	-126	-391.041176	-112
$\text{TS2(2)3}_{(3,2)}$	-391.009544	-29	-390.994376	10
$\text{I23}_{(3,2)}$	-391.028581	-79	-	-
$\text{TS233}_{(3,2)}$	-391.028658	-80	-	-
$\text{I3}_{(3,2)}$	-391.069541	-187	-	-
$\text{TS3P}_{\text{gem}2(3,2)}$	-390.997073	3	-	-
$\text{P}_{\text{gem}2(3,2)}$	-391.052855	-143	-	-
$\text{TS3P}_{(3,2)}$	-390.985179	35	-	-
$\text{P}_{(3,2)}$	-391.028346	-79	-	-
$\text{TS3P}_{\text{gem}(3,2)}$	-391.011091	-33	-	-
$\text{P}_{\text{gem}(3,2)}$	-391.112219	-299	-	-
$\text{TSPP}_{\text{gem}(3,2)}$	-391.019789	-56	-	-
$\text{TSP}_{\text{gem}}\text{P}_{\text{vic}(3,2)}$	-391.092113	-246	-	-
$\text{P}_{\text{vic}(3,2)}$	-391.138270	-367	-	-

4. Cryo IR Spectroscopy and Cryo Kinetics of Dinitrogen Activation and Cleavage by Small Tantalum Cluster Cations

Table S13: Calculated energies of the cluster adsorbate complex $[\text{Ta}_3(\text{N}_2)_2]^+$ in the triplet state along the activation pathways a and b of the second N_2 molecule on a Ta_3^+ cluster complex. The ΔE values are determined with respect to the initial triplet state (${}^3\text{P}_{\text{gem}}^{\text{ES}}, \text{N}_2$). For graphical representation, see Fig. 4 and Fig. S4.

	pathway a		pathway b	
	energy E / Ha	energy E / Ha	energy E / Ha	ΔE / kJ/mol
$\text{P}_{\text{gem}(3,1)}^{\text{ES}}, \text{N}_2$	-390.998358	0	-390.998358	0
$\text{I1}_{(3,2)}$	-391.014498	-42	-391.023354	-66
$\text{TS12}_{(3,2)}$	-390.997176	3	-391.005324	-18
$\text{I2}_{(3,2)}$	-391.040611	-111	-391.032980	-91
$\text{TS2(2)3}_{(3,2)}$	-391.015834	-46	-391.006259	-21
$\text{I23}_{(3,2)}$	-391.026634	-74	-	-
$\text{TS233}_{(3,2)}$	-391.008292	-26	-	-
$\text{I3}_{(3,2)}$	-391.027629	-77	-	-
$\text{TS3P}_{\text{gem}2(3,2)}$	-391.012715	-38	-	-
$\text{P}_{\text{gem}2(3,2)}$	-391.015599	-45	-	-
$\text{P}_{(3,2)}$	-391.005182	-18	-	-
$\text{TS3P}_{\text{gem}(3,2)}$	-391.017505	-50	-	-
$\text{P}_{\text{gem}(3,2)}$	-391.131018	-348	-	-
$\text{TSP}_{\text{gem}}\text{P}_{\text{vic}(3,2)}$	-391.121676	-324	-	-
$\text{P}_{\text{vic}(3,2)}$	-391.145559	-386	-	-

Table S14: Calculated distances in Å of atoms within PES_{gem} , N_2 and $[Ta_3(N_2)_2]^+$ in the singlet state along the activation pathway a of N_2 on PES_{gem} from the initial state to $I3_{(3,2)}$.

	$1PES_{gem(3,1)}$	$1N_2$	$1I1_{(3,2)}$	$1TS12_{(3,2)}$	$1I2_{(3,2)}$	$1TS223_{(3,2)}$	$1I23_{(3,2)}$	$1TS233_{(3,2)}$	$1I3_{(3,2)}$
									
Ta1-Ta2	2.35659	-	2.47948	2.42545	2.4587	3.14179	2.91311	2.89602	2.71408
Ta2-Ta3	2.6757	-	2.64931	2.65247	2.69208	2.64563	2.60044	2.56524	2.44093
Ta1-Ta3	2.59123	-	2.47958	2.52265	2.66177	2.62513	2.54387	2.56045	2.69978
Ta1-N1	1.92889	-	2.13953	2.05533	1.98044	1.86173	1.83198	1.82903	1.79692
Ta1-N3	-	-	2.08351	2.05023	1.91333	1.85914	1.95422	1.93821	1.87347
Ta2-N1	1.88216	-	1.92942	2.04994	2.03767	1.86867	1.89745	1.90375	1.95661
Ta2-N2	2.37736	-	1.86239	1.87177	1.85123	1.77432	1.78172	1.78725	1.89458
Ta2-N3	-	-	-	-	-	-	-	-	2.39661
Ta2-N4	-	-	-	-	-	-	-	-	2.05256
Ta3-N1	1.81628	-	1.92936	1.89656	2.00501	-	-	-	-
Ta3-N2	1.8845	-	1.86235	1.83991	1.8592	1.96652	1.9648	1.96026	1.85752
Ta3-N3	-	-	-	2.54154	2.07327	2.08032	2.06777	2.08086	2.23426
Ta3-N4	-	-	-	-	2.01943	1.91454	2.05819	2.03837	2.04184
N3-N4	-	1.08948	1.10815	1.12437	1.22842	1.28341	1.22861	1.24318	1.35776

4. Cryo IR Spectroscopy and Cryo Kinetics of Dinitrogen Activation and Cleavage by Small Tantalum Cluster Cations

Table S15: Calculated distances in Å of atoms within PES_{gem} , N_2 and $[Ta_3(N_2)_2]^+$ in the triplet state along the activation pathway a of N_2 on PES_{gem} from the initial state to $I3_{(3,2)}$.

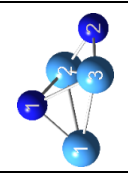
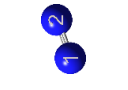







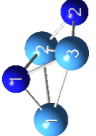

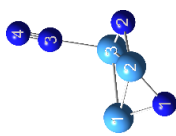
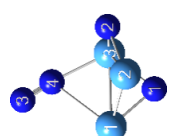


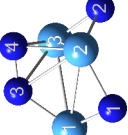
	${}^3PES_{gem(3,1)}$	1N_2	${}^3I1_{(3,2)}$	${}^3TS12_{(3,2)}$	${}^3I2_{(3,2)}$	${}^3TS223_{(3,2)}$	${}^3I23_{(3,2)}$	${}^3TS233_{(3,2)}$	${}^3I3_{(3,2)}$
									
Ta1-Ta2	2.47986	-	2.53825	2.5123	2.63017	2.57787	2.81907	2.8961	2.74471
Ta2-Ta3	2.68493	-	2.60494	2.7072	2.75403	2.79869	2.80393	2.56535	2.47746
Ta1-Ta3	2.47993	-	2.53806	2.66058	2.71447	2.52018	2.53612	2.56054	3.07571
Ta1-N1	1.84976	-	2.23617	1.88376	1.86288	1.97281	1.87355	1.82904	1.78323
Ta1-N3	-	-	2.17187	2.0564	1.90184	1.99266	2.01391	1.93821	1.88472
Ta2-N1	2.10539	-	1.92712	2.06134	2.06097	1.83901	1.84243	1.90373	1.97237
Ta2-N2	1.84797	-	1.85272	1.85398	1.80675	1.84791	1.84124	1.78729	1.89997
Ta2-N3	-	-	-	-	-	-	-	-	2.37077
Ta2-N4	-	-	-	-	-	-	-	-	2.02339
Ta3-N1	2.10566	-	1.927	2.0162	2.06756	-	-	-	-
Ta3-N2	1.84797	-	1.85283	1.8429	1.90733	1.87299	1.8742	1.96032	1.84418
Ta3-N3	-	-	-	2.67147	2.10879	2.07388	2.10485	2.08085	2.29065
Ta3-N4	-	-	-	-	2.01169	1.98365	2.06804	2.03833	2.04438
N3-N4	-	1.08948	1.10145	1.12045	1.2336	1.24756	1.21996	1.24321	1.34542

Table S16: Calculated distances in Å of atoms within PES_{gem} , N_2 and $[Ta_3(N_2)_2]^+$ in the singlet state along the activation pathway b of N_2 on PES_{gem} from the initial state to $I3_{(3,2)}$.

	$^1PES_{gem(3,1)}$	1N_2	$^1I1_{(3,2)}$	$^1TS12_{(3,2)}$	$^1I2_{(3,2)}$	$^1TS23_{(3,2)}$	$^1I3_{(3,2)}$
							
Ta1-Ta2	2.35659	-	2.48374	2.38157	2.47874	2.41793	2.71408
Ta2-Ta3	2.6757	-	2.79257	2.68198	2.6948	2.75278	2.44093
Ta1-Ta3	2.59123	-	2.48516	2.57509	2.76924	2.72429	2.69978
Ta1-N1	1.92889	-	1.88979	1.88882	2.19881	1.9551	1.79692
Ta1-N3	-	-	-	2.66476	2.13527	2.14456	1.87347
Ta1-N4	-	-	-	-	1.90639	1.95994	-
Ta2-N1	1.88216	-	1.85822	-	1.90792	-	1.95661
Ta2-N2	2.37736	-	1.88639	1.88903	1.87651	1.85203	1.89458
Ta2-N3	-	-	-	-	-	-	2.39661
Ta2-N4	-	-	-	-	-	-	2.05256
Ta3-N1	1.81628	-	-	1.96975	1.96211	1.92241	-
Ta3-N2	1.8845	-	1.82228	1.82017	1.84086	1.85868	1.85752
Ta3-N3	-	-	2.12215	2.10406	1.87323	1.8674	2.23426
Ta3-N4	-	-	-	-	-	-	2.04184
N3-N4	-	1.08948	1.1019	1.11408	1.2671	1.34735	1.35776

4. Cryo IR Spectroscopy and Cryo Kinetics of Dinitrogen Activation and Cleavage by Small Tantalum Cluster Cations

Table S17: Calculated distances in Å of atoms within $P_{ES_gem}^{ES_gem}$, N_2 and $[Ta_3(N_2)_2]^+$ in the triplet state along the activation pathway b of N_2 on $P_{ES_gem}^{ES_gem}$ from the initial state to $I3_{(3,2)}$.




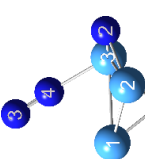
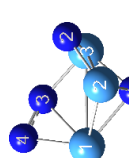
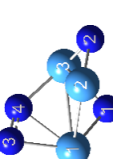

	${}^3P_{ES_gem(3,1)}^{ES_gem}$	1N_2	${}^3I1_{(3,2)}$	${}^3TS12_{(3,2)}$	${}^3I2_{(3,2)}$	${}^3TS23_{(3,2)}$	${}^3I3_{(3,2)}$
							
Ta1-Ta2	2.47986	-	2.47582	2.50955	2.66762	2.72096	2.74471
Ta2-Ta3	2.68493	-	2.70529	2.70333	2.74705	2.8569	2.47746
Ta1-Ta3	2.47993	-	2.52064	2.49924	2.72702	2.59563	3.07571
Ta1-N1	1.84976	-	1.83176	1.83232	2.04599	1.94865	1.78323
Ta1-N3	-	-	-	2.60975	2.06121	2.01481	1.88472
Ta1-N4	-	-	-	-	1.89866	1.96272	-
Ta2-N1	2.10539	-	2.08746	2.11712	2.01263	-	1.97237
Ta2-N2	1.84797	-	1.85574	1.82665	1.83193	1.79122	1.89997
Ta2-N3	-	-	-	-	-	-	2.37077
Ta2-N4	-	-	-	-	-	-	2.02339
Ta3-N1	2.10566	-	-	2.11256	1.90772	1.81947	-
Ta3-N2	1.84797	-	1.8472	1.8943	1.87438	1.94196	1.84418
Ta3-N3	-	-	2.23243	2.02821	1.87239	1.93541	2.29065
Ta3-N4	-	-	-	-	-	-	2.04438
N3-N4	-	1.08948	1.09763	1.13448	1.29448	1.2909	1.34542

Table S18: Calculated energies of the cluster adsorbate complex $[\text{Ta}_3(\text{N}_2)_3]^+$ in the singlet state along the activation pathways a and b of the third N_2 molecule on a Ta_3^+ cluster complex. The ΔE values are determined with respect to the initial singlet state ($^1\text{I}_{3(3,2)}$, N_2). For a graphical representation, see Fig. 5. Calculated IR frequencies (unscaled) $\nu_{\text{N}_5\text{N}_6}$ are given for relevant intermediates.

	pathway a			pathway b		
	energy E / Ha	ΔE / kJ/mol	$\nu_{\text{N}_5\text{N}_6}$ (unscaled.) / cm^{-1}	energy E / Ha	ΔE / kJ/mol	$\nu_{\text{N}_5\text{N}_6}$ (unscaled.) / cm^{-1}
$\text{I}_{3(3,2)}$, N_2	-500.510160	0	-	-500.510160	0	-
$\text{I}_{1(3,2)}$	-500.530739	-54	2474	-500.531292	-55	2427
$\text{TS}_{12(3,2)}$	-500.511166	-3	-	-500.511640	-4	-
$\text{I}_{2(3,2)}$	-500.523605	-35	1816	-500.526068	-42	1764
$\text{TS}_{2\text{III}(3,2)}$	-500.482478	39	-	-500.494330	42	-
$\text{I}_{\text{III}(3,2)}$	-500.491574	38	1023	-500.495495	38	1144
$\text{TS}_{\text{III IV}(3,2)}$	-500.421648	218	-	-	-	-
$\text{I}_{\text{IV}(3,2)}$	-500.502414	20	-	-	-	-

4. Cryo IR Spectroscopy and Cryo Kinetics of Dinitrogen Activation and Cleavage by Small Tantalum Cluster Cations

Table S19: Optimized structure/geometry, calculated IR frequencies (unscaled) $\nu_{N_5N_6}$ and calculated energies of singlet state isomers (3,4).

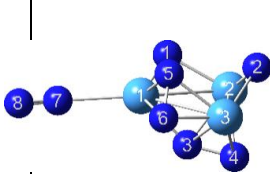
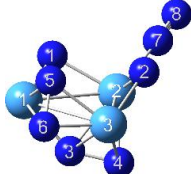
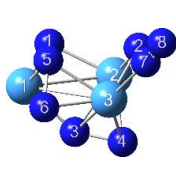
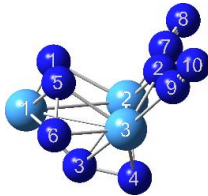
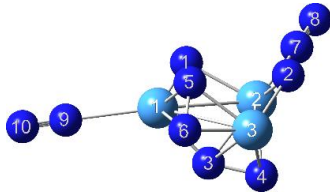
	$1(3,4)^{Ta1}$	$1(3,4)^{Ta2}$	$1(3,4)^{Ta3}$
			
$\nu_{N_7N_8}$ (unscal.) / cm^{-1}	2445	2488	2455
energy E / Ha	-609.963841	-609.966799	-609.964753
ΔE / kJ/mol	+8	0	+6

Table S20: Optimized structure/geometry, calculated IR frequencies (unscaled) $\nu_{N_5N_6}$ and calculated energies of singlet state isomers (3,5).

	$1(3,5)^{Ta2,Ta3}$	$1(3,5)^{Ta1,Ta2}$
		
$\nu_{N_7N_8}$ (unscal.) / cm^{-1}	2487	2485
$\nu_{N_9N_{10}}$ (unscal.) / cm^{-1}	2447	2435
energy E / Ha	-719.434536	-719.434429
ΔE / kJ/mol	0	0

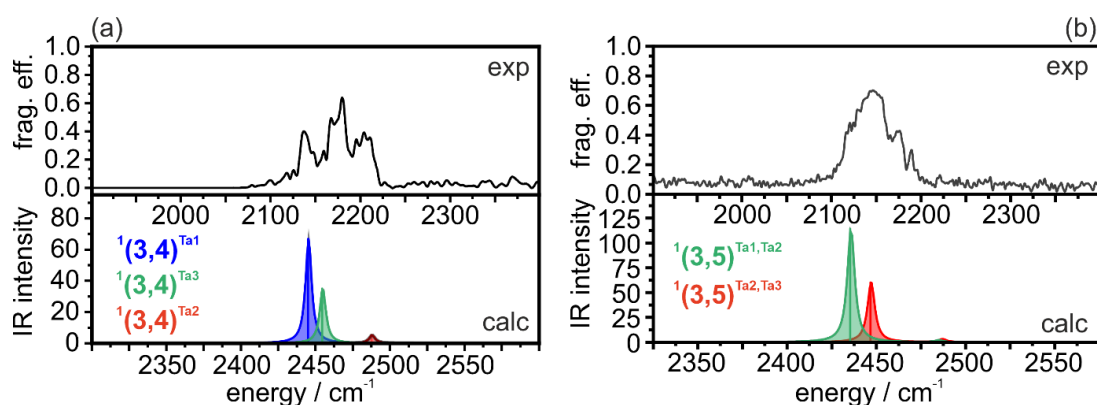


Figure S6: Experimental IR-PD spectra and DFT modelling of (3,4), (a), and (3,5), (b), respectively. The DFT modelling for (3,4) provides for predictions on the harmonic frequencies of the N_2 stretching vibrations at three sites, and they agree qualitatively. The predicted splittings of the (3,5) bands agree well with the observed ones.

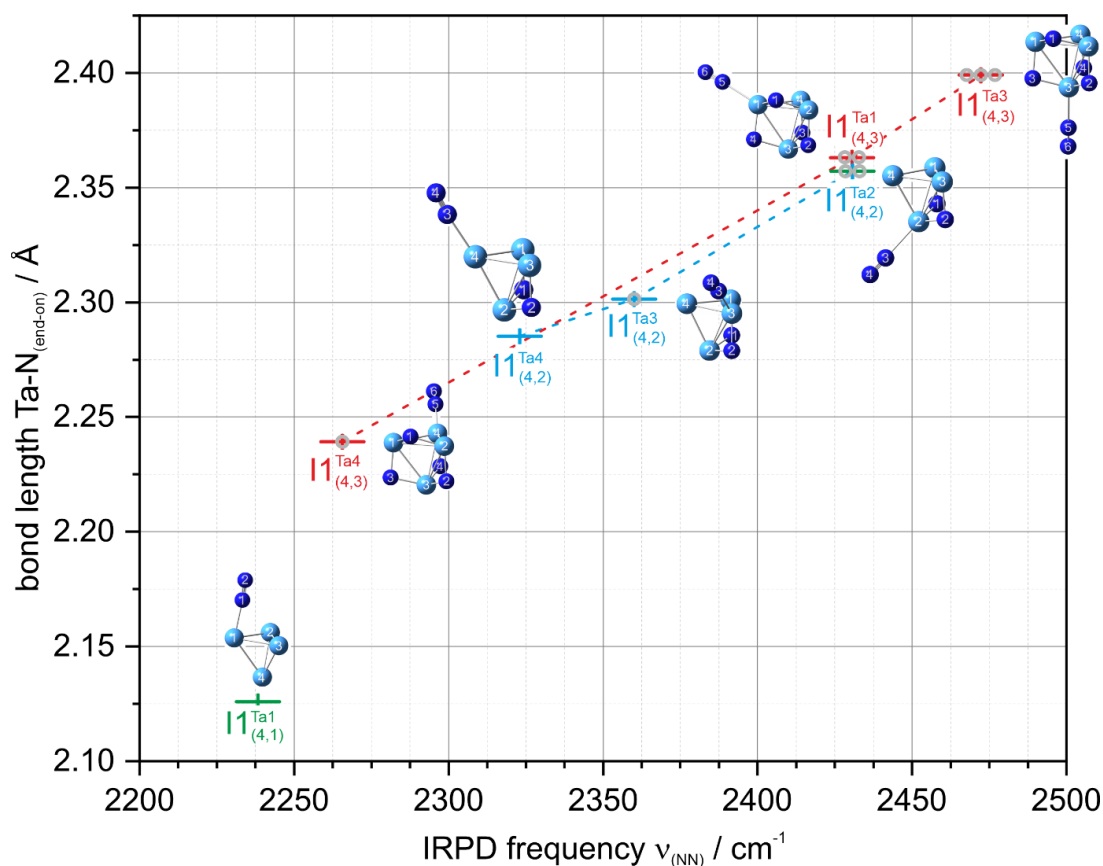


Figure S7: Multitude of I1 type model structures and their simulated IR frequencies from the reaction paths of the first second and third N_2 activation of our prior publication on the cationic Ta_4^+ cluster.⁷ The N_2 coordinating Ta atom is crucial, and in particular its involvement into nitride bonds (none, one, two or up to three). In consequence the red shift of IR frequency diminishes with respect to free N_2 (2330 cm^{-1})⁹. The dotted lines serve to guide the eye. None, one, two or three open black circles at the computed data points indicate an according number of nitride bonds of the N_2 end-on coordinating Ta atom. An according trend in the N-N bond length' is found in Fig. 8.

4. Cryo IR Spectroscopy and Cryo Kinetics of Dinitrogen Activation and Cleavage by Small Tantalum Cluster Cations

Table S21: Tabular summary of the specific values on the relationship between the I1 type model structures and their simulated IR frequencies from the reaction paths of the first second and third N₂ activation of our prior publication on the cationic Ta₄⁺ cluster.

⁷ For graphical representations, see Fig. 8 and Fig. S6.

	number of involvements in nitride bonds	Ta-N _(end-on) / Å	N-N _(end-on) / Å	$\nu_{\text{NN(unscal.)}}$ / cm ⁻¹
I1 _(4,1)	0	2.12602	1.10833	2238
I1 ^{Ta2} _(4,2)	2	2.36296	1.09143	2431
I1 ^{Ta3} _(4,2)	1	2.30132	1.09618	2360
I1 ^{Ta4} _(4,2)	0	2.28513	1.09805	2323
I1 ^{Ta1} _(4,3)	2	2.35714	1.09095	2431
I1 ^{Ta3} _(4,3)	3	2.39913	1.08899	2472
I1 ^{Ta4} _(4,3)	1	2.23915	1.09963	2266

Table S22a: Calculated energies and IR frequencies (scaling factor 0.9736) of the cluster adsorption isomers (4,3) in the doublet state. Isomers shown in bold are chosen for further discussion. For graphical representation of those, see Fig. S7.

	$\nu_{\text{NNend-on}}$ cm ⁻¹	$\nu_{\text{NNend-on(scaled)}}$ cm ⁻¹	$\nu_{\text{NNside-on}}$ cm ⁻¹	$\nu_{\text{NNside-on(scaled)}}$ cm ⁻¹	energy E Ha	ΔE kJ/mol
	-	-	1515	1475	-556.267561	-

Table S22b: Calculated energies and IR frequencies (scaling factor 0.9736) of the cluster adsorption isomers (4,4) in the doublet state. Isomers shown in bold are chosen for further discussion. For graphical representation of those, see Fig. S7.

	$\nu_{\text{NNend-on}}$ cm ⁻¹	$\nu_{\text{NNend-on(scaled)}}$ cm ⁻¹	$\nu_{\text{NNside-on}}$ cm ⁻¹	$\nu_{\text{NNside-on(scaled)}}$ cm ⁻¹	energy E Ha	ΔE kJ/mol
a	2481	2416	1474	1435	-665.730583	+4.3
b	2462	2397	1518	1478	-665.732204	0
c	2403	2340	1491	1451	-665.731950	+0.7
d	2493	2427	1475	1436	-665.731882	+0.8

Table S22c1: Calculated energies and IR frequencies (scaling factor 0.9736) of the cluster adsorption isomers (4,5) in the doublet state. Isomers shown in bold are chosen for further discussion. For graphical representation of those, see Fig. S8.

	$\nu_{\text{NNend-on}}$ cm ⁻¹	$\nu_{\text{NNend-on(scaled)}}$ cm ⁻¹	$\nu_{\text{NNside-on}}$ cm ⁻¹	$\nu_{\text{NNside-on(scaled)}}$ cm ⁻¹	energy E Ha	ΔE kJ/mol
a	2423, 2481	2359, 2416	1475	1436	-775.194814	+3.5
b	2405, 2477	2342, 2411	1422	1385	-775.194645	+3.9
c	2480, 2492	2415, 2426	1458	1420	-775.19197	+11.0
d	2415, 2493	2351, 2427	1479	1440	-775.196146	0
e	2407, 2488	2343, 2422	1414	1377	-775.194758	+3.6
f	2400, 2476	2336, 2411	1475	1436	-775.195133	+2.7

4. Cryo IR Spectroscopy and Cryo Kinetics of Dinitrogen Activation and Cleavage by Small Tantalum Cluster Cations

Table S22c2: Calculated energies and IR frequencies (scaling factor 0.9736) of the cluster adsorption isomers (4,5) in the doublet state. Isomers shown in bold are chosen for further discussion. For graphical representation of those, see Fig. S8.

	$\nu_{\text{NNend-on}}$ cm ⁻¹	$\nu_{\text{NNend-on}}$ (scaled) cm ⁻¹	$\nu_{\text{NNside-on}}$ cm ⁻¹	$\nu_{\text{NNside-on}}$ (scaled) cm ⁻¹	energy E Ha	ΔE kJ/mol
g	2406, 2444	2343, 2379	1690	1645	-775.176142	+52.5
h	2367, 2457	2304, 2392	1448	1409	-775.18705	+23.9
i	2492, 2494	2426, 2428	1471	1432	-775.181075	+39.6
j	2482, 2487	2417, 2421	1472	1433	-775.178382	+46.6

Table S22d1: Calculated energies and IR frequencies (scaling factor 0.9736) of the cluster adsorption isomers (4,6) in the doublet state. Isomers shown in bold are chosen for further discussion. For graphical representation of those, see Fig. S8.

	$\nu_{\text{NNend-on}}$ cm ⁻¹	$\nu_{\text{NNend-on}}$ (scaled) cm ⁻¹	$\nu_{\text{NNside-on}}$ cm ⁻¹	$\nu_{\text{NNside-on}}$ (scaled) cm ⁻¹	energy E Ha	ΔE kJ/mol
a	2376, 2478, 2493	2313, 2413, 2427	1466	1428	-884.656946	+1.8
b	2402, 2433, 2475	2339, 2369, 2410	1419	1382	-884.657565	+0.1
c	2389, 2466, 2489	2326, 2401, 2423	1427	1390	-884.655971	+4.3
d	2406, 2430, 2489	2342, 2366, 2423	1417	1380	-884.657634	0
e	2391, 2438, 2445	2327, 2373, 2381	1709	1664	-884.639037	+48.8
f	2434, 2483, 2487	2370, 2417, 2421	1471	1432	-884.641718	+41.7
g	2356, 2455, 2480	2294, 2390, 2415	1447	1409	-884.648786	+23.2
h	2409, 2478, 2491	2345, 2412, 2425	1394	1357	-884.637658	+52.4
i	2388, 2433, 2466	2325, 2369, 2401	1440	1402	-884.636852	+54.5
j	2482, 2484, 2495	2416, 2418, 2429	1458	1420	-884.639729	+47.0
k	2476, 2491, 2493	2411, 2425, 2427	1455	1417	-884.640348	+45.3
l	2350, 2451, 2491	2288, 2387, 2426	1440	1402	-884.650706	+18.1
o	2411, 2492, 2493	2347, 2426, 2428	1470	1431	-884.644619	+34.1
p	2397, 2427, 2485	2333, 2363, 2419	1406	1369	-884.636227	+56.2
q	2406, 2489, 2494	2342, 2423, 2428	1414	1377	-884.643834	+36.2

Table S22d2: Calculated energies and IR frequencies (scaling factor 0.9736) of the cluster adsorption isomers (4,6) in the doublet state. Isomers shown in bold are chosen for further discussion. For graphical representation of those, see Fig. S8.

	$\nu_{\text{N}^{\text{Nend-on}}}$ cm ⁻¹	$\nu_{\text{N}^{\text{Nend-on}}(\text{scaled})}$ cm ⁻¹	$\nu_{\text{N}^{\text{Nside-on}}}$ cm ⁻¹	$\nu_{\text{N}^{\text{Nside-on}}(\text{scaled})}$ cm ⁻¹	energy E Ha	ΔE kJ/mol
r	2391, 2438, 2445	2328, 2373, 2381	1708	1663	-884.639035	+48.8
s	2364, 2385, 2456	2301, 2322, 2391	1492	1453	-884.649605	+21.0
t	2346, 2458, 2473	2285, 2393, 2407	1464	1426	-884.625406	+84.6
u	2441, 2452, 2462	2377, 2388, 2397	1454	1415	-884.633351	+63.7
v	2493, 2494, 2495	2427, 2428, 2429	1462	1423	-884.629845	+72.9
w	2483, 2487, 2489	2417, 2422, 2423	1433	1395	-884.622050	+93.4

Table S22e1: Calculated energies and IR frequencies (scaling factor 0.9736) of the cluster adsorption isomers (4,7) in the doublet state. Isomers shown in bold are chosen for further discussion. For graphical representation of those, see Fig. S9.

	$\nu_{\text{N}^{\text{Nend-on}}}$ cm ⁻¹	$\nu_{\text{N}^{\text{Nend-on}}(\text{scaled})}$ cm ⁻¹	$\nu_{\text{N}^{\text{Nside-on}}}$ cm ⁻¹	$\nu_{\text{N}^{\text{Nside-on}}(\text{scaled})}$ cm ⁻¹	energy E Ha	ΔE kJ/mol
a	2384, 2396, 2464, 2490	2321, 2332, 2399, 2424	1438	1400	-994.116470	0
b	2381, 2482, 2485, 2494	2318, 2416, 2420, 2428	1466	1427	-994.103679	+33.6
c	2336, 2452, 2482, 2492	2274, 2387, 2417, 2426	1444	1406	-994.109306	+8.8
d	2372, 2477, 2491, 2493	2309, 2412, 2425, 2427	1465	1427	-994.105871	+27.8
e	2402, 2411, 2472, 2489	2339, 2347, 2407, 2424	1397	1360	-994.100559	+41.8
f	2349, 2402, 2456, 2477	2287, 2338, 2391, 2412	1409	1372	-994.110648	+15.3
g	2303, 2349, 2463, 2469	2242, 2287, 2398, 2404	1477	1438	-994.103079	35.2
h	2382, 2475, 2481, 2494	2320, 2409, 2416, 2428	1433	1395	-994.104166	+32.3
i	2388, 2449, 2471, 2485	2325, 2385, 2405, 2420	1520	1480	-994.097926	+48.7
j	2380, 2468, 2489, 2491	2317, 2403, 2424, 2425	1426	1388	-994.105464	+28.9
k	2372, 2405, 2444, 2489	2310, 2341, 2380, 2424	1591	1549	-994.100616	+41.6
l	2345, 2404, 2452, 2487	2283, 2340, 2387, 2421	1407	1370	-994.111071	+14.2
o	2396, 2436, 2490, 2493	2333, 2371, 2424, 2427	1414	1376	-994.106028	+27.4

4. Cryo IR Spectroscopy and Cryo Kinetics of Dinitrogen Activation and Cleavage by Small Tantalum Cluster Cations

Table S22e2: Calculated energies and IR frequencies (scaling factor 0.9736) of the cluster adsorption isomers (4,7) in the doublet state. Isomers shown in bold are chosen for further discussion. For graphical representation of those, see Fig. S9.

	$\nu_{\text{NNend-on}}$ cm ⁻¹	$\nu_{\text{NNend-on}}$ (scaled) cm ⁻¹	$\nu_{\text{NNside-on}}$ cm ⁻¹	$\nu_{\text{NNside-on}}$ (scaled) cm ⁻¹	energy E Ha	ΔE kJ/mol
p	2343, 2393, 2418, 2457	2281, 2330, 2354, 2392	1654	1610	-994.093597	+60.1
q	2356, 2456, 2483, 2488	2294, 2391, 2417, 2423	1451	1413	-994.095001	+56.3
r	2274, 2457, 2466, 2480	2214, 2393, 2401, 2414	1493	1454	-994.084788	+84.2
s	2482, 2484, 2490, 2494	2416, 2418, 2424, 2428	1462	1423	-994.087321	+76.5
t	2346, 2452, 2491, 2493	2284, 2387, 2426, 2428	1442	1404	-994.098529	+47.1

Table S22f1: Calculated energies and IR frequencies (scaling factor 0.9736) of the cluster adsorption isomers (4,8) in the doublet state. Isomers shown in bold are chosen for further discussion. For graphical representation of those, see Fig. S9.

	$\nu_{\text{NNend-on}}$ cm ⁻¹	$\nu_{\text{NNend-on}}$ (scaled) cm ⁻¹	$\nu_{\text{NNside-on}}$ cm ⁻¹	$\nu_{\text{NNside-on}}$ (scaled) cm ⁻¹	energy E Ha	ΔE kJ/mol
a	2369, 2393, 2463, 2490, 2492	2306, 2330, 2398, 2424, 2426	1408	1371	-1103.562814	+19.1
b	2321, 2385, 2455, 2470, 2487	2260, 2322, 2390, 2405, 2421	1412	1374	-1103.570101	0
c	2329, 2353, 2473, 2476, 2491	2267, 2290, 2407, 2411, 2425	1415	1377	-1103.561204	+23.4
d	2379, 2394, 2464, 2490, 2492	2316, 2330, 2399, 2424, 2426	1435	1398	-1103.568104	+5.2
e	2335, 2453, 2483, 2486, 2492	2273, 2388, 2418, 2420, 2426	1446	1408	-1103.555511	+38.3
f	2367, 2481, 2484, 2491, 2493	2305, 2416, 2419, 2426, 2428	1469	1431	-1103.551773	+48.1
g	2330, 2453, 2481, 2491, 2493	2268, 2388, 2416, 2426, 2427	1444	1406	-1103.556679	+35.2
h	2347, 2399, 2456, 2480, 2485	2285, 2336, 2391, 2415, 2419	1410	1373	-1103.556888	+34.7
i	2400, 2417, 2447, 2480, 2483	2337, 2354, 2382, 2415, 2418	1502	1462	-1103.546551	+61.8
j	2384, 2411, 2467, 2477, 2490	2321, 2347, 2402, 2411, 2424	1442	1404	-1103.546016	+63.2
k	2377, 2477, 2481, 2490, 2492	2314, 2411, 2415, 2424, 2425	1428	1390	-1103.552198	+47.0
l	2390, 2446, 2470, 2488, 2491	2327, 2381, 2405, 2423, 2425	1504	1464	-1103.546609	+61.7

Table S22f2: Calculated energies and IR frequencies (scaling factor 0.9736) of the cluster adsorption isomers (4,8) in the doublet state. Isomers shown in bold are chosen for further discussion. For graphical representation of those, see Fig. S9.

	$\nu_{\text{NNend-on}}$ cm ⁻¹	$\nu_{\text{NNend-on}}$ (scaled) cm ⁻¹	$\nu_{\text{NNside-on}}$ cm ⁻¹	$\nu_{\text{NNside-on}}$ (scaled) cm ⁻¹	energy E Ha	ΔE kJ/mol
o	2324, 2384, 2434, 2455, 2490	2263, 2321, 2370, 2390, 2424	1554	1513	-1103.554421	+41.2
p	2339, 2403, 2449, 2489, 2492	2277, 2340, 2384, 2423, 2427	1409	1372	-1103.548410	+28.6
q	2370, 2407, 2453, 2490, 2493	2308, 2343, 2388, 2424, 2427	1546	1505	-1103.559223	+56.9

Table S22g1: Calculated energies and IR frequencies (scaling factor 0.9736) of the cluster adsorption isomers (4,9) in the doublet state. Isomers shown in bold are chosen for further discussion. For graphical representation of those, see Fig. S10.

	$\nu_{\text{NNend-on}}$ cm ⁻¹	$\nu_{\text{NNend-on}}$ (scaled) cm ⁻¹	$\nu_{\text{NNside-on}}$ cm ⁻¹	$\nu_{\text{NNside-on}}$ (scaled) cm ⁻¹	energy E Ha	ΔE kJ/mol
a	2374, 2389, 2474, 2484, 2490, 2492	2311, 2326, 2409, 2419, 2424, 2426	1417	1380	-1213.009991	+19.8
b	2309, 2372, 2455, 2467, 2488, 2490	2248, 2310, 2391, 2402, 2423, 2424	1397	1360	-1213.012694	+12.7
c	2349, 2365, 2410, 2462, 2479, 2487	2287, 2302, 2346, 2397, 2413, 2421	1452	1414	-1213.008334	+24.1
d	2375, 2389, 2464, 2488, 2490, 2492	2313, 2326, 2399, 2423, 2424, 2426	1418	1380	-1213.010897	+17.4
e	2311, 2392, 2438, 2459, 2474, 2487	2250, 2329, 2374, 2394, 2409, 2421	1477	1438	-1213.012252	+13.8
f	2315, 2379, 2454, 2465, 2488, 2492	2254, 2317, 2389, 2400, 2422, 2426	1407	1370	-1213.017514	0
g	2274, 2313, 2456, 2468, 2489, 2490	2213, 2252, 2391, 2403, 2423, 2424	1480	1441	-1213.011748	+15.1
h	2286, 2323, 2440, 2449, 2466, 2487	2226, 2262, 2376, 2384, 2401, 2422	1457	1418	-1213.011403	+16.0

4. Cryo IR Spectroscopy and Cryo Kinetics of Dinitrogen Activation and Cleavage by Small Tantalum Cluster Cations

Table S22g2: Calculated energies and IR frequencies (scaling factor 0.9736) of the cluster adsorption isomers (4,9) in the doublet state. Isomers shown in bold are chosen for further discussion. For graphical representation of those, see Fig. S10.

	$\nu_{\text{N}^{\text{end-on}}}$ cm ⁻¹	$\nu_{\text{N}^{\text{end-on}}}$ (scaled) cm ⁻¹	$\nu_{\text{N}^{\text{side-on}}}$ cm ⁻¹	$\nu_{\text{N}^{\text{side-on}}}$ (scaled) cm ⁻¹	energy E Ha	ΔE kJ/mol
i	2392, 2423, 2435, 2464, 2468, 2486	2329, 2359, 2371, 2399, 2403, 2420	1417	1380	-1213.014875	+6.9
j	2377, 2390, 2462, 2491, 2492, 2494	2314, 2327, 2397, 2426, 2426, 2428	1440	1402	-1213.016128	+3.6
k	2436, 2457, 2483, 2486, 2489, 2493	2372, 2392, 2417, 2421, 2423, 2427	1447	1409	-1212.993414	+63.3
l	2415, 2439, 2459, 2483, 2485, 2492	2351, 2374, 2394, 2417, 2420, 2426	1448	1410	-1213.000187	+45.5
o	2431, 2454, 2480, 2484, 2490, 2493	2367, 2389, 2415, 2419, 2425, 2427	1470	1431	-1212.997943	+51.4
p	2291, 2341, 2448, 2472, 2482, 2484	2231, 2279, 2383, 2406, 2416, 2419	1484	1444	-1213.00168	+41.6
q	2375, 2406, 2469, 2477, 2486, 2489	2313, 2343, 2404, 2412, 2420, 2424	1437	1399	-1212.99369	+62.5
r	2316, 2397, 2427, 2450, 2490, 2492	2255, 2334, 2363, 2385, 2424, 2426	1543	1503	-1213.00182	+41.2

Table S22h1: Calculated energies and IR frequencies (scaling factor 0.9736) of the cluster adsorption isomers (4, 10) in the doublet state. Isomers shown in bold are chosen for further discussion. For graphical representation of those, see Fig. S10.

	$\nu_{\text{NNend-on}}$	$\nu_{\text{NNend-on}}$ (scaled)	$\nu_{\text{NNside-on}}$	$\nu_{\text{NNside-on}}$ (scaled)	energy E	ΔE
	cm^{-1}	cm^{-1}	cm^{-1}	cm^{-1}	Ha	kJ/mol
a	2265, 2303, 2473, 2474, 2483, 2485, 2490	2205, 2242, 2408, 2408, 2417, 2420, 2425	1451	1413	-1322.450917	+38.4
b	2297, 2352, 2454, 2478, 2482, 2488, 2491	2237, 2290, 2389, 2413, 2417, 2423, 2425	1405	1368	-1322.459726	+15.3
c	2375, 2393, 2475, 2484, 2489, 2490, 2491	2312, 2330, 2410, 2418, 2423, 2424, 2425	1416	1378	-1322.456881	+22.8
d	2283, 2357, 2464, 2474, 2478, 2490, 2493	2223, 2295, 2399, 2408, 2413, 2424, 2427	1383	1346	-1322.453885	+30.7
e	2306, 2358, 2456, 2472, 2488, 2489, 2496	2246, 2296, 2391, 2406, 2422, 2423, 2426	1399	1362	-1322.46056	+13.1
f	2334, 2357, 2417, 2460, 2478, 2487, 2492	2273, 2294, 2353, 2395, 2413, 2422, 2426	1460	1422	-1322.455478	+26.5
g	2308, 2380, 2446, 2461, 2476, 2490, 2493	2247, 2318, 2381, 2396, 2410, 2424, 2427	1472	1433	-1322.459304	+16.4
h	2267, 2363, 2446, 2453, 2469, 2474, 2489	2208, 2300, 2382, 2388, 2404, 2409, 2423	1459	1420	-1322.461932	+9.5
i	2280, 2318, 2446, 2449, 2467, 2489, 2491	2220, 2257, 2381, 2385, 2402, 2424, 2425	1471	1432	-1322.459411	+16.1
j	2273, 2315, 2428, 2462, 2470, 2483, 2491	2213, 2254, 2364, 2397, 2404, 2418, 2425	1466	1427	-1322.455679	+25.9
k	2309, 2357, 2452, 2469, 2471, 2472, 2484	2248, 2295, 2387, 2404, 2406, 2406, 2419	1474	1435	-1322.456212	+24.5
l	2378, 2419, 2435, 2464, 2469, 2488, 2491	2316, 2355, 2371, 2399, 2404, 2423, 2425	1412	1374	-1322.462004	+9.3
o	2385, 2423, 2435, 2463, 2476, 2482, 2492	2322, 2359, 2371, 2398, 2410, 2417, 2427	1419	1382	-1322.460731	+12.7

4. Cryo IR Spectroscopy and Cryo Kinetics of Dinitrogen Activation and Cleavage by Small Tantalum Cluster Cations

Table S22h2: Calculated energies and IR frequencies (scaling factor 0.9736) of the cluster adsorption isomers (4, 10) in the doublet state. Isomers shown in bold are chosen for further discussion. For graphical representation of those, see Fig. S10.

	$\nu_{\text{N}^{\text{Nend-on}}}$ cm ⁻¹	$\nu_{\text{N}^{\text{Nend-on}}(\text{scaled})}$ cm ⁻¹	$\nu_{\text{N}^{\text{Nside-on}}}$ cm ⁻¹	$\nu_{\text{N}^{\text{Nside-on}}(\text{scaled})}$ cm ⁻¹	energy E Ha	ΔE kJ/mol
p	2264, 2307, 2452, 2468, 2490, 2491, 2492	2205, 2246, 2387, 2403, 2424, 2425, 2427	1477	1438	-1322.458636	+18.2
q	2301, 2357, 2456, 2466, 2491, 2493, 2494	2241, 2295, 2391, 2401, 2425, 2427, 2428	1405	1368	-1322.465562	0
r	2373, 2391, 2472, 2481, 2491, 2492, 2493	2311, 2328, 2407, 2416, 2425, 2426, 2428	1440	1402	-1322.461815	+9.8

Table S22i1: Calculated energies and IR frequencies (scaling factor 0.9736) of the cluster adsorption isomers (4, 11) in the doublet state. Isomers shown in bold are chosen for further discussion. For graphical representation of those, see Fig. S11.

	$\nu_{\text{N}^{\text{Nend-on}}}$ cm ⁻¹	$\nu_{\text{N}^{\text{Nend-on}}(\text{scaled})}$ cm ⁻¹	$\nu_{\text{N}^{\text{Nside-on}}}$ cm ⁻¹	$\nu_{\text{N}^{\text{Nside-on}}(\text{scaled})}$ cm ⁻¹	energy E Ha	ΔE kJ/mol
a	2276, 2320, 2425, 2467, 2468, 2485, 2490, 2492	2215, 2259, 23601, 2402, 2403, 2419, 2424, 2426	1441	1403	-1431.898733	+27.4
b	2278, 2385, 2430, 2439, 2475, 2481, 2481, 2488	2218, 2322, 2366, 2374, 2410, 2415, 2415, 2423	1441	1403	-1431.902694	+17.4
c	2349, 2363, 2401, 2466, 2480, 2484, 2489, 2490	2287, 2301, 2337, 2401, 2415, 2418, 2423, 2424	1434	1396	-1431.898049	+29.4
d	2294, 2351, 2454, 2474, 2483, 2488, 2492, 2493	2233, 2289, 2389, 2409, 2417, 2422, 2426, 2427	1407	1370	-1431.906262	+7.9
e	2309, 2411, 2434, 2455, 2479, 2481, 2489, 2492	2248, 2348, 2369, 2390, 2413, 2416, 2424, 2426	1455	1416	-1431.90424	+13.2
f	2259, 2362, 2444, 2452, 2469, 2474, 2487, 2488	2199, 2300, 2379, 2387, 2404, 2409, 2421, 2422	1457	1418	-1431.90384	+14.2

Table S22i2: Calculated energies and IR frequencies (scaling factor 0.9736) of the cluster adsorption isomers (4, 11) in the doublet state. Isomers shown in bold are chosen for further discussion. For graphical representation of those, see Fig. S11.

	$\nu_{\text{NNend-on}}$ cm ⁻¹	$\nu_{\text{NNend-on}}$ (scaled) cm ⁻¹	$\nu_{\text{NNside-on}}$ cm ⁻¹	$\nu_{\text{NNside-on}}$ (scaled) cm ⁻¹	energy E Ha	ΔE kJ/mol
g	2388, 2399, 2433, 2439, 2467, 2473, 2485, 2488	2325, 2336, 2369, 2374, 2402, 2408, 2419, 2423	1487	1448	-1431.89877	+27.5
h	2379, 2411, 2444, 2464, 2471, 2488, 2488, 2491	2316, 2348, 2379, 2399, 2405, 2422, 2422, 2425	1409	1371	-1431.90443	+12.7
i	2294, 2350, 2456, 2467, 2488, 2490, 2493, 2494	2234, 2288, 2391, 2402, 2423, 2425, 2427, 2428	1400	1363	-1431.90777	+3.9
j	2274, 2314, 2441, 2464, 2469, 2482, 2487, 2490	2214, 2253, 2377, 2399, 2404, 2417, 2422, 2424	1479	1440	-1431.90316	+16.0
k	2336, 2354, 2408, 2460, 2479, 2488, 2491, 2493	2274, 2292, 2344, 2395, 2414, 2422, 2426, 2427	1449	1410	-1431.90236	+18.1
l	2272, 2346, 2452, 2463, 2470, 2470, 2490, 2493	2212, 2284, 2388, 2398, 2404, 2405, 2424, 2427	1474	1435	-1431.908339	+2.4
o	2387, 2410, 2423, 2440, 2468, 2472, 2488, 2491	2324, 2347, 23599, 2376, 2403, 2407, 2422, 2426	1484	1444	-1431.902889	+16.7
p	2299, 2420, 2429, 2454, 2467, 2490, 2493, 2494	2239, 2356, 2365, 2389, 2401, 2425, 2427, 2428	1441	1403	-1431.906237	+7.9
q	2272, 2362, 2447, 2450, 2469, 2474, 2486, 2489	2212, 2299, 2382, 2386, 2404, 2408, 2421, 2423	1459	1421	-1431.903685	+14.6
r	2267, 2309, 2441, 2448, 2468, 2491, 2491, 2492	2207, 2248, 2376, 2383, 2403, 2425, 2426, 2427	1468	1429	-1431.905999	+8.6
s	2380, 2416, 2432, 2464, 2464, 2491, 2492, 2493	2318, 2352, 2368, 2398, 2399, 2425, 2426, 2427	1418	1380	-1431.909262	0
t	2386, 2419, 2436, 2462, 2478, 2484, 2488, 2492	2323, 2355, 2372, 2397, 2412, 2418, 2423, 2426	1413	1376	-1431.903569	+14.9
u	2373, 2387, 2474, 2483, 2488, 2491, 2492, 2493	2311, 2324, 2408, 2418, 2423, 2425, 2426, 2427	1430	1393	-1431.904656	+12.1

4. Cryo IR Spectroscopy and Cryo Kinetics of Dinitrogen Activation and Cleavage by Small Tantalum Cluster Cations

Table S22j1: Calculated energies and IR frequencies (scaling factor 0.9736) of the cluster adsorption isomers (4, 12) in the doublet state. Isomers shown in bold are chosen for further discussion. For graphical representation of those, see Fig. S11.

	$\nu_{\text{N}^{\text{end-on}}}$	$\nu_{\text{N}^{\text{end-on}}(\text{scaled})}$	$\nu_{\text{N}^{\text{side-on}}}$	$\nu_{\text{N}^{\text{side-on}}(\text{scaled})}$	energy E Ha	ΔE kJ/mol
	cm^{-1}	cm^{-1}	cm^{-1}	cm^{-1}		
a	2253, 2369, 2437, 2450, 2476, 2481, 2485, 2489, 2492	2194, 2306, 2373, 2385, 2410, 2416, 2419, 2424, 2426	1446	1408	-1541.347853	+7.9
b	2273, 2312, 2439, 2466, 2469, 2484, 2486, 2489, 2489	2213, 2251, 2375, 2401, 2404, 2418, 2420, 2423, 2423	1453	1415	-1541.345918	+23.0
c	2279, 2376, 2426, 2441, 2477, 2481, 2484, 2488, 2488	2219, 2313, 2362, 2376, 2412, 2415, 2418, 2422, 2422	1435	1397	-1541.348569	+16.0
d	2389, 2416, 2437, 2461, 2477, 2483, 2485, 2488, 2492	2326, 2353, 2372, 2396, 2411, 2418, 2420, 2423, 2426	1412	1374	-1541.345464	+24.2
e	2329, 2350, 2408, 2463, 2482, 2487, 2488, 2491, 2492	2268, 2288, 2344, 2398, 2416, 2421, 2422, 2425, 2426	1444	1405	-1541.345093	+25.1
f	2381, 2418, 2430, 2462, 2474, 2483, 2487, 2491, 2492	2318, 2354, 2366, 2397, 2409, 2418, 2421, 2425, 2426	1415	1378	-1541.349737	+12.9
g	2293, 2341, 2455, 2476, 2483, 2488, 2491, 2492, 2493	2233, 2279, 2390, 2411, 2418, 2422, 2425, 2426, 2427	1403	1366	-1541.353303	+3.6
h	2378, 2424, 2433, 2461, 2477, 2481, 2485, 2489, 2490	2316, 2360, 2369, 2396, 2411, 2415, 2420, 2423, 2424	1414	1377	-1541.349092	+14.6
i	2255, 2348, 2444, 2454, 2479, 2479, 2484, 2487, 2490	2195, 2286, 2379, 2389, 2414, 2414, 2418, 2421, 2424	1470	1431	-1541.350435	+11.1
j	2268, 2365, 2433, 2446, 2472, 2481, 2491, 2491, 2493	2208, 2302, 2368, 2382, 2407, 2415, 2425, 2426, 2427	1423	1385	-1541.352053	+6.9
k	2265, 2356, 2445, 2451, 2468, 2472, 2486, 2486, 2487	2205, 2294, 2380, 2387, 2403, 2407, 2420, 2421, 2422	1459	1421	-1541.345544	+24.0
l	2381, 2414, 2431, 2464, 2465, 2487, 2491, 2492, 2493	2318, 2351, 2366, 2399, 2400, 2422, 2425, 2426, 2427	1414	1377	-1541.351472	+8.4
o	2379, 2422, 2435, 2461, 2478, 2483, 2488, 2489, 2490	2316, 2358, 2370, 2396, 2413, 2417, 2422, 2423, 2424	1409	1372	-1541.349839	+12.7

Table S22j2: Calculated energies and IR frequencies (scaling factor 0.9736) of the cluster adsorption isomers (4, 12) in the doublet state. Isomers shown in bold are chosen for further discussion. For graphical representation of those, see Fig. S11.

	$\nu_{\text{N}^{\text{Nend-on}}}$ cm ⁻¹	$\nu_{\text{N}^{\text{Nend-on}}}$ (scaled) cm ⁻¹	$\nu_{\text{N}^{\text{Nside-on}}}$ cm ⁻¹	$\nu_{\text{N}^{\text{Nside-on}}}$ (scaled) cm ⁻¹	energy E Ha	ΔE kJ/mol
p	2258, 2303, 2438, 2462, 2471, 2483, 2490, 2491, 2492	2199, 2243, 2373, 2397, 2406, 2418, 2424, 2425, 2426	1472	1433	-1541.34871	+15.6
q	2334, 2387, 2415, 2451, 2460, 2466, 2471, 2489, 2491	2272, 2324, 2351, 2386, 2395, 2401, 2406, 2423, 2426	1474	1435	-1541.34924	+14.3
r	2263, 2343, 2448, 2462, 2470, 2471, 2490, 2491, 2493	2204, 2281, 2384, 2397, 2405, 2406, 2424, 2426, 2427	1469	1431	-1541.354668	0
s	2398, 2403, 2421, 2442, 2465, 2469, 2490, 2492, 2493	2335, 2339, 2357, 2377, 2400, 2403, 2424, 2426, 2427	1440	1402	-1541.349248	+14.2

4. Cryo IR Spectroscopy and Cryo Kinetics of Dinitrogen Activation and Cleavage by Small Tantalum Cluster Cations

Table S23a: DFT optimized structures of cluster adsorption isomers (4,3) in the doublet state. Isomers shown in bold are chosen for further discussion. For calculated energies, IR frequencies and graphical representation of those, see Tab. S22a, Fig. S7.

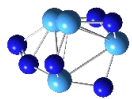
(4,3)							
--------------	---	--	--	--	--	--	--

Table S23b: DFT optimized structures of cluster adsorption isomers (4,4) in the doublet state. Isomers shown in bold are chosen for further discussion. For calculated energies, IR frequencies and graphical representation of those, see Tab. S22b, Fig. S7.

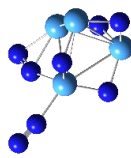
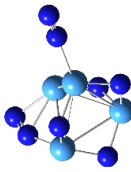
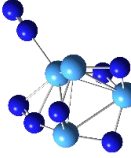
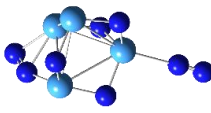
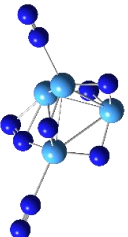
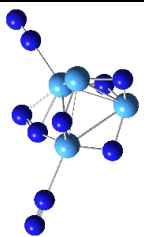
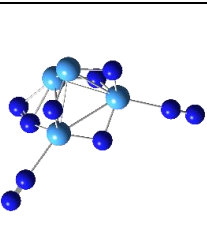
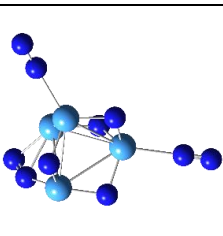
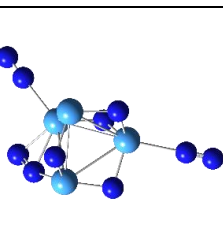
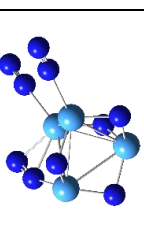
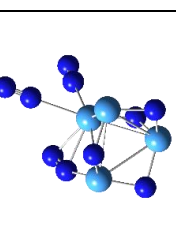
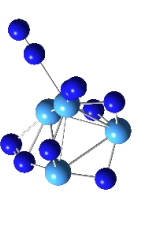
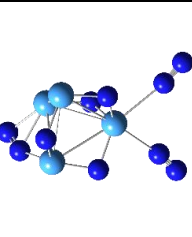
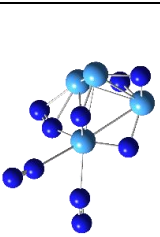
(4,4)a		(4,4)b		(4,4)c		(4,4)d	
---------------	--	---------------	--	---------------	--	---------------	--

Table S23c: DFT optimized structures of cluster adsorption isomers (4,5) in the doublet state. Isomers shown in bold are chosen for further discussion. For calculated energies, IR frequencies and graphical representation of those, see Tab. S22c, Fig. S8.

(4,5)a		(4,5)b		(4,5)c		(4,5)d		(4,5)e		(4,5)f		(4,5)g	
(4,5)h		(4,5)i		(4,5)j									

4. Cryo IR Spectroscopy and Cryo Kinetics of Dinitrogen Activation and Cleavage by Small Tantalum Cluster Cations

Table S23d: DFT optimized structures of cluster adsorption isomers (4,6) in the doublet state. Isomers shown in bold in the caption are chosen for further discussion. For calculated energies, IR frequencies and graphical representation of those, see Tab. S22d, Fig. S8.

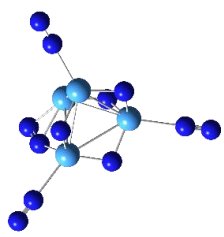
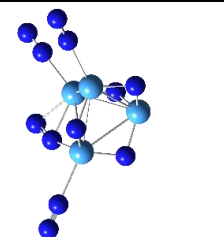
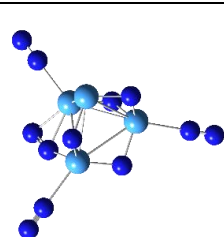
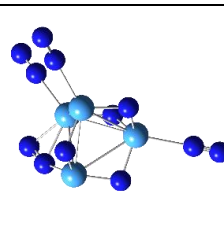
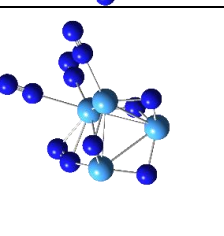
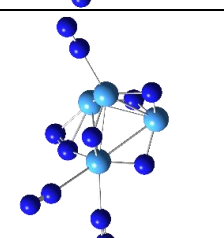
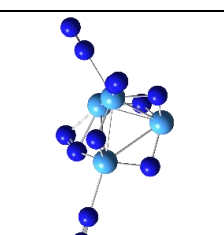
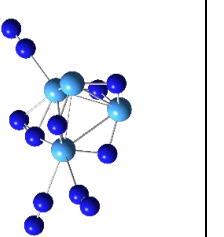
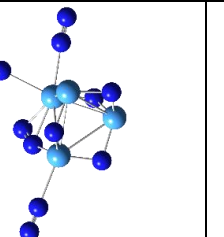
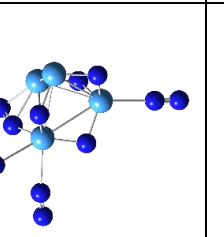
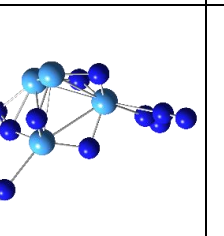
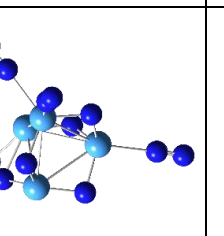
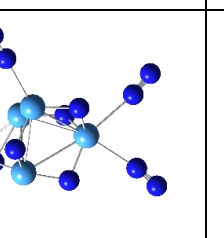
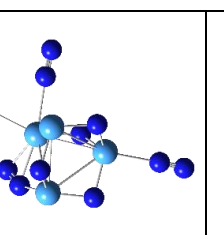
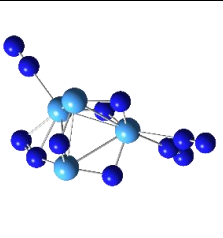
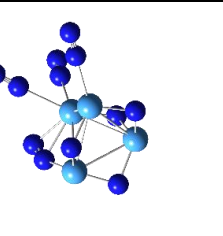
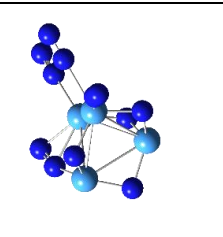
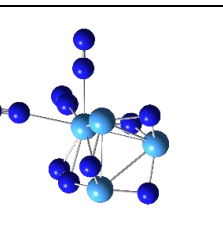
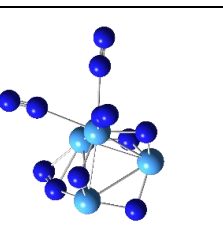
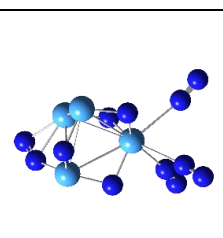
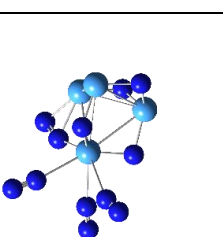
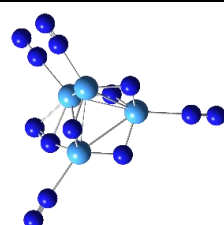
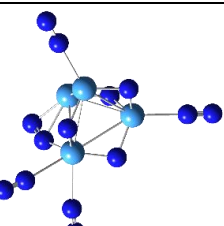
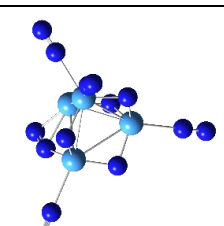
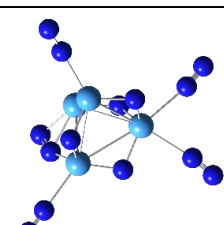
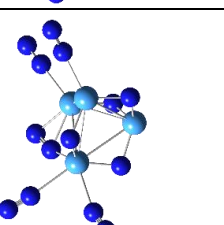
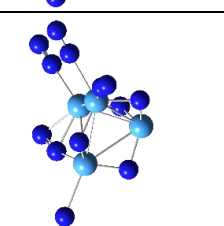
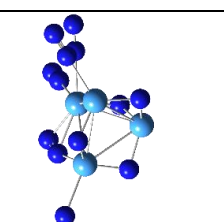
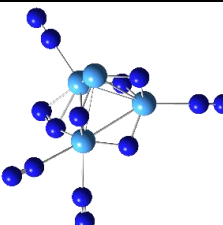
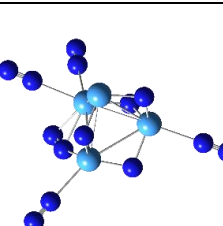
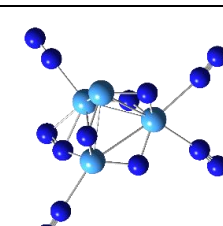
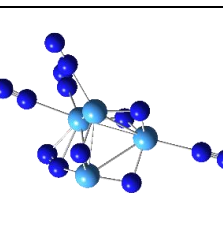
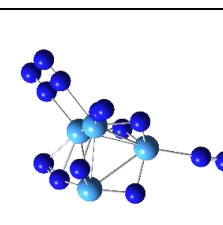
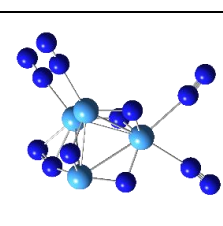
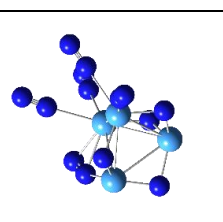
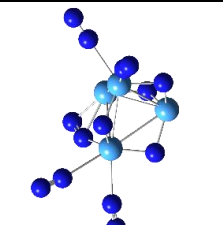
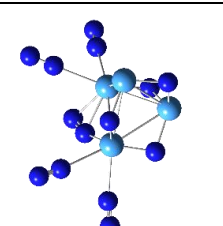
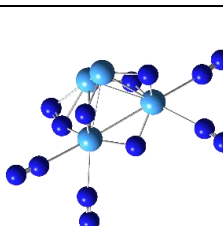
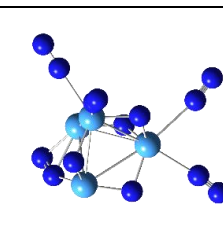
						
(4,6)a	(4,6)b	(4,6)c	(4,6)d	(4,6)e	(4,6)f	(4,6)g
						
(4,6)h	(4,6)i	(4,6)j	(4,6)k	(4,6)l	(4,6)o	(4,6)p
						
(4,6)q	(4,6)r	(4,6)s	(4,6)t	(4,6)u	(4,6)v	(4,6)w

Table S23e: DFT optimized structures of cluster adsorption isomers (4,7) in the doublet state. Isomers shown in bold are chosen for further discussion. For calculated energies, IR frequencies and graphical representation of those, see Tab. S22e, Fig. S9.

						
(4,7)a	(4,7)b	(4,7)c	(4,7)d	(4,7)e	(4,7)f	(4,7)g
						
(4,7)h	(4,7)i	(4,7)j	(4,7)k	(4,7)l	(4,7)o	(4,7)p
						
(4,7)q	(4,7)r	(4,7)s	(4,7)t			

4. Cryo IR Spectroscopy and Cryo Kinetics of Dinitrogen Activation and Cleavage by Small Tantalum Cluster Cations

Table S23f: DFT optimized structures of cluster adsorption isomers (4,8) in the doublet state. Isomers shown in bold in the table are chosen for further discussion. For calculated energies, IR frequencies and graphical representation of those, see Tab. S22f, Fig. S9.

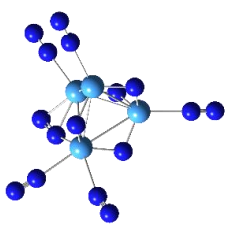
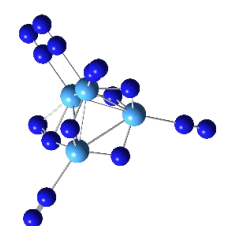
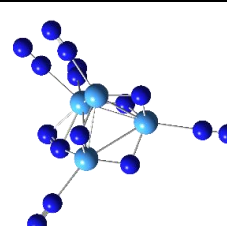
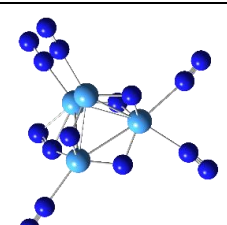
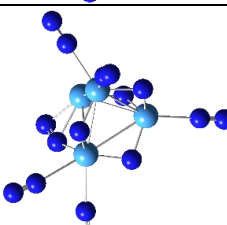
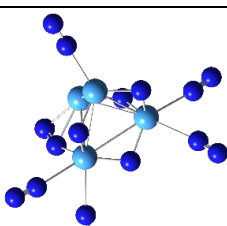
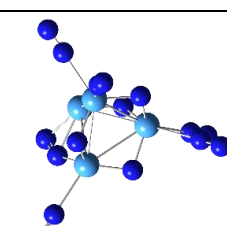
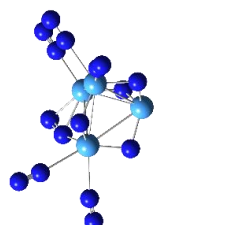
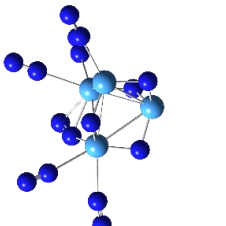
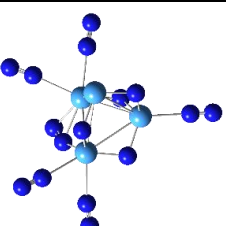
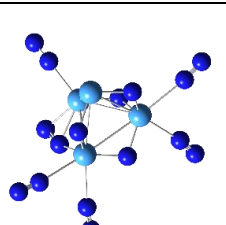
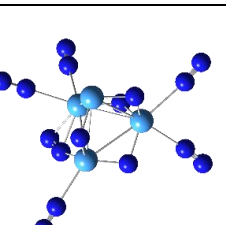
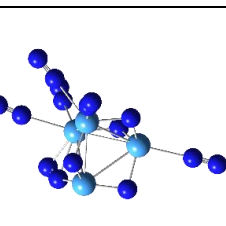
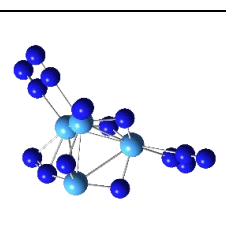
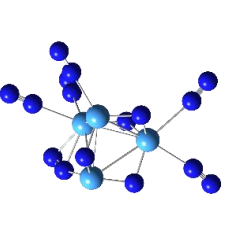
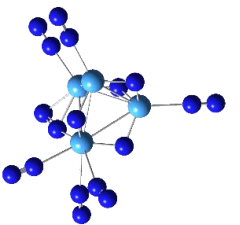
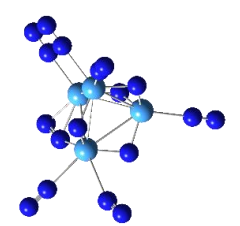
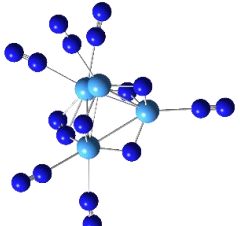
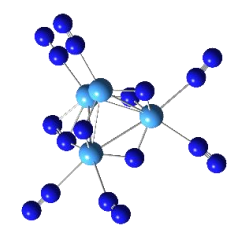
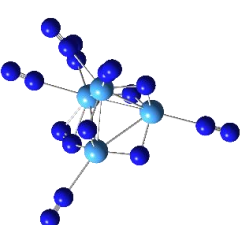
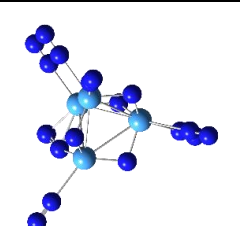
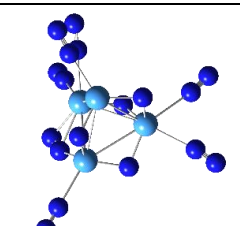
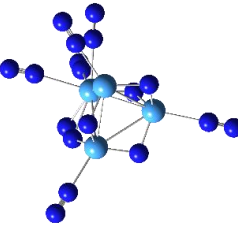
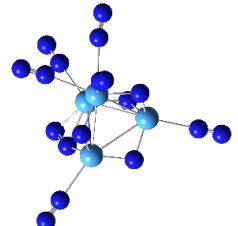
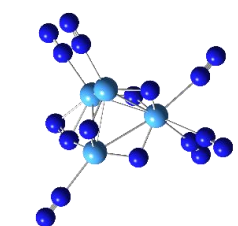
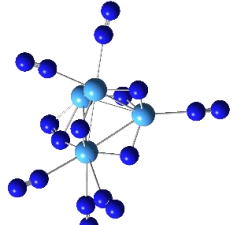
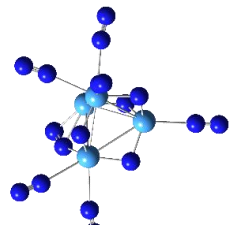
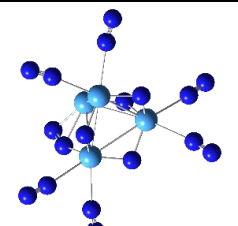
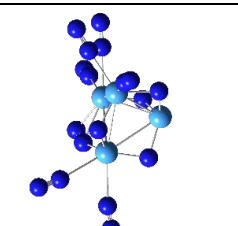
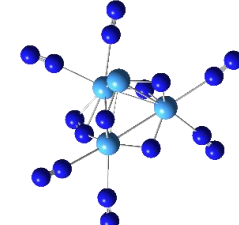
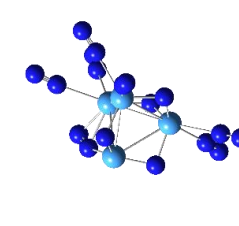
(4,8)a	(4,8)b	(4,8)c	(4,8)d	(4,8)e	(4,8)f	(4,8)g
						
(4,8)h	(4,8)i	(4,8)j	(4,8)k	(4,8)l	(4,8)o	(4,8)p
						
(4,8)q						
						

Table S23g: DFT optimized structures of cluster adsorption isomers (4,9) in the doublet state. Isomers shown in bold are chosen for further discussion. For calculated energies, IR frequencies and graphical representation of those, see Tab. S22g, Fig. S10.

						
(4,9)a	(4,9)b	(4,9)c	(4,9)d	(4,9)e	(4,9)f	(4,9)g
						
(4,9)h	(4,9)i	(4,9)j	(4,9)k	(4,9)l	(4,9)o	(4,9)p
						
(4,9)q	(4,9)r					

4. Cryo IR Spectroscopy and Cryo Kinetics of Dinitrogen Activation and Cleavage by Small Tantalum Cluster Cations

Table S23h: DFT optimized structures of cluster adsorption isomers (4,10) in the doublet state. Isomers shown in bold are chosen for further discussion. For calculated energies, IR frequencies and graphical representation of those, see Tab. S22h, Fig. S10.

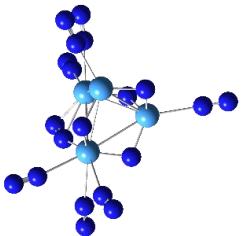
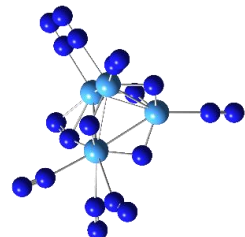
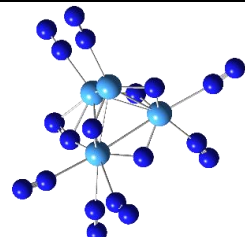
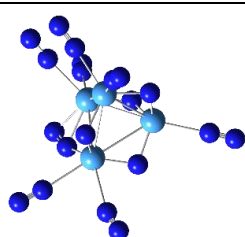
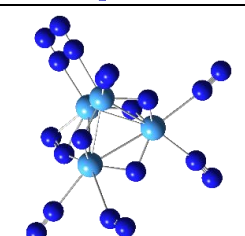
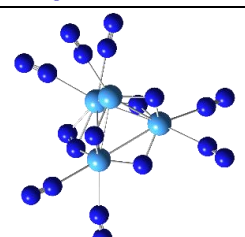
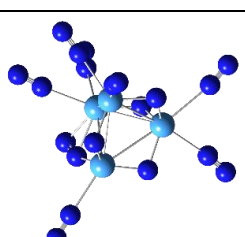
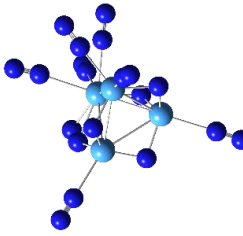
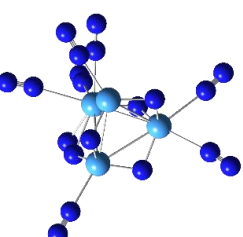
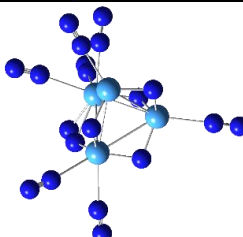
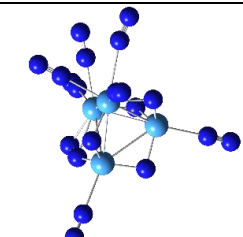
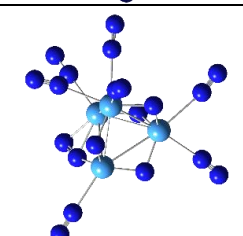
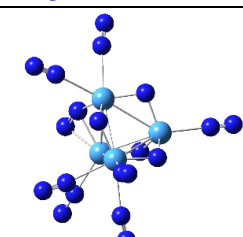
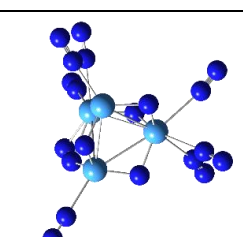
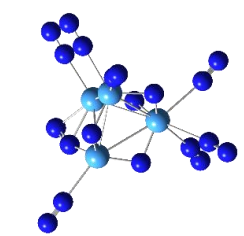
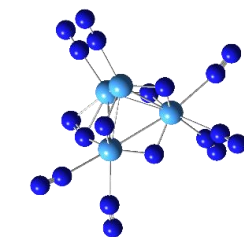
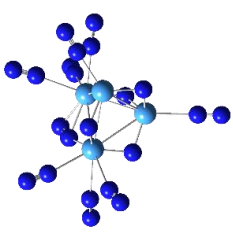
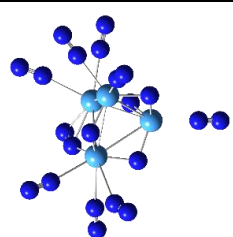
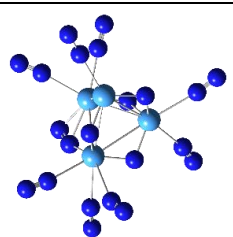
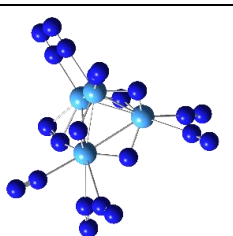
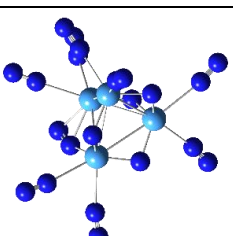
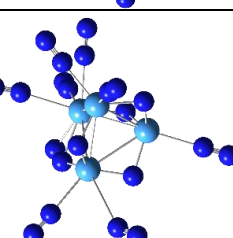
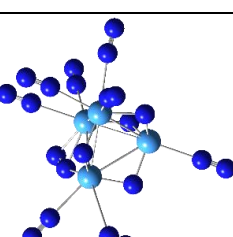
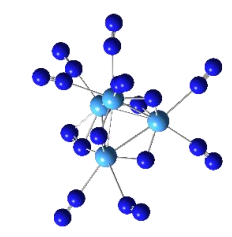
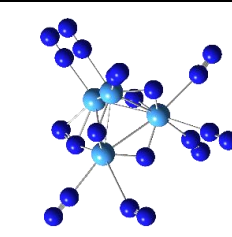
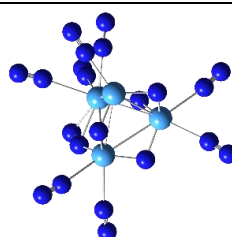
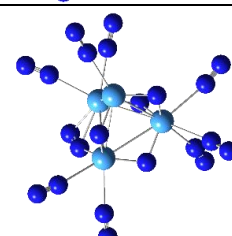
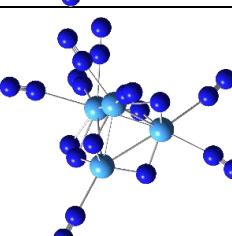
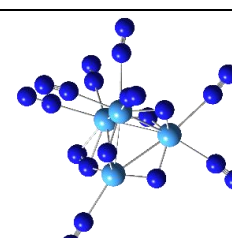
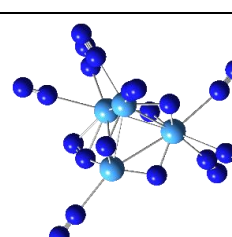
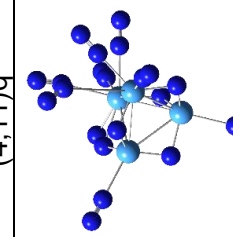
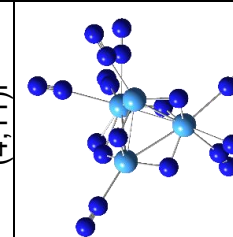
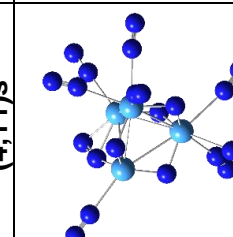
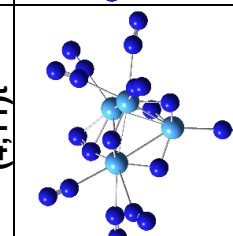
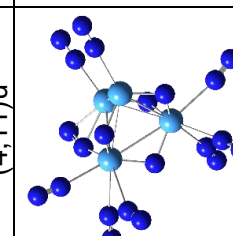
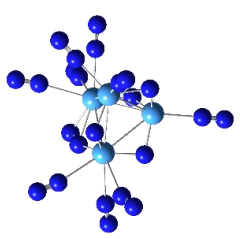
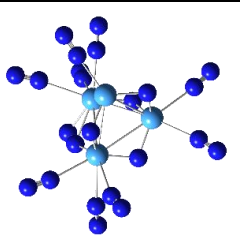
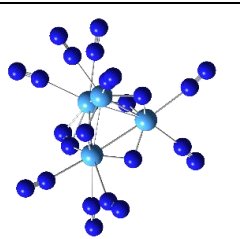
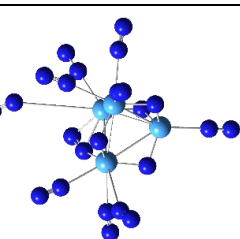
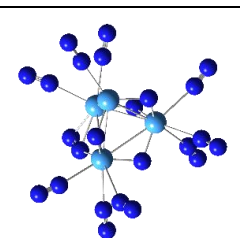
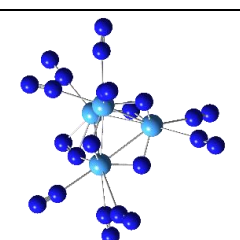
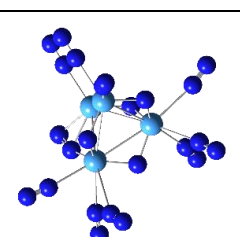
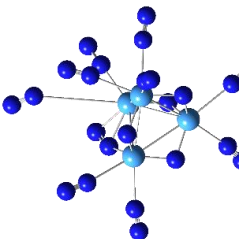
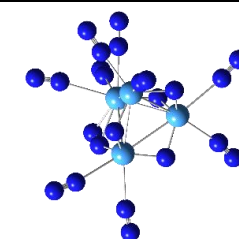
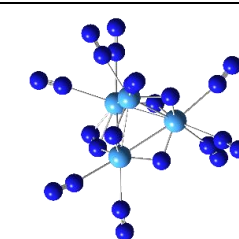
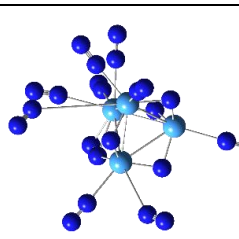
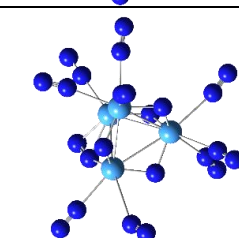
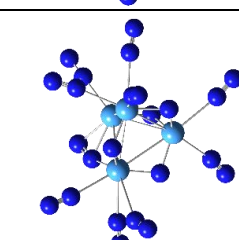
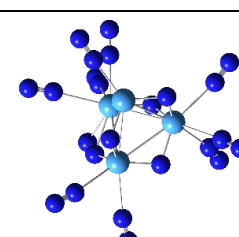
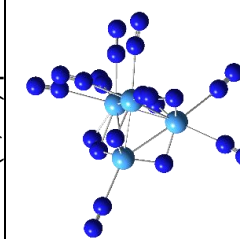
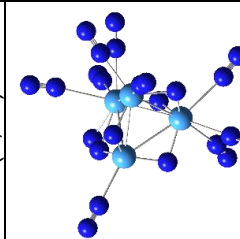
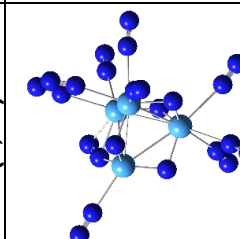
						
(4,10)h	(4,10)i	(4,10)j	(4,10)k	(4,10)l	(4,10)o	(4,10)p
						
(4,10)q	(4,10)r					
						

Table S23i: DFT optimized structures of cluster adsorption isomers (4,11) in the doublet state. Isomers shown in bold are chosen for further discussion. For calculated energies, IR frequencies and graphical representation of those, see Tab. S22j, Fig. S11.

(4,11)a	(4,11)b	(4,11)c	(4,11)d	(4,11)e	(4,11)f	(4,11)g
						
(4,11)h	(4,11)i	(4,11)j	(4,11)k	(4,11)l	(4,11)o	(4,11)p
						
(4,11)q	(4,11)r	(4,11)s	(4,11)t	(4,11)u		
						

4. Cryo IR Spectroscopy and Cryo Kinetics of Dinitrogen Activation and Cleavage by Small Tantalum Cluster Cations

Table S23j: DFT optimized structures of cluster adsorption isomers (4, 12) in the doublet state. Isomers shown in bold are chosen for further discussion. For calculated energies, IR frequencies and graphical representation of those, see Tab. S22j, Fig. S11.

(4,12)a	(4,12)b	(4,12)c	(4,12)d	(4,12)e	(4,12)f	(4,12)g
						
(4,12)h	(4,12)i	(4,12)j	(4,12)k	(4,12)l	(4,12)o	(4,12)p
						
(4,12)q	(4,12)r	(4,12)s				
						

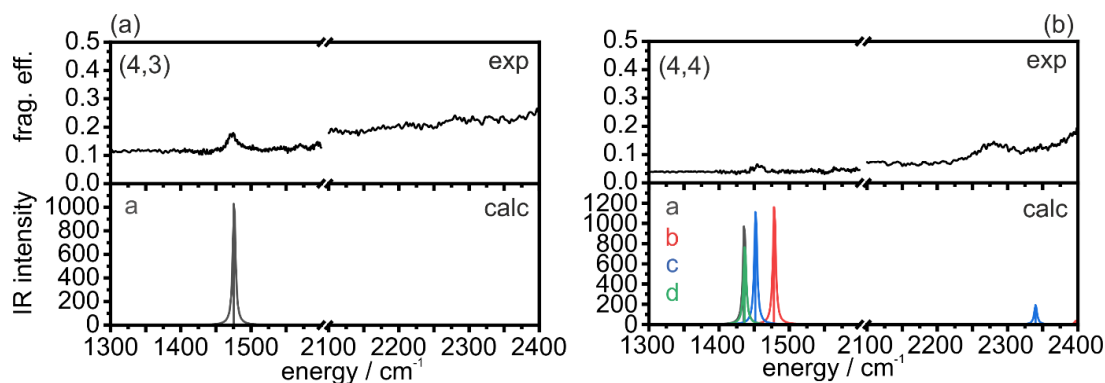


Figure S8: Experimental IR-PD spectra and DFT modelling of (4,3), (a), and (4,4), (b), respectively. The predicted IR frequencies are scaled by a factor of 0.9736. For calculated energies and IR frequencies of the shown structural isomers of (4,3), see Tab. S22a and Tab. S23a. For calculated energies and IR frequencies of the shown structural isomers of (4,4), see Tab. S22b and Tab. S23b.

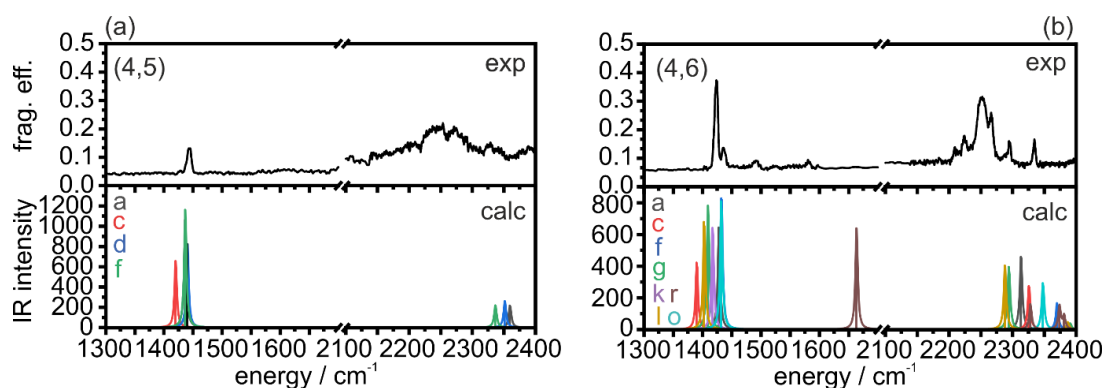


Figure S9: Experimental IR-PD spectra and DFT modelling of (4,5), (a), and (4,6), (b), respectively. The predicted IR frequencies are scaled by a factor of 0.9736. For calculated energies and IR frequencies of the shown structural isomers of (4,5), see Tab. S22c and Tab. S23c. For calculated energies and IR frequencies of the shown structural isomers of (4,6), see Tab. S22d and Tab. S23d.

4. Cryo IR Spectroscopy and Cryo Kinetics of Dinitrogen Activation and Cleavage by Small Tantalum Cluster Cations

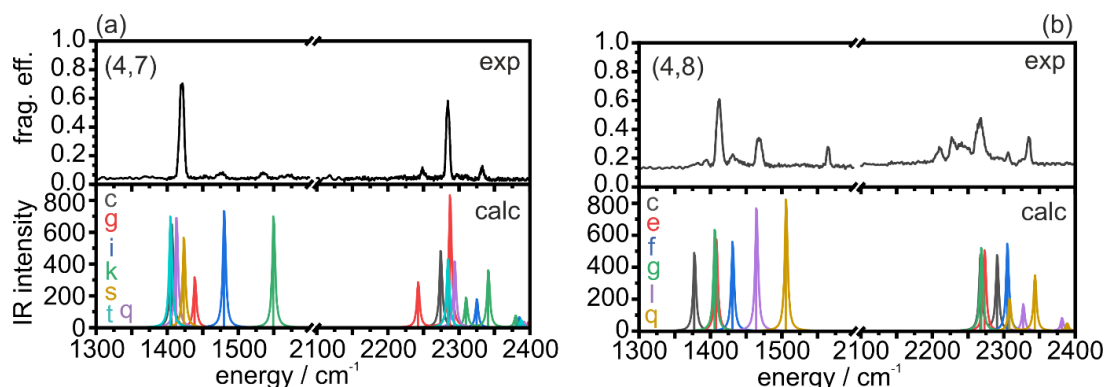


Figure S10: Experimental IR-PD spectra and DFT modelling of (4,7), (a), and (4,8), (b), respectively. The predicted IR frequencies are scaled by a factor of 0.9736. For calculated energies and IR frequencies of the shown structural isomers of (4,7), see Tab. S22e and Tab. S23e. For calculated energies and IR frequencies of the shown structural isomers of (4,8), see Tab. S22f and Tab. S23f.

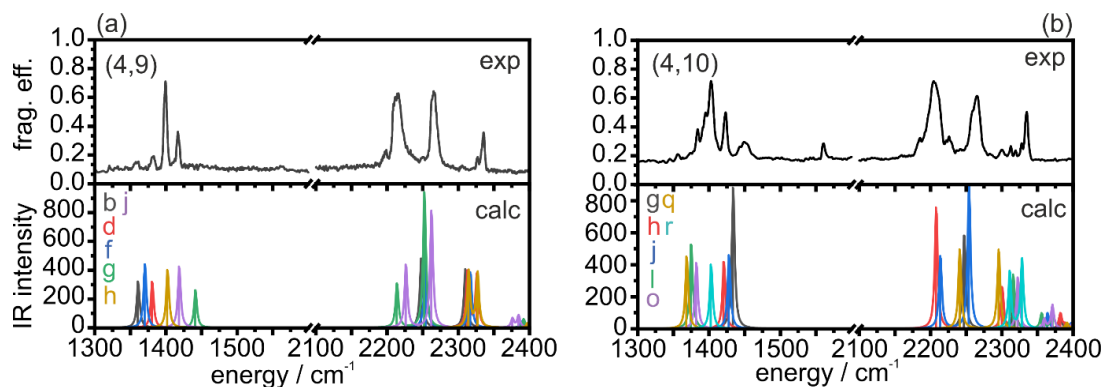


Figure S11: Experimental IR-PD spectra and DFT modelling of (4,9), (a), and (4,10), (b), respectively. The predicted IR frequencies are scaled by a factor of 0.9736. For calculated energies and IR frequencies of the shown structural isomers of (4,9), see Tab. S22g and Tab. S23g. For calculated energies and IR frequencies of the shown structural isomers of (4,10), see Tab. S22h and Tab. S23h.

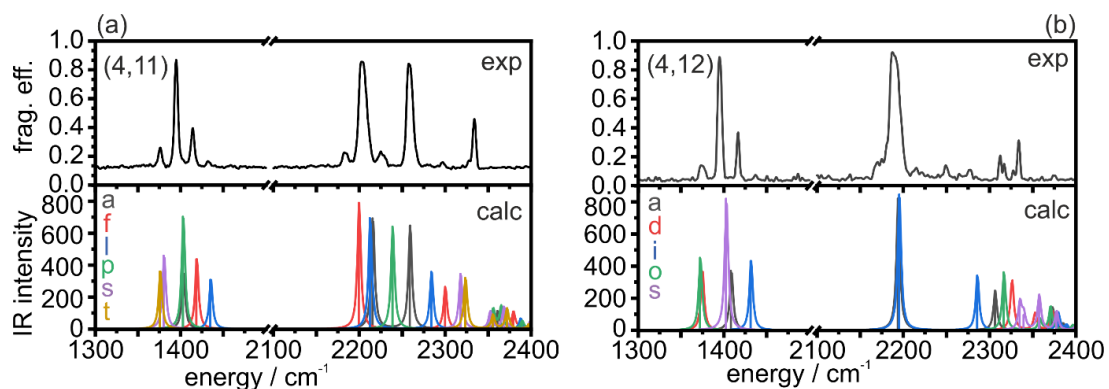


Figure S12: Experimental IR-PD spectra and DFT modelling of (4,11), (a), and (4,12), (b), respectively. The predicted IR frequencies are scaled by a factor of 0.9736. For calculated energies and IR frequencies of the shown structural isomers of (4,11), see Tab. S22i and Tab. S23i. For calculated energies and IR frequencies of the shown structural isomers of (4,12), see Tab. S22j and Tab. S23j.

4. Cryo IR Spectroscopy and Cryo Kinetics of Dinitrogen Activation and Cleavage by Small Tantalum Cluster Cations

Table S24: Bond distances $d(\text{Ta4-N6})$ and angles $\angle(\text{Ta4-Ta1-N6})$ of computed isomers of the cluster species (4,6) and (4,7) indicate increase an increasing tilt of the $\mu_2\text{-}\kappa\text{N}:\kappa\text{N,N N5N6}_{(\text{side-on})}$ ligand with the observed red shift of its IR vibrational frequency. The predicted IR frequencies are scaled by a factor of 0.9736.

isomer	$d(\text{Ta4-N6}) / \text{\AA}$	$\angle(\text{Ta4-Ta1-N6}) / ^\circ$	$\nu_{\text{N5N6}(\text{scaled})} / \text{cm}^{-1}$
(4,6)	a	2.09973	1428
	c	2.14642	1390
	f	2.11304	1432
	g	2.09858	1409
	k	2.10872	1417
	l	2.08409	1402
	o	2.09961	1431
	r	2.21526	1663
(4,7)	c	2.09482	1406
	g	2.09580	1438
	i	2.18669	1480
	k	2.19734	1549
	q	2.10059	1413
	s	2.11287	1423
	t	2.08385	1404

Table S25a: Calculated IR spectrum of isomer (4,7)c. The predicted IR frequencies are scaled by a factor of 0.9736. The bending vibration of the side-on $\mu_2\text{-}\kappa\text{N}:\kappa\text{N},\text{N N}_2$ ligand at 111 cm^{-1} , and a wagging mode of the $\text{N}_{2(\text{end-on})}$ ligand on Ta2 at 51 cm^{-1} might couple to the side-on N_2 stretching mode at 1406 cm^{-1} (scaled).

energy / cm^{-1}	energy (scaled)/ cm^{-1}	IR intensity
10.2176	9.94786	0.236
19.4926	18.978	0.3352
28.0593	27.31853	0.5486
31.3014	30.47504	0.3857
40.7778	39.70127	0.2029
45.9992	44.78482	0.0341
51.0843	49.73567	0.2107
78.5286	76.45544	1.0929
111.2524	108.31534	1.0825
127.0588	123.70445	13.6358
134.0777	130.53805	2.3684
138.5869	134.92821	4.3126
147.5874	143.69109	4.9026
156.436	152.30609	3.936
175.3051	170.67705	3.5226
180.6536	175.88434	1.5561
182.9975	178.16637	1.7801
192.7846	187.69509	8.6015
194.0439	188.92114	1.5496
197.268	192.06012	4.8152
202.2491	196.90972	0.3241
206.1974	200.75379	0.6953
217.267	211.53115	3.5302
229.2133	223.16207	9.0562
239.9958	233.65991	5.8766
245.6397	239.15481	1.7916
260.0053	253.14116	11.4239
269.5148	262.39961	1.9784
287.8441	280.24502	11.1669
309.9114	301.72974	3.683
329.1736	320.48342	1.4535
362.6268	353.05345	10.321
375.3322	365.42343	3.2833
478.0506	465.43006	1.6939
569.475	554.44086	3.6997
599.5951	583.76579	11.5988
643.6079	626.61665	76.492
708.6674	689.95858	125.6325
713.3993	694.56556	131.5728
729.9125	710.64281	103.222
772.3713	751.9807	35.4663

4. Cryo IR Spectroscopy and Cryo Kinetics of Dinitrogen Activation and Cleavage by Small Tantalum Cluster Cations

Table S25b: Calculated IR spectrum of isomer (4,7)c. The predicted IR frequencies are scaled by a factor of 0.9736. The bending vibration of the side-on $\mu_2\text{-}\kappa\text{N}:\kappa\text{N},\text{N N}_2$ ligand at 111 cm^{-1} , and a wagging mode of the $\text{N}_{2(\text{end-on})}$ ligand on Ta2 at 51 cm^{-1} might couple to the side-on N_2 stretching mode at 1406 cm^{-1} (scaled).

energy / cm^{-1}	energy (scaled)/ cm^{-1}	IR intensity
821.8665	800.16922	34.2319
886.3202	862.92135	245.9894
1444.0647	1405.94139	648.6374
2335.7668	2274.10256	481.549
2451.7051	2386.98009	47.3735
2482.118	2416.59008	0.589
2492.1804	2426.38684	8.4558

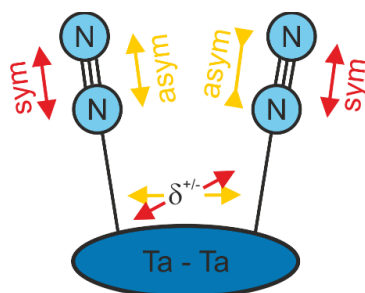


Figure S13: Scheme of electron density shuffling across the metallic Ta-Ta bond with the N_2 stretching motion.

Text S2: Introduction with a focus on kinetic studies

The paramount significance of catalytic conversions renders it necessary to augment process optimization with fundamental knowledge. It is e.g. the catalytically enabled valorization of ubiquitous N_2 which accounts for around 2 % of total final energy consumption worldwide.¹⁰ Heterogeneous catalysis is the backbone of such conversions, and it most often utilizes catalysts that incorporate Transition Metals (TM), either in the form of bulk or nanostructured materials.^{11, 12} Any further optimization of this and other catalyzed processes thus promises for economic benefits, and it would help to launch sustainability and provide for environmental protection. Thus, the afore mentioned fundamental knowledge may well assist and support such practical optimization.

The investigation of isolated TM clusters may seem vaguely related to these quests, at first glance. However, it is mandatory to describe and understand materials and elementary processes at the molecular level, and atomically precise TM clusters may serve in this regard.^{13, 14} Reaction enthalpies and prevailing barriers determine the kinetics: Catalytic macro kinetics manifest in the magnitudes of empirical turn over numbers, and micro kinetics in the reaction rates of chosen elementary steps. Most often, the bimolecular reaction rates of TM clusters with single molecules reveal size-dependent variations, that are deeply interweaved with the electronic and geometric structures of the bare TM cluster and of the cluster adsorbate product complexes.^{15, 16} Several reactivity studies of various TM cluster kinetics with small molecules have revealed remarkable cluster size dependencies, in particular for small clusters.¹⁷⁻²⁶

The kinetics of N_2 adsorption on Ag_n^+ clusters reveal first step rate coefficients that increase exponentially from $n = 1 - 7$, which was interpreted in terms of an increase of internal degrees of freedom with cluster size.¹⁷ Extensive reaction studies of nickel group cluster anions with N_2 , O_2 , CO_2 , and N_2O found parallel trends of the first step rate coefficients and the adsorption limits, both of which increase with cluster size. Notably, the observed saturation effects imply rearrangements in the cluster core upon high reactant loads.^{19, 27} A wealth of extensive kinetic reactivity studies with Rhodium cations was reviewed before.²⁰ The relative reaction rates of small Rh_n clusters with N_2 and D_2 were found to increase sharply from $n = 3$ and $n = 5$ on, respectively,²¹ and kinetic investigations of Rh_n^+ , $n = 6 - 16$ with NO managed to distinguish various

4. Cryo IR Spectroscopy and Cryo Kinetics of Dinitrogen Activation and Cleavage by Small Tantalum Cluster Cations

cluster sizes for their highly reactive or largely inert cluster surface morphologies, with biexponential reaction kinetics of Rh_6^+ that signify coexisting isomers.^{18, 22} Small Rh_n^+ clusters revealed a cooperative auto enhancement of NO adsorption rather than cluster size dependencies which are small up to saturation of vacant adsorption sites.²⁸

Temperature-dependent reaction kinetics of cationic tantalum clusters Ta_n^+ , $n = 13 - 40$, with molecular oxygen indicate a change in the reaction mechanism from dissociative to molecular adsorption upon saturation of active surface sites.²⁹ Tantalum clusters are susceptible to oxide formation by O_2 and CO_2 .^{30, 31} We review other than kinetic investigations of tantalum clusters in the introduction sections of **[IRS1, IRS2]**

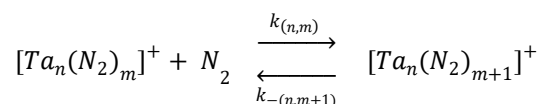
By virtue of our previous studies, we have established cryo kinetic measurements of isolated TM clusters under single collision conditions as a strong tool for the elucidation of elementary adsorption and reaction processes, as e.g. on Nb_n^+ ³², Ni_n^+ ^{4, 33}, Rh_n^+ ³⁴, Rh_iFe_j^+ ³⁵ and Fe_n^+ ³⁶. As in the current case, we have complemented our kinetic studies with cryo IR spectroscopic studies of the resulting cluster adsorbate species.^{1, 3, 4, 34-36} Our third line of experimental methodology, gas phase studies by the X-ray magnetic circular dichroism (XMCD) technique, would serve to elucidate high spin states and possible orbital contributions to magnetic moments of isolated clusters.^{37 38} Our quantum chemical modelling by DFT reveal, however, low spin states of all clusters and complexes of relevance in the current study.

Text S3: Further Information about Experimental and Computational Methods

The transition metal cluster ions are generated in a home-built laser vaporization (LAVP) source.^{39, 40} The second harmonic of a pulsed Nd:YAG (Innolas Spitlight 300, 20 Hz) evaporates the metal atoms from a rotating tantalum foil (99.95 %, 0.5 mm thick, Alfa Aesar). The hot plasma consisting of atoms and ions thus generated is captured by a He gas pulse (40 μ s, 15 bar) from a home-built piezoelectric valve⁴¹. This valve operates in synchronization with the laser. The gas pulse entrains the plasma through a 69 mm long channel (2 mm diameter). The atoms and ions cool and aggregate into clusters during the subsequent jet expansion into vacuum (10^{-7} mbar). The resulting cluster size distribution passes electrostatic lenses and reaches a 90° ion beam bender. The cluster ions can be selected by size using the following quadrupole mass filter. Subsequently the (mass selected) ions are injected into the cryogenic hexapole ion trap which is cooled to 26 K by a closed cycle He cryostat. Thereby, we are able to trap required mass complexes and to continuously introduce buffer and/or reaction gas. For the present study we introduced He as buffer gas and N₂ as reaction gas. To achieve sufficient N₂ attachment to the Ta_n⁺ cluster we increased the pressure in the ion trap from 1.2×10^{-7} mbar up to a maximum of 3.5×10^{-7} mbar. The additional continuously introduced He gas ensures efficient trapping and cooling of the ions. Thus, the pressure in the ion trap increases up to 6.8×10^{-6} mbar. The ions are trapped in the hexapole ion trap for various storage times (0 – 20 s) according to the investigation procedure. For detection, the manipulated ions, [Ta_n(N₂)_m]⁺ = (n,m), are steered into the FT-ICR cell by a series of electrostatic lenses. The so-called “infinity” type cell⁴² is cooled down to 10 K by a closed cycle He cryostat to prevent heating of the clusters by black body radiation. If required, it is possible to isolate the ion complexes within the ICR cell. This was necessary when recording IRPD spectra for the cryogenic infrared spectroscopy studies [IRS1], this work, and [IRS2], our adjoined IR-PD study on larger tantalum clusters, to ensure sufficient irradiation of the ions. For the kinetic studies of N₂ adsorption to Ta_n⁺ clusters, the ICR cell served only for ion detection. Instead, the storage of ions in the hexapole filled with N₂ is of particular interest for the study of adsorption kinetics. Storage of the cluster adsorbate species (n,m) occurs under isothermal conditions at 26 K. In order to investigate the cationic tantalum clusters and their nitrogen adducts we performed reaction delay scans. The recorded mass spectrum for each reaction delay consists of an average of 40 scans. We receive a temporal evolution of mass spectra, which we

4. Cryo IR Spectroscopy and Cryo Kinetics of Dinitrogen Activation and Cleavage by Small Tantalum Cluster Cations

evaluate to obtain signal intensities and assigned storage times for each adsorbate complex. These data serve as input for evaluation by evofit⁴³, our in-house genetic algorithm fitting routine. The pseudo-first-order fits performed yield relative rate constants for all adsorption $k_{(n,m)}$ and desorption $k_{-(n,m+1)}$ steps.



The chosen nomenclature is in line with our previous publications⁷. For further explanation of the nomenclature for the Ta_n^+ cluster and their adsorbates we refer the reader to the supporting information.

From the relative rate constants $k_{(n,m)}$ and $k_{-(n,m+1)}$ we determine the absolute rate constants $k_{(n,m)}^{abs}$ using the absolute collision gas number densities $\rho_{N_2}(T)$ as conversion factor.

$$k_{(n,m)}^{abs} = \frac{k_{(n,m)}}{\rho_{N_2}(T)}$$

The pressure in the surrounding chamber $p_c^{(300 K)}$ and an effective geometry factor c_{app} serve to obtain approximate values for the absolute collision gas number densities $\rho_{N_2}(T)$.

$$\rho_{N_2}(26 K) = \frac{c_{app} p_c^{(300 K)}}{k_B T_{300 K}}$$

We determined the geometry factor as 1.8(9) at 26 K. Calculating the quotient of the absolute rate constants k^{abs} and the collision rates k^{coll} give the absolute reaction efficiency γ .

$$\gamma = \frac{k^{abs}}{k^{coll}}$$

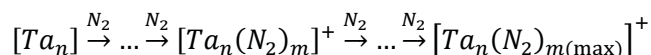
Three models serve for determination of collision rates: The average dipole orientation (ADO) theory is based on a concept of a classical trajectory of a linear dipole in the field of a point charge where μ is the reduced mass of the cluster adsorbate complex, μ_D indicates the dipole moment and α gives the polarizability.^{44, 45}

$$k^{ADO} = \frac{q}{2 \varepsilon_0 \sqrt{\mu}} \left(\sqrt{\alpha'} + c \mu_D \sqrt{\frac{2}{\pi k_B T}} \right)$$

The parameter for the polarizable volume α' and the dipole moment μ_D express parameter c which can take values from 0 to 1.⁴⁶ Note, that a vanishing dipole moment, as of N₂, causes k^{ADO} to become identical to the Langevin rate constant. Additional effects may prevail upon TM clusters reacting with small molecules, and Kummerlöwe and Beyer⁴⁷ devised two models to approximate collision rates of ionic clusters with neutral molecules: the hard sphere average dipole orientation (HAS) model and the surface charge capture (SCC) theory. Both models share the idea that clusters and the neutral reactants are hard spheres and charge is point charge. The former one assumes the point charge in the center of the ionic cluster and according the latter one is the charge able to migrate to the cluster surface by its attractive interaction with the neutral collision partner.

Text S4: Trends and limits of N₂ adsorption on tantalum cluster

To investigate the adsorption behavior of nitrogen molecules on Ta_n⁺ clusters of cluster sizes $n = 2 - 8$, each cluster species was isolated in the quadrupole mass filter and stored in the hexapole ion trap at 26 K. At the same time, nitrogen (up to $3.5 \cdot 10^{-7}$ mbar) was continuously introduced as reaction gas into the hexapole. For all cluster sizes, a progression $\Delta m = 28$ m/z was observed, which implies a stepwise adsorption of molecular nitrogen according to:



The N₂ adsorption to each cluster Ta_n⁺ reaches a limit $m_{(\max)}$, which depends on cluster size n . (Fig S14, disk symbols) Beyond this limit neither an increase of N₂ pressure nor an increase of storage time leads to further N₂ adsorption. While the tantalum dimer cation, Ta₂⁺, merely adsorb a single nitrogen molecule, the tantalum trimer cation, Ta₃⁺, manages to accommodate up to 11 N₂ molecules. In remarkable contrast to this steep incline, the Ta₄⁺ and Ta₅⁺ accept another two and three nitrogen molecules,

4. Cryo IR Spectroscopy and Cryo Kinetics of Dinitrogen Activation and Cleavage by Small Tantalum Cluster Cations

respectively. Ta_5^+ and all larger clusters up to Ta_8^+ accept 16 N_2 irrespective of their size; there is no further incline.

The steep increase in N_2 adsorption from Ta_2^+ to Ta_3^+ is remarkable, and it is in equally remarkable contrast to the plateau at Ta_5^+ and beyond. Our previous investigation of N_2 adsorption limits of other transition metal clusters have revealed an increasing trend of N_2 adsorption limits with increasing cluster size with a close to 1:1 stoichiometry in cases of Fe_n^+ ³⁶, Ni_n^+ ³³, and a close to 1:2 stoichiometry in the case of Rh_n^+ ³⁴ (cf. Fig. S15). This may be due to the fact that the transition metals Fe and Ni are 3d metals, Rh is a 4d metal, while tantalum is a 5d transition metal.

Further findings deserve attention: In the cases of Ta_2^+ and Ta_3^+ the largest observable cluster adsorbate complex $[Ta_2(N_2)_{m(max)}]^+$ and $[Ta_3(N_2)_{m(max)}]^+$, respectively, are the most abundant complexes in equilibrium m^* (Fig. S14, solid triangles). This is clearly not the case for larger tantalum clusters. In equilibrium there are three distinct levels of N_2 adsorption: highest amount and lowest amount of N_2 observed, $m_{(max)}$ and $m_{(min)}$ (Fig. S14, open circles and open triangles, respectively), and most intense species with m^* N_2 adsorbates (Fig. S14 solid triangles). The most abundant cluster adsorbate complex in equilibrium possesses one to 4 N_2 adsorbates less. The orange shaded area in figure 1 emphasizes the observed range of N_2 adsorption in equilibrium. For observed intensities of all $[Ta_n(N_2)_m]^+$ species in equilibrium refer to Fig. S16.

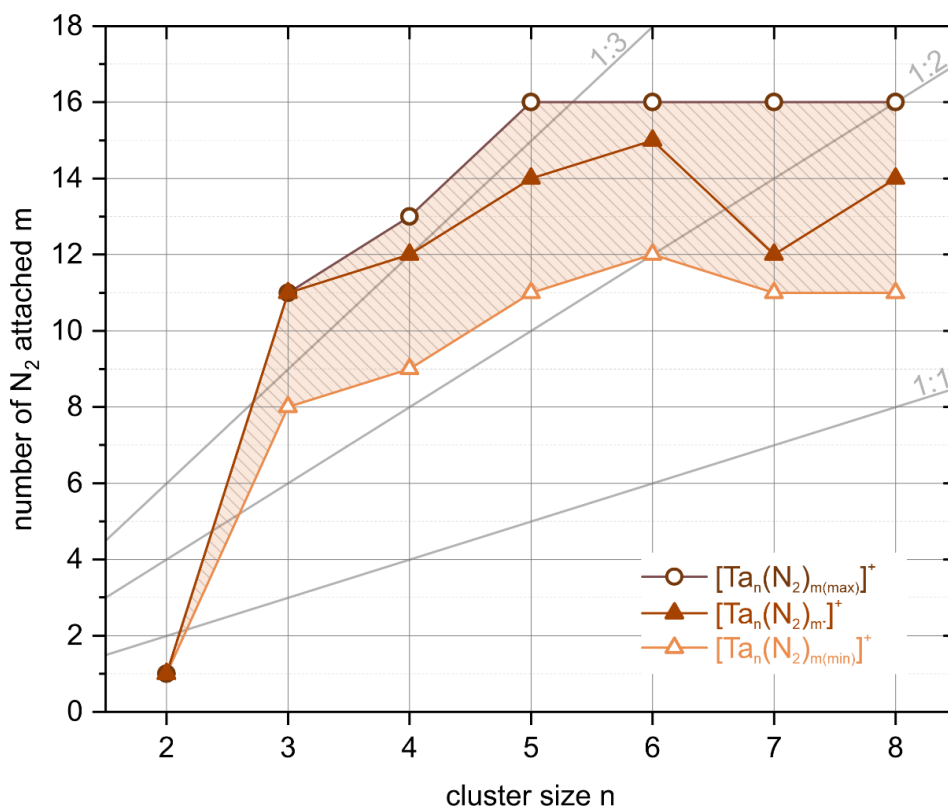


Figure S14: Plot of the experimentally determined adsorption limits $m_{(\max)}$ (open circles) of N₂ on Ta_n⁺ clusters, $n = 2-8$, when stored in the hexapole ion trap with 26 K Helium buffer gas. In equilibrium (at up to 20 s, exposure to $3.5 \cdot 10^{-7}$ mbar N₂) there are two more distinct levels of N₂ adsorption: lowest amount of N₂ observed $m_{(\min)}$ (open triangles) and most intense species with m^* N₂ adsorbates (solid triangles). The orange shaded area emphasizes the observed range of N₂ adsorption in equilibrium.

4. Cryo IR Spectroscopy and Cryo Kinetics of Dinitrogen Activation and Cleavage by Small Tantalum Cluster Cations

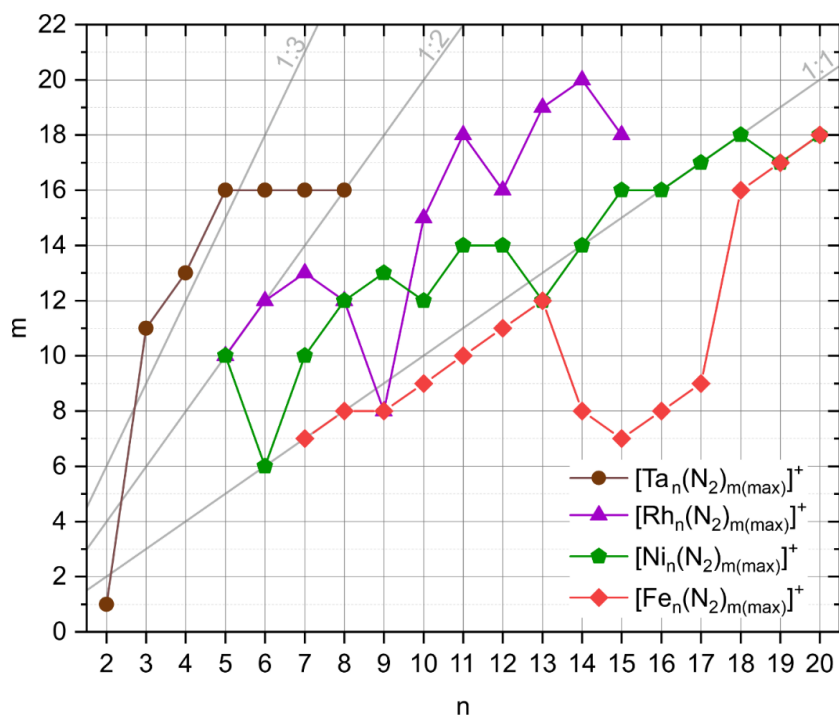


Figure S15: Plot of the experimentally determined adsorption limits $m_{(\max)}$ of N_2 on Ta_n^+ , Rh_n^{+34} , Ni_n^{+33} and Fe_n^{+36} clusters when stored in the hexapole ion trap with 26 K Helium buffer gas.

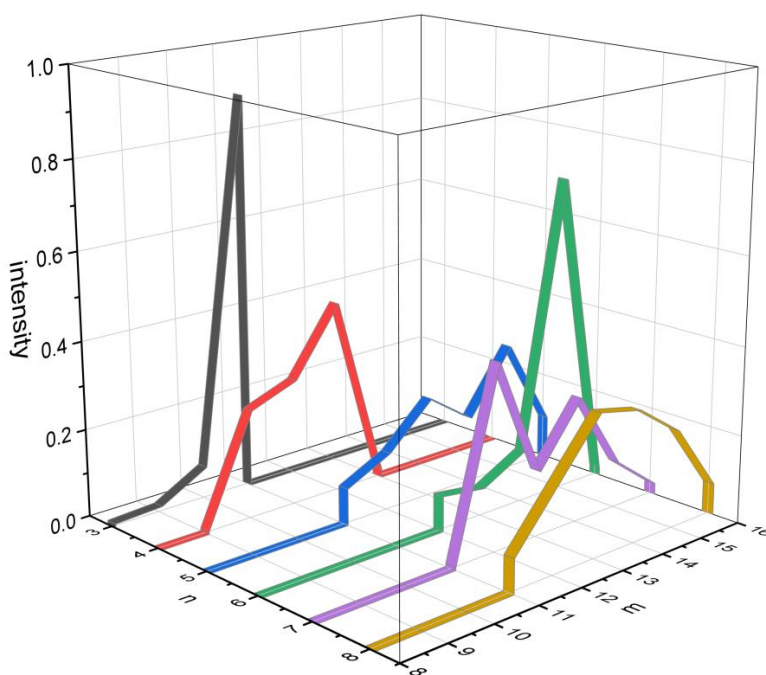


Figure S16: 3D plot of observed intensities of all $[\text{Ta}_n(\text{N}_2)_m]^+$, (n,m) , species in equilibrium. Supporting plot to the orange shaded area in Fig. S14.

Text S5: Cryo kinetics and rate constants of N_2 adsorption to tantalum clusters

Our kinetic measurements reveal the temporal evolution of the adsorbate intensities for each N_2 adsorption step onto the Tantalum clusters Ta_n^+ , $n = 2 - 8$. We fit the intensity data with a pseudo-first-order kinetic approach using our genetic algorithm routine *evofit*⁴³. The obtained fits confirm consecutive N_2 adsorption steps to Ta_n^+ cluster, $n = 2 - 8$, and varying amounts of N_2 desorption at higher levels of N_2 loads.

Text S6: Absolute rate constants of the initial N_2 adsorption steps

Before we start a presentation and discussion of the kinetics of each cluster size, we have a glance at the magnitude of the initial rate constant of adsorption as a function of Tantalum cluster size (Fig. S17). By normalization to the collision gas density, we derive these absolute rate constants $k_{(n,0)}^{\text{abs}}$ from the pseudo-first-order fit of relative rate constants $k_{(n,m)}$, as fitted for all steps of N_2 uptake and release and as to discuss later.

4. Cryo IR Spectroscopy and Cryo Kinetics of Dinitrogen Activation and Cleavage by Small Tantalum Cluster Cations

We have observed before in the case of Rhodium clusters Rh_n^+ a gradual increase of the absolute rate constants $k^{abs}_{(n,0)}$ with increasing n starting at $n = 5$ ³⁴. Neutral Rhodium clusters seem to reveal same behavior²¹. Ta_n^+ cluster, $n \leq 4$, are almost unreactive towards CO; for larger clusters above $n = 5$, the CO binding rate increases abruptly by at least three orders of magnitude.²⁶ We find a like increase of rate constants in the current study of cationic Tantalum clusters (Figs. S17 and S18). Effective $n = 7$ and beyond, both Rh_n^+ and Ta_n^+ assume N_2 adsorption rates $k^{abs}_{(n,0)}$ of same values, void of further increase. The steep rise from $k^{abs}_{(5,0)}$ to $k^{abs}_{(7,0)}$ may find an interpretation in terms of $[Ta_n(N_2)_1]^+$ heat capacities: The larger the internal heat bath – roughly scaling with the cluster size n – the more irreversible the N_2 adsorption enthalpy redistributes, and at some point – here $n = 7$ – the N_2 desorption fades out. Prior modelling of Kummerlöwe et al. devised a Surface Charge Capture Model (SCC, k^{SCC}), and a Hard Sphere Average Dipole Orientation Model (HAS, k^{HSA})⁴⁷. These serve to complement the established Average Dipole Orientation Theory (ADO, k^{ADO}), and the Langevin capture cross section. Application of these models to the current case of $Ta_n^+ + N_2$ adsorption compares well with the determined absolute rate constants $k^{abs}_{(7,0)}$ and $k^{abs}_{(8,0)}$, which fall in between of k^{SCC} and k^{HSA} (Fig. S17, Tab. S26). Under present conditions, values of k^{ADO} , $k^{Langevin}$, and k^{HSA} coincide.

The most noteworthy cases of $k^{abs}_{(2,0)}$, $k^{abs}_{(3,0)}$, and $k^{abs}_{(4,0)}$ do require special attention: from Geng et. al.⁸ we know, that Ta_2^+ activates N_2 . Our combined IR-PD and DFT studies⁷ and [IRS1] confirm like abilities of Ta_3^+ and Ta_4^+ . All of these activations are highly exothermic, and they reveal most stable nitride products which are resilient against N_2 release. Void of entrance barriers, the Ta_2^+ and Ta_3^+ and Ta_4^+ clusters experience no kinetic hindrance. While Ta_3^+ and Ta_4^+ digest N_2 collision partners with collision rate, the Ta_2^+ cluster seem to experience some steric hindrance, and it might happen that unfavorable N_2 orientations upon mutual approach are highly likely. While the entrance channel barrier of N_2 activation by Ta_2^+ is submerged, the concomitant transition state thus seems to be narrow, and it reduces the effective capture rate $k^{abs}_{(2,0)}$ by more than an order of magnitude as observed.

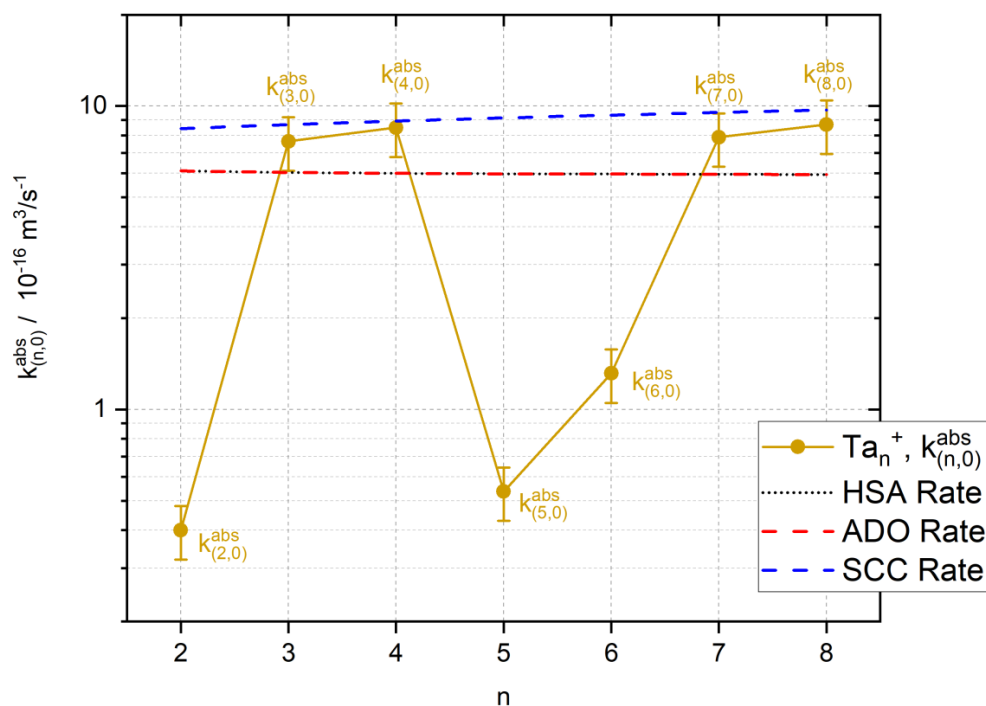


Figure S17: Absolute experimental rate constants $k_{(n,0)}^{abs}$ of for the adsorption of the first N_2 molecule to the Tantalum clusters Ta_n^+ , $n = 2 - 8$ as a function of cluster size n (solid dots), collision rates by average dipole orientation (ADO) theory (red dashed line), and by the hard sphere average (HSA) dipole orientation model (black dotted line), and by the surface charge capture (SCC) model (blue dashed line). Numerical values are listed in Tab. S26.

4. Cryo IR Spectroscopy and Cryo Kinetics of Dinitrogen Activation and Cleavage by Small Tantalum Cluster Cations

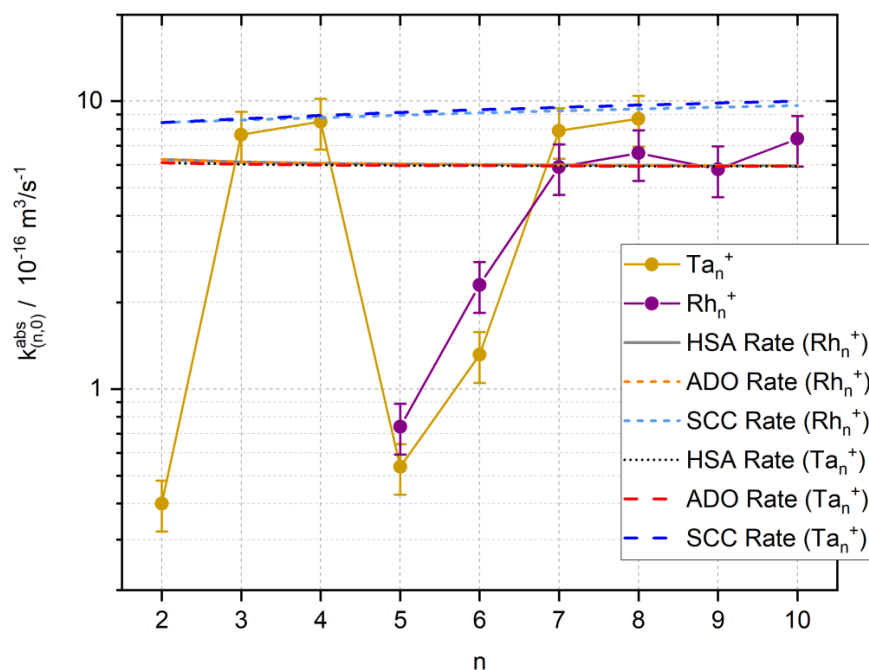


Figure S18: Absolute rate constants $k_{(n,0)}^{abs}$ of for the adsorption of the first N_2 molecule to the Tantalum clusters Ta_n^+ , $n = 2 - 8$ and Rh_n^+ , $n = 5 - 10$ ³⁴, as a function of cluster size n (green dots, estimated error bars), compared to classical average dipole orientation (ADO) theory (red dashed line), to the hard sphere average (HAS) dipole orientation model (black dotted line), and to the surface charge capture (SCC) model (blue dashed line). Numerical values for Ta_n^+ are listed in Table S26.

Table S26: Relative experimental and derived absolute N₂ adsorption rate constants for the initial N₂ adsorption to Ta_n⁺ clusters in comparison to the calculated rate constants by classical ADO theory, the HSA model, and the SCC model (see Tab. S2). The experimental values, recorded at 2.8 – 6.8*10⁻⁶ mbar He buffer gas and 2.0 – 3.5*10⁻⁷ mbar N₂ within the RF hexapole ion trap at 26 K, bear an estimated uncertainty of ±20 %.

n	k _(n,0) s ⁻¹	k ^{abs} _(n,0) 10 ⁻¹⁶ m ³ s ⁻¹	k ^{ADO} _(n,0) 10 ⁻¹⁶ m ³ s ⁻¹	K ^{HSA} _(n,0) 10 ⁻¹⁶ m ³ s ⁻¹	K ^{SCC} _(n,0) 10 ⁻¹⁶ m ³ s ⁻¹
2	0.56	0.40	6.11	6.11	8.42
3	8.30	7.64	6.04	6.04	8.68
4	9.58	8.48	6.00	6.00	8.92
5	0.60	0.54	5.98	5.98	9.14
6	2.00	1.31	5.96	5.96	9.33
7	8.91	7.88	5.95	5.95	9.52
8	7.55	8.69	5.95	5.95	9.69

4. Cryo IR Spectroscopy and Cryo Kinetics of Dinitrogen Activation and Cleavage by Small Tantalum Cluster Cations

Table S27: Input data for determination of absolute rate constants according to the theories of Average Dipole Orientation (ADO), Hard-Sphere (HAS) and Surface Capture (SCC) theory. We compared our absolute rate constants with the three models employed by Kummerloewe and Beyer and used their software.⁴⁷ We used the viscosity of N₂ at 300K.

Entity (unit)	value
$m(\text{N}_2) / 10^{-26} \text{ kg}$	4.65
$k_B / 10^{-23} \text{ J}\cdot\text{K}^{-1}$	1.38
T / K	300
$\eta / 10^{-6} \text{ Pa}\cdot\text{s}$ ⁴⁸	17.9
$\alpha(\text{N}_2) 10^{-40} \text{ C}\cdot\text{m}^2\cdot\text{V}^{-1}$	1.97
$\mu(\text{N}_2) / 10^{-30} \text{ C}\cdot\text{m}$	0
Dipole licking constant	0
$m(\text{N}_2) / \text{amu}$	28
$r(\text{N}_2) / \text{Å}$	1.85
Maximum cluster size	8
Monomer mass / amu	181
$\delta(\text{Ta}) / \text{g}\cdot\text{cm}^{-3}$ ⁹	16.63
Temperature / K (used in ADO/HSA)	26
Cluster charge state	1

Text S7: $[\text{Ta}_2(\text{N}_2)_m]^+$ - Cryo kinetics and rate constants

The Ta_2^+ cluster attaches a single nitrogen molecule utmost, and without any indication of desorption (Fig. S19). We performed further kinetic studies of $\text{Ta}_2^+ + \text{N}_2$ under N_2 pressure variation (Fig. S20(a)-(c)), which reveal the intuitively expected and simple effect of increasing N_2 pressure inducing a faster N_2 adsorption. With no exact pressure gauging at hand, we leave it with the qualitative finding of a close to linear relation.

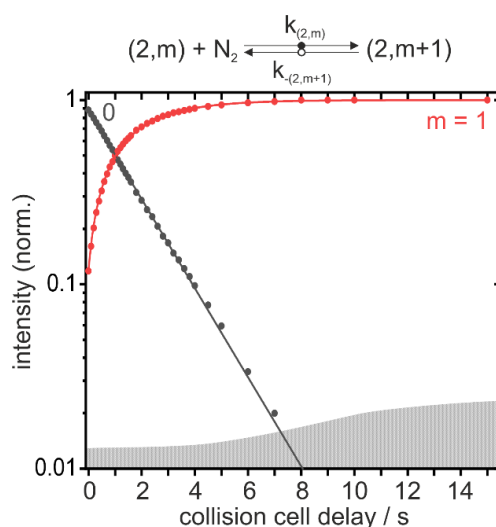


Figure S19: Isothermal kinetics of N_2 adsorption by isolated Ta_2^+ clusters at 26 K, He buffer gas ($6.8 \cdot 10^{-6}$ mbar) and $2.5 \cdot 10^{-7}$ mbar N_2 pressure. The fitting curves (solid lines) of the recorded data (solid dots) confirm pseudo-first-order kinetics for the adsorption of a single N_2 molecule onto Ta_2^+ clusters, no subsequent processes becoming discernible. The gray shaded area indicates the background noise level.

4. Cryo IR Spectroscopy and Cryo Kinetics of Dinitrogen Activation and Cleavage by Small Tantalum Cluster Cations

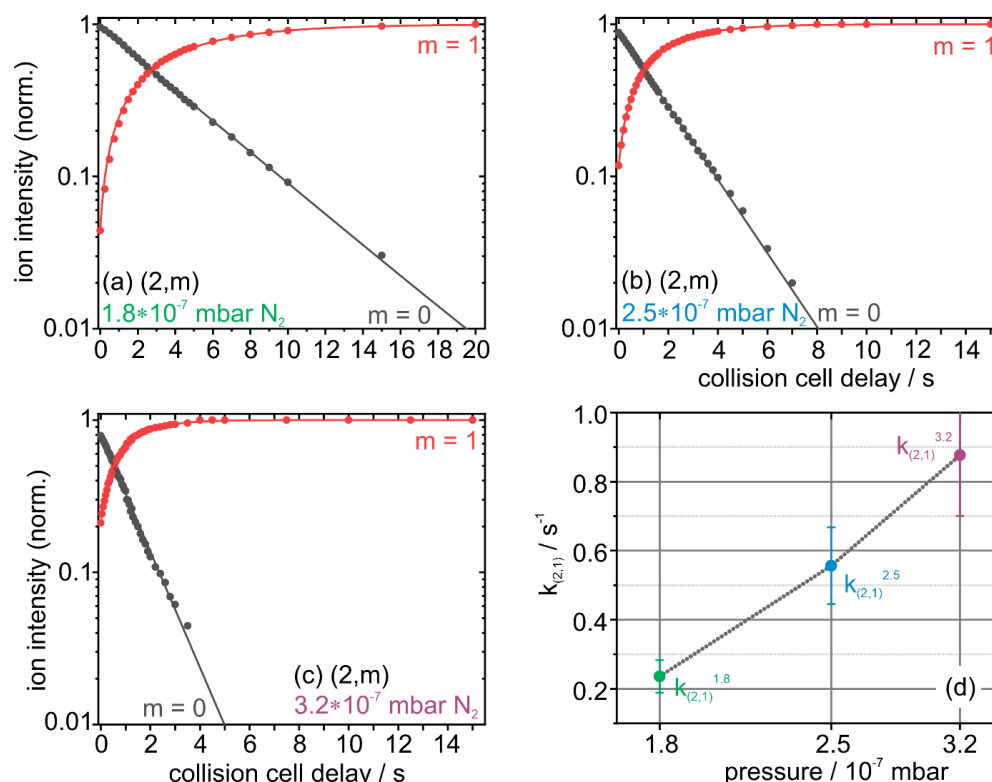


Figure S20: Isothermal kinetics of the N_2 adsorption by isolated Ta_2^+ cluster at 26 K, He buffer gas and various N_2 pressure: (a) 1.8×10^{-7} mbar, (b) 2.5×10^{-7} mbar, (c) 3.2×10^{-7} mbar. The fitting curves (solid lines) of the recorded data (solid dots) confirm pseudo-first-order kinetics for the adsorption of the one N_2 molecule to Ta_2^+ clusters. (d): Observed rate constants ($k_{(2,1)}^{1.8}$, $k_{(2,1)}^{2.5}$, $k_{(2,1)}^{3.2}$, where the superscripts 1.8, 2.6 and 3.2 indicate the N_2 pressure in units of 10^{-7} mbar) resulting from pseudo first order fits of measured kinetic data of Ta_2^+ cluster complexes as function of exposed N_2 pressure.

Table S28: Pseudo-first-order rate constants for the N₂ adsorption and desorption at various N₂ pressure: (a) $1.8 \cdot 10^{-7}$ mbar, (b) $2.5 \cdot 10^{-7}$ mbar, (c) $3.2 \cdot 10^{-7}$ mbar on (2,m) clusters ($k_{(2,m)}$ and $k_{-(2,m+1)}$), the related absolute rate constants ($k^{\text{abs}}_{(2,m)}$), the calculated collision rates ($k^{\text{coll}}_{(2,m)}$) and the absolute reaction efficiency ($\gamma_{(2,m)}$). Statistical uncertainties of the relative rate constants are +/- 20%, and the absolute rate constants acquire an additional uncertainty from pressure calibration of +/- 50%.

	m	$k_{(2,m)}$ s ⁻¹	$k_{-(2,m+1)}$ s ⁻¹	$k^{\text{abs}}_{(2,m)}$ 10 ⁻¹⁶ m ³ s ⁻¹	$k^{\text{coll}}_{(2,m)}$ 10 ⁻¹⁶ m ³ s ⁻¹	$\gamma_{(2,m)}$
a	0	0.24	< 0.001	0.17	6.11	0.03
b	0	0.56	< 0.001	0.40	6.11	0.06
c	0	0.87	< 0.001	0.63	6.11	0.10

Text S8: [Ta₃(N₂)_m]⁺ - Cryo kinetics and rate constants

The high N₂ uptake of the Tantalum trimer cluster Ta₃⁺ occurs through a stepwise N₂ adsorption (Fig. S21) up to an adsorption limit $m_{(\text{max})}$ of 11 N₂ molecules. On the long term, this is the most intense cluster adsorbate complex m^* .

In accordance with our typical evaluation routine of kinetic measurements we fitted the measured intensity data with a pseudo-first-order kinetic approach using our genetic algorithm routine *evofit*⁴³, by which we managed to obtain an overall fit of high quality (Fig. S21, correlation coefficient $\rho = 0.982$). The thereby fitted rate constants of stepwise N₂ adsorption occur close to or even at collision rate. However, we find two dips at $k_{(3,2)}$ and $k_{(3,5)}$. These indicate particularly slow uptake of the third and sixth N₂ molecule. Accordingly, the reactant species (3,2) (Fig. S21(a), dark blue curve) is most abundant up to a reaction delay of 0.3 s, and its N₂ uptake is significantly diminished. In the further course of N₂ adsorption this species (3,2) converts stepwise into species (3,5) which thereby becomes most abundant beyond 0.4 s collision cell delay (Fig. S21(a), dark yellow curve). This indicates an especially slower adsorption for the 6th N₂ molecule as well. At collision cell delays of 10 s and beyond the $m_{(\text{max})}$ species is in a dynamic adsorption/desorption equilibrium with its precursor (3,10). It proved beneficial to include the adsorbate species (3,8) and (3,9) into this equilibrium, some ambiguities remaining. While the adsorption constants $k_{(3,8)}$, $k_{(3,9)}$ and $k_{(3,10)}$ diminish significantly with respect to those of prior adsorption steps, and it is at this level of N₂

4. Cryo IR Spectroscopy and Cryo Kinetics of Dinitrogen Activation and Cleavage by Small Tantalum Cluster Cations

uptake that desorption starts to set in, yielding significant contributions by rate constants $k_{-(3,11)}$ and $k_{-(3,9)}$. Note, that prior desorption seems insignificant, yielding vanishing values of $k_{-(3,0)}$ to $k_{-(3,7)}$ up to our experimental limits (Fig. S21 (b)).

We checked for possible size specific back reactions at early stage, namely high desorption rates of $k_{-(3,3)}$ and $k_{-(3,6)}$, which would cause fitted forward reaction rate values $k_{(3,2)}$ and $k_{(3,5)}$ to take values better in line with prior and subsequent steps, overall close to collision rate. This would yield an alternative fit (variant 2) of the recorded kinetics (Fig. S21, Fig. S23), with a slightly reduced correlation coefficient ($\rho = 0.980$).

We refer to our associated cryogenic infrared spectroscopy study for more detailed insight into the first few N₂ adsorption processes and the species involved [IRS1]. There we present IR-PD spectra of the first five adsorbate species (3,1), (3,2), (3,3), (3,4) and (3,5). The experimental findings are combined with DFT modelling for feasible N₂ adsorption, activation and cleavage pathways. For the absorption of the first N₂ molecule to Ta₃⁺, we identified an overall declining reaction path (-504 kJ/mol) towards ultimate N₂ cleavage, which is much in line with our previously identified across edge above surface (AEAS) mechanism of Ta₄⁺⁷. These findings about a highly exothermic cleavage mechanism for the first N₂ adsorption nicely agree with the observation of a fast initial N₂ adsorption process ($k_{(3,0)}$) from Ta₃⁺ kinetic measurements (Fig. S21(b)). Our DFT modelling of the second N₂ adsorption revealed an exothermic N₂ activation pathway as well, and it elucidates the experimental findings of our IR-PD measurements which signify the absence of NN fingerprints between 1200 and 2400 cm⁻¹. Thus, these findings are in line with a fast adsorption process $k_{(3,1)}$ for the second N₂ molecule – which we indeed obtain by our kinetic studies discussed above. Note, that the determined absence of N₂ desorption from (3,1) and (3,2) lends further support to our interpretation that the first two N₂ adsorbates likely undergo spontaneous activation.

The adsorption of the third and sixth N₂ molecule occur discernably slower, and the desorption is facile as evidenced by high values of $k_{-(3,3)}$ and $k_{-(3,6)}$. This indicates a likely meta stability of the formed (3,3)^{*} and (3,6)^{*} complexes. While the interpretation of the latter case would be much involved, the prior case of three N₂ adsorbates is well

in line with the DFT predictions of [IRS1]: (3,3) swiftly forms by N₂ adsorption from a “hot” precursor I3_(3,2), and it likely converts much of its stabilization into internal excitation. The next, subsequent N₂ adsorption event thus take place at elevated internal energy, and it might suffer from competition with swift desorption – as suggested by the alternative fit with significant desorption rate constant $k_{-(3,3)}$ (cf. Fig. S21, Fig. S23). Note, that the larger the complex, which involves increasing amounts of N₂ adsorbates, the swifter thermal relaxation and collisional cooling becomes, and the larger the density of states becomes. Thus, the subsequent formation of larger complexes seems much less hampered by internal excitation.

In search of a possible, plausible explanation for the noticeable slow adsorption rate $k_{(3,5)}$ or rather a feasible desorption rate $k_{-(3,6)}$, we performed DFT calculations for conceivable adsorption sites for, and arrangements of further N₂ molecules on the III_(3,3) cluster surface as discussed in [IRS1]. It seems likely that cluster adsorbate complex sustains its priory achieved structural motifs: an I3 above surface coordination motif, one double-bridged triangular edge and two one single-bridged triangular edge. In effect, the additional end-on coordinating N₂ ligands may assume any of three available adsorption sites, Ta1, Ta2 or Ta3. These differ in the number of nearest neighbors. Geometry optimization of (3,4) isomers yield three almost degenerated states. We expect all three isomers likely populated in agreement with experimental IR results. Starting from these three isomers for (3,4), we again obtained two almost degenerate isomers for (3,5) by subsequent adsorption of a fifth N₂ molecule. As the fourth and fifth N₂ molecule adsorb to merely two out of three possible coordination sites there is a single coordination site vacant for adsorption of a sixth N₂ molecule filling up the second adsorption shell of N₂ on the Ta₃⁺ cluster for (3,6). Therefore, the 6th N₂ molecule must bind to the already highly occupied Ta center, which is not yet occupied by another terminally bound N₂ – a center where the acceptance angle of attack for the N₂ molecule to be adsorbed is small due to the already adsorbed N₂ molecules sterically shielding the center. This is likely to complicate adsorption and it might cause the low adsorption rate constant $k_{(3,5)}$ or rather a high desorption rate $k_{-(3,6)}$, either of which evidence by the observed temporal enhancement of (3,5).

4. Cryo IR Spectroscopy and Cryo Kinetics of Dinitrogen Activation and Cleavage by Small Tantalum Cluster Cations

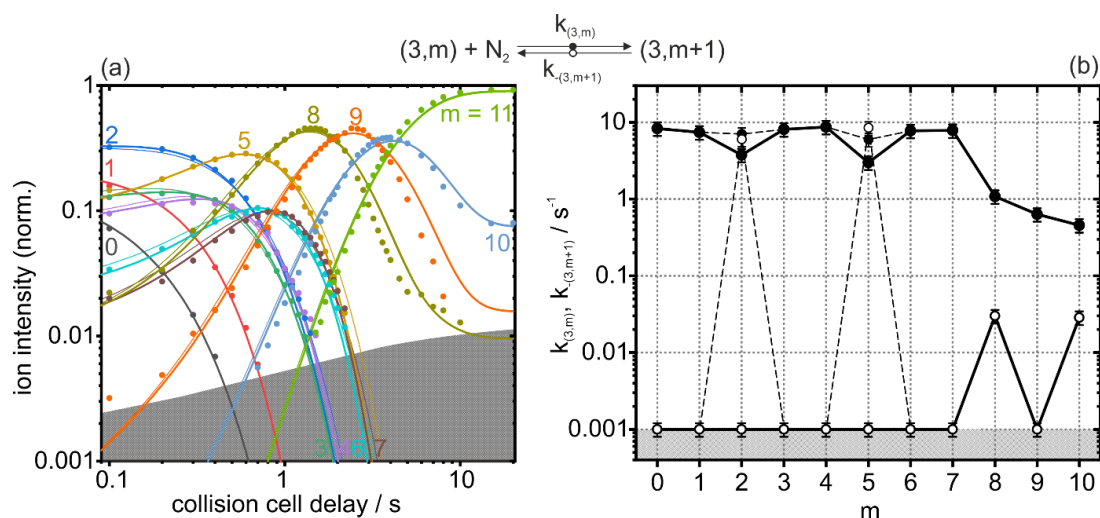


Figure S21: (a) Isothermal kinetics of N_2 adsorption by isolated Ta_3^+ clusters at 26 K, He buffer gas ($6.8 \cdot 10^{-6}$ mbar) and $2.5 \cdot 10^{-7}$ mbar N_2 pressure. The fitting curves (solid lines) of the recorded data (solid dots) confirm pseudo-first-order kinetics for the adsorption in a reaction chain of up to 11 consecutive steps for Ta_3^+ clusters. The chosen log-log plot allows for enhanced visibility of the initial adsorption curves. (b) Fitted values of relative rate constants of Ta_3^+ for the adsorption ($k_{(3,m)}$, solid circles) and the desorption ($k_{-(3,m+1)}$, open circles) as a function of stepwise N_2 adsorption. The gray shaded areas indicate the background noise level. Note an alternative fit (variant 2) with enhanced rates $k_{(3,3)}$, $k_{-(3,3)}$, $k_{(3,6)}$, and $k_{-(3,6)}$, indicated by delicate lines in the kinetic plot (a) and by dotted line in the rate constants plot (b). For separate plots and exact values, we refer to Fig. S22, Fig. S23, Tab. S29 and Tab. S30.

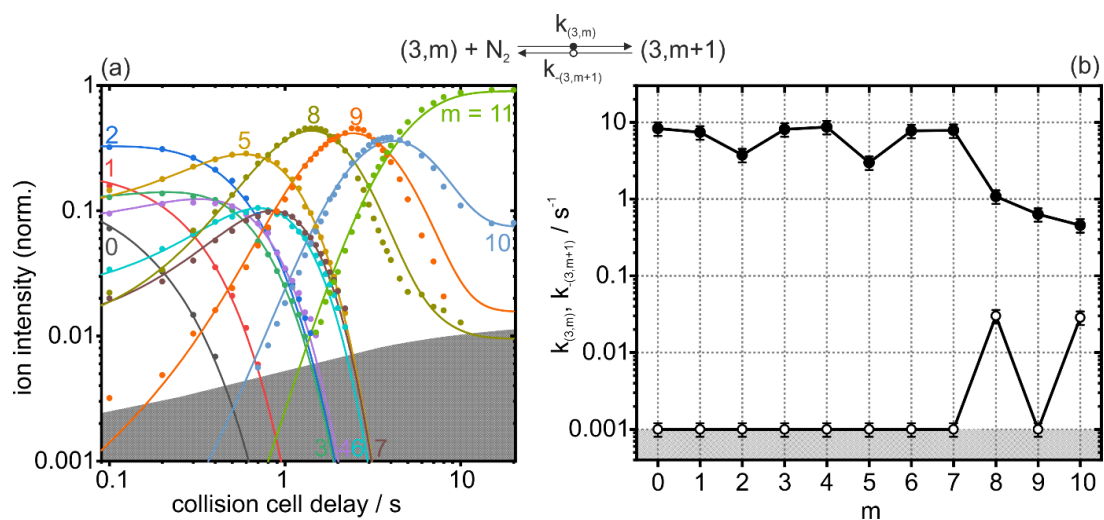


Figure S22: (a) Isothermal kinetics of N_2 adsorption by isolated Ta_3^+ clusters at 26 K, He buffer gas ($6.8 \cdot 10^{-6}$ mbar) and $2.6 \cdot 10^{-7}$ mbar N_2 pressure (variant 1). The fitting curves (solid lines) of the recorded data (solid dots) confirm pseudo-first-order kinetics for the adsorption in a reaction chain of up to 11 consecutive steps for Ta_3^+ clusters. We chose a log-log plot for better visibility of the initial adsorption curves. (b) Fitted values of relative rate constants of Ta_3^+ for the adsorption ($k_{(3,m)}$, solid circles) and the desorption ($k_{-(3,m+1)}$, open circles) as a function of stepwise N_2 adsorption. The gray shaded areas indicate the background noise level.

4. Cryo IR Spectroscopy and Cryo Kinetics of Dinitrogen Activation and Cleavage by Small Tantalum Cluster Cations

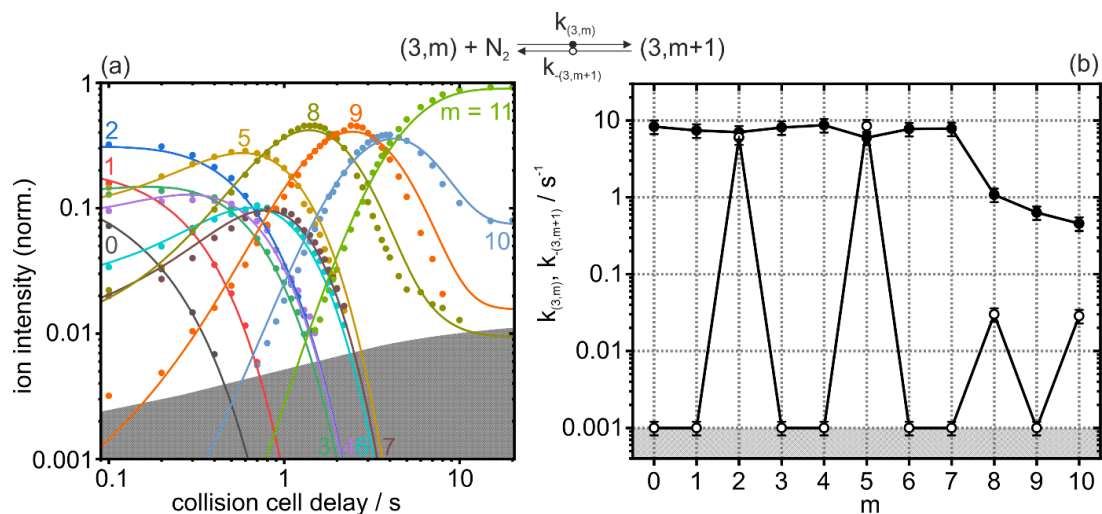


Figure S23: (a) Isothermal kinetics of N_2 adsorption by isolated Ta_3^+ clusters at 26 K, He buffer gas ($6.8 \cdot 10^{-6}$ mbar) and $2.6 \cdot 10^{-7}$ mbar N_2 pressure (variant 2). The fitting curves (solid lines) of the recorded data (solid dots) confirm pseudo-first-order kinetics for the adsorption in a reaction chain of up to 11 consecutive steps for Ta_3^+ clusters. We chose a log-log plot for better visibility of the initial adsorption curves. (b) Fitted values of relative rate constants of Ta_3^+ for the adsorption ($k_{(3,m)}$, solid circles) and the desorption ($k_{-(3,m+1)}$, open circles) as a function of stepwise N_2 adsorption. The gray shaded areas indicate the background noise level.

Table S29: Pseudo-first-order rate constants for the N₂ adsorption and desorption ($p(\text{N}_2)=2.6 \cdot 10^{-7}$ mbar) on [Ta₃(N₂)_m]⁺ clusters ($k_{(3,m)}$ and $k_{-(3,m+1)}$, variant 1, cf. Fig. S22), the related absolute rate constants ($k^{\text{abs}}_{(3,m)}$ and $k^{\text{abs}}_{-(3,m+1)}$), the calculated collision rates ($k^{\text{coll}}_{(3,m)}$) and the absolute reaction efficiency ($\gamma_{(3,m)}$). Statistical uncertainties of the relative rate constants are +/-20%, and the absolute rate constants acquire an additional uncertainty from pressure calibration of +/-50%.

m	$k_{(3,m)}$ s ⁻¹	$k_{-(3,m+1)}$ s ⁻¹	$k^{\text{abs}}_{(3,m)}$ 10 ⁻¹⁶ m ³ s ⁻¹	$k^{\text{abs}}_{-(3,m+1)}$ 10 ⁻¹⁹ m ³ s ⁻¹	$k^{\text{coll}}_{(3,m)}$ 10 ⁻¹⁶ m ³ s ⁻¹	$\gamma_{(3,m)}$
0	8.30	< 0.001	7.64	< 1.10	6.04	1.27
1	7.41	< 0.001	6.82	< 1.10	4.99	1.37
2	3.76	< 0.001	3.46	< 1.10	4.37	1.49
3	8.11	< 0.001	7.46	< 1.10	3.96	1.89
4	8.69	< 0.001	8.00	< 1.10	3.65	2.19
5	2.99	< 0.001	2.75	< 1.10	3.42	1.61
6	7.74	< 0.001	7.12	< 1.10	3.23	2.20
7	7.83	< 0.001	7.20	< 1.10	3.08	2.34
8	1.08	0.03	9.95	27.6	2.95	0.34
9	0.63	< 0.001	5.83	< 1.10	2.84	0.21
10	0.46	0.03	4.21	26.4	2.75	0.15

4. Cryo IR Spectroscopy and Cryo Kinetics of Dinitrogen Activation and Cleavage by Small Tantalum Cluster Cations

Table S30: Pseudo-first-order rate constants for the N₂ adsorption and desorption ($p(\text{N}_2)=2.6 \cdot 10^{-7}$ mbar) on [Ta₃(N₂)_m]⁺ clusters ($k_{(3,m)}$ and $k_{-(3,m+1)}$, variant 2, cf. Fig. S23), the related absolute rate constants ($k^{\text{abs}}_{(3,m)}$), the calculated collision rates ($k^{\text{coll}}_{(3,m)}$) and the absolute reaction efficiency ($\gamma_{(3,m)}$). Statistical uncertainties of the relative rate constants are +/-20%, and the absolute rate constants acquire an additional uncertainty from pressure calibration of +/-50%.

m	$k_{(3,m)}$ s ⁻¹	$k_{-(3,m+1)}$ s ⁻¹	$k^{\text{abs}}_{(3,m)}$ 10 ⁻¹⁶ m ³ s ⁻¹	$k^{\text{coll}}_{(3,m)}$ 10 ⁻¹⁶ m ³ s ⁻¹	$\gamma_{(3,m)}$
0	8.30	< 0.001	7.64	6.04	1.27
1	7.41	< 0.001	6.82	4.99	1.37
2	7.06	6.00	6.50	4.37	0.79
3	8.11	< 0.001	7.46	3.96	1.89
4	8.69	< 0.001	8.00	3.65	2.19
5	5.99	8.50	5.52	3.42	0.81
6	7.74	< 0.001	7.12	3.23	2.20
7	7.83	< 0.001	7.20	3.08	2.34
8	1.08	0.03	9.95	2.95	0.34
9	0.63	< 0.001	5.83	2.84	0.21
10	0.46	0.03	4.21	2.75	0.15

Text S9: Ta₄(N₂)_m⁺ - Cryo kinetics and rate constants

In the case of Ta₄⁺ we found stepwise N₂ adsorption up to an adsorption limit $m_{(\max)}$ of 13 N₂ molecules. On the long term equilibrium, its precursor species (4,12) becomes the most intense cluster adsorbate complex m^* . In the course of our prior published study on cryo N₂ cleavage by the Ta₄⁺ cluster we have provided some discussion of N₂ adsorption kinetics on the tantalum tetramer ⁷. We found kinetic curves and fitted rate constants of the first two N₂ adsorptions that differ from the subsequent ones: the first N₂ adsorption proceeds much faster and the second adsorption proceeds much slower than the subsequent seven adsorption steps. We analyzed these kinetic findings in combination with results from IR-PD measurements and DFT modelling and found evidence for facile N₂ activation and cleavage of the first two N₂ molecules on the Ta₄⁺ cluster. The adsorption, activation and cleavage of the first N₂ molecule by Ta₄⁺ proved to be a highly exothermic and thus fast process. As the barriers along the activation pathway of a second N₂ molecule are merely submerged the activation and cleavage process proceeds much slower than the cleavage of the prior first N₂ molecule. Subsequent to these two facile N₂ cleavages a complete NN triple bond splitting of a third N₂ molecule is kinetically hindered. All further N₂ molecules likely adsorb end-on to single Ta centers. This nicely agrees with the six similar adsorption rates $k_{(4,2)}$ to $k_{(4,7)}$ which we determined by fitting the recorded kinetics. Despite an in general quite good fit, some conceptual deviation of recorded kinetics and fit remained, namely in the cases of (4,7) to (4,11) and at intermediate reaction times. There seems to operate some mechanism beyond our simple model of stepwise N₂ adsorption/desorption to a homogeneous sample of Ta₄⁺ clusters. It seems most likely that we have to consider further species – e.g. adsorption isomers - and / or processes – such as e.g. adsorbate shell reordering, as supported and discussed at length by our accompanying IR-PD study [IRS1]. At long reaction times, beyond a collision cell delay of 8 s we reveal horizontal and parallel curves for the generation of the ultimate products (4,9) to (4,13) which indicates that these five adsorbate complexes are in a dynamic equilibrium. Our fitting supports this conclusion by significant rate constants for the desorption.

4. Cryo IR Spectroscopy and Cryo Kinetics of Dinitrogen Activation and Cleavage by Small Tantalum Cluster Cations

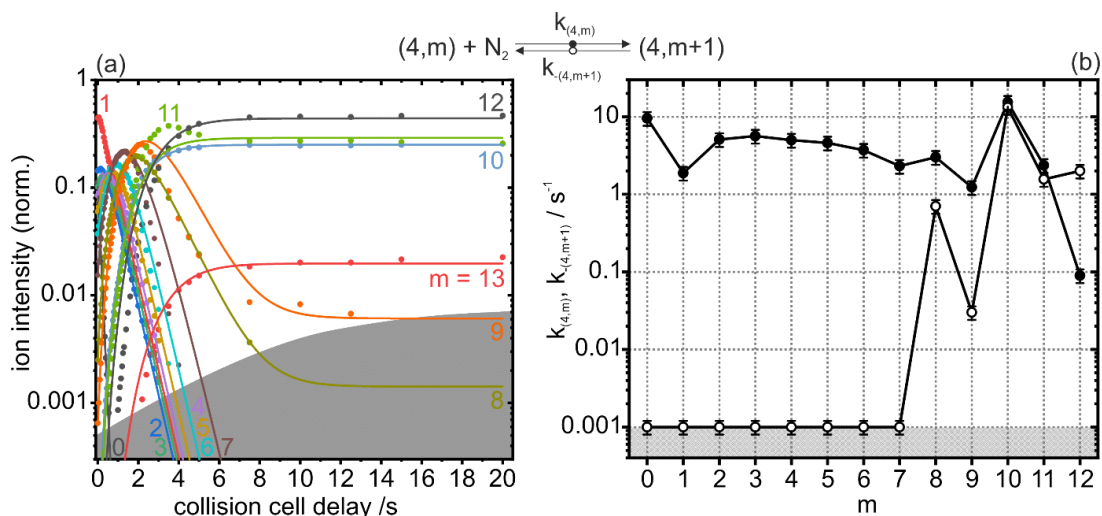


Figure S24: (a) Isothermal kinetics of N_2 adsorption by isolated Ta_4^+ clusters at 26 K, He buffer gas and $2.6 \cdot 10^{-7}$ mbar N_2 pressure. The fitting curves (solid lines) of the recorded data (solid dots) confirm pseudo-first-order kinetics for the adsorption in a reaction chain of up to 13 consecutive steps for Ta_4^+ clusters. (b) Fitted values of relative rate constants of Ta_4^+ for the adsorption ($k_{(4,m)}$, solid circles) and the desorption ($k_{-(4,m+1)}$, open circles) as a function of stepwise N_2 adsorption. The gray shaded areas indicate the background noise level. A log-log plot of (a) may be found in the our prior $\text{Ta}_4^+ + \text{N}_2$ study ⁷).

Table S31: Pseudo-first-order rate constants for the N₂ adsorption and desorption ($p(\text{N}_2)=2.6 \cdot 10^{-7}$ mbar) on $[\text{Ta}_4(\text{N}_2)_m]^+$ clusters ($k_{(4,m)}$), the related absolute rate constants ($k_{(4,m)}^{\text{abs}}$ and $k_{-(4,m+1)}^{\text{abs}}$), the calculated collision rates ($k_{(4,m)}^{\text{coll}}$) and the absolute reaction efficiency ($\gamma_{(4,m)}$). Statistical uncertainties of the relative rate constants are +/-20%, and the absolute rate constants acquire an additional uncertainty from pressure calibration of +/-50%.

m	$k_{(4,m)}$ s ⁻¹	$k_{-(4,m+1)}$ s ⁻¹	$k_{(4,m)}^{\text{abs}}$ 10 ⁻¹⁶ m ³ s ⁻¹	$k_{(4,m)}^{\text{coll}}$ 10 ⁻¹⁶ m ³ s ⁻¹	$\gamma_{(4,m)}$
0	9.58	< 0.001	8.48	6.00	1.41
1	1.88	< 0.001	1.67	4.94	0.34
2	5.10	< 0.001	4.51	4.32	1.04
3	5.65	< 0.001	5.00	3.90	1.28
4	5.01	< 0.001	4.43	6.80	0.65
5	4.60	< 0.001	4.07	3.35	1.22
6	3.72	< 0.001	3.29	3.16	1.04
7	2.31	< 0.001	2.05	3.01	0.68
8	3.02	0.70	2.67	1.16	2.30
9	1.23	0.03	1.09	2.76	0.40
10	15.4	13.3	13.7	2.67	5.12
11	2.37	1.56	2.09	2.58	0.81
12	0.09	2.00	0.08	2.51	0.03

4. Cryo IR Spectroscopy and Cryo Kinetics of Dinitrogen Activation and Cleavage by Small Tantalum Cluster Cations

References

1. A. Straßner, C. Wiehn, M. P. Klein, D. V. Fries, S. Dillinger, J. Mohrbach, M. H. Prosenc, P. B. Armentrout and G. Niedner-Schatteburg, *J. Chem. Phys.* **155** (24), 244305 (2021).
2. S. Dillinger, J. Mohrbach, J. Hower, M. Gaffga and G. Niedner-Schatteburg, *Phys. Chem. Chem. Phys.* **17** (16), 10358-10362 (2015).
3. S. Dillinger, J. Mohrbach and G. Niedner-Schatteburg, *J. Chem. Phys.* **147** (18), 184305 (2017).
4. J. Mohrbach, S. Dillinger and G. Niedner-Schatteburg, *J. Phys. Chem. C* **121** (20), 10907-10918 (2017).
5. S. Dillinger, M. P. Klein, A. Steiner, D. C. McDonald, M. A. Duncan, M. M. Kappes and G. Niedner-Schatteburg, *J. Phys. Chem. Lett.* **9** (4), 914-918 (2018).
6. M. P. Klein, A. A. Ehrhard, J. Mohrbach, S. Dillinger and G. Niedner-Schatteburg, *Top. Catal.* **61** (1), 106-118 (2018).
7. D. V. Fries, M. P. Klein, A. Steiner, M. H. Prosenc and G. Niedner-Schatteburg, *Phys. Chem. Chem. Phys.* **23** (19), 11345-11354 (2021).
8. C. Geng, J. Li, T. Weiske and H. Schwarz, *Proc. Natl. Acad. Sci.* **115** (46), 11680-11687 (2018).
9. W. M. Haynes, *CRC Handbook of Chemistry and Physics*. (CRC Press Taylor & Francis Group, 2014).
10. IEA, *Ammonia Technology Roadmap CC BY-NC 3.0 IGO*. (2021).
11. F. Schüth, *Chem. unserer Zeit* **40** (2), 92-103 (2006).
12. A. Wang, J. Li and T. Zhang, *Nat. Rev. Chem.* **2** (6), 65-81 (2018).
13. D. K. Böhme and H. Schwarz, *Angew. Chem. Int. Ed.* **44** (16), 2336-2354 (2005).
14. P. B. Armentrout, *Catal. Sci. Technol.* **4** (9), 2741-2755 (2014).
15. M. B. Knickelbein, *Annu. Rev. Phys. Chem.* **50** (1), 79-115 (1999).
16. S. J. Riley, *Ber. Bunsenges. Phys. Chem.* **96** (9), 1104-1109 (1992).
17. T. Ito, M. Arakawa, Y. Taniguchi and A. Terasaki, *Z. Phys. Chem.* **233** (6), 759-770 (2019).
18. M. S. Ford, M. L. Anderson, M. P. Barrow, D. P. Woodruff, T. Drewello, P. J. Derrick and S. R. Mackenzie, *Phys. Chem. Chem. Phys.* **7** (5), 975-980 (2005).
19. P. A. Hintz and K. M. Ervin, *J. Chem. Phys.* **100** (8), 5715-5725 (1994).

20. Y.-X. Zhao, X.-G. Zhao, Y. Yang, M. Ruan and S.-G. He, *J. Chem. Phys.* **154** (18), 180901 (2021).
21. M. R. Zakin, D. M. Cox and A. Kaldor, *J. Chem. Phys.* **89** (2), 1201-1202 (1988).
22. M. L. Anderson, M. S. Ford, P. J. Derrick, T. Drewello, D. P. Woodruff and S. R. Mackenzie, *J. Phys. Chem. A* **110** (38), 10992-11000 (2006).
23. M. D. Morse, M. E. Geusic, J. R. Heath and R. E. Smalley, *J. Chem. Phys.* **83** (5), 2293-2304 (1985).
24. W. F. Hoffman, E. K. Parks, G. C. Nieman, L. G. Pobo and S. J. Riley, *Z. Phys. D: At. Mol. Clusters* **7** (1), 83-89 (1987).
25. P. Fayet, A. Kaldor and D. M. Cox, *J. Chem. Phys.* **92** (1), 254-261 (1990).
26. I. Balteanu, U. Achatz, O. P. Balaj, B. S. Fox, M. K. Beyer and V. E. Bondybey, *Int. J. Mass spectrom.* **229** (1), 61-65 (2003).
27. P. A. Hintz and K. M. Ervin, *J. Chem. Phys.* **103** (18), 7897-7906 (1995).
28. Y. Tawarayama, S. Kudoh, K. Miyajima and F. Mafuné, *J. Phys. Chem. A* **119** (31), 8461-8468 (2015).
29. D. Neuwirth, J. F. Eckhard, B. R. Visser, M. Tschurl and U. Heiz, *Phys. Chem. Chem. Phys.* **18** (11), 8115-8119 (2016).
30. J. F. Eckhard, D. Neuwirth, C. Panosetti, H. Oberhofer, K. Reuter, M. Tschurl and U. Heiz, *Phys. Chem. Chem. Phys.* **19** (8), 5985-5993 (2017).
31. N. Levin, J. T. Margraf, J. Lengyel, K. Reuter, M. Tschurl and U. Heiz, *Phys. Chem. Chem. Phys.* **24** (4), 2623-2629 (2022).
32. B. Pfeffer, S. Jaberg and G. Niedner-Schatteburg, *J. Chem. Phys.* **131** (19) (2009).
33. J. Mohrbach, S. Dillinger and G. Niedner-Schatteburg, *J. Chem. Phys.* **147** (18), 184304 (2017).
34. A. A. Ehrhard, M. P. Klein, J. Mohrbach, S. Dillinger and G. Niedner-Schatteburg, *Mol. Phys.* **119** (17-18), e1953172 (2021).
35. A. A. Ehrhard, M. P. Klein, J. Mohrbach, S. Dillinger and G. Niedner-Schatteburg, *J. Chem. Phys.* **156** (5), 054308 (2022).
36. A. Straßner, M. P. Klein, D. V. Fries, C. Wiehn, M. E. Huber, J. Mohrbach, S. Dillinger, D. Spelsberg, P. B. Armentrout and G. Niedner-Schatteburg, *J. Chem. Phys.* **155** (24), 244306 (2021).

4. *Cryo IR Spectroscopy and Cryo Kinetics of Dinitrogen Activation and Cleavage by Small Tantalum Cluster Cations*

37. S. Peredkov, M. Neeb, W. Eberhardt, J. Meyer, M. Tombers, H. Kampschulte and G. Niedner-Schatteburg, *Phys. Rev. Lett.* **107** (23), 233401 (2011).
38. J. Meyer, M. Tombers, C. van Wüllen, G. Niedner-Schatteburg, S. Peredkov, W. Eberhardt, M. Neeb, S. Palutke, M. Martins and W. Wurth, *J. Chem. Phys.* **143** (10) (2015).
39. C. Berg, T. Schindler, G. Niedner-Schatteburg and V. E. Bondybey, *J. Chem. Phys.* **102** (12), 4870-4884 (1995).
40. V. Bondybey and J. English, *J. Chem. Phys.* **74**, 6978-6979 (1981).
41. D. Proch and T. Trickl, *Rev. Sci. Instrum.* **60** (4), 713-716 (1989).
42. P. Caravatti and M. Allemann, *Org. Mass Spectrom.* **26** (5), 514-518 (1991).
43. M. Graf, Diploma Thesis, Technische Universität Kaiserslautern, 2006.
44. T. Su and M. T. Bowers, *J. Am. Chem. Soc.* **95** (23), 7609-7610 (1973).
45. T. Su and M. T. Bowers, *J. Chem. Phys.* **58** (7), 3027-3037 (1973).
46. T. Su and M. T. Bowers, *Int. J. Mass Spectrom. Ion Phys.* **12** (4), 347-356 (1973).
47. G. Kummerlöwe and M. K. Beyer, *Int. J. Mass spectrom.* **244** (1), 84-90 (2005).
48. Dortmund Data Bank (2020).

5 CRYO-IR SPECTROSCOPY AND CRYO-KINETICS OF CLUSTER N₂ ADSORBATE COMPLEXES OF TANTALUM CLUSTER CATIONS Ta₅₋₈⁺

5.1 Preamble

The following chapter is a reprint of a publication in the journal "*The Journal of Chemical Physics*"

The experiments were performed by myself - partly together with A. Straßner, M. P. Klein and M. E. Huber. The evaluation of the measured data was carried out by myself and it was accompanied by discussions with Straßner, M. P. Klein and G. Niedner-Schatteburg. I wrote the first full paper draft of the manuscript plus supplementary information, and G. Niedner-Schatteburg and I revised it together. Subsequently, it was revised and approved by all other authors.

Full Reference

Cryo-IR Spectroscopy and Cryo-Kinetics of Cluster N₂ Adsorbate Complexes of Tantalum Cluster Cations Ta₅₋₈⁺

D. V. Fries, M. P. Klein, A. Straßner, M. E. Huber, G. Niedner-Schatteburg, *The Journal of Chemical Physics* **2023**, 159, 164306.

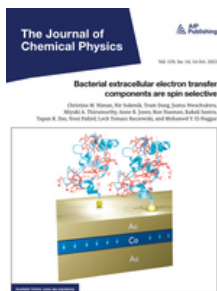
<https://doi.org/10.1063/5.0157218>

5. Cryo-IR Spectroscopy and Cryo-Kinetics of Cluster N_2 Adsorbate Complexes of Tantalum Cluster Cations Ta_{5-8}^+

5.2 Reprint

Reprint permission

Reproduced with permission of AIP Publishing.



Cryo-IR spectroscopy and cryo-kinetics of cluster N_2 adsorbate complexes of tantalum cluster cations Ta_{5-8}

Author: Fries, Daniela V.; Klein, Matthias P.

Publication: Journal of Chemical Physics

Publisher: AIP Publishing

Date: Oct 25, 2023

Rights managed by AIP Publishing.

Creative Commons

This is an open access article distributed under the terms of the [Creative Commons CC BY](https://creativecommons.org/licenses/by/4.0/) license, which permits unrestricted use, distribution, and reproduction in any medium, provided the original work is properly cited.

You are not required to obtain permission to reuse this article.

Cryo-IR spectroscopy and cryo-kinetics of cluster N₂ adsorbate complexes of tantalum cluster cations Ta₅₋₈⁺

Cite as: J. Chem. Phys. 159, 164306 (2023); doi: 10.1063/5.0157218

Submitted: 5 May 2023 • Accepted: 12 September 2023 •

Published Online: 25 October 2023



Daniela V. Fries,¹ Matthias P. Klein,¹ Annika Straßner,¹ Maximilian E. Huber,¹ and Gereon Niedner-Schatteburg¹

AFFILIATIONS

Department of Chemistry and State Research Center OPTIMAS, Rheinland-Pfälzische Technische Universität (RPTU) Kaiserslautern-Landau, 67663 Kaiserslautern, Germany

¹Author to whom correspondence should be addressed: gns@rptu.de

ABSTRACT

We present an IR-PD study of tantalum cluster adsorbate complexes [Ta_n(N₂)_m]⁺, abbreviated (n,m), n = 5–8. We utilize infrared spectroscopy of isolated and size selected clusters as prepared and characterized by a cryogenic tandem ion trap setup, and we augment our experiments with quantum chemical simulations at the level of density functional theory. The cluster adsorbate complexes (n,m) reveal vibrational bands above 2000 cm⁻¹, which indicate end-on coordinated μ₁-N₂ oscillators, and bands below 2000 cm⁻¹, which indicate side-on μ₂-κN:κN,N coordinated ones. We observe a general increase in spectral complexity and an inhomogeneous broadening, mainly towards the red, at certain points of N₂ loading m, which originates from an increasingly higher amount of double and triple N₂ coordination at Ta sites, eventually at all of them. Other than the small tantalum clusters Ta_n⁺, n = 2–4, the IR-PD spectra of the initial N₂ adsorbate species (n,1), n = 5–8, provide strong evidence for a lack of spontaneous N₂ cleavage. Spontaneous N₂ cleavage by Ta_n⁺, n = 5–8, seems suppressed. Therefore, the ability of a small Ta cluster to cleave dinitrogen disappears with one more tantalum core atom. The study of stepwise N₂ adsorption on size selected Ta_n⁺, n = 5–8 clusters revealed adsorption limits m_(max) of [Ta_n(N₂)_m]⁺ that are independent of cluster size within this size range. Cryo-adsorption kinetics at 26 K allowed for kinetic fits to consecutive N₂ adsorption steps, and the fits revealed significant N₂ desorption rates upon higher N₂ loads, and the cluster adsorbate complexes eventually reached equilibrium. Some enhanced N₂ desorption rates point towards likely adsorbate shell reorganization, and there is also some evidence for the coexistence of isomeric cluster adsorbate complexes.

© 2023 Author(s). All article content, except where otherwise noted, is licensed under a Creative Commons Attribution (CC BY) license (<http://creativecommons.org/licenses/by/4.0/>). <https://doi.org/10.1063/5.0157218>

INTRODUCTION

The application of transition metals (TM) in heterogeneous catalysis is the basis for numerous industrial processes.^{2–7} Mechanistic understanding of the catalytic reactions was early on postulated to take place at so-called active sites⁸ that are part of the solid surface of a catalyst, which is most often less characterized when *in operando*. Transition metal clusters serve as model systems for these active sites in order to provide insights into elemental catalytic processes at the molecular level.^{9–15} All of this research elucidates cluster size effects on their structure and on their reactivity.

In particular, there are numerous studies that demonstrate the interaction and reactivity of tantalum clusters and their alloys,

carbides and chalcogenides, with small molecules such as N₂,^{1,16–23} CH₄,^{17,24–26} CO₂,²⁷ and O₂.²⁸ Interaction, leading towards adsorption, is understood to yield adsorbates on the cluster surfaces. The cluster adsorbate complexes may act as precursor states for the activation and bond cleavage of these adsorbates. The issue of N≡N bond cleavage, for example, plays a role in the ongoing research efforts to develop an energetically optimized protocol, e.g., for Haber–Bosch NH₃ production, a catalytic process of paramount significance to mankind on this planet and beyond.^{29,30}

N₂ activation has also been observed to proceed by small clusters of Co and Rh when assisted by surface plasma radiation,^{31,32} and bare TM clusters of V, Gd, and Sc,^{33–35} and homo- and heterometallic cluster carbides, with some subsequent C–N bond

5. Cryo-IR Spectroscopy and Cryo-Kinetics of Cluster N₂ Adsorbate Complexes of Tantalum Cluster Cations Ta₅₋₈⁺

formation,^{16,17,36,37} and ultimately through lithiated TM complexes.³⁸

Size effects, an intrinsic propriety of clusters, prevail in tantalum clusters as well. The governing thermochemistry drives tantalum cluster cations of six atoms and less to reduce CO₂ to CO, while larger ones form adducts.²⁷ There are further size effects in the oxidation of such tantalum cluster cations, with the Ta₈⁺ cluster cation sticking out by its oxidative cleavage towards Ta₄O₄⁺.²⁸ Furthermore, size effects arise from small tantalum clusters (n = 1–4) dehydrogenating CH₄ and concurrently eliminating H₂, yielding the product of the stoichiometry [Ta_nC₂H]⁺, while larger clusters (n = 5–10) enable mere molecular adsorption.²⁶ While the bare Ta₅⁺ cluster is inert towards CH₄, its monoxide, Ta₅O⁺, activates CH₄.²⁴

The elucidation of such size effects asks for a structural characterization of participating species that may arise through spectroscopic experiments, which elucidate characteristic vibrations of, e.g., cluster adsorbate complexes and eventual reaction products.

Historically, inelastic electron scattering off N₂ layered surfaces has proved valuable, but it has suffered from limited spectral resolution.^{39,40} The technical advancement of infrared photon dissociation (IR-PD) spectroscopy by either free electron lasers (FEL) or Optical Parametric Oscillator (OPO) technology has helped to identify characteristic vibrational bands, in particular when applied to isolated clusters and their complexes, and thereby achieve sufficient spectral resolution (as low as ±5 cm⁻¹),^{41–44} and this method is widely applicable and well established by now.^{45–54}

In any case, it is mandatory to augment recorded vibrational spectra with quantum chemical modeling by density functional theory (DFT) methods in order to enable sound structural and dynamic interpretation. A successful example of such an approach is, e.g., the subsequent elucidation of the afore-mentioned tantalum product complex [4Ta₄C₂H]⁺²⁴ by IR-MPD spectroscopy and first principles quantum calculations, which identified a dihydride carbide formation, H₂Ta₄C⁺, and ruled out any other CH bond containing species.²⁵ Another study complements experimental results from vibrational spectra and theoretical modeling of bare Ta_n⁺ clusters, n = 6–20, and it managed to identify cluster geometries, their relative stabilities, and electronic properties.^{55,56} An early study on the chemisorption properties of small tantalum clusters has revealed an oxygen adatom effect on the N₂ uptake rate.¹⁸ Several studies including DFT modeling of small tantalum clusters provide strong evidence for dissociative N₂ adsorption.^{19–23,57} A 2022 perspective summarizes recent progress in the field of nitrogen activation by TM species in the gas phase, and it shows that a systematic understanding of cluster reactivity towards N₂ is lacking to date.⁵⁸

With this work, we build on our earlier study of Ta₄⁺ and complement it with a study of cationic clusters of n = 5–8 tantalum atoms. We reacted the bare clusters with N₂ at 26 K and recorded IR-PD spectra of the adsorption species [Ta_n(N₂)_m]⁺, similar to our earlier studies on Ni_n⁺, Rh_n⁺, Rh_iFe_j⁺, and Fe_n⁺ clusters.^{59–64} In the adjoined IR-PD study [IRS1], we discuss the N₂ adsorption onto the three small clusters Ta₂₋₄⁺. In our current study [IRS2], we actually present findings for the N₂ adsorption onto the cluster sizes Ta₅₋₈⁺. The findings of both studies, which we refer to in the following as [IRS1] and [IRS2], respectively, find strong support through our complementary cryogenic kinetic study (cf., supplementary material). The combination of IR-PD measurements and DFT modeling with kinetic studies provides insights into

the structures of the N₂ adsorbate species (5,m), (6,m), (7,m), and (8,m). We gain insight into the coordination motifs of the N₂ ligands and find strong size effects, especially in terms of the first few adsorbates. We clarify and extend the overall picture and provide a systematic study of N₂ adsorption on small tantalum clusters Ta_n⁺, n = 2–8. While we find complete cleavage of the N₂ triple bond of the very first adsorbed N₂ molecule on Ta₂⁺, Ta₃⁺, and Ta₄⁺, the present study provides strong evidence for a lack of cleavage for clusters from Ta₅⁺ on and beyond. Instead, adsorption of the first N₂ molecule occurs in end-on orientation to the cluster core exclusively.

EXPERIMENTAL AND COMPUTATIONAL METHODS

It is a tandem cryo-ion trap instrument that serves as a platform for all of the experiments conducted. It consists of a customized Fourier transform ion cyclotron resonance (FT-ICR) mass spectrometer (Apex Ultra, Bruker Daltonics) that encompasses cluster ion generation, size selection, N₂ coordination, cluster adsorbate complex selection, and eventually infrared photon dissociation (IR-PD) spectroscopy of the respective cluster adsorption species. Note that this protocol comprises an MS³ procedure. Detailed descriptions of the ion generation and adsorption processes of the metal clusters can be found elsewhere^{1,59,60,64–67} and also in the supplementary material, where we present and discuss adjoined kinetic studies.

Briefly, we trap the cluster ions in an RF hexapole ion trap using the routine described in Text S3 in the supplementary material and guide the thus generated cluster N₂ adsorbate complexes into the cryogenic (~10 K) FT-ICR cell. For recording IR-PD spectra, we trap and select each cluster adsorbate species of interest in the IRC cell and irradiate each isolated ion packet by a tunable IR laser system with 7–10 laser pulses with an energy of 0.5–3.0 mJ each. These IR photon pulses stem from a pulsed injection seeded Nd:YAG laser (10 Hz, PL8000, Continuum), which pumps a KTP/KTA optical parametric oscillator/amplifier (OPO/OPA, LaserVision). An AgGaSe₂ crystal generates the difference frequency (DF) of the OPA's signal and the idler waves, whereby we generate the applied IR irradiation in the range of 1100 and 2400 cm⁻¹. Absolute values of the DFM frequencies were derived from the online monitored OPO signal frequencies (continuous online wavemeter monitoring, Bristol Instruments, 8721B-NIR) and the pre-recorded value of the Nd:YAG frequency. Fragmentation mass spectra are recorded during continuous scans of the IR wavelength, and the recorded IR-PD signal transforms into a fragmentation efficiency via evaluation of $\frac{\sum_i F_i}{\sum_i F_i + \sum_i P_i}$, where F_i and P_i are fragment and parent ion intensities. The plotted fragmentation efficiency as a function of laser frequency finally yields the IR-PD spectrum. In all cases, single or multiple N₂ losses were the only observed fragmentation channels.

Quantum chemical modeling by Density Functional Theory (DFT) served to obtain optimized cluster (adsorbate) geometries and vibrational eigenmodes, as achieved by the program packages Gaussian 09 and 16.^{68,69} We employed the hybrid functional PBE0^{70,71} along with the Def2-TZVP basis set^{72,73} for all atoms in (5,0) cases, the Def2-TZVP basis set⁷² for N atoms, and the cc-pVTZ-pp basis set⁷⁴ for Ta atoms in all (6,m) and (7,m) cases. We did so in continuity with prior studies that have succeeded to model N₂

adsorption before^{60,61,64,66,67}—particularly for the adsorption, activation, and cleavage of N₂ on Ta₄⁺ clusters.¹ We tolerated relaxed SCF convergence criteria of 10⁻⁶ (as compared to 10⁻⁸ in “standard” DFT calculations) in order to achieve swift SCF convergence. The vibrational eigenmode spectra of all optimized geometries were inspected for the absence of any imaginary frequency. We applied optimized scaling factors of 0.9586 and 0.9512 for (6,m) and (7,m), respectively, for the cluster sizes to account for the prevailing anharmonicities, documenting unscaled IR frequencies in the supplementary material. We arrive at theoretical IR absorption spectra by convolution of the predicted and scaled IR frequencies with a Gaussian profile of FWHM = 5 cm⁻¹. Natural Population Analysis (NPA) was performed via the NBO 5.9 option as implemented in Gaussian 09.⁷⁵

RESULTS AND DISCUSSION

The current IR-PD spectroscopic study of the N₂ adsorbates of Ta_n⁺ clusters, n = 5–8, was conducted under adiabatic conditions, and it is complemented by some N₂ adsorption kinetics studies (cf. supplementary material). Here, we extend and complete our IR-PD study on the small cluster adsorbates (n,m), n = 2–4, as discussed in the adjoined infrared study [IRS1]. Once more, we recorded IR-PD patterns that vary remarkably by the size of the Ta_n⁺ clusters, n, which in turn vary by the amount of N₂ adsorbate, m. In keeping with the adjoint study [IRS1], we arrange the studied cluster adsorbates in a (n,m) matrix and discuss the respective IR-PD spectra of each cluster size n in separate chapters.

The adsorbed N₂ chromophores in each of the cluster adsorbate complexes possess vibrational bands, which we record as IR-PD features. Therefore, for all cluster adsorbate complexes (n,m) studied, we observe a specific and individual variation of IR-PD features as a function of the tantalum cluster size n and the nitrogen adsorbate loading m. In all cases, the recorded N₂ fingerprint features range from 2000 to 2350 cm⁻¹, and they most likely correspond to end-on N₂ adsorbates that coordinate in a μ₁ fashion to individual tantalum centers, with little to no interaction with other neighboring tantalum centers. This interpretation is in line with previously reported cases for Fe_n⁺,⁶⁴ Co_n⁺,⁶⁵ Ni_n⁺,^{59,60} Ru_n⁺,⁶⁶ Rh_n⁺,⁶⁷ and even Ta₄⁺.¹ In addition to these end-on bands, there are some cases where we observe IR-PD bands in the range of 1300–1700 cm⁻¹, which indicate the most likely presence of a side-on μ₂-κN:κN₂ N₂ ligand within the respective cluster adsorbate complex. This conclusion follows from the results of our previous study of N₂ on a Ta₄⁺ cluster.¹

[Ta₅(N₂)_m]⁺

We recorded IR-PD spectra of all cluster adsorbate complexes from (5,1) up to (5,13) (Fig. 1). We observe bands in the end-on N₂ stretching range at 2000–2300 cm⁻¹ for all investigated cluster adsorbate complexes, while there are little and weak IR-PD bands in the side-on N₂ range below 2000 cm⁻¹. There are IR-PD signals in the end-on N₂ stretching range at all levels of N₂ adsorption, m = 1–13. There is no indication for N₂ activation and nitride formation whatsoever. While Nitride formation would be highly exothermic (cf. Table S3 in the supplementary material), the recorded IR-PD signatures signify intact N₂ adsorbates, and it seems to prevail an extensive kinetic hindrance by unsurmountable barriers. If activated

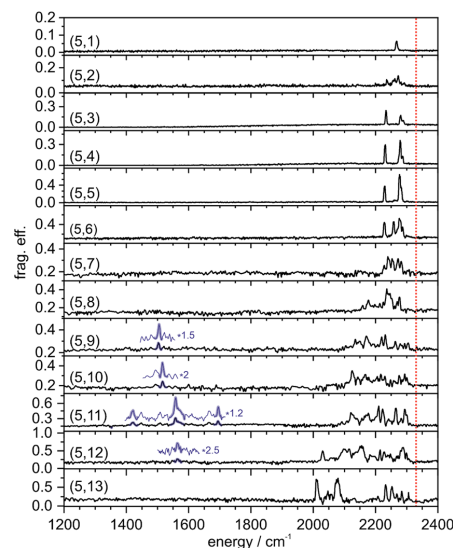


FIG. 1. IR-PD spectra of sequentially increasing cluster N₂ adsorbate complexes [Ta₅(N₂)_m]⁺, m = 1–13, as recorded after prior 26 K He buffer gas cooling. Note the significant red-shift of the IR-PD bands with respect to the free N₂ stretching vibrational frequency (2330 cm⁻¹,⁷⁶ red dotted line).

nitrides form at all, they seem to be minor and leave no fingerprint. Instead of N₂ cleavage, we find a manifold of bands that persist at any level of N₂ adsorption and shift slightly to the red with increasing N₂ adsorption. In parallel, at (5,8) and beyond, we observe some broad and some sharp bands appearing to the red and spreading out to almost 2000 cm⁻¹. It seems appropriate to account for the observed redshifts with respect to the free N₂ stretching vibration at 2330 cm⁻¹ in terms of a σ-donor and π-acceptor synergism as before. Up to species (5,8), we found no evidence of a N₂ stretching vibrational band in the side-on range. For species (5,9) to (5,12), the IR-PD spectra indicate the presence of some weak adsorptions in the range between 1400 and 1700 cm⁻¹. In the following, we will briefly discuss the recorded IR-PD spectra (5,m) and some of their IR-PD bands in some more detail.

For single N₂ adsorption m = 1, (5,1), we found a sharp single band at 2268 cm⁻¹, which is red-shifted by 62 cm⁻¹ with respect to the free N₂ stretching vibration at 2330 cm⁻¹.⁷⁶ The (5,2) spectrum shows a more complex IR-PD band pattern, and we identify bands at 2236, 2257, 2262, and 2273 cm⁻¹. Instead of merely two bands, e.g., from a single isomer with two end-on coordinated N₂ molecules, we observe a manifold of at least four weak bands between 2200 and 2300 cm⁻¹ and thus conclude on some co-existing isomers with comparable stabilization energies. The recorded IR-PD spectra of the species (5,3), (5,4), and (5,5) reveal no significant changes, and we observe three bands: An intense single band shifts slightly to the red from 2234, (5,3), to 2229 cm⁻¹, (5,5); another intense band shifts to the red from 2281, (5,3) to 2277 cm⁻¹, (5,5). Finally, there is

5. Cryo-IR Spectroscopy and Cryo-Kinetics of Cluster N_2 Adsorbate Complexes of Tantalum Cluster Cations Ta_{5-8}^+

another weak band at 2289 cm^{-1} (5,3) that shifts less with increasing m and thus merges into a mere shoulder of the second band in the IR-PD spectrum (5,5) (2282 cm^{-1}). The slight redshift of the measured IR-PD bands with m cross-references to our prior studies on the N_2 adsorption to other transition metal clusters such as Fe_n^{+64} and Ni_n^{+59} . In both cases, we found similar effects, and we took them as an indication of rough cluster surfaces. The adsorption of one and two more N_2 molecules onto the formal monolayer at (5,5) yields a more complicated IR-PD band pattern for species (5,6)—and even more so for (5,7). The prior (5,5) IR-PD spectrum is augmented by one more band at 2259 cm^{-1} in (5,6) and another band on top at 2240 cm^{-1} in (5,7). The spectral broadening continues through the adsorption of the eighth N_2 molecule, and the recorded IR-PD bands for (5,8) stretch out across a significantly wider range, from 2150 to 2300 cm^{-1} . Nevertheless, we identify some partially resolved maxima at 2159 , 2177 , 2214 , 2225 , 2236 , 2241 , 2246 , 2252 , 2269 , and 2277 cm^{-1} . The new, most red-shifted bands might arise either from a variation of Ta center next neighbor coordination or from a triple end-on N_2 occupation at a single Ta center. The IR-PD spectra of (5,9), (5,10), and (5,11) largely resemble that of (5,8), and we observe broad IR-PD patterns spread out across 2130 – 2310 cm^{-1} , with some IR-PD bands partially resolved. The observed excess of IR-PD bands over present N_2 oscillators clearly indicates co-existing isomers, which likely differ in the very structure of the N_2 adsorbate shell or less likely differ in some parameters of the relaxed cluster core. In contrast to the prior IR-PD spectra, the spectra of the three species (5,9), (5,10), and (5,11) reveal a weak IR-PD band at 1504 , 1516 , and 1558 cm^{-1} , respectively, which indicates the most likely presence of a side-on μ_2 - $\kappa N:\kappa N,N$ N_2 ligand. In addition, (5,11) reveals two more bands at 1422 and 1694 cm^{-1} that indicate further side-on N_2 coordination at other sites and with varying coordination parameters such as, e.g., the tilting angle. The IR-PD spectra of species (5,12) and (5,13) reveal another increase in the maximum of redshifts and an eventual gain in spectral structure and reduction of broadening. In (5,13), the end-on coordinated N_2 ligands seems to separate into two classes, as indicated by high and low redshifted bands at 2010 – 2080 cm^{-1} and 2208 – 2306 cm^{-1} , with less to no options in between other than before. A side-on μ_2 - $\kappa N:\kappa N,N$ N_2 indicating band of (5,12) at 1563 cm^{-1} continues the trend of such bands in (5,9) – (5,12), and it terminates this series, as (5,13) does not reveal any such or similar IR-PD signal. It seems as if at this point the shell of N_2 adsorbates has become so sterically crowded that a two Ta center coordinating N_2 tilt is not possible anymore. Instead, the lack of wagging space leads to an increase in stiffness in this N_2 adsorbate shell, which might manifest in a highly structured and well-resolved IR-PD spectrum of (5,13).

In summary, we found numerous IR-PD bands in the IR-PD spectra of species (5, m), $m = 1$ – 13 , which are located mainly in the end-on coordinated N_2 stretching range of 2000 – 2310 cm^{-1} . Some of these species ($m = 9$ – 12) indicate weak IR-PD signals below 2000 cm^{-1} , which we assign to side-on μ_2 - $\kappa N:\kappa N,N$ N_2 ligands. Starting with a few single and distinguishable end-on N_2 bands of the less occupied species (5, m), m small, we observe with increasing m an overall increase of spectral complexity and an asymmetric broadening, largely towards the red. Finally, the spectrum of (5,13) reveals some sharp bands. While intermediate N_2 loads (moderate m values) allow for much spectral complexity and likely isomerism, the highly loaded species with much of a filled N_2 shell exhibit reduced spectral

complexity and less isomerism. This indicates the onset of orientational stiffness and a less wagging disorder. Side-on μ_2 - $\kappa N:\kappa N,N$ N_2 coordination seems to die out.

Other than the smaller tantalum clusters Ta_n^+ , $n = 2$ – 4 (cf. Fries *et al.*¹ and the adjoined study [IRS1]), the (5, m) spectra provide strong evidence for a lack of any spontaneous N_2 cleavage. Note that we found IR-PD fingerprints of end-on bound N_2 molecules on otherwise bare Ta_5^+ clusters and a lack of side-on μ_2 - $\kappa N:\kappa N,N$ N_2 fingerprints. It appears as if an enhanced entrance channel barrier prevents spontaneous tilting and further activation. It takes further N_2 adsorption to find some weak side-on μ_2 - $\kappa N:\kappa N,N$ N_2 fingerprints. Spontaneous N_2 cleavage by Ta_5^+ seems suppressed.

In order to investigate the effects of stepwise N_2 adsorption on the cluster structure and possible spin relaxations in the course of adsorption, we optimized the Ta_5^+ cluster core together with the adsorbate shell of (5, m) in the cases of $m = 0, 1, 2, 5, 10$ comprising end-on N_2 ligands. For each m , we started with several conceivable adsorption shell isomers, which adsorb N_2 onto a reasonable trigonal bipyramid (tbp) cluster framework. We obtained fully converged structures for singlet to nonet multiplicities in most cases (Fig. 2). Vertical offsets of the (5, m) curves depict N_2 adsorption and desorption energies—each of these curves resembling the spin valley⁶¹ of a single (5, m) complex. We find triplet and singlet isomers most stable in all cases and sometimes almost degenerate.

The bare Ta_5^+ cluster finds itself most stable in a triplet trigonal bipyramidal (tbp) minimum structure³tbp, independent of starting geometries. Two apical Ta atoms coordinate three next neighbors each, and the three equatorial Ta atoms coordinate four next neighbors each. This most stable isomer is close to D_{3h} symmetry. The singlet electromer is slightly less stable, by a mere 14 kJ/mol . Higher multiplicities are more expensive by at least 90 kJ/mol and much

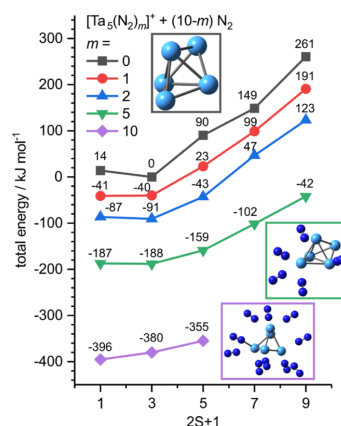


FIG. 2. Total energies of computed $[Ta_5(N_2)_m]^+$ cluster adsorbate complexes (5, m) as a function of the spin multiplicity $2S + 1$, and normalized to the most stable (5,0) spin isomer (trigonal bipyramid, 3tbp, triplet). The calculated minimum structures for (5,0), (5,5), and (5,10) are shown as insets; the geometries of other multiplicities may differ slightly.

beyond. Through single N_2 adsorption, singlet and triplet multiplicities become degenerate. This degeneracy persists throughout further N_2 adsorption, up to $m = 5$. Note that high multiplicities seem to stabilize as well, and the spin valleys become more shallow. The energy difference between each curve's minimum and the quintet state decreases from 63 kJ/mol ($m = 1$) over 48 kJ/mol ($m = 2$) to 29 kJ/mol ($m = 5$).

The most stable (5,5) cluster adsorbate complex has its N_2 adsorbate shell concentrating on one side of the tbp cluster core: two of the equatorial Ta atoms are singly occupied, and one of the two apical Ta atoms has adsorbed three N_2 molecules. Upon adsorption of ten N_2 molecules, yielding the most stable (5,10) cluster adsorbate complex, the tbp cluster core has received some significant distortion towards an oblate geometry. Two opposite (apical) Ta atoms adsorb only a single N_2 molecule. Two other Ta atoms adsorb a triplet of N_2 molecules each. In (5,10), the singlet state is favored over the triplet state by 16 kJ/mol. We thus assume that adsorption-induced spin quenching could occur at high N_2 coverage, $m \geq 5$.

We extract adsorption energies from the spin valley curves by evaluating their offsets, which yield both vertical (spin conserving) and adiabatic (including relaxation of the spin state) adsorption energies (cf. Fig. S2 and Table S2). In most cases, the vertical and adiabatic energies are very similar, as singlet and triplet states are close to degenerate. The adsorption energies increase from about -40 kJ/mol ($m = 0$) to about -50 kJ/mol ($m = 1$), irrespective of multiplicity. From $m = 2$ to $m = 4$, we interpolate values of about -32.4 kJ/mol per N_2 adsorbate. From $m = 5$ to $m = 9$, we interpolate adiabatic adsorption energies of -41.5 kJ/mol per N_2 , which are slightly larger than the vertical ones (-38.4 kJ/mol per N_2).

Through natural population analysis (NPA), we obtained more information on the charge and spin distributions of some selected clusters and on the influence of the first N_2 adsorption.

The NPA of the most stable (5,0) ${}^3\text{tbp}$ isomer reveals a concentration of the positive charge on the equatorial Ta atoms (Fig. S4). The two apical Ta atoms possess less positive charge density and more spin density than the three equatorial ones. A spin density of ~ 1 at each of the two apical Ta atoms indicates the localization of a single unpaired electron at each of them.

All of the three considered (5,1) isomers a, b, and c (Fig. S5) are tbp type structures, and they are equally stable (within the uncertainty of the DFT modeling, about 4 kJ/mol), with all other structures being less stable by +18 kJ/mol and beyond. The isomers a, b, and c reveal minor changes in singlet or triplet spin preference and in the predicted orientation of the end-on coordinated N_2 adsorbate. In effect, isomers a and b find themselves in close proximity to C_5 symmetry, whereas c possesses C_{2v} symmetry. Their computed linear absorption spectra are depicted in the supplementary material, Fig. S3. Application of the successfully applied scaling factor of our prior Ta_4^+ study (see the adjoined study [IRS1]) 0.9736 finds isomer b interpreting the recorded IR-PD spectrum well, isomer a less likely, while isomer c may be ruled out. These assumptions find nice correspondence in the spin valley prediction— ${}^1(5,1)$ is slightly less stable than ${}^3(5,1)$ —and in structural motifs of N_2 coordination to TM centers such as Rh and Ta, where we found a preferred “90° to surface normal” N_2 coordination that persists for many species along the adsorption chain.^{1,77}

As in the naked (5,0) Ta cluster, the (5,1) N_2 adsorbate complex locates a large fraction of positive charge on the three equatorial Ta

atoms and the majority of electron density in triplet states at the two apical Ta atoms. Note that the N_2 molecule prefers to adsorb onto either of the three equatorial Ta atoms, which serve as better electron acceptors than the two apical ones.

In the case of the triplet isomers b and c, both apical Ta atoms comprise an unpaired electron each, and their charge density is reduced with respect to the singlet isomer a by $0.04e$ per Ta atom. Upon adsorption, the N_2 molecule is polarized ($\Delta q < 0.29e$) but obtains little net charge and little net spin density. The electron population of the adsorbing Ta atom strongly depends on the isomer (spin and mainly angle), in particular if compared with the other equatorial Ta atoms: it varies between $0.255e$, b, and $0.174e$, c. In the singlet isomer a, the adsorbing Ta atom is the most positive equatorial atom with a charge density of $0.255e$. The charge density of the adsorbing Ta atom in triplet isomer b is in between the other equatorial atoms $0.219e < 0.259e < 0.279e$. In the highly symmetric triplet isomer c, the adsorbing isomer comprises the least charge density of the equatorial Ta atoms ($0.174e < 0.26e$).

In summary, the observed weak IR-PD bands below 2000 cm^{-1} of several species (5,m), $m \geq 9$, indicate isomers that might contain a side-on coordinated $\mu_2\text{-}\kappa\text{N}:\kappa\text{N}:\text{N}$ N_2 ligand. However, the measured IR-PD spectra for the adsorbate species (5,m) provide no evidence for N_2 cleavage. We found IR-PD bands of end-on-bound N_2 molecules to single Ta centers for all species along the adsorption chain. It is remarkable, that the addition of a single metal atom to the Ta_4^+ cluster framework eliminates the ability of the cluster to cleave N_2 molecules.

We speculate that the adsorption of a single N_2 molecule induces little change in the electron distribution within the Ta_5^+ cluster core, likely the computed isomer b, and it has almost no effect on the spin density distribution. These effects are specific for each coordination isomer of the (5,1) complex, and they depend strongly on the orientation of the adsorbed N_2 molecule. It remains to elucidate how this changes along the further N_2 adsorption chain.

$[\text{Ta}_6(\text{N}_2)_m]^+$

Next, we inspect in detail the IR-PD spectra of the tantalum cluster adsorbate species $\text{Ta}_6(\text{N}_2)_m^+$: (6,m), $m = 1\text{--}15$. We took IR-PD spectra for (6,m) in the $1200\text{--}2400\text{ cm}^{-1}$ range (cf. Fig. 3), as we did before for smaller tantalum clusters. That is, we analyzed each adsorbate species for IR-PD vibration bands in the end-on region above 2000 cm^{-1} and in the side-on region below 2000 cm^{-1} . The recorded IR-PD spectra reveal an end-on N_2 fingerprinting fragmentation signal in all investigated cases (6,m) up to $m = 15$ —even for the very first N_2 adsorbate species (6,1). All of these bands are shifted to the red with respect to the stretching frequency of free N_2 at 2330 cm^{-1} ,⁷⁶ but by varying amounts. All of these shifts originate from an interplay of σ -donor and π -acceptor interactions at work, and in a cluster size modulated manner.

In the following, we briefly discuss the recorded IR-PD spectra (6,m) (cf. Fig. 3) and the obtained characteristic bands separately. The IR-PD spectrum of (6,1) reveals merely a single weak IR-PD induced fragmentation at 2293 cm^{-1} . The presence of this IR-PD band reveals strong evidence for a lack of N_2 cleavage on the Ta_6^+ cluster. This is well in line with the observed lack of N_2 cleavage by

5. Cryo-IR Spectroscopy and Cryo-Kinetics of Cluster N_2 Adsorbate Complexes of Tantalum Cluster Cations Ta_{5-8}^+

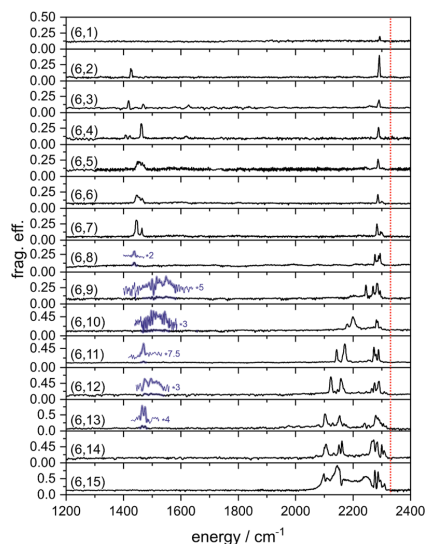


FIG. 3. IR-PD spectra of sequentially increasing cluster N_2 adsorbate complexes $[Ta_6(N_2)_m]^+$, $m = 1-15$, as recorded after prior 26 K He buffer gas cooling. Note the significant red-shift of the IR-PD bands with respect to the free N_2 stretching vibrational frequency (2330 cm^{-1} , red dotted line).

Ta_5^+ , which makes for a trend: the N_2 cleavage ability of small tantalum clusters vanishes upon an increase in cluster size. Finally, there is no IR-PD evidence for tilted N_2 side coordination in (6,1).

The IR-PD spectrum of (6,2) reveals a single band at 1425 cm^{-1} and another one at 2292 cm^{-1} . The former one is in accordance with similar bands of smaller tantalum clusters, which we assigned to N_2 molecules acting as $\mu_2\text{-}\kappa\text{N}:\kappa\text{N},\text{N}$ ligands that bind side-on across a Ta-Ta edge of the cluster cores. Our DFT calculations will confirm this interpretation, the presence of a single side-on N_2 ligand in the (6,2) complex (cf. below). The other IR-PD band of (6,2), above 2000 cm^{-1} , corresponds to a like band in (6,1), and we assign it to the N_2 stretching vibration of the other N_2 adsorbate, which binds end-on to single tantalum centers.

The IR-PD spectrum of (6,3) reveals evidence for the onset of co-existing adsorption isomers: There are three IR-PD bands in the side-on range, at 1416 , 1468 , and 1625 cm^{-1} , and a strong band in the end-on range, at 2289 cm^{-1} , with an additional weak and broad IR-PD induced adsorption at 2255 cm^{-1} . Therefore, the number of IR-PD bands (6,3) exceeds the amount of adsorbed N_2 molecules. We interpret this necessarily as strong evidence for the co-existence of adsorbate isomers in a cluster adsorbate complex with a persistent Ta_6^+ cluster core framework. This would be similar to our findings for N_2 adsorbate complexes of the Ta_4^+ (cf. [IRS1]) and Ta_5^+ clusters. The IR-PD spectrum reveals a wide spread of IR-PD bands in the side-on range, from 1400 to 1650 cm^{-1} . This reminds us of the Ta_4^+ case in our adjoined study [IRS1], where we assigned some observed bands with a diminished redshift to N_2 complexes with a

smaller tilt of the side-on $\mu_2\text{-}\kappa\text{N}:\kappa\text{N},\text{N}$ N_2 ligand. Therefore, we speculate on multiple isomers, each of which contains a single side-on $\mu_2\text{-}\kappa\text{N}:\kappa\text{N},\text{N}$ N_2 ligand across an edge of the cluster core and which likely differ slightly in the degree of tilting. However, co-existing isomers that contain two of these side-on $\mu_2\text{-}\kappa\text{N}:\kappa\text{N},\text{N}$ N_2 ligands are conceivable as well. The subsequent DFT calculations will help to clarify.

We observe five distinguishable IR-PD bands for species (6,4): four of them are located in the side-on range at 1406 , 1423 , 1462 , and 1620 cm^{-1} (weak), and a single one is located at 2289 cm^{-1} in the end-on range. Note that the integrated IR-PD signals of the side-on region (below 2000 cm^{-1}) exceed those of the end-on region for all cluster adsorbate species with N_2 loads as in (6,8) and beyond.

The IR-PD spectrum of (6,5) comes somewhat as a surprise: it reveals merely two bands, one of which is significantly broadened, around 1448 cm^{-1} , and the other is a sharp IR band at 2287 cm^{-1} , the latter one known as an end-on coordinated N_2 ligand, as observed in all spectra of less loaded clusters. There are little to no shifts with respect to the equivalent bands of (6,4). The broadening of the side-on peak suggests the presence of multiple coordination isomers of two or up to three side-on coordinated N_2 ligands.

The IR-PD spectrum of (6,6) resembles very much that of (6,5), with merely an additional weak band at 2300 cm^{-1} . This new band is located 14 cm^{-1} to the blue of the persistent N_2 end-on band, which might signify a splitting that originates from two N_2 oscillators and their symmetrically/asymmetrically coupled stretching vibrations. Note that our prior investigations of related species have ongoingly found such effects in N_2 adsorbates to other types of transition metal clusters.^{39,64} The broad adsorption below 2000 cm^{-1} persists, as observed in (6,5).

The IR-PD spectrum of species (6,7) shows a similar band pattern as (6,6). However, the side-on region of (6,7) yields two well separate bands at 1445 and 1464 cm^{-1} . The ratio of integrated IR-PD signals in the side-on region to those in the end-on region indicates once again a strong contribution of side-on coordinated N_2 chromophores, two or three of them in total.

The side-on IR-PD signal diminishes significantly in (6,8), with a single weak adsorption at 1438 cm^{-1} . In contrast, the IR-PD signal in the end-on range builds up and reveals a strong quartet at 2276 , 2284 , 2289 , and 2294 cm^{-1} , which might either signify various types of symmetric/asymmetric couplings or distinguishable coordination sites and motifs. In any case, all of these IR-PD bands are located in the same frequency range ($2250\text{--}2300\text{ cm}^{-1}$) as the singlet and doublet bands of the less loaded adsorbate species.

Starting with the adsorption of the ninth N_2 molecule, the range of observed end-on IR-PD bands widens to the red; in (6,9), it extends down to 2200 cm^{-1} . Features of (6,8) largely persist in (6,9) through three partially overlapping bands at 2269 , 2283 , and 2294 cm^{-1} . Two new features arise: a sharp band at 2245 cm^{-1} and a further red-shifted broad adsorption around 2202 cm^{-1} . There is a significant change in the IR-PD signal in the side-on range: any discernible IR-PD signal of (6,9) diminishes to some very weak and widely broadened signal around 1525 cm^{-1} , which is less to the red than the intensive peaks of the less loaded species (6,2) to (6,7).

The IR-PD spectrum of species (6,10) merely hints at some broad and very weak adsorption in the side-on range that is hardly discernible and might peak around 1515 cm^{-1} . On its own, this

feature might be questionable. Similar broad IR-PD bands in (6,9) and (6,11) lend some credibility to our speculation. In the end-on region, the weak band of (6,9) at 2202 cm^{-1} rises to a prominent doublet of (6,10) at 2180 and 2199 cm^{-1} . Quite the opposite, the four strong bands of (6,9) above 2200 cm^{-1} reduce to a single band of (6,10) at 2283 cm^{-1} .

The observable IR-PD signal of (6,11) in the end-on range broadens to the red and extends from 2140 to 2300 cm^{-1} . There are five distinguishable IR-PD bands at 2143 , 2171 , 2273 , 2280 , and 2288 cm^{-1} . The side-on spectral range of the recorded IR-PD spectrum of (6,11) reveals a weak but sharp adsorption at 1470 cm^{-1} , which hints towards a single (6,11) isomer with a side-on μ_2 - $\kappa\text{N}:\kappa\text{N},\text{N}$ coordinated N_2 ligand.

The IR-PD spectra of species (6,12) and (6,13) reveal band patterns that are most similar to those of (6,11). Some IR-PD bands of end-on coordinated N_2 stretching modes reach out slightly further to the red, down to 2100 cm^{-1} . The weak side-on adsorption at 1474 cm^{-1} persists in (6,12), as observed in (6,11), and it reveals a small but discernible splitting in (6,13).

In the IR-PD spectrum of species (6,14), there are no IR-PD bands in the side-on range below 2000 cm^{-1} , and despite a sufficient signal-to-noise ratio. This indicates that the addition of the fourteenth N_2 molecule suppresses any side-on μ_2 - $\kappa\text{N}:\kappa\text{N},\text{N}$ N_2 ligand, and it likely converts any prior one. We speculate that spatial crowding of the many ligands may well favor the slimmer end-on N_2 coordination over the space consuming side-on N_2 coordination. In the IR-PD region of end-on N_2 coordination, above 2000 cm^{-1} , we observe numerous resolved IR-PD bands: 2100 , 2106 , 2133 , 2151 , and 2161 cm^{-1} , as well as at 2266 , 2272 , 2284 , 2300 , and 2308 cm^{-1} . All in all, these bands are significantly better resolved than in the spectra of (6,12) and (6,13). We take this as a hint towards a reduced degree of disorder in N_2 wagging coordinates.

Reaching out for feasibility limits, we managed to record an IR-PD spectrum of species (6,15). This spectrum revealed numerous IR-PD bands at the end-on coordinated N_2 stretching range above 2000 cm^{-1} . We observe intensive adsorptions at 2098 , 2108 , 2145 , 2276 , 2287 , 2295 , and 2310 cm^{-1} . Moreover, there are some broad IR-PD absorptions without resolved structures between 2168 and 2245 cm^{-1} . It appears as if the fifteenth N_2 ligand induces some enhanced couplings towards and among the other N_2 ligands. This might be well understood in terms of threefold N_2 coordinated Ta centers. At medium N_2 load, $m = 9$ – 14 , there are one or two such centers, and they may assume distal positions in the octahedral Ta scaffold. Any third center with a threefold N_2 load must, of course, come close to either of the previous ones. Which induces many opportunities for inter-center N_2 stretching mode couplings. In effect, the recorded IR-PD spectrum yields broad and largely unstructured bands—as observed and on display in the (6,15) spectrum of Fig. 3.

In summary, we found numerous IR-PD bands in various wavenumber ranges for the N_2 adsorption species (6,m), $m = 1$ – 15 , mainly in the range of 1400 – 1650 cm^{-1} and 2000 to 2310 cm^{-1} . We assign the discernible IR-PD bands below 2000 cm^{-1} to side-on bound μ_2 - $\kappa\text{N}:\kappa\text{N},\text{N}$ N_2 molecules and those above 2000 cm^{-1} to μ_1 end-on coordinated N_2 molecules. The end-on bound N_2 coordination signature in (6,1) corresponds to a similar finding in (5,1). Therefore, Ta_6^+ provides strong evidence for a lack of any spontaneous N_2 cleavage as well. For some species, explicitly (6,3) and

(6,4), the total number of IR-PD bands exceeds the total number of N_2 adsorbates, which provides strong evidence of coordination isomers. The μ_1 coordination dominates the end-on range of the IR-PD spectra at low N_2 loads up to $m = 5$. With increasing N_2 coverage, we observe an overall asymmetrical spread out to the red of the end-on bands. At the highest recorded N_2 load, in the IR-PD spectrum of (6,15), the end-on bands assume a range of more than 200 cm^{-1} , between 2100 and 2310 cm^{-1} . We attribute the observation of such a wide spreading out to an increasingly higher amount of double and triple N_2 coordination at Ta sites of the cluster scaffold, eventually at all of them. The higher the N_2 coordination of Ta, the more the vibrational frequencies of the corresponding N_2 ligands shift to the red.

The side-on μ_2 - $\kappa\text{N}:\kappa\text{N},\text{N}$ N_2 coordination motifs emerge in most of the IR-PD spectra, except (6,1), (6,14), and (6,15). At low N_2 loads, up to (6,7), the side-on fingerprints are roughly as strong as the end-on ones. At high N_2 loads (6,8) and beyond, there is an undisputable propensity for favorable end-on signatures, and side-on ones diminish. Therefore, it appears as if highly loaded clusters prefer, upon saturation, an exclusive end-on N_2 coordination, and partially loaded ones enable a mixture of some side-on N_2 coordination with some end-on N_2 coordination. Steric overcrowding seems to enforce the spatially less demanding end-on N_2 coordination in (6,14) and (6,15).

We undertook DFT modeling for conceivable clusters (6,m) in order to investigate the structure and geometry of the bare Ta_6^+ cluster ($m = 0$) and its first N_2 adsorbate species up to $m = 3$.

We found the bare Ta_6^+ cluster most stable in a slightly compressed octahedral structure, with four slightly elongated equatorial bonds (cf. Table S9) and a doublet state ($M = 2$). We also found some less stable structure, a nido-pentagonal pyramid with a quartet state ($M = 4$, $+66\text{ kJ/mol}$). Other test structures were optimized into either of these two. Energetics of other spin states/multiplicities and further details are to be found in the supplement (cf. Table S4). Our present conclusions on the naked Ta_6^+ cluster are well in line with a previous study.⁵⁶ Beyond that study, we went on and modeled the stepwise adsorption of N_2 molecules to the favored octahedral Ta_6^+ structure.

The slightly compressed octahedron provides for two distinguishable adsorption sites of likely end-on coordinated N_2 molecules, with either of the two polar Ta sites of the octahedron proving most favorable (cf. Table S4, isomer a). Note that the compression-distortion of the octahedral cluster did receive slight changes from the polar N_2 adsorption. In such (6,1), comprising a polar N_2 adsorbate, the prior equal equatorial bonds elongate ($+0.10\text{ \AA}$) and compress (-0.12 \AA) in concert with a minor tilting of 2° of the N_2 ligand with respect to the polar symmetry axis. This, in turn, makes the four equatorial Ta sites pairwise distinguishable. Alternatively, an N_2 adsorption onto either of the other four equatorial Ta centers (cf. Table S4, isomer b) would stabilize less, by $+7\text{ kJ/mol}$, and the according quartet states even less, $+22$ and $+17\text{ kJ/mol}$, respectively. Spin states seem to persist upon N_2 adsorption in the present case, and any spin raise seems unlikely. This is even more so in view of our spin-valley curves of the Ta_5^+ cluster species (5,m) (see above) and of several prior studies of adsorbate induced spin quenching in other TM clusters.^{61,64} From here on, we constrain ourselves to consider doublet states of (6,m).

5. Cryo-IR Spectroscopy and Cryo-Kinetics of Cluster N_2 Adsorbate Complexes of Tantalum Cluster Cations Ta_{5-8}^+

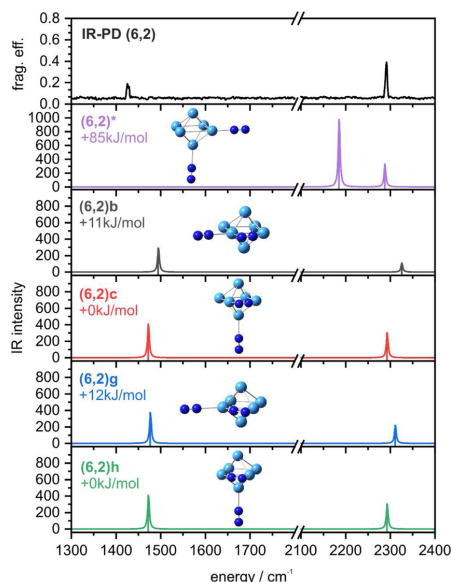


FIG. 4. Experimental IR-PD spectrum of (6,2) and DFT modeled spectra of selected structural isomers in the doublet state, their relative energies indicated with respect to the most stable isomer (6,2)c and the optimized cluster adsorbate structures. The predicted IR frequencies are scaled by a factor of 0.9586. For calculated energies and IR frequencies of all modeled isomers of (6,2), see Tables S6(b) and S7(b).

The recorded IR-PD bands of the (6,2) cluster complex at 1425 cm^{-1} motivate a computational quest for either of two N_2 molecules coordinating in a side-on ($\mu_2\text{-}\kappa\text{N}:\kappa\text{N},\text{N}$) motif. Indeed, such a motif proved more favorable by at least $+85\text{ kJ/mol}$ [cf. Fig. 4 and Table S6(b)], than that of mere end-on coordination, whose predicted IR spectrum deviates from the measured IR-PD spectrum anyway (cf. Fig. 4). The identified most stable isomers (6,2)c and (6,2)h both comprise a side-on $\mu_2\text{-}\kappa\text{N}:\kappa\text{N},\text{N}$ N_2 ligand that is coordinated to two equatorial Ta centers, next neighbors to the polar N_2 end-on coordinating Ta center (cf. Fig. 4). They differ by chirality, and they are degenerate, as expected [cf. Table S6(b) in the supplementary material]. The bond of the side-on N_2 coordinating Ta pair shortens by -0.07 \AA (cf. Table S9).

We identified further $N_{2(\text{side-on})}/N_{2(\text{end-on})}$ ligand combinations, and we found them less stable by $+11$ to $+20\text{ kJ/mol}$. [cf. Tables S6(b) and S7(b)]. Obviously, both N_2 ligands seek proximity, and they benefit from a cooperative gain on the order of up to 20 kJ/mol in achieving such proximity. Indeed, our modeling confirms that the most stable degenerate isomer pairs [isomers (6,2)b/g and (6,2)c/h] reveal identical IR spectra, respectively. Moreover, all four IR spectra match the recorded IR-PD spectra (Fig. 4). In contrast, the computed IR spectra of the isomer pair (6,2)e,j, and further ones do not coincide with the recorded IR-PD spectrum [cf. Table S6(b)]. Most notably, it shows that the side-on N_2 orientation proves negli-

gible, and hence, only the location of the coordinating Ta pair over which the side-on ligand is located is more relevant for searching for a matching minimum structure for the measured (6,2) IR-PD spectrum. The orientation of the side-on ligand over the edge seems to be less relevant. Furthermore, we have identified a cooperative effect between the end-on N_2 and the side-on N_2 .

In order to model the observed stepwise uptake of a third N_2 ligand by Ta_6^+ , we added a second end-on bound N_2 ligand to the prior end-on and side-on $\mu_2\text{-}\kappa\text{N}:\kappa\text{N},\text{N}$ N_2 ligands [cf. Tables S6(c1) and S7(c1)]. It emerges from a favorable arrangement of the two end-on N_2 ligands at Ta centers on the opposite Ta corners of the octahedral core [cf. Fig. 5, structures (6,3)j and (6,3)w]. Both end-on N_2 ligands are located at distal coordination sites. The side-on $\mu_2\text{-}\kappa\text{N}:\kappa\text{N},\text{N}$ N_2 ligand is located in between and proximal to either end-on N_2 ligand. The orientation of the side-on N_2 ligand across its coordinating Ta-Ta edge is degenerate. By virtue of the high symmetry, the modeled IR spectrum provides for merely two bands that match well the observed IR-PD bands at 2289 and 1468 cm^{-1} . Furthermore, observed IR-PD bands at 1416 , 1625 , and 2255 cm^{-1} point towards other isomers.

Up to now, we have not yet succeeded in identifying such candidates that would provide for two end-on and a single side-on ligand [cf. Fig. 5 and Fig. S7 (a)], and we wonder about some isomer with another degree of tilting of the N_2 side-on ligand. Note

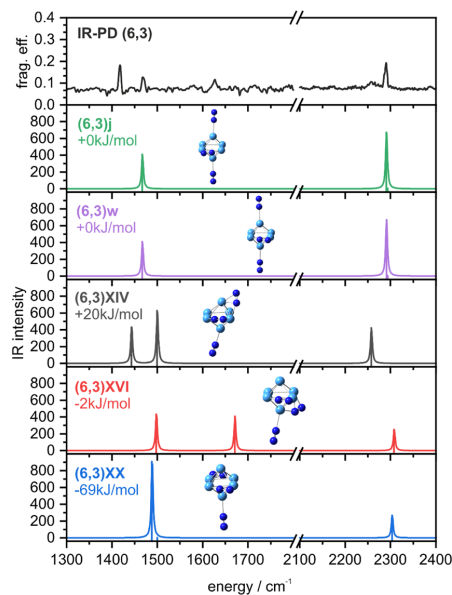


FIG. 5. Experimental IR-PD spectrum of (6,3) and DFT modeled spectra of selected structural isomers in the doublet state, their relative energies indicated with respect to isomers (6,3)j/w, and optimized cluster adsorbate structures included as insets. The predicted IR frequencies are scaled by a factor of 0.9586. For calculated energies and IR frequencies of all modeled isomers of (6,3), see Tables S6(c) and S7(c).

that our adjoined study of Ta_4^+ [IRS1] confirms such effects. We find support for our hypothesis by a closer look at the bond distances $Ta_{k(N,N)}-N_{side-on(\mu 1)}$ and the angles $Ta_{k(N,N)}-Ta_{k(N)}-N_{side-on(\mu 1)}$ of the twenty-two isomers at hand (6,3)a-w. Indeed, there is a correlation between an increase in the tilt of the side-on $\mu_2-kN:kN,N$ N_2 ligand and the observed redshift of its IR-PD vibrational frequency (cf. Table S8). This correlation seems independent of cluster size and cluster core structure, and it seems that the local $Ta-(N-N)-Ta$ geometry dominates the observed effects.

In order to assign the IR-PD bands at 1416, 1625, and 2255 cm^{-1} , we consider isomers with two side-on $\mu_2-kN:kN,N$ N_2 adsorbates. Our modeling of several conceivable arrangements [cf. Tables S6(c) and 6(c)] yielded three isomers (6,3)XIV, (6,3)XVI, and (6,3)XX with a bunch of IR frequencies that agree quite well with the experimental IR-PD bands [cf. Fig. 5 and Fig. S7 (b)]. Within these three isomers, the arrangement of the end-on ligand and one of the side-on ligands corresponds to the structure of the most favorable isomer (6,2), as described earlier. Differences arise from varying positions of the second side-on ligand.

In the two isomers (6,3)XIV and (6,3)XVI, all three N_2 ligands are located in proximity to each other, and they share common Ta sites for coordination. These two isomers suffice to interpret all five experimental IR-PD bands at 1416, 1468, 1625, 2255, and 2289 cm^{-1} (cf. Fig. 5 and Fig. S7). The third isomer (6,3)XX, which is actually the most stable one at -69 kJ/mol , manages to locate its three N_2 ligands while avoiding shared Ta sites.

This yields a highly symmetric arrangement of the N_2 ligands, and it causes merely a single IR band in the side-on range and merely another single IR band in the end-on range. Both match the experimental IR-PD bands at 1468 and 2289 cm^{-1} . Note that this isomer (6,3)XX on its own does not explain all observed IR-PD bands. However, we interpret the recorded IR-PD spectrum of (6,3) in terms of likely isomers (6,3) XIV and XVI, and we acknowledge possible contributions from other isomers.

In summary, DFT modeling provided insights into the structure of the first three adsorbate species (6,1), (6,2), and (6,3) on the Ta_6^+ cluster octahedron. The first N_2 ligand yielding (6,1) adsorbs most likely end-on to the cluster core followed by two N_2 adsorption steps giving two $\mu_2-kN:kN,N$ N_2 ligands in (6,3). This sequence of end-on adsorption before side-on adsorption of the first three N_2 ligands differs from the results of N_2 adsorption on the Ta_4^+ cluster (cf. Fries *et al.*¹ and the adjoined study [IRS1]) and highlights once more the differential behavior between cluster sizes Ta_n^+ , $n \leq 4$, and Ta_n^+ , $n \geq 5$.

At this point, we want to address the question of whether the DFT predictions and the recorded IR-PD spectra are in line with the recorded adsorption kinetics (cf. supplementary material, Text S9, Fig. S22). The kinetics show an N_2 adsorption cascade to the bare Ta_6^+ cluster. The possible isomers for (6,1), (6,2), and (6,3) identified by DFT modeling correspond in structure/geometry to this chain of successive N_2 adsorption steps. The isomer identified as most likely to be populated in each case serves as the initial geometry for the adsorption of the next N_2 molecule.

$[Ta_7(N_2)_m]^+$

From our kinetic studies presented and discussed in the supplementary material (cf. Text S10, Fig. S23), we know that the

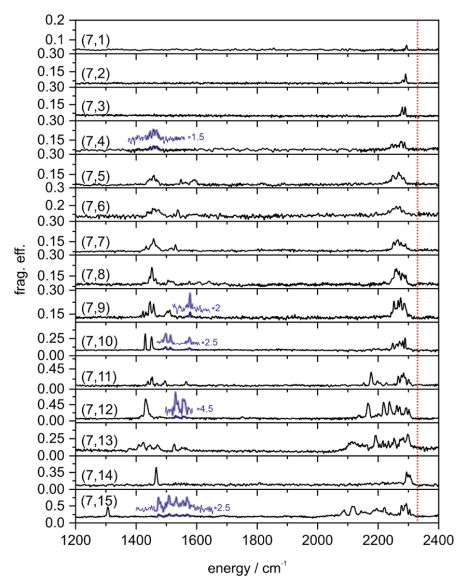


FIG. 6. IR-PD spectra of sequentially increasing cluster N_2 adsorbate complexes $[Ta_7(N_2)_m]^+$, $m = 1-15$, as recorded after prior 26 K He buffer gas cooling. Note the significant red-shift of the IR-PD bands with respect to the free N_2 stretching vibrational frequency (2330 cm^{-1} ,⁷⁶ red dotted line).

Ta_7^+ cluster adsorbs up to 16 N_2 molecules onto its cluster surface. We found an equilibrium between adsorbed species (7,10) to (7,16) at long reaction times. However, (7,16) is a very small, low-intensity product in equilibrium. Therefore, (7,15) became the largest N_2 adsorbate complex in our current IR-PD study of N_2 adsorption on Ta_7^+ (cf. Fig. 6). As before, we searched for IR-PD induced bands in the 1200 to 2400 cm^{-1} range and found numerous vibrational bands in two frequency ranges: below 2000 cm^{-1} for N_2 oscillators binding in a side-on $\mu_2-kN:kN,N$ motif to the Ta_7^+ cluster core, and beyond 2000 cm^{-1} for those binding end-on to single Ta centers. In the following, we discuss the experimental IR-PD spectra of the species in detail.

The N_2 adsorption chain on Ta_7^+ starts with the initial adsorbate species (7,1). For this species, we observe a single IR-PD band at 2294 cm^{-1} and thus a redshift with respect to the free N_2 stretching oscillation of -36 cm^{-1} . Once more, it seems reasonable to explain this redshift by a σ -donor and π -acceptor synergism. The presence of this IR-PD band provides strong evidence that spontaneous N_2 cleavage by Ta_7^+ does not proceed. Instead, Ta_7^+ appears to continue the trend that at a cluster size of $n = 5$ and beyond, adsorption of the first N_2 molecule occurs in end-on orientation to the cluster core and without further activation.

There are strong similarities in the IR-PD spectra of the subsequent two adsorbate species (7,2) and (7,3). Both spectra reveal a doublet with a splitting of 9 cm^{-1} : at 2282 and 2291 cm^{-1} for (7,2) and at 2280 and 2289 cm^{-1} for (7,3), respectively. The second

5. Cryo-IR Spectroscopy and Cryo-Kinetics of Cluster N_2 Adsorbate Complexes of Tantalum Cluster Cations Ta_{5-8}^+

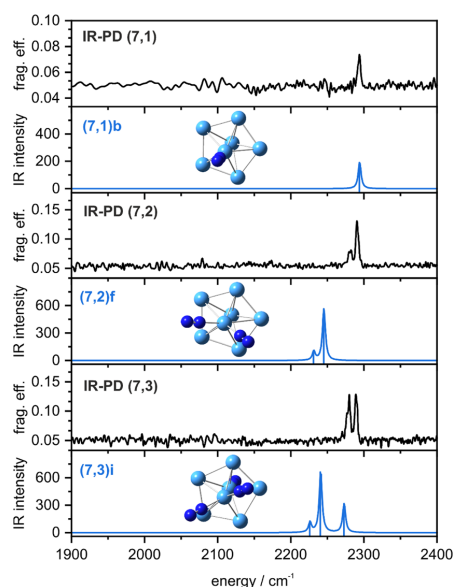


FIG. 7. Experimental IR-PD spectra of (7,1), (7,2), and (7,3) and DFT modeled spectra of selected structural isomers in the triplet state and the corresponding optimized cluster adsorbate structures as insets. The predicted IR frequencies are scaled by a factor of 0.9586. For calculated energies and IR frequencies of all modeled isomers of (7,m), see Tables S11(a)–S11(c) and S12(a)–S12(c).

N_2 molecule adsorbs to a site of the cluster such that another IR-PD band arises. A detailed examination of the (7,3) spectrum shows a very weak IR-PD sideband at 2277 cm^{-1} (Fig. 7). Our DFT modeling will reveal conceivable geometries and vibrational modes that will help to clarify.

For all of the species from (7,4) to (7,10), we observe a similar IR-PD band pattern in the end-on range above 2000 cm^{-1} . These spectra reveal induced fragmentation from 2234 cm^{-1} [the lowest end-on IR-PD fingerprint in the case of species (7,6)] to 2292 cm^{-1} [the highest end-on IR-PD fingerprint in the case of species (7,8)]. The number count of clearly identifiable IR-PD bands in the respective range varies between four and six.

The experimental IR-PD band patterns in the side-on region below 2000 cm^{-1} vary somewhat by the N_2 load, but they also show some recurring band patterns. For the adsorbate species (7,4), we observe a broad and weak IR-PD band around 1457 cm^{-1} with some partially resolved band structure. The IR-PD spectrum of the next larger adsorbate complexes (7,5) and beyond reveals a much more complex band pattern of side-on N_2 oscillators. Instead of a single broad IR-PD band around 1457 cm^{-1} (7,4), we now observe up to three bands for (7,5), (7,6), (7,7), and (7,8), which partially overlap and reveal some variation in their width but little shifts. This trend does not continue for the adsorbate species (7,9) and (7,10); instead, the spectra of both species show four and merely two sharp

bands, respectively, all of which reveal clearly less bandwidth than the smaller adsorbate species.

In addition, for (7,5) and beyond, we observe some IR-PD adsorptions at up to 1600 cm^{-1} : There is some side-on N_2 stretching doublet structure that shifts to the red with N_2 load from 1548 to 1563 cm^{-1} in (7,5) to 1498 and 1513 cm^{-1} in (7,10). The IR-PD spectra of (7,5), (7,9), and (7,10) reveal an additional single band just below 1600 cm^{-1} , which also shifts to the red with N_2 load, from 1594 in (7,5) to 1576 cm^{-1} in (7,10).

With the adsorption of the eleventh N_2 molecule onto the cluster adsorbate complex, the range of the end-on IR-PD band pattern successively expands to the red, down to 2100 cm^{-1} in (7,13). Within this range, the IR-PD spectra of the three species (7,11), (7,12), and (7,13) show an average of ten bands, which is twice as much as for the previous adsorbate species (7,4) to (7,10).

In the side-on region below 2000 cm^{-1} , the adsorption of the eleventh N_2 preserves the band pattern of the (7,10) species, and the same largely holds for (7,13). In contrast, the IR-PD spectra of the species (7,12) reveal particularly different IR-PD fingerprints: There is a single intensive band at 1431 cm^{-1} , which is accompanied by some weak bands at 1530 and 1554 cm^{-1} . The occurrence of such a sharp and intense band indicates multiple side-on N_2 adsorbates in equivalent arrangements, likely $\mu_2\text{-}\kappa\text{N}:\kappa\text{N},\text{N}$ type, that experience like next neighbor interactions and concomitant couplings of their stretching bands. Astonishing as it is, larger and smaller adsorbate complexes, namely (7,11) and (7,13), behave differently and provide for disliked next neighbor interactions among their side-on coordinated N_2 ligands.

The experimental IR-PD spectrum of the species (7,14) is conspicuous for its low number count of IR-PD bands. The (7,14) species provides for a formal N_2 double layer of two ligands per Ta site. If truly occupied in such a stoichiometric manner, it would provide for all equivalent ligands and high symmetry. Indeed, the IR-PD spectrum provides for a single intensive band at 1467 cm^{-1} , indicating side-on $\mu_2\text{-}\kappa\text{N}:\kappa\text{N},\text{N}$ N_2 oscillators, and a single intensive broad band around 2301 cm^{-1} , originating from some end-on N_2 oscillators. It is thus clearly evident that the formal “double layer” species does provide for two types of clearly distinguishable N_2 adsorbates, with the exact count of each of them remaining undisclosed.

From (7,4) to (7,13), the number of measured IR-PD bands corresponded to or even exceeded the number of adsorbed N_2 molecules, which indicates the likely presence of multiple isomers of these species. In contrast, the IR-PD band number count of species (7,14) strongly suggests the occurrence of a single isomer.

It is surprising to recognize the positions and number count of the IR-PD bands of (7,15). There are at least twelve distinguishable adsorption maxima in the end-on range between 2088 and 2304 cm^{-1} . Even more surprisingly, the prior intense IR-PD band of (7,14) at 1467 cm^{-1} shifts by adsorption of the 15th N_2 ligand down to 1307 cm^{-1} , by as much as -160 cm^{-1} , which is quite significant. Some more weak bands arise between 1475 and 1568 cm^{-1} .

The recorded IR-PD spectra of (7,m) reveal numerous bands that provide information about the structure of the coordinated N_2 ligands within the respective cluster adsorbate complexes. The spectra of the first three adsorbate species, (7,1) to (7,3), indicate N_2 oscillators that bind end-on to single Ta centers. From (7,4) and beyond, we find evidence for N_2 oscillators binding in a side-on

μ_2 - $\kappa\text{N}:\kappa\text{N},\text{N}$ motif to the Ta_7^+ cluster core. We recognize the large number of IR-PD bands below 2000 cm^{-1} . Together with the IR-PD bands above 2000 cm^{-1} , the total number of IR-PD bands for all species from (7,4) and beyond, but (7,12) and (7,14), exceeds the number of N_2 oscillators of the respective cluster adsorbates. We take this as strong evidence for several co-existing adsorbate isomers. However, there is the case of (7,14), where the number of IR-PD bands clearly falls below the number of adsorbed N_2 ligands. This in turn indicates a highly symmetric arrangement of the N_2 ligands on the Ta_7^+ cluster framework within the formal double layer of N_2 oscillators.

In order to gain deeper insights into the N_2 adsorption on the Ta_7^+ cluster and the involved structures of the cluster adsorbate complexes, we performed DFT modeling of conceivable geometries.

First of all, we wondered about the bare framework of the Ta_7^+ cluster. We chose four geometries as starting points: a capped octahedron (coh), a pentagonal bipyramid (pbp), and two types of capped trigonal prism (ctp1: capped over square plane, ctp2: capped over triangle plane). The pentagonal bipyramid (pbp) in a triplet state turned out to be the most stable (cf. Table S10). Our conclusions on this naked Ta_7^+ cluster are well in line with a previous study.⁵⁶ Singlet and quintet states of the same geometry are less stable by +35 and +37 kJ/mol, respectively. As listed in the supplement (cf. Table S10), all other investigated geometries are less stable, e.g. +162 kJ/mol for the capped octahedral (³coh) geometry. We, therefore, take the pentagonal bipyramidal (pbp) geometry for the Ta_7^+ framework as a starting point to investigate N_2 adsorption.

The highly symmetric pentagonal bipyramidal core structure of Ta_7^+ provides two distinguishable binding sites for the adsorption of a first N_2 molecule in end-on orientation. DFT modeling predicts that the two preferred triplet structures differ by 11 kJ/mol [cf. Tables S11(a) and S12(a)]. N_2 adsorption on one of the two tips of the pentagonal bipyramid is preferred as compared to adsorption on one of the Ta atoms of the pentagonal plane of the framework. The predicted IR band of the end-on N_2 oscillator comes close to the single experimental IR-PD band at 2294 cm^{-1} (cf. Fig. 7 and Fig. S8).

DFT modeling of conceivable geometries of species (7,2) [cf. Tables S11(b) and S12(b)] yielded merely a single isomer whose predicted IR band pattern matches the experimentally observed twin IR-PD bands at 2282 and 2291 cm^{-1} (cf. Fig. 7 and Fig. S8) but for some shift. The characteristic splitting of the IR-PD band results from an arrangement of both N_2 oscillators onto a single Ta atom. In consistency with the most stable isomer (7,1)b, which might serve as a precursor to this isomer (7,2)f, both N_2 molecules adsorb to either of the two tips of the pentagonal bipyramid. Unfortunately, this (7,2) isomer with this arrangement of N_2 ligands is 29 kJ/mol less stable than the most stable one in our DFT study. Nevertheless, we take this isomer to be the most likely, and we presume unknown issues on the DFT modeling side.

For species (7,3), our DFT modeling yields several isomers that differ in stability by a mere 19 kJ/mol [cf. Tables S11(c) and S12(c)]. None of the predicted IR band patterns reveal satisfactory predictions. The third most stable isomer (+6 kJ/mol) shows some resemblance with the observed IR-PD spectrum of (7,3) (cf. Fig. 7 and Fig. S9). In this isomer, the three N_2 oscillators would be distributed over the two tips of the pentagonal bipyramid. At this point, it becomes obvious that DFT modeling with our methods at hand

reaches its limits, and we look very much forward to seeing other researcher pick up this topic, hopefully in the near future.

In summary, we conclude from our DFT modeling for conceivable geometries of the bare Ta_7^+ cluster (7,0) and of the first three adsorbate species (7,1), (7,2), (7,3) that the N_2 molecules adsorb in an end-on motif to the pentagonal bipyramid prior to an adsorption to one of the five Ta atoms forming the pentagonal plane of the framework.

At this point, our IR-PD spectra and our concomitant DFT modeling strongly suggest a consecutive uptake of N_2 adsorbates into end-on coordination geometries onto a presumed most stable Ta_7^+ isomer without any indication of its scaffold to rearrange or the spin states to relay. These findings are much in line with our kinetic studies of N_2 adsorption to Ta_7^+ , as documented in the supplementary material (cf. Text S10, Fig. S23). There, we do observe stepwise N_2 uptake by the Ta_7^+ cluster, and we managed to perform a pseudo-first-order kinetic fit that does not indicate neither any isomerization nor any activation throughout the first four N_2 adsorption steps. The second and third N_2 adsorption processes proceed somewhat slower than the first step. This might correspond to the reasonable conclusion of sterically limited N_2 adsorption to the tips of the pentagonal bipyramidal framework of the Ta_7^+ cluster core.

The almost abrupt increase in the number of IR-PD bands from (7,4) and beyond, which we interpret as a clear indication of the presence of multiple isomers for each of the species, coincides with the increasing desorption rates from $k_{(7,4)}$ onward and beyond. Therefore, the isomers for all species from (7,4) onward appear to adsorb additional N_2 molecules with likely simultaneous isomerization of the adsorbate shell. There is further coincidence of a particular feature in the (7,11)th IR-PD spectra with the kinetics (cf. supplementary material, Fig. S23) of the eleventh N_2 adsorption onto Ta_7^+ : The IR-PD spectrum of (7,11) reveals a significant extension of the end-on coordinated IR-PD bands to the red, and the recorded N_2 adsorption kinetics demonstrate an equilibrium of all cluster adsorbates from (7,10) and beyond. Therefore, our IR-PD studies and our kinetic studies come to the same conclusions. The increase in multiple N_2 coordination at the same tantalum centers causes likely isomerization, e.g., N_2 adsorbate site hopping.

$[\text{Ta}_8(\text{N}_2)_m]^+$

The Ta_8^+ cluster is the largest one that we characterized by recording the IR-PD spectra of (8,m), $m = 1-8$ (Fig. 8 and Fig. S10). We found no IR induced fragmentation in the low wavenumber range below 2000 cm^{-1} and, therefore, we have no indications for the formation of side-on μ_2 - $\kappa\text{N}:\kappa\text{N},\text{N}$ coordinated N_2 oscillators in the investigated cluster adsorbate complexes. We observe several IR-PD bands above 2000 cm^{-1} , which likely stem from μ_1 end-on coordinated N_2 ligands of the Ta_8^+ cluster. The low yields of higher loaded adsorbate species ($m > 8$, cf. Fig. S25, supplementary material) hampered the recording of their IR-PD spectra, and the obtained signal-to-noise ratio is meager. Once more, it seems reasonable to assume weak σ -donation and considerable π -acceptance at work.

We observe a strong IR-PD band at 2261 cm^{-1} and a very weak band at 15 cm^{-1} to the blue, which indicates a second less likely isomer. With the current DFT modeling at hand, we cannot assign

5. Cryo-IR Spectroscopy and Cryo-Kinetics of Cluster N_2 Adsorbate Complexes of Tantalum Cluster Cations Ta_{5-8}^+

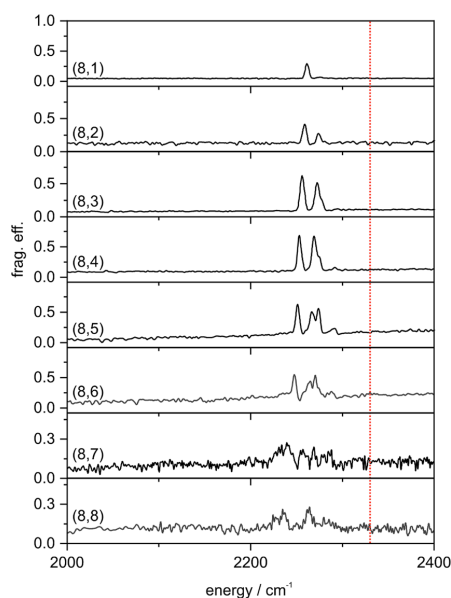


FIG. 8. IR-PD spectra of sequentially increasing cluster N_2 adsorbate complexes $[Ta_8(N_2)_m]^+$, $m = 1-8$, as recorded after prior 26 K He buffer gas cooling. Note the significant red-shift of the IR-PD bands with respect to the free N_2 stretching vibrational frequency (2330 cm^{-1} ,⁷⁶ red dotted line). For IR-PD spectra in the range of $1200-2400\text{ cm}^{-1}$, see Fig. S10 in the supplementary material.

particular geometries to these isomers. We are left with the speculation that some coordination isomers form, which finds some support in our kinetic studies (cf. supplementary material, Text S11, Figs. S24 and S25). It is noteworthy to emphasize at this point that the presence of end-on coordinated N_2 fingerprinting IR-PD bands is a compelling argument for the lack of N_2 cleavage ability of the Ta_8^+ cluster.

The IR-PD band pattern of (8,1) persists in the IR-PD spectrum of (8,2), slightly shifted to 2259 and 2274 cm^{-1} . The latter one intensifies significantly. With the adsorption of the third N_2 molecule onto the Ta_8^+ cluster, this very IR-PD band pattern is preserved in (8,3), but for some shoulder of the blue band.

The species (8,4) reveals two intensive IR-PD bands at 2253 and 2269 cm^{-1} . The vaguely discernible blue shoulder of (8,3) has evolved into a clear feature of (8,4) at 2274 cm^{-1} . In addition, one notes a weak IR-PD band at 2292 cm^{-1} . It is this band pattern that persists in the IR-PD spectrum of (8,5) but with some intensity variations and minor shifts.

Besides an inferior signal-to-noise ratio, the (8,5) IR-PD bands persist in (8,6), and an additional band arises at 2241 cm^{-1} , which is to the red of all previous (8,m) bands. We found such behavior in (5,m), (6,m), and (7,m) at some point as well. The IR-PD spectra of species (8,6), (8,7), and (8,8) reveal six to eight bands at similar locations.

The cross-reference to our cryo-kinetics study of N_2 adsorption on the Ta_n^+ cluster, $n = 2-8$, supplementary material, yields further insights. The kinetic curve of the first adsorbate species (8,1), Fig. S25, provides strong indications for two isomers, which signify their different reactivity. Our interpretation of the IR-PD spectrum (8,1) concludes as well that there are two isomers, one of which is less populated.

CONCLUSION

We present an IR-PD study of tantalum cluster adsorbate complexes $[Ta_n(N_2)_m]^+$, abbreviated (n,m), $n = 5-8$, [IRS2], and in the adjoined IR-PD study [IRS1], we present findings for the N_2 adsorption to the smaller cluster adsorbate complexes $[Ta_{2-4}(N_2)_m]^+$.

We found numerous bands in the IR-PD spectra of species (5,m), $m = 1-13$, which are located mainly in the end-on coordinated N_2 stretching range. Some of these species ($m = 9-12$) indicate weak IR-PD signals, which we assign to side-on $\mu_2\text{-}\kappa\text{N}:\kappa\text{N},\text{N}$ N_2 ligands. DFT calculations allowed us to tentatively assign cluster structures on the basis of trigonal bipyramidal (bp) cluster cores. The evaluation of spin valley curves allows us to evaluate the spin-state-dependent stability of cluster adsorbate complexes in the course of N_2 adsorption. Triplet and singlet isomers reveal themselves to be most stable in all cases. We assume some spin quenching from triplet to singlet states upon adsorption of the fifth to tenth N_2 molecule. It is the subject of ongoing work to conduct extensive quantum chemical modeling of the seemingly hindered reaction path of (5,1) and of all of the stationary points.

We found numerous IR-PD bands of the N_2 adsorption species (6,m), $m = 1-15$, in two spectral ranges, 1400 to 1650 cm^{-1} and 2000 to 2310 cm^{-1} . DFT modeling revealed a sequence of initial N_2 end-on coordination and a subsequent mix of N_2 side-on adsorption. The recorded IR-PD spectra of (7,m) reveal numerous bands indicating N_2 oscillators that bind end-on to single Ta centers in complexes (7,1) to (7,3). From (7,4) on and beyond, we find evidence for N_2 oscillators binding in a side-on $\mu_2\text{-}\kappa\text{N}:\kappa\text{N},\text{N}$ motif to the Ta_7^+ cluster core. We observe several IR-PD bands of (8,m), which likely stem from μ_1 -end-on coordinated N_2 ligands. Starting from a few single and distinguishable end-on N_2 bands of the less occupied adsorbate complexes (n,m), $n = 5-7$, we observe a general increase in spectral complexity and an inhomogeneous broadening of bands, mainly towards the red, at certain points of N_2 loading m. We attribute this observation to an increasingly higher amount of double and triple N_2 coordination of Ta sites, eventually at all of them. The more N_2 ligands coordinate with single Ta sites, the more the vibrational frequencies shift to the red.

Other than the IR-PD spectra of the small tantalum clusters Ta_n^+ , $n = 2-4$ (cf. Fries *et al.*¹ and the adjoined study [IRS1]), the present IR-PD spectra of the initial adsorbate species (n,1), $n = 5-8$, provide strong evidence for a lack of spontaneous N_2 cleavage. Instead, there are significant IR-PD fingerprints of end-on bound N_2 molecules on otherwise bare Ta_n^+ , $n = 5-8$, clusters throughout. It appears as if an enhanced entrance channel barrier prevents spontaneous tilting and further activation. In the cases of $n = 5-8$, it takes further N_2 adsorption to find some weak side-on $\mu_2\text{-}\kappa\text{N}:\kappa\text{N},\text{N}$ N_2 fingerprints, and the reasoning for the onset of these features at (5,9), (6,2), and (7,4) is an open question as of now. One

may speculate on a conceivable N_2 - N_2 cooperativity that is highly sensitive to cluster surface morphologies and thereby also to the cluster sizes. In any case, it is a sound finding that the spontaneous N_2 cleavage by Ta_n^+ , $n = 5-8$, is suppressed. Therefore, the ability of a small Ta cluster to cleave dinitrogen (cf. Fries *et al.*¹ and [IRS1]) disappears by adding a single, fifth metal atom to the cluster core.

The above-mentioned findings find strong support in our cryogenic kinetic studies, as documented in the supplementary material. There, we present a study of stepwise N_2 adsorption on size selected Ta_n^+ , $n = 5-8$ clusters, yielding $[Ta_n(N_2)_m]^+$. The N_2 adsorption reaches a limit $m_{(\max)} = 16$, which does not depend on cluster size n , and we observe a final equilibrium among those adsorbate complexes that possess up to three to five N_2 adsorbates less than $m_{(\max)}$, and the kinetic fits revealed significant N_2 desorption rates upon higher N_2 loads. The variations of absolute rates find reasonable interpretation in terms of simple thermodynamic arguments. We find some evidence for spin quenching, and it mixes in a conceivable coexistence of isomeric cluster adsorbate complexes.

SUPPLEMENTARY MATERIAL

Online supplementary material comprises a nomenclature for the clusters and their adsorbates, comprehensive listings of energetics, structures, and IR frequencies of computed structures, further experimental and computed IR spectra, and multiple text blocks and viewgraphs on the conducted kinetic experiments, kinetic fits, and their interpretation in detail.

ACKNOWLEDGMENTS

This work was supported by the German research foundation DFG within the trans-regional collaborative research center Grant No. SFB/TRR 88 (Cooperative effects in homo and heterometallic complexes, 3MET.de) and by the research center OPTIMAS. We acknowledge Thomas Kolling for his technical assistance and valuable discussion. Quantum chemical modeling took place at the "Regionales Hochschulrechenzentrum Kaiserslautern" (RHRK).

AUTHOR DECLARATIONS

Conflict of Interest

The authors have no conflicts to disclose.

Author Contributions

The experiments were performed by D.V.F.—partly together with A.S., M.P.K., and M.E.H. D.V.F. and M.P.K. performed the quantum chemical calculations. The evaluation of the measured data was carried out by D.V.F., and it was accompanied by discussions with A.S., M.P.K., and G.N.-S. D.V.F. and G.N.-S. wrote the manuscript, which all the authors revised and agreed to.

Daniela V. Fries: Data curation (lead); Formal analysis (lead); Investigation (lead); Validation (equal); Writing – original draft (equal);

Writing – review & editing (equal). **Matthias P. Klein:** Conceptualization (supporting); Data curation (supporting); Investigation (supporting); Methodology (supporting); Validation (supporting); Writing – review & editing (supporting). **Annika Straßner:** Data curation (supporting); Investigation (supporting); Methodology (supporting); Resources (supporting); Validation (supporting); Writing – review & editing (supporting). **Maximilian E. Huber:** Data curation (supporting); Formal analysis (supporting); Investigation (supporting); Project administration (supporting); Validation (supporting); Writing – review & editing (supporting). **Gereon Niedner-Schatteburg:** Conceptualization (lead); Formal analysis (equal); Funding acquisition (lead); Investigation (supporting); Methodology (lead); Project administration (lead); Resources (lead); Supervision (lead); Validation (equal); Writing – original draft (equal); Writing – review & editing (equal).

DATA AVAILABILITY

The data that support the findings of this study are available from the corresponding author upon reasonable request.

REFERENCES

- D. V. Fries, M. P. Klein, A. Steiner, M. H. Prosenč, and G. Niedner-Schatteburg, *Phys. Chem. Chem. Phys.* **23**(19), 11345–11354 (2021).
- A. Mittasch, *Geschichte der Ammoniaksynthese* (Verlag Chemie, 1951).
- K. Ziegler, H. Breil, E. Hilzkamp, and H. Martin, Germany Patent No. DE973626C (14 April 1960).
- W. Ostwald, United Kingdom Patent No. GB190200698A (20 March 1902).
- BASF, Germany Patent No. DE235421C (13 October 1908).
- F. Fischer and H. Tropsch, Germany Patent No. DE524468C (7 May 1931).
- F. Fischer and H. Tropsch, Germany Patent No. DE484337C (16 October 1929).
- H. S. Taylor, *Proc. R. Soc. London, Ser. A* **108**(745), 105–111 (1925).
- S. M. Lang and T. M. Bernhardt, *Phys. Chem. Chem. Phys.* **14**(26), 9255–9269 (2012).
- D. K. Böhme and H. Schwarz, *Angew. Chem., Int. Ed.* **44**(16), 2336–2354 (2005).
- R. A. J. O'Hair and G. N. Khairallah, *J. Cluster Sci.* **15**(3), 331–363 (2004).
- P. Armentrout, *Annu. Rev. Phys. Chem.* **52**(1), 423–461 (2001).
- M. M. Kappes, *Chem. Rev.* **88**(2), 369–389 (1988).
- P. B. Armentrout, *Catal. Sci. Technol.* **4**(9), 2741–2755 (2014).
- M. D. Morse, M. E. Geusic, J. R. Heath, and R. E. Smalley, *J. Chem. Phys.* **83**(5), 2293–2304 (1985).
- L.-H. Mou, Y. Li, Z.-Y. Li, Q.-Y. Liu, H. Chen, and S.-G. He, *J. Am. Chem. Soc.* **143**(45), 19224–19231 (2021).
- L.-H. Mou, Y. Li, G.-P. Wei, Z.-Y. Li, Q.-Y. Liu, H. Chen, and S.-G. He, *Chem. Sci.* **13**(32), 9366–9372 (2022).
- M. R. Zakin, D. M. Cox, and A. Kaldor, *J. Chem. Phys.* **87**(8), 5046–5048 (1987).
- G.-D. Jiang, L.-H. Mou, J.-J. Chen, Z.-Y. Li, and S.-G. He, *J. Phys. Chem. A* **124**(38), 7749–7755 (2020).
- C. Geng, J. Li, T. Weiske, and H. Schwarz, *Proc. Natl. Acad. Sci. U. S. A.* **115**(46), 11680–11687 (2018).
- C. Geng, J. Li, T. Weiske, and H. Schwarz, *Proc. Natl. Acad. Sci. U. S. A.* **116**(43), 21416–21420 (2019).
- F. Mafuné, Y. Tawarayama, and S. Kudoh, *J. Phys. Chem. A* **120**(24), 4089–4095 (2016).
- M. Kumar Yadav and A. Mookerjee, *Physica B* **405**(18), 3940–3942 (2010).
- J. F. Eckhardt, T. Masubuchi, M. Tschuri, R. N. Barnett, U. Landman, and U. Heiz, *J. Phys. Chem. C* **122**(44), 25628–25637 (2018).
- J. Lengyel, N. Levin, F. J. Wensink, O. V. Lushchikova, R. N. Barnett, U. Landman, U. Heiz, J. M. Bakker, and M. Tschuri, *Angew. Chem., Int. Ed.* **59**(52), 23631–23635 (2020).

5. Cryo-IR Spectroscopy and Cryo-Kinetics of Cluster N₂ Adsorbate Complexes of Tantalum Cluster Cations Ta₅₋₈⁺

- ²⁶J. F. Eckhard, T. Masubuchi, M. Tschurl, R. N. Barnett, U. Landman, and U. Heiz, *J. Phys. Chem. A* **125**(24), 5289–5302 (2021).
- ²⁷N. Levin, J. T. Margraf, J. Lengyel, K. Reuter, M. Tschurl, and U. Heiz, *Phys. Chem. Chem. Phys.* **24**(4), 2623–2629 (2022).
- ²⁸J. F. Eckhard, D. Neuwirth, C. Panosetti, H. Oberhofer, K. Reuter, M. Tschurl, and U. Heiz, *Phys. Chem. Chem. Phys.* **19**(8), 5985–5993 (2017).
- ²⁹R. Schlögl, *Angew. Chem., Int. Ed.* **42**(18), 2004–2008 (2003).
- ³⁰H. Liu, *Chin. J. Catal.* **35**(10), 1619–1640 (2014).
- ³¹L. Geng, Y. Jia, H. Zhang, C. Cui, and Z. Luo, *ChemPhysChem* **23**(17), e202200288 (2022).
- ³²C. Cui, Y. Jia, H. Zhang, L. Geng, and Z. Luo, *J. Phys. Chem. Lett.* **11**(19), 8222–8230 (2020).
- ³³M. Zhou, X. Jin, Y. Gong, and J. Li, *Angew. Chem., Int. Ed.* **46**(16), 2911–2914 (2007).
- ³⁴X. Cheng, Z.-Y. Li, L.-H. Mou, Y. Ren, Q.-Y. Liu, X.-L. Ding, and S.-G. He, *Chem. – A Eur. J.* **25**(72), 16523–16527 (2019).
- ³⁵Y. Gong, Zhao, and M. Zhou, *J. Phys. Chem. A* **111**(28), 6204–6207 (2007).
- ³⁶Z.-Y. Li, Y. Li, L.-H. Mou, J.-J. Chen, Q.-Y. Liu, S.-G. He, and H. Chen, *J. Am. Chem. Soc.* **142**(24), 10747–10754 (2020).
- ³⁷Z.-Y. Li, F. Horn, Y. Li, L.-H. Mou, W. Schöllkopf, H. Chen, S.-G. He, and K. R. Asmis, *Chem. Eur. J.* **29**(14), e202203384 (2022).
- ³⁸Y.-Q. Ding, Z.-Y. Chen, Z.-Y. Li, X. Cheng, M. Wang, and J.-B. Ma, *J. Phys. Chem. A* **126**(9), 1511–1517 (2022).
- ³⁹M. C. Tsai, U. Ship, I. C. Bassignana, J. Küppers, and G. Ertl, *Surf. Sci.* **155**(2), 387–399 (1985).
- ⁴⁰H. J. Freund, B. Bartos, R. P. Messmer, H. Grunze, H. Kühlenbeck, and M. Neumann, *Surf. Sci.* **185**(1), 187–202 (1987).
- ⁴¹A. Fielicke, A. Kirilyuk, C. Ratsch, J. Behler, M. Scheffler, G. Von Helden, and G. Meijer, *Phys. Rev. Lett.* **93**(2), 023401 (2004).
- ⁴²J. Oomens, B. G. Sartakov, G. Meijer, and G. von Helden, *Int. J. Mass Spectrom.* **254**(1), 1–19 (2006).
- ⁴³J. R. Eyler, *Mass Spectrom. Rev.* **28**(3), 448–467 (2009).
- ⁴⁴P. Maitre, D. Scuderi, D. Corinti, B. Chiavarino, M. E. Crestoni, and S. Fornarini, *Chem. Rev.* **120**(7), 3261–3295 (2020).
- ⁴⁵J. Roithová, *Chem. Soc. Rev.* **41**(2), 547–559 (2012).
- ⁴⁶G. Altinay and R. B. Metz, *Int. J. Mass Spectrom.* **297**(1–3), 41–45 (2010).
- ⁴⁷B. Chiavarino, M. E. Crestoni, M. Schütz, A. Bouchet, S. Piccirillo, V. Steinmetz, O. Dopfer, and S. Fornarini, *J. Phys. Chem. A* **118**(34), 7130–7138 (2014).
- ⁴⁸O. Dopfer, *J. Phys. Org. Chem.* **19**(8–9), 540–551 (2006).
- ⁴⁹N. I. Hammer, J. W. Shin, J. M. Headrick, E. G. Diken, J. R. Roscioli, G. H. Weddle, and M. A. Johnson, *Science* **306**(5696), 675–679 (2004).
- ⁵⁰J. M. Headrick, E. G. Diken, R. S. Walters, N. I. Hammer, R. A. Christie, J. Cui, E. M. Myshakin, M. A. Duncan, M. A. Johnson, and K. D. Jordan, *Science* **308**(5729), 1765–1769 (2005).
- ⁵¹A. M. Rijs and J. Oomens, *Top. Curr. Chem.* **364**, 1–42 (2015).
- ⁵²T. R. Rizzo and O. V. Boyarkina, *Top. Curr. Chem.* **364**, 43–97 (2015).
- ⁵³T. R. Rizzo, J. A. Stearns, and O. V. Boyarkina, *Int. Rev. Phys. Chem.* **28**(3), 481–515 (2009).
- ⁵⁴W. H. Robertson and M. A. Johnson, *Annu. Rev. Phys. Chem.* **54**, 173–213 (2003).
- ⁵⁵P. Gruene, A. Fielicke, and G. Meijer, *J. Chem. Phys.* **127**(23), 234307 (2007).
- ⁵⁶J. Du, X. Sun, and G. Jiang, *J. Chem. Phys.* **136**(9), 094311 (2012).
- ⁵⁷X. Sun and X. Huang, *ACS Omega* **7**(26), 22682–22688 (2022).
- ⁵⁸L.-H. Mou, Z.-Y. Li, and S.-G. He, *J. Phys. Chem. Lett.* **13**(18), 4159–4169 (2022).
- ⁵⁹J. Mohrbach, S. Dillinger, and G. Niedner-Schatteburg, *J. Phys. Chem. C* **121**(20), 10907–10918 (2017).
- ⁶⁰S. Dillinger, J. Mohrbach, and G. Niedner-Schatteburg, *J. Chem. Phys.* **147**(18), 184305 (2017).
- ⁶¹A. A. Ehrhard, M. P. Klein, J. Mohrbach, S. Dillinger, and G. Niedner-Schatteburg, *Mol. Phys.* **119**(17–18), e1953172 (2021).
- ⁶²A. A. Ehrhard, M. P. Klein, J. Mohrbach, S. Dillinger, and G. Niedner-Schatteburg, *J. Chem. Phys.* **156**(5), 054308 (2022).
- ⁶³A. Straßner, M. P. Klein, D. V. Fries, C. Wiehn, M. E. Huber, J. Mohrbach, S. Dillinger, D. Spelsberg, P. B. Armentrout, and G. Niedner-Schatteburg, *J. Chem. Phys.* **155**(24), 244306 (2021).
- ⁶⁴A. Straßner, C. Wiehn, M. P. Klein, D. V. Fries, S. Dillinger, J. Mohrbach, M. H. Prosen, P. B. Armentrout, and G. Niedner-Schatteburg, *J. Chem. Phys.* **155**(24), 244305 (2021).
- ⁶⁵S. Dillinger, J. Mohrbach, J. Hewer, M. Gaffga, and G. Niedner-Schatteburg, *Phys. Chem. Chem. Phys.* **17**(16), 10358–10362 (2015).
- ⁶⁶S. Dillinger, M. P. Klein, A. Steiner, D. C. McDonald, M. A. Duncan, M. M. Kappes, and G. Niedner-Schatteburg, *J. Phys. Chem. Lett.* **9**(4), 914–918 (2018).
- ⁶⁷M. P. Klein, A. A. Ehrhard, J. Mohrbach, S. Dillinger, and G. Niedner-Schatteburg, *Top. Catal.* **61**(1), 106–118 (2018).
- ⁶⁸M. J. Frisch, G. W. Trucks, H. B. Schlegel, G. E. Scuseria, M. A. Robb, J. R. Cheeseman, G. Scalmani, V. Barone, B. Mennucci, G. A. Petersson, H. Nakatsuji, M. Caricato, X. Li, H. P. Hratchian, A. F. Izmaylov, J. Bloino, G. Zheng, J. L. Sonnenberg, M. Hada, M. Ehara, K. Toyota, R. Fukuda, J. Hasegawa, M. Ishida, T. Nakajima, Y. Honda, O. Kitao, H. Nakai, T. Vreven, J. A. Montgomery, Jr., J. E. Peralta, F. Ogliaro, M. Bearpark, J. J. Heyd, E. Brothers, K. N. Kudin, V. N. Staroverov, R. Kobayashi, J. Normand, K. Raghavachari, A. Rendell, J. C. Burant, S. S. Iyengar, J. Tomasi, M. Cossi, N. Rega, J. M. Millam, M. Klene, J. E. Knox, J. B. Cross, V. Bakken, C. Adamo, J. Jaramillo, R. Gomperts, R. E. Stratmann, O. Yazyev, A. J. Austin, R. Cammi, C. Pomelli, J. W. Ochterski, R. L. Martin, K. Morokuma, V. G. Zakrzewski, G. A. Voth, P. Salvador, J. J. Dannenberg, S. Dapprich, A. D. Daniels, Ö. Farkas, J. B. Foresman, J. V. Ortiz, J. Cioslowski, and D. J. Fox, *GAUSSIAN 09, Revision E.01*, Gaussian, Inc., Wallingford, CT, 2009.
- ⁶⁹M. J. Frisch, G. W. Trucks, H. B. Schlegel, G. E. Scuseria, M. A. Robb, J. R. Cheeseman, G. Scalmani, V. Barone, G. A. Petersson, H. Nakatsuji, X. Li, M. Caricato, A. V. Marenich, J. Bloino, B. G. Janesko, R. Gomperts, B. Mennucci, H. P. Hratchian, J. V. Ortiz, A. F. Izmaylov, J. L. Sonnenberg, D. Williams-Young, F. Ding, F. Lipparini, F. Egidi, J. Goings, B. Peng, A. Petrone, T. Henderson, D. Ranasinghe, V. G. Zakrzewski, J. Gao, N. Rega, G. Zheng, W. Liang, M. Hada, M. Ehara, K. Toyota, R. Fukuda, J. Hasegawa, M. Ishida, T. Nakajima, Y. Honda, O. Kitao, H. Nakai, T. Vreven, K. Throssell, J. A. Montgomery, Jr., J. E. Peralta, F. Ogliaro, M. J. Bearpark, J. J. Heyd, E. N. Brothers, K. N. Kudin, V. N. Staroverov, T. A. Keith, R. Kobayashi, J. Normand, K. Raghavachari, A. P. Rendell, J. C. Burant, S. S. Iyengar, J. Tomasi, M. Cossi, J. M. Millam, M. Klene, C. Adamo, R. Cammi, J. W. Ochterski, R. L. Martin, K. Morokuma, O. Farkas, J. B. Foresman, and D. J. Fox, *GAUSSIAN 16, Revision C.01*, Gaussian, Inc., Wallingford, CT, 2016.
- ⁷⁰J. P. Perdew, K. Burke, and M. Ernzerhof, *Phys. Rev. Lett.* **78**(7), 1396 (1997).
- ⁷¹C. Adamo and V. Barone, *J. Chem. Phys.* **110**(13), 6158–6170 (1999).
- ⁷²F. Weigend and R. Ahlrichs, *Phys. Chem. Chem. Phys.* **7**(18), 3297–3305 (2005).
- ⁷³D. Andrae, U. Häußermann, M. Dolg, H. Stoll, and H. Preuß, *Theor. Chim. Acta* **77**(2), 123–141 (1990).
- ⁷⁴D. Figgen, K. A. Peterson, M. Dolg, and H. Stoll, *J. Chem. Phys.* **130**(16), 164108 (2009).
- ⁷⁵E. D. Glendening, J. K. Badenhoop, A. E. Reed, J. E. Carpenter, J. A. Bohmann, C. M. Morales, and F. Weinhold, *NBO 5.9*, 2009.
- ⁷⁶W. M. Haynes, *CRC Handbook of Chemistry and Physics* (CRC Press Taylor & Francis Group, 2014).
- ⁷⁷M. P. Klein, Ph.D. thesis, Technische Universität Kaiserslautern, 2021.

5.3 Supplementary Information

Supplementary material to

**Cryo IR Spectroscopy and Cryo Kinetics
of Cluster N₂ Adsorbate Complexes
of Tantalum Cluster Cations Ta₅₋₈⁺**

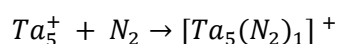
Daniela V. Fries, Matthias P. Klein, Annika Straßner, Maximilian E. Huber,
and Gereon Niedner-Schatteburg^{a)}

Department of Chemistry and State Research Center OPTIMAS,
Rheinland-Pfälzische Technische Universität (RPTU) Kaiserslautern-Landau,
67663 Kaiserslautern, Germany

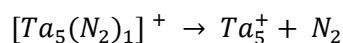
a) Author to whom correspondence should be addressed: gns@rptu.de

Text S1: Nomenclature for the Ta_n^+ clusters and their adsorbates

Nitrogen adsorption on the tantalum clusters yields cluster adsorbate complexes, which are referred to as $[Ta_n(N_2)_m]^+$ in typical chemical complex nomenclature. Continuing the series studies on transition metal (TM) clusters¹⁻⁷ and for better reference, we have again chosen an abridged (n,m) nomenclature for these tantalum clusters $[Ta_n(N_2)_m]^+$. In this nomenclature, n represents the size of the cluster; e. g., n = 5 represents a cluster of five tantalum atoms. This cluster size consequently corresponds to the shortened notation (5,m). According to our investigations there are 16 complexes of the form (5,m), where m stands for the number of N_2 molecules attached to the cluster. Hence, for the cluster size n = 5 the index m ranges from 0 to 16. The 16 (5,m) complexes are interlinked by 16 processes, respectively, in the form of adsorption and desorption reactions. The rate constants for these adsorption and desorption processes are labelled as k_m and $k_{-(m+1)}$. Therefore, m can assume values from 0 to 15. We use e.g. $k_0 := k_{0 \rightarrow 1}$ for the adsorption step:



and $k_{-1} := k_{1 \rightarrow 0}$ for the desorption step:



We assume that the so called “side-on” motif originates from initial “end-on” $\mu_{1-\kappa}N$ N_2 coordination to some Ta center, designated $Ta_{\kappa N}$. Subsequent tilting of the N_2 ligand towards a neighboring Ta center adds another “side-on” $\mu_{2-\kappa}N,N$ N_2 coordination at this very Ta neighbor, designated $Ta_{\kappa N,N}$. Note that the prior end-on $\mu_{1-\kappa}N$ coordination persists. It thus should actually be designated most correctly as a combined side-on/end-on motif, while we utilize the shorthand notation of a mere “side-on” designation for simplicity.

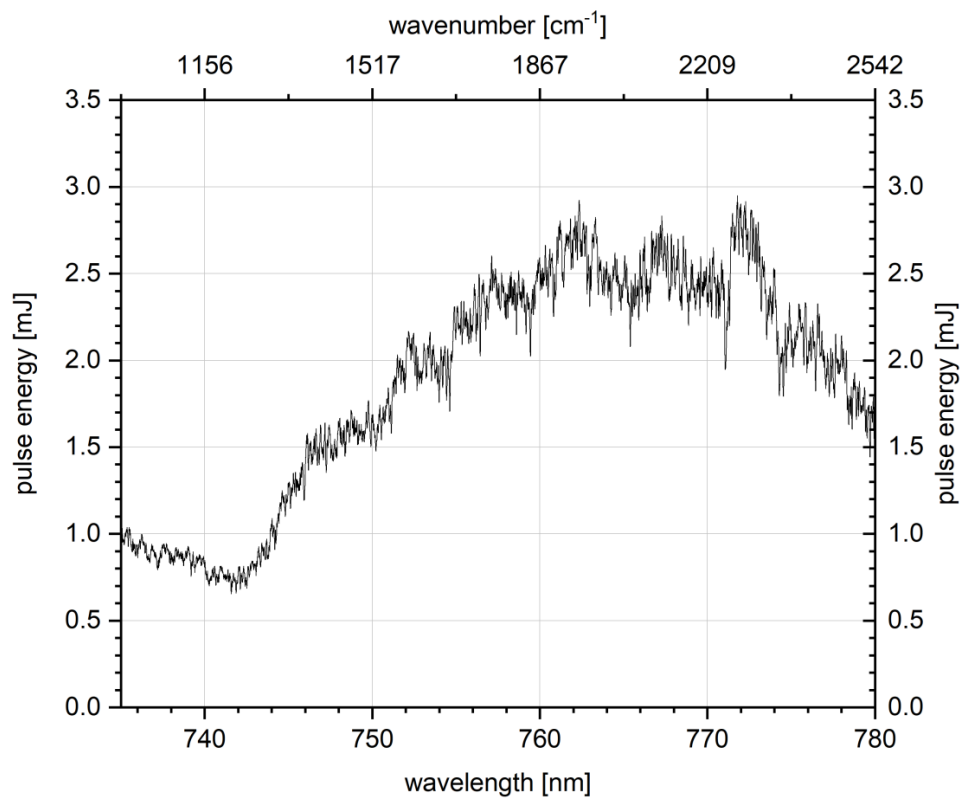


Figure S1: Laser pulse energy in dependence of wavelength and wavenumber.

5. Cryo-IR Spectroscopy and Cryo-Kinetics of Cluster N_2 Adsorbate Complexes of Tantalum Cluster Cations Ta_{5-8}^+

Table S1: Energies of the isomers constituting the spin valley: (a) absolute energies of the cluster adsorbate complexes ($E_{abs(5,m)}$); (b) absolute energies of the “(5,m) + (10-m) N_2 ” systems, and (c) the relative energies of the “(5,m) + (10-m) N_2 ” systems. The most stable isomer for each m is shown in bold.

		$E_{abs(5,m)} / \text{a.u.}$				
(a)		m = 0	m = 1	m = 2	m = 5	m = 10
2S+1						
1		-284.636154	-394.103318	-503.567109	-831.944199	-1379.254958
3		-284.641462	-394.102967	-503.568665	-831.944565	-1379.249108
5		-284.607070	-394.078960	-503.550502	-831.933369	-1379.239387
7		-284.584741	-394.050024	-503.516246	-831.911559	
15		-284.542173	-394.015054	-503.487011	-831.888831	
<hr/>						
(b)		$E_{abs(5,m)+(10-m)N_2} / \text{a.u.}$				
2S+1		m = 0	m = 1	m = 2	m = 5	m = 10
1		-1379.098937	-1379.119823	-1379.137335	-1379.175591	-1379.254958
3		-1379.104245	-1379.119472	-1379.138892	-1379.175956	-1379.249108
5		-1379.069853	-1379.095464	-1379.120729	-1379.164761	-1379.239387
7		-1379.047524	-1379.066529	-1379.086473	-1379.142951	
10		-1379.004956	-1379.031558	-1379.057238	-1379.120223	
<hr/>						
(c)		$E_{abs(5,m)+(10-m)N_2} / \text{kJ/mol}$				
2S+1		m = 0	2S+1	m = 0	2S+1	m = 0
1		13.94	-40.90	-86.88	-187.32	-395.70
3		0.00	-39.98	-90.97	-188.28	-380.34
5		90.29	23.05	-43.28	158.89	-354.82
7		148.92	99.02	46.66	-101.62	
15		260.68	190.84	123.42	-41.95	

Table S2: Vertical (triplet) and adiabatic adsorption energies as derived from our calculated (5.m) $m = 0, \dots, 2, 5, 10$ isomers. The values represent the steps 0 and 1 as well as the values for triple adsorption (5.2) \rightarrow (5.5) and fivefold adsorption (5.5) \rightarrow (5.10). For the latter two larger steps. We also present interpolated values in an additional column (bold).

step m	adsorption energy / kJ/mol			
	vertical triplet		adiabatic	
0	-40.0		-40.9	
1	-50.1		-51.0	
2	-97.3	-32.4	-97.3	-32.4
3		-32.4		-32.4
4		-32.4		-32.4
5	-192.1	-38.4	-207.4	-41.5
6		-38.4		-41.5
7		-38.4		-41.5
8		-38.4		-41.5
9		-38.4		-41.5

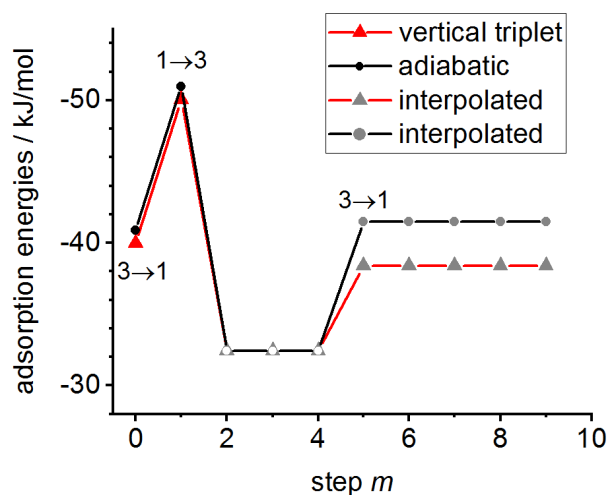


Fig. S2: Vertical (triplet) and adiabatic adsorption energies ΔE_{ads} of the adsorption steps $m = 0$ through $m = 10$. The grey points represent interpolated values between (5,2) – (5,5) and (5,5) – (5,10), respectively. The labelling indicates transition between spin states.

5. Cryo-IR Spectroscopy and Cryo-Kinetics of Cluster N_2 Adsorbate Complexes of Tantalum Cluster Cations Ta_{5-8}^+

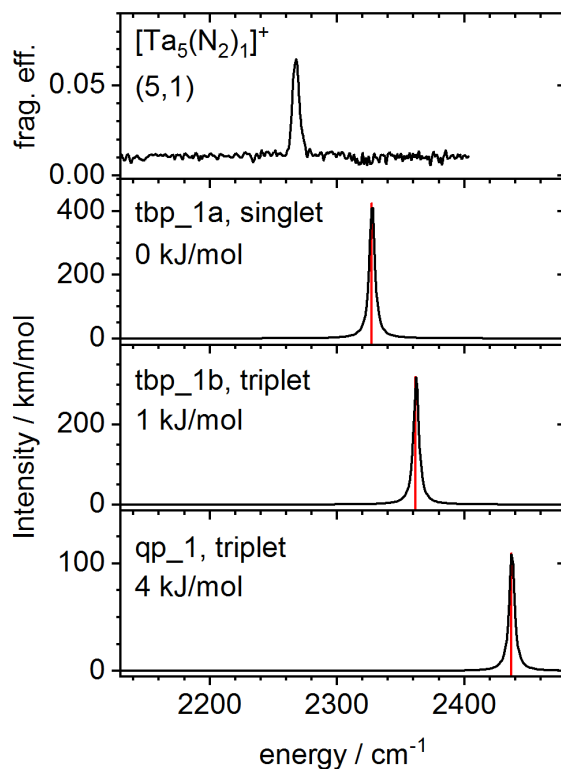


Fig. S3: Experimental IR-PD spectra and calculated linear absorption spectra of the most stable isomers for the (5,1) cluster adsorbate complex. The calculated IR spectra are not scaled. The structures of the assigned isomers are shown in Fig. 5.

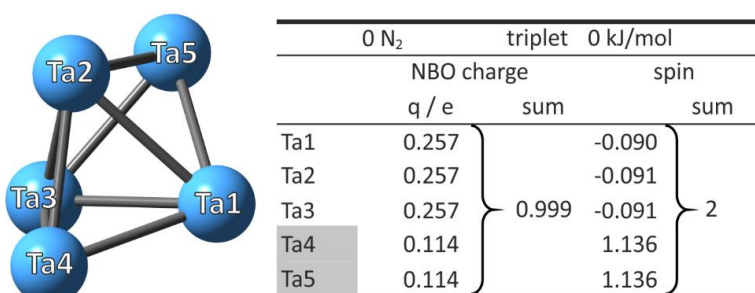


Fig.S4: Most stable isomers of the (5,0) cluster 3tbp . The charge and spin distribution of each isomer is given. The grey shading indicates the apical Ta atoms.

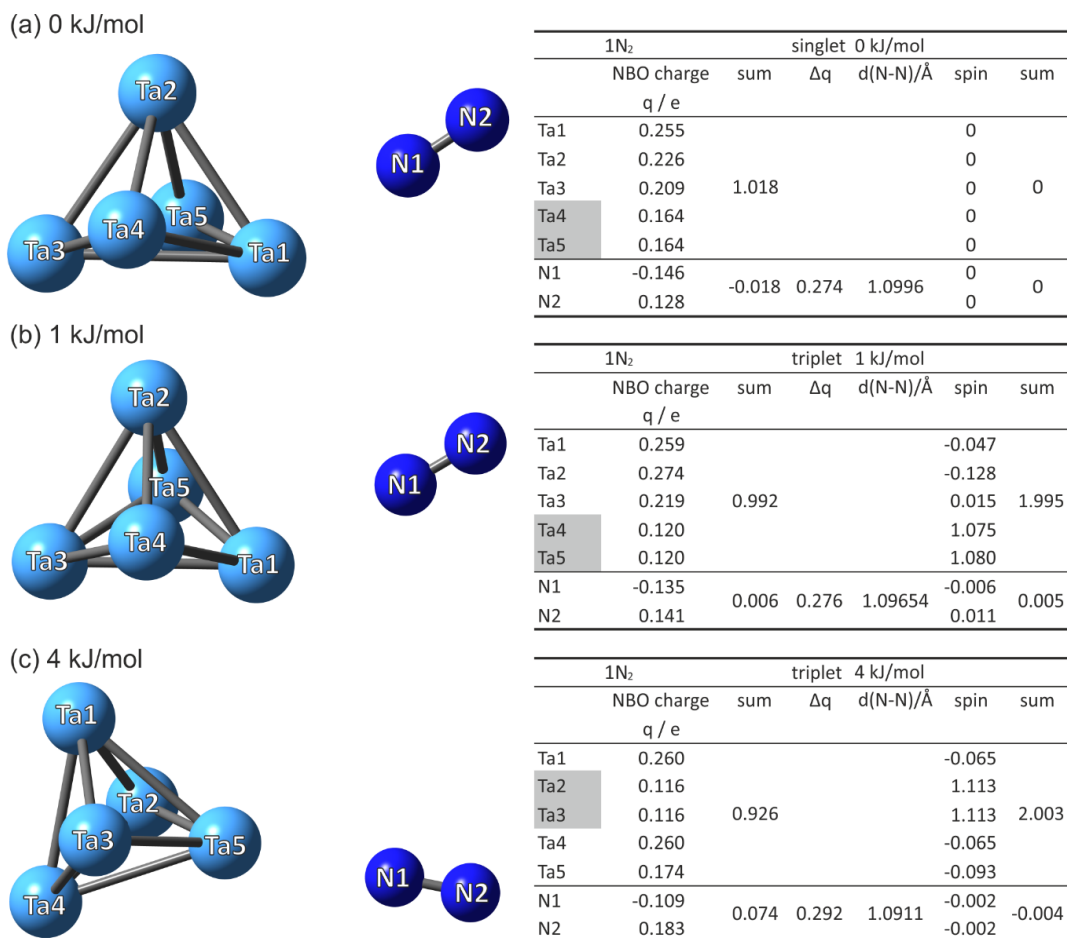


Fig. S5: Three most stable isomers of the (5, 1) cluster adsorbate complex with N₂ end on coordination. The isomers are equally stable. The corresponding calculated linear absorption spectra are given in Fig. S3. The charge and spin distribution of each isomer is given. The grey shading indicates the apical Ta atoms. The asterisk emphasizes the adsorbing Ta1 atom.

Table S3: DFT modeling and optimization of a (5, 1) isomer with a dissociated N₂ ligand in comparison to stable isomers with a molecular N₂ ligand (cf. Fig S5).

	multiplicity	energy E / Ha	ΔE / kJ/mol
	3	-394.25199444	-412
tbp_1b, triplet (b)	3	-394.10296748	+1
qp_1, triplet (c)	3	-394.10190331	+4

5. Cryo-IR Spectroscopy and Cryo-Kinetics of Cluster N_2 Adsorbate Complexes of Tantalum Cluster Cations Ta_{5-8}^+

Table S4: DFT modeling and optimization of the bare cluster Ta_6^+ with even multiplications 2 – 10 revealed the symmetric octahedron in the doublet state as the most favorable geometry for the Ta_6^+ cluster framework.

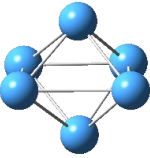
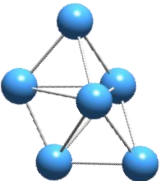
(a) octrahedron 	multiplicity	energy E / Ha	ΔE / kJ/mol
	2	-344.420939	0
	4	-344.411923	+24
	6	-344.386124	+91
	8	-344.375529	+119
	10	-344.351041	+184
(b) nido-pentagonal bipyramid 	multiplicity	energy E / Ha	ΔE / kJ/mol
	2	-	-
	4	-344.395731	+66
	6	-344.381343	+104
	8	-344.359671	+161
	10	-344.317150	+272

Table S5: DFT modelling and optimization of (6,1) isomers a and b. N_2 adsorption to the corners of the octahedron in the doublet state shows the most favorable cluster geometry. Adsorption of the N_2 molecule onto one of the other four Ta centers (isomer b) yields less favorable geometry structure.

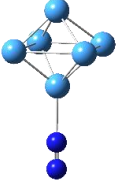
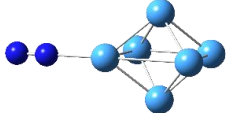
a 	multiplicity	energy E / Ha	ΔE / kJ/mol
	2	-453.878948	0
	4	-453.870466	+22
b 	multiplicity	energy E / Ha	ΔE / kJ/mol
	2	-453.876221	+7
	4	-453.869620	+24

Table S6a: Calculated energies and IR frequencies (scaling factor 0.9586) of the cluster adsorption isomers (6,1) in the doublet state. Isomers shown in bold are chosen for further discussion. For graphical representation of those, see Fig. S6.

	$\nu_{\text{NNend-on}}$ cm ⁻¹	$\nu_{\text{NNend-on}}$ (scaled) cm ⁻¹	$\nu_{\text{NNside-on}}$ cm ⁻¹	$\nu_{\text{NNside-on}}$ (scaled) cm ⁻¹	energy E Ha	ΔE kJ/mol
a	2392	2293	-	-	-453.878948	0
b	2287	2192	-	-	-453.876221	+7

Table S6b: Calculated energies and IR frequencies (scaling factor 0.9586) of the cluster adsorption isomers (6,2) in the doublet state. Isomers shown in bold are chosen for further discussion. For graphical representation of those, see Fig. S6. The isomer * is the most stable found for an adsorption shell of two end-on coordinated N₂ ligands on the Ta₆⁺ framework.

	$\nu_{\text{NNend-on}}$ cm ⁻¹	$\nu_{\text{NNend-on}}$ (scaled) cm ⁻¹	$\nu_{\text{NNside-on}}$ cm ⁻¹	$\nu_{\text{NNside-on}}$ (scaled) cm ⁻¹	energy E Ha	ΔE kJ/mol
*	2279, 2386	2185, 2288	-	-	-563.335670	+85
a	2377	2278	1555	1490	-563.361120	+18
b	2426	2325	1559	1494	-563.363559	+11
c	2392	2293	1535	1472	-563.367873	+0
d	2341	2244	1541	1478	-563.363138	+12
e	2348	2251	1544	1480	-563.363348	+12
f	2411	2311	1540	1476	-563.360154	+20
g	2396	2296	1547	1482	-563.363348	+12
h	2411	2311	1540	1476	-563.367874	+0
i	2392	2293	1536	1472	-563.360814	+19
j	2426	2325	1559	1495	-563.363557	+11

5. Cryo-IR Spectroscopy and Cryo-Kinetics of Cluster N_2 Adsorbate Complexes of Tantalum Cluster Cations Ta_{5-8}^+

Table S6c1: Calculated energies and IR frequencies (scaling factor 0.9586) of the cluster adsorption isomers (6,3) in the doublet state. Isomers shown in bold are chosen for further discussion. For graphical representation of those, see Fig. S7.

	$\nu_{NNend-on}$ cm ⁻¹	$\nu_{NNend-on}(scaled)$ cm ⁻¹	$\nu_{NNside-on}$ cm ⁻¹	$\nu_{NNside-on}(scaled)$ cm ⁻¹	energy E Ha	ΔE kJ/mol
a	2367, 2420	2269, 2320	1571	1506	-672.816180	+30
b	2372, 2390	2274, 2291	1549	1485	-672.820648	+18
c	2330, 2371	2234, 2272	1554	1490	-672.816317	+29
d	2376, 2412	2277, 2312	1553	1488	-672.816005	+30
e	2399, 2421	2300, 2321	1554	1489	-672.81871	+23
f	2387, 2425	2288, 2325	1549	1485	-672.823264	+11
g	2387, 2424	2288, 2323	1565	1500	-672.815669	+31
h	2390, 2411	2291, 2311	1533	1469	-672.822668	+13
i	2331, 2387	2234, 2288	1535	1472	-672.822935	+12
j	2390, 2393	2291, 2294	1530	1467	-672.827548	+0
k	2333, 2410	2236, 2310	1534	1471	-672.818476	+24
l	2377, 2409	2278, 2309	1551	1487	-672.815284	+32
o	2384, 2390	2285, 2291	1540	1476	-672.819673	+21
p	2367, 2383	2269, 2284	1561	1496	-672.812620	+39
q	2388, 2424	2289, 2323	1565	1500	-672.815671	+31
r	2399, 2421	2300, 2321	1554	1489	-672.818708	+23
s	2390, 2411	2291, 2312	1533	1469	-672.822667	+13
t	2376, 2412	2278, 2312	1552	1488	-672.816011	+30
u	2387, 2425	2288, 2325	1549	1485	-672.823262	+11
v	2372, 2390	2274, 2291	1549	1485	-672.820646	+18
w	2390, 2393	2291, 2294	1530	1467	-672.827547	+0
x	2367, 2421	2269, 2320	1571	1506	-672.816177	+30

Table S6c2: Calculated energies and IR frequencies (scaling factor 0.9586) of the cluster adsorption isomers (6,3) in the doublet state. Isomers shown in bold are chosen for further discussion. For graphical representation of those, see Fig. S7.

	$\vartheta_{\text{NNend-on}}$ cm ⁻¹	$\vartheta_{\text{NNend-on}}(\text{scaled})$ cm ⁻¹	$\vartheta_{\text{NNside-on}}$ cm ⁻¹	$\vartheta_{\text{NNside-on}}(\text{scaled})$ cm ⁻¹	energy E Ha	ΔE kJ/mol
I	2342	2245	1665, 1688	1596, 1618	-672.814170	+35
II	2295	2200	1619, 1639	1552, 1571	-672.829025	-4
III	2297	2202	1591, 1611	1525, 1544	-672.829663	-6
IV	2312	2216	1600, 1677	1534, 1607	-672.814559	+34
V	2281	2186	1554, 1577	1490, 1511	-672.828832	-3
VI	2366	2268	1553, 1678	1488, 1609	-672.829582	-5
VII	2374	2276	1588, 1592	1522, 1527	-672.829611	-5
VIII	2374	2276	1588, 1592	1522, 1527	-672.821596	+16
IX	2323	2226	1575, 1804	1510, 1729	-672.822778	+13
X	2425	2324	1596, 1610	1530, 1543	-672.845881	-48
XI	2373	2275	1599, 1683	1533, 1613	-672.823409	+11
XII	2413	2313	1547, 1566	1483, 1501	-672.849327	-57
XIII	2386	2287	1546, 1794	1482, 1720	-672.824559	+8
XIV	2355	2257	1505, 1564	1443, 1500	-672.8200247	+20
XV	2384	2285	1655, 1680	1586, 1610	-672.821152	+17
XVI	2408	2308	1562, 1743	1498, 1671	-672.828465	-2
XVII	2408	2308	1611, 1630	1544, 1563	-672.832616	-13
XVIII	2414	2314	1562, 1606	1497, 1540	-672.827907	-1
XIX	2387	2288	1587, 1600	1522, 1534	-672.850717	-61
XX	2403	2303	1553, 1565	1488, 1500	-672.853795	-69
XXI	2361	2263	1554, 1570	1490, 1505	-672.832061	-12

5. Cryo-IR Spectroscopy and Cryo-Kinetics of Cluster N_2 Adsorbate Complexes of Tantalum Cluster Cations Ta_{5-8}^+

Table S7a: DFT optimized structures of cluster adsorption isomers (6,1) in the doublet state. Isomers shown in bold are chosen for further discussion. For calculated energies, IR frequencies and graphical representation of those, see Tab. S6a, Fig. S6.

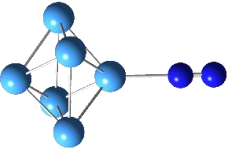
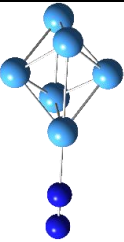
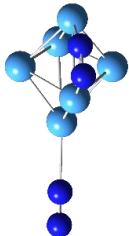
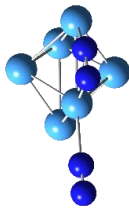
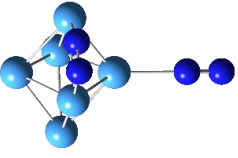
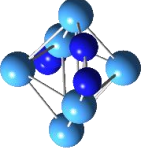
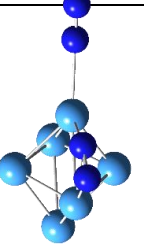
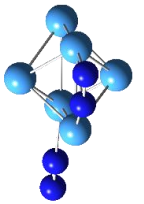
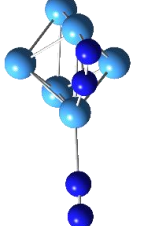
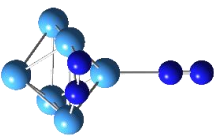
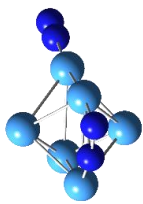
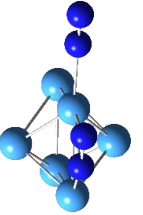
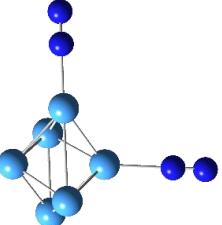
(6,1)a	(6,1)b					
						

Table S7b: DFT optimized structures of cluster adsorption isomers (6,2) in the doublet state. Isomers shown in bold are chosen for further discussion. For calculated energies, IR frequencies and graphical representation of those, see Tab. S6b, Fig. S6.

(6,2)a	(6,2)b	(6,2)c	(6,2)d	(6,2)e	(6,2)f	(6,2)g
						
(6,2)h	(6,2)i	(6,2)j	(6,2)*			
						

5. Cryo-IR Spectroscopy and Cryo-Kinetics of Cluster N_2 Adsorbate Complexes of Tantalum Cluster Cations Ta_{5-8}^+

Table S7c1: DFT optimized structures of cluster adsorption isomers (6,3) in the doublet state. Isomers shown in bold in the caption are chosen for further discussion. For calculated energies, IR frequencies and graphical representation of those, see Tab. S6c1 Fig. S7.

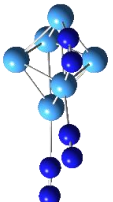
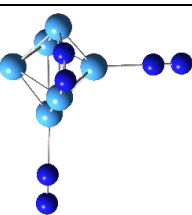
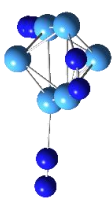
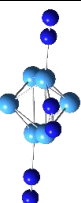
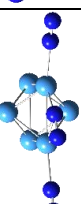
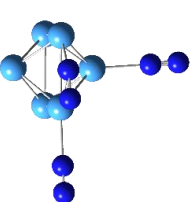
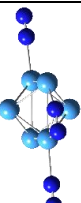
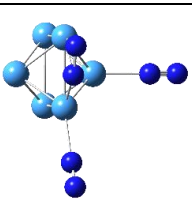
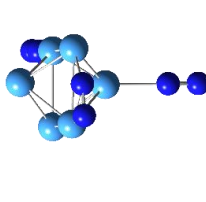
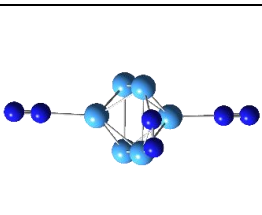
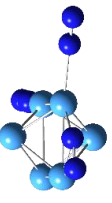
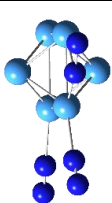
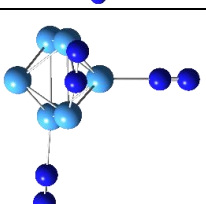
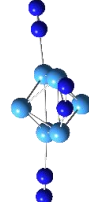
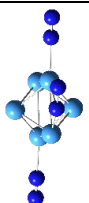
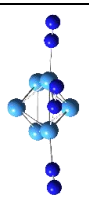
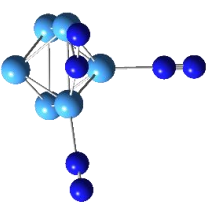
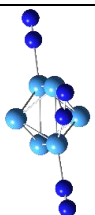
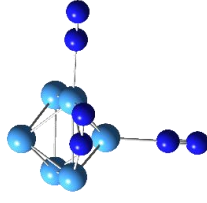
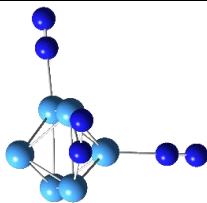
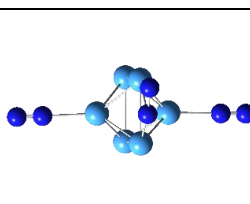
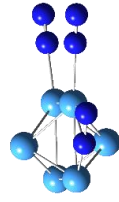



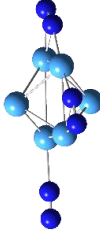
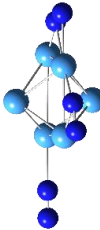
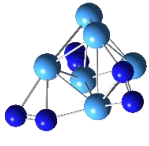
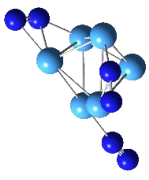
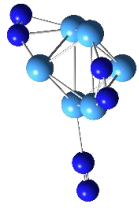
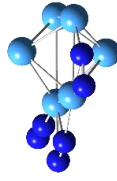
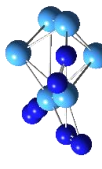
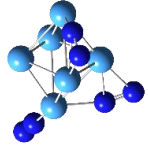
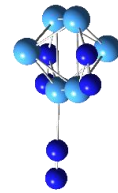
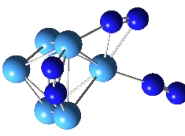
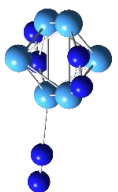
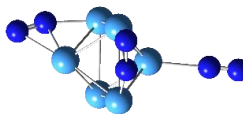
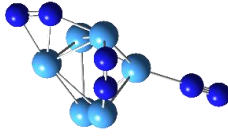
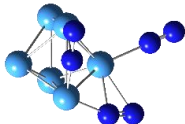
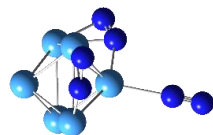
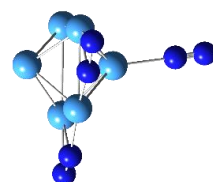
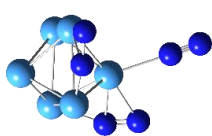
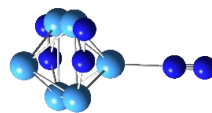
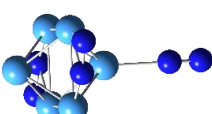
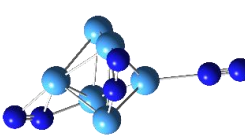
							
(6,3)a	(6,3)b	(6,3)c	(6,3)d	(6,3)e	(6,3)f	(6,3)g	(6,3)h
e							
							
(6,3)i	(6,3)j	(6,3)k	(6,3)l	(6,3)o	(6,3)p	(6,3)q	(6,3)r
(6,3)j							
							
(6,3)s	(6,3)t	(6,3)u	(6,3)v	(6,3)w	(6,3)x	(6,3)y	(6,3)z

Table S7c2: DFT optimized structures of cluster adsorption isomers (6,3) in the doublet state. Isomers shown in bold are chosen for further discussion. For calculated energies, IR frequencies and graphical representation of those, see Tab. S6c2, Fig. S7.

						
(6,3)I	(6,3)II	(6,3)III	(6,3)IV	(6,3)V	(6,3)VI	(6,3)VII
						
(6,3)VIII	(6,3)IX	(6,3)X	(6,3)XI	(6,3)XII	(6,3)XIII	(6,3)XIV
						
(6,3)XV	(6,3)XVI	(6,3)XVII	(6,3)XVIII	(6,3)XIX	(6,3)XX	(6,3)XXI

5. Cryo-IR Spectroscopy and Cryo-Kinetics of Cluster N_2 Adsorbate Complexes of Tantalum Cluster Cations Ta_{5-8}^+

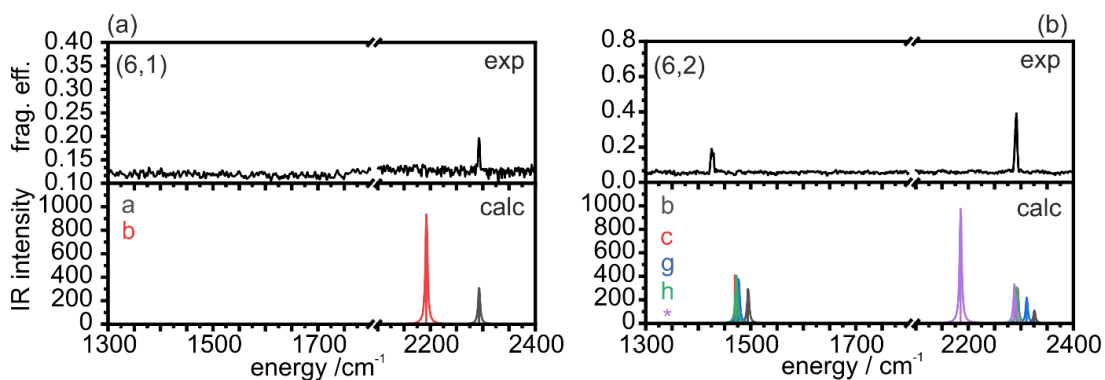


Figure S6: Experimental IR-PD spectra and DFT modelling of (6,1), (a), and (6,2), (b), respectively. The predicted IR frequencies are scaled by a factor of 0.9586. For calculated energies and IR frequencies of the shown structural isomers of (6,1) see Tab. S6a and Tab. S7a. For calculated energies and IR-PD frequencies of the shown structural isomers of (6,2), see Tab. S6b and Tab. S7b.

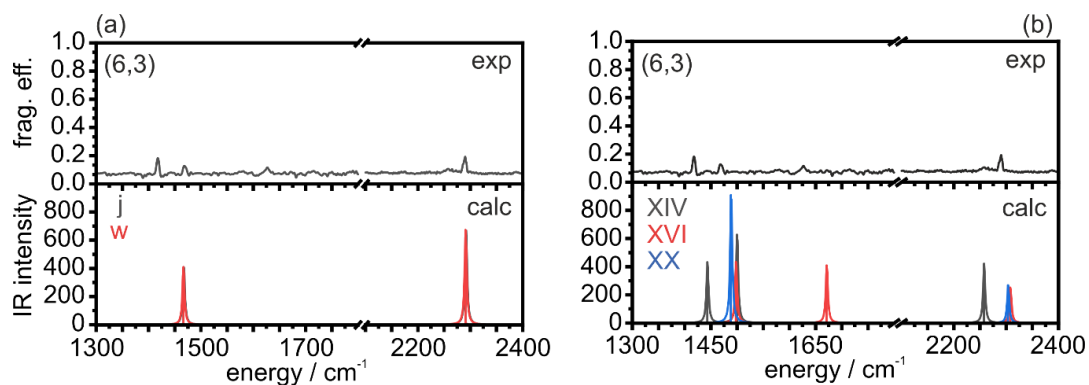


Figure S7: Experimental IR-PD spectra and DFT modelling of (6,3). The predicted IR frequencies are scaled by a factor of 0.9586. For calculated energies and IR frequencies of the shown structural isomers of (6,3), see Tab. S6c and Tab. S7c.

Table S8: Bond distances $d(\text{Ta}_{\kappa(\text{N},\text{N})}\text{-N}_{\text{side-on}(\mu 1)})$ and angles $\angle(\text{Ta}_{\kappa(\text{N},\text{N})}\text{-Ta}_{\kappa(\text{N})}\text{-N}_{\text{side-on}(\mu 1)})$ of computed isomers of the cluster species (6,3) indicate increase an increasing tilt of the $\mu 2\text{-}\kappa\text{N}:\kappa\text{N},\text{N}$ $\text{N}_{2(\text{side-on})}$ ligand with the observed red shift of its IR-PD vibrational frequency. The predicted IR frequencies are scaled by a factor of 0.9586.

	$d(\text{Ta}_{\kappa(\text{N},\text{N})}\text{-N}_{\text{side-on}(\mu 1)}) / \text{\AA}$	$\angle(\text{Ta}_{\kappa(\text{N},\text{N})}\text{-Ta}_{\kappa(\text{N})}\text{-N}_{\text{side-on}(\mu 1)}) / ^\circ$	$\nu_{\text{N}_{2(\text{side-on})}(\text{scaled})} / \text{cm}^{-1}$
a	2.08947	40.91829	1506
b	2.05810	40.68829	1485
c	2.06306	40.79344	1490
d	2.06156	40.67260	1488
e	2.07524	40.39410	1489
f	2.07297	40.49036	1485
g	2.08019	40.53546	1500
h	2.04623	40.29155	1469
i	2.04860	40.42159	1472
j	2.04338	40.31689	1467
k	2.0464	40.28260	1471
l	2.05502	40.35606	1487
o	2.04568	40.28351	1476
p	2.06233	40.72937	1496
q	2.08014	40.53481	1500
r	2.07528	40.39470	1490
s	2.04626	40.29202	1469
t	2.06133	40.66508	1488
u	2.07299	40.49033	1485
v	2.05811	40.68883	1485
w	2.04342	40.31785	1467
x	2.08949	40.91941	1506

Table S9: Calculated bond length in \AA of atoms within several (6,m) cluster complexes in the doublet state. The four elongated bonds (marked in bold) form an equatorial square.

	(6,0)	(6,1)	(6,2)c	(6,2)h
Ta1-Ta6	2.49747	2.55366	2.56514	2.66571
Ta1-Ta2	2.94797	2.74873	2.67640	2.68645
Ta1-Ta5	2.49752	2.55005	2.55672	2.65279
Ta1-Ta3	2.94991	2.96555	3.25006	3.06375
Ta4-Ta2	2.75581	2.74882	3.06371	3.25010
Ta4-Ta6	2.57804	2.55353	2.55881	2.53633
Ta4-Ta3	2.75606	2.96578	2.70891	2.70893
Ta4-Ta5	2.57808	2.55003	2.55113	2.54359
Ta3-Ta6	2.54477	2.50116	2.53625	2.55879
Ta3-Ta5	2.54483	2.49811	2.54350	2.55121
Ta2-Ta6	2.54512	2.60137	2.66564	2.56518

5. Cryo-IR Spectroscopy and Cryo-Kinetics of Cluster N_2 Adsorbate Complexes of Tantalum Cluster Cations Ta_{5-8}^+

Table S10: DFT modeling and optimization of the bare cluster Ta_7^+ with multiplications 1 – 9 revealed the highly symmetric pentagonal bipyramid (pbp) in the triplet state as the most favorable geometry for the Ta_7^+ cluster framework.

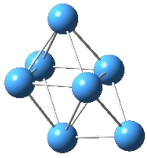
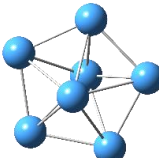
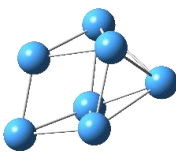
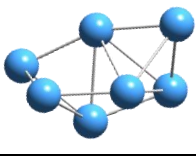
(a) capped octahedron (coh) 	multiplicity	energy E / Ha	ΔE / kJ/mol
	1	-401.867197	+174
	3	-401.871694	+162
	5	-401.873511	+157
	7	-401.864513	+181
	9	-401.833692	+262
(b) pentagonal bipyramid (pbp) 	multiplicity	energy E / Ha	ΔE / kJ/mol
	1	-401.920208	+35
	3	-401.933469	0
	5	-401.91925	+37
	7	-401.901773	+83
	9	-401.854847	+206
(c) capped trigonal prism (ctp1) 	multiplicity	energy E / Ha	ΔE / kJ/mol
	1	-401.871933	+162
	3	-401.870444	+165
	5	-401.873716	+157
	7	-401.864513	+181
	9	-401.834897	+259
(d) capped trigonal prism (ctp2) 	multiplicity	energy E / Ha	ΔE / kJ/mol
	1	-401.837909	+251
	3	-401.847564	+226
	5	-401.845557	+231
	7	-401.864516	+181
	9	-401.833692	+262

Table S11a: Calculated energies and IR frequencies (scaling factor 0.9512) of the cluster adsorption isomers (7,1) in the triplet state. Isomers shown in bold are chosen for further discussion. For graphical representation of those, see Fig. S8.

	$\nu_{\text{NNend-on}}$ cm ⁻¹	$\nu_{\text{NNend-on}}$ (scaled) cm ⁻¹	$\nu_{\text{NNside-on}}$ cm ⁻¹	$\nu_{\text{NNside-on}}$ (scaled) cm ⁻¹	energy E Ha	ΔE kJ/mol
a	2325	2212	-	-	-511.390076	+11
b	2412	2294	-	-	-511.394375	0

Table S11b: Calculated energies and IR frequencies (scaling factor 0.9512) of the cluster adsorption isomers (7,2) in the triplet state. Isomers shown in bold are chosen for further discussion. For graphical representation of those, see Fig. S8.

	$\nu_{\text{NNend-on}}$ cm ⁻¹	$\nu_{\text{NNend-on}}$ (scaled) cm ⁻¹	$\nu_{\text{NNside-on}}$ cm ⁻¹	$\nu_{\text{NNside-on}}$ (scaled) cm ⁻¹	energy E Ha	ΔE kJ/mol
a	2319, 2326	2205, 2213	-	-	-620.844428	+28
b	2318, 2322	2205, 2208	-	-	-620.847154	+20
c	2319, 2397	2205, 2280	-	-	-620.851052	+10
d	2408, 2409	2290, 2292	-	-	-620.854919	0
e	2301, 2325	2189, 2211	-	-	-620.846087	+23
f	2346, 2360	2231, 2245	-	-	-620.843849	+29

5. Cryo-IR Spectroscopy and Cryo-Kinetics of Cluster N_2 Adsorbate Complexes of Tantalum Cluster Cations Ta_{5-8}^+

Table S11c: Calculated energies and IR frequencies (scaling factor 0.9512) of the cluster adsorption isomers (7,3) in the triplet state. Isomers shown in bold are chosen for further discussion. For graphical representation of those, see Fig. S9.

	$\nu_{NNend-on}$ cm ⁻¹	$\nu_{NNend-on}(scaled)$ cm ⁻¹	$\nu_{NNside-on}$ cm ⁻¹	$\nu_{NNside-on}(scaled)$ cm ⁻¹	energy E Ha	ΔE kJ/mol
a	2317, 2319, 2354	2204, 2206, 2239	-	-	-730.300715	+18
b	2317, 2335, 2353	2204, 2221, 2238	-	-	-730.301611	+16
c	2332, 2349, 2380	2218, 2235, 2264	-	-	-730.304946	+7
d	2310, 2318, 2383	2197, 2205, 2267	-	-	-730.307690	0
e	2294, 2320, 2341	2182, 2207, 2227	-	-	-730.300511	+19
f	2296, 2321, 2327	2184, 2208, 2213	-	-	-730.303481	+11
g	2289, 2322, 2382	2177, 2208, 2265	-	-	-730.307294	+1
h	2314, 2338, 2354	2201, 2224, 2239	-	-	-730.301947	+15
i	2340, 2355, 2389	2226, 2241, 2273	-	-	-730.305408	+6

Table S12a: DFT optimized structures of cluster adsorption isomers (7,1) in the triplet state. Isomers shown in bold are chosen for further discussion. For calculated energies, IR frequencies and graphical representation of those, see Tab. S11a, Fig. S8.

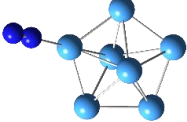
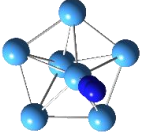
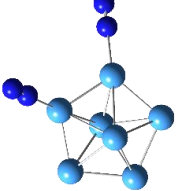
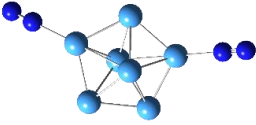
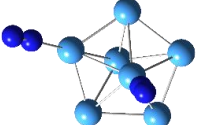
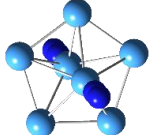
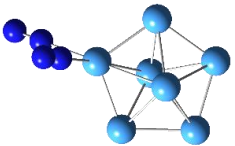
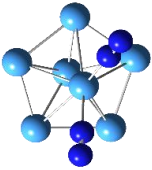
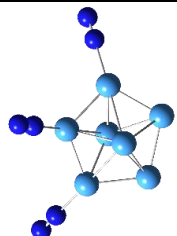
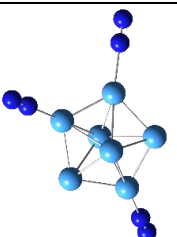
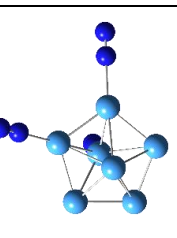
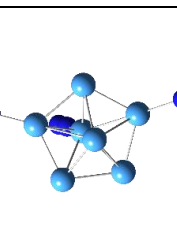
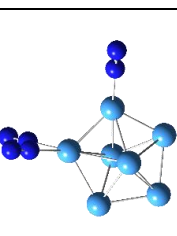
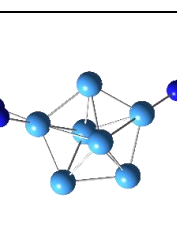
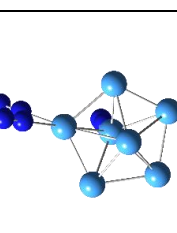
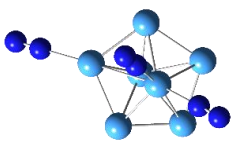
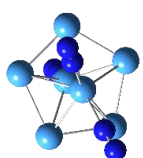
(7,1)a	(7,1)b				
					

Table S12b: DFT optimized structures of cluster adsorption isomers (7,2) in the triplet state. Isomers shown in bold are chosen for further discussion. For calculated energies, IR frequencies and graphical representation of those, see Tab. S11b, Fig. S8.

(7,2)a	(7,2)b	(7,2)c	(7,2)d	(7,2)e	(7,2)f
					

5. Cryo-IR Spectroscopy and Cryo-Kinetics of Cluster N_2 Adsorbate Complexes of Tantalum Cluster Cations Ta_{5-8}^+

Table S12c: DFT optimized structures of cluster adsorption isomers (7,3) in the triplet state. Isomers shown in bold in the caption are chosen for further discussion. For calculated energies, IR frequencies and graphical representation of those, see Tab. S11c, Fig. S9.

(7,3)a		(7,3)b		(7,3)c		(7,3)d		(7,3)e		(7,3)f		(7,3)g	
(7,3)h		(7,3)i											

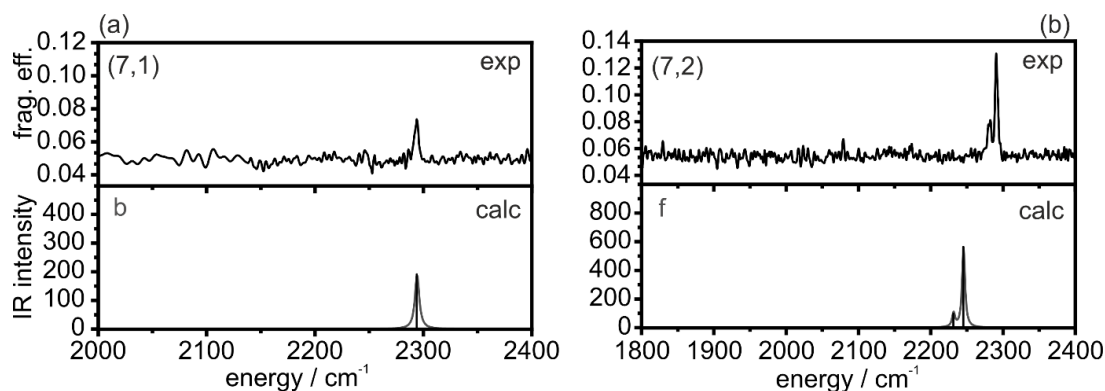


Figure S8: Experimental IR-PD spectra and DFT modelling of (7,1), (a), and (7,2), (b), respectively. The predicted IR frequencies are scaled by a factor of 0.9512. For calculated energies and IR frequencies of the shown structural isomers of (7,1), see Tab. S9a and Tab. S11a. For calculated energies and IR-PD frequencies of the shown structural isomers of (7,2), see Tab. S9b and Tab. S11b.

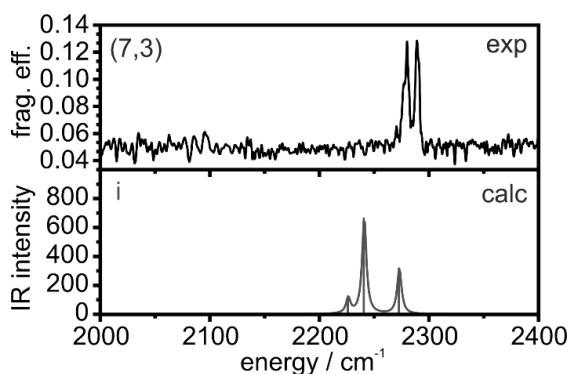


Figure S9: Experimental IR-PD spectrum and DFT modelling of (7,3). The predicted IR frequencies are scaled by a factor of 0.9512. For calculated energies and IR frequencies of the shown structural isomers of (7,1), see Tab. S10c and Tab. S11c.

5. Cryo-IR Spectroscopy and Cryo-Kinetics of Cluster N_2 Adsorbate Complexes of Tantalum Cluster Cations Ta_{5-8}^+

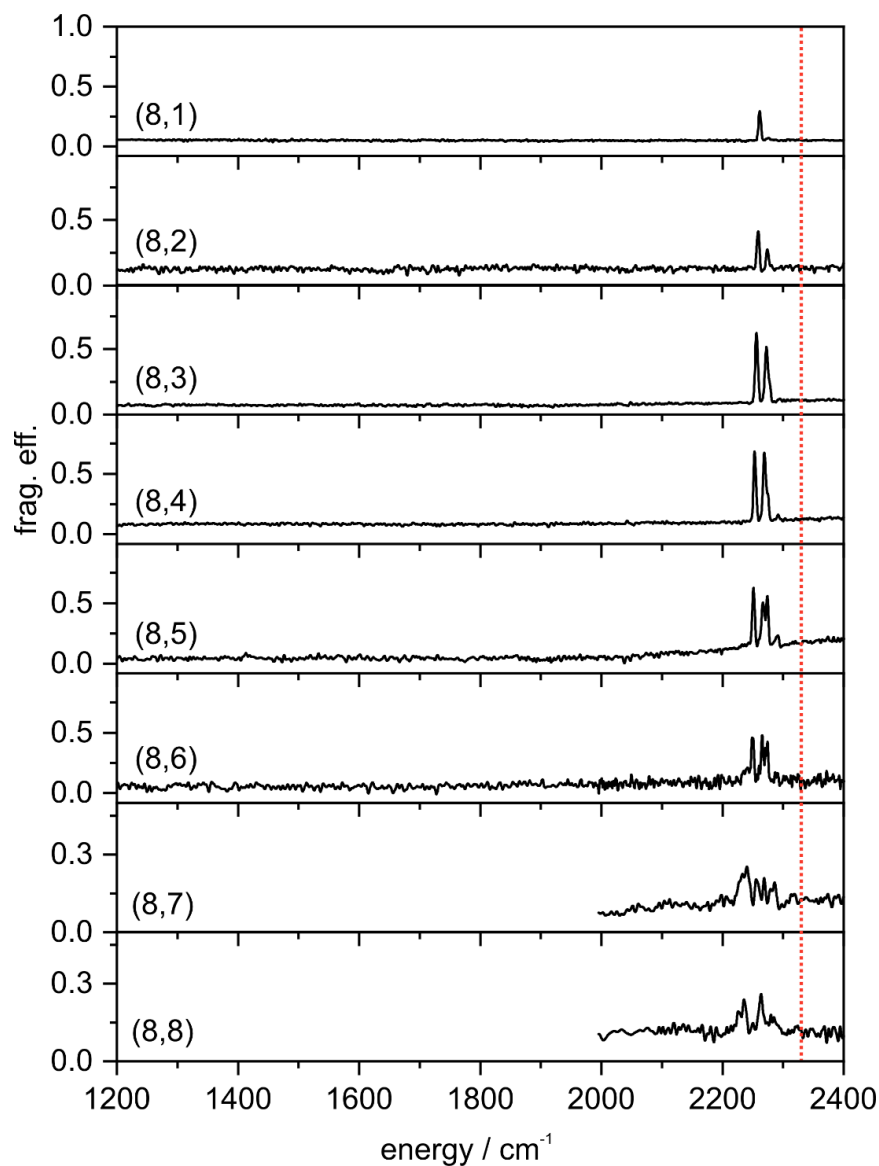


Figure S10: IR-PD spectra of sequential N_2 adsorption steps onto Ta_8^+ cluster cations $[Ta_8(N_2)_m]^+$, $m = 1 - 8$ as recorded after 26 K He buffer gas cooling. Note the significant red-shift of the IR-PD bands with respect to the free N_2 stretching vibrational frequency (2330 cm^{-1} ⁸, red dotted line).

Text S2: Introduction with a focus on kinetic studies

The paramount significance of catalytic conversions renders it necessary to augment process optimization with fundamental knowledge. It is e.g. the catalytically enabled valorization of ubiquitous N_2 which accounts for around 2 % of total final energy consumption worldwide.⁹ Heterogeneous catalysis is the backbone of such conversions, and it most often utilizes catalysts that incorporate Transition Metals (TM), either in the form of bulk or nanostructured materials.^{10, 11} Any further optimization of this and other catalyzed processes thus promises for economic benefits, and it would help to launch sustainability and provide for environmental protection. Thus, the afore mentioned fundamental knowledge may well assist and support such practical optimization.

The investigation of isolated TM clusters may seem vaguely related to these quests, at first glance. However, it is mandatory to describe and understand materials and elementary processes at the molecular level, and atomically precise TM clusters may serve in this regard.^{12, 13} Reaction enthalpies and prevailing barriers determine the kinetics: Catalytic macro kinetics manifest in the magnitudes of empirical turn over numbers, and micro kinetics in the reaction rates of chosen elementary steps. Most often, the bimolecular reaction rates of TM clusters with single molecules reveal size-dependent variations, that are deeply interweaved with the electronic and geometric structures of the bare TM cluster and of the cluster adsorbate product complexes.^{14, 15} Several reactivity studies of various TM cluster kinetics with small molecules have revealed remarkable cluster size dependencies, in particular for small clusters.¹⁶⁻²⁵

The kinetics of N_2 adsorption on Ag_n^+ clusters reveal first step rate coefficients that increase exponentially from $n = 1 - 7$, which was interpreted in terms of an increase of internal degrees of freedom with cluster size.¹⁶ Extensive reaction studies of nickel group cluster anions with N_2 , O_2 , CO_2 , and N_2O found parallel trends of the first step rate coefficients and the adsorption limits, both of which increase with cluster size. Notably, the observed saturation effects imply rearrangements in the cluster core upon high reactant loads.^{18, 26} A wealth of extensive kinetic reactivity studies with Rhodium cations was reviewed before.¹⁹ The relative reaction rates of small Rh_n clusters with N_2 and D_2 were found to increase sharply from $n = 3$ and $n = 5$ on, respectively,²⁰ and kinetic investigations of Rh_n^+ , $n = 6 - 16$ with NO managed to distinguish various

5. Cryo-IR Spectroscopy and Cryo-Kinetics of Cluster N_2 Adsorbate Complexes of Tantalum Cluster Cations Ta_{5-8}^+

cluster sizes for their highly reactive or largely inert cluster surface morphologies, with biexponential reaction kinetics of Rh_6^+ that signify coexisting isomers.^{17, 21} Small Rh_n^+ clusters revealed a cooperative auto enhancement of NO adsorption rather than cluster size dependencies which are small up to saturation of vacant adsorption sites.²⁷

Temperature-dependent reaction kinetics of cationic tantalum clusters Ta_n^+ , $n = 13 - 40$, with molecular oxygen indicate a change in the reaction mechanism from dissociative to molecular adsorption upon saturation of active surface sites.²⁸ Tantalum clusters are susceptible to oxide formation by O_2 and CO_2 .^{29, 30} We review other than kinetic investigations of tantalum clusters in the two main papers presenting our IR-PD spectroscopy studies about $Ta_{2-4}^+ + N_2$, [IRS1], and $Ta_{5-8}^+ + N_2$, [IRS2].

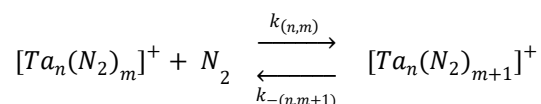
By virtue of our previous studies, we have established cryo kinetic measurements of isolated TM clusters under single collision conditions as a strong tool for the elucidation of elementary adsorption and reaction processes, as e.g. on Nb_n^+ ³¹, Ni_n^+ ^{4, 32}, Rh_n^+ ³³, $Rh_iFe_j^+$ ³⁴ and Fe_n^+ ³⁵. As in the current case, we have complemented our kinetic studies with cryo IR spectroscopic studies of the resulting cluster adsorbate species.^{1, 3, 4, 33-35} Our third line of experimental methodology, gas phase studies by the X-ray magnetic circular dichroism (XMCD) technique, would serve to elucidate high spin states and possible orbital contributions to magnetic moments of isolated clusters.^{36 37} Our quantum chemical modelling by DFT reveal, however, low spin states of all clusters and complexes of relevance in the current study.

Text S3: Further Information about Experimental and Computational Methods

The transition metal cluster ions are generated in a home-built laser vaporization (LAVP) source.^{38, 39} The second harmonic of a pulsed Nd:YAG (Innolas Spitlight 300, 20 Hz) evaporates the metal atoms from a rotating tantalum foil (99.95 %, 0.5 mm thick, Alfa Aesar). The hot plasma consisting of atoms and ions thus generated is captured by a He gas pulse (40 μ s, 15 bar) from a home-built piezoelectric valve⁴⁰. This valve operates in synchronization with the laser. The gas pulse entrains the plasma through a 69 mm long channel (2 mm diameter). The atoms and ions cool and aggregate into clusters during the subsequent jet expansion into vacuum (10^{-7} mbar). The resulting cluster size distribution passes electrostatic lenses and reaches a 90° ion beam bender. The cluster ions can be selected by size using the following quadrupole mass filter. Subsequently the (mass selected) ions are injected into the cryogenic hexapole ion trap which is cooled to 26 K by a closed cycle He cryostat. Thereby, we are able to trap required mass complexes and to continuously introduce buffer and/or reaction gas. For the present study we introduced He as buffer gas and N₂ as reaction gas. To achieve sufficient N₂ attachment to the Ta_n⁺ cluster we increased the pressure in the ion trap from 1.2×10^{-7} mbar up to a maximum of 3.5×10^{-7} mbar. The additional continuously introduced He gas ensures efficient trapping and cooling of the ions. Thus, the pressure in the ion trap increases up to 6.8×10^{-6} mbar. The ions are trapped in the hexapole ion trap for various storage times (0 – 20 s) according to the investigation procedure. For detection, the manipulated ions, [Ta_n(N₂)_m]⁺ = (n,m), are steered into the FT-ICR cell by a series of electrostatic lenses. The so-called “infinity” type cell⁴¹ is cooled down to 10 K by a closed cycle He cryostat to prevent heating of the clusters by black body radiation. If required, it is possible to isolate the ion complexes within the ICR cell. This was necessary when recording IR-PD spectra for the cryogenic infrared spectroscopy studies [IRS2], this work, and [IRS1], our adjoined IR-PD study on smaller tantalum clusters, to ensure sufficient irradiation of the ions. For the kinetic studies of N₂ adsorption to Ta_n⁺ clusters, the ICR cell served only for ion detection. Instead, the storage of ions in the hexapole filled with N₂ is of particular interest for the study of adsorption kinetics. Storage of the cluster adsorbate species (n,m) occurs under isothermal conditions at 26 K. In order to investigate the cationic tantalum clusters and their nitrogen adducts we performed reaction delay scans. The recorded mass spectrum for each reaction delay consists of an average of 40 scans. We receive a temporal evolution of mass spectra, which we

5. Cryo-IR Spectroscopy and Cryo-Kinetics of Cluster N_2 Adsorbate Complexes of Tantalum Cluster Cations Ta_{5-8}^+

evaluate to obtain signal intensities and assigned storage times for each adsorbate complex. These data serve as input for evaluation by *evofit*⁴², our in-house genetic algorithm fitting routine. The pseudo-first-order fits performed yield relative rate constants for all adsorption $k_{(n,m)}$ and desorption $k_{-(n,m+1)}$ steps.



The chosen nomenclature is in line with our previous publications⁷. For further explanation of the nomenclature for the Ta_n^+ cluster and their adsorbates we refer the reader to the supporting information.

From the relative rate constants $k_{(n,m)}$ and $k_{-(n,m+1)}$ we determine the absolute rate constants $k_{(n,m)}^{abs}$ using the absolute collision gas number densities $\rho_{N_2}(T)$ as conversion factor.

$$k_{(n,m)}^{abs} = \frac{k_{(n,m)}}{\rho_{N_2}(T)}$$

The pressure in the surrounding chamber $p_c^{(300\text{ K})}$ and an effective geometry factor c_{app} serve to obtain approximate values for the absolute collision gas number densities $\rho_{N_2}(T)$.

$$\rho_{N_2}(26\text{ K}) = \frac{c_{app} p_c^{(300\text{ K})}}{k_B T_{300\text{ K}}}$$

We determined the geometry factor as 1.8(9) at 26 K. Calculating the quotient of the absolute rate constants k^{abs} and the collision rates k^{coll} give the absolute reaction efficiency γ .

$$\gamma = \frac{k^{abs}}{k^{coll}}$$

Three models serve for determination of collision rates: The average dipole orientation (ADO) theory is based on a concept of a classical trajectory of a linear dipole in the field of a point charge where μ is the reduced mass of the cluster adsorbate complex, μ_D indicates the dipole moment and α gives the polarizability.^{43, 44}

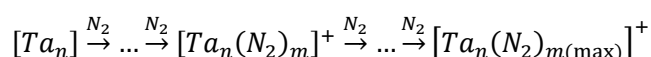
$$k^{ADO} = \frac{q}{2 \varepsilon_0 \sqrt{\mu}} \left(\sqrt{\alpha'} + c \mu_D \sqrt{\frac{2}{\pi k_B T}} \right)$$

The parameter for the polarizable volume α' and the dipole moment μ_D express parameter c which can take values from 0 to 1.⁴⁵ Note, that a vanishing dipole moment, as of N_2 , causes k^{ADO} to become identical to the Langevin rate constant. Additional effects may prevail upon TM clusters reacting with small molecules, and Kummerlöwe and Beyer⁴⁶ devised two models to approximate collision rates of ionic clusters with neutral molecules: the hard sphere average dipole orientation (HAS) model and the surface charge capture (SCC) theory. Both models share the idea that clusters and the neutral reactants are hard spheres and charge is point charge. The former one assumes the point charge in the center of the ionic cluster and according the latter one is the charge able to migrate to the cluster surface by its attractive interaction with the neutral collision partner.

5. Cryo-IR Spectroscopy and Cryo-Kinetics of Cluster N_2 Adsorbate Complexes of Tantalum Cluster Cations Ta_{5-8}^+

Text S4: Trends and limits of N_2 adsorption on tantalum cluster

To investigate the adsorption behavior of nitrogen molecules on Ta_n^+ clusters of cluster sizes $n = 2 - 8$, each cluster species was isolated in the quadrupole mass filter and stored in the hexapole ion trap at 26 K. At the same time, nitrogen (up to $3.5 \cdot 10^{-7}$ mbar) was continuously introduced as reaction gas into the hexapole. For all cluster sizes, a progression $\Delta m = 28$ m/z was observed, which implies a stepwise adsorption of molecular nitrogen according to:



The N_2 adsorption to each cluster Ta_n^+ reaches a limit $m_{(\max)}$, which depends on cluster size n . (Fig S11, disk symbols) Beyond this limit neither an increase of N_2 pressure nor an increase of storage time leads to further N_2 adsorption. While the tantalum dimer cation, Ta_2^+ , merely adsorb a single nitrogen molecule, the tantalum trimer cation, Ta_3^+ , manages to accommodate up to 11 N_2 molecules. In remarkable contrast to this steep incline, the Ta_4^+ and Ta_5^+ accept another two and three nitrogen molecules, respectively. Ta_5^+ and all larger clusters up to Ta_8^+ accept 16 N_2 irrespective of their size; there is no further incline.

The steep increase in N_2 adsorption from Ta_2^+ to Ta_3^+ is remarkable, and it is in equally remarkable contrast to the plateau at Ta_5^+ and beyond. Our previous investigation of N_2 adsorption limits of other transition metal clusters have revealed an increasing trend of N_2 adsorption limits with increasing cluster size with a close to 1:1 stoichiometry in cases of Fe_n^+ ³⁵, Ni_n^+ ³², and a close to 1:2 stoichiometry in the case of Rh_n^+ ³³ (cf. Fig. S12). This may be due to the fact that the transition metals Fe and Ni are 3d metals, Rh is a 4d metal, while tantalum is a 5d transition metal.

Further findings deserve attention: In the cases of Ta_2^+ and Ta_3^+ the largest observable cluster adsorbate complex $[Ta_2(N_2)_{m(\max)}]^+$ and $[Ta_3(N_2)_{m(\max)}]^+$, respectively, are the most abundant complexes in equilibrium m^* (Fig. S11, solid triangles). This is clearly not the case for larger tantalum clusters. In equilibrium there are three distinct levels of N_2 adsorption: highest amount and lowest amount of N_2 observed, $m_{(\max)}$ and $m_{(\min)}$ (Fig. S11, open circles and open triangles, respectively), and most intense species with m^* N_2 adsorbates (Fig. S11 solid triangles). The most abundant cluster adsorbate

complex in equilibrium possesses one to 4 N_2 adsorbates less. The orange shaded area in figure 1 emphasizes the observed range of N_2 adsorption in equilibrium. For observed intensities of all $[Ta_n(N_2)_m]^+$ species in equilibrium refer to Fig. S13.

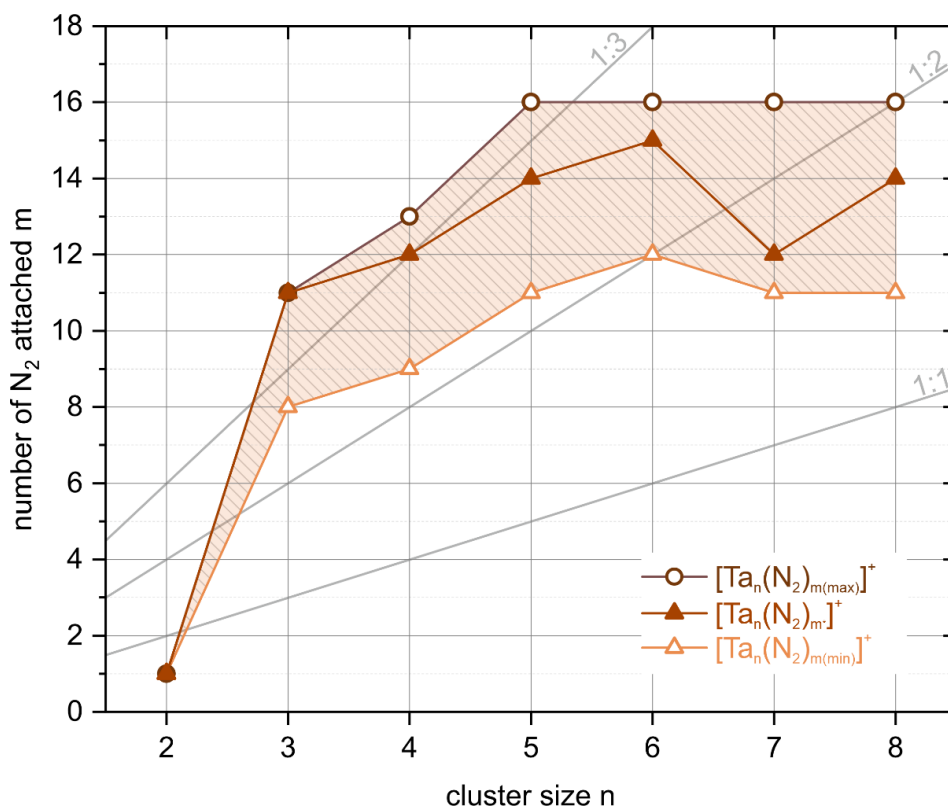


Figure S11: Plot of the experimentally determined adsorption limits $m_{(\max)}$ (open circles) of N_2 on Ta_n^+ clusters, $n = 2-8$, when stored in the hexapole ion trap with 26 K Helium buffer gas. In equilibrium (at up to 20 s, exposure to $3.5 \cdot 10^{-7}$ mbar N_2) there are two more distinct levels of N_2 adsorption: lowest amount of N_2 observed $m_{(\min)}$ (open triangles) and most intense species with m^* N_2 adsorbates (solid triangles). The orange shaded area emphasizes the observed range of N_2 adsorption in equilibrium.

5. Cryo-IR Spectroscopy and Cryo-Kinetics of Cluster N_2 Adsorbate Complexes of Tantalum Cluster Cations Ta_{5-8}^+

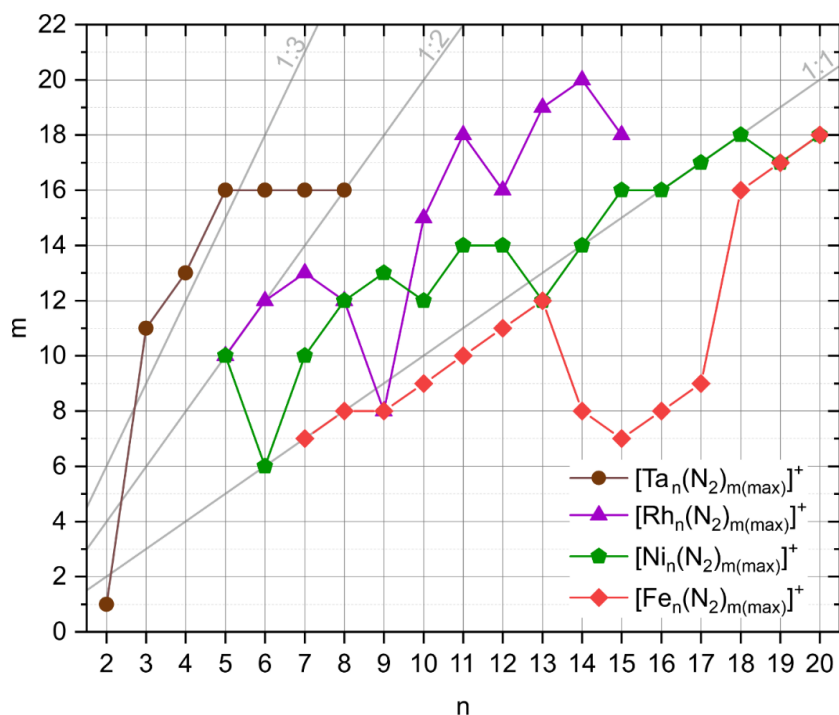


Figure S12: Plot of the experimentally determined adsorption limits $m_{(max)}$ of N_2 on Ta_n^+ , Rh_n^{+33} , Ni_n^{+32} and Fe_n^{+35} clusters when stored in the hexapole ion trap with 26 K Helium buffer gas.

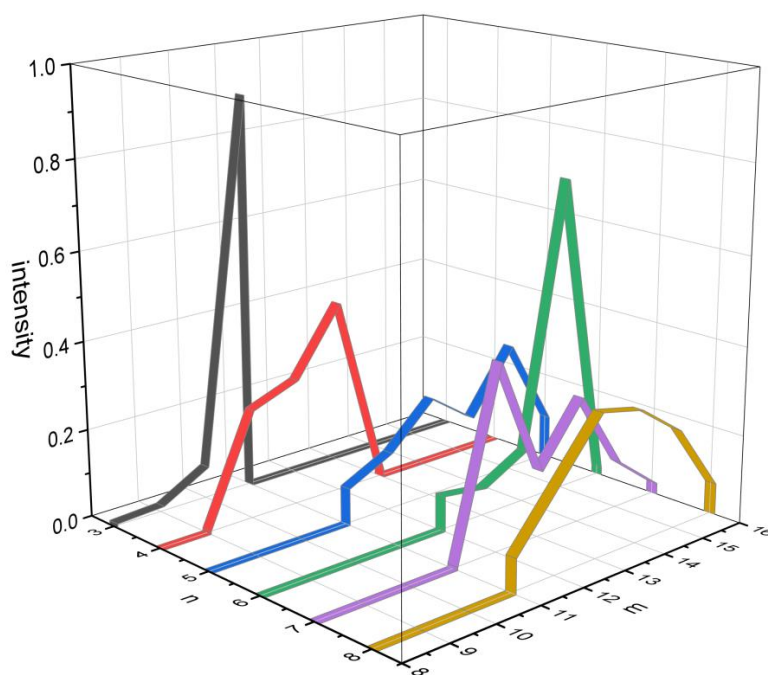


Figure S13: 3D plot of observed intensities of all $[\text{Ta}_n(\text{N}_2)_m]^+$, (n,m) , species in equilibrium. Supporting plot to the orange shaded area in Fig. S11.

Text S5: Cryo kinetics and rate constants of N_2 adsorption to tantalum clusters

Our kinetic measurements reveal the temporal evolution of the adsorbate intensities for each N_2 adsorption step onto the Tantalum clusters Ta_n^+ , $n = 2 - 8$. We fit the intensity data with a pseudo-first-order kinetic approach using our genetic algorithm routine *evofit*⁴². The obtained fits confirm consecutive N_2 adsorption steps to Ta_n^+ cluster, $n = 2 - 8$, and varying amounts of N_2 desorption at higher levels of N_2 loads.

Text S6: Absolute rate constants of the initial N_2 adsorption steps

Before we start a presentation and discussion of the kinetics of each cluster size, we have a glance at the magnitude of the initial rate constant of adsorption as a function of Tantalum cluster size (Fig. S17). By normalization to the collision gas density, we derive these absolute rate constants $k_{(n,0)}^{\text{abs}}$ from the pseudo-first-order fit of relative rate constants $k_{(n,m)}$, as fitted for all steps of N_2 uptake and release and as to discuss later.

5. Cryo-IR Spectroscopy and Cryo-Kinetics of Cluster N_2 Adsorbate Complexes of Tantalum Cluster Cations Ta_{5-8}^+

We have observed before in the case of Rhodium clusters Rh_n^+ a gradual increase of the absolute rate constants $k^{\text{abs}}_{(n,0)}$ with increasing n starting at $n = 5$ ³³. Neutral Rhodium clusters seem to reveal same behavior.²⁰ Ta_n^+ cluster, $n \leq 4$, are almost unreactive towards CO; for larger clusters above $n = 5$, the CO binding rate increases abruptly by at least three orders of magnitude.²⁵ We find a like increase of rate constants in the current study of cationic Tantalum clusters (Figs. S17 and S18). Effective $n = 7$ and beyond, both Rh_n^+ and Ta_n^+ assume N_2 adsorption rates $k^{\text{abs}}_{(n,0)}$ of same values, void of further increase. The steep rise from $k^{\text{abs}}_{(5,0)}$ to $k^{\text{abs}}_{(7,0)}$ may find an interpretation in terms of $[Ta_n(N_2)_1]^+$ heat capacities: The larger the internal heat bath – roughly scaling with the cluster size n – the more irreversible the N_2 adsorption enthalpy redistributes, and at some point – here $n = 7$ – the N_2 desorption fades out. Prior modelling of Kummerlöwe et al. devised a Surface Charge Capture Model (SCC, k^{SCC}), and a Hard Sphere Average Dipole Orientation Model (HAS, k^{HSA})⁴⁶. These serve to complement the established Average Dipole Orientation Theory (ADO, k^{ADO}), and the Langevin capture cross section. Application of these models to the current case of $Ta_n^+ + N_2$ adsorption compares well with the determined absolute rate constants $k^{\text{abs}}_{(7,0)}$ and $k^{\text{abs}}_{(8,0)}$, which fall in between of k^{SCC} and k^{HSA} (Fig. S17, Tab. S13). Under present conditions, values of k^{ADO} , k^{Langevin} , and k^{HSA} coincide.

The most noteworthy cases of $k^{\text{abs}}_{(2,0)}$, $k^{\text{abs}}_{(3,0)}$, and $k^{\text{abs}}_{(4,0)}$ do require special attention: from Geng et. al.⁴⁷ we know, that Ta_2^+ activates N_2 . Our combined IR-PD and DFT studies Fries et. al.⁷ and **[IRS1]**, main paper, confirm like abilities of Ta_3^+ and Ta_4^+ . All of these activations are highly exothermic, and they reveal most stable nitride products which are resilient against N_2 release. Void of entrance barriers, the Ta_2^+ and Ta_3^+ and Ta_4^+ clusters experience no kinetic hindrance. While Ta_3^+ and Ta_4^+ digest N_2 collision partners with collision rate, the Ta_2^+ cluster seem to experience some steric hindrance, and it might happen that unfavorable N_2 orientations upon mutual approach are highly likely. While the entrance channel barrier of N_2 activation by Ta_2^+ is submerged, the concomitant transition state thus seems to be narrow, and it reduces the effective capture rate $k^{\text{abs}}_{(2,0)}$ by more than an order of magnitude as observed.

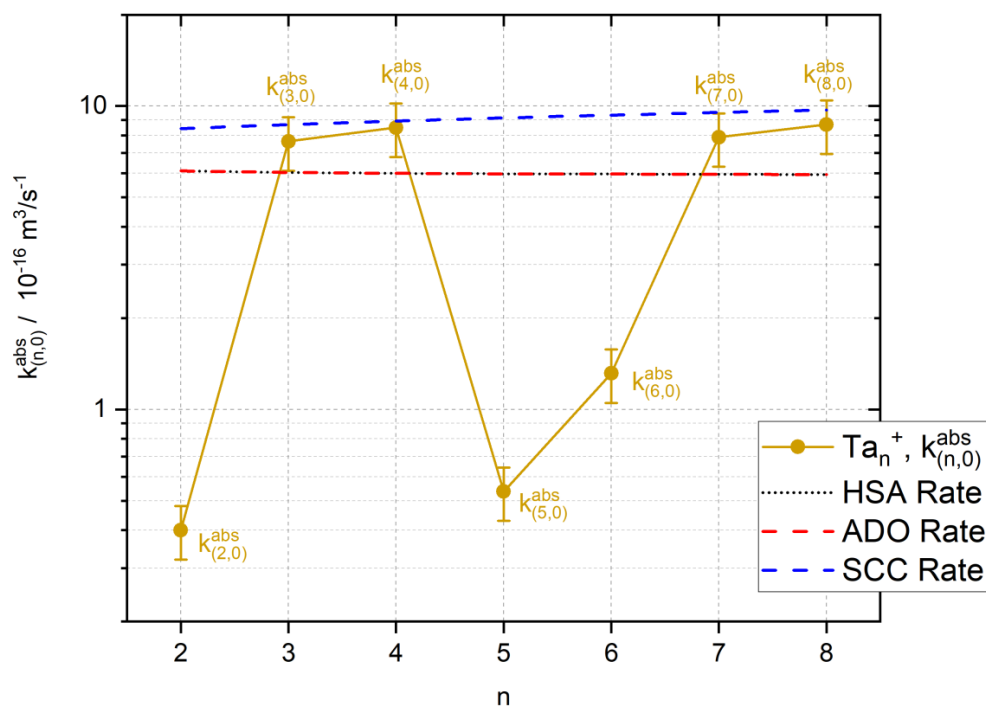


Figure S17: Absolute experimental rate constants $k_{(n,0)}^{abs}$ of for the adsorption of the first N_2 molecule to the Tantalum clusters Ta_n^+ , $n = 2 - 8$ as a function of cluster size n (solid dots), collision rates by average dipole orientation (ADO) theory (red dashed line), and by the hard sphere average (HSA) dipole orientation model (black dotted line), and by the surface charge capture (SCC) model (blue dashed line). Numerical values are listed in Tab. S13.

5. Cryo-IR Spectroscopy and Cryo-Kinetics of Cluster N_2 Adsorbate Complexes of Tantalum Cluster Cations Ta_{5-8}^+

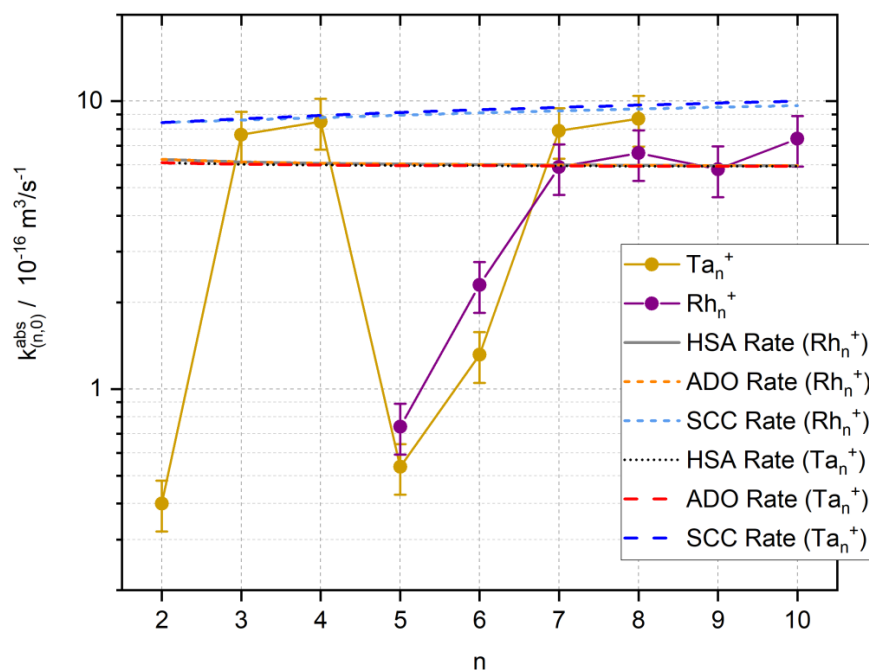


Figure S18: Absolute rate constants $k_{(n,0)}^{abs}$ of for the adsorption of the first N_2 molecule to the Tantalum clusters Ta_n^+ , $n = 2 - 8$ and Rh_n^+ , $n = 5 - 10$ ³³, as a function of cluster size n (green dots, estimated error bars), compared to classical average dipole orientation (ADO) theory (red dashed line), to the hard sphere average (HAS) dipole orientation model (black dotted line), and to the surface charge capture (SCC) model (blue dashed line). Numerical values for Ta_n^+ are listed in Table S13.

Table S13: Relative experimental and derived absolute N₂ adsorption rate constants for the initial N₂ adsorption to Ta_n⁺ clusters in comparison to the calculated rate constants by classical ADO theory, the HSA model, and the SCC model (see Tab. S2). The experimental values, recorded at 2.8 – 6.8*10⁻⁶ mbar He buffer gas and 2.0 – 3.5*10⁻⁷ mbar N₂ within the RF hexapole ion trap at 26 K, bear an estimated uncertainty of ±20 %.

n	k _(n,0) s ⁻¹	k ^{abs} _(n,0) 10 ⁻¹⁶ m ³ s ⁻¹	k ^{ADO} _(n,0) 10 ⁻¹⁶ m ³ s ⁻¹	K ^{HSA} _(n,0) 10 ⁻¹⁶ m ³ s ⁻¹	K ^{SCC} _(n,0) 10 ⁻¹⁶ m ³ s ⁻¹
2	0.56	0.40	6.11	6.11	8.42
3	8.30	7.64	6.04	6.04	8.68
4	9.58	8.48	6.00	6.00	8.92
5	0.60	0.54	5.98	5.98	9.14
6	2.00	1.31	5.96	5.96	9.33
7	8.91	7.88	5.95	5.95	9.52
8	7.55	8.69	5.95	5.95	9.69

5. Cryo-IR Spectroscopy and Cryo-Kinetics of Cluster N₂ Adsorbate Complexes of Tantalum Cluster Cations Ta₅₋₈⁺

Table S14: Input data for determination of absolute rate constants according to the theories of Average Dipole Orientation (ADO), Hard-Sphere (HAS) and Surface Capture (SCC) theory. We compared our absolute rate constants with the three models employed by Kummerloewe and Beyer and used their software.⁴⁶ We used the viscosity of N₂ at 300K.

Entity (unit)	value
m(N ₂) / 10 ⁻²⁶ kg	4.65
k _B / 10 ⁻²³ J*K ⁻¹	1.38
T / K	300
η / 10 ⁻⁶ Pa*s ⁴⁸	17.9
α(N ₂) 10 ⁻⁴⁰ C*m ² *V ⁻¹	1.97
μ(N ₂) / 10 ⁻³⁰ C*m	0
Dipole licking constant	0
m(N ₂) / amu	28
r(N ₂) / Å	1.85
Maximum cluster size	8
Monomer mass / amu	181
δ(Ta) / g*cm ⁻³ ⁸	16.63
Temperature / K (used in ADO/HSA)	26
Cluster charge state	1

Text S7: Ta₅(N₂)_m⁺ - Cryo kinetics and rate constants

We recorded the cryo kinetics, at 26 K, of the N₂ adsorption onto a Ta₅⁺ cluster (cf. Fig. S19, S20 and S21). The Ta₅⁺ cluster adsorbs N₂ up to saturation at (5,m), m = 16. Up to a collision cell delay of 2 s we observe such stepwise uptake of 14 N₂ molecules (cf. Fig. S19(a)). These recorded kinetic curves allow for a fitting with a pseudo-first-order model kinetic of stepwise adsorption and concurrent desorption of N₂ adsorbates. The application of our genetic algorithm routine *evofit*⁴² manages to achieve such an overall fit of high quality (cf. Fig. S19, correlation coefficient $\rho = 0.993$). The thereby fitted rate constant for the adsorption of the first N₂ molecule results in a low value of $k_{(5,0)} = 0.61 \text{ s}^{-1}$ which indicates a slow adsorption process, as obvious by the slow decrease of (5,0). Seven subsequent adsorption steps up to (5,8) proceed with successively increasing adsorption rate constants. The adsorption of the eighth N₂ molecule appears to be the fastest, $k_{(5,7)} = 9.80 \text{ s}^{-1}$, in the course of the 14 fitted adsorption steps. From then on, the adsorption rate constants decrease successively from 4.61 s^{-1} , $k_{(5,8)}$ to 0.34 s^{-1} , $k_{(5,13)}$. Note, that for all adsorption processes up to species (5,4) the N₂ desorption appears to be insignificant, yielding vanishing values of $k_{-(5,1)}$ through $k_{-(5,5)}$, within our experimental limits. It is for $k_{-(5,6)}$ and beyond, that desorption rate constants become significant. The “smooth surface” like ⁴ parallel evolution of ion intensities at a collision delay time of 2 s suggests all equivalent adsorption sites. The fitted values of the corresponding desorption rate constants are significant, despite a lack of visual recognition in the recorded ion intensity data at first glance.

Beyond a collision cell delay of 2 s, the recorded data of ion intensities reveal some counter-intuitive trends of (5,0) and (5,1) (cf. Fig. S20a), and these are much beyond an unequivocal interpretation. The occurrence of these counter-intuitive trends was reproducible, but their magnitude varied. There is no clear correlation with measurement parameters such as reaction and collision gas pressures as well as ion-optical potentials. (cf. Fig. S20 and S21). Moreover, we were not able to provide a reasonable kinetic model that would fit these recorded kinetic data at long reaction times. For further discussion refer to Text S8 in the supplement.

Despite these intermediate uncertainties, the long time kinetics of collision cell delays of 10 s and beyond reveal meaningful and reproducible data. We observe horizontal

5. Cryo-IR Spectroscopy and Cryo-Kinetics of Cluster N_2 Adsorbate Complexes of Tantalum Cluster Cations Ta_{5-8}^+

and parallel ion intensity curves for the ultimate adsorbate species (5,m), $m = 11 - 16$. Under all circumstances, (5,15) dominates. This indicates that these six species are in a dynamic equilibrium of adsorption and desorption reactions at these long reaction times.

Text S8: Discussion of long time kinetics of (5,m)

Beyond a collision cell delay of 2 s, the recorded data of ion intensities reveal some counter-intuitive trends of (5,0) and (5,1) (cf. Fig. S20a), and these are subject of interpretation with a significant level of speculation. Despite high effort, we did not achieve any satisfactory fit of the intensity data from 2 s to 20 s. Acquiescing this defeat, we tempt to speculate on the basis of findings from prior cases of N_2 adsorption on tantalum clusters of other sizes and transition metal clusters in general ^{4, 32-35}:

Hypothetical concept #1: Spin quenching. At a certain point of N_2 loading, all previously adsorbed ligands might desorb at some point all at once, for some reason, and release naked Ta_5^+ clusters, which enables the “belly” of (5,0) intensities at 2 s and beyond. The necessary driving force is questionable: From DFT modeling we know N_2 binding energies of about 40 kJ/mol per adsorption step (cf. Fig. 2, S2 and Table S2). A sudden N_2 boiling off would require copious amounts of activation, likely up to 100 kJ/mol and beyond. The product species (5,0)' and (5,1)' would need to possess equal amounts of enhanced stabilities with respect to the original/prior (5,0) and (5,1) species. Adsorption-induced spin quenching and/or structural relaxation at high N_2 coverage might provide for such a delayed stabilization. Note, that our modeled spin-valley curves in Fig. 2 suggest some spin quenching of triplet to singlet states upon N_2 loads of 5 adsorbates and beyond. The computed energetics, however, are not fully in line with this hypothesis. Further computations at enhanced levels of theory, such as e.g. multi reference modelling, would be highly ambitious.

Hypothetical concept #2: Isomers. Further deliberations on course of the recorded ion intensities, in particular the one of (5,0), at collision cell delays between 2 s and 5 s as plateau, might open up a new interpretation approach. One might consider two initial isomers of (5,0) which differ either in geometries or electronic states. One of them might show a delayed N_2 adsorption ability and thus causes the shifted decrease of ion intensities as recorded. This might continue with a diminishing amplitude along the

progressing chain of further stepwise N₂ adsorptions. We failed, however, to achieve a satisfactory fit of the recorded ion intensities by an according kinetic model.

Hypothetical concept #3: Ion trap issues. N₂ adsorption events take place within a cryogenized RF hexapole trap, and under isothermal conditions by virtue of an inert He buffer gas. Spurious RF ion heating effects are known for their hardly predictable mass dependencies.⁴⁹⁻⁵² It might be the case, that we experience such artefact like effects in the present cases of (5,m) kinetics. It truly the case it would remain to explain why some multiple (5,m) species are affected, while seemingly all of the (3,m) and (4,m) and (6,m) and (7,m) species do not experience such effects.

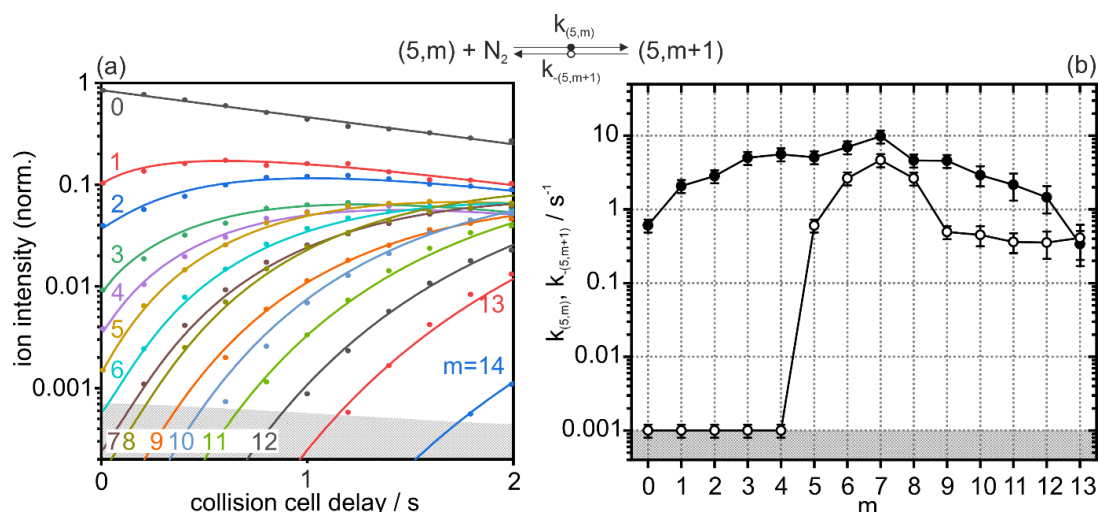


Figure S19: (a) Isothermal kinetics of N₂ adsorption by isolated Ta₅⁺ clusters at 26 K, He buffer gas and 2.6*10⁻⁷ mbar N₂ pressure. The fitting curves (solid lines) of the recorded data (solid dots) confirm pseudo-first-order kinetics for the adsorption in a reaction chain of up to 14 consecutive steps for Ta₅⁺ clusters. Figure S20(a) shows the ion intensities up to a collision cell delay of 20 s. **(b)** Fitted values of relative rate constants of Ta₅⁺ for the adsorption ($k_{(5,m)}$, solid circles) and the desorption ($k_{-(5,m+1)}$, open circles) as a function of stepwise N₂ adsorption. The gray shaded areas indicate the background noise level.

5. Cryo-IR Spectroscopy and Cryo-Kinetics of Cluster N₂ Adsorbate Complexes of Tantalum Cluster Cations Ta₅₋₈⁺

Table S15: Pseudo-first-order rate constants for the N₂ adsorption and desorption ($p(\text{N}_2)=2.6 \cdot 10^{-7}$ mbar) on [Ta₅(N₂)_m]⁺ clusters ($k_{(5,m)}$ and $k_{-(5,m+1)}$) up to a collision cell delay of 2 s. The related absolute rate constants ($k^{\text{abs}}_{(5,m)}$), the calculated collision rates ($k^{\text{coll}}_{(5,m)}$) and the absolute reaction efficiency ($\gamma_{(5,m)}$) are given as well. Statistical uncertainties of the relative rate constants are +/- 20%, and the absolute rate constants acquire an additional uncertainty from pressure calibration of +/- 50%.

m	$k_{(5,m)}$ s ⁻¹	$k_{-(5,m+1)}$ s ⁻¹	$k^{\text{abs}}_{(5,m)}$ 10 ⁻¹⁶ m ³ s ⁻¹	$k^{\text{coll}}_{(5,m)}$ 10 ⁻¹⁶ m ³ s ⁻¹	$\gamma_{(5,m)}$
0	0.61	< 0.001	0.54	5.98	0.09
1	2.08	< 0.001	1.84	4.92	0.38
2	2.84	< 0.001	2.51	4.29	0.59
3	5.01	< 0.001	4.44	3.86	1.15
4	5.60	< 0.001	4.96	3.55	1.39
5	5.10	0.60409	4.51	3.31	1.36
6	6.98	2.64434	6.18	3.12	1.98
7	9.80	4.67054	8.68	2.96	2.93
8	4.61	2.63079	4.08	2.83	1.44
9	4.56	0.49302	4.04	2.72	1.49
10	2.91	0.45094	2.58	2.62	0.99
11	2.17	0.36279	1.92	2.53	0.76
12	1.46	0.3545	1.29	2.45	0.52
13	0.34	0.41115	0.30	2.39	0.13

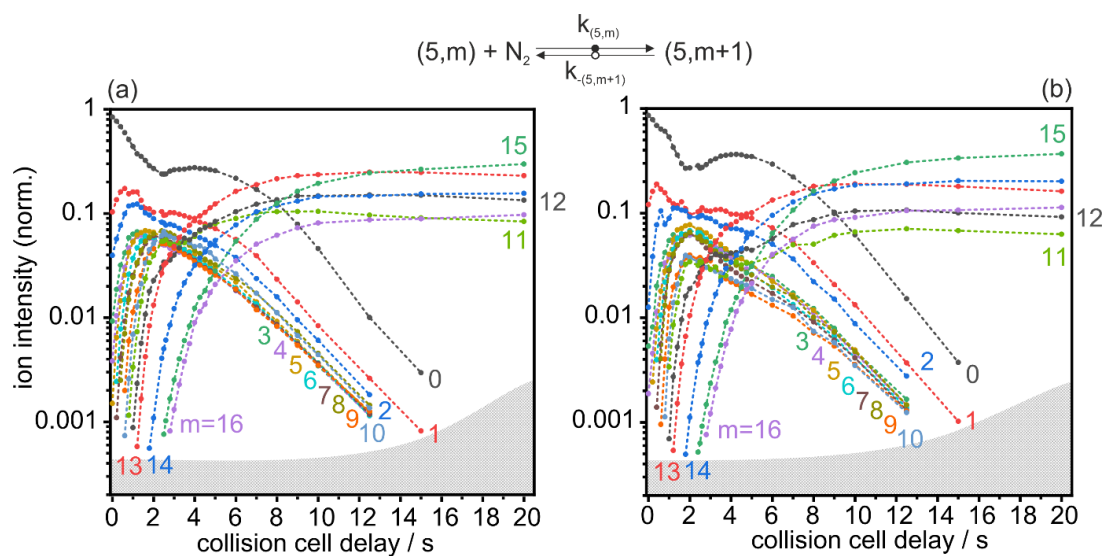


Figure S20: (a) Isothermal kinetics of N_2 adsorption by isolated Ta_5^+ clusters at 26 K, He buffer gas ($6.8 \cdot 10^{-6}$ mbar) and $2.6 \cdot 10^{-7}$ mbar N_2 pressure (date of measurement: 15.01.2020). (b) Isothermal kinetics of N_2 adsorption by isolated Ta_5^+ clusters at 26 K, He buffer gas ($4.9 \cdot 10^{-6}$ mbar) and $2.5 \cdot 10^{-7}$ mbar N_2 pressure (date of measurement: 21.01.2020). Measured Data are presented as solid circles are connected by dashed lines to guide the eye. The gray shaded areas indicate the background noise level.

5. Cryo-IR Spectroscopy and Cryo-Kinetics of Cluster N_2 Adsorbate Complexes of Tantalum Cluster Cations Ta_{5-8}^+

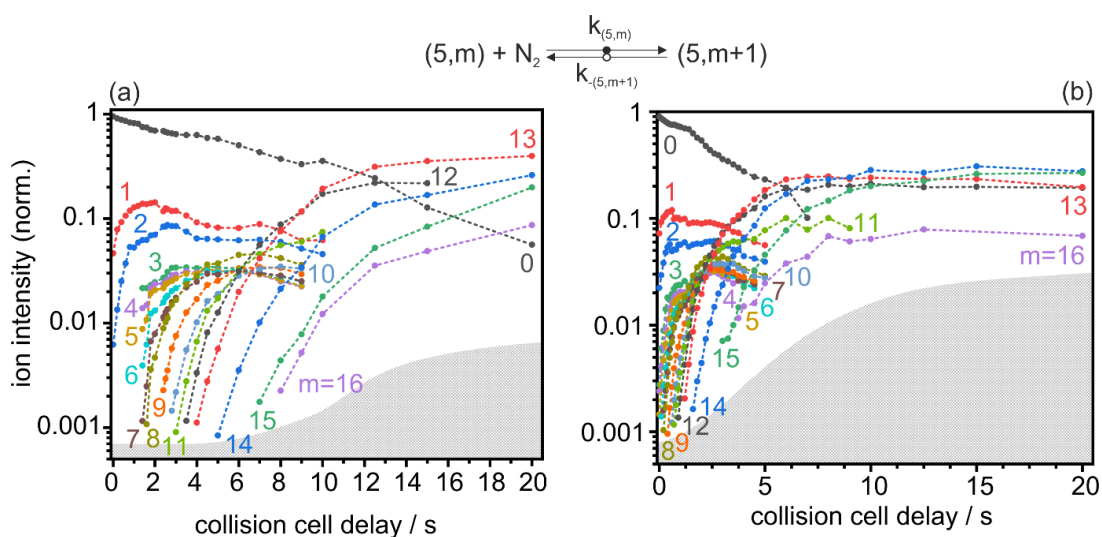


Figure S21: (a) Isothermal kinetics of N_2 adsorption by isolated Ta_{5}^+ clusters at 26 K, He buffer gas ($6.7 \cdot 10^{-6}$ mbar) and $1.8 \cdot 10^{-7}$ mbar N_2 pressure (date of measurement: 22.02.2019). (b) Isothermal kinetics of N_2 adsorption by isolated Ta_{5}^+ clusters at 26 K, He buffer gas ($5.9 \cdot 10^{-6}$ mbar) and $3.1 \cdot 10^{-7}$ mbar N_2 pressure (date of measurement: 12.03.2019). Measured Data are presented as solid circles are connected by dashed lines to guide the eye. The gray shaded areas indicate the background noise level.

Text S9: Ta₆(N₂)_m⁺ - Cryo kinetics and rate constants

The recorded kinetics of the cluster species (6,m) reveal typical stepwise adsorption of up to 16 N₂ molecules to the cluster, and we manage to achieve a fit of high quality by pseudo-first order kinetics (cf. Fig. 22). The chain of N₂ adsorption to Ta₆⁺ starts with a particularly slow first step, adsorption rate $k_{(6,0)}$ of mere 2.00 s⁻¹ (cf. Fig. 22(b)). This is more than a factor of two less than that of the second N₂ adsorption step, $k_{(6,1)}=4.63$ s⁻¹, which seems accelerated. It is also faster than the subsequent N₂ adsorption steps, $k_{(6,2)}$, $k_{(6,3)}$ and $k_{(6,4)}$ of the third, fourth and fifth N₂ adsorption to (6,2), (6,3) and (6,4), respectively. All subsequent adsorption steps up to the 11th N₂ adsorption step are faster than the second step, and they assume rates of up to $k_{(6,9)}=7.93$ s⁻¹, which is the maximum rate, for the 10th N₂ adsorption to (6,9).

There, at $k_{(6,9)}$, the adsorption rates reach a plateau up to $k_{(6,11)}$. The three subsequent N₂ adsorption steps $k_{(6,12)}$ through $k_{(6,14)}$ reveal particularly high adsorption rates $k_{(6,12)}=20.2$ s⁻¹, $k_{(6,13)}=12.0$ s⁻¹, and $k_{(6,14)}=17.6$ s⁻¹, ultimately yielding species (6,15). On the long term, at reaction times of up to 6 s and beyond, this (6,15) species is the most intense cluster adsorbate complex, denoted $m^* = 15$. The final adsorption step of the adsorption chain yields, however, an adsorption limit $m_{(max)}$ of 16 N₂ molecules. Beyond a collision cell delay of 4 s, the kinetic plot reveals horizontal and parallel curves for the corresponding adsorption complex (6,16) and its four precursors species (6,12), (6,13), (6,14) and (6,15). This indicates a dynamic equilibrium amongst these five adsorbate complexes. Our fitting supports this conclusion by particularly high values of the participating desorption rate constants $k_{-(6,13)}$ to $k_{-(6,16)}$. Note, that prior desorption seems insignificant, yielding vanishing values of $k_{-(6,1)}$ to $k_{-(6,12)}$ up to our experimental limits (Fig. 22(b)).

At this point, we want to address the question, whether the recorded adsorption kinetics are in line with available DFT predictions and the recorded IR-PD spectra in the main paper (cf. Fig. 5). The kinetics show an N₂ adsorption cascade to the bare Ta₆⁺ cluster. Conceivable isomers for (6,1), (6,2) and (6,3), as identified by DFT modeling, correspond in structure/geometry to this chain of successive N₂ adsorption steps. The isomers which are identified as most likely to be populated serve as starting geometries for the next N₂ adsorption.

5. Cryo-IR Spectroscopy and Cryo-Kinetics of Cluster N_2 Adsorbate Complexes of Tantalum Cluster Cations Ta_{5-8}^+

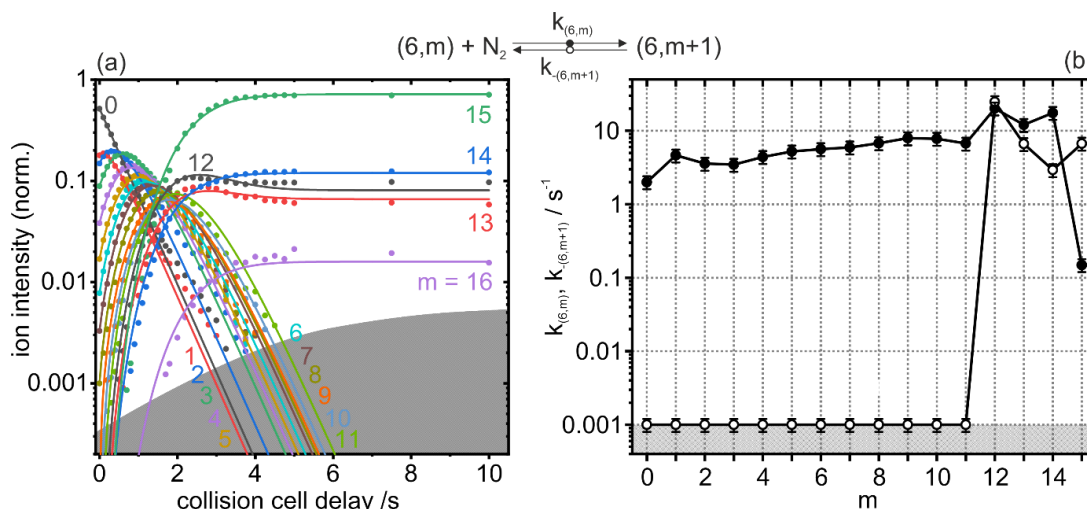


Figure S22: (a) Isothermal kinetics of N_2 adsorption by isolated Ta_6^+ clusters at 26 K, He buffer gas ($3.8 \cdot 10^{-6}$ mbar) and $3.5 \cdot 10^{-7}$ mbar N_2 pressure. The fitting curves (solid lines) of the recorded data (solid dots) confirm pseudo-first-order kinetics for the adsorption in a reaction chain of up to 16 consecutive steps for Ta_6^+ clusters. (b) Fitted values of relative rate constants of Ta_6^+ for the adsorption ($k_{(6,m)}$, solid circles) and the desorption ($k_{-(6,m+1)}$, open circles) as a function of stepwise N_2 adsorption. The gray shaded areas indicate the background noise level.

Table S16: Pseudo-first-order rate constants for the N₂ adsorption and desorption ($p(\text{N}_2)=3.5 \cdot 10^{-7}$ mbar) on $[\text{Ta}_6(\text{N}_2)_m]^+$ clusters ($k_{(6,m)}$ and $k_{-(6,m+1)}$), the related absolute rate constants ($k^{\text{abs}}_{(6,m)}$), the calculated collision rates ($k^{\text{coll}}_{(6,m)}$) and the absolute reaction efficiency ($\gamma_{(6,m)}$). Statistical uncertainties of the relative rate constants are +/- 20%, and the absolute rate constants acquire an additional uncertainty from pressure calibration of +/- 50%.

m	$k_{(6,m)}$ s ⁻¹	$k_{-(6,m+1)}$ s ⁻¹	$k^{\text{abs}}_{(6,m)}$ 10 ⁻¹⁶ m ³ s ⁻¹	$k^{\text{coll}}_{(6,m)}$ 10 ⁻¹⁶ m ³ s ⁻¹	$\gamma_{(6,m)}$
0	2.00	< 0.001	1.31E-16	5.96	0.22
1	4.63	< 0.001	3.05E-16	4.90	0.62
2	3.58	< 0.001	2.35E-16	4.27	0.55
3	3.46	< 0.001	2.27E-16	3.84	0.59
4	4.41	< 0.001	2.90E-16	3.53	0.82
5	5.23	< 0.001	3.44E-16	3.29	1.05
6	5.64	< 0.001	3.70E-16	3.09	1.20
7	5.94	< 0.001	3.90E-16	2.93	1.33
8	6.78	< 0.001	4.46E-16	2.80	1.59
9	7.93	< 0.001	5.21E-16	2.68	1.94
10	7.81	< 0.001	5.14E-16	2.58	1.99
11	6.72	< 0.001	4.42E-16	2.50	1.77
12	20.2	24.7	1.33E-15	2.42	5.49
13	12.0	6.63	7.92E-16	2.35	3.37
14	17.6	2.93	1.15E-15	2.29	5.05
15	0.15	6.70	9.79E-18	2.23	0.04

Text S10: Ta₇(N₂)_m⁺ - Cryo kinetics and rate constants

The investigation of Ta₇⁺ reveals successive adsorption of up to 16 N₂ molecules. This adsorption chain starts with a first, particularly fast N₂ adsorption step. With an adsorption rate $k_{(7,0)}$ of 8.01 s⁻¹, this first N₂ adsorption proceeds faster than all subsequent steps. Accordingly, the (6,0) intensity curve of the kinetic plot (cf. Fig. 23(a), black dots and line) decreases rapidly. The subsequent three N₂ adsorptions up to (7,4) proceed much slower, with rates declining to $k_{(7,3)}$ at 4.06 s⁻¹. The following adsorption rates increase to $k_{(7,9)} = 7.61$ s⁻¹ before gradually decreasing to $k_{(7,15)} = 0.83$ s⁻¹. Beyond this trend, the adsorption of the 13 N₂ molecule takes place with a somewhat higher adsorption rate of $k_{(7,12)} = 5.98$ s⁻¹. With the adsorption of a 16th N₂ molecule to the cluster adsorbate complex the adsorption chain terminates at the adsorption limit $m_{(max)}$, species (7,16). Beyond a collision cell delay of 4 s, the kinetic plot reveals horizontal and parallel curves of the six adsorbate species (7,10), (7,11), (7,12), (7,13), (7,14) and (7,15). This indicates a dynamic equilibrium of these seven species. Our fitting supports this conclusion by peculiar high desorption rate constants $k_{-(7,11)}$ to $k_{-(7,16)}$. The desorption rate $k_{-(7,13)}$ sticks out, and it exceeds any adsorption rate. Accordingly, on the long term, the corresponding species (7,12) is the most intense cluster adsorbate complex, $m^* = 12$. The intermediate range of desorption steps proceeds with moderate rates $k_{-(7,5)}$ through $k_{-(7,10)}$, cf. Fig. 23(b). Any desorption from smaller adsorbate complexes appears to be insignificant, and the predicted desorption rates $k_{-(7,1)}$ to $k_{-(7,4)}$ disappear in our experimental limits.

We refer to the main paper “cryogenic infrared spectroscopy study” (cf. Fig.8 and 9) for some more detailed insight into the first few N₂ adsorbate cluster complexes. The concomitant DFT modelling revealed a pentagonal bipyramidal (pbp) geometry for the bare Ta₇⁺ framework which sustains throughout N₂ adsorption steps. Predicted IR adsorption spectra and recorded IR-PD spectra of (7,1), (7,2) and (7,3) agree well, and we find no indication of isomerization at this point. From (7,4) on and beyond we observed an almost abrupt increase in the number of IR-PD bands, which we interpret as a clear indication of the presence of multiple adsorbate isomers upon high levels of N₂ load. These findings agree well with the increasing desorption rates of $k_{-(7,5)}$ and beyond. Thus, the isomers of all species from (7,4) onwards appear to adsorb additional N₂ molecules with simultaneous isomerization of the adsorbate shell. At this stage, we like to point out a compelling correspondence amongst the kinetic findings

of the present study and the insights of the IR-PD study: The adsorption process of the eleventh N_2 molecule onto the Ta_7^+ cluster seems special. While the measured N_2 adsorption kinetics demonstrate an equilibrium for all cluster from (7,10) and beyond, we note a significant extension to the red of the IR-PD bands within the range of end-on N_2 coordination. The latter was found to indicate multiple N_2 coordination to the same Ta coordination site/atom. Thus, we conclude in a correspondence of the onset of multiple N_2 coordination with the onset of likely adsorbate shell reorganization, and with the onset of significant N_2 desorption.

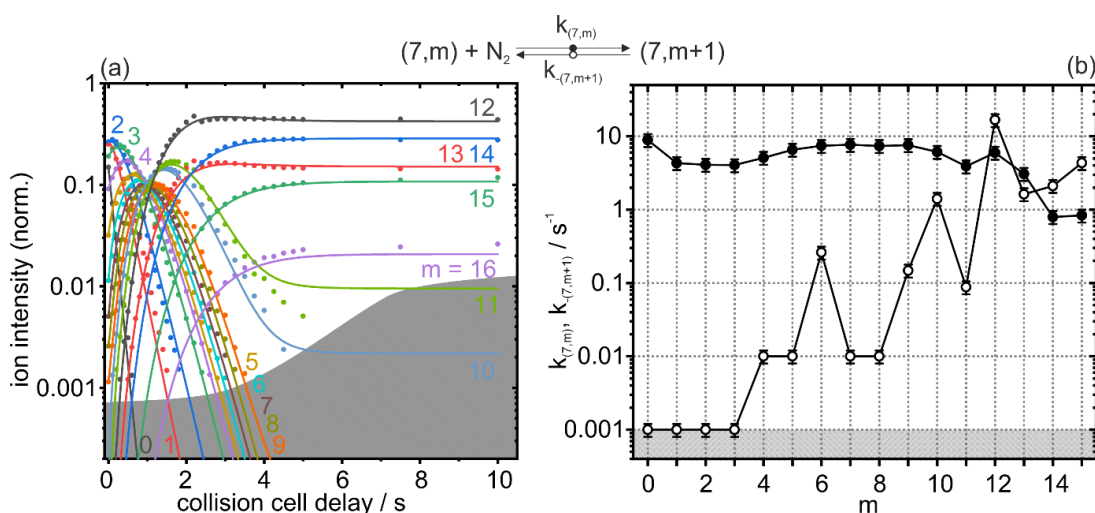


Figure S23: (a) Isothermal kinetics of N_2 adsorption by isolated Ta_7^+ clusters at 26 K, He buffer gas ($3.0 \cdot 10^{-6}$ mbar) and $2.6 \cdot 10^{-7}$ mbar N_2 pressure. The fitting curves (solid lines) of the recorded data (solid dots) confirm pseudo-first-order kinetics for the adsorption in a reaction chain of up to 16 consecutive steps for Ta_7^+ clusters. (b) Fitted values of relative rate constants of Ta_7^+ for the adsorption ($k_{(7,m)}$, solid circles) and the desorption ($k_{-(7,m+1)}$, open circles) as a function of stepwise N_2 adsorption. For pressure normalized absolute values of adsorption rate constants refer to the supplement. The gray shaded areas indicate the background noise level.

5. Cryo-IR Spectroscopy and Cryo-Kinetics of Cluster N_2 Adsorbate Complexes of Tantalum Cluster Cations Ta_{5-8}^+

Table S17: Pseudo-first-order rate constants for the N_2 adsorption and desorption ($p(N_2)=3.0 \cdot 10^{-7}$ mbar) on $[Ta_7(N_2)_m]^+$ clusters ($k_{(7,m)}$ and $k_{-(7,m+1)}$), the related absolute rate constants ($k^{abs}_{(7,m)}$), the calculated collision rates ($k^{coll}_{(7,m)}$) and the absolute reaction efficiency ($\gamma_{(7,m)}$). Statistical uncertainties of the relative rate constants are +/- 20%, and the absolute rate constants acquire an additional uncertainty from pressure calibration of +/- 50%.

m	$k_{(7,m)}$ s ⁻¹	$k_{-(7,m+1)}$ s ⁻¹	$k^{abs}_{(7,m)}$ 10 ⁻¹⁶ m ³ s ⁻¹	$k^{coll}_{(7,m)}$ 10 ⁻¹⁶ m ³ s ⁻¹	$\gamma_{(7,m)}$
0	8.91	< 0.001	7.88	5.95	1.32
1	4.32	< 0.001	3.82	4.89	0.78
2	4.10	< 0.001	3.63	4.25	0.85
3	4.06	< 0.001	3.59	3.82	0.94
4	5.10	0.01	4.51	3.51	1.29
5	6.57	0.01	5.82	3.27	1.78
6	7.43	0.26	6.58	3.07	2.14
7	7.67	< 0.001	6.79	2.91	2.33
8	7.40	< 0.001	6.55	2.77	2.36
9	7.61	0.15	6.73	2.66	2.53
10	6.14	1.41	5.44	2.56	2.12
11	3.90	0.09	3.45	2.47	1.40
12	5.98	16.7	5.29	2.39	2.21
13	3.08	1.63	2.72	2.32	1.17
14	0.79	2.11	0.70	2.26	0.31
15	0.83	4.34	0.74	2.20	0.34

Text S11: Ta₈(N₂)_m⁺ - Cryo kinetics and rate constants

Ta₈⁺ is the largest tantalum cluster in this cryo kinetic study of N₂ adsorption. We observe an overall N₂ adsorption chain of 16 steps yielding (8,16) as maximum adsorbate species (cf. Fig. S25). We managed to obtain a fit of high quality (Fig. 24, correlation coefficient $\rho = 0.995$) for the measured data up to a collision cell delay of 1 s. The thereby fitted relative rate constant for the adsorption of the first N₂ molecule (cf. Fig. S17) indicates a very effective adsorption process close to unit sticking probability, and it manifests by the steep decrease of (8,0) intensities within short time. The subsequent three adsorption steps proceed somewhat faster, cf. Fig. 24(b). The adsorption of the fourth N₂ molecule appears to be the fastest in the course of 11 consecutive adsorption steps, $k_{(8,3)} = 10.39 \text{ s}^{-1}$. From then on, the adsorption rate constants decrease successively, with each N₂ adsorption step, from 8.83 s^{-1} , $k_{(8,4)}$, to 1.56 s^{-1} , (8,10). However, the adsorption rate constant of the tenth N₂ molecule drops out of trends by a significantly lower $k_{(8,9)}$ value of 0.48 s^{-1} . This slow adsorption process delays further N₂ uptake and leads to a retarded growth of species (8,10) and (8,11). Note, that competitive N₂ desorption is significant along the entire adsorption chain, from the very first N₂ adsorbate. This behavior seems to be characteristic for the cluster size $n = 8$. All other cases ($n = 2 - 7$) did not reveal such significant desorption rates for the initial adsorption steps. All fits of rates of $m = 9$ and beyond would be questionable, when assuming stepwise adsorption and desorption to single isomers only, which is our present kinetic model. However, above a collision cell delay of more than 1 s, the recorded intensities of all species (8,m) assume a counter-intuitive course (cf. Fig. S25a), which is reproducible. At this point, we were not able to obtain a satisfactory fit of these recorded long term kinetics to a simple kinetic model in line with stepwise adsorption/desorption processes to and from single isomers only. However, the recorded (8,m) kinetics reveal features which are reminiscent of the (17,m) and (18,m) cases of cationic iron clusters³⁵. In those cases, we invoked three much involved scenarios of delayed activation conversion (DAC), minimum conversion (MIC), and maximum conversion (MAC). All of them have in common the involvement of multiple isomers, up to three, which may interconvert upon N₂ adsorption. We managed to draw some conclusions from the application of these alternative modelling schemes to the Fe₁₇⁺ and Fe₁₈⁺ cases. We plan to apply these scenarios to the present Ta₅⁺ and Ta₈⁺ cases in the near future. In summary at this stage, we may speculate about concurrent and likely interconverting isomers of (8,m) species. We find support

5. Cryo-IR Spectroscopy and Cryo-Kinetics of Cluster N_2 Adsorbate Complexes of Tantalum Cluster Cations Ta_{5-8}^+

for this suggestion in our infrared spectroscopy study (cf. Fig. 10). The interpretation of the IR-PD spectrum (8,1) concludes in two isomers one of which is less populated. This is in line with the kinetic curve of (8,1) which provides strong indication for two isomers with fast and slow N_2 adsorption.

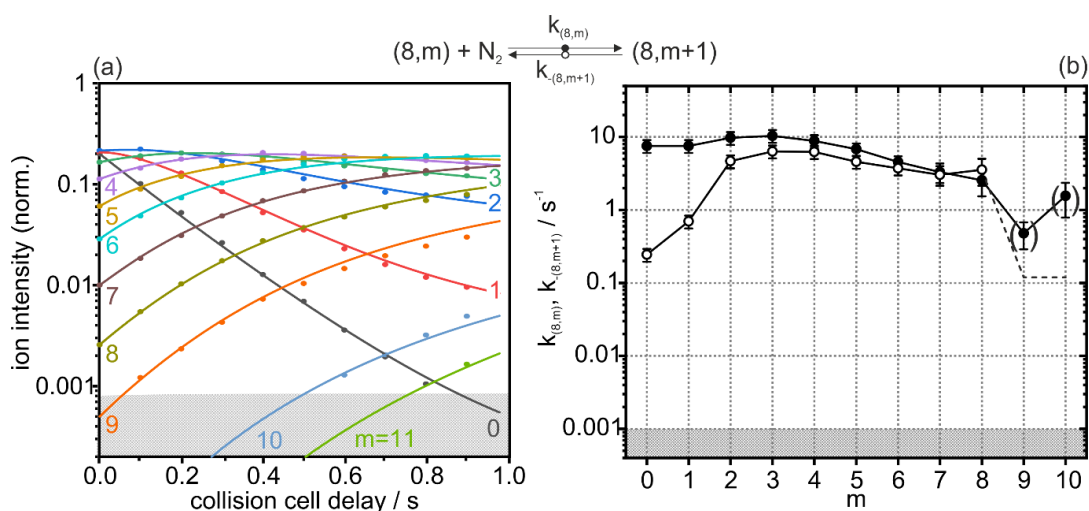


Figure S24: (a) Isothermal kinetics of N_2 adsorption by isolated Ta_8^+ clusters at 26 K, He buffer gas and $2.0 \cdot 10^{-7}$ mbar N_2 pressure. The fitting curves (solid lines) of the recorded data (solid dots) confirm pseudo-first-order kinetics for the adsorption in a reaction chain of up to 11 consecutive steps for Ta_8^+ clusters. Figure S25 shows the ion intensities up to a collision cell delay of 10 s. **(b)** Fitted values of relative rate constants of Ta_8^+ for the adsorption ($k_{(8,m)}$, solid circles) and the desorption ($k_{-(8,m+1)}$, open circles) as a function of stepwise N_2 adsorption. The gray shaded areas indicate the background noise level.

Table S18: Pseudo-first-order rate constants for the N₂ adsorption and desorption ($p(\text{N}_2)=2.0 \cdot 10^{-7}$ mbar) on $[\text{Ta}_8(\text{N}_2)_m]^+$ clusters ($k_{(8,m)}$ and $k_{-(8,m+1)}$) up to a collision cell delay of 1 s. The related absolute rate constants ($k^{\text{abs}}_{(8,m)}$), the calculated collision rates ($k^{\text{coll}}_{(8,m)}$) and the absolute reaction efficiency ($\gamma_{(8,m)}$) are given as well. Statistical uncertainties of the relative rate constants are +/- 20%, and the absolute rate constants acquire an additional uncertainty from pressure calibration of +/- 50%.

m	$k_{(8,m)}$ s ⁻¹	$k_{-(8,m+1)}$ s ⁻¹	$k^{\text{abs}}_{(8,m)}$ 10 ⁻¹⁶ m ³ s ⁻¹	$k^{\text{coll}}_{(8,m)}$ 10 ⁻¹⁶ m ³ s ⁻¹	$\gamma_{(8,m)}$
0	7.55	0.24	8.69	5.94	1.46
1	7.54	0.70	8.68	4.88	1.78
2	9.75	4.67	11.2	4.24	2.64
3	10.4	6.34	12.0	3.81	3.14
4	8.83	6.26	10.2	3.50	2.91
5	6.81	4.59	7.84	3.25	2.41
6	4.54	3.73	5.22	3.06	1.71
7	3.31	3.04	3.81	2.89	1.32
8	2.55	3.56	2.94	2.76	1.07

5. Cryo-IR Spectroscopy and Cryo-Kinetics of Cluster N_2 Adsorbate Complexes of Tantalum Cluster Cations Ta_{5-8}^+

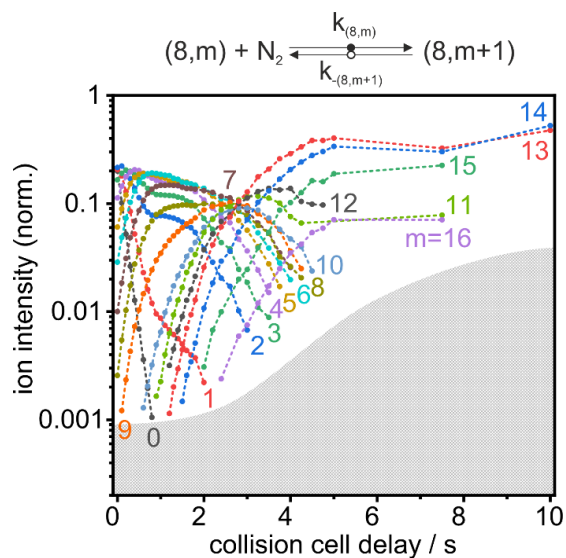


Figure S25: Isothermal kinetics of N_2 adsorption by isolated Ta_8^+ clusters at 26 K, He buffer gas ($2.8 \cdot 10^{-6}$ mbar) and $2.0 \cdot 10^{-7}$ mbar N_2 pressure. Measured Data are presented as solid circles are connected by dashed lines to guide the eye. The gray shaded areas indicate the background noise level.

References

1. A. Straßner, C. Wiehn, M. P. Klein, D. V. Fries, S. Dillinger, J. Mohrbach, M. H. Prosenc, P. B. Armentrout and G. Niedner-Schatteburg, *J. Chem. Phys.* **155** (24), 244305 (2021).
2. S. Dillinger, J. Mohrbach, J. Hewer, M. Gaffga and G. Niedner-Schatteburg, *Phys. Chem. Chem. Phys.* **17** (16), 10358-10362 (2015).
3. S. Dillinger, J. Mohrbach and G. Niedner-Schatteburg, *J. Chem. Phys.* **147** (18), 184305 (2017).
4. J. Mohrbach, S. Dillinger and G. Niedner-Schatteburg, *J. Phys. Chem. C* **121** (20), 10907-10918 (2017).
5. S. Dillinger, M. P. Klein, A. Steiner, D. C. McDonald, M. A. Duncan, M. M. Kappes and G. Niedner-Schatteburg, *J. Phys. Chem. Lett.* **9** (4), 914-918 (2018).
6. M. P. Klein, A. A. Ehrhard, J. Mohrbach, S. Dillinger and G. Niedner-Schatteburg, *Top. Catal.* **61** (1), 106-118 (2018).
7. D. V. Fries, M. P. Klein, A. Steiner, M. H. Prosenc and G. Niedner-Schatteburg, *Phys. Chem. Chem. Phys.* **23** (19), 11345-11354 (2021).
8. W. M. Haynes, *CRC Handbook of Chemistry and Physics*. (CRC Press Taylor & Francis Group, 2014).
9. IEA, *Ammonia Technology Roadmap CC BY-NC 3.0 IGO*. (2021).
10. F. Schüth, *Chem. unserer Zeit* **40** (2), 92-103 (2006).
11. A. Wang, J. Li and T. Zhang, *Nat. Rev. Chem.* **2** (6), 65-81 (2018).
12. D. K. Böhme and H. Schwarz, *Angew. Chem. Int. Ed.* **44** (16), 2336-2354 (2005).
13. P. B. Armentrout, *Catal. Sci. Technol.* **4** (9), 2741-2755 (2014).
14. M. B. Knickelbein, *Annu. Rev. Phys. Chem.* **50** (1), 79-115 (1999).
15. S. J. Riley, *Ber. Bunsenges. Phys. Chem.* **96** (9), 1104-1109 (1992).
16. T. Ito, M. Arakawa, Y. Taniguchi and A. Terasaki, *Z. Phys. Chem.* **233** (6), 759-770 (2019).
17. M. S. Ford, M. L. Anderson, M. P. Barrow, D. P. Woodruff, T. Drewello, P. J. Derrick and S. R. Mackenzie, *Phys. Chem. Chem. Phys.* **7** (5), 975-980 (2005).
18. P. A. Hintz and K. M. Ervin, *J. Chem. Phys.* **100** (8), 5715-5725 (1994).
19. Y.-X. Zhao, X.-G. Zhao, Y. Yang, M. Ruan and S.-G. He, *J. Chem. Phys.* **154** (18), 180901 (2021).

5. Cryo-IR Spectroscopy and Cryo-Kinetics of Cluster N_2 Adsorbate Complexes of Tantalum Cluster Cations Ta_{5-8}^+

20. M. R. Zakin, D. M. Cox and A. Kaldor, *J. Chem. Phys.* **89** (2), 1201-1202 (1988).
21. M. L. Anderson, M. S. Ford, P. J. Derrick, T. Drewello, D. P. Woodruff and S. R. Mackenzie, *J. Phys. Chem. A* **110** (38), 10992-11000 (2006).
22. M. D. Morse, M. E. Geusic, J. R. Heath and R. E. Smalley, *J. Chem. Phys.* **83** (5), 2293-2304 (1985).
23. W. F. Hoffman, E. K. Parks, G. C. Nieman, L. G. Pobo and S. J. Riley, *Z. Phys. D - Atoms, Molecules and Clusters* **7** (1), 83-89 (1987).
24. P. Fayet, A. Kaldor and D. M. Cox, *J. Chem. Phys.* **92** (1), 254-261 (1990).
25. I. Balteanu, U. Achatz, O. P. Balaj, B. S. Fox, M. K. Beyer and V. E. Bondybey, *Int. J. Mass spectrom.* **229** (1), 61-65 (2003).
26. P. A. Hintz and K. M. Ervin, *J. Chem. Phys.* **103** (18), 7897-7906 (1995).
27. Y. Tawaraya, S. Kudoh, K. Miyajima and F. Mafuné, *J. Phys. Chem. A* **119** (31), 8461-8468 (2015).
28. D. Neuwirth, J. F. Eckhard, B. R. Visser, M. Tschurl and U. Heiz, *Phys. Chem. Chem. Phys.* **18** (11), 8115-8119 (2016).
29. J. F. Eckhard, D. Neuwirth, C. Panosetti, H. Oberhofer, K. Reuter, M. Tschurl and U. Heiz, *Phys. Chem. Chem. Phys.* **19** (8), 5985-5993 (2017).
30. N. Levin, J. T. Margraf, J. Lengyel, K. Reuter, M. Tschurl and U. Heiz, *Phys. Chem. Chem. Phys.* **24** (4), 2623-2629 (2022).
31. B. Pfeffer, S. Jaberg and G. Niedner-Schatteburg, *J. Chem. Phys.* **131** (19) (2009).
32. J. Mohrbach, S. Dillinger and G. Niedner-Schatteburg, *J. Chem. Phys.* **147** (18), 184304 (2017).
33. A. A. Ehrhard, M. P. Klein, J. Mohrbach, S. Dillinger and G. Niedner-Schatteburg, *Mol. Phys.* **119** (17-18), e1953172 (2021).
34. A. A. Ehrhard, M. P. Klein, J. Mohrbach, S. Dillinger and G. Niedner-Schatteburg, *J. Chem. Phys.* **156** (5), 054308 (2022).
35. A. Straßner, M. P. Klein, D. V. Fries, C. Wiehn, M. E. Huber, J. Mohrbach, S. Dillinger, D. Spelsberg, P. B. Armentrout and G. Niedner-Schatteburg, *J. Chem. Phys.* **155** (24), 244306 (2021).
36. S. Peredkov, M. Neeb, W. Eberhardt, J. Meyer, M. Tombers, H. Kampschulte and G. Niedner-Schatteburg, *Phys. Rev. Lett.* **107** (23), 233401 (2011).

37. J. Meyer, M. Tombers, C. van Wüllen, G. Niedner-Schatteburg, S. Peredkov, W. Eberhardt, M. Neeb, S. Palutke, M. Martins and W. Wurth, *J. Chem. Phys.* **143** (10) (2015).
38. C. Berg, T. Schindler, G. Niedner-Schatteburg and V. E. Bondybey, *J. Chem. Phys.* **102** (12), 4870-4884 (1995).
39. V. Bondybey and J. English, *J. Chem. Phys.* **74**, 6978-6979 (1981).
40. D. Proch and T. Trickl, *Rev. Sci. Instrum.* **60** (4), 713-716 (1989).
41. P. Caravatti and M. Allemann, *Org. Mass Spectrom.* **26** (5), 514-518 (1991).
42. M. Graf, Diploma Thesis, Technische Universität Kaiserslautern, 2006.
43. T. Su and M. T. Bowers, *J. Am. Chem. Soc.* **95** (23), 7609-7610 (1973).
44. T. Su and M. T. Bowers, *J. Chem. Phys.* **58** (7), 3027-3037 (1973).
45. T. Su and M. T. Bowers, *Int. J. Mass Spectrom. Ion Phys.* **12** (4), 347-356 (1973).
46. G. Kummerlöwe and M. K. Beyer, *Int. J. Mass spectrom.* **244** (1), 84-90 (2005).
47. C. Geng, J. Li, T. Weiske and H. Schwarz, *Proc. Natl. Acad. Sci.* **115** (46), 11680-11687 (2018).
48. Dortmund Data Bank (2020).
49. L. Deslauriers, S. Olmschenk, D. Stick, W. K. Hensinger, J. Sterk and C. Monroe, *Phys. Rev. Lett.* **97** (10), 103007 (2006).
50. A. V. Tolmachev, A. N. Vilkov, B. Bogdanov, L. PĀsa-Tolić, C. D. Masselon and R. D. Smith, *J. Am. Soc. Mass. Spectrom.* **15** (11), 1616-1628 (2004).
51. V. L. Ryjkov, X. Zhao and H. A. Schuessler, *Phys. Rev. A* **71** (3), 033414 (2005).
52. D. A. Hite, K. S. McKay, S. Kotler, D. Leibfried, D. J. Wineland and D. P. Pappas, *MRS Advances* **2** (41), 2189-2197 (2017).

6 KINETICS OF H₂ ADSORPTION ONTO Ta₂₋₈⁺ CLUSTERS UNDER CRYOGENIC CONDITIONS

Daniela V. FRIES, Annika STRAßNER, Matthias P. KLEIN, and Gereon
NIEDNER-SCHATTEBURG

Department of Chemistry and State Research Center OPTIMAS,
Rheinland-Pfälzische Technische Universität (RPTU) Kaiserslautern-Landau,
67663 Kaiserslautern, Germany

6.1 Preamble

The experiments were performed by myself - partly together with A. Straßner and M. P. Klein. The evaluation of the measured data was carried out by me, and it was accompanied by discussions with G. Niedner-Schatteburg. I wrote the manuscript.

6.2 Paper draft

6.2.1 Abstract

In this paper we present a study of stepwise H₂ adsorption on size-selected tantalum cluster cations Ta_n⁺, n = 2-8, in a hexapole ion trap at 18 K. The observed adsorption limits and kinetic processes exhibit distinct dependencies on cluster size n. The smallest tantalum cluster cation, Ta₂⁺, proved to be inert toward H₂. The first few H₂ adsorption reactions of Ta_n⁺ cluster, n = 3-5, proceed very fast and without competitive desorption reactions, up to a seeming threshold which is the completion of the first adsorbate shell. From then on, the adsorption chain proceeds slowly, and it is accompanied by several desorption reactions. The H₂ adsorption chain of Ta₇⁺ proceeds similarly, but with less significant desorption steps than the H₂ adsorption kinetics of Ta₃₋₅⁺. The characteristics of the present kinetics of H₂ adsorption onto Ta₆⁺ and Ta₈⁺ differ considerably: We observe slow initial H₂ adsorption processes for Ta₆⁺, delaying the adsorption chain process. However, several adsorption steps in the further course of the adsorption chain proceed remarkably fast. The recorded ion intensities of the Ta₈⁺ kinetic reveal at first the stepwise adsorption of five H₂ molecules yielding [Ta₈(N₂)₅]⁺ as intermittent adsorption limit. This species adsorbs further H₂ molecules in a delayed manner. The ion intensities of species [Ta₈(N₂)₇]⁺ lead us to speculate on adsorbate shell reorganization and/or adsorbate-induced cluster relaxation processes.

6.2.2 Introduction

Most of the earthly hydrogen is in molecular form with a strong covalent H₂ bond (436 kJ mol⁻¹ [1]). Hydrogenases metabolize H₂ enzymatically by their active centers which contain a metal component. [2-4] For all chemical engineering and many related fields, heterogeneous catalysis is the key technology. [5] The majority of engineered chemical processes utilize transition metals (TM) as catalysts. [6-11] At first glance, the study of isolated TM clusters may seem only vaguely related to these questions. Actually, it is imperative to describe and understand underlying materials and elementary processes at the molecular level. Atomic precise TM clusters can serve in this regard. Several review publications demonstrate size effects for structure, chemical and physical properties and for the reactivity of TM clusters. [12-18] It is known that the interaction of H₂ with TM clusters, TM

complexes, and with metal surfaces leads to the formation of activated and dissociated hydrogen. [19–21] There are numerous experimental studies - mainly spectroscopic in nature - and quantum chemical calculations at DFT level on the adsorption of H_2 to various TM clusters: H_2 adsorption to $[Sc_nO]^+$, V_n^+ , Fe_n^+ , and Co_n^+ yields exclusively hydride species. In contrast, both atomic and molecularly chemisorbed hydrogen is present for Ni_n^+ clusters. [22] The cluster hydride complexes $[Fe_nH_m]^+$ and $[Co_nH_m]^+$ take up further physisorbed H_2 molecules. [23, 24] While H_2 molecules binds exclusively dissociatively on Ni_5^+ and Ni_6^+ the special case of Ni_4^+ can adsorb H_2 molecularly. [25] IR spectroscopy and DFT studies reveal large binding energies for Cu_5^+ , corresponding to dissociative adsorption, and small binding energies for Cu_4^+ , implying significant amounts of molecular H_2 adsorption. [26] In addition, H_2 adsorption onto Pt_n^+ clusters yields cluster adsorbate complexes in which the H_2 ligands coordinate both molecularly and dissociatively. [27] Early studies on Fe_n^+ [28] and Ni_n^+ [29] reveal a reactivity with H_2 that varies strongly by the cluster size n , sometimes by several orders of magnitude, especially for small clusters.

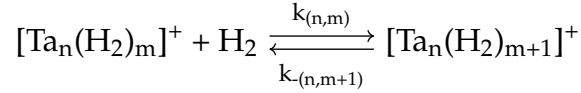
In the particular case of small cationic tantalum clusters Ta_n^+ , vibrational spectra and theoretical modeling successfully provide for the geometries of the bare clusters, their relative stabilities and electronic properties. [30, 31] Further, extensive experimental and quantum chemical studies have addressed the reactions of Ta_n^+ clusters with small molecules such as CO_2 [32], O_2 [33], N_2 [34–37] or CH_4 [38–40]. Theory predicts that Ta_2^+ is capable of mediating the formation of NH_3 from N_2 and H_2 . [41] We have worked extensively in the past on the N_2 activation and cleavage capabilities of small tantalum clusters. The experimental results of adsorption kinetics and IR spectroscopy, supported by DFT modeling, show that the smallest clusters Ta_2^+ , Ta_3^+ , and Ta_4^+ are able to adsorb, activate, and even cleave at least one N_2 molecule. [42–44] The activation and cleavage of the N_2 triple bond is of particular interest considering the overall picture of industrial ammonia formation [45, 46] where, however, cleavage of the H_2 bond is also required. With this study, we contribute to answering the question whether the small tantalum clusters Ta_n^+ , $n = 2 - 8$, are also able to activate and cleave H_2 molecules. We reacted the bare clusters with H_2 at 18 K in a hexapole ion trap and measured the adsorption kinetics by recording ion intensities of the adsorption species $[Ta_n(H_2)_m]^+$, abbreviated (n,m), as a function of storage time. This is in line with our earlier N_2 adsorption studies on Ta_4^+ , Ni_n^+ , Rh_n^+ , $[Rh_iFe_j]^+$ and Fe_n^+ clusters. [39, 42–44, 47–51] The present kinetic

study reveals two different processes for H₂ adsorption onto Ta₃⁺, Ta₄⁺, Ta₅⁺ and Ta₇⁺: initial fast adsorption processes without competing desorption reactions at low H₂ loadings, indicating dissociative adsorption processes, and subsequent slow adsorption steps accompanied by multiple desorption reactions at high H₂ loadings, indicating molecular H₂ adsorption. We identify the threshold between these two types of adsorption behavior as the completion of a first shell of adsorbate. ($m = n$). The findings of this study, which we refer to in the following as [CKS], finds strong support by our complementary IR-PD and DFT study [IRS], chapter 7.

6.2.3 Experimental and Computational Methods

We perform our kinetic measurements using a customized Fourier Transform Ion Cyclotron Resonance (FT-ICR) mass spectrometer (*Apex Ultra*, Bruker Daltonics). A home built laser vaporization (LVAP) source [52, 53] generates transition metal clusters TM_n[±] of various cluster sizes n : The second harmonic of a pulsed Nd:YAG (Innolas Spitlight 300, 20 Hz) evaporates metal atoms from a rotating tantalum foil (99.95 %, 0.5 mm thick, Alfa Aesar). A He gas pulse (40 μs, 15 bar) from a home-built piezoelectric valve [54] captures the hot plasma consisting of atoms and ions and entrains it through a 69 mm long channel (2 mm diameter). The atoms and ions cool down and aggregate yielding clusters during the subsequent jet expansion into vacuum (10⁻⁷ mbar). The resulting cluster size distribution passes through electrostatic lenses and reaches a 90° ion beam bender which deflects the ion beam onto the magnetic field axis. A quadrupole mass filter is used to size-select the cluster ions before they are injected into a cryogenic hexapole ion trap. A closed-cycle He cryostat cools the ion trap down to 18 K. The setup allows to continuously introduce buffer and/or reaction gas. For the present study, we introduced He as buffer gas and H₂ as reaction gas. To achieve sufficient H₂ attachment to the Ta_n⁺ clusters, the H₂ pressure in the ion trap was increased from 1.2 × 10⁻⁷ mbar up to a maximum of 6.0 × 10⁻⁷ mbar. Additionally, He gas was continuously introduced up to a pressure of 6.6 × 10⁻⁶ mbar in order to ensure efficient trapping and cooling of the ions. Required ions can be trapped in the hexapole ion trap for various storage times (collision cell delay) up to 30 s according to the investigation procedure. The manipulated ions are steered into the FT-ICR cell by a series of electrostatic lenses. The so-called *infinity* type cell [55] serves for ion detection and is cooled down to 10 K by a closed He cryostat to prevent heating of the clusters and cluster adsorbate complexes by black body radiation. The ICR cell offers opportunity to store ions

therein. This was not used for the present experiments but for the associated cryogenic infrared spectroscopy study [IRS]. Instead, the cluster ions Ta_n^+ were stored in the hexapole ion trap filled with H_2/He under isothermal conditions at 18 K. We recorded mass spectra (40 spectra per storage time/delay) for several storage times in order to determine the temporal evolution of the H_2 adsorption onto the cluster adsorbate complexes. We evaluate pseudo-first order kinetic fits from storage times and the assigned signal intensities of each cluster adsorbate complex using the fitting routine `evofit` [56]. This yields relative rate constants for all adsorption $k_{(n,m)}$ and desorption $k_{-(n,m+1)}$ steps along the H_2 adsorption chain.



The nomenclature is in line with our previous publications on Ta_n^+ . [42–44] We refer the reader to the supplementary information for a detailed explanation of the nomenclature for the clusters and their adsorbates.

We convert the relative rate constants $k_{(n,m)}$ and $k_{-(n,m+1)}$ into the corresponding absolute rate constants $k_{(n,m)}^{\text{abs}}$ using the absolute collision gas number densities $\rho_{\text{H}_2}(T)$.

$$k_{(n,m)}^{\text{abs}} = \frac{k_{(n,m)}}{\rho_{\text{H}_2}(T)}$$

We obtain approximate values for the absolute collision gas number densities $\rho_{\text{H}_2}(T)$ from the pressure in the surrounding chamber $p_c^{300\text{K}}$ and an effective geometry factor c_{app} .

$$\rho_{\text{H}_2}(18\text{K}) = \frac{c_{\text{app}} \cdot p_c^{300\text{K}}}{k_B \cdot T_{300\text{K}}}$$

The geometry factor c_{app} is 1.8 at 26 K with an uncertainty of $\pm 50\%$. The quotient of the absolute rate constants k^{abs} and the collision rates k^{coll} give the absolute reaction efficiency $\gamma_{(3,m)}$.

$$\gamma_{(3,m)} = \frac{k^{\text{abs}}}{k^{\text{coll}}}$$

6.2.4 Results and Discussion

Trends and Limits of H₂ Adsorption to Ta₂₋₈⁺ Clusters

Mass spectrometric measurements provided preliminary information on H₂ adsorption to Ta_n⁺ clusters, n = 2-8. For this purpose, each cluster size was isolated in a quadrupole mass filter and stored in the hexapole ion trap at 18 K, into which we continuously introduced hydrogen as reaction gas. We observe a series of H₂ adsorbates ($\Delta m = +2 m/z$) for all cluster sizes except Ta₂⁺. At a certain point, H₂ adsorption to each cluster reaches a limit which depends on cluster size n. Beyond this limit neither an increase of H₂ pressure nor an increase of storage time leads to further H₂ adsorption. Figure 1 depicts the observed H₂ adsorption limits m_{\max} for the investigated cluster sizes n = 2-8.

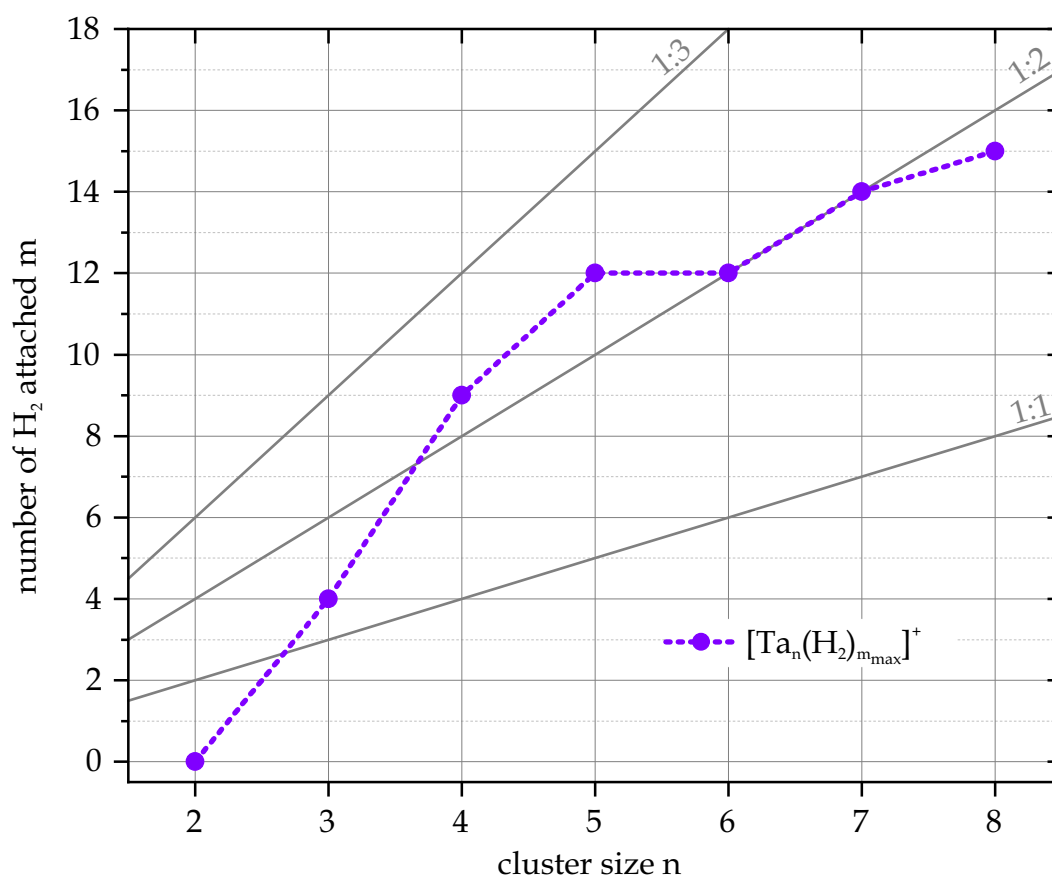


Figure 1: Plot of the experimentally determined adsorption limits m_{\max} of H₂ adsorption to Ta_n⁺ clusters, n = 2-8. The cluster ions were stored for up to 30 s within the hexapole ion trap with 18 K He buffer gas and up to 6.0×10^{-7} mbar H₂ as reaction gas. The gray lines indicate stoichiometries of n:m_{max}.

The tantalum trimer cation, Ta_3^+ , is the smallest cluster which adsorbs H_2 under the conditions of our experiment. It accumulates up to four H_2 molecules. For the cationic tantalum tetramer, Ta_4^+ , we observe an increase in the H_2 adsorption of up to nine H_2 molecules. The mass spectra of Ta_5^+ and Ta_6^+ reveal that both cluster species adsorb up to twelve H_2 molecules. For Ta_7^+ and Ta_8^+ , the H_2 adsorption limit increases up to 14 and 15 H_2 molecules, respectively. Overall, we observe an increasing trend in the adsorption limits m_{max} with increasing cluster size n at a stoichiometry close to $n:m = 1:2$. This is an order of stoichiometry less than we observed for the adsorption of N_2 onto the clusters of sizes $n = 3-6$ (*cf.* Figure S1 in the supplementary information, chapter 6.3). Since we did not observe any further increase in N_2 adsorption limits for Ta_5^+ and all larger clusters up to Ta_8^+ , the curves of the experimentally determined adsorption limits m_{max} of H_2 and N_2 converge for large Ta_n^+ clusters, $n = 7, 8$.

Cryo Kinetics and Rate Constants of H_2 Adsorption to Ta_{2-8}^+ Cluster

The series of mass spectra recorded at various increasing storage times show the temporal evolution of the adsorbate intensities for each step of H_2 adsorption to the tantalum clusters Ta_n^+ , $n = 2-8$. We obtain rate constants for each reaction process by fitting the intensity data with a pseudo-first-order kinetic approach [56]. The fits confirm consecutive H_2 adsorption steps for Ta_n^+ cluster of all investigated sizes. In parallel with the H_2 adsorption reactions, varying amounts of H_2 desorption reactions show up at higher H_2 loads. Note, that we use an abridged (n,m) nomenclature for the tantalum cluster adsorbate complexes $[\text{Ta}_n(\text{H}_2)_m]^+$. The chosen nomenclature for the Ta_n^+ clusters and their hydrogen adsorbates are more explicitly described in the supplementary information.

$[\text{Ta}_2(\text{H}_2)_m]^+$ The inertness of Ta_2^+ towards H_2 is striking. This is despite a particularly long storage time of up to 30 s and exposure to 5.4×10^{-7} mbar H_2 within the hexapole ion trap. The kinetic study of Ta_2^+ illustrates this finding (*cf.* Figure S2 in the supplementary information, chapter 6.3). Therefore, our experiments cannot confirm that a reaction of Ta_2^+ with H_2 is possible, as predicted by Geng *et al.* [41] in quantum chemical calculations.

6. Kinetics of H₂ Adsorption onto Ta₂₋₈⁺ Clusters under Cryogenic Conditions

[Ta₃(H₂)_m]⁺ The uptake of H₂ molecules onto the tantalum trimer cation, Ta₃⁺, occurs through stepwise H₂ adsorption up to an adsorption limit m_{max} of four H₂ molecules. Using our genetic algorithm, we obtained pseudo-first-order fits that were of satisfactory overall quality (*cf.* Figure 2(a), correlation coefficient $\chi = 0.974$). Unfortunately, at this point, fitting the somewhat deviating ion intensity of (3,2) to the recorded intensities goes beyond our simple adsorption model.

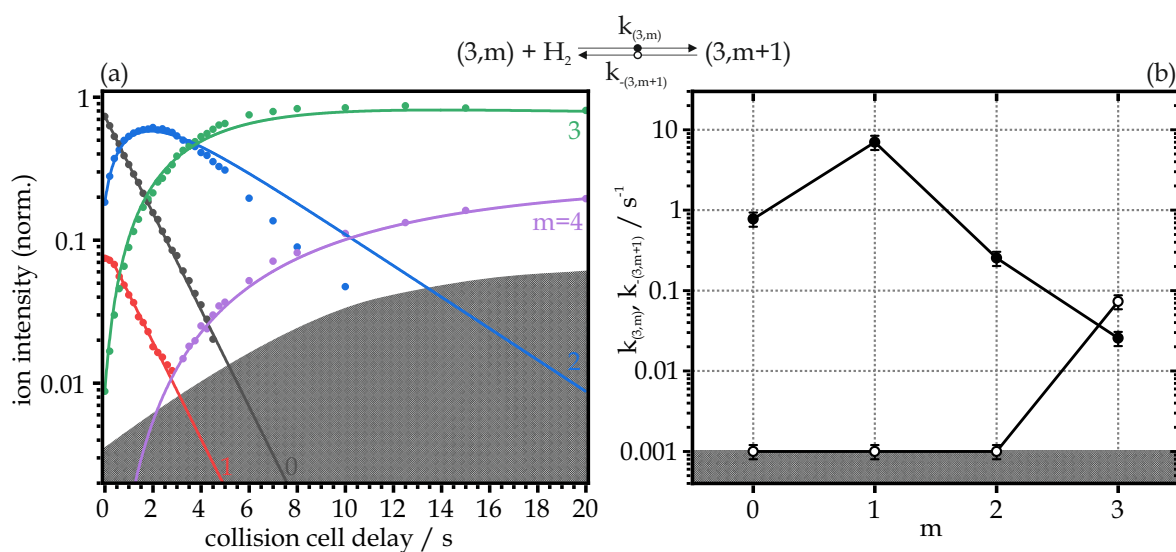


Figure 2: (a) Isothermal kinetics of H₂ adsorption by isolated Ta₃⁺ clusters at 18 K, He buffer gas (3.0×10^{-6} mbar) and 1.8×10^{-7} mbar H₂ pressure. The fitting curves (solid lines) of the recorded data (solid dots) confirm pseudo-first-order kinetics for the adsorption in a reaction chain of up to four consecutive steps for Ta₃⁺ clusters. (b) Fitted values of relative rate constants of Ta₃⁺ for the adsorption ($k_{(3,m)}$, solid circles) and the desorption ($k_{-(3,m+1)}$, open circles) as a function of stepwise H₂ adsorption. For pressure-normalized absolute values of adsorption rate constants refer to the supplementary information, chapter 6.3. The gray shaded areas indicate the background noise level.

Nevertheless, these kinetics show a slow process for the adsorption of the first H₂ molecule onto the Ta₃⁺ cluster, as indicated by a particularly low adsorption rate $k_{(3,0)}$ of 0.779 s^{-1} (*cf.* Figure 2(b)). In contrast, the comparatively high rate constant $k_{(3,1)}$ of 7.000 s^{-1} indicates a considerably fast adsorption process for the uptake of the second H₂ molecule. The adsorption process of the third H₂ molecule proceeds slower than the prior two adsorption processes ($k_{(3,2)} = 0.253 \text{ s}^{-1}$) and yields the cluster adsorbate complex with a (n,m) = 1:1 stoichiometry of the number of metal atoms

and ligand molecules. The Ta_3^+ cluster loaded with a formal monolayer of H_2 ligand molecules manages to take up a fourth H_2 molecule but with a significantly low adsorption rate constant $k_{(3,3)}$ of 0.036 s^{-1} . Desorption, as reflected by the non-negligible contribution of the desorption rate constant $k_{-(3,4)}$, begins at this level of H_2 load. Note, that prior desorption seems insignificant, yielding vanishing values of $k_{-(3,1)}$, $k_{-(3,2)}$ and $k_{-(3,3)}$ up to our experimental limits. Finally, the cluster adsorbate complexes (3,3) and (3,4) are in equilibrium at high collision times.

At this point we refer to our associated cryogenic infrared spectroscopy study [IRS] for a more detailed understanding of the $[\text{Ta}_3(\text{H}_2)_m]^+$ adsorbate species. From the structural information, we might infer the underlying reaction processes. The IR-PD spectra of the three adsorbate species (3,1), (3,2) and (3,3) reveal no IR-induced fragmentation. According to the findings from the IR-PD experiments of hydrogen adsorbate species (4,m) and (5,m) we speculate about three dissociatively adsorbed H_2 molecules on the Ta_3^+ cluster. We also find similarities in the adsorption rate constants for the H_2 uptake comparing the present H_2 kinetics of Ta_3^+ with the ones of Ta_4^+ and Ta_5^+ . In both latter cases, the significant decrease in adsorption rates indicate that adsorption of molecular H_2 starts to occur. All H_2 molecules completing the formal first adsorbate shell adsorb dissociatively to the cluster. We take the liberty of assuming that such behavior is also present for Ta_3^+ . The low ion intensities of (3,4) hindered the recording of its IR-PD spectra and thus any experimental confirmation of this assumption. Therefore, further experiment-based conclusions about the adsorption process of H_2 and the structures involved remain open at this point.

$[\text{Ta}_4(\text{H}_2)_m]^+$ Adsorption kinetics of the tantalum tetramer cation, Ta_4^+ , recorded at a pressure of 1.4×10^{-7} mbar H_2 , show the uptake of up to four H_2 molecules (*cf.* Figure 3(a)). The adsorption process of H_2 onto the Ta_4^+ clusters appears to reach its limit m_{max} at a collision cell delay of about 2.5 s. The first three H_2 adsorption processes proceed remarkably fast. Accordingly, the kinetic fit yields high adsorption rate constants between 9.363 s^{-1} , $k_{(4,0)}$, and 13.23 s^{-1} , $k_{(4,3)}$. In contrast, the uptake of the fourth H_2 molecule proceeds significantly slower: $k_{(4,3)} = 1.560 \text{ s}^{-1}$. The resulting cluster adsorbate complex (4,4) appears to be inert towards further adsorption of H_2 . Note, that desorption seems insignificant up to this point, yielding vanishing values of $k_{-(4,1)}$, $k_{-(4,2)}$, $k_{-(4,3)}$, and $k_{-(4,4)}$ up to our experimental limits. However, we performed an additional H_2 kinetic measurement of Ta_4^+ at a H_2 pressure of

6. Kinetics of H₂ Adsorption onto Ta₂₋₈⁺ Clusters under Cryogenic Conditions

5.4×10^{-7} mbar. Indeed, the earlier apparently inert adsorbate complex (4,4) now shows uptake of additional H₂ molecules after all (*cf.* Figure 3(b)). The actual limit of adsorption m_{\max} thus increases to nine H₂ molecules. Despite the high H₂ pressure, which favors the adsorption of the molecules, especially the uptake of the fifth H₂ molecule proves to be particularly slow. The corresponding adsorption rate constant $k_{(4,4)}$ of 0.037 s^{-1} appears to be the lowest overall in the entire H₂ adsorption chain. We obtained somewhat higher rate constants of 0.391 and 2.143 s^{-1} for the adsorption of the sixth and seventh H₂ molecules, respectively. The rate constants of the two final adsorption steps of H₂ eventually both settle at about 0.545 s^{-1} . Besides the fact that the adsorption processes beyond the formally first adsorbate shell are slower by Ta₄⁺ than the previous reactions up to the monolayer of H₂ molecules, it is noticeable that desorption also starts from this H₂ loading. This yields significant contributions by the desorption rate constants $k_{-(4,5)}$ to $k_{-(4,9)}$. The desorption rates $k_{-(4,5)}$, and $k_{-(4,6)}$ exceed the corresponding adsorption rates $k_{(4,4)}$, and $k_{(4,5)}$. The kinetic curves reveal horizontal and parallel curves for the generation of the adsorption limit species [Ta₄(N₂)_m]⁺, $m = 5-9$, already at a collision delay of less than 5 s. This clearly indicates that all cluster adsorbate complexes from (4,5) and beyond are in a dynamic equilibrium throughout the overall kinetic measurement.

To obtain an overall picture of the H₂ adsorption to Ta₄⁺ we merged both rate constant plots of the two kinetic measurements using $\frac{1.4}{5.4}$ as scaling factor for all rate constants $m \geq 4$. Pressure dependent three body processes seem negligible in this case. Figure S3 in the supplementary information shows the unscaled rate constants of the two kinetic fits in separate plots. The plot of the merged rate constants (*cf.* Figure 3(c)) shows even more clearly the steep drop in adsorption rate constants once the H₂ loading reaches the formal first adsorbate shell and more H₂ molecules are adsorbed onto the cluster. At the same time, with the completion of the formal first adsorbate shell, desorption reactions set in. We conclude that there are two different adsorption processes that run in sequence: The first few H₂ adsorption processes proceed very fast and without competitive desorption reactions. The second type process is characteristic for slow adsorption reactions accompanied by fast desorption reactions. The threshold is the completion of the first adsorbate shell.

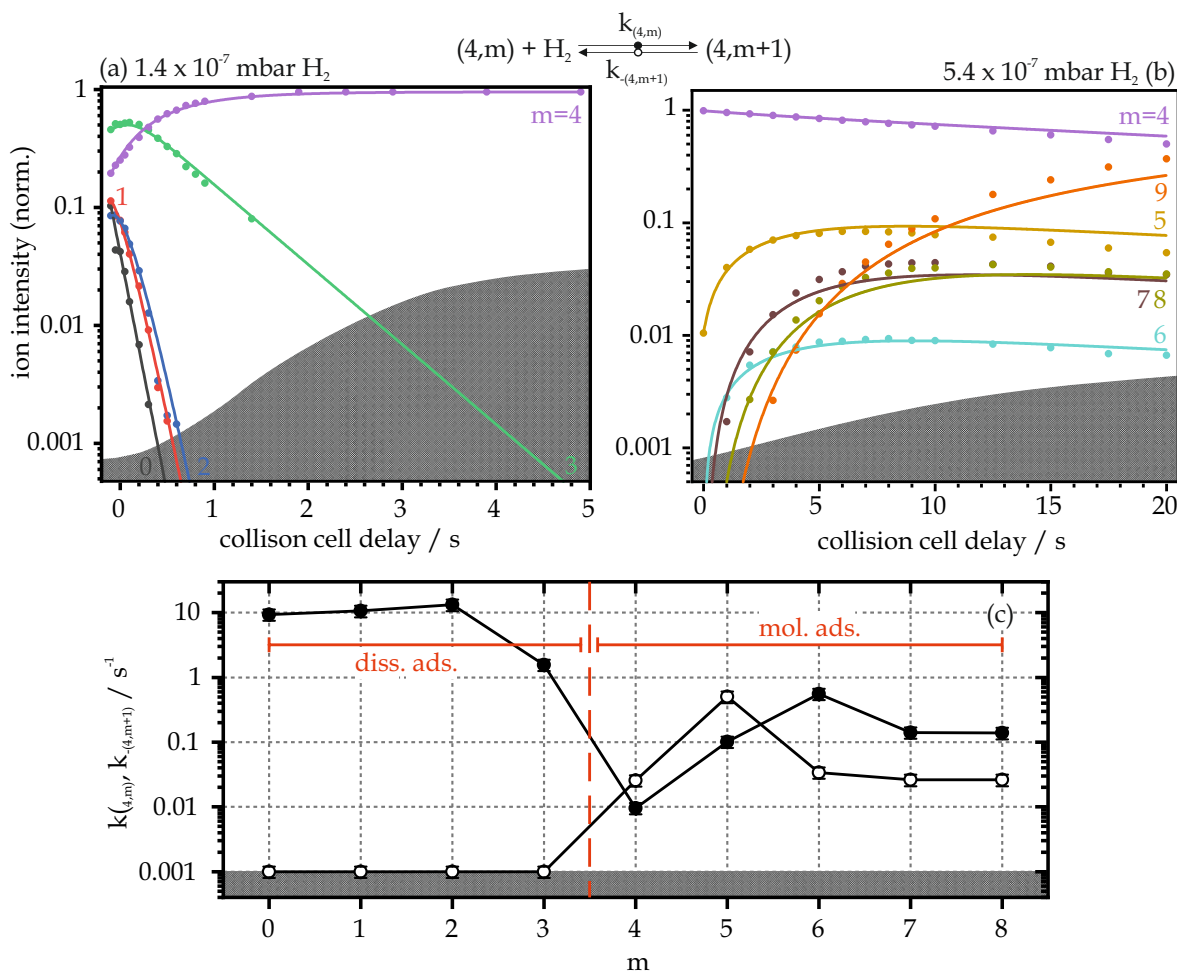


Figure 3: Isothermal kinetics of H_2 adsorption by isolated Ta_4^+ clusters at 18 K, He buffer gas (6.6×10^{-6} mbar) and 1.4×10^{-7} mbar H_2 pressure (a), and 3.0×10^{-6} mbar He buffer gas with 5.4×10^{-7} mbar H_2 pressure (b), respectively. The fitting curves (lines) of the recorded data (dots) confirm pseudo-first-order kinetics for the adsorption in a reaction chain of up to nine consecutive steps for Ta_4^+ clusters. (c) Fitted values of corresponding relative rate constants of Ta_4^+ for the adsorption ($k_{(4,m)}$, solid circles) and the desorption ($k_{(4,m+1)}$, open circles) as a function of stepwise H_2 adsorption. For pressure-normalized absolute values of adsorption rate constants refer to the supplementary information 6.3. The values of the rate constants $k_{(4,m)}$ and $k_{(4,m+1)}$, $m = 4-8$, are scaled by the pressure ratio $\frac{1.4}{5.4}$. Figures S3(c) and S3(d) in the supplementary information (*cf.* chapter 6.3) give unscaled rate constants for all adsorption and desorption steps. The gray shaded areas indicate the background noise level.

6. Kinetics of H₂ Adsorption onto Ta₂₋₈⁺ Clusters under Cryogenic Conditions

At this point we refer to our associated cryogenic infrared spectroscopy study [IRS] for a more detailed structural understanding of the adsorbate species [Ta₄(H₂)_m]⁺, (4,m). With our IR-PD setup we are able to probe Ta-H bands and to infer structural information about the corresponding cluster adsorbate complexes from the measured IR-PD bands. The IR-PD spectra of the first four adsorbate species (4,1), (4,2), (4,3) and (4,4) reveal no IR-induced fragmentation. For (4,5), we observe multiple IR-PD bands in a spectral range between 1100 and 1500 cm⁻¹.

Our DFT modeling for conceivable (4,5) cluster geometries, yielding a corresponding vibrational band pattern, resulted in the following cluster geometry: Four H₂ molecules are dissociatively adsorbed onto a tantalum tetrahedron core. Two opposite Ta-Ta edges of the Ta₄⁺ tetrahedron are bridged by two hydrogen atoms and each of the remaining four Ta-Ta edges is bridged by one hydrogen atom. The fifth H₂ is adsorbed in a side-on motif to one of the Ta atoms of the cluster. We conclude four dissociatively adsorbed H₂ molecules, whose adsorption reaction likely is a fast process. This is in line with findings from our prior study on N₂ adsorption onto small tantalum cluster cations Ta₂₋₄⁺ [42, 43]. In all three cases, the rate constants for the adsorption reactions of the first N₂ molecules are comparatively high. These first N₂ molecules undergo dissociative adsorption on the cluster. The adsorption chain of H₂ onto Ta₄⁺ continues in reactions leading to molecularly adsorbed H₂ molecules for (4,5) and beyond. These molecularly adsorption processes proceed much more slowly. Furthermore, these molecularly adsorbed H₂ molecules are less strongly bound to the cluster core than the dissociatively adsorbed ones and are thus able to undergo desorption reactions.

[Ta₅(H₂)_m]⁺ To gain insight into the individual processes along the H₂ adsorption chain on Ta₅⁺, we performed kinetic studies of Ta₅⁺ + H₂. The measured data at 1.4 × 10⁻⁷ mbar H₂ pressure in the hexapole ion trap show the uptake of up to nine H₂ molecules on Ta₅⁺ in the first place (*cf.* Figure 4(a) and (c)). The obtained pseudo-first-order kinetic fit is of high overall quality (correlation coefficient $\chi = 0.994$). It is noticeable that the adsorption of the initial five H₂ molecules proceeds so rapidly that the ion intensities of the corresponding cluster adsorbate species (5,m), m = 0-4, disappear in the noise within a collision cell delay of less than 2 s. Accordingly, the kinetic fits yield adsorption rate constants of 6.838 and 6.063 s⁻¹ for k_(5,0), and k_(5,1), respectively. The subsequent three adsorption rate constants k_(5,2), k_(5,3) and k_(5,4) have even higher values of 10.54, 11.38, and 10.29 s⁻¹. The adsorption of the

sixth H₂ proceeds significantly slower and the according rate constant $k_{(5,5)}$ constant drops down to 0.182 s^{-1} . The following three steps of H₂ adsorption are again slightly faster, but the rate constants are still far below those of the fast initial five adsorption steps.

It is noticeable that desorption also starts for these H₂ loads. This yields significant contributions by the desorption rate constants $k_{-(5,7)}$, $k_{-(5,8)}$ and $k_{-(5,9)}$. The latter seems to actually exceed the corresponding adsorption rate $k_{(5,8)}$. The kinetics plot (*cf.* Figure 4(a)) shows both rising and falling curves instead of horizontal and parallel curves for the generation of the ultimate adsorption limit species $[\text{Ta}_5(\text{N}_2)_m]^+$, $m = 5-9$. This clearly shows that no dynamic equilibrium has been established throughout the whole adsorption chain. Instead, these curves indicate that the H₂ adsorption processes are not yet complete and that further H₂ adsorption on Ta_5^+ could possibly follow.

It is for this reason, that we performed additional kinetic measurements at a H₂ pressure of 4.0×10^{-7} mbar. Indeed, we now observe the uptake of additional H₂ molecules (*cf.* Figure 4(b)). The limit of adsorption m_{max} thus increases to twelve H₂ molecules. The measured intensity data show that the adsorption chain yields an adsorption species (5,12), which remains the only species present at long storage times above 4 s. The obtained pseudo-first-order kinetics fit are of good overall quality (correlation coefficient $\chi = 0.985$).

The two measured kinetics (a) and (b) both include the five adsorbate species (5,5) to (5,9). In this case, high order processes of three body collisions seem to induce non-linear pressure dependencies. Therefore, in this case of Ta_5^+ kinetics, we did not merge the plots of the rate constants with a scaling factor from the quotient of the two H₂ pressures. Nevertheless, it seemed reasonable to us to consider the rate constants over the entire adsorption chain in a joint plot. Figure S4 in the supplementary information (*cf.* chapter 6.3) shows the overlapping rate constants: solid black circles for the adsorption rates of the kinetics measured at 1.4×10^{-7} mbar and solid blue squares for the adsorption rates of the kinetics measured at 4.0×10^{-7} mbar.

6. Kinetics of H_2 Adsorption onto Ta_{2-8}^+ Clusters under Cryogenic Conditions

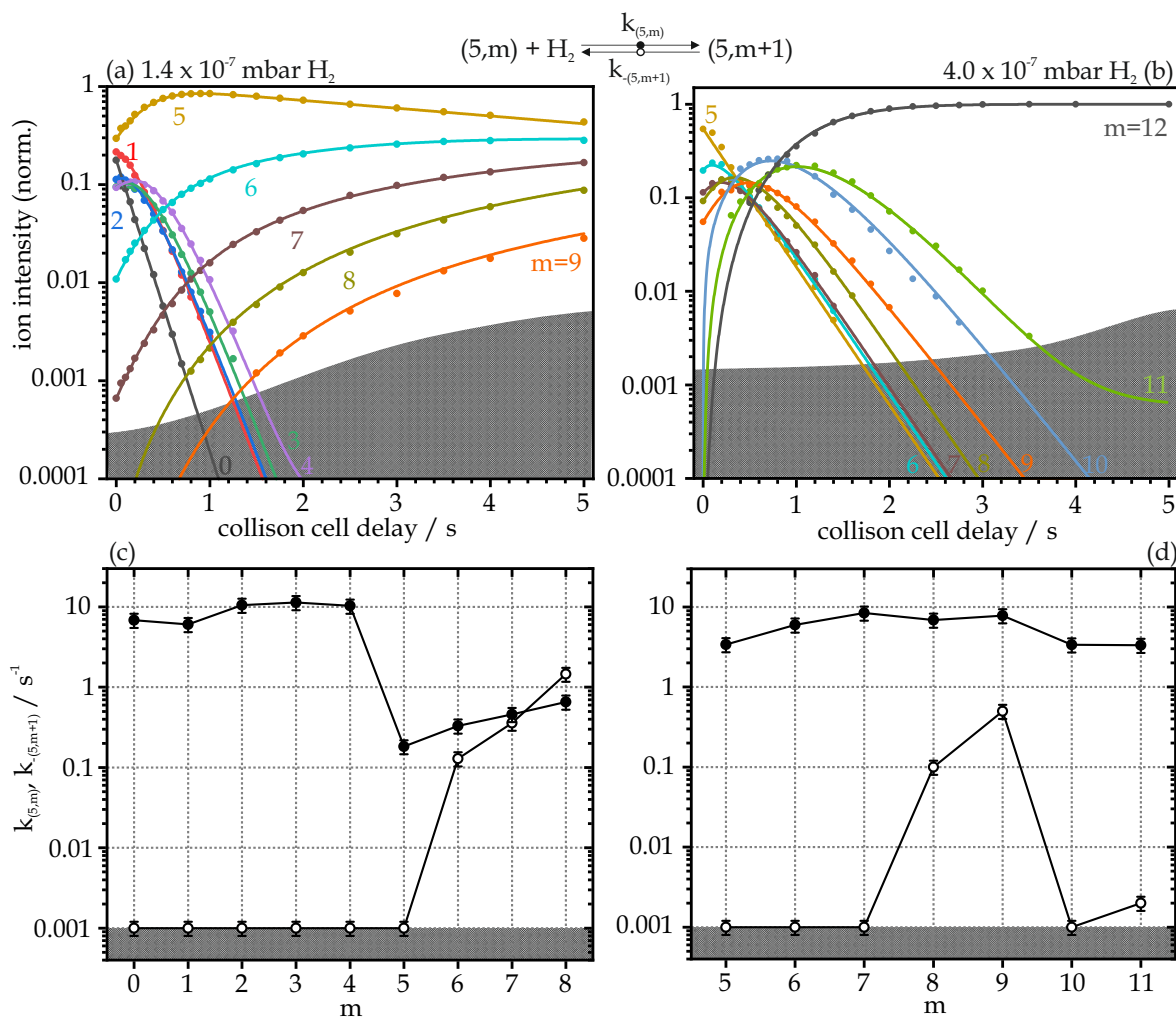


Figure 4: Isothermal kinetics of H_2 adsorption by isolated Ta_5^+ clusters at 18 K, He buffer gas (6.5×10^{-6} mbar) and 1.4×10^{-7} mbar H_2 pressure (a), and 5.4×10^{-6} mbar He buffer gas with 4.0×10^{-7} mbar H_2 pressure (b), respectively. The fitting curves (lines) of the recorded data (dots) confirm pseudo-first-order kinetics for the adsorption in a reaction chain of up to twelve consecutive steps for Ta_5^+ clusters. Fitted values of corresponding relative rate constants of Ta_5^+ for the adsorption ($k_{(5,m)}$, solid circles) and the desorption ($k_{-(5,m+1)}$, open circles) as a function of stepwise H_2 adsorption. (c) gives the rate constants obtained from the fit of kinetic (a). (d) gives the rate constants obtained from the fit of kinetic (b). For pressure-normalized absolute values of adsorption rate constants refer to the supplementary information, chapter 6.3. The gray shaded areas indicate the background noise level.

For the “overlapping” rate constants $k_{(5,m)}^{1.4 \times 10^{-7} \text{ mbarH}_2}$ and $k_{-(5,m)}^{4.0 \times 10^{-7} \text{ mbarH}_2}$, $m = 5 - 8$, we observe parallel increasing values, albeit partly shifted. They are separated by an order of magnitude. The value for $k_{(5,9)}$ is similarly high as $k_{(5,8)}$. The final adsorption rate constants $k_{(5,10)}$ and $k_{(5,11)}$ are considerably lower. In parallel, the rate constants for the desorption of a H_2 molecule from (5,11) and (5,12), $k_{-(5,m+1)}$ $m = 10$ and $m = 11$, decrease to (almost) insignificant values of 0.001 and 0.002 s^{-1} , respectively. Thus, the adsorption limit species ($5, m_{\text{max}}=12$) is the only species present at long storage times, consistent with the measured ion intensity kinetics shown in Figure 4(b).

The overall picture of H_2 adsorption onto Ta_5^+ indicates a steep drop in adsorption rate constants once the H_2 loading reaches the formal first adsorbate shell ($n, m = n$) and more H_2 molecules are adsorbed onto the cluster. At the same time, beyond a completion of the formal first adsorbate shell, several desorption reactions set in. We observe a similar behavior for the H_2 adsorption onto the smaller tantalum clusters Ta_3^+ and Ta_4^+ . Also in the present case we conclude that there are two different H_2 adsorption processes that follow each other: The first few H_2 adsorption reactions proceed very fast and without competitive desorption reactions. The second type process is characteristic for slow adsorption reactions accompanied by several desorption reactions. The threshold is the completion of the first adsorbate shell. Based on these parallels, we estimate a general trend for H_2 adsorption on small Ta_n^+ clusters.

At this point we refer to our associated cryogenic infrared spectroscopy study [IRS] for a more detailed understanding of the adsorbate species $[\text{Ta}_5(\text{H}_2)_m]^+$, (5,m). Our IR-PD routine probing the Ta-H bands of the cluster adsorbate species reveals no IR-induced fragmentation for all species (5,0) to (5,5). For all subsequent adsorbate species from (5,6) and beyond, we observe multiple IR-PD bands in a spectral range between 1100 and 1800 cm^{-1} . Our DFT modeling for conceivable cluster geometries, yielding corresponding IR band patterns, predicts five dissociatively adsorbed H_2 molecules on a trigonal bipyramidal Ta_5^+ cluster framework. In other words, all H_2 molecules forming the first formal adsorbate shell bind to the cluster framework in dissociative motifs. All further H_2 molecules adsorb molecularly to the cluster. The prediction of dissociative adsorption processes for the initial five H_2 molecules correspond to the fast rate constants $k_{(5,m)}$, $m = 0 - 4$. This is in line with the findings for H_2 on Ta_3^+ and Ta_4^+ . For both species we found a convincing justification

6. Kinetics of H₂ Adsorption onto Ta₂₋₈⁺ Clusters under Cryogenic Conditions

in the assumption of fast dissociative adsorption processes up to the formal first adsorption shell species (n,m = n) and much slower molecular adsorption processes beyond. These molecularly adsorbed H₂ molecules are less strongly bound to the cluster core than the dissociatively adsorbed ones and are thus able to undergo desorption reaction. The final adsorption process leading to species (5,11) and (5,12), forms the formal third adsorption shell of H₂ on Ta₅⁺. Here, the low adsorption rate constants and (almost) insignificant values of desorption rate constants are in good agreement with the predicted cluster geometry of (5,12), which provides the reason for the characteristic IR-PD band at 1700 cm⁻¹. This ultimate shell consists of two H₂ ligands coordinating in a combined side-on/end-on $\mu_2\text{-}\kappa\text{H}:\kappa\text{H},\text{H}$ motif and are thus strongly activated. This activated coordination is associated with high adsorption energies coming with reduced H₂ desorption.

We assume that the overall picture of dissociative adsorption up to a formal first adsorbate shell and molecular adsorption beyond is a general procedure for the adsorption of H₂ on small tantalum clusters, since we find this behavior for the adsorption of H₂ on Ta₃⁺ and Ta₄⁺ as well as on the present Ta₅⁺.

[Ta₆(H₂)_m]⁺ For Ta₆⁺ we find stepwise H₂ adsorption up to an adsorption limit m_{max} of twelve H₂ molecules. However, we do not observe all species (6,m) along the adsorption chain. Using our typical evaluation routine we fitted the measured intensity data and managed to obtain an overall fit of high overall quality (*cf.* Figure 5(a), correlation coefficient $\chi = 0.990$). Figure 5(b) shows the thereby fitted rate constants for each H₂ adsorption and desorption step. The ion intensity of the bare Ta₆⁺ cluster decreases very slowly over the course of the kinetics measurement and is still the ion species with the third highest intensity even at a very long collision cell delay of 30 s. This indicates that the adsorption reaction on Ta₆⁺ continues well beyond our measurement period. The adsorption rate constant $k_{(6,0)}$ gives a correspondingly low value at 0.074 s⁻¹. The adsorption of a second H₂ molecules yielding the cluster adsorbate species (6,2) proceeds even slower: $k_{(6,1)} = 0.033 \text{ s}^{-1}$. Surprisingly, the next significant larger cluster adsorbate species is (6,6), comprising a full formal first adsorbate shell. We hardly find very low intensity indications of complexes between (6,2) and (6,6). They may exist merely as adsorption intermediates. In effect, any fits inevitably need to involve high values of $k_{(6,m)}$, $m = 2 - 5$, which rise by more than one or two orders of magnitude with respect to the values of the initial

adsorption steps. The adsorption of another H₂ molecule beyond the formal first adsorbate shell is still fast, but much slower than the previous three adsorption steps. This yields the observable species (6,7). From this H₂ loading, additional competitive desorption reactions of H₂ start. This yields significant contributions by the desorption rate constants $k_{-(6,7)}$ to $k_{-(6,12)}$. None of them appear to actually exceed the corresponding adsorption rate constants. However, the high values of the desorption rates correspond to the horizontal and parallel course of the respective ion intensity curves. Note, that desorption seems insignificant up to this point, yielding values of $k_{-(6,1)}$ to $k_{-(6,6)}$ below our background noise level. We observe significant ion intensities for all cluster adsorbate species (6,9) to (6,12) while the ion intensities of species (6,8) disappear again in the background noise. In effect, the adsorption rate constant $k_{(6,8)}$ has an exceptionally high value of 30.63 s^{-1} . The corresponding desorption rate $k_{-(6,9)}$, on the other hand, has a particularly low value. The fits reveal gradually decreasing values for the rate constants of the last three adsorption and desorption reaction processes of H₂, which lead to the adsorption limit (6,12).

In summary, the characteristic of the present kinetics of H₂ adsorption onto Ta₆⁺ differs significantly from the adsorption kinetics observed for Ta₃⁺, Ta₄⁺ and Ta₅⁺: We do not observe fast adsorption processes for the first few H₂ molecules indicative of dissociative adsorption steps as we did for the kinetics of (3,m), (4,m) and (5,m). The slow initial adsorption processes delay the entire adsorption chain. In fact, (6,1) is the most intense species even with a long storage time of 30 s. However, an adsorption chain in which individual steps occur so rapidly that not every species can be detected by mass spectrometry is very unusual for our experimental setup. We have only observed a similar behavior in N₂ adsorption onto the Fe₁₃⁺ and Fe₁₄⁺ clusters [50]. None of the cluster sizes of other investigated transition metal clusters [39, 47–49], in particular also the tantalum clusters [42], showed such a behavior so far. Only the onset of desorption reactions after reaching a full formal first adsorbate shell ($n, m = n$) is in agreement with the previously measured kinetics of (n,m), $n = 3 - 5$.

We now know about the rates of all adsorption and desorption steps up to the adsorption limit species (6,12). To understand the big picture of H₂ adsorption on Ta_n⁺ clusters, it is beneficial to also know the structures of the species involved in these processes. We therefore refer to our associated cryogenic infrared spectroscopy study [IRS]. The IR-PD spectra reveal no IR-induced fragmentation for species (6,1)

6. Kinetics of H₂ Adsorption onto Ta₂₋₈⁺ Clusters under Cryogenic Conditions

but multiple IR-PD bands in a spectral range between 1100 and 1400 cm⁻¹ for species (6,12). Without further information from DFT modeling on various cluster geometries at hand, we can only speculate at this point. Based on the findings of the (n,m) cluster adsorbates of size n=4 and n=5, we assume a dissociatively adsorbed H₂ molecule for (6,1) while the maximum adsorption species (6,12) additionally has intact H₂ molecules in its adsorbate shell. The low ion intensities of the other adsorbate species, especially at short storage times as required for IR-PD spectroscopic studies, hamper the recording of their IR-PD spectra and thus prevent obtaining further structural information.

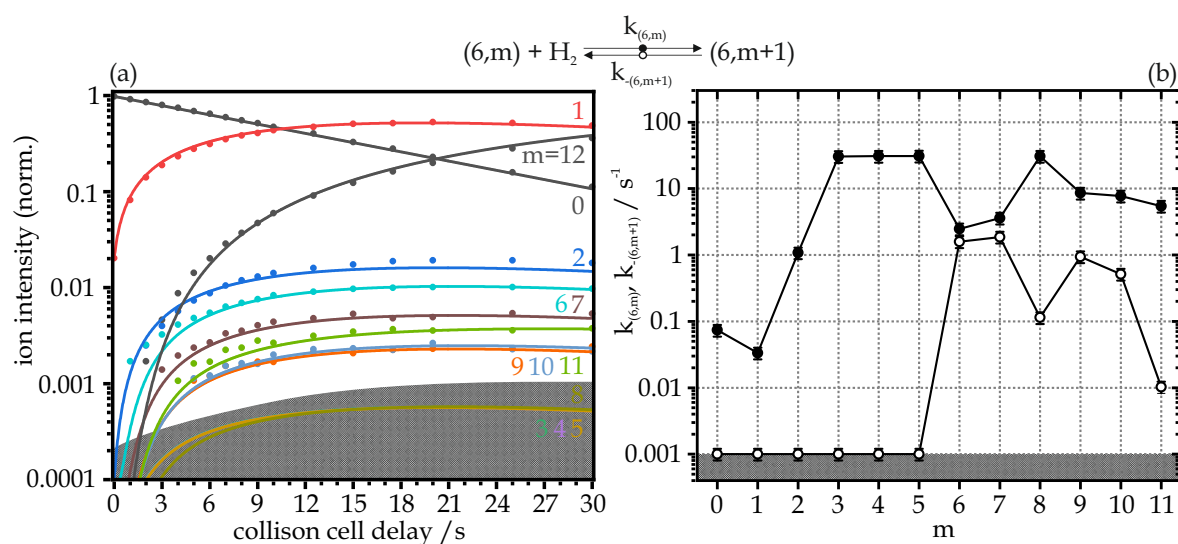


Figure 5: (a) Isothermal kinetics of H₂ adsorption by isolated Ta₆⁺ clusters at 18 K, He buffer gas (3.0×10^{-6} mbar) and 6.0×10^{-7} mbar H₂ pressure. The fitting curves (solid lines) of the recorded data (solid dots) confirm pseudo-first-order kinetics for the adsorption in a reaction chain of up to twelve consecutive steps for Ta₆⁺ clusters. (b) Fitted values of corresponding relative rate constants of Ta₆⁺ for the adsorption ($k_{(6,m)}$, solid circles) and the desorption ($k_{-(6,m+1)}$, open circles) as a function of stepwise H₂ adsorption. For pressure-normalized absolute values of adsorption rate constants refer to the supplementary information, chapter 6.3. The gray shaded areas indicate the background noise level.

[Ta₇(H₂)_m]⁺ We performed kinetic measurements of H₂ adsorption onto Ta₇⁺ clusters. The obtained pseudo-first-order kinetic fit of the measured intensity data is of good overall quality (correlation coefficient $\chi=0.987$). We find stepwise uptake of 14 H₂ molecules onto Ta₇⁺ yielding the adsorption limit species (7,14). It is noteworthy that this species reached the highest intensity of all species within less than 3 s of collision cell delay at an exposure of only 1.4×10^{-7} mbar. Accordingly, we obtain high adsorption rate constants between 8.596 and 15.12 s^{-1} for the first six adsorption processes. The adsorption of the seventh H₂ molecule, which completes the formal first adsorbate shell on Ta₇⁺, appears to be the fastest process in the course of the entire adsorption chain. In fact, a very high value of 21.06 s^{-1} is predicted for the corresponding adsorption rate $k_{(7,6)}$. All further adsorption processes proceed considerably slower and the corresponding adsorption rate constants decrease successively to 1.295 s^{-1} . For the cluster adsorbate species (7,6) and the three subsequent species (7,7), (7,8), and (7,9), additional desorption reactions of H₂ become significant. In fact, the predicted desorption rates are considerably high and only an order of magnitude lower than the corresponding adsorption rates. Note, that desorption seems insignificant for all prior adsorption processes, yielding values of $k_{-(7,1)}$ to $k_{-(7,5)}$ below our background noise level. The contributions of desorption rates $k_{-(7,10)}$, $k_{-(7,11)}$ and $k_{-(7,12)}$ also appear to be insignificant before $k_{-(7,13)}$ and $k_{-(7,14)}$ slightly increase to 0.004 s^{-1} . As a consequence, at long storage times of 8 s and beyond the m_{max} species (7,14) is in dynamic equilibrium with its precursor (7,9).

The overall picture of the processes along the H₂ adsorption chain shows a less significant decrease in adsorption rates beyond the formal first adsorption shell than observed for the H₂ adsorption kinetics of the smaller tantalum clusters Ta₃⁺, Ta₄⁺, and Ta₅⁺. It is also noteworthy that the desorption reactions start before the completion of the first adsorbate shell. While four desorption processes are significant in the middle of the adsorption chain, the desorption reactions become irrelevant or of little influence towards the end. A threshold dividing the adsorption chain into two sections along the first adsorbate shell is not evident.

6. Kinetics of H₂ Adsorption onto Ta₂₋₈⁺ Clusters under Cryogenic Conditions

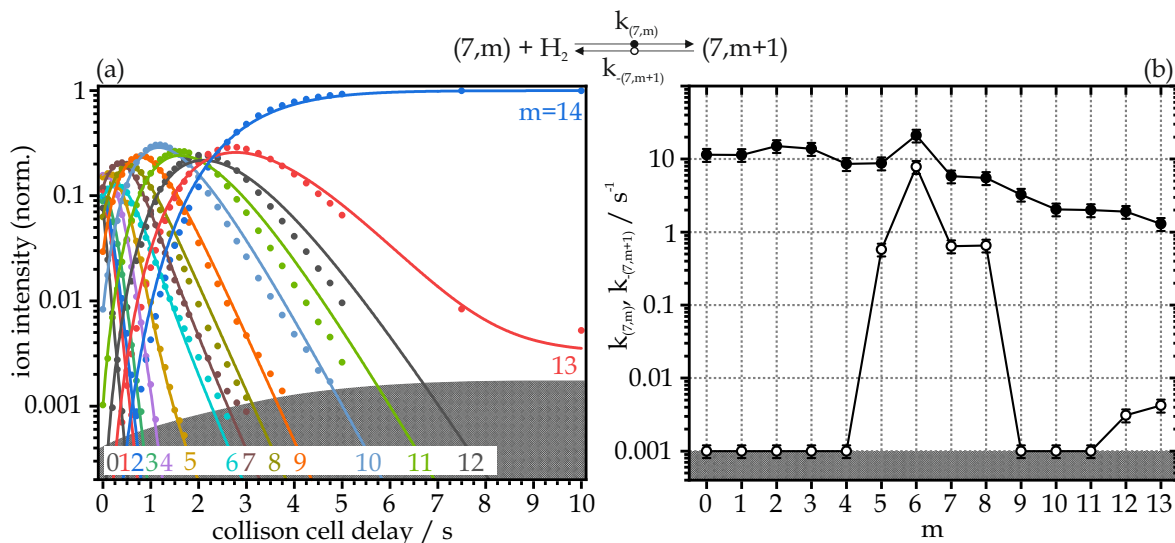


Figure 6: (a) Isothermal kinetics of H₂ adsorption by isolated Ta₇⁺ clusters at 18 K, He buffer gas (3.0×10^{-6} mbar) and 1.4×10^{-7} mbar H₂ pressure. The fitting curves (lines) of the recorded data (dots) confirm pseudo-first-order kinetics for the adsorption in a reaction chain of up to 14 consecutive steps for Ta₇⁺ clusters. (b) Fitted values of corresponding relative rate constants of Ta₇⁺ for the adsorption ($k_{(7,m)}$, solid circles) and the desorption ($k_{-(7,m+1)}$, open circles) as a function of stepwise H₂ adsorption. For pressure-normalized absolute values of adsorption rate constants refer to the supplementary information, chapter 6.3. The gray shaded areas indicate the background noise level.

Our associated cryogenic infrared spectroscopy study [IRS] sheds light on the species involved in the processes along the adsorption chain of H₂ to Ta₇⁺. The recorded IR-PD spectra provide evidence for dissociatively adsorbed H₂ molecules within the formal first adsorbate shell on the Ta₇⁺ cluster. All further H₂ molecules are very likely bound in molecular motifs to the cluster. Without further information from DFT modeling on cluster geometries whose IR band patterns match those measured, we speculate on this conclusion by comparing our present results with those obtained in our study of H₂ adsorption to Ta₄⁺ and Ta₅⁺ (*cf.* [IRS]). If these findings hold, it is counterintuitive that the kinetic fit predicts desorption rates with high rate constants for the desorption of H₂ molecules likely to be dissociatively adsorbed. We consider it realistic that the Ta₇⁺ cluster core contains at least one Ta center that does not accept hydrides due to a high level of next neighbor coordination to other Ta

centers. Thus, a Ta_7^+ cluster could accommodate only five H_2 molecules for dissociative adsorption, while all subsequent molecules are molecularly adsorbed. This hypothesis is consistent with the results of the measured kinetics presented here. However, the dissociative adsorption of a sixth and a seventh H_2 molecule could be possible in principle, although initially inaccessible. The photon energy introduced into the respective cluster adsorbates while recording IR-PD spectra could cause a reorganization of the Ta hydride cluster core, so that the additional molecularly adsorbed H_2 molecules eventually dissociate on the cluster and form hydrides. This results in the absence of IR-PD bands in the corresponding spectra, *cf.* [IRS].

$[\text{Ta}_8(\text{H}_2)_m]^+ \text{Ta}_8^+$ is the largest cluster in our cryo kinetic study of H_2 adsorption on tantalum cluster cations. We performed the kinetic measurement at a H_2 pressure of 1.4×10^{-7} mbar (*cf.* Figure 7). The recorded ion intensities reveal at first the stepwise adsorption of five H_2 molecules. This yields species (8,5) as an intermittent adsorption limit that adsorbs additional H_2 molecules in a delayed manner. The ion intensity of the subsequent adsorbate species (8,6) rises with collision cell delay. The next intense cluster adsorbate species actually appears to be the maximum adsorption species (8,15). We observe low ion intensities for all species along the adsorbate chain between (8,6) and (8,15). This indicates fast reaction processes for the corresponding adsorption steps. The ion intensities of species (8,7) (dark brown circles in the kinetic plot Figure 7) show a striking course. Starting with low intensities within the first 0.5 s of the measurement, the ion intensities of (8,7) reaches their first intensity maximum at 1 s collision cell delay. Thereupon, the ion intensity decreases until a collision cell delay of 3 s. From this point on, the ion intensities increase again until the end of the measurement (15 s). The ion intensities of another adsorbate species along the adsorption chain, (8,11), also show a second increase. However, the effect for (8,11) is less pronounced than for the species (8,7). Appropriate kinetic fits are necessary to interpret the measured intensities. However, the H_2 adsorption processes taking place go beyond our simple stepwise adsorption model. Thus, we remain speculating for processes which might involve adsorbate shell reorganization and/or adsorbate induced cluster relaxation. Both possibilities may result in the desorption of some H_2 ligands and, as a consequence, species with less adsorbed H_2 regain ion intensity. The kinetic plot shows a nearly horizontal and parallel progression of ion intensities for species (8,4), (8,5), (8,6), (8,7), (8,11), and (8,15) at collision cell delays beyond 10 s. This indicates that these six adsorbate complexes are in dynamic equilibrium.

6. Kinetics of H₂ Adsorption onto Ta₂₋₈⁺ Clusters under Cryogenic Conditions

At this point we refer to our associated cryogenic infrared spectroscopy study [IRS]. The recorded IR-PD spectra might provide information about the structure of the involved adsorbate species. Indeed, we managed to perform IR-PD spectra for (8,m), m = 1-6 and m = 15. The low yields of the other adsorbate species, especially at short storage times as required for IR-PD spectroscopic studies, hamper the recording of their IR-PD spectra. However, the IR-PD spectra of the first five adsorbate species show no IR-induced fragmentation, indicating dissociative adsorbed H₂ molecules. This is in line with the probably fast adsorption processes yielding the intermittent adsorption limit (8,5). We observe weak IR-PD bands for species (8,6) indicative of a molecularly adsorbed sixth H₂ molecule. Adsorption of this molecule is likely a slow process, as indicated by the present kinetic measurement. As an interpretation, we assume that at the cluster size n = 8 the first adsorbate shell can already be complete if it consists of five H₂ ligands, m = 5, instead of m = n as observed for the smaller clusters n = 3-5.

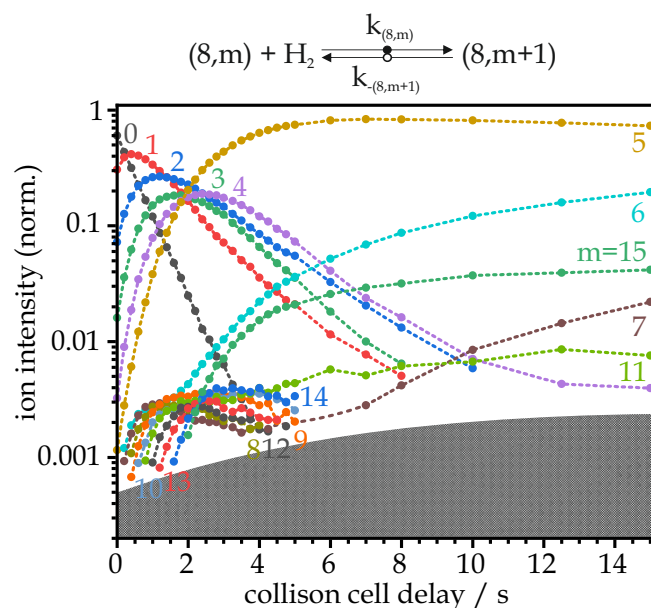


Figure 7: (a) Isothermal kinetics of H₂ adsorption by isolated Ta₈⁺ clusters at 18 K, He buffer gas (3.1×10^{-6} mbar) and 1.4×10^{-7} mbar H₂ pressure. Measured data are presented as circles and are connected by dashed lines to guide the eye. The gray shaded areas indicate the background noise level.

6.2.5 Conclusion

In this paper we present a study of stepwise H₂ adsorption on size-selected tantalum cluster cations Ta_n⁺, n = 2 - 8. We observe an increasing trend in the adsorption limits m_{max} with increasing cluster size n at a stoichiometry close to 1:2. The total number of adsorbed H₂ molecules is less than the N₂ adsorption limit. This is likely due to the dissociation of the first adsorbed H₂ molecules on the cluster, resulting in a faster occupation of more binding sites than the molecular adsorbed ligands. We recorded adsorption kinetics at 18 K in a hexapole ion trap and performed pseudo-first order kinetic fits to the measured intensity data. We received fits with high overall quality and rate constants for all adsorption and desorption steps along the respective adsorption chain. The results show that the H₂ adsorption to Ta_n⁺ cluster exhibit dependencies on cluster size n. The smallest tantalum cluster cation, Ta₂⁺, proved to be inert towards H₂ under the conditions of our experiments. The heat bath of this small cluster seems to be insufficient to dissociate H₂.

For Ta_n⁺ cluster, n = 3 - 5, we conclude that there are two different H₂ adsorption processes that follow each other: The first few H₂ adsorption reactions proceed very fast and without competitive desorption reactions. The second type process is characteristic for slow adsorption reactions accompanied by several desorption reactions. The threshold is the completion of the first adsorbate shell. From our associated cryogenic infrared study [IRS] and some DFT modeling for conceivable (n,m) geometries we found a convincing justification in the assumption of fast dissociative adsorption processes up to the formal first adsorption shell species (n,m = n) and much slower molecular adsorption processes beyond that. These molecularly adsorbed H₂ molecules are more weakly bound to the cluster core than the dissociatively adsorbed ones and are thus able to undergo desorption reactions.

The characteristic of the present kinetic of H₂ adsorption onto Ta₆⁺ differs significantly from the adsorption kinetics observed for Ta₃⁺, Ta₄⁺ and Ta₅⁺: We do not observe fast adsorption processes for the first few H₂ molecules indicative of dissociative adsorption steps. These slow initial adsorption processes delay the entire adsorption chain. However, we do not observe all species (6,m) along the adsorption chain as their reaction processes are too fast. The fitted rate constants reveal the onset of desorption reactions after reaching a full formal first adsorbate shell.

The overall picture of the processes along the H₂ adsorption chain of Ta₇⁺ reveals a decrease in adsorption rates beyond the formal first adsorption shell, but it is less significant than observed for the H₂ adsorption kinetics of the smaller tantalum clusters Ta₃⁺, Ta₄⁺ and Ta₅⁺. However, the recorded IR-PD spectra [IRS] provide evidence for dissociatively adsorbed H₂ molecules within the formal first adsorbate shell on the Ta₇⁺ cluster. All further H₂ molecules are very likely bound in molecular motifs to the cluster.

We again observe an unusual behavior for the adsorption kinetics of H₂ and Ta₈⁺. The recorded ion intensities reveal at first the stepwise adsorption of five H₂ molecules. Thus, (8,5) is as an *intermittent adsorption limit* that adsorbs additional H₂ molecules in a delayed manner. The ion intensities of species (8,7) lead us to speculate on adsorbate shell reorganization and/or adsorbate-induced cluster relaxation processes.

6.2.6 Acknowledgements

This work was supported by the German research foundation DFG within the trans-regional collaborative research center SFB/TRR 88 “Cooperative effects in homo and heterometallic complexes” (3met.de) and by the state research center OP-TIMAS. We thank Thomas Kolling for technical assistance and valuable discussion.

6.2.7 References

- [1] W. M. Haynes, *CRC Handbook of Chemistry and Physics, Vol. 95th*, CRC Press Taylor & Francis Group, **2014**.
- [2] M. Frey, *ChemBioChem* **2002**, 3, 153–160.
- [3] S. Shima, R. K. Thauer, *The Chemical Record* **2007**, 7, 37–46.
- [4] M. Bruschi, M. Tiberti, A. Guerra, L. De Gioia, *Journal of the American Chemical Society* **2014**, 136, 1803–1814.
- [5] F. Schüth, *Chemie in unserer Zeit* **2006**, 40, 92–103.
- [6] A. Mittasch, *Geschichte der Ammoniaksynthese*, Verlag Chemie, **1951**.
- [7] H. Breil, E. Holzkamp, H. Martin, K. E. H. Ziegler, DE973626C, **1960**.

-
- [8] W. Ostwald, GB190200698A, **1902**.
- [9] Badische Anilin- und Soda-Fabrik, DE235421C, **1911**.
- [10] F. Fischer, H. Tropsch, DE524468C, **1931**.
- [11] F. Fischer, H. Tropsch, DE484337C, **1925**.
- [12] P. B. Armentrout, *Catalysis Science & Technology* **2014**, *4*, 2741–2755.
- [13] S. M. Lang, T. M. Bernhardt, *Physical Chemistry Chemical Physics* **2012**, *14*, 9255–9269.
- [14] D. K. Böhme, H. Schwarz, *Angewandte Chemie International Edition* **2005**, *44*, 2336–2354.
- [15] R. A. J. O’Hair, G. N. Khairallah, *Journal of Cluster Science* **2004**, *15*, 331–363.
- [16] P. B. Armentrout, *Annual Reviews* **2001**, *52*, 423–461.
- [17] E. L. Muetterties, *Science* **1977**, *196*, 839–848.
- [18] M. B. Knickelbein, *Annual Reviews* **1999**, *50*, 79–115.
- [19] M. E. Geusic, M. D. Morse, R. E. Smalley, *The Journal of Chemical Physics* **1985**, *82*, 590–591.
- [20] G. J. Kubas, *Accounts of Chemical Research* **1988**, *21*, 120–128.
- [21] K. Christmann, *Surface Science Reports* **1988**, *9*, 1–163.
- [22] D. A. Hite, K. S. McKay, S. Kotler, D. Leibfried, D. J. Wineland, D. P. Pappas, *MRS Advances* **2017**, *2*, 2189–2197.
- [23] M. B. Knickelbein, G. M. Koretsky, K. A. Jackson, M. R. Pederson, Z. Hajnal, *The Journal of Chemical Physics* **1998**, *109*, 10692–10700.
- [24] K. García-Díez, J. Fernández-Fernández, J. A. Alonso, M. J. López, *Physical Chemistry Chemical Physics* **2018**, *20*, 21163–21176.
- [25] I. Swart, P. Gruene, A. Fielicke, G. Meijer, B. M. Weckhuysen, F. M. F. de Groot, *Physical Chemistry Chemical Physics* **2008**, *10*, 5743–5745.
- [26] O. V. Lushchikova, H. Tahmasbi, S. Reijmer, R. Platte, J. Meyer, J. M. Bakker, *The Journal of Physical Chemistry A* **2021**, *125*, 2836–2848.

6. Kinetics of H₂ Adsorption onto Ta₂₋₈⁺ Clusters under Cryogenic Conditions

- [27] C. Kerpál, D. J. Harding, D. M. Rayner, A. Fielicke, *The Journal of Physical Chemistry A* **2013**, *117*, 8230–8237.
- [28] S. C. Richtsmeier, E. K. Parks, K. Liu, L. G. Pobo, S. J. Riley, *The Journal of Chemical Physics* **1985**, *82*, 3659–3665.
- [29] W. F. Hoffman, E. K. Parks, G. C. Nieman, L. G. Pobo, S. J. Riley, *Zeitschrift für Physik D Atoms Molecules and Clusters* **1987**, *7*, 83–89.
- [30] P. Gruene, A. Fielicke, G. Meijer, *The Journal of Chemical Physics* **2007**, *127*, 234307.
- [31] J. Du, X. Sun, G. Jiang, *The Journal of Chemical Physics* **2012**, *136*, 094311.
- [32] N. Levin, J. T. Margraf, J. Lengyel, K. Reuter, M. Tschurl, U. Heiz, *Physical Chemistry Chemical Physics* **2022**, *24*, 2623–2629.
- [33] J. F. Eckhard, D. Neuwirth, C. Panosetti, H. Oberhofer, K. Reuter, M. Tschurl, U. Heiz, *Physical Chemistry Chemical Physics* **2017**, *19*, 5985–5993.
- [34] C. Geng, J. Li, T. Weiske, H. Schwarz, *Proceedings of the National Academy of Sciences* **2019**, *116*, 21416–21420.
- [35] X. Sun, X. Huang, *ACS Omega* **2022**, *7*, 22682–22688.
- [36] G.-D. Jiang, L.-H. Mou, J.-J. Chen, Z.-Y. Li, S.-G. He, *The Journal of Physical Chemistry A* **2020**, *124*, 7749–7755.
- [37] M. Kumar Yadav, A. Mookerjee, *Physica B: Condensed Matter* **2010**, *405*, 3940–3942.
- [38] J. F. Eckhard, T. Masubuchi, M. Tschurl, R. N. Barnett, U. Landman, U. Heiz, *The Journal of Physical Chemistry C* **2018**, *122*, 25628–25637.
- [39] A. A. Ehrhard, M. P. Klein, J. Mohrbach, S. Dillinger, G. Niedner-Schatteburg, *The Journal of Chemical Physics* **2022**, *0*, 054308.
- [40] J. Lengyel, N. Levin, F. J. Wensink, O. V. Lushchikova, R. N. Barnett, U. Landman, U. Heiz, J. M. Bakker, M. Tschurl, *Angewandte Chemie International Edition* **2020**, *59*, 23631–23635.
- [41] C. Geng, J. Li, T. Weiske, H. Schwarz, *Proceedings of the National Academy of Sciences* **2018**, *115*, 11680–11687.

-
- [42] D. V. Fries, M. P. Klein, A. Steiner, M. H. Prosenc, G. Niedner-Schatteburg, *Physical Chemistry Chemical Physics* **2021**, 23, 11345–11354.
- [43] D. V. Fries, M. P. Klein, A. Straßner, M. E. Huber, M. Luczak, C. Wiehn, G. Niedner-Schatteburg, *The Journal of Chemical Physics* **2023**, 159, 164303.
- [44] D. V. Fries, M. P. Klein, A. Straßner, M. E. Huber, G. Niedner-Schatteburg, *The Journal of Chemical Physics* **2023**, 159, 164306.
- [45] G. Ertl, *Catalysis Reviews* **1980**, 21, 201–223.
- [46] G. Ertl, *Angewandte Chemie International Edition* **2008**, 47, 3524–3535.
- [47] J. Mohrbach, S. Dillinger, G. Niedner-Schatteburg, *The Journal of Physical Chemistry C* **2017**, 121, 10907–10918.
- [48] S. Dillinger, J. Mohrbach, G. Niedner-Schatteburg, *The Journal of Chemical Physics* **2017**, 147, 184305.
- [49] A. A. Ehrhard, M. P. Klein, J. Mohrbach, S. Dillinger, G. Niedner-Schatteburg, *Molecular Physics* **2021**, 119, e1953172.
- [50] A. Straßner, M. P. Klein, D. V. Fries, C. Wiehn, M. E. Huber, J. Mohrbach, S. Dillinger, D. Spelsberg, P. B. Armentrout, G. Niedner-Schatteburg, *The Journal of Chemical Physics* **2021**, 155, 244306.
- [51] A. Straßner, C. Wiehn, M. P. Klein, D. V. Fries, S. Dillinger, J. Mohrbach, M. H. Prosenc, P. B. Armentrout, G. Niedner-Schatteburg, *The Journal of Chemical Physics* **2021**, 155, 244305.
- [52] C. Berg, T. Schindler, G. Niedner-Schatteburg, B. V. E., *The Journal of Chemical Physics* **1995**, 102, 4870–4884.
- [53] V. Bondybey, J. English, *The Journal of Chemical Physics* **1981**, 74, 6978–6979.
- [54] D. Proch, T. Trickl, *Review of Scientific Instruments* **1989**, 60, 713–716.
- [55] P. Caravatti, M. Allemann, *Organic Mass Spectrometry* **1991**, 26, 514–518.
- [56] M. Graf, *Diploma Thesis*, Technische Universität Kaiserslautern, **2006**.

6.3 Supplementary Information

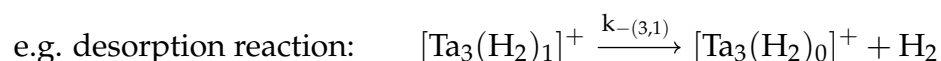
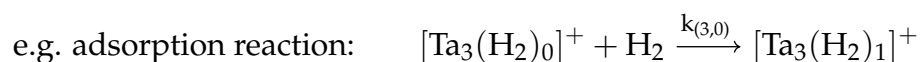
KINETICS OF H₂ ADSORPTION ONTO TA₂₋₈⁺ CLUSTER UNDER CRYOGENIC CONDITIONS

Daniela V. FRIES, Annika STRAßNER, Matthias P. KLEIN, and Gereon
NIEDNER-SCHATTEBURG

Department of Chemistry and State Research Center OPTIMAS,
Rheinland-Pfälzische Technische Universität (RPTU) Kaiserslautern-Landau,
67663 Kaiserslautern, Germany

Text S1: Nomenclature for the Ta_n^+ clusters and their hydrogen adsorbates

The adsorption of H_2 onto Ta_n^+ clusters yield cluster adsorbate complexes whose typical chemical nomenclature is $[Ta_n(H_2)_m]^+$. In line with our prior studies on a series of transition metal clusters [1-9] we have again chosen an abridged (n,m) nomenclature for the cluster adsorbate complexes $[Ta_n(H_2)_m]^+$. In this nomenclature, n stands for the size of the cluster; e.g., n = 3 stands for a cluster of three tantalum atoms. The corresponding shortened notation for hydrogen adsorbates is (3,m), where m stands for the number of H_2 molecules adsorbed to the cluster. As Ta_3^+ adsorbs up to four H_2 molecules we observe four complexes (3,m) which are interlinked by four processes, respectively, in the form of adsorption and desorption reactions. Each of these processes is described by a relative rate constant, either $k_{(3,m)}$ for an adsorption reaction or $k_{-(3,m+1)}$ for a desorption reaction. In this case n = 3, the index m of the rate constants ranges from 0 to 3.



6. Kinetics of H_2 Adsorption onto Ta_{2-8}^+ Clusters under Cryogenic Conditions

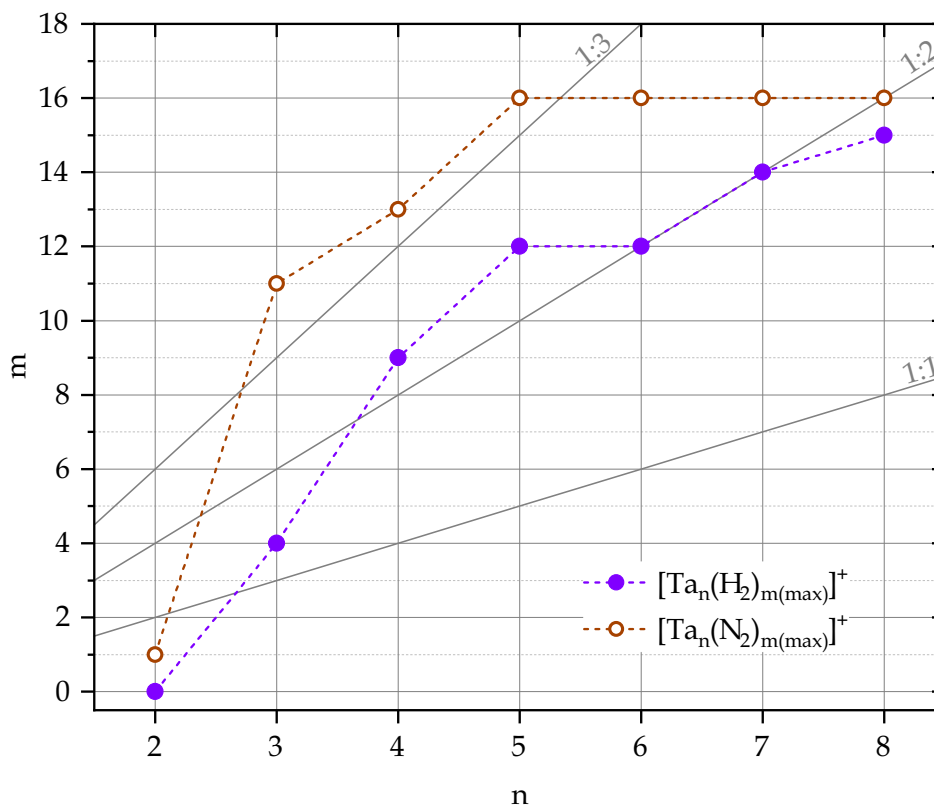


Figure S1: Plot of the experimentally determined adsorption limits m_{\max} of H_2 adsorption to Ta_n^+ clusters, $n=2-8$ (solid circles). The cluster ions were stored for up to 30 s within the hexapole ion trap with 18 K He buffer gas and up to 6.0×10^{-7} mbar H_2 as reaction gas. The open circles represent the experimentally determined adsorption limits m_{\max} of N_2 adsorption to Ta_n^+ clusters, $n=2-8$ (up to 20 s, exposure to 3.5×10^{-7} mbar H_2). The gray lines indicate stoichiometries of $n:m_{\max}$.

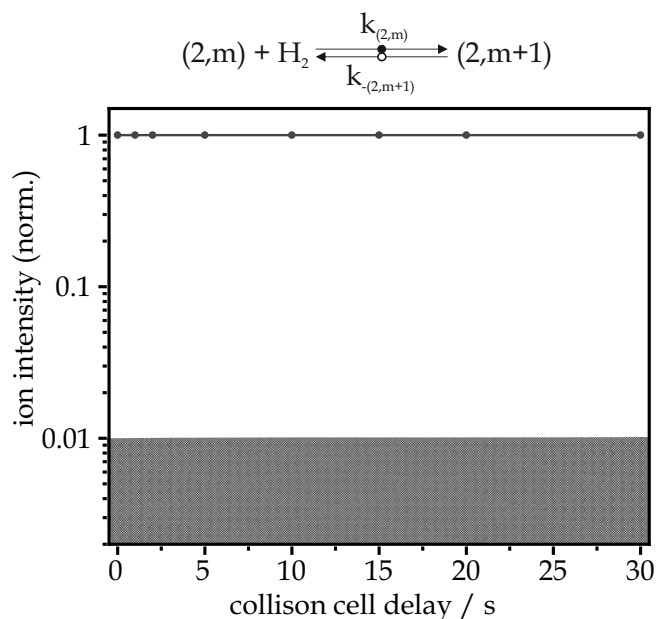


Figure S2: Isothermal kinetics of H_2 adsorption by isolated Ta_2^+ clusters at 18 K, He buffer gas (3.0×10^{-6} mbar) and 5.4×10^{-7} mbar H_2 pressure. Measured data are presented as circles and the fits (shown as lines) assume pseudo-first-order kinetics illustrating the inertness of Ta_2^+ towards H_2 .

Table S1: Pseudo-first-order rate constants for the H_2 adsorption and desorption ($p(\text{H}_2)=1.8 \times 10^{-7}$ mbar) on $[\text{Ta}_3(\text{H}_2)_m]^+$ clusters ($k_{(3,m)}$ and $k_{-(3,m+1)}$, cf. Figure 2), the related absolute rate constants ($k_{(3,m)}^{\text{abs}}$), the calculated collision rates ($k_{(3,m)}^{\text{coll}}$) and the absolute reaction efficiencies ($\gamma_{(3,m)}$). Statistical uncertainties of the relative rate constants are $\pm 20\%$, and the absolute rate constants acquire an additional uncertainty from pressure calibration of $\pm 50\%$.

m	$k_{(3,m)}$ s^{-1}	$k_{-(3,m+1)}$ s^{-1}	$k_{(3,m)}^{\text{abs}}$ $10^{-16} \text{ m}^3 \text{ s}^{-1}$	$k_{(3,m)}^{\text{coll}}$ s^{-1}	$\gamma_{(3,m)}$
0	0.779	<0.001	0.996	4.105	0.243
1	7.000	<0.001	8.949	3.393	2.638
2	0.253	<0.001	0.324	2.973	0.109
3	0.026	0.073	0.033	2.690	0.012

6. Kinetics of H₂ Adsorption onto Ta₂₋₈⁺ Clusters under Cryogenic Conditions

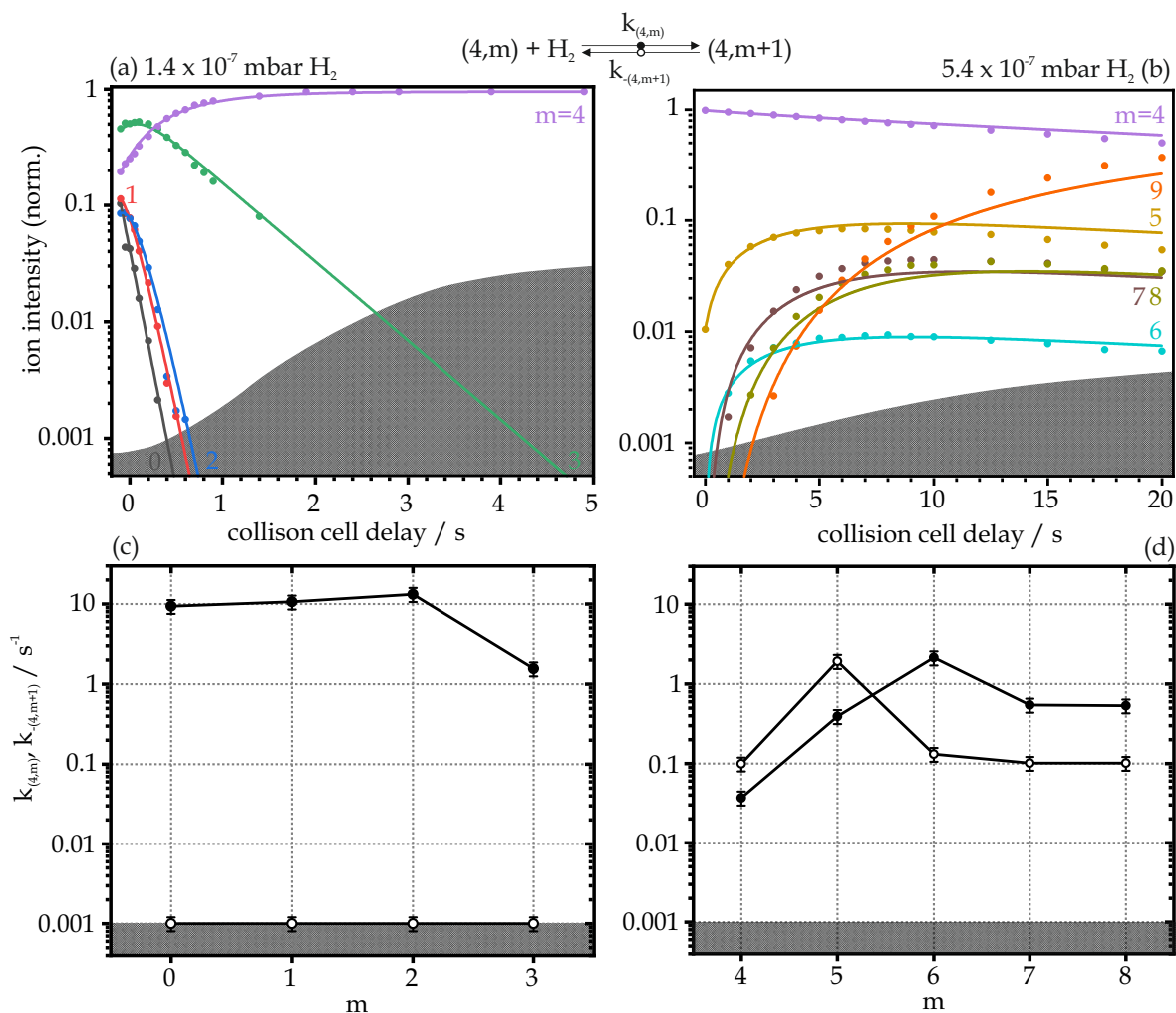


Figure S3: (a) Isothermal kinetics of H₂ adsorption by isolated Ta₄⁺ clusters at 18 K, He buffer gas (6.6×10^{-6} mbar) and 1.4×10^{-7} mbar H₂ pressure ((a)), and 3.0×10^{-6} mbar He buffer gas with 5.4×10^{-7} mbar H₂ pressure ((b)), respectively. The fitting curves (solid lines) of the recorded data (solid dots) confirm pseudo-first-order kinetics for the adsorption in a reaction chain of up to nine consecutive steps for Ta₄⁺ clusters. (c) and (d) Fitted values of corresponding relative rate constants of Ta₄⁺ for the adsorption ($k_{(4,m)}$, solid circles) and the desorption ($k_{-(4,m+1)}$, open circles) as a function of stepwise H₂ adsorption. The gray shaded areas indicate the background noise level.

Table S2: Pseudo-first-order rate constants for the H₂ adsorption and desorption ($p(\text{H}_2)=1.4 \times 10^{-7}$ mbar) on $[\text{Ta}_4(\text{H}_2)_m]^+$ clusters ($k_{(4,m)}$ and $k_{-(4,m+1)}$, *cf.* Figure S3(a)), the related absolute rate constants ($k_{(4,m)}^{\text{abs}}$), the calculated collision rates ($k_{(4,m)}^{\text{coll}}$) and the absolute reaction efficiencies ($\gamma_{(4,m)}$). Statistical uncertainties of the relative rate constants are $\pm 20\%$, and the absolute rate constants acquire an additional uncertainty from pressure calibration of $\pm 50\%$.

m	$k_{(4,m)}$ s^{-1}	$k_{-(4,m+1)}$ s^{-1}	$k_{(4,m)}^{\text{abs}}$ $10^{-16} \text{ m}^3 \text{ s}^{-1}$	$k_{(4,m)}^{\text{coll}}$ $10^{-16} \text{ m}^3 \text{ s}^{-1}$	$\gamma_{(4,m)}$
0	9.363	<0.001	15.39	4.080	3.772
1	10.63	<0.001	17.48	3.362	5.200
2	13.23	<0.001	21.75	2.938	7.402
3	1.560	<0.001	2.565	2.652	0.972

Table S3: Pseudo-first-order rate constants for the H₂ adsorption and desorption ($p(\text{H}_2)=5.4 \times 10^{-7}$ mbar) on $[\text{Ta}_4(\text{H}_2)_m]^+$ clusters ($k_{(4,m)}$ and $k_{-(4,m+1)}$, *cf.* Figure S3(b)), the related absolute rate constants ($k_{(4,m)}^{\text{abs}}$), the calculated collision rates ($k_{(4,m)}^{\text{coll}}$) and the absolute reaction efficiencies ($\gamma_{(4,m)}$). Statistical uncertainties of the relative rate constants are $\pm 20\%$, and the absolute rate constants acquire an additional uncertainty from pressure calibration of $\pm 50\%$.

m	$k_{(4,m)}$ s^{-1}	$k_{-(4,m+1)}$ s^{-1}	$k_{(4,m)}^{\text{abs}}$ $10^{-16} \text{ m}^3 \text{ s}^{-1}$	$k_{(4,m)}^{\text{coll}}$ $10^{-16} \text{ m}^3 \text{ s}^{-1}$	$\gamma_{(4,m)}$
4	0.037	0.099	0.016	4.623	<0.010
5	0.391	1.934	0.167	2.280	0.073
6	2.143	0.131	0.913	2.151	0.425
7	0.545	0.101	0.232	2.045	0.114
8	0.533	0.101	0.227	0.788	0.289

6. Kinetics of H₂ Adsorption onto Ta₂₋₈⁺ Clusters under Cryogenic Conditions

Table S4: Pseudo-first-order rate constants for the H₂ adsorption and desorption ($p(\text{H}_2)=1.4 \times 10^{-7}$ mbar) on $[\text{Ta}_5(\text{H}_2)_m]^+$ clusters ($k_{(5,m)}$ and $k_{-(5,m+1)}$), *cf.* Figure 4(a)), the related absolute rate constants ($k_{(5,m)}^{\text{abs}}$), the calculated collision rates ($k_{(5,m)}^{\text{coll}}$) and the absolute reaction efficiencies ($\gamma_{(5,m)}$). Statistical uncertainties of the relative rate constants are $\pm 20\%$, and the absolute rate constants acquire an additional uncertainty from pressure calibration of $\pm 50\%$.

m	$k_{(5,m)}$ s^{-1}	$k_{-(5,m+1)}$ s^{-1}	$k_{(5,m)}^{\text{abs}}$ $10^{-16} \text{ m}^3 \text{ s}^{-1}$	$k_{(5,m)}^{\text{coll}}$ $10^{-16} \text{ m}^3 \text{ s}^{-1}$	$\gamma_{(5,m)}$
0	6.838	<0.001	11.24	4.065	2.765
1	6.063	<0.001	9.966	3.344	2.980
2	10.54	<0.001	17.33	2.917	5.940
3	11.38	<0.001	18.70	2.628	7.115
4	10.38	<0.001	16.91	2.416	7.000
5	0.182	<0.001	0.300	2.253	0.133
6	0.331	0.129	0.544	2.122	0.256
7	0.459	0.359	0.755	2.014	0.375
8	0.655	1.456	1.076	1.924	0.560

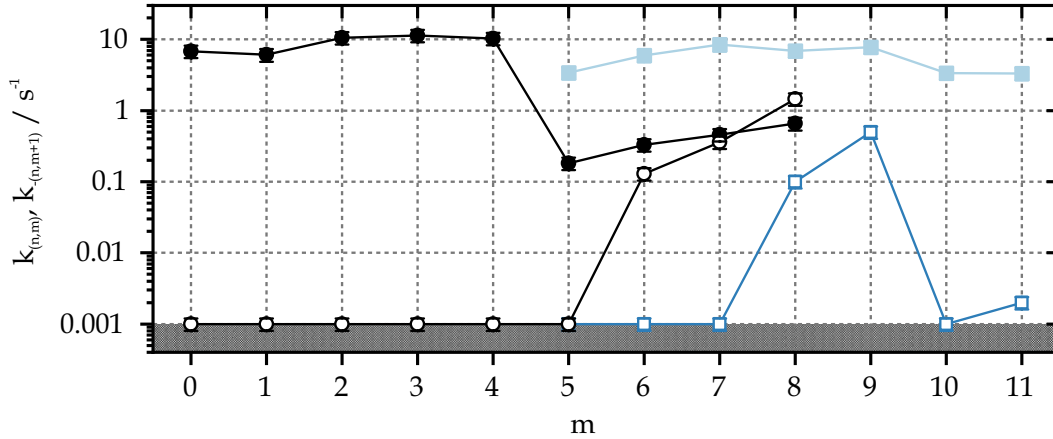


Figure S4: Fitted values of corresponding relative rate constants of Ta₅⁺ for the adsorption ($k_{(5,m)}$, solid symbols) and the desorption ($k_{-(5,m+1)}$, open symbols) as a function of stepwise H₂ adsorption. The black symbols show the rate constants resulting from the fitted kinetics recorded at 1.4×10^{-7} mbar H₂ pressure (*cf.* Figure 4(a) and (c)). The blue symbols show the rate constants resulting from the fitted kinetics recorded at 4.0×10^{-7} mbar H₂ pressure (*cf.* Figure 4(b) and (d)). The gray shaded area indicate the background noise level.

Table S5: Pseudo-first-order rate constants for the H₂ adsorption and desorption ($p(\text{H}_2)=4.0 \times 10^{-7}$ mbar) on $[\text{Ta}_5(\text{H}_2)_m]^+$ clusters ($k_{(5,m)}$ and $k_{-(5,m+1)}$, *cf.* Figure 4(b)), the related absolute rate constants ($k_{(5,m)}^{\text{abs}}$), the calculated collision rates ($k_{(5,m)}^{\text{coll}}$) and the absolute reaction efficiencies ($\gamma_{(5,m)}$). Statistical uncertainties of the relative rate constants are $\pm 20\%$, and the absolute rate constants acquire an additional uncertainty from pressure calibration of $\pm 50\%$.

m	$k_{(5,m)}$ s^{-1}	$k_{-(5,m+1)}$ s^{-1}	$k_{(5,m)}^{\text{abs}}$ $10^{-16} \text{m}^3 \text{s}^{-1}$	$k_{(5,m)}^{\text{coll}}$ $10^{-16} \text{m}^3 \text{s}^{-1}$	$\gamma_{(5,m)}$
5	3.397	<0.001	1.954	2.253	0.867
6	5.978	<0.001	3.439	2.122	1.621
7	8.441	<0.001	4.856	2.014	2.411
8	6.875	0.100	3.955	1.924	2.056
9	7.811	0.500	4.493	1.847	2.433
10	3.381	<0.001	1.945	1.780	1.093
11	3.333	0.002	1.918	1.721	1.114

Table S6: Pseudo-first-order rate constants for the H₂ adsorption and desorption ($p(\text{H}_2)=4.0 \times 10^{-7}$ mbar) on $[\text{Ta}_6(\text{H}_2)_m]^+$ clusters ($k_{(6,m)}$ and $k_{-(6,m+1)}$, *cf.* Figure 5(a)), the related absolute rate constants ($k_{(6,m)}^{\text{abs}}$), the calculated collision rates ($k_{(6,m)}^{\text{coll}}$) and the absolute reaction efficiencies ($\gamma_{(6,m)}$). Statistical uncertainties of the relative rate constants are $\pm 20\%$, and the absolute rate constants acquire an additional uncertainty from pressure calibration of $\pm 50\%$.

m	$k_{(6,m)}$ s^{-1}	$k_{-(6,m+1)}$ s^{-1}	$k_{(6,m)}^{\text{abs}}$ $10^{-16} \text{m}^3 \text{s}^{-1}$	$k_{(6,m)}^{\text{coll}}$ $10^{-16} \text{m}^3 \text{s}^{-1}$	$\gamma_{(6,m)}$
0	0.074	<0.001	0.028	4.055	0.007
1	0.033	<0.001	0.013	3.331	0.004
2	1.077	<0.001	0.413	2.903	0.142
3	30.50	<0.001	11.70	2.612	4.478
4	30.76	<0.001	11.80	2.399	4.917
5	30.81	<0.001	11.82	2.234	5.288
6	2.470	1.581	0.947	2.102	0.451
7	3.585	1.862	1.375	1.994	0.689
8	30.64	0.114	11.75	1.902	6.177
9	8.571	0.941	3.287	1.824	1.802
10	7.721	0.514	2.961	1.756	1.686
11	5.443	0.010	2.088	1.697	1.230

6. Kinetics of H₂ Adsorption onto Ta₂₋₈⁺ Clusters under Cryogenic Conditions

Table S7: Pseudo-first-order rate constants for the H₂ adsorption and desorption ($p(\text{H}_2)=1.4 \times 10^{-7}$ mbar) on [Ta₇(H₂)_m]⁺ clusters ($k_{(7,m)}$ and $k_{-(7,m+1)}$), cf. Figure 6(a)), the related absolute rate constants ($k_{(7,m)}^{\text{abs}}$), the calculated collision rates ($k_{(7,m)}^{\text{coll}}$) and the absolute reaction efficiencies ($\gamma_{(7,m)}$). Statistical uncertainties of the relative rate constants are $\pm 20\%$, and the absolute rate constants acquire an additional uncertainty from pressure calibration of $\pm 50\%$.

m	$k_{(7,m)}$ s ⁻¹	$k_{-(7,m+1)}$ s ⁻¹	$k_{(7,m)}^{\text{abs}}$ 10 ⁻¹⁶ m ³ s ⁻¹	$k_{(7,m)}^{\text{coll}}$ 10 ⁻¹⁶ m ³ s ⁻¹	$\gamma_{(7,m)}$
0	11.47	<0.001	18.85	4.047	4.657
1	11.42	<0.001	18.76	3.323	5.647
2	15.12	<0.001	24.85	2.893	8.589
3	13.82	<0.001	22.71	2.601	8.730
4	8.596	<0.001	14.13	2.387	5.919
5	8.764	0.577	14.40	2.221	6.485
6	21.06	7.828	34.62	2.088	16.58
7	5.813	0.640	9.554	1.979	4.828
8	5.513	0.656	9.061	1.887	4.802
9	3.263	<0.001	5.364	1.808	2.967
10	2.048	<0.001	3.367	1.739	1.936
11	2.002	<0.001	3.290	1.679	1.959
12	1.899	0.003	3.122	1.626	1.920
13	1.295	0.004	2.128	1.578	1.348

References

- [1] D. V. Fries, M. P. Klein, A. Steiner, M. H. Prosenc, G. Niedner-Schatteburg, *Physical Chemistry Chemical Physics* **2021**, 23, 11345–11354.
- [2] D. V. Fries, M. P. Klein, A. Straßner, M. E. Huber, M. Luczak, C. Wiehn, G. Niedner-Schatteburg, *The Journal of Chemical Physics* **2023**, 159, 164303.
- [3] D. V. Fries, M. P. Klein, A. Straßner, M. E. Huber, G. Niedner-Schatteburg, *The Journal of Chemical Physics* **2023**, 159, 164306.
- [4] J. Mohrbach, S. Dillinger, G. Niedner-Schatteburg, *The Journal of Physical Chemistry C* **2017**, 121, 10907–10918.
- [5] S. Dillinger, J. Mohrbach, G. Niedner-Schatteburg, *The Journal of Chemical Physics* **2017**, 147, 184305.
- [6] A. Straßner, C. Wiehn, M. P. Klein, D. V. Fries, S. Dillinger, J. Mohrbach, M. H. Prosenc, P. B. Armentrout, G. Niedner-Schatteburg, *The Journal of Chemical Physics* **2021**, 155, 244305.
- [7] S. Dillinger, J. Mohrbach, J. Hower, M. Gaffga, G. Niedner-Schatteburg, *Physical Chemistry Chemical Physics* **2015**, 17, 10358–10362.
- [8] S. Dillinger, M. P. Klein, A. Steiner, D. C. McDonald, M. A. Duncan, M. M. Kappes, G. Niedner-Schatteburg, *The Journal of Physical Chemistry Letters* **2018**, 9, 914–918.
- [9] M. P. Klein, A. A. Ehrhard, J. Mohrbach, S. Dillinger, G. Niedner-Schatteburg, *Topics in Catalysis* **2018**, 61, 106–118.

7 CRYO IR SPECTROSCOPY OF H₂ ADSORPTION TO TA₂₋₈⁺ CLUSTERS

Daniela V. FRIES, Annika STRAßNER, Matthias P. KLEIN, and Gereon
NIEDNER-SCHATTEBURG

Department of Chemistry and State Research Center OPTIMAS,
Rheinland-Pfälzische Technische Universität (RPTU) Kaiserslautern-Landau,
67663 Kaiserslautern, Germany

7.1 Preamble

The experiments were performed by myself - partly together with A. Straßner and M. P. Klein. The quantum chemical modelling calculations and the evaluation of the experimental data were conducted by myself. The evaluation of the measured data was carried out by me, and it was accompanied by discussions with G. Niedner-Schatteburg. I wrote the manuscript.

7.2 Paper draft

7.2.1 Abstract

We present an IR-PD study of tantalum cluster adsorbate complexes [Ta_n(H₂)_m]⁺ species, abbreviated (n,m), n = 3 - 8. We utilize infrared spectroscopy of the isolated and size-selected clusters under cryogenic conditions within a buffer gas filled ion trap, and we augment our experiments by quantum chemical simulations (at DFT level). For the cases n = 3 - 5 and n = 7, the absence of any vibrational bands in the IR-PD spectra of all adsorbate species up to (n,m = n) is striking. In contrast, all investigated species with higher H₂ loading show multiple IR-PD bands corresponding to Ta-H binding vibrations. The overall picture for the H₂ adsorption on Ta_n⁺ clusters is supported by DFT modeling for conceivable cluster geometries (4,m) and (5,m): All H₂ molecules building the formal first adsorbate shell are dissociatively adsorbed to the clusters before all further H₂ molecules are molecularly adsorbed. In the very special case of the (5,12) cluster, we conclude that activation of H₂ seems to be possible even late in the adsorption chain. For Ta₆⁺ and Ta₈⁺ the formal first adsorbate shell is most likely completed before m = n is reached.

7.2.2 Introduction

Hydrogen on earth exists partly in molecular form, with a strong covalent H-H bond (436 kJ mol⁻¹ [1]). In microorganisms, a family of enzymes - hydrogenases - metabolizes hydrogen. The activation and cleavage of the H-H bond takes place at an active site, which contains a metal component. [2-4] Such heterogeneous catalysis is also a key technology for chemical engineering and many related fields. [5] Numerous industrial processes are based on transition metal (TM) catalysts. [6-11] TM clusters can serve as model systems for active sites, providing insights into elemental catalytic processes at the molecular level. [12-18] All of these cited review publications document size effects for structure, chemical and physical properties and the reactivity of the metal clusters. The interaction of H₂ with TM clusters and complexes and with metal surfaces showed the formation of activated and dissociated hydrogen. [19-21] In particular, for TM complexes, a synergistic bonding similar to the Dewar-Chatt-Duncanson model for the interaction of CO with transition metals [22] is described for coordinated H₂: An elongated H-H bond (prior to complete cleavage) results from a σ -donation of charge density from the filled

H-H σ -bonding orbital into an empty d orbital of the metal and a simultaneous π back donation from a filled d orbital of the metal into the empty σ^* anti-bonding orbital of the H₂ molecule. Silbaugh *et al.* summarized in 2016 the experimental enthalpies and energies of numerous molecular and dissociative adsorption reactions measured on various metallic single-crystal surfaces of late TM, as well as the standard enthalpies of formation of the adsorbates produced, to serve as benchmarks for validating computational methods and for estimating surface reaction energies. [23]

In co-adsorption of CO and H₂ on cationic cobalt and vanadium clusters, hydrogen acts as a co-factor controlling the interaction (dissociative or molecular chemisorption) of CO molecules with the cluster. [24, 25] Interestingly, dissociatively adsorbed hydrogen yielding distal and proximal hydrogen atom positions on a Ru₈⁺ cluster are hindered in their migration by pre-loaded nitrogen molecules but are not affected by subsequent nitrogen adsorption. [26] Moreover, several researchers have already investigated the adsorption of H₂ on various transition metal clusters - mostly 3d transition metal clusters - experimentally and theoretically using DFT calculations. It is shown that the geometries of hydrogen adsorption depend to some extent on both elemental composition and cluster size. The adsorption of H₂ is found to be exclusively dissociative on Sc_nO⁺, V_n⁺, Fe_n⁺, and Co_n⁺, and both atomic and molecularly chemisorbed hydrogen is present for Ni_n⁺ clusters. [27] In the case of Fe_n⁺, the cluster hydride complexes Fe_nH_m⁺ take up additional H₂ molecules, which are physisorbed to give Ni_nH_m(H₂)_p⁺ species. [28] A theoretical study of H₂ adsorption on Co_{6,13}⁺ clusters predicts the mechanisms for H₂ adsorption and dissociation, and the competition between the two processes: At low coverage, dissociative H₂ adsorption is the preferred adsorption channel. Further molecular H₂ adsorption leads to saturated clusters. The H atoms of the dissociatively adsorbed H₂ ligands sit across Co-Co bonds, like metal hydrides. When H₂ is molecularly adsorbed onto the cluster, it coordinates side-on to a Co atom. [29] The reactivity of Ni_n⁺ clusters with H₂ appear a strong dependency on size, in particular for small clusters. [30] While an H₂ molecule binds exclusively dissociatively on Ni₅⁺ and Ni₆⁺ the special case of Ni₄⁺ adsorbs H₂ molecularly. The resulting Ni₄H₂⁺ isomer might serve as model system for a precursor state for dissociation. [31] IR spectroscopy and DFT studies on small Cu_n⁺ cluster reveal that binding energies are largest for Cu₅⁺, corresponding to dissociative adsorption, and smaller binding energies for Cu₄⁺, implying significant amount of molecular adsorption. [32] In addition to the d-element clusters, Pt_n⁺ clusters with molecular H₂ form cluster

complexes that contain molecularly bound H₂ alongside bridging and atop binding H atoms. [33] In computational studies, heterometallic cluster complexes Mn_nRh and Mn_nCo [34, 35] act as effective catalytic agents for H₂ adsorption and dissociation, as well as carbon-supported palladium clusters [36, 37].

For the particular case of cationic tantalum clusters Ta_n⁺, some efforts have already been made in the form of experiments and quantum chemical calculations to study their reactivity, especially with respect to the activation ability towards small molecules such as CO₂ [38], O₂ [39], N₂ [40–43] or CH₄ [93, 94]. Experimental results from vibrational spectra and theoretical modeling of Ta_n⁺ clusters, n = 6 – 20, successfully provide for the geometries of the bare clusters, their relative stabilities and electronic properties. [44, 45] IR spectroscopy of the product complex [4Ta,C,2H]⁺ of methane dehydrogenation by Ta₄⁺ shows an IR band at 1400 cm⁻¹, which is assigned by DFT modeling to the Ta-H vibration of a dihydride motif in H₂Ta₄C⁺. [46] The activation and cleavage of the nitrogen triple bond is of particular interest considering the overall picture of industrial ammonia formation [47, 48]. Theory predicts that Ta₂⁺ is capable of mediating the formation of NH₃ from N₂ and H₂. [49] We have also extensively investigated the N₂ activation and cleavage capabilities of small tantalum clusters. The experimental results of adsorption kinetics and IR spectroscopy measurements, supported by DFT modeling, show that the smallest clusters Ta₂⁺, Ta₃⁺, and Ta₄⁺ are able to adsorb, activate, and even cleave at least one N₂ molecule. [50–52] With this study we contribute to answer the question whether the small tantalum clusters Ta_n⁺, n = 2 - 8, are also able to activate and cleave H₂ molecules. We reacted these clusters with H₂ at 18 K and recorded IR-PD spectra of the adsorption species [Ta_n(H₂)_m]⁺, similar to our earlier N₂ adsorption studies on Ta_n⁺ [50–52], Ni_n⁺ [53–55], Rh_n⁺ [56, 57], Rh_iFe_j⁺ [58, 59] and Fe_n⁺ [60, 61] clusters. Indeed, the present IR-PD study, supported by DFT modeling, provides strong evidence that all the clusters Ta₃⁺, Ta₄⁺, Ta₅⁺, Ta₆⁺, Ta₇⁺ and Ta₈⁺ dissociatively adsorb those H₂ ligands that build up the formal first adsorbate shell of the cluster complexes (n,m). The findings of this study, which we refer in the following as [IRS], finds strong support though our complementary cryogenic kinetic study [CKS], chapter 6.

7.2.3 Experimental and Computational Methods

A custom-built Fourier transform ion cyclotron resonance (FT-ICR) mass spectrometer (*Apex Ultra*, Bruker Daltonics) allows to perform adsorption kinetics and IR-PD measurements. Transition metal clusters TM_n^\pm of various cluster sizes n are generated in a home built laser vaporization (LVAP) source [62, 63] from a rotating tantalum foil (99.95 %, 0.5 mm thick, Alfa Aesar). The metal atoms are evaporated by the second harmonic of a pulsed Nd:YAG laser (Innolas Spitlight 300, 20 Hz). The resulting hot plasma consisting of atoms and ions is captured by a He gas pulse (40 μ s, 15 bar) from a home-bult piezoelectric valve [64]. The atoms and ions cool and aggregate into clusters during the subsequent jet expansion through a 69 mm long channel (2 mm diameter) into vacuum (10^{-7} mbar). The resulting cluster size distribution passes through electrostatic lenses and reaches a 90° ion beam bender which deflects the ion beam onto the magnetic field axis. A quadrupole mass filter serves for size-selection of the cluster ions before they are introduced into a cryogenic hexapole ion trap (18 K, reaction gas H_2 up to 6.0×10^{-7} mbar and collision gas He up to 6.6×10^{-6} mbar). Therein the cluster ions are trapped and can react with reaction gases using the routine described in [CKS]. The manipulated ions are guided into the cryogenic (10 K) ICR cell for detection.

Our experimental setup allows us to couple an IR-OPO/OPA laser system into this ICR cell. A pulsed injection seeded Nd:YAG laser (10 Hz, PL8000, Continuum) pumps a KTP/KTA optical parametric oscillator/amplifier (OPO/OPA, LaserVision). An AgGaSe₂ crystal generates the difference frequency (DF) between the OPA signal and idler waves. This laser setup provides IR radiation in the range of 1000 and 2400 cm^{-1} , which is used to irradiate the selected cluster adsorbate complexes, so that the isolated ion packages are treated with 7 to 10 laser pulses, each with an energy of 0.5 to 3.0 mJ. For measuring IR-PD spectra we record a series of fragmentation mass spectra during continuous scanning of the IR wavelength. From the measured IR-PD signal we evaluate the fragmentation efficiency $= \left(\frac{\sum_i F_i}{\sum_i F_i + \sum_i P_i} \right)$, F_i and P_i are fragment and parent ion intensities. The fragmentation efficiency thus determined is plotted as a function of laser frequency to obtain the IR-PD spectrum. H_2 loss was the only observed fragmentation channel for all species investigated. For

DFT modeling, geometry optimization, and vibrational analysis were performed using the program package Gaussian 16 [65]. We employed the functional PBE0 [66, 67] and the cc-pVTZ-pp basis set [68] for Ta atoms and the Def2-TZVP basis set [69] for H atoms. In this way, we follow up on previous studies in which we succeeded in modeling the adsorption of N₂ and, to some extent, H₂ onto cationic transition metal clusters. [26, 50–52, 55, 56, 61, 70] Therefore, we justify our choice of these level of theory. We tolerated relaxed SCF convergence criteria of 10⁻⁶ (as compared to 10⁻⁸ in “standard” DFT calculations) to achieve SCF convergence in all cases. All stationary points were checked for no imaginary frequency to ensure that they were true minimum structures. For predicted vibrational frequencies we applied a scaling factor of 0.9434 and 0.9619 for (4,m) and (5,m), respectively, to account for the prevailing anharmonicities. Unscaled IR frequencies for all cases are documented in the supplementary information (*cf.* chapter 7.3). The predicted and scaled IR frequencies are simulated using a gaussian profile of fwhm = 5 cm⁻¹.

7.2.4 Results and Discussion

IR-PD spectroscopy studies of TM cluster adsorbate complexes provide for structural information on the geometries of the investigated complexes. Actually, we are able to probe Ta-H bands and from the measured IR-PD bands we infer structural information about the corresponding [Ta_n(H₂)_m]⁺ species, abbreviated (n,m). These findings extend our cryo kinetic study [CKS] of H₂ adsorption on size-selected tantalum clusters Ta_n⁺, n = 2 - 8.

We found a concise variation of recorded IR-PD features as a function of the tantalum cluster size n and of H₂ adsorbate loading m. The recorded IR-PD features of Ta-H fingerprints locate in the majority of the cases in the spectral range of 1100 to 1700 m/z. However, there are some spectra that do not show IR-PD bands in this spectral range. One could attribute this to low vibrational mode densities and infer single photon adsorption processes leading to dark IR-PD bands. Two color experiments might provide sufficient photon energie to unreavel such dark IR-PD bands. Note, that we have observed the unexpected absence of IR-PD bands in previous studies for several cases of nitrogen adsorbate species of small tantalum cluster cations. [50, 51] For all these cases it was explained by swift N₂ activation and cleavage after initial N₂ adsorption to the cluster surface. A similar behavior could be possible in the present case of H₂ adsorption and will be discussed in the

following. We choose to organise the measured IR-PD spectra in an (n,m) matrix, where n is given per section, one after the other.

[Ta₂(H₂)_m]⁺ The smallest tantalum cluster, the dimer species Ta₂⁺, appears to be inert towards H₂ under the conditions of our experiment. In our related cryokinetic study [CKS], we illustrated this by measuring a constant intensity for the bare Ta₂⁺ cluster at particularly long storage times and exposure to 5.4×10^{-7} mbar H₂. The recorded kinetic shows no evidence of mass signals from an adsorbed species. [Ta₂(H₂)_m]⁺.

[Ta₃(H₂)_m]⁺ The trimer species Ta₃⁺ is the smallest cationic tantalum cluster for which we found adsorption of H₂ and thus were able to perform IR-PD studies of the cluster adsorbate species (3,m), m = 1 - 3. The low yield of the higher loaded adsorbate species (3,4), *cf.* [CKS], hampered our efforts to record its IR-PD spectra. The absence of any vibrational bands for the three species (3,1), (3,2) and (3,3) is striking. We have found convincing arguments that the absence of IR-PD bands can be explained in other ways than by dark IR-PD bands resulting from low vibrational mode densities. Indeed, it seems plausible that the small tantalum cluster cations might be able to activate and cleave H₂ adsorbates. Quantum chemical calculations of Geng *et al.* [49] predict activation of H₂ by Ta₂⁺. Although we could not confirm this experimentally in the case of Ta₂⁺, we suspect a corresponding activation of H₂ by the naked Ta₃⁺ cluster. Specific DFT modeling for conceivable cluster geometries and reaction pathways for adsorption, activation, and probably even cleavage of H₂ would help to clarify. Without having these at hand, we interpret the results utilizing our findings from the adsorption of H₂ on larger tantalum clusters Ta_n⁺ (n > 3 as presented in this work) and from our previous study on adsorption of N₂ on Ta_n⁺. [50, 51] Indeed, for all the tantalum cluster cations studied [Ta_n(H₂)_m]⁺, we observe no IR-PD bands for the first adsorbed species. In particular, the IR-PD measurements of (4,m) and (5,m) provide strong evidence that all H₂ molecules adsorb dissociatively onto the cluster yielding (n,m = n), the species with a complete formal first adsorbate shell. We take the liberty of assuming that Ta₃⁺ behaves in a similar way.

At this point we refer to our associated cryo kinetic study [CKS] for a more detailed understanding of the adsorption processes of H₂ on Ta₃⁺. The kinetic plot and corresponding rate constants show that Ta₃⁺ loaded with a formal monolayer

7. Cryo IR Spectroscopy of H₂ Adsorption to Ta₂₋₈⁺ Clusters

of H₂ ligand molecules can accommodate a fourth H₂ molecule. However, the corresponding adsorption rate constant is significantly lower than that of the previous three adsorption processes. Furthermore, at this level of H₂ load desorption sets in. We observe similar behaviors for the H₂ kinetics of Ta₄⁺ and Ta₅⁺. In both cases, the significant decrease in adsorption rates accompanied by significant desorption rates is an indication that adsorption of molecular H₂ starts to occur. This supports our thesis of dissociatively adsorbed H₂ ligands for all adsorbate species (3,1), (3,2) and (3,3). The hydride ligands are more strongly bound to the cluster core than molecularly adsorbed ligands. Therefore, they cannot act as IR-PD tags, resulting in the absence of bands in the IR-PD spectra.

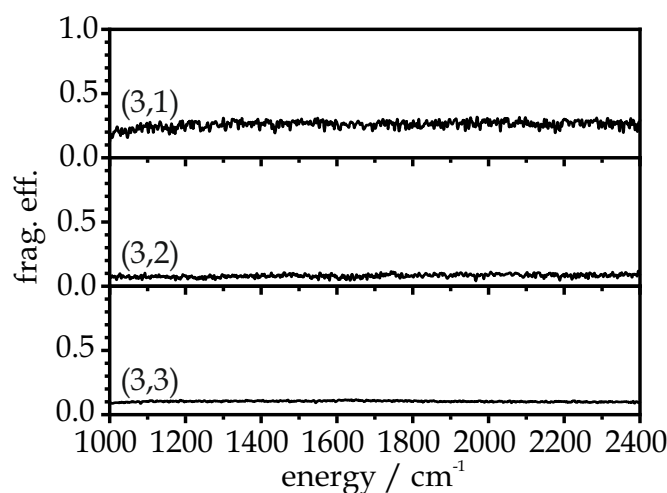


Figure 1: IR-PD spectra of [Ta₃(H₂)_m]⁺ (simplified nomenclature: (3,m)), m = 1–3, in the spectral range between 1000 and 2400 cm⁻¹. Note the absence of vibrational bands in all cases.

[Ta₄(H₂)_m]⁺ From our associated cryo kinetic study [CKS], we know that Ta₄⁺ adsorbs up to nine H₂ molecules onto its cluster surface. Our IR spectroscopic studies may provide for additional structural information. We actually succeeded in obtaining IR-PD spectra for (4,m), m = 1–5 (*cf.* Figure 2). The low yields of the higher loaded adsorbate species, m ≥ 6, especially at short storage times in the hexapole ion trap as required for time-efficient IR-PD spectroscopic studies, hamper the recording of their IR-PD spectra. The absence of any IR-PD bands for (4,1), (4,2), (4,3) and (4,4) is striking. For (4,5), we observe several IR-PD bands in a spectral range of 1100 to 1500 cm⁻¹. Bands within this range would correspond to Ta-H bond vibrations. DFT modeling for conceivable cluster geometries yield a corresponding IR band

pattern and allow for identification of the cluster structure present when compared with the measured measured IR-PD spectra of (4,5).

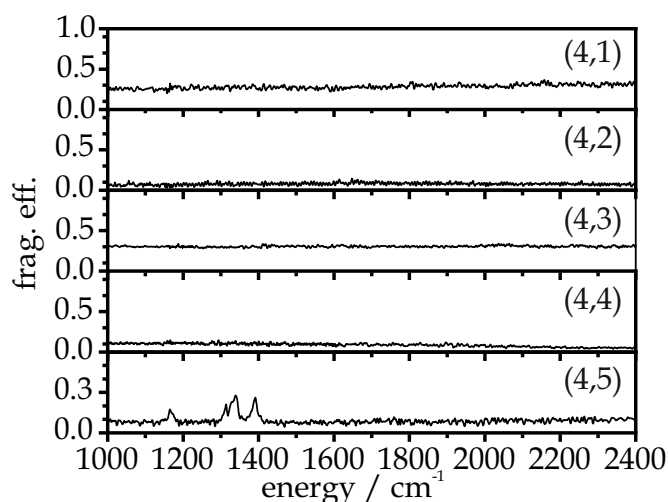


Figure 2: IR-PD spectra of $[\text{Ta}_4(\text{H}_2)_m]^+$ (simplified nomenclature: (4,m)), $m = 1 - 5$, in the spectral range between 1000 and 2400 cm^{-1} . Note the absence of vibrational bands in the cases (4,1), (4,2), (4,3) and (4,4).

Our DFT modeling for (4,5) yielded several isomers each in the doublet or quartet state (*cf.* Figure S2 and Tables S1 and S2). We have chosen a tetrahedral geometry for the bare Ta_4^+ cluster core. This is consistent with our previous study in which we successfully used such a tetrahedral cluster structure for the adsorption of N_2 on Ta_4^+ [50] [51]. For the hydrogen adsorbates we found the doublet state species favored over the corresponding quartet state species by at least 48 kJ mol^{-1} . The most favored doublet species is $^2(4,5)\text{a}$. The other two doublet isomers $^2(4,5)\text{b}$ and $^2(4,5)\text{c}$ are somewhat less favored with 10 kJ mol^{-1} and 3 kJ mol^{-1} , respectively. The DFT calculations of $^2(4,5)\text{a}$ predicts an IR band pattern which is in a very good agreement with the experiment. Figure 3 shows a comparison of the measured IR-PD bands of (4,5) and the predicted ones for $^2(4,5)\text{a}$. We managed to simulate all spectral features and observe a good overall agreement not only in band positions, but also in band splitting. This holds despite differences in predicted IR strengths and observed IR-PD intensities. The structure of $^2(4,5)\text{a}$ comprises a formal first adsorbate shell, which consists of eight hydrogen atoms: Two opposite Ta-Ta edges of the Ta_4^+ tetrahedron are bridged by two hydrogen atoms and each of the remaining four Ta-Ta edges is bridged by one hydrogen atom. The fifth H_2 molecule is adsorbed in a side-on motive to one of the Ta atoms of the cluster. All measured IR-PD bands result

7. Cryo IR Spectroscopy of H₂ Adsorption to Ta₂₋₈⁺ Clusters

from coupled vibrations of all Ta-H bonds constituting the formal first adsorbate shell. The predicted frequency (3729 cm⁻¹) of molecularly adsorbed H₂ molecule is outside the accessible measurement range.

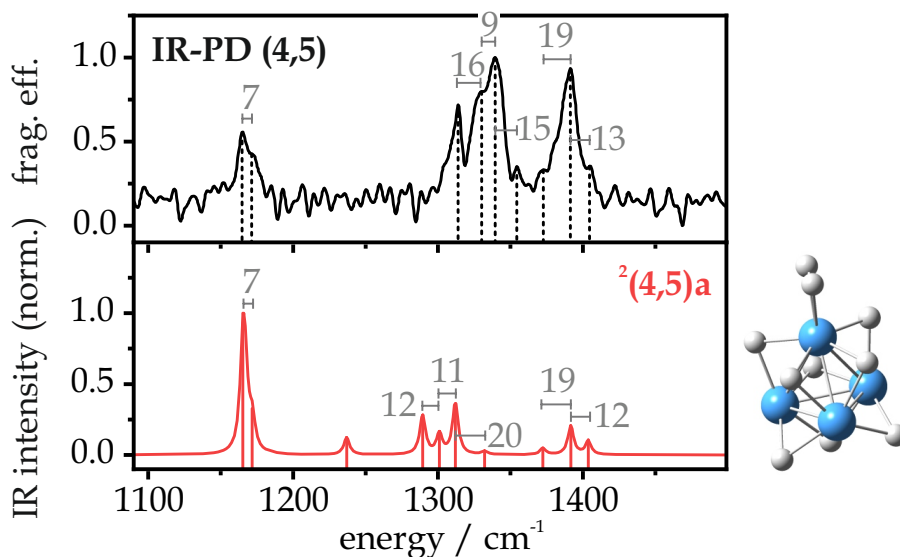


Figure 3: IR-PD spectra of [Ta₄(H₂)₅]⁺ (simplified nomenclature: (4,5)) in the spectral range between 1100 and 1500 cm⁻¹ in comparison with DFT modeled spectra of selected structural isomer ²(4,5)a. The predicted IR frequencies are scaled by a factor of 0.9434. Note, that the predicted splittings correspond well with the observed ones, and this holds despite differences in predicted IR strengths and observed IR-PD intensities. For calculated energy and IR frequencies of isomer ²(4,5)a, see Table S1. The calculated structure is a tetrahedral cluster core with two opposing Ta-Ta edges, each bridged by two hydrogen atoms, and one hydrogen atom bridging each of the remaining four Ta-Ta edges. The fifth H₂ molecule is adsorbed in a side-on motif on one of the Ta atoms.

Since we are actually studying Ta-H vibrations, the measured IR-PD band pattern gives not only direct information about the structure of (4,5), but also indirect information about the structure of the lower loaded species. We performed DFT modeling for minimum doublet structures of (4,m) species from m = 0 to m = 4 along a stepwise adsorption chain finally leading to the identified (4,5) species (*cf.* Figure 4). Note that this study does not consider possible transition states and reaction pathways between adsorption steps. The starting point of the adsorption chain is the bare Ta₄⁺ with a tetrahedral geometry and the diatomic H₂ molecule.

The minimum structure for (4,1) shows dissociative H₂ adsorption over two adjacent edges of the tetrahedron. The subsequent second H₂ molecule yields again two neighboring hydrogen bridged Ta-Ta edges. The third H₂ molecule still adsorbs dissociatively, but remarkably, the two H atoms do not bridge two adjacent free Ta-Ta edges. Instead, one of the dissociated hydrogen atoms arranges itself over a Ta-Ta edge that is already bridged by a hydrogen atom, and the other bridges a Ta-Ta edge that was still free until then. This yields an adsorbate geometry of (4,3) comprising one double hydrogen-bridged Ta-Ta edge, four single hydrogen-bridged Ta-Ta edges, and one completely free, unbridged Ta-Ta edge. The fourth H₂ molecule adsorbs again dissociatively, but over the same edge, namely the still free, unbridged Ta-Ta edge of the tetrahedral cluster core. Each of these dissociative adsorption steps is strongly exothermic. However, as the H₂ loading increases, the energy difference steadily decreases: While the DFT calculations predict an exothermic adsorption of 192.5 kJ mol⁻¹ for the first H₂ molecule, it is only 143.3 kJ mol⁻¹ for the fourth adsorption step. Adsorption of the fifth H₂, which coordinates molecularly to the cluster, is much less exothermic at only 27.2 kJ mol⁻¹. Obviously, a pair of H atoms is more strongly bound to the cluster surface than a molecularly adsorbed H₂ molecule.

In summary, our IR-PD study and DFT modeling reveal that the first four H₂ molecules adsorb dissociatively to the Ta₄⁺ cluster prior to molecular adsorption of the fifth H₂ molecule. At this point, we address the question, whether the DFT predictions and the recorded IR-PD spectra are in line with the recorded adsorption kinetics [CKS]. The H₂ kinetics of (4,m) reveal particularly fast adsorption processes for the first four H₂ molecules. Once the H₂ loading reaches the formal first adsorbate shell, we observe a steep drop in adsorption rate constants for the uptake of all further H₂ molecules. At the same time, desorption reactions set in.

Combining all the information from kinetics, IR-PD spectra and DFT modeling gives an overall picture of the adsorption of H₂ on Ta₄⁺. There are two different adsorption processes that follow each other in the course of H₂ adsorption: The first few H₂ adsorption reactions proceed very fast and without competitive desorption reactions. All H₂ molecules adsorbed in these processes coordinate dissociatively and form hydrogen-bridged Ta-Ta edges of the cluster core. The second type process is characteristic for slow adsorption reactions. These molecularly adsorbed H₂ molecules are less strongly bound to the cluster core than pairs of H atoms and are

thus able to undergo desorption reaction. The threshold between first and second type processes is the completion of the first adsorbate shell.

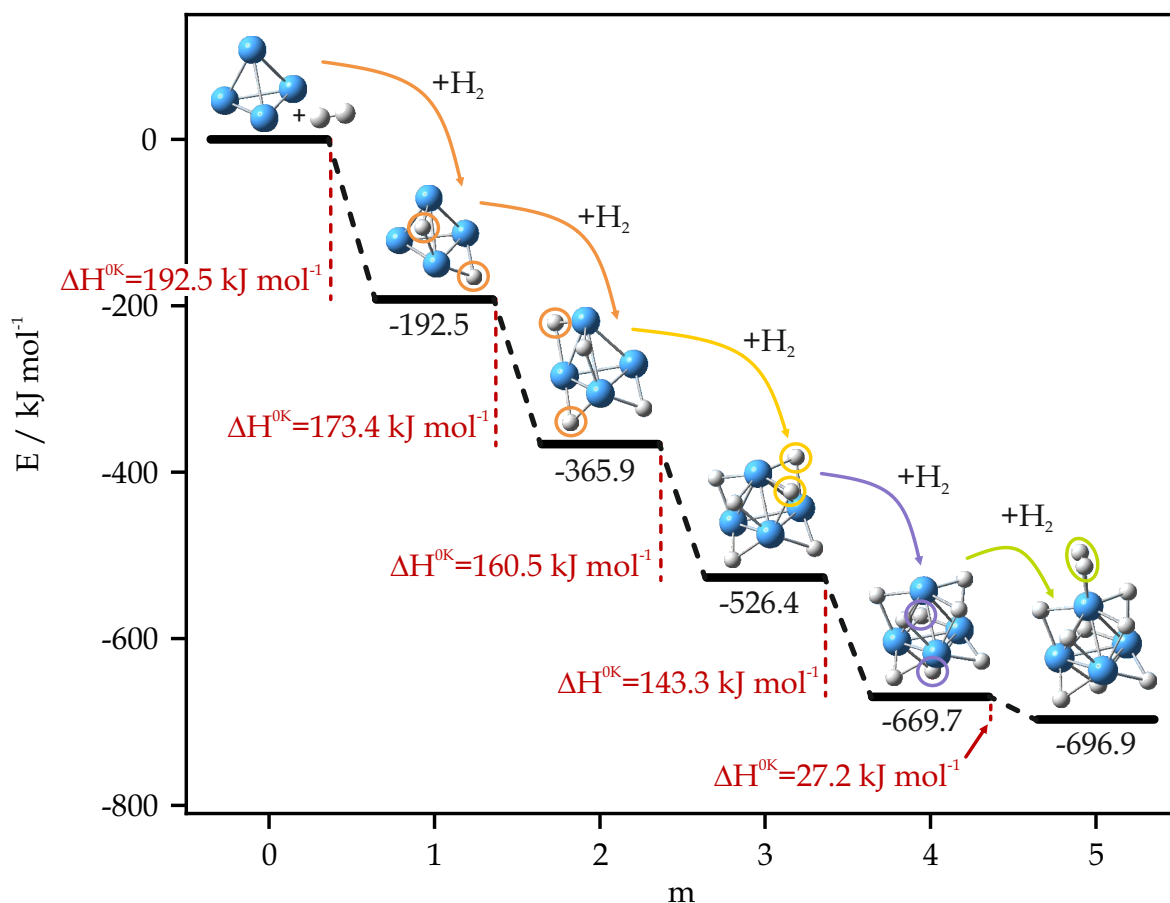


Figure 4: Computed energetics of stepwise H₂ adsorption onto Ta₄⁺ cluster up to species (4,5). The H atoms added in the respective adsorption step are highlighted by colored circles. Note that this study does not consider possible transition states and reaction pathways between adsorption steps. The given values are relative energies of doublet states with respect to the free cluster adsorbate complex components (in black), and with respect to desorption of single H₂ (in red).

[Ta₅(H₂)_m]⁺ For Ta₅⁺, we succeeded in studying all cluster adsorbate species (5,m), m = 1 - 12, by IR-PD spectroscopy. The IR-PD spectra of (5,1), (5,2), (5,3), (5,4) and (5,5) reveal no IR-induced fragmentation. For (5,6) and beyond, we observe several IR-PD bands in a spectral range between 1100 and 1800 cm⁻¹. The IR-PD spectra can be divided into three sections according to the affiliation of the species to the adsorbate shells: All species of the formal first adsorbate shell show no IR-PD

bands in the recorded spectra, indicating hydride complexes for all of them. The IR-PD spectra of all species of the formal second adsorbate shell show a characteristic IR-PD band at 1180 cm^{-1} while a sharp and intense band at 1700 cm^{-1} (*cf.* Figure 5, orange) is characteristic for the the third adsorbate shell species. The spectrum of species (5,10), which completes the formal second adsorbate shell, exhibits the properties of the second and third adsorbate shell species.

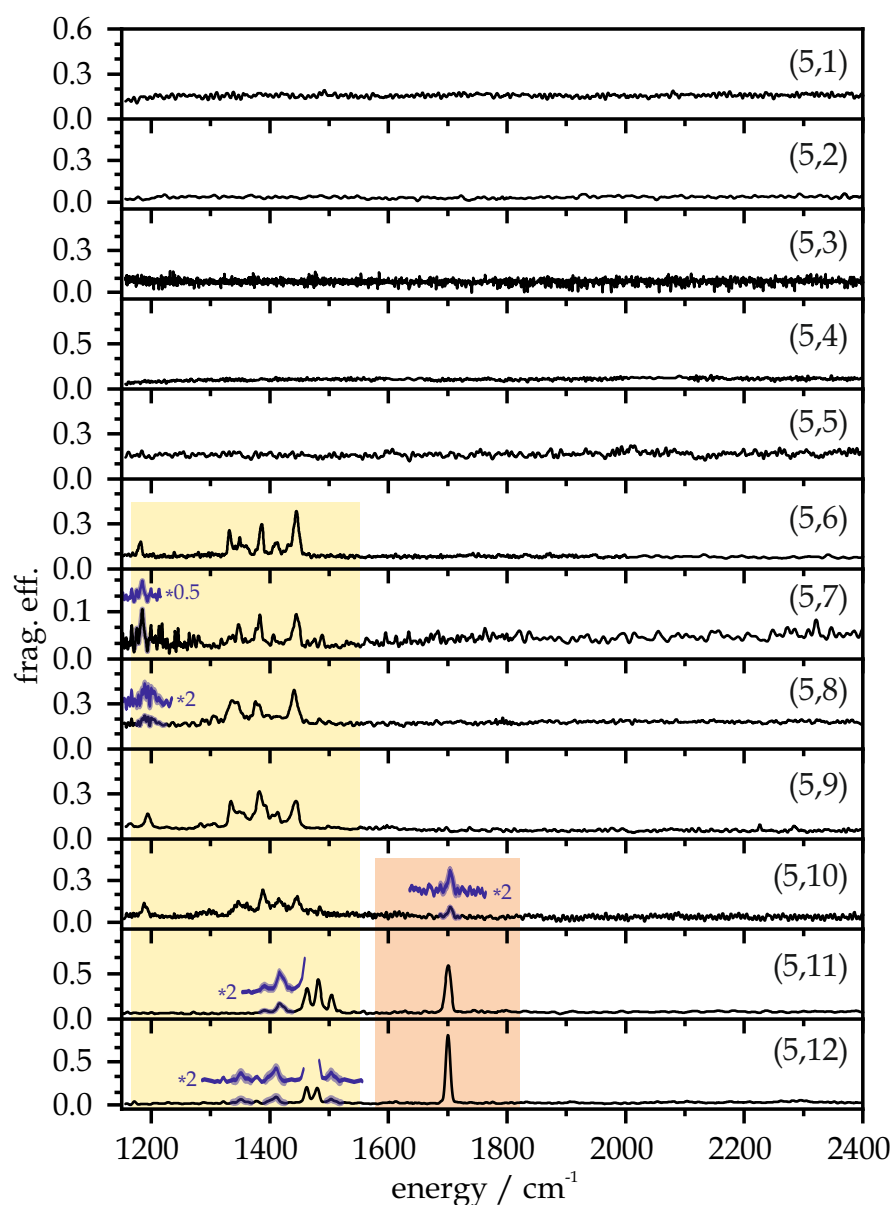


Figure 5: IR-PD spectra of sequential H_2 adsorption steps onto Ta_5^+ cluster cations $[\text{Ta}_5(\text{N}_2)_m]^+$, $m = 1 - 13$, as recorded after 18 K He buffer gas cooling. The spectral range is between 1150 and 2400 cm^{-1} . For IR-PD spectra in the range of 1000 to 2400 cm^{-1} , see Figure S3 in the supplementary information.

Both the IR-PD spectra of the second adsorbate shell species and the third adsorbate shell species show IR-PD bands between 1300 and 1500 cm⁻¹ (Figure 5, yellow). However, the band pattern differs significantly between second adsorbate shell species and third adsorbate shell species: For the case of (5,6) we find five IR-PD bands at 1331, 1349, 1386, 1409, and 1445 cm⁻¹. This IR-PD band pattern persists for all species of the second adsorbate shell up to (5,9), but with some minor shifts. With species (5,10), the IR-PD bands around 1345 cm⁻¹ decrease in intensity, while at the same time a new IR-PD band appears at 1484 cm⁻¹. This shift of the IR-PD band pattern to the blue for the species beyond the formal second adsorbate shell results in four bands at 1415, 1462, 1481, and 1504 cm⁻¹ for (5,11) and (5,12). Based on the IR-PD band patterns, the characteristics of the measured H₂ adsorption kinetics [CKS] and in analogy to the results of species (4,m), we assume dissociatively adsorbed H₂ molecules within the formal first adsorbate shell of five ligands on the Ta₅⁺ cluster. All other H₂ ligands likely coordinate molecularly. DFT modeling will help to clarify.

Since we study Ta-H vibrations, the measured IR-PD band pattern of (5,6) gives indirect information about the structure of the lower loaded and formal first adsorbate shell species (5,5) as species (5,6) corresponds to (5,5+1). We have chosen a trigonal bipyramidal (tbp) geometry for the bare Ta₅⁺ cluster. Two apical atoms Ta^{ap} coordinate three next neighbors each, the three equatorial atoms Ta^{eq} coordinate four next neighbors each. This is consistent with our previous study in which we successfully used such a tbp cluster structure for the adsorption of N₂ on Ta₅⁺. [52]

In order to verify our assumption, we performed DFT modeling for conceivable cluster geometries of (5,5) containing five dissociatively adsorbed H₂ ligands on a tbp Ta₅⁺ cluster core, yielding a corresponding IR band pattern. We consider singlet and triplet spin states. For calculated energies, IR frequencies, and structures we refer to Tables S5 and S6 as well as Figure S4 in the supplementary information (*cf.* chapter 7.3). Our DFT modeling was successful and we found isomer ¹(5,5)e, whose predicted IR frequencies agree very well with the measured IR-PD band pattern of Ta-H vibrations of (5,6) (*cf.* Figure S4). The predicted geometry of (5,5)e comprises a trigonal bipyramidal (tbp) Ta₅⁺ cluster core coordinating ten hydrogen atoms across its Ta-Ta edges. More precisely, eight hydrogen atoms bridge pairwise four Ta^{eq}-Ta^{ap} edges - two pairs above and two below the equatorial plane of the

tbp cluster core. This results in two free edges in a Ta^{ap}-Ta^{eq}-Ta^{ap} triangle. The two remaining hydrogen atoms both coordinate to Ta^{eq}-Ta^{eq} edges of the Ta^{eq}-Ta^{eq}-Ta^{eq} triangle, which is perpendicular to the free Ta^{ap}-Ta^{eq}-Ta^{ap} triangle (*cf.* Table S6).

This structure serves as starting geometry for the next H₂ adsorption step. It provides for three distinguishable adsorption sites for likely end-on coordinating H₂ molecules: one of the two apical sites Ta^{ap}, one of the two fivefold coordinated equatorial sites Ta^{eq}, and the twofold coordinated equatorial site Ta^{eq}. The resulting singlet and triplet isomers (5,6)a, (5,6)b and (5,6)c differ by up to 26 kJ mol⁻¹. The IR frequencies of the ¹(5,6)b isomer agree well with the measured IR-PD band pattern, albeit somewhat shifted (*cf.* Figure 3). In particular, the characteristic IR-PD band at 1180 cm⁻¹ is well reproduced. The same cluster geometry in the triplet state does not provide a suitable IR frequency for the IR-PD band at 1180 cm⁻¹, but the predicted frequency at 1386 cm⁻¹ complements the predicted singlet state frequencies and completes the overall IR-PD band pattern of the measurement (*cf.* Figure 6(a)). The singlet and triplet isomer are degenerate (*cf.* Table S7). We conclude that the sixth H₂ molecule adsorbs side-on to one of the two fivefold coordinated equatorial sites Ta^{eq} of the cluster adsorbate complex, yielding the isomer (5,6)b, which probably occurs in both singlet and triplet spin states.

Our DFT modeling for conceivable isomers of the subsequent cluster-adsorbate complex (5,7) suggests a likely coordination of the seventh H₂ molecule to the other fivefold coordinated equatorial site Ta^{eq}. Again, singlet and triplet isomer are degenerate (*cf.* Table S9). The predicted IR frequencies of the two spin state isomers together agree with the measured IR-PD band pattern (*cf.* Figure 6(b)). We therefore consider a co-existence of singlet and triplet isomer ^{1,3}(5,6)b likely. Coordination of the seventh H₂ molecule instead at the doubly coordinated equatorial site Ta^{eq} yields isomers (5,7)a (*cf.* Table S10). The predicted IR frequencies are similar to those of the (5,7)b isomers (*cf.* Figure S6). However, the ¹(5,6)a and ³(5,6)a isomers are less stable than ¹(5,6)b and ³(5,6)b by 10 and 14 kJ mol⁻¹, respectively, so we consider the formation of the (5,7)a isomers to be less likely than that of (5,7)b isomers.

7. Cryo IR Spectroscopy of H₂ Adsorption to Ta₂₋₈⁺ Clusters

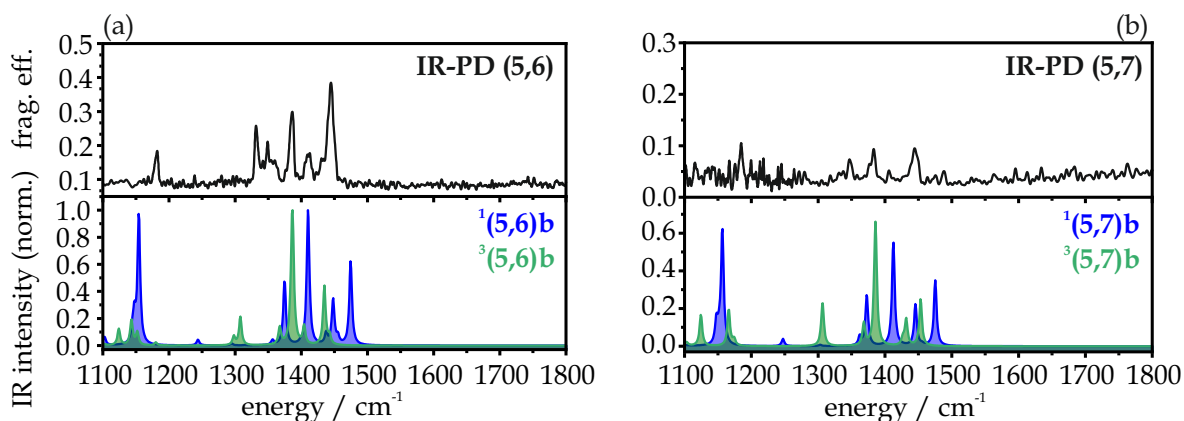


Figure 6: Experimental IR-PD spectra and DFT modeling of (5,6), (a), and (5,7), (b), respectively. The predicted IR frequencies are scaled by a factor of 0.9619. Coexistence of singlet and triplet isomers seems likely. For calculated energies and IR frequencies of the shown structural isomers of (5,6), see Table S7 and Table S8. For calculated energies and IR-PD frequencies of the shown structural isomers of (5,7), see Table S9 and Table S10.

Our DFT modeling for conceivable isomers of the subsequent cluster adsorbate complex (5,8) reveals isomer (5,8)a whose predicted IR frequencies of the two spin state isomers together agree well with the measured IR-PD band pattern (*cf.* Figure 7(a)). The isomers ¹(5,8)a and ³(5,8)a comprise three side-on and molecularly adsorbed H₂ ligands, each coordinating to one of the equatorial sites Ta^{eq} of the cluster adsorbate complex (*cf.* Table S12). Our DFT modeling predicted three additional structural isomers, some of which are actually up to 30 kJ mol⁻¹ more stable. However, some of the alternative isomers are not directly accessible from the former (5,7)b isomer, but would require expensive reorganisation of the adsorbate shell, which we consider unlikely. Finally, we consider a good agreement of the predicted IR frequencies with the experimentally measured IR-PD band pattern as the most important argument to identify the most likely structural isomer. In this case, we conclude that coexistence of the spin isomers ¹(5,8)a and ³(5,8)a seems likely. Up to this point of the adsorption chain, we thus conclude for dissociative adsorption of five H₂ molecules before molecular adsorption starts from the sixth H₂ molecule and beyond. The first three of these molecularly adsorbed H₂ molecules prefer to coordinate at the three equatorial sites Ta^{eq} rather than at the apical sites Ta^{ap} of the cluster adsorbate complex. Coordination of these apical sites Ta^{ap} seems to start only with the adsorption of the ninth H₂ molecule.

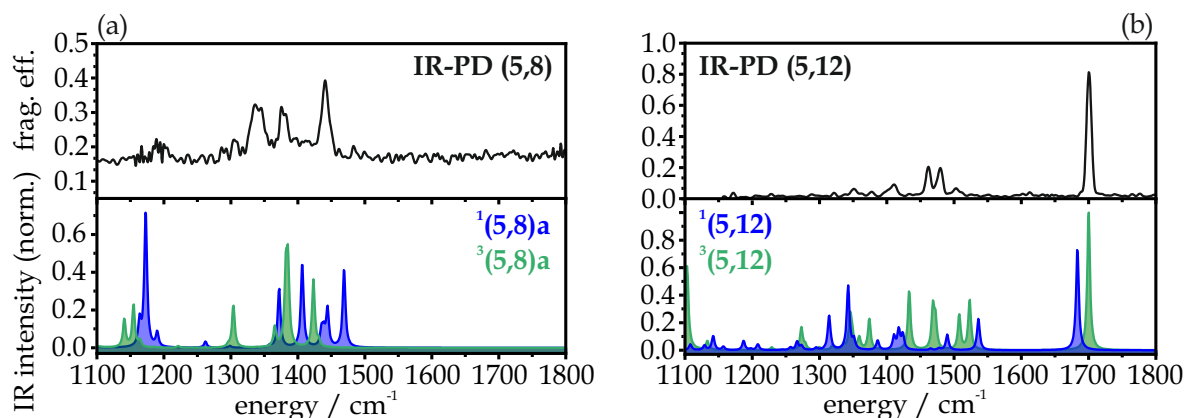


Figure 7: Experimental IR-PD spectra and DFT modeling of (5,8), (a), and (5,12), (b), respectively. The predicted IR frequencies are scaled by a factor of 0.9619. It seems likely that singlet and triplet isomers coexist for (5,8), while we assume that (5,12) is most likely a triplet state species. For calculated energies and IR frequencies of the shown structural isomers of (5,8), see Table S11 and Table S12. For calculated energies and IR-PD frequencies of the shown structural isomers of (5,12), see Table S13 and Table S14.

We managed to model a structure for the adsorption limit species (5,12). The IR frequencies of the triplet state isomer $^3(5,12)$ agree well with the measured IR-PD band pattern, albeit somewhat shifted. Some IR-PD bands below 1400 cm^{-1} , although predicted by DFT modeling, are of low intensity in the measured spectra due to decreasing IR laser energy. (*cf.* Figure S8). However, the characteristic IR-PD band at 1700 cm^{-1} is well reproduced. The corresponding singlet state species $^1(5,12)$ is slightly less stable by 7 kJ mol^{-1} and the predicted IR frequencies are in poor agreement with the measured (5,12) IR-PD band pattern. We thus assume that the triplet state species $^3(5,12)$ is formed.

The predicted structure of the cluster adsorbate complex $^3(5,12)$ bases on the already identified (5,8)a structure, to which two of the four additional H_2 ligands coordinate side-on and molecularly to the two apical sites Ta^{ap} - one H_2 to each apical Ta atom. The two further H_2 ligands coordinate also side-on to each of the apical sites, respectively. However, these H_2 ligands are strongly activated and the H-H distance is increased to 2.00 \AA , so that one of the two H atoms of each ligand is arranged like a hydride over one of the two previously free edges in the $\text{Ta}^{\text{ap}}\text{-Ta}^{\text{eq}}\text{-Ta}^{\text{ap}}$ motif. This results in a combined side-on/end-on $\mu_2\text{-}\kappa\text{H}:\kappa\text{H},\text{H}$ coordination

7. Cryo IR Spectroscopy of H₂ Adsorption to Ta₂₋₈⁺ Clusters

motif for these H₂ ligands (*cf.* Table S14). A detailed frequency analysis shows that this particular coordination motif is the origin of the characteristic IR-PD band at 1700 kJ mol⁻¹ observed for species (5,m), m = 10 - 12. Ta-H vibrations involving the H atoms that do not bridge the Ta-Ta edge allow such high wavenumbers.

At this point we refer to Figure 8 for a overall picture of H₂ adsorption to Ta₅⁺. Note that this study does not consider possible transition states and reaction pathways between adsorption steps. The starting point of the adsorption chain is the bare Ta₅⁺ and the diatomic H₂ molecule. All given energies are relative energies of triplet states with respect to the free cluster adsorbate complex components. DFT calculations predict an exothermic adsorption of 654.3 kJ mol⁻¹ for the sum of the first five H₂ molecules. From this, the average adsorption energy for each of the first five H₂ molecules can be estimated to be about 130.9 kJ mol⁻¹. The magnitude of these adsorption energies agrees well with those predicted by DFT calculations for the adsorption of H₂ on Ta₄⁺. These high values of exothermic adsorption energy are a consequence of dissociative adsorption of the corresponding H₂ molecules. Accordingly, the predicted adsorption energies for the subsequent three H₂ molecules are much less exothermic, ranging from only 34.6 to 20.6 kJ mol⁻¹. The magnitude of these adsorption energies agrees again well with those predicted by DFT calculations for the adsorption of H₂ on Ta₄⁺.

In contrast, it is noteworthy that DFT calculations predict an exothermic adsorption of 245.8 kJ mol⁻¹ for the sum of the terminal four H₂ molecules, yielding (5,12) from (5,8). From this, the average adsorption energy for each of these terminal four H₂ molecules can be estimated to be about 61.5 kJ mol⁻¹ which is two to three times the adsorption energies of the prior molecularly adsorbed H₂ molecules. This can be explained considering the predicted cluster geometry of (5,12) which comprises two H₂ ligands which coordinate in a combined side-on/end-on $\mu_2\text{-}\kappa\text{H}:\kappa\text{H,H}$ motif and are thus highly activate. This activated coordination is associated with higher adsorption energies than molecular adsorption without further activation. Understanding the driving force for this late activation of H₂ would require further detailed and extensive DFT studies on conceivable reaction pathways and transition states. This could be a starting point for further studies.

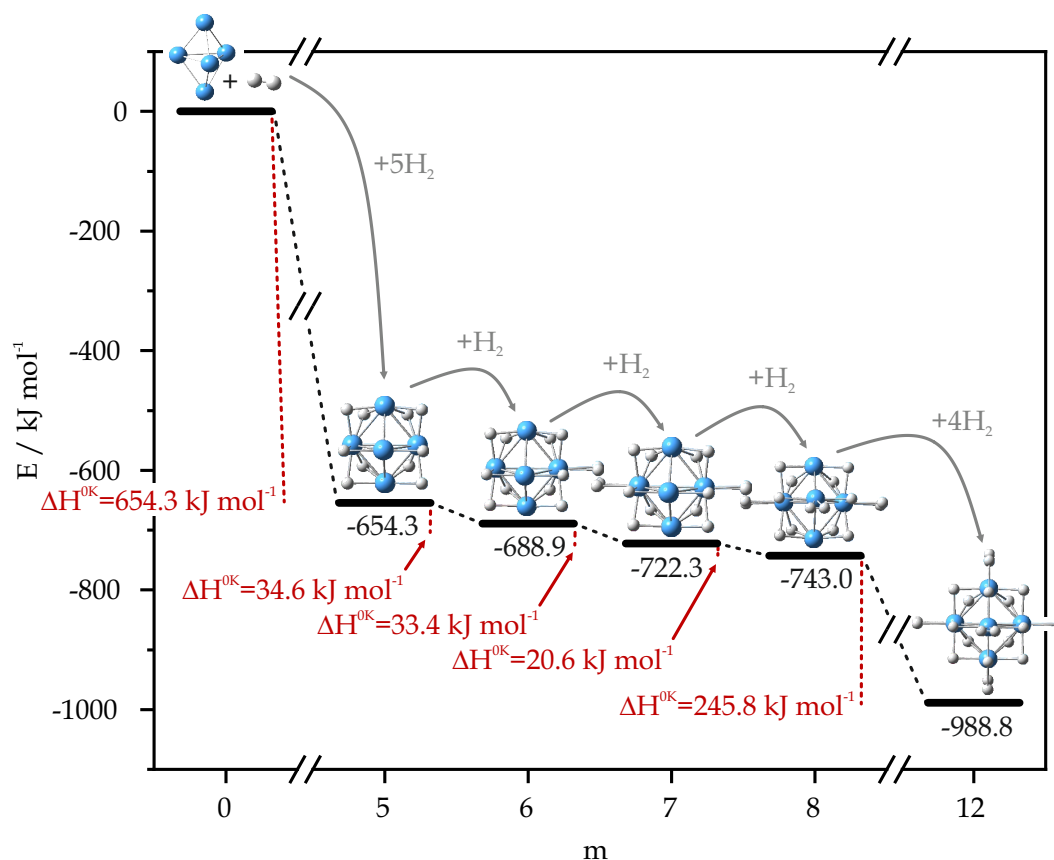


Figure 8: Computed Energetics of stepwise H₂ adsorption onto Ta₅⁺ cluster up to species (5,12). The shown cluster adsorbate structures are triplet state structures. Note that this study does not consider possible transition states and reaction pathways between adsorption steps. The given values are relative energies of triplet states with respect to the free cluster adsorbate complex components (in black), and with respect to desorption of single H₂ (in red).

In summary, our IR-PD study and DFT modeling reveal that the first five H₂ molecules adsorb dissociatively to the Ta₅⁺ cluster prior to molecular adsorption starting with the sixth H₂ molecule. In species (5,12), two of the four last adsorbed H₂ molecules are highly activated. At this point we want to address the question, whether these findings and conclusions are in line with the recorded H₂ adsorption kinetics of Ta₅⁺ [CKS]. The fast first five adsorption processes are consistent with the absence of IR-PD bands in the measured spectra of the corresponding cluster adsorbate complexes and their predicted structure comprising exclusively dissociatively coordinated H₂ ligands. Beyond this formal first adsorbate shell - within the formal second adsorbate shell - decreasing adsorption rate constants and the onset of significant desorption processes are accompanied by several IR-PD bands in the

measured spectra and DFT calculated cluster adsorbate structures. This behavior indicates that molecular H₂ adsorption occurs first at equatorial Ta^{eq} sites before apical Ta^{ap} sites are also coordinated by H₂ in the further course of the adsorption chain. The final adsorption processes lead to species (5,11) and (5,12), which form the formal third adsorption shell of H₂ to Ta₅⁺, proceed significantly slower than the five preceding adsorption steps. In parallel, the rate constants for desorption decrease to (almost) insignificant values. This is in good agreement with the predicted cluster geometry of (5,12). It consists of two H₂ ligands coordinating in a combined side-on/end-on $\mu_2\text{-}\kappa\text{H}:\kappa\text{H}_2$ motif and is thus strongly activated. This activated coordination is associated with high adsorption energies coming with reduced H₂ desorption capacity. We assume that this over all picture of H₂ adsorption on Ta₅⁺ might be a general procedure for the adsorption of H₂ on small tantalum clusters, since we found this behavior for the adsorption of H₂ on Ta₄⁺ before.

[Ta₆(H₂)_m]⁺ We extended our kinetic study of the adsorption of H₂ to Ta₆⁺ **[CKS]** by performing IR-PD spectroscopy on accessible cluster adsorbate complexes. In fact, we recorded IR-PD spectra of the first adsorbate species (6,1) and the adsorption limit species (6, m_{max} = 12) (*cf.* Figure 9 and S9). The low yields of all adsorbate species in between (m = 2 - 11, *cf.* **[CKS]**), especially at short storage times as required for time-efficient IR-PD spectroscopic studies, hampered recording of their IR-PD spectra, and the obtained signal to noise ratio is meager. We find no IR-induced fragmentation for the first adsorbate species (6,1). In contrast, the IR-PD spectrum of (6,12) reveals three broad IR-PD bands at 1151, 1320, and 1360 cm⁻¹.

The interpretation of the recorded IR-PD spectra would benefit from DFT modeling for conceivable geometries of the cluster adsorbate complexes. Since we do not have this at hand, we attempt to speculate based on findings from previous cases of H₂ adsorption on tantalum clusters of other sizes, in particular Ta₄⁺ and Ta₅⁺. For both cases we managed to understand the process of H₂ adsorption as well as the adsorbate species involved. On this basis, we assume a dissociatively adsorbed H₂ molecule on the Ta₆⁺ cluster core for (6,1). The absence of IR-PD bands in the recorded spectrum is indicative of such a cluster geometry. The dissociatively coordinated H₂ probably forms two hydride bridged Ta-Ta edges. As a result, fragmentation of such a cluster adsorbate complex is not possible under the conditions of our IR-PD experiment. The observed IR-PD bands in the spectrum of the adsorption limit species (6,12) can be assigned to Ta-H vibrational frequencies. We are able

to measure these bands because the molecularly adsorbed H_2 ligands likely act as a tag which detaches upon adsorption of a single IR photon. The presence of Ta-H bands in the IR-PD spectrum of (6,12) support the interpretation of dissociatively adsorbed H_2 within the formal first adsorbate shell.

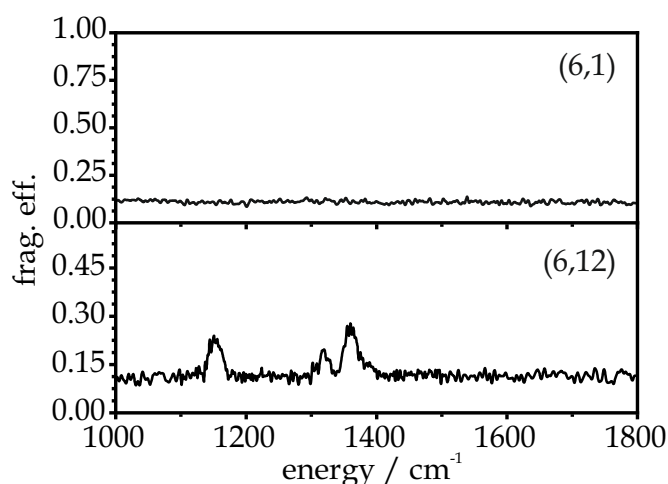


Figure 9: IR-PD spectra of sequential H_2 adsorption steps onto Ta_6^+ cluster cations $[\text{Ta}_6(\text{N}_2)_m]^+$, $m=1$ and $m=12$ as recorded after 18 K He buffer gas cooling. The wavenumber range is between 1000 and 1800 cm^{-1} . For IR-PD spectra in the range of 1000 to 2400 cm^{-1} , see Figure S9 in the supplementary information.

$[\text{Ta}_7(\text{H}_2)_m]^+$ For the cationic tantalum heptamer, Ta_7^+ we observe stepwise adsorption of up to 14 H_2 molecules (*cf.* kinetic study [CKS]). In the following, we discuss the associated IR-PD spectra to obtain structural information about these adsorbate species. We actually succeeded in obtaining IR-PD spectra of all adsorbate species along the H_2 adsorption chain: $(7,m)$, $m=1-14$ (*cf.* Figure 10). The absence of IR-induced fragmentation for the first seven adsorbate species $(7,1)$ to $(7,7)$ is striking. This is consistent with our results for the adsorbate species of the smaller Ta_n^+ clusters, $n=3-5$, whose IR-PD spectra show no bands for all species (n,m) up to $m=n$. Based on the parallels in the results, we assume that all tantalum clusters behave similarly. Accordingly, we observe multiple IR-PD bands for all species comprising eight or more H_2 ligands building up their second adsorbate shell. Note, that we do not observe any characteristics of a third adsorbate shell which would be similar to the sharp IR-PD band at 1700 cm^{-1} for the high loaded adsorbate species of Ta_5^+). The single band at 1120 cm^{-1} for species $(7,8)$ shifts slightly but gradually towards the blue to 1138 cm^{-1} for species $(7,14)$. The pattern of the bundle of IR-PD bands between 1200 and 1500 cm^{-1} is preserved for

7. Cryo IR Spectroscopy of H₂ Adsorption to Ta₂₋₈⁺ Clusters

species $m = 8 - 14$ along the adsorbate chain, but with some minor shifts: The IR-PD spectra of (7,8) and (7,9) reveal six IR-PD bands at 1274, 1295, 1327, 1348, 1374 and 1390 cm⁻¹, respectively. For (7,10) and all adsorbate species beyond, the range of these IR-PD bands broadens symmetrically, leading to the following IR-PD band pattern for the final adsorbate species (7,14): 1237, 1267, 1284, 1297, 1309, 1348, 1384, and 1397 cm⁻¹.

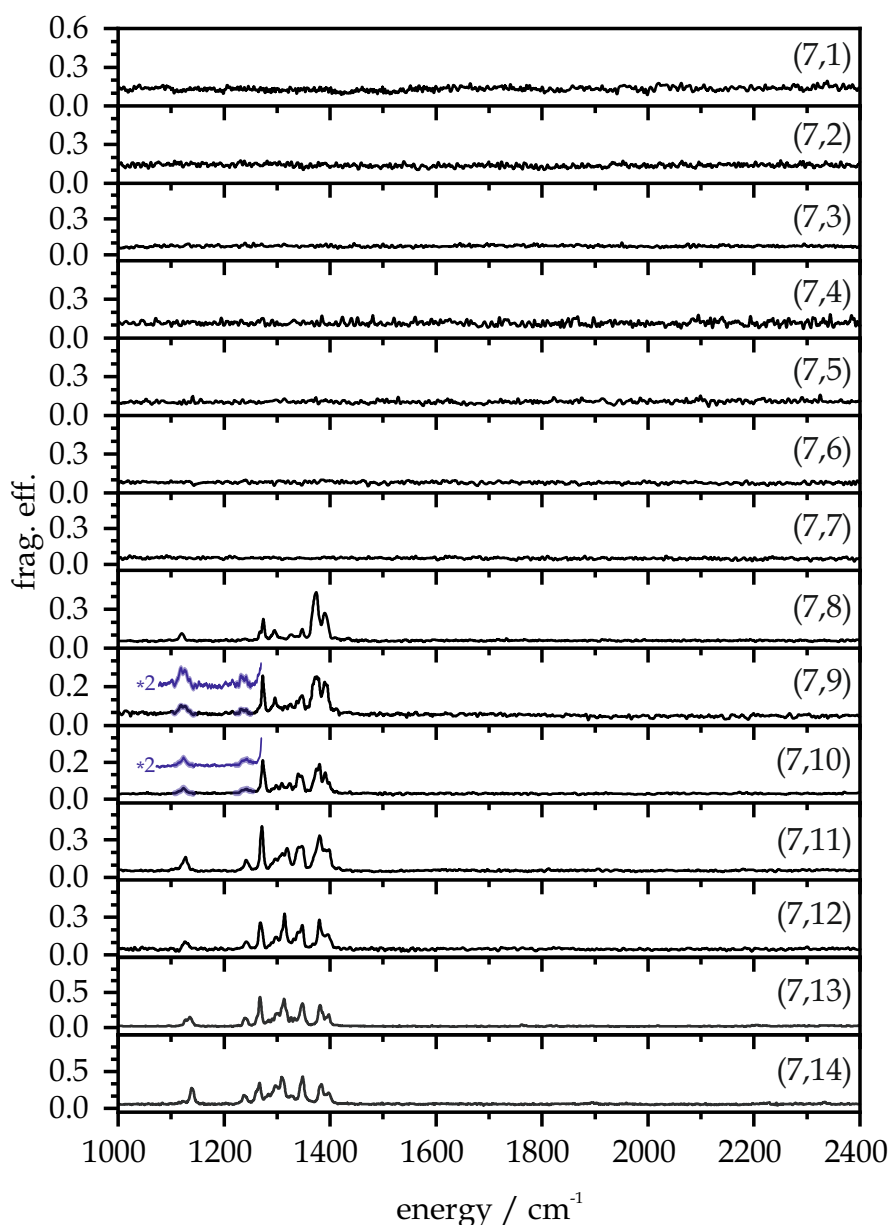


Figure 10: IR-PD spectra of sequential H₂ adsorption steps onto Ta₇⁺ cluster cations [Ta₇(N₂)_m]⁺, $m = 1 - 14$, as recorded after 18 K He buffer gas cooling. The spectral range is between 1000 and 2400 cm⁻¹.

The parallels in the IR-PD spectra to those of (4,m) and (5,m) encouraged us to make the following interpretations: The absence of IR-PD bands in spectra of (7,1) to (7,7) indicates dissociatively adsorbed H₂ ligands. Their H atoms probably coordinate as bridges over Ta-Ta edges of the cluster core. We suggest molecular adsorption for all H₂ molecules beyond the formal first adsorbate shell. For their adsorption motif, we propose a side-on coordination at a single Ta atom of the cluster core. These interpretive hypotheses would benefit from DFT modeling for conceivable cluster adsorbate structures (7,m) whose predicted IR band patterns match the experimental IR-PD spectrum. Without such DFT predictions, we make do with these reasoned but speculative structural assumption at this point. However, it may be worth consulting our related cryokinetic study [CKS] of H₂ and Ta₇⁺. The overall picture of the processes along the H₂ adsorption chain shows a less significant decrease in adsorption rates beyond the formal first adsorption shell than observed for the H₂ adsorption kinetics of the smaller tantalum clusters Ta₃⁺, Ta₄⁺, and Ta₅⁺. Nevertheless, we can clearly assign higher rate constants to adsorption processes that are probably dissociative ($k_{(7,0)}$ to $k_{(7,6)}$) than to adsorption processes that are probably molecular ($k_{(7,7)}$ to $k_{(7,13)}$). Admittedly, it is counterintuitive that the kinetic fit predicts desorption rates with high rate constants for the desorption of molecules likely to be dissociatively adsorbed. It seems plausible to us that there is at least one Ta core atom of the bare Ta₇⁺ cluster which may not accept hydrides in the first place due to its high level of next neighbor coordination to other Ta centers. Therefore, the sixth and seventh H₂ molecules initially adsorb molecularly onto the cluster. While measuring the IR-PD spectra of (7,6) and (7,7), the photon energy introduced into the cluster adsorbate complexes could induce a reorganization of the cluster core, so that the initially molecularly adsorbed H₂ molecules eventually dissociate on the cluster and form highly stable hydrides. This results in the observed absence of IR-PD bands in the corresponding spectra. Thus, significant desorption reactions in kinetic measurements do not necessarily contradict IR-PD fingerprints indicating dissociatively adsorbed H₂ ligands.

[Ta₈(H₂)_m]⁺ For the tantalum cluster cation Ta₈⁺ we managed to perform IR-PD spectroscopy of the adsorbate species (8,m), m = 1 - 6 and m = 15. The low yields of all adsorbate species in between (m = 7 - 15, *cf.* [CKS]), especially at short storage times as required for time-efficient IR-PD spectroscopic studies, hampered recording of their IR-PD spectra, and the obtained signal to noise ratio is meager. We do not observe IR-induced fragmentation for the first adsorbate species (8,1) to (8,5). The

7. Cryo IR Spectroscopy of H₂ Adsorption to Ta₂₋₈⁺ Clusters

IR-PD spectrum of (8,6) shows three weak bands at 1112, 1401, and 1721 cm⁻¹. For the adsorption limit species (8,15), we observe IR-PD bands at 1179 and 1261 cm⁻¹ and a doublet at 1307 and 1314 cm⁻¹. It is noteworthy that Ta₈⁺ deviates from the previously observed trend of smaller tantalum clusters and shows distinct IR-PD bands for species (8,6), which comprises an incomplete formal first adsorbate shell. The location of the IR-PD bands in the spectrum is also noteworthy: They extend over a very broad spectral range from 1100 to 1750 cm⁻¹. We have observed a similarly broad splitting of the band pattern only for (5,10) which is the formal second adsorbate shell species of Ta₅⁺. This is - at first glance - obviously not the case for the present species (8,6). The early appearance of IR-PD bands and the broad band distribution indicates the occurrence of additional species and processes that go beyond our previously identified correlation between formal adsorbate shells and resulting adsorption processes and species.

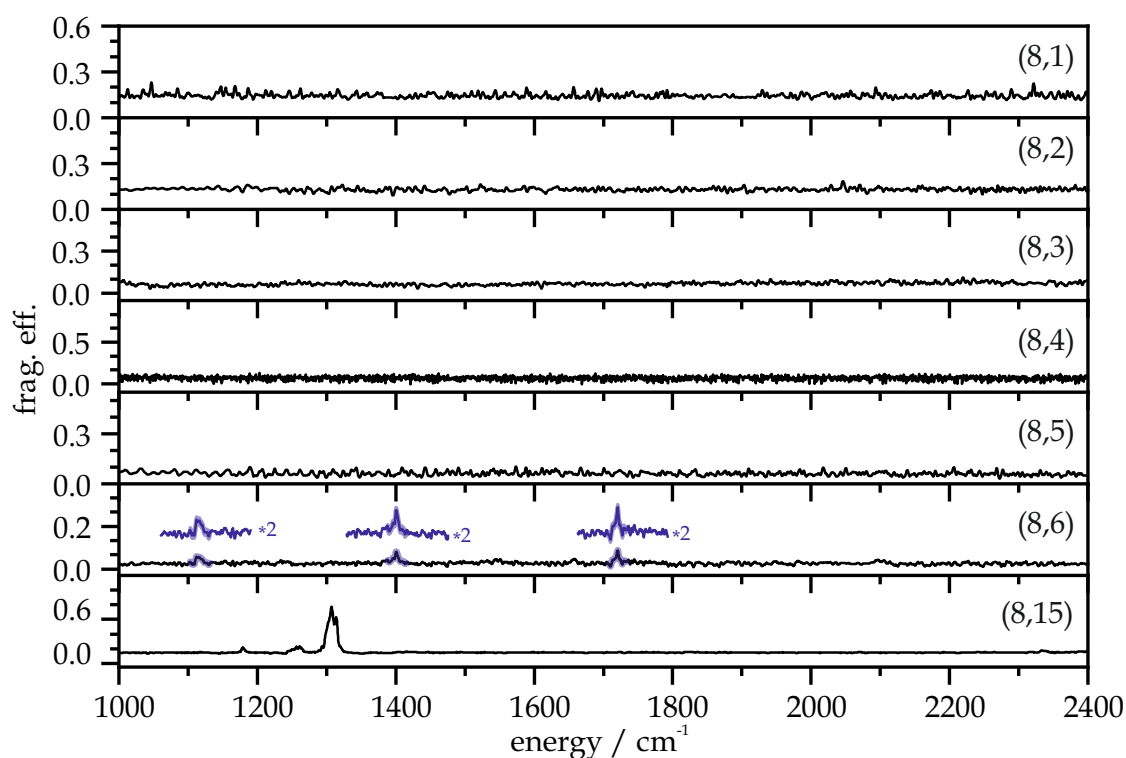


Figure 11: IR-PD spectra of sequential H₂ adsorption steps onto Ta₈⁺ cluster cations [Ta₈(N₂)_m]⁺, m = 1 - 6 and m = 15, as recorded after 18 K He buffer gas cooling. The spectral range is between 1000 and 2400 cm⁻¹.

At this point it may be worth consulting our related cryokinetic study [CKS] of H₂ and Ta₈⁺. The measured temporal evolution of ion intensities reveal at first

the stepwise adsorption of five H₂ molecules yielding species (8,5) as an intermittent adsorption limit. Further adsorption of H₂ molecules proceeds in a delayed manner. The slowly formed (8,6) is the first species, for which we observe IR-PD bands. Based on this correlation, we speculate that for the cluster size $n=8$ the first adsorbate shell may already be completed if it consists of five H₂ ligands, $m=5$, instead of $m=n$ as observed for the smaller clusters $n=3-5$. The slow adsorption indicates molecular coordination that allows this sixth H₂ ligand to act as a tag and to record IR-PD bands as observed. It seems plausible to us that the bare Ta₈⁺ cluster might comprise at least one, maybe more, highly coordinated Ta atoms (high number of next neighbor Ta atoms) which are reluctant to cleave H₂. Thus, the sixth H₂ ligand of (8,6) opens the second adsorbate shell around the cluster. These interpretive hypotheses would benefit from DFT modeling for conceivable cluster adsorbate structures (8, m) whose predicted IR band patterns match the experimental IR-PD spectrum. Without such DFT predictions, we are content at this point with these reasoned but speculative structural hypotheses.

7.2.5 Conclusion

We present an IR-PD study of tantalum cluster adsorbate complexes [Ta _{n} (H₂) _{m}]⁺ species, abbreviated (n, m), $n=3-8$. We found a concise variation of recorded IR-PD features as a function of the tantalum cluster size n and of H₂ adsorbate loading m . The recorded IR-PD features locate in the majority of the cases in the spectral range between 1100 and 1700 cm⁻¹.

However, we did not find IR-PD bands within our accessible spectral range for all species studied (n, m). More precisely, the absence of any vibrational bands for all adsorbate species of Ta₃⁺, Ta₄⁺, Ta₅⁺ and Ta₇⁺ up to (n, $m=n$), the species with a complete formal first adsorbate shell, is striking. In contrast, all investigated species with higher H₂ loading show multiple IR-PD bands corresponding to Ta-H binding vibrations. Thus, the IR-PD band patterns provide structural information about the respective species and indirectly about the structures of the previous complexes of the adsorption chain. In particular, DFT modeling for conceivable cluster geometries (4, m) and (5, m), whose predicted IR frequencies match the experimental IR-PD band patterns, yield the following overall picture for H₂ adsorption to Ta _{n} ⁺ clusters: All H₂ molecules building the formal first adsorbate shell adsorb dissociatively to the clusters before all further H₂ molecules are molecularly adsorbed from there on.

In the very special case of the (5,12) cluster, the last two H₂ ligands even coordinate in a formal third adsorbate shell. The predicted cluster geometry comprises two H₂ ligands coordinated in a combined side-on/end-on $\mu_2\text{-}\kappa\text{H}:\kappa\text{H},\text{H}$ motif. Thus, we conclude that activation of H₂ seems to be possible even late in the adsorption chain. These results are in full agreement with the findings from our associated cryo kinetic study [CKS], which shows very fast adsorption processes without competing desorption reactions until the completion of the first adsorbate shell. From then on, the adsorption chain proceeds with slow adsorption reactions accompanied by several desorption reactions.

For Ta₆⁺ and Ta₈⁺ we assume a different adsorption behavior of H₂, for the interpretation of which we rely on the findings of (4,m) and (5,m). Again, the first H₂ molecules adsorb dissociatively to the clusters. For the further course of the H₂ adsorption chain, we assume that the formal first adsorbate shell might be completed before $m = n$ is reached. There may be at least one, maybe more, highly coordinated Ta cluster core atoms that do not accept hydrides and cause this premature completion of the first adsorbate shell. Without any findings from DFT modelling, we are content at this point with these reasoned but speculative structural hypotheses.

7.2.6 Acknowledgements

This work was supported by the German research foundation DFG within the trans-regional collaborative research center SFB/TRR 88 "Cooperative effects in homo and heterometallic complexes" (3met.de) and by the state research center OPTIMAS. We thank Thomas Kolling for technical assistance and valuable discussion. Quantum chemical modeling took place at the "Regionales Hochschulrechenzentrum Kaiserslautern" (RHRK).

7.2.7 References

- [1] W. M. Haynes, *CRC Handbook of Chemistry and Physics, Vol. 95th*, CRC Press Taylor & Francis Group, **2014**.
- [2] M. Frey, *ChemBioChem* **2002**, 3, 153–160.
- [3] S. Shima, R. K. Thauer, *The Chemical Record* **2007**, 7, 37–46.

-
- [4] M. Bruschi, M. Tiberti, A. Guerra, L. De Gioia, *Journal of the American Chemical Society* **2014**, *136*, 1803–1814.
- [5] F. Schüth, *Chemie in unserer Zeit* **2006**, *40*, 92–103.
- [6] A. Mittasch, *Geschichte der Ammoniaksynthese*, Verlag Chemie, **1951**.
- [7] H. Breil, E. Holzkamp, H. Martin, K. E. H. Ziegler, DE973626C, **1960**.
- [8] W. Ostwald, GB190200698A, **1902**.
- [9] Badische Anilin- und Soda-Fabrik, DE235421C, **1911**.
- [10] F. Fischer, H. Tropsch, DE524468C, **1931**.
- [11] F. Fischer, H. Tropsch, DE484337C, **1925**.
- [12] P. B. Armentrout, *Catalysis Science & Technology* **2014**, *4*, 2741–2755.
- [13] S. M. Lang, T. M. Bernhardt, *Physical Chemistry Chemical Physics* **2012**, *14*, 9255–9269.
- [14] D. K. Böhme, H. Schwarz, *Angewandte Chemie International Edition* **2005**, *44*, 2336–2354.
- [15] R. A. J. O’Hair, G. N. Khairallah, *Journal of Cluster Science* **2004**, *15*, 331–363.
- [16] P. B. Armentrout, *Annual Reviews* **2001**, *52*, 423–461.
- [17] E. L. Muetterties, *Science* **1977**, *196*, 839–848.
- [18] M. B. Knickelbein, *Annual Reviews* **1999**, *50*, 79–115.
- [19] M. E. Geusic, M. D. Morse, R. E. Smalley, *The Journal of Chemical Physics* **1985**, *82*, 590–591.
- [20] G. J. Kubas, *Accounts of Chemical Research* **1988**, *21*, 120–128.
- [21] K. Christmann, *Surface Science Reports* **1988**, *9*, 1–163.
- [22] J. Chatt, L. A. Duncanson, *Journal of the Chemical Society (Resumed)* **1953**, 2939–2947.
- [23] T. L. Silbaugh, C. T. Campbell, *The Journal of Physical Chemistry C* **2016**, *120*, 25161–25172.

- [24] I. Swart, A. Fielicke, B. Redlich, G. Meijer, B. M. Weckhuysen, F. M. F. de Groot, *Journal of the American Chemical Society* **2007**, *129*, 2516–2520.
- [25] I. Swart, A. Fielicke, D. M. Rayner, G. Meijer, B. M. Weckhuysen, F. M. F. de Groot, *Angewandte Chemie International Edition* **2007**, *46*, 5317–5320.
- [26] S. Dillinger, M. P. Klein, A. Steiner, D. C. McDonald, M. A. Duncan, M. M. Kappes, G. Niedner-Schatteburg, *The Journal of Physical Chemistry Letters* **2018**, *9*, 914–918.
- [27] D. A. Hite, K. S. McKay, S. Kotler, D. Leibfried, D. J. Wineland, D. P. Pappas, *MRS Advances* **2017**, *2*, 2189–2197.
- [28] M. B. Knickelbein, G. M. Koretsky, K. A. Jackson, M. R. Pederson, Z. Hajnal, *The Journal of Chemical Physics* **1998**, *109*, 10692–10700.
- [29] K. García-Díez, J. Fernández-Fernández, J. A. Alonso, M. J. López, *Physical Chemistry Chemical Physics* **2018**, *20*, 21163–21176.
- [30] W. F. Hoffman, E. K. Parks, G. C. Nieman, L. G. Pobo, S. J. Riley, *Zeitschrift für Physik D Atoms Molecules and Clusters* **1987**, *7*, 83–89.
- [31] I. Swart, P. Gruene, A. Fielicke, G. Meijer, B. M. Weckhuysen, F. M. F. de Groot, *Physical Chemistry Chemical Physics* **2008**, *10*, 5743–5745.
- [32] O. V. Lushchikova, H. Tahmasbi, S. Reijmer, R. Platte, J. Meyer, J. M. Bakker, *The Journal of Physical Chemistry A* **2021**, *125*, 2836–2848.
- [33] C. Kerpál, D. J. Harding, D. M. Rayner, A. Fielicke, *The Journal of Physical Chemistry A* **2013**, *117*, 8230–8237.
- [34] R. Trivedi, D. Bandyopadhyay, *International Journal of Hydrogen Energy* **2016**, *41*, 20113–20121.
- [35] R. Trivedi, D. Bandyopadhyay, *International Journal of Hydrogen Energy* **2015**, *40*, 12727–12735.
- [36] L. Warczinski, C. Hättig, *Physical Chemistry Chemical Physics* **2019**, *21*, 21577–21587.
- [37] I. Cabria, M. J. López, S. Fraile, J. A. Alonso, *The Journal of Physical Chemistry C* **2012**, *116*, 21179–21189.

-
- [38] N. Levin, J. T. Margraf, J. Lengyel, K. Reuter, M. Tschurl, U. Heiz, *Physical Chemistry Chemical Physics* **2022**, *24*, 2623–2629.
- [39] J. F. Eckhard, D. Neuwirth, C. Panosetti, H. Oberhofer, K. Reuter, M. Tschurl, U. Heiz, *Physical Chemistry Chemical Physics* **2017**, *19*, 5985–5993.
- [40] C. Geng, J. Li, T. Weiske, H. Schwarz, *Proceedings of the National Academy of Sciences* **2019**, *116*, 21416–21420.
- [41] X. Sun, X. Huang, *ACS Omega* **2022**, *7*, 22682–22688.
- [42] G.-D. Jiang, L.-H. Mou, J.-J. Chen, Z.-Y. Li, S.-G. He, *The Journal of Physical Chemistry A* **2020**, *124*, 7749–7755.
- [43] M. Kumar Yadav, A. Mookerjee, *Physica B: Condensed Matter* **2010**, *405*, 3940–3942.
- [44] P. Gruene, A. Fielicke, G. Meijer, *The Journal of Chemical Physics* **2007**, *127*, 234307.
- [45] J. Du, X. Sun, G. Jiang, *The Journal of Chemical Physics* **2012**, *136*, 094311.
- [46] J. Lengyel, N. Levin, F. J. Wensink, O. V. Lushchikova, R. N. Barnett, U. Landman, U. Heiz, J. M. Bakker, M. Tschurl, *Angewandte Chemie International Edition* **2020**, *59*, 23631–23635.
- [47] G. Ertl, *Catalysis Reviews* **1980**, *21*, 201–223.
- [48] G. Ertl, *Angewandte Chemie International Edition* **2008**, *47*, 3524–3535.
- [49] C. Geng, J. Li, T. Weiske, H. Schwarz, *Proceedings of the National Academy of Sciences* **2018**, *115*, 11680–11687.
- [50] D. V. Fries, M. P. Klein, A. Steiner, M. H. Prosenc, G. Niedner-Schatteburg, *Physical Chemistry Chemical Physics* **2021**, *23*, 11345–11354.
- [51] D. V. Fries, M. P. Klein, A. Straßner, M. E. Huber, M. Luczak, C. Wiehn, G. Niedner-Schatteburg, *The Journal of Chemical Physics* **2023**, *159*, 164303.
- [52] D. V. Fries, M. P. Klein, A. Straßner, M. E. Huber, G. Niedner-Schatteburg, *The Journal of Chemical Physics* **2023**, *159*, 164306.

- [53] J. Mohrbach, S. Dillinger, G. Niedner-Schatteburg, *The Journal of Physical Chemistry C* **2017**, *121*, 10907–10918.
- [54] S. Dillinger, J. Mohrbach, G. Niedner-Schatteburg, *The Journal of Chemical Physics* **2017**, *147*, 184305.
- [55] J. Mohrbach, S. Dillinger, G. Niedner-Schatteburg, *The Journal of Chemical Physics* **2017**, *147*, 184304.
- [56] A. A. Ehrhard, M. P. Klein, J. Mohrbach, S. Dillinger, G. Niedner-Schatteburg, *Molecular Physics* **2021**, *119*, e1953172.
- [57] M. P. Klein, *PhD Thesis*, Technische Universität Kaiserslautern, **2021**.
- [58] A. A. Ehrhard, M. P. Klein, J. Mohrbach, S. Dillinger, G. Niedner-Schatteburg, *The Journal of Chemical Physics* **2022**, *0*, 054308.
- [59] M. P. Klein, A. A. Ehrhard, M. E. Huber, A. Straßner, D. V. Fries, S. Dillinger, J. Mohrbach, G. Niedner-Schatteburg, *The Journal of Chemical Physics* **2022**, *156*, 014302.
- [60] A. Straßner, M. P. Klein, D. V. Fries, C. Wiehn, M. E. Huber, J. Mohrbach, S. Dillinger, D. Spelsberg, P. B. Armentrout, G. Niedner-Schatteburg, *The Journal of Chemical Physics* **2021**, *155*, 244306.
- [61] A. Straßner, C. Wiehn, M. P. Klein, D. V. Fries, S. Dillinger, J. Mohrbach, M. H. Prosenc, P. B. Armentrout, G. Niedner-Schatteburg, *The Journal of Chemical Physics* **2021**, *155*, 244305.
- [62] C. Berg, T. Schindler, G. Niedner-Schatteburg, B. V. E., *The Journal of Chemical Physics* **1995**, *102*, 4870–4884.
- [63] V. Bondybey, J. English, *The Journal of Chemical Physics* **1981**, *74*, 6978–6979.
- [64] D. Proch, T. Trickl, *Review of Scientific Instruments* **1989**, *60*, 713–716.
- [65] M. J. Frisch, G. W. Trucks, H. B. Schlegel, G. E. Scuseria, M. A. Robb, J. R. Cheeseman, G. Scalmani, V. Barone, G. A. Petersson, H. Nakatsuji, X. Li, M. Caricato, A. V. Marenich, J. Bloino, B. G. Janesko, R. Gomperts, B. Menucci, H. P. Hratchian, J. V. Ortiz, A. F. Izmaylov, J. L. Sonnenberg, Williams, F. Ding, F. Lipparini, F. Egidi, J. Goings, B. Peng, A. Petrone, T. Henderson, D. Ranasinghe, V. G. Zakrzewski, J. Gao, N. Rega, G. Zheng, W. Liang,

- M. Hada, M. Ehara, K. Toyota, R. Fukuda, J. Hasegawa, M. Ishida, T. Nakajima, Y. Honda, O. Kitao, H. Nakai, T. Vreven, K. Throssell, J. A. Montgomery Jr., J. E. Peralta, F. Ogliaro, M. J. Bearpark, J. J. Heyd, E. N. Brothers, K. N. Kudin, V. N. Staroverov, T. A. Keith, R. Kobayashi, J. Normand, K. Raghavachari, A. P. Rendell, J. C. Burant, S. S. Iyengar, J. Tomasi, M. Cossi, J. M. Millam, M. Klene, C. Adamo, R. Cammi, J. W. Ochterski, R. L. Martin, K. Morokuma, O. Farkas, J. B. Foresman, D. J. Fox, *Wallingford CT* **2016**.
- [66] J. P. Perdew, K. Burke, M. Ernzerhof, *Physical Review Letters* **1997**, *78*, 1396–1396.
- [67] C. Adamo, V. Barone, *The Journal of Chemical Physics* **1999**, *110*, 6158–6170.
- [68] D. Figgen, K. A. Peterson, M. Dolg, H. Stoll, *The Journal of Chemical Physics* **2009**, *130*, 164108.
- [69] F. Weigend, R. Ahlrichs, *Physical Chemistry Chemical Physics* **2005**, *7*, 3297–3305.
- [70] M. P. Klein, A. A. Ehrhard, J. Mohrbach, S. Dillinger, G. Niedner-Schatteburg, *Topics in Catalysis* **2018**, *61*, 106–118.

7.3 Supplementary Information

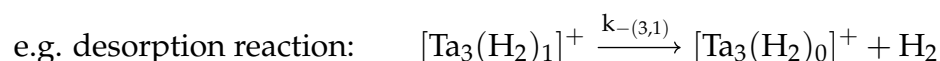
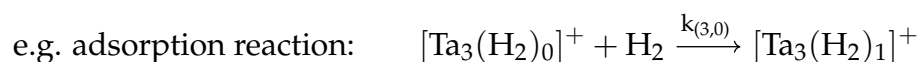
CRYO IR SPECTROSCOPY OF H₂ ADSORPTION TO TA₂₋₈⁺ CLUSTERS

Daniela V. FRIES, Annika STRAßNER, Matthias P. KLEIN, and Gereon
NIEDNER-SCHATTEBURG

Department of Chemistry and State Research Center OPTIMAS,
Rheinland-Pfälzische Technische Universität (RPTU) Kaiserslautern-Landau,
67663 Kaiserslautern, Germany

Text S1: Nomenclature for the Ta_n^+ cluster and their hydrogen adsorbates

The adsorption of H_2 onto Ta_n^+ cluster yield cluster adsorbate complexes whose typical chemical nomenclature is $[Ta_n(H_2)_m]^+$. In line with our prior studies on a series of transition metal clusters [1-9] we have again chosen an abridged (n,m) nomenclature for the cluster adsorbate complexes $[Ta_n(H_2)_m]^+$. In this nomenclature, n stands for the size of the cluster; e.g., n = 3 stands for a cluster of three tantalum atoms. The corresponding shortened notation for hydrogen adsorbates is (3,m), where m stands for the number of H_2 molecules adsorbed to the cluster. As Ta_3^+ adsorbs up to four H_2 molecules we observe four complexes (3,m) which are interlinked by four processes, respectively, in the form of adsorption and desorption reactions. Each of these processes is described by a relative rate constant, either $k_{(3,m)}$ for an adsorption reaction or $k_{-(3,m+1)}$ for a desorption reaction. In this case n = 3, the index m of the rate constants ranges from 0 to 3.



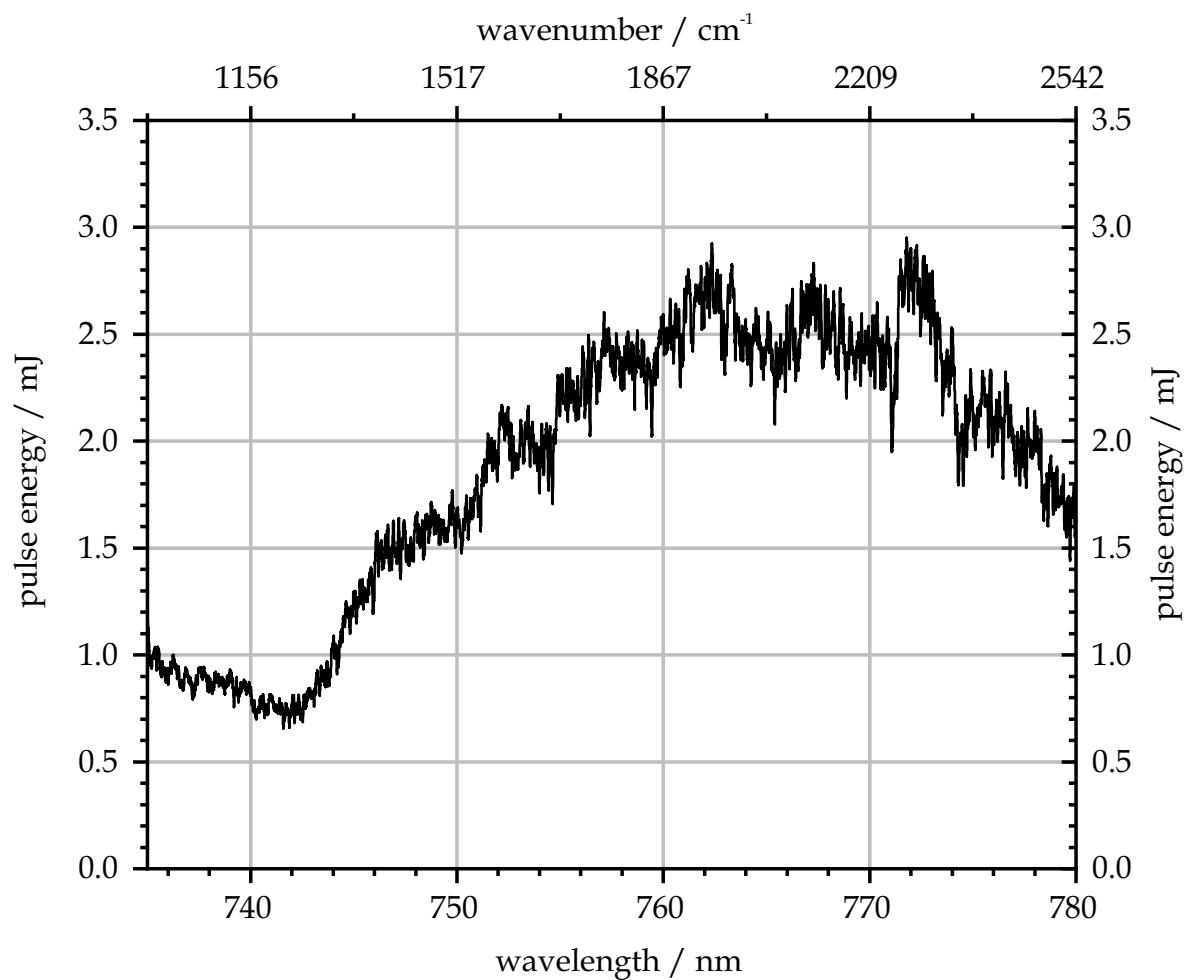


Figure S1: Laser pulse energy in dependency of wavelength and wavenumber.

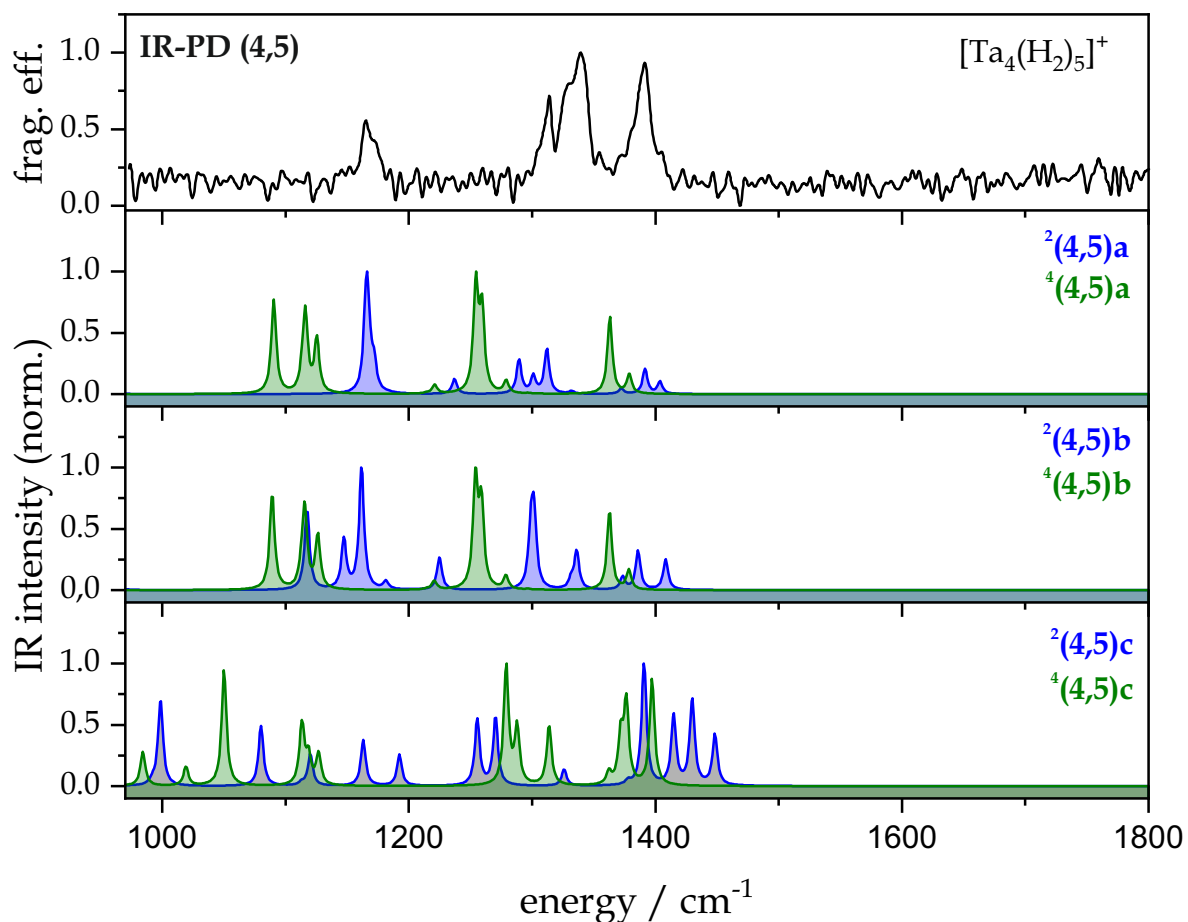


Figure S2: IR-PD spectra of $[\text{Ta}_4(\text{H}_2)_5]^+$ (simplified nomenclature: (4,5)) in the spectral range between 1000 and 1800 cm^{-1} . DFT modeled spectra of selected structural isomers in the doublet and quartet state, respectively. The predicted IR frequencies are scaled by a factor of 0.9434. For calculated energies and IR frequencies of all modeled isomers of (4,5), see Table S1.

Table S1: Calculated energies and IR frequencies (scaling factor 0.9434) of the cluster adsorption isomers (4,5) in the doublet and quartet state between 1000 and 2400 cm⁻¹. The minimum energy isomer is shown in bold. For graphical representation of the IR spectra, see Figure S2, for geometries and structures of the isomers see Table S2.

	$\tilde{\nu}_{\text{TaH}} / \text{cm}^{-1}$	$\tilde{\nu}_{\text{TaH}}^{\text{scaled}} / \text{cm}^{-1}$	energy E / Ha	$\Delta E / \text{kJ mol}^{-1}$
² (4,5)a	1016.11, 1235.26, 1242.06, 1311.19, 1366.70, 1379.00, 1390.67, 1412.04, 1454.62, 1475.08, 1487.90	958.60, 1165.345, 1171.76, 1236.97, 1289.34, 1300.95, 1311.96, 1332.12, 1372.29, 1391.59, 1403.69	-235.493572	0
⁴ (4,5)a	1155.86, 1180.42, 1183.02, 1192.86, 1287.14, 1294.20, 1329.63, 1334.89, 1355.70, 1374.48, 1444.85, 1461.51	1090.44, 1113.61, 1116.06, 1125.34, 1214.29, 1220.95, 1254.37, 1259.34, 1278.97, 1296.68, 1363.07, 1378.79	-235.476251	+48
² (4,5)b	1013.69, 1051.42, 1058.53, 1144.89, 1179.73, 1187.27, 1232.80, 1263.92, 1330.84, 1346.53, 1405.43, 1460.45, 1474.24, 1499.67, 1515.62, 1535.19	956.31, 991.91, 998.62, 1080.09, 1112.96, 1120.07, 1163.03, 1192.38, 1255.51, 1270.32, 1325.88, 1377.79, 1390.80, 1414.79, 1429.84, 1448.30	-235.490939	+10
⁴ (4,5)b	1014.41, 1043.28, 1080.29, 1113.16, 1179.12, 1180.32, 1185.78, 1194.38, 1355.72, 1365.06, 1392.60, 1444.08, 1454.16, 1458.96, 1481.12	957.00, 984.23, 1019.14, 1050.15, 1112.38, 1113.51, 1118.66, 1126.78, 1278.98, 1287.79, 1313.78, 1362.35, 1371.85, 1376.38, 1397.29	-235.474521	+53
² (4,5)c	1021.49, 1184.49, 1216.16, 1231.35, 1252.24, 1298.34, 1376.92, 1379.70, 1411.54, 1416.33, 1455.81, 1469.08, 1492.78	963.67, 1117.45, 1147.32, 1161.65, 1181.37, 1224.86, 1298.99, 1301.61, 1331.65, 1336.16, 1373.41, 1385.93, 1408.29	-235.493572	+3
⁴ (4,5)c	1154.48, 1179.12, 1182.43, 1193.71, 1286.77, 1293.91, 1329.32, 1334.47, 1355.49, 1374.18, 1444.53, 1461.15	1089.14, 1112.38, 1115.51, 1126.14, 1213.94, 1220.68, 1254.08, 1258.94, 1278.77, 1296.40, 1362.77, 1378.45	-235.476269	+48

Table S2: DFT optimized structures of cluster adsorption isomers (4,5) in the doublet and quartet state. The minimum energy isomer is indicated in bold. For calculated energies, IR frequencies and plots of the calculated IR spectra, see Table S1 and Figure S2.

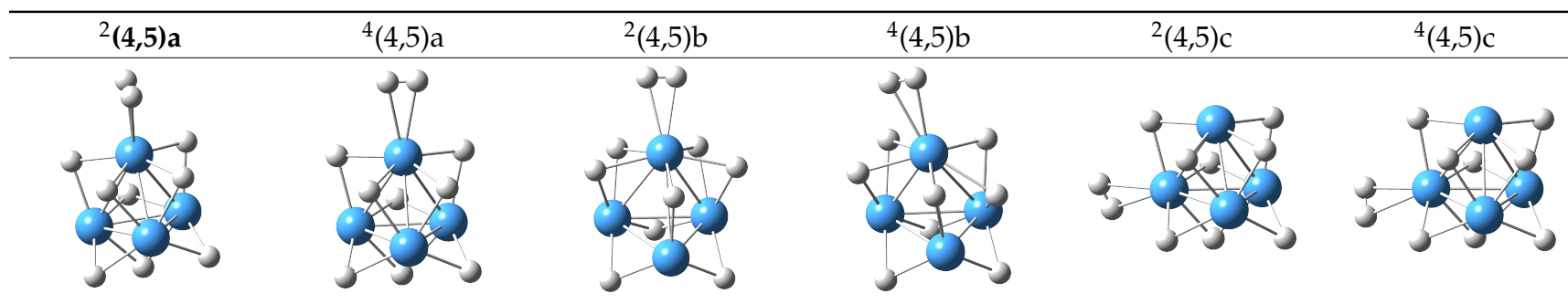
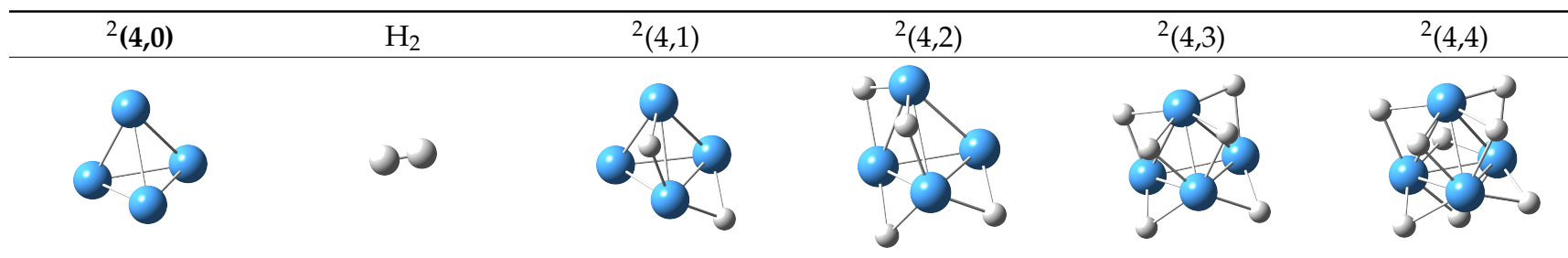


Table S3: DFT optimized structures of cluster adsorption isomers (4,m) in the doublet state. For calculated energies see Table S4.



7. Cryo IR Spectroscopy of H₂ Adsorption to Ta₂₋₈⁺ Clusters

Table S4: DFT optimized energies of cluster adsorption isomers (4,m) in the doublet state. ΔE are relative energies with respect to the free cluster adsorbate complex components. $\Delta\Delta E$ are relative energies for each adsorption step. For structures and graphical representation see Figure 4.

	energy E / Ha	ΔE / kJ mol ⁻¹	$\Delta\Delta E$ / kJ mol ⁻¹
² (4,0)	-229.438526	-	-
H ₂	-1.158150	-	-
<hr/>			
² (4,0) + H ₂	-230.596676	-	-
² (4,1)	-230.669995	-192.5	-192.5
² (4,2)	-231.894199	-365.9	-173.4
² (4,3)	-233.113487	-526.4	-160.5
² (4,4)	-234.326208	-669.7	-143.3
² (4,5)a	-235.494717	-696.9	-27.2

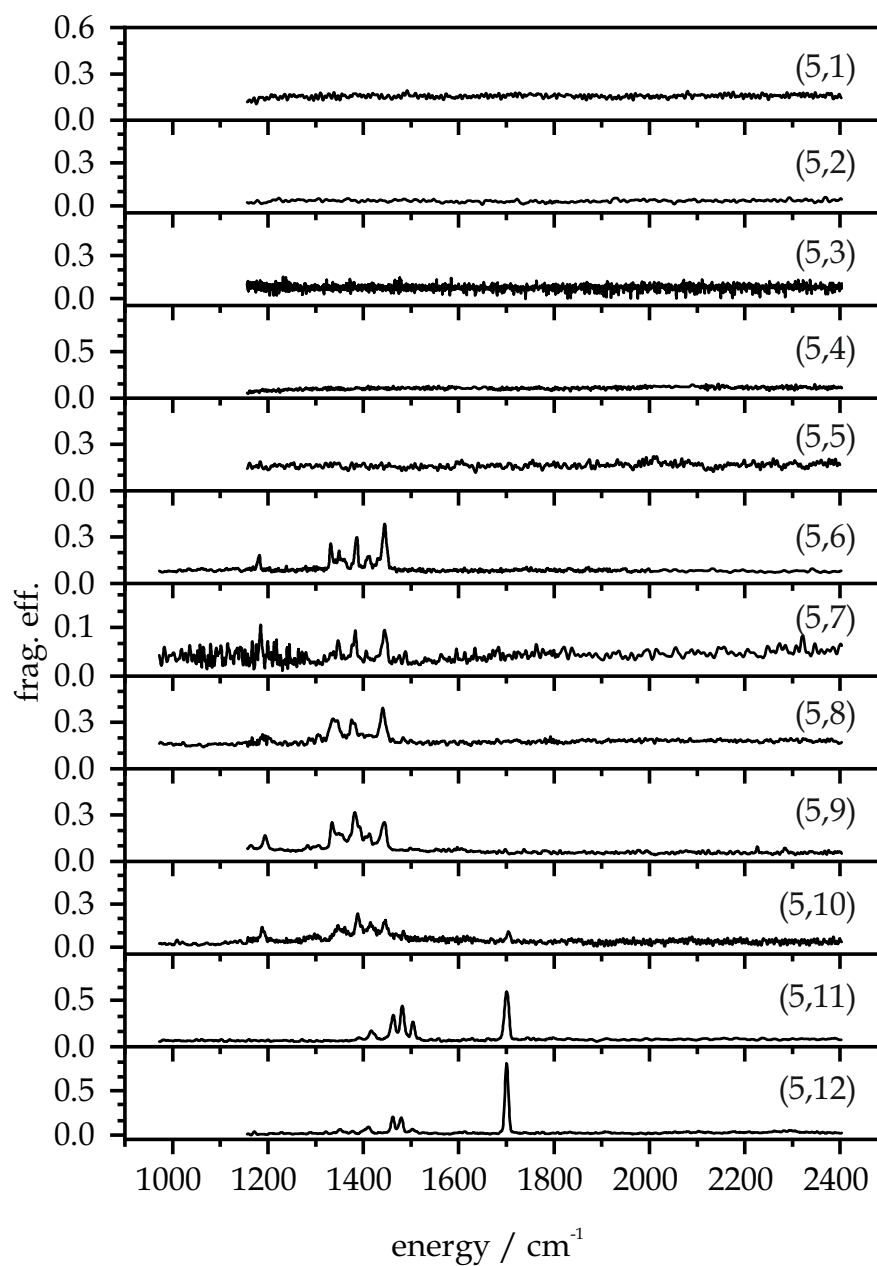


Figure S3: IR-PD spectra of sequential H₂ adsorption steps onto Ta₅⁺ cluster cations [Ta₅(N₂)_m]⁺, m = 1 – 13, as recorded after 18 K He buffer gas cooling.

Table S5: Calculated energies and IR frequencies (not scaled) of the cluster adsorption isomers (5,5) in the singlet and triplet state between 1000 and 2400 cm^{-1} . The isomer indicated in bold is chosen for further discussion. For graphical representation of the IR spectra, see Figure S4, for geometries and structures of the isomers see Table S6.

	$\tilde{\nu}_{\text{TaH}}$ cm^{-1}	energy E Ha	ΔE kJ mol^{-1}
$^1(5,5)\text{a}$	1020.68, 1050.09, 1123.04, 1158.33, 1159.78, 1194.01, 1236.35, 1276.92, 1293.76, 1383.61, 1397.91, 1429.28, 1445.76, 1470.19, 1472.43, 1515.77, 1573.29, 1621.30, 1661.18	-290.718726	0
$^3(5,5)\text{a}$	1002.26, 1094.04, 1119.64, 1177.88, 1183.60, 1222.96, 1268.11, 1292.49, 1314.72, 1355.33, 1386.97, 1398.37, 1431.79, 1438.49, 1450.84, 1460.71, 1467.49, 1490.71, 1533.60	-290.70432	+38
$^1(5,5)\text{b}$	1024.85, 1051.89, 1120.97, 1163.22, 1181.31, 1214.57, 1246.49, 1334.57, 1352.40, 1378.15, 1389.24, 1411.56, 1438.28, 1454.56, 1493.78, 1522.07, 1534.51, 1587.68	-290.701273	+46
$^3(5,5)\text{b}$	1006.27, 1084.96, 1116.99, 1162.93, 1184.69, 1203.83, 1258.15, 1299.18, 1341.03, 1347.84, 1367.43, 1380.28, 1398.84, 1417.07, 1424.15, 1428.59, 1455.41, 1477.27, 1499.98	-290.702285	+43
$^1(5,5)\text{c}$	1135.84, 1172.29, 1189.95, 1218.14, 1286.26, 1320.58, 1331.43, 1352.79, 1387.12, 1394.76, 1400.54, 1428.57, 1437.92, 1470.13, 1513.77, 1515.93, 1526.19	-290.715786	+8
$^3(5,5)\text{c}$	1005.65, 1084.96, 1117.30, 1163.12, 1184.72, 1203.82, 1256.96, 1298.63, 1340.50, 1347.27, 1367.52, 1379.81, 1398.78, 1418.05, 1424.39, 1429.18, 1455.67, 1477.17, 1500.18	-290.702287	+43
$^1(5,5)\text{d}$	1044.47, 1056.05, 1140.35, 1215.09, 1247.41, 1252.85, 1278.16, 1290.14, 1306.88, 1343.01, 1367.71, 1373.50, 1387.93, 1412.27, 1420.68, 1432.09, 1444.83, 1505.11	-290.6956153	+61
$^3(5,5)\text{d}$	1008.23, 1030.85, 1071.51, 1075.02, 1138.53, 1182.99, 1189.98, 1207.81, 1215.87, 1238.56, 1330.25, 1356.74, 1371.06, 1389.56, 1399.15, 1405.43, 1412.73, 1414.74, 1428.62, 1479.49	-290.691193	+72
$^1(5,5)\text{e}$	1040.69, 1074.44, 1084.42, 1089.03, 1108.19, 1120.70, 1187.97, 1194.58, 1199.20, 1287.42, 1336.53, 1367.80, 1400.05, 1428.67, 1453.53, 1463.58, 1490.74, 1497.45, 1504.99, 1532.62	-290.678177	+106
$^3(5,5)\text{e}$	1047.75, 1064.15, 1088.97, 1102.08, 1130.51, 1141.35, 1176.96, 1228.95, 1262.94, 1339.71, 1367.54, 1403.91, 1407.35, 1419.23, 1432.14, 1449.25, 1451.10, 1473.74, 1500.82	-290.678579	+105

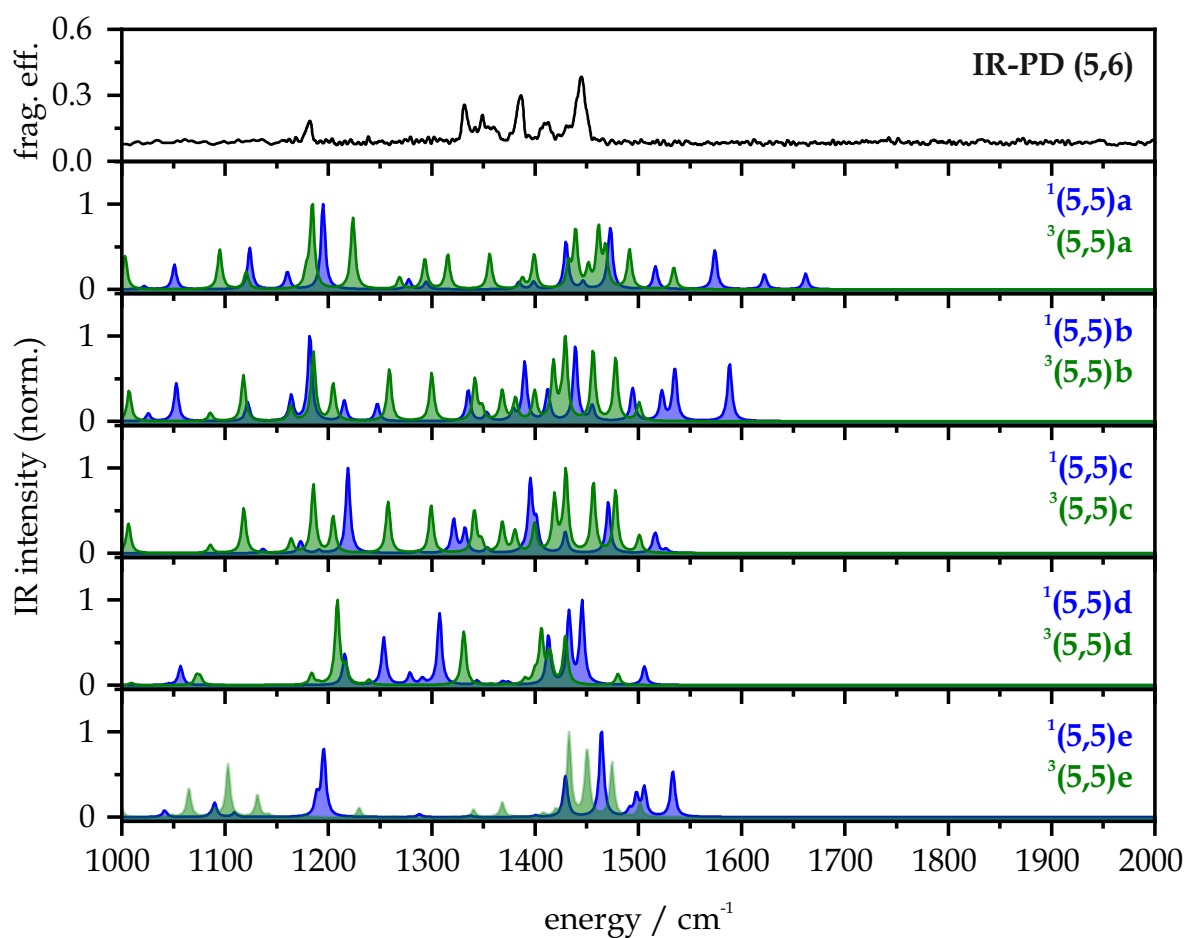


Figure S4: IR-PD spectra of $[\text{Ta}_5(\text{H}_2)_6]^+$ (simplified nomenclature: (5,6)) in the spectral range between 1000 and 2000 cm^{-1} . DFT modeled spectra of structural isomers (5,5) in the singlet and triplet state, respectively. The predicted IR frequencies are not scaled. For calculated energies and IR frequencies of all modeled isomers of (5,5), see Table S5.

7. Cryo IR Spectroscopy of H₂ Adsorption to Ta₂₋₈⁺ Clusters

Table S6: DFT optimized structures of cluster adsorption isomers (5,5) in the singlet and triplet state. The isomer indicated in bold is chosen for further discussion. For calculated energies, IR frequencies and a plot of calculated IR spectra, see Table S5 and Figure S4.

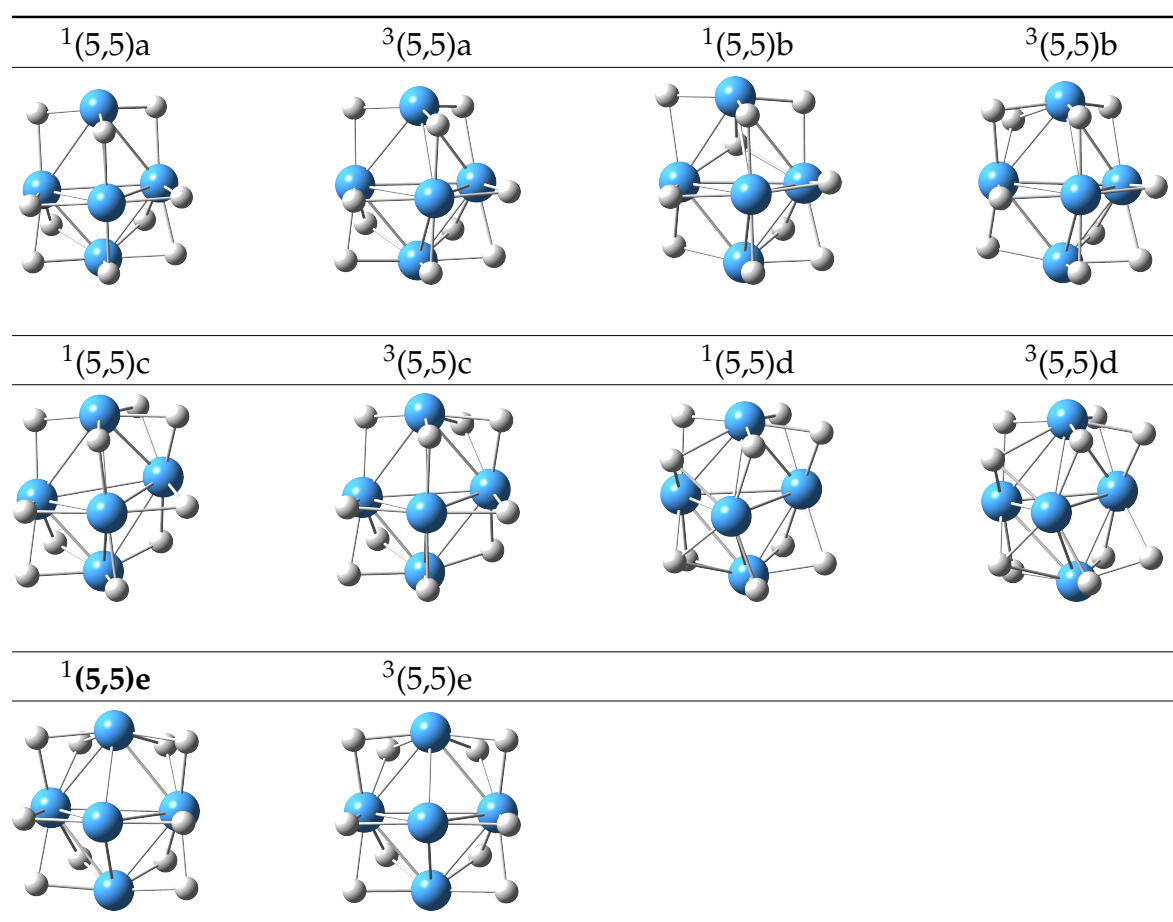


Table S7: Calculated energies and IR frequencies (not scaled) of the cluster adsorption isomers (5,6) in the singlet and triplet state between 1000 and 2400 cm^{-1} . The isomer indicated in bold is chosen for further discussion. For a plot of calculated IR spectra, see Figure S5, for geometries and structures of the isomers see Table S8.

	$\tilde{\nu}_{\text{TaH}}$ cm^{-1}	energy E Ha	ΔE kJ mol^{-1}
$^1(5,6)\text{a}$	1006.47, 1029.90, 1064.46, 1091.22, 1112.52, 1158.67, 1165.71, 1177.88, 1201.84, 1311.66, 1404.19, 1429.11, 1445.01, 1459.38, 1482.95, 1502.47, 1519.67, 1538.46, 1564.74, 1579.48, 1595.74	-291.853692	0
$^3(5,6)\text{a}$	1066.13, 1071.12, 1087.12, 1099.79, 1125.12, 1136.73, 1193.82, 1206.36, 1229.00, 1272.89, 1339.18, 1370.42, 1406.73, 1419.04, 1422.32, 1464.98, 1468.64, 1483.23, 1508.24, 1525.03	-291.847925	+15
$^1(5,6)\text{b}$	1034.75, 1074.51, 1077.17, 1112.78, 1122.64, 1130.15, 1145.43, 1189.35, 1192.37, 1199.37, 1292.33, 1345.10, 1365.13, 1409.53, 1428.40, 1453.82, 1465.32, 1493.73, 1504.65, 1512.28, 1532.21	-291.849492	+11
$^3(5,6)\text{b}$	1006.31, 1053.33, 1075.98, 1097.90, 1113.12, 1145.46, 1167.87, 1187.76, 1196.96, 1226.07, 1261.72, 1348.64, 1358.87, 1395.87, 1403.73, 1420.79, 1439.90, 1441.41, 1459.05, 1490.92, 1499.09	-291.84952	+11
$^1(5,6)\text{c}$	1057.28, 1079.53, 1085.73, 1105.83, 1113.37, 1139.16, 1212.018, 1218.48, 1238.57, 1310.98, 1328.20, 1370.07, 1391.26, 1427.72, 1445.19, 1454.05, 1474.50, 1485.51, 1506.39, 1532.97	-291.843803	+26
$^3(5,6)\text{c}$	1049.26, 1099.14, 1117.78, 1156.93, 1162.21, 1184.83, 1205.35, 1225.64, 1231.29, 1303.16, 1337.17, 1340.52, 1388.19, 1397.92, 1409.19, 1457.34, 1462.50, 1473.66, 1504.53, 1514.56	-291.84473	+26

7. Cryo IR Spectroscopy of H₂ Adsorption to Ta₂₋₈⁺ Clusters

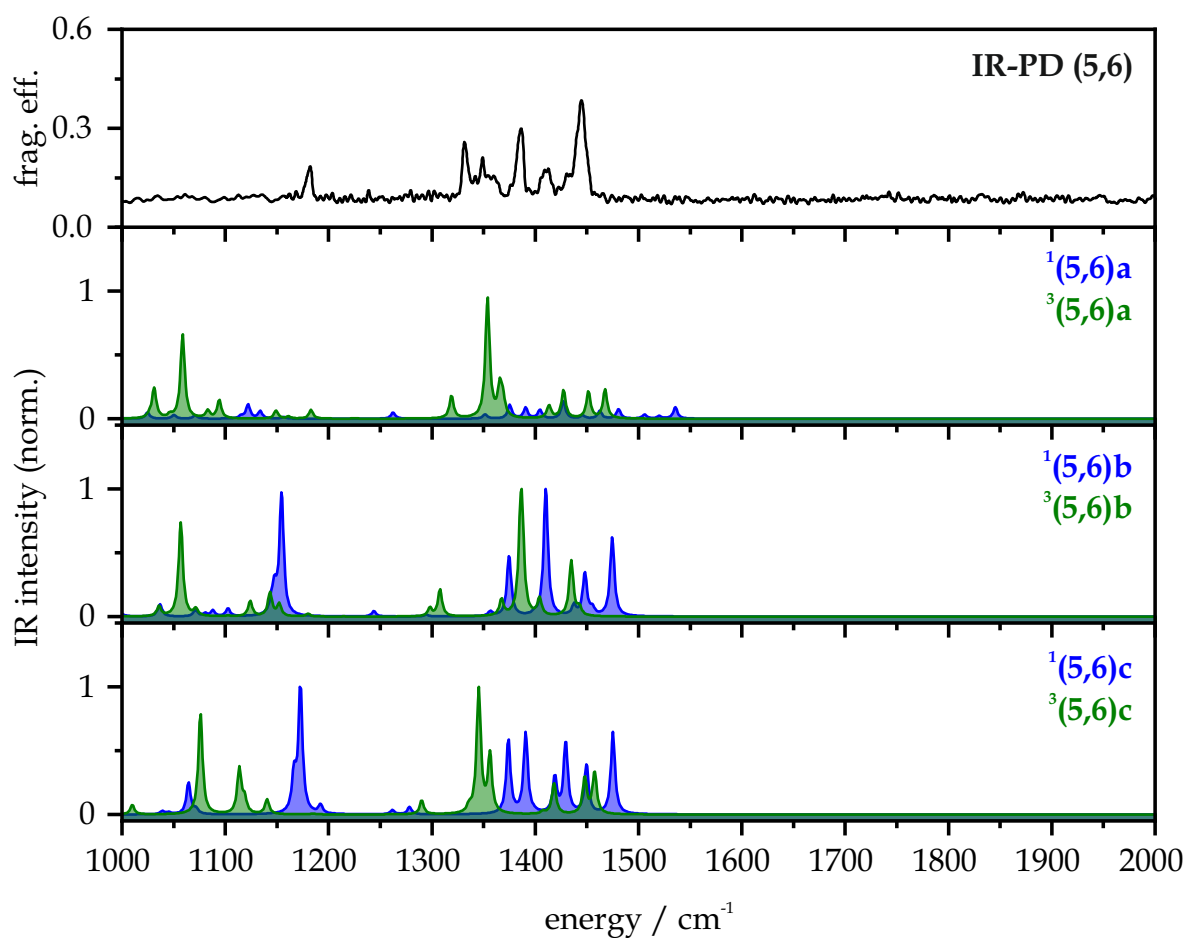


Figure S5: IR-PD spectra of [Ta₅(H₂)₆]⁺ (simplified nomenclature: (5,6)) in the spectral range between 1000 and 2000 cm⁻¹. DFT modeled spectra of structural isomers (5,6) in the singlet and triplet state, respectively. The predicted IR frequencies are scaled by a factor of 0.9619. For calculated energies and IR frequencies of all modeled isomers of (5,6), see Table S7.

Table S8: DFT optimized structures of cluster adsorption isomers (5,6) in the singlet and triplet state. The isomer indicated in bold is chosen for further discussion. For calculated energies, IR frequencies and a plot of calculated IR spectra, see Table S7 and Figure S5.

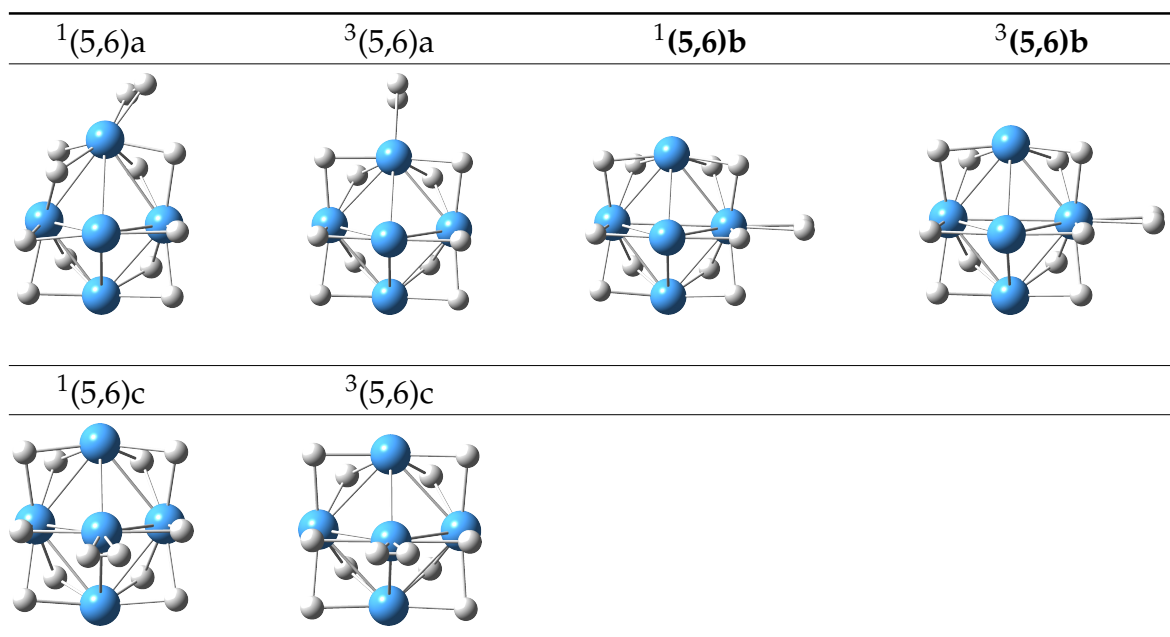


Table S9: Calculated energies and IR frequencies (not scaled) of the cluster adsorption isomers (5,7) in the singlet and triplet state (abbreviated nomenclature e.g. ¹a stands for ¹(5,7)a) between 1000 and 2400 cm⁻¹. The isomers indicated in bold are chosen for further discussion. For a plot of calculated IR spectra, see Figure S6, for geometries and structures of the isomers see Table S10.

	$\tilde{\nu}_{\text{TaH}}$ cm ⁻¹	energy E Ha	ΔE kJ mol ⁻¹
¹ a	1048.77, 1067.88, 1076.32, 1123.89, 1133.89, 1139.15, 1143.06, 1210.41, 1217.90, 1218.62, 1310.94, 1337.64, 1366.74, 1401.35, 1427.35, 1448.80, 1455.04, 1479.96, 1490.55, 1505.34, 1530.44	-293.014827	+30
³ a	1039.36, 1058.35, 1089.89, 1104.37, 1120.49, 1143.18, 1170.05, 1185.49, 1198.87, 1219.22, 1265.51, 1347.41, 1353.59, 1394.30, 1402.17, 1415.02, 1426.75, 1441.12, 1444.95, 1469.14, 1492.84	-293.015854	+27
¹b	1046.99, 1091.32, 1101.23, 1106.73, 1128.17, 1129.36, 1130.99, 1131.80, 1192.34, 1196.23, 1201.64, 1296.00, 1353.80, 1362.45, 1415.45, 1426.40, 1451.19, 1467.74, 1502.13, 1511.91, 1513.43, 1532.957	-293.020328	+16
³b	1018.21, 1052.51, 1072.13, 1098.27, 1121.13, 1139.90, 1146.18, 1168.25, 1211.54, 1219.97, 1239.30, 1269.66, 1348.79, 1357.52, 1394.09, 1401.78, 1421.80, 1439.33, 1440.35, 1482.51, 1487.72, 1510.22	-293.020394	+16
¹ c	1030.17, 1121.87, 1136.76, 1156.21, 1162.48, 1175.07, 1193.51, 1203.30, 1210.35, 1222.69, 1315.83, 1354.91, 1369.70, 1391.39, 1422.01, 1447.33, 1474.13, 1498.95, 1503.58, 1519.40, 1534.66, 1727.48	-293.024865	+3
³ c	1047.01, 1072.73, 1088.27, 1112.60, 1152.29, 1181.70, 1214.07, 1219.98, 1266.96, 1283.74, 1317.96, 1338.04, 1377.99, 1397.48, 1413.16, 1423.60, 1432.56, 1457.73, 1464.37, 1489.21, 1507.18, 1641.38	-293.026413	0
¹ d	1029.98, 1045.47, 1053.45, 1082.32, 1125.21, 1144.69, 1185.97, 1240.18, 1302.43, 1398.17, 1413.42, 1429.02, 1432.60, 1444.04, 1480.80, 1493.23, 1503.44, 1520.58, 1538.50, 1579.03, 1620.25	-293.02527	+3
³ d	1032.11, 1067.62, 1071.86, 1107.48, 1122.42, 1140.69, 1175.00, 1187.57, 1227.74, 1271.83, 1339.80, 1360.96, 1405.71, 1409.57, 1413.67, 1421.99, 1448.55, 1458.24, 1462.26, 1502.56	-293.012863	+36

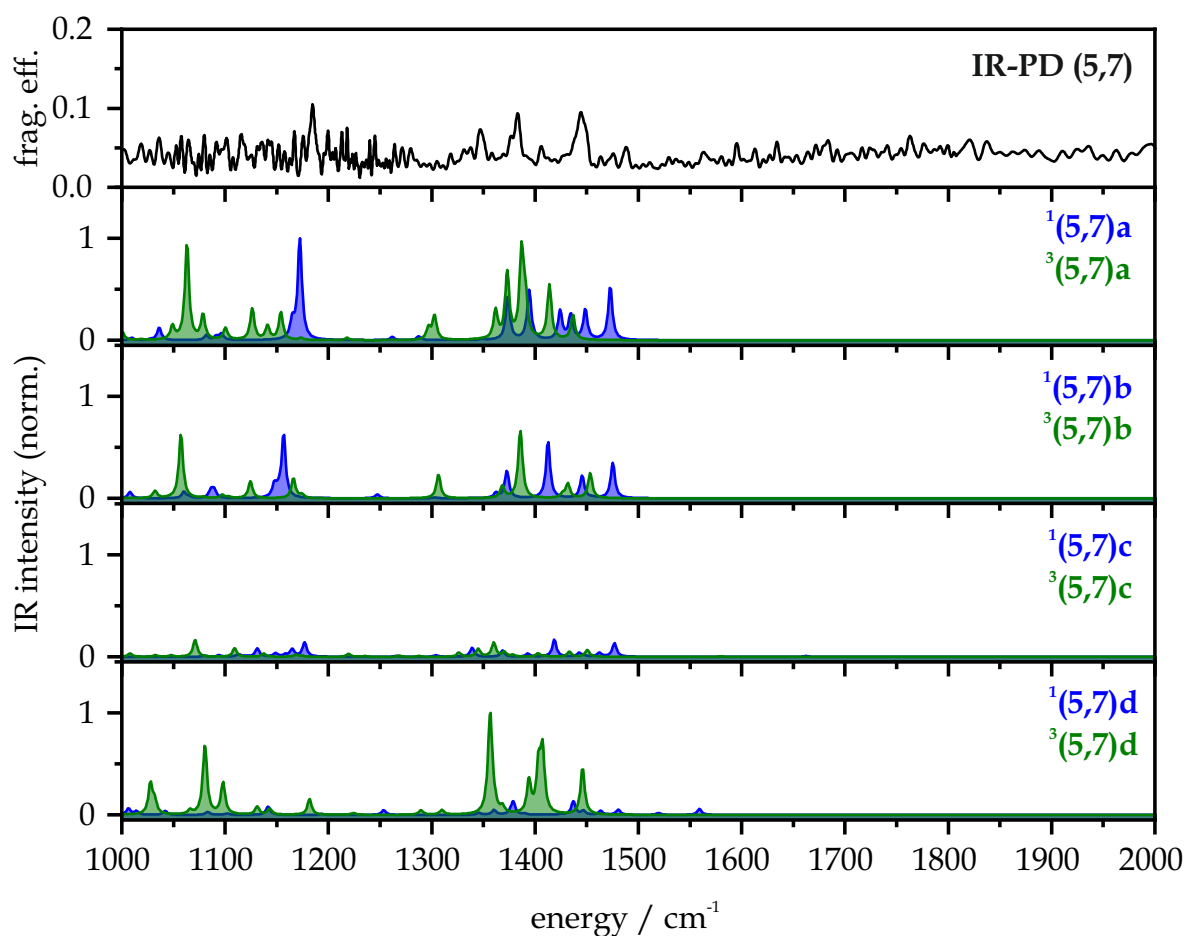


Figure S6: IR-PD spectra of $[\text{Ta}_5(\text{H}_2)_7]^+$ (simplified nomenclature: (5,7)) in the spectral range between 1000 and 2000 cm^{-1} . DFT modeled spectra of structural isomers (5,7) in the singlet and triplet state, respectively. The predicted IR frequencies are scaled by a factor of 0.9619. For calculated energies and IR frequencies of all modeled isomers of (5,7), see Table S9.

7. Cryo IR Spectroscopy of H₂ Adsorption to Ta₂₋₈⁺ Clusters

Table S10: DFT optimized structures of cluster adsorption isomers (5,7) in the singlet and triplet state. The isomers indicated in bold are chosen for further discussion. For calculated energies, IR frequencies and a plot of calculated IR spectra, see Table S9 and Figure S6.

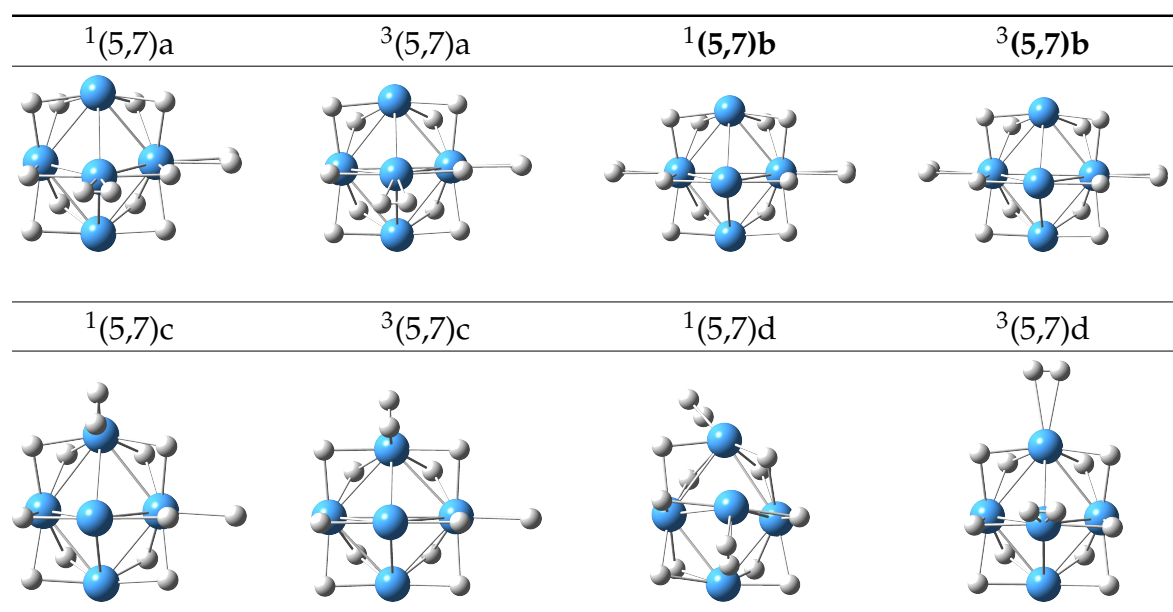


Table S11: Calculated energies and IR frequencies (not scaled) of the cluster adsorption isomers (5,8) in the singlet and triplet state (e.g. ¹a stands for ¹(5,8)a) between 1000 and 2400 cm⁻¹. The isomers indicated in bold are chosen for further discussion. For a plot of calculated IR spectra, see Figure S7, for geometries and structures of the isomers see Table S12.

	$\tilde{\nu}_{\text{TaH}}$ cm ⁻¹	energy E Ha	ΔE kJ mol ⁻¹
¹ a	1079.48, 1096.01, 1108.77, 1111.32, 1114.93, 1115.85, 1131.45, 1144.96, 1209.08, 1218.45, 1236.41, 1311.28, 1349.13, 1363.90, 1411.37, 1425.63, 1449.96, 1461.49, 1491.43, 1495.03, 1500.77, 1526.46	-294.185279	+30
³ a	1046.45, 1058.78, 1088.00, 1103.92, 1119.99, 1120.14, 1131.65, 1185.33, 1199.63, 1209.69, 1232.36, 1269.08, 1346.48, 1354.62, 1391.28, 1398.29, 1418.85, 1436.06, 1439.45, 1452.13, 1478.88, 1486.93	-294.186408	+27
³ b	1014.05, 1041.67, 1060.45, 1106.62, 1117.07, 1130.96, 1154.34, 1173.48, 1185.23, 1195.02, 1211.94, 1260.71, 1344.38, 1349.81, 1394.00, 1412.17, 1416.39, 1429.48, 1447.23, 1457.16, 1475.90, 1495.57	-294.183863	+34
¹ c	1048.39, 1060.12, 1107.51, 1123.29, 1149.57, 1156.25, 1159.19, 1234.98, 1249.53, 1272.06, 1291.64, 1321.01, 1332.13, 1377.61, 1378.59, 1399.25, 1414.27, 1441.28, 1456.31, 1483.76, 1551.13, 1599.78	-294.181479	+40
³ c	1052.35, 1064.53, 1085.64, 1114.27, 1152.45, 1174.23, 1197.15, 1226.22, 1252.78, 1270.38, 1321.90, 1337.39, 1364.91, 1389.68, 1400.92, 1410.73, 1421.85, 1447.08, 1460.90, 1483.60, 1501.84, 1659.95	-294.192575	+11
¹ d	1044.86, 1124.42, 1153.32, 1163.71, 1164.16, 1178.51, 1190.71, 1196.64, 1204.19, 1214.70, 1225.11, 1319.29, 1358.53, 1370.68, 1388.41, 1429.41, 1444.10, 1473.68, 1494.37, 1516.45, 1525.75, 1544.54, 1742.60	-294.196742	0
³ d	1011.66, 1035.16, 1064.34, 1087.05, 1114.61, 1134.69, 1147.41, 1153.28, 1167.78, 1185.75, 1192.09, 1229.64, 1271.48, 1355.61, 1369.96, 1393.49, 1400.11, 1417.13, 1427.67, 1451.33, 1485.91, 1487.43, 1511.85	-294.191489	+14

7. Cryo IR Spectroscopy of H₂ Adsorption to Ta₂₋₈⁺ Clusters

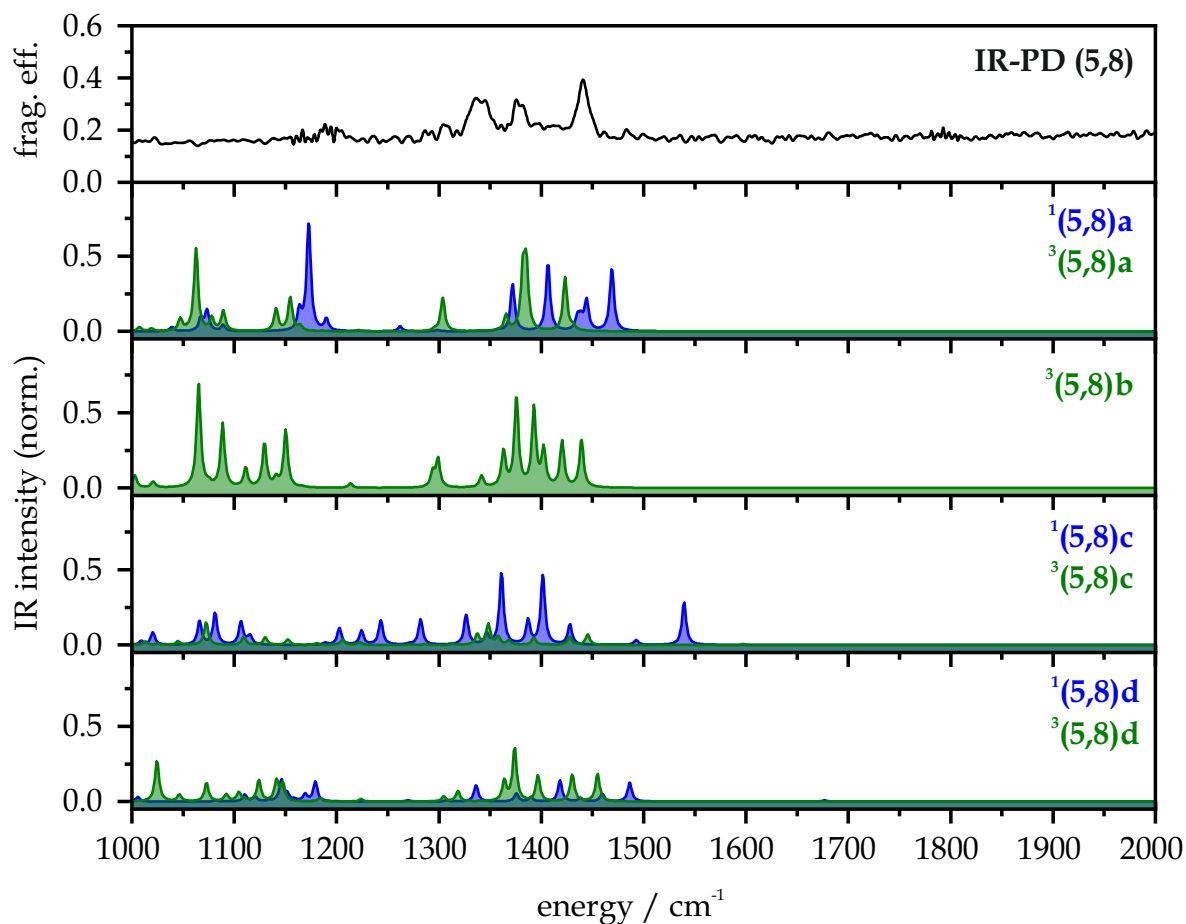


Figure S7: IR-PD spectra of [Ta₅(H₂)₈]⁺ (simplified nomenclature: (5,8)) in the spectral range between 1000 and 2000 cm⁻¹. DFT modeled spectra of structural isomers (5,8) in the singlet and triplet state, respectively. The predicted IR frequencies are scaled by a factor of 0.9619. For calculated energies and IR frequencies of all modeled isomers of (5,8), see Table S11.

Table S12: DFT optimized structures of cluster adsorption isomers (5,8) in the singlet and triplet state. The isomers indicated in bold are chosen for further discussion. For calculated energies, IR frequencies and a plot of calculated IR spectra, see Table S11 and Figure S7.

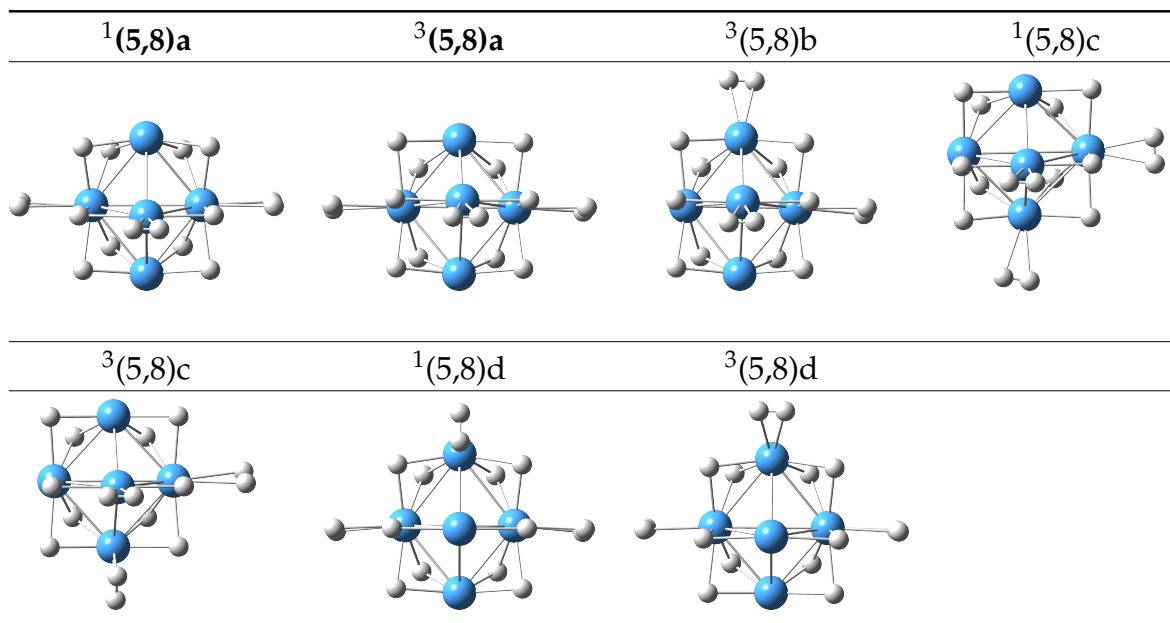


Table S13: Calculated energies and IR frequencies (not scaled) of the cluster adsorption species (5,12) in the singlet and triplet state between 1000 and 2400 cm^{-1} . The spin state species indicated in bold are chosen for further discussion. For a plot of calculated IR spectra, see Figure S8, for geometries and structures of the isomers see Table S14.

	$\tilde{\nu}_{\text{TaH}}$ cm^{-1}	energy E Ha	ΔE kJ mol^{-1}
$^1(5,12)$	1056.86, 1079.93, 1093.54, 1151.14, 1173.12, 1186.44, 1201.86, 1233.27, 1244.17, 1255.24, 1292.85, 1306.12, 1316.27, 1322.75, 1345.64, 1365.60, 1395.01, 1403.87, 1438.18, 1440.69, 1465.80, 1473.15, 1479.55, 1522.50, 1535.91, 1548.26, 1596.69, 1749.24, 1751.36	-298.909869	+7
$^3(5,12)$	1002.54, 1066.02, 1081.93, 1083.21, 1132.89, 1146.12, 1177.44, 1208.00, 1276.97, 1304.60, 1322.69, 1328.71, 1350.11, 1350.43, 1366.24, 1370.68, 1387.84, 1398.04, 1401.18, 1412.22, 1427.72, 1444.54, 1481.76, 1489.38, 1526.05, 1530.03, 1566.70, 1582.75, 1766.71, 1769.39	-298.912626	0

7. Cryo IR Spectroscopy of H_2 Adsorption to Ta_2-8^+ Clusters

Table S14: DFT optimized structures of cluster adsorption isomer (5,12) in the singlet and triplet state. For calculated energies, IR frequencies and graphical representation of those, see Table S13 and Figure S8.

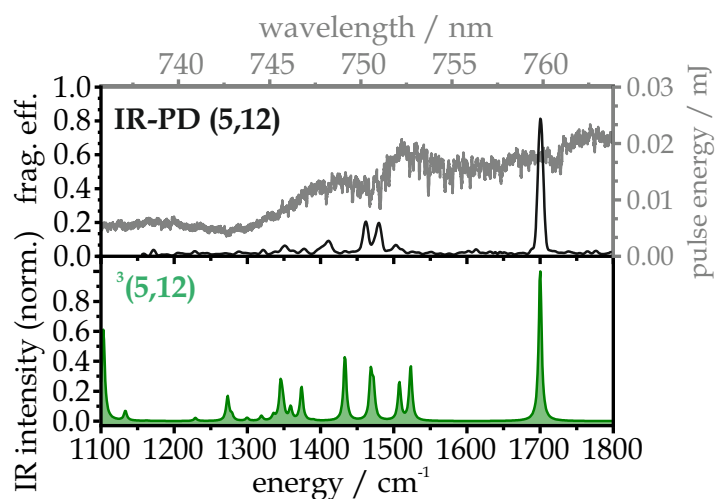
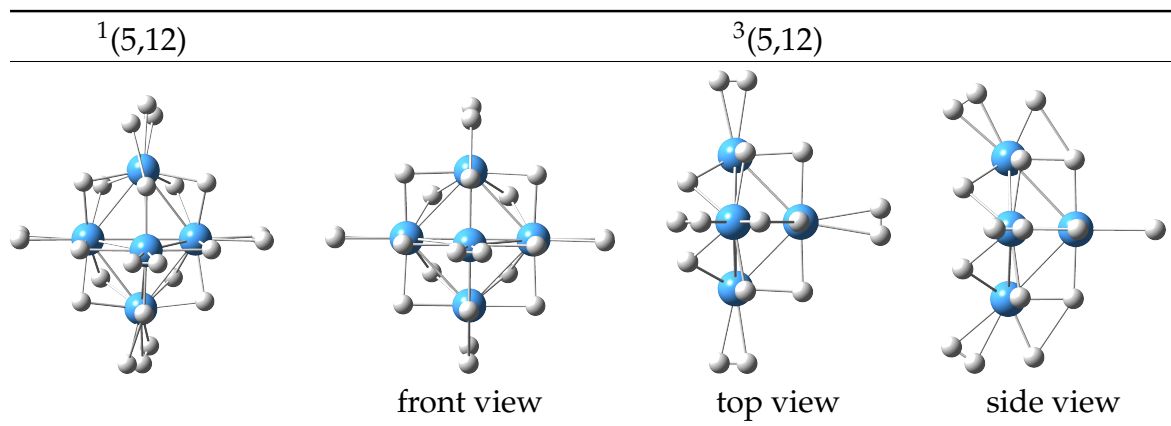


Figure S8: IR-PD spectra of $[Ta_5(H_2)_{12}]^+$ (simplified nomenclature: (5,12)) in the spectral range between 1100 and 1800 cm^{-1} . Laser pulse energy in dependency of wavelength and wavenumber for the IR-PD measurements of (5,12) is shown in grey. DFT modeled spectrum of structural isomers (5,12) in the triplet state. The predicted IR frequencies are scaled by a factor of 0.9619. For calculated energies and IR frequencies of the modeled isomer, see Table S13.

Table S15: DFT optimized energies of cluster adsorption isomers (5,m) in the triplet state. ΔE are relative energies with respect to the free cluster adsorbate complex components. $\Delta\Delta E$ are relative energies for each adsorption step. For structures and graphical representation see Figure 8.

	energy E / Ha	$\Delta E / \text{kJ mol}^{-1}$	$\Delta\Delta E / \text{kJ mol}^{-1}$
$^3(5,0)$	-284.638231	-	-
H_2	-1.158150	-	-
$^3(5,0) + \text{H}_2$	-285.796381	-	-
$^3(5,5)\text{e}$	-290.684135	-654.3	-654.3
$^3(5,6)\text{b}$	-291.849520	-688.9	-34.6
$^3(5,7)\text{b}$	-293.020394	-722.4	-33.4
$^3(5,8)\text{a}$	-294.186408	-743.0	-20.6
$^3(5,12)$	-298.912626	-988.8	-245.8

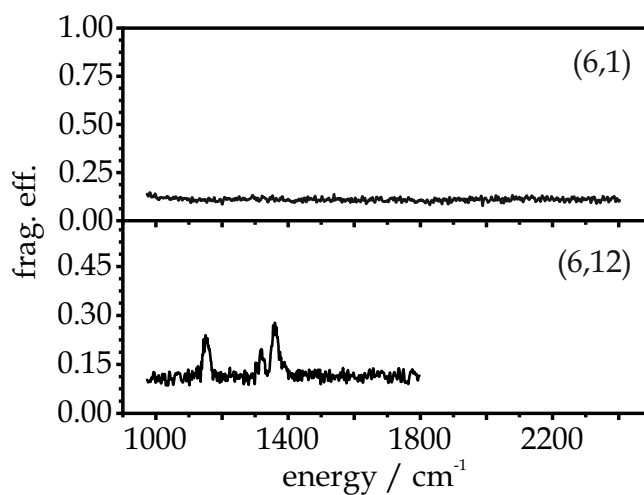


Figure S9: IR-PD spectra of H_2 adsorption steps onto Ta_6^+ cluster cations $[\text{Ta}_6(\text{N}_2)_m]^+$, $m = 1$ and $m = 12$, as recorded after 18 K He buffer gas cooling.

References

- [1] D. V. Fries, M. P. Klein, A. Steiner, M. H. Prosenc, G. Niedner-Schatteburg, *Physical Chemistry Chemical Physics* **2021**, 23, 11345–11354.
- [2] D. V. Fries, M. P. Klein, A. Straßner, M. E. Huber, M. Luczak, C. Wiehn, G. Niedner-Schatteburg, *The Journal of Chemical Physics* **2023**, 159, 164303.
- [3] D. V. Fries, M. P. Klein, A. Straßner, M. E. Huber, G. Niedner-Schatteburg, *The Journal of Chemical Physics* **2023**, 159, 164306.
- [4] J. Mohrbach, S. Dillinger, G. Niedner-Schatteburg, *The Journal of Physical Chemistry C* **2017**, 121, 10907–10918.
- [5] S. Dillinger, J. Mohrbach, G. Niedner-Schatteburg, *The Journal of Chemical Physics* **2017**, 147, 184305.
- [6] A. Straßner, C. Wiehn, M. P. Klein, D. V. Fries, S. Dillinger, J. Mohrbach, M. H. Prosenc, P. B. Armentrout, G. Niedner-Schatteburg, *The Journal of Chemical Physics* **2021**, 155, 244305.
- [7] S. Dillinger, J. Mohrbach, J. Hewer, M. Gaffga, G. Niedner-Schatteburg, *Physical Chemistry Chemical Physics* **2015**, 17, 10358–10362.
- [8] S. Dillinger, M. P. Klein, A. Steiner, D. C. McDonald, M. A. Duncan, M. M. Kappes, G. Niedner-Schatteburg, *The Journal of Physical Chemistry Letters* **2018**, 9, 914–918.
- [9] M. P. Klein, A. A. Ehrhard, J. Mohrbach, S. Dillinger, G. Niedner-Schatteburg, *Topics in Catalysis* **2018**, 61, 106–118

8 SIZE DEPENDENCE OF N₂ ADSORPTION ONTO TA₄-10⁻ CLUSTER ANIONS

Daniela V. FRIES, Maximilian LUCZAK, Christopher WIEHN, and Gereon
NIEDNER-SCHATTEBURG

Department of Chemistry and State Research Center OPTIMAS,
Rheinland-Pfälzische Technische Universität (RPTU) Kaiserslautern-Landau,
67663 Kaiserslautern, Germany

8.1 Preamble

The experiments were performed by myself. For a few measurements I was supported by my colleagues M. Luczak and C. Wiehn. The evaluation of the measured data was carried out by me, and it was accompanied by discussions with G. Niedner-Schatteburg. I wrote the manuscript.

8.2 Paper draft

8.2.1 Abstract

Herein, we present our findings for the adsorption of N₂ on small tantalum cluster anions Ta_n⁻, n = 4-10, under cryogenic conditions using a Fourier Transform Ion Cyclotron Resonance (FT-ICR) mass spectrometer. The cluster size n = 9 proved to be the minimum size for N₂ adsorption and stabilization of the resulting cluster adsorbate complexes [Ta_n(N₂)_m]⁻. The adsorption of N₂ onto smaller anionic clusters and the stabilization of the resulting cluster adsorbate complexes [Ta₄₋₈(N₂)_m]⁻ does not seem possible. Thus, this work shows that the ability of anionic tantalum clusters to absorb and stabilize N₂ depends strongly on the cluster size n.

8.2.2 Introduction

The potential of cluster chemistry for modeling chemisorption and catalytic processes on surfaces was recognized early on. [1] Numerous reviews summarize the respective current state of research on gas phase transition metal (TM) clusters reacting with small molecules and provide insights into elementary catalytic processes at the molecular level. [2-7] All of these publications emphasize the strong size dependence of the reactivity of the metal clusters. Their charge is also of interest for reactivity of the TM clusters.

Nitric oxide decomposition studies of anionic and cationic rhodium clusters reveal that cations react significantly faster than the corresponding anions. [8] While for the reaction of Nb anions with CO the relative rates show qualitatively similar behavior as reported for cations, the reaction with nitrogen shows stronger differences in the rates for different cluster sizes. [9] A detailed study of the chemisorption and oxidation reactions of nickel group cluster anions with various small molecules shows a strong dependence of the reactivity on the elemental composition of the clusters. Nevertheless, the authors can conclude a rough trend for the reactivity of the cluster anions: especially N₂ reactions are generally reported to have a very low reaction efficiency. [10] Another publication makes the effect of charge upon CO adsorption onto group 5 and group 9 transition metal cluster cations and anions a subject of discussion. The most striking anomaly noted by the authors is the behavior of the anionic group 5 clusters, which exhibit a significantly shifted threshold of

reactivity to larger cluster sizes compared to the cationic group 5 and cationic and anionic group 9 clusters. Finally, anions and cations of large clusters comprising 17 or 18 metal atoms show very similar reactivity. [11]

Furthermore, there are several studies on the reaction of homo- and heteronuclear metal clusters as carbides with nitrogen. The C_n ligands of the tantalum carbide clusters are capable of modifying the natural charge, electron configuration, composition, and relative orientation of orbitals of the Ta atom, thereby controlling the reactivity of TaC_n^- , $n = 1-4$, towards N_2 . [12] The heteronuclear metal cluster anions $FeTaC_2^-$ and $CoTaC_2^-$ reveal the ability to cleave the N_2 triple bond. Once more, carbon plays an important role within these systems as it stabilizes critical cluster units or polarizes the cluster itself to enable the N_2 adsorption and activation. Moreover, these metal carbide clusters offer the opportunity of subsequent C-N bond formation. [13, 14]

The anionic tantalum nitride cluster $Ta_3N_2^-$ is able to efficiently dehydrogenate an ethene molecule, forming two H_2 molecules and a $Ta_3N_2C_2^-$ cluster, which in turn is also reactive towards ethene and releases another H_2 molecule. [15] PES experiments and theoretical calculations show that $Ta_3N_3H_{0-1}^-$ can adsorb and cleave nitrogen. The reactivity of $Ta_3N_3H^-$ proved to be significantly higher than that of the dehydrated $Ta_3N_3^-$ clusters. The presence of the hydrogen atom does not directly affect the reaction process, but changes the charge distribution and geometry of $Ta_3N_3H^-$, thus increasing the reactivity of the cluster. [16] $^{15}N/^{14}N$ isotope exchange experiments and DFT modeling of dissociative adsorption of N_2 on tantalum nitride cluster anions $Ta_3N_3^-$ demonstrate that preferential sites such as nitrogen vacancies are required for the activation of N_2 on nitride surfaces at the molecular level. [17] Computational investigations predict a thermodynamically accessible stepwise cleavage of the triple bond of two N_2 molecules by Ta_3^- clusters. [18] A study of gas-phase reactions of Ta_n^- , $n = 5-27$, with nitrogen in a Re-TOF-MS-VMI instrument shows that N_2 adsorbate products appear only from $n \geq 14$. Ta_{10}^- clusters react slowly with N_2 . Quantumchemical calculations reveal that well-organized superatomic orbitals pertain the origin of this unique Ta_{10}^- cluster stability. [19]

Following numerous studies on N₂ adsorption on cationic TM clusters [20–26] we present here our cryogenic mass spectrometric experiments on Ta_n⁻ cluster anions, n = 4–10, in which we investigate their ability to react with N₂. This complements our previous studies on Ta_n⁺ with N₂. [27–29] Here, we show that the ability of anionic Ta_n⁻ clusters to adsorb N₂ depends strongly on the cluster size n, and we discuss the differences with the adsorption of N₂ onto cationic Ta_n⁺ clusters.

8.2.3 Experimental and Computational Methods

The experimental data was recorded using a customized Fourier Transform Ion Cyclotron Resonance Mass Spectrometer (FT-ICR MS, *Apex Ultra*, Bruker Daltonics). This instrument is equipped with a home built laser vaporization (LVAP) [30, 31] source which was used for cluster generation. The second harmonic of a pulsed Nd:YAG (Innolas Spitlight 300, 20 Hz) evaporates the metal atoms from a rotating Ta-target (99,95 %, 0.5 mm thick, Alfa Aesar) generating a hot plasma which consists of atoms and ions. A He gas pulse (40 μs, 15 bar) from a home built piezoelectric valve [32] captures the hot plasma and entrains it through an ion channel (69 mm long, 2 mm diameter). During this jet expansion into vacuum (10⁻⁷ mbar) the atoms and ions in the plasma cool down and aggregate into cluster ions. A variation of the source parameters (backing pressure, laser-valve-delay, valve opening time, source voltage) affects the generated intensity maximum of the cluster size distribution. The cluster ions are guided by electrostatic lenses through a 90° ion bender. Next, the cluster size distribution passes a quadrupole mass filter for mass selection before the ions of the selected cluster size are introduced into a cryogenic hexapole ion trap. A closed-cycle He cryostat cools the hexapole to 26 K. Therein, we are able to continuously introduce buffer and/or reaction gas. We used He (up to 6.8 × 10⁻⁶ mbar) as buffer gas and N₂ (up to 6.0 × 10⁻⁷ mbar) as reaction gas for the experiments of this study. The introduced He gas ensures efficient trapping and cooling of the ions. It is possible to store respective cluster ions within the hexapole ion trap. In order to record the present data we stored the ions up to 0.5 s. For detection, the manipulated ions, [Ta_n(N₂)_m]⁻ = (n,m), are steered into the ICR cell by a series of electrostatic lenses. This ICR cell is a *infinity* type cell [33]. A closed cycle He cryostat cools down the ICR cell to 10 K to prevent heating of the clusters by black body radiation.

The setup of our FT-ICR MS instrument allows us not only to record mass spectra but also to perform kinetic studies on adsorption processes of reaction gases to the cluster ions. Furthermore, it is possible to couple a tunable IR-OPO/OPA laser into the ICR cell in order to investigate the cluster adsorbate species using IR spectroscopy. However, due to the low intensity of the cluster species, further studies beyond the acquisition of simple mass spectra of the tantalum cluster anions could not be performed in the frame of the present study.

8.2.4 Results and Discussion

Using our FT-ICR MS instrument we investigated the N₂ adsorption ability of Ta_n⁻. As shown in Figure 1 the laser vaporization source produces anionic tantalum clusters of various cluster sizes. For mass spectra of the raw measured data of anionic tantalum clusters optimized for small and larger clusters sizes we refer the reader to the supplementary information (*cf.* Figure S1 and S2, chapter 8.3).

Within our measurement range up to 2000 m/z we found the cluster sizes $n = 4 - 10$. In addition to the bare tantalum clusters, numerous tantalum oxides are also formed during the cluster formation process in the laser vaporization source. We assign the experimental cluster signals by simulating the masses of the bare cluster and their oxides. For Ta₄⁻ the bare cluster signal is still more intense than the signals of the oxides [Ta₄O_x]⁻. At Ta₅⁻ and above, the oxide signals become much more intense and exceed the signal intensity of the bare metal clusters.

Compared to our studies on tantalum cation clusters [27–29], the signal intensity of the anions is significantly lower. This does not seem surprising to us, since anions have an additional reaction channel: the loss of an electron. The neutral, uncharged clusters resulting from this electron loss are not detectable with our instrument. Hence, this additional reaction channel for cluster anions reduces the measured signal intensities of the cluster anions compared to cluster cations of the same transition metal. Unfortunately, the magnitude of this effect on the signal intensity of the Ta_n⁻ clusters is so large that we are reaching the limit of measurability with our experimental methods.

To study nitrogen adsorption to anionic tantalum clusters, the reaction gas nitrogen is continuously introduced into the cryogenic hexapole ion trap of our FT-ICR

8. Size Dependence of N_2 Adsorption onto Ta_{4-10}^- Cluster Anions

MS instrument. Despite the introduced high N_2 pressure (5.5×10^{-7} mbar), the mass spectrum of the cluster distribution without cluster size isolation in the quadrupole mass filter (Figure 2(a)) still shows only the mass signals of the bare Ta_4^- cluster and its oxides. The oxide species are likely formed during cluster generation. This findings become even clearer in Figure 2(b).

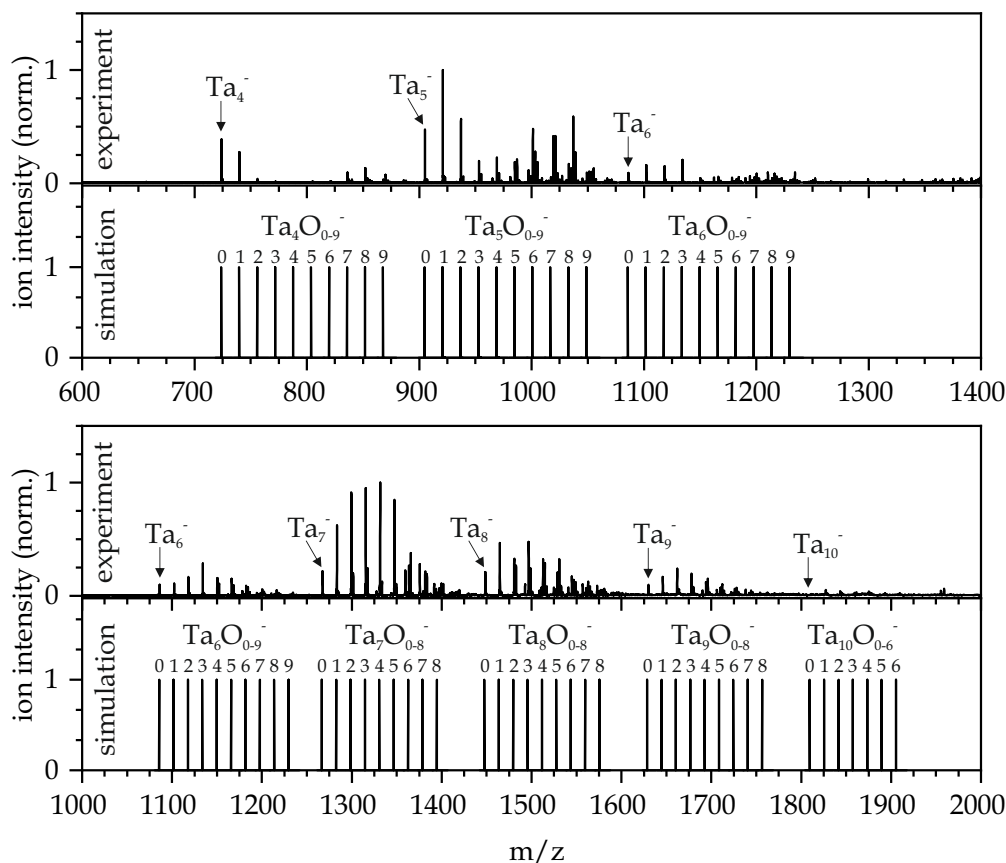


Figure 1: Experimental mass spectra of anionic tantalum cluster distributions from the laser vaporization source in the mass ranges of 600–1400 m/z for small tantalum clusters (Ta_4^- to Ta_6^-) and 1000–2000 m/z for larger clusters (Ta_6^- to Ta_{10}^-) at 26 K. To assign the experimental cluster signals, the simulated masses of the bare tantalum clusters and their oxides are shown below the overview spectra.

We isolated the bare Ta_4^- cluster in a quadrupole mass filter (indicated in the spectrum by “iso Ta_4^- ”), and after the ions pass the hexapole ion trap (6.0×10^{-7} mbar) filled with nitrogen, the mass spectrum still shows exclusively the bare Ta_4^- signal. We observe no mass signals of N_2 adsorbed species. For comparison, the simulation shows the theoretical mass of the first nitrogen adsorbate species $[Ta_4(N_2)_1]^-$. When trying to store the cluster ions in the hexapole, the ion signal disappeared

in the noise. This absence of mass signals of N_2 adsorbed species indicates that the anionic tantalum cluster Ta_4^- is either chemically inert towards nitrogen or the cluster adsorbate species formation is accompanied by the loss of an electron. This so-called reactive detachment yields neutral cluster adsorbate species which in turn are not detectable in our experimental setup. However, the adsorption of N_2 onto anionic Ta_4^- clusters and the stabilisation of the resulting cluster adsorbate complexes $[Ta_4(N_2)_m]^-$ does not seem possible.

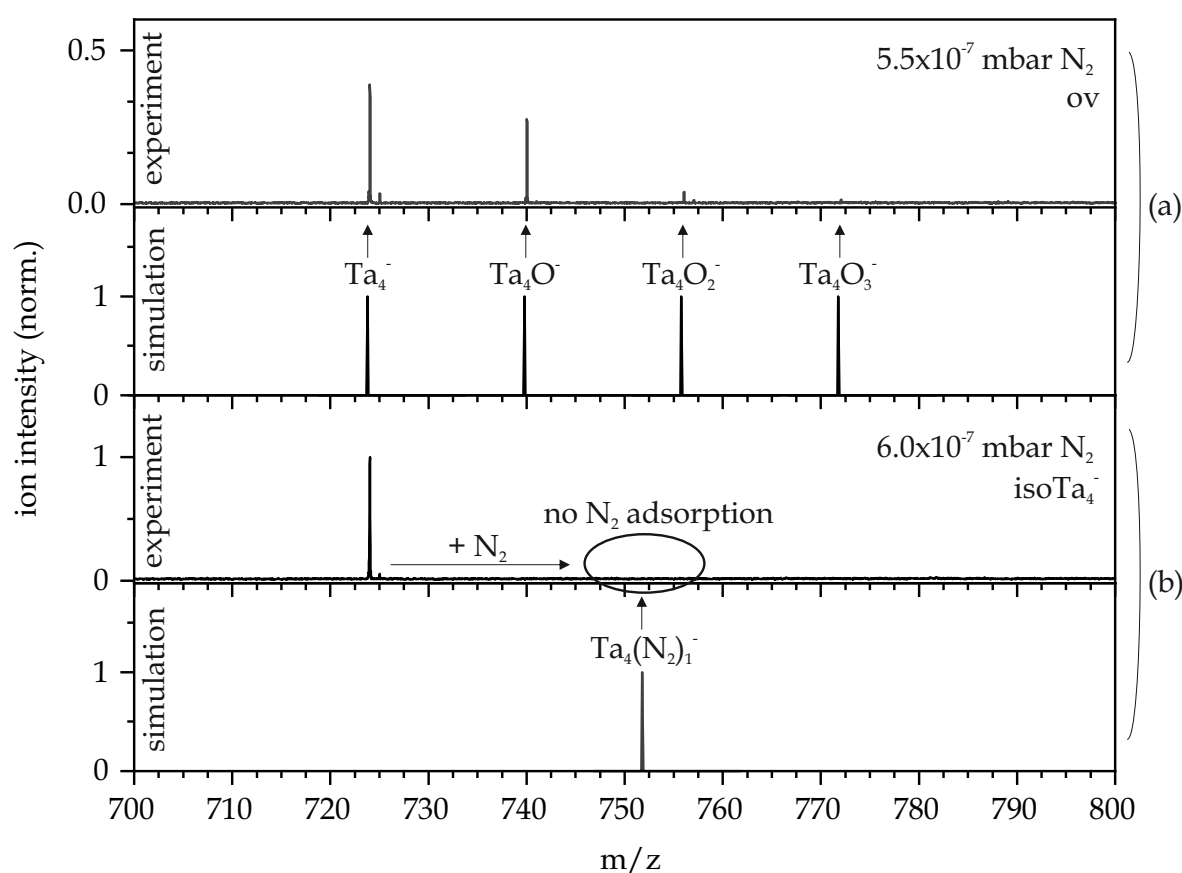


Figure 2: (a) Experimental mass spectrum of the anionic tantalum cluster distribution from the laser evaporation source in the mass range of 700–800 m/z at 26 K (without mass isolation in the quadrupole). The simulated masses of the bare tantalum cluster Ta_4^- and its oxides $[Ta_4O_1]^-$, $[Ta_4O_2]^-$ and $[Ta_4O_3]^-$ are shown below for assignment of the experimental cluster signals. (b) Experimental mass spectrum at 26 K with isolation of Ta_4^- in the quadrupole mass filter and nitrogen (6.0×10^{-7} mbar) introduced as reaction gas in the cryogenic hexapole ion trap. The simulation shows the theoretical mass of the first nitrogen adsorbate species $[Ta_4(N_2)_1]^-$.

8. Size Dependence of N_2 Adsorption onto Ta_{4-10}^- Cluster Anions

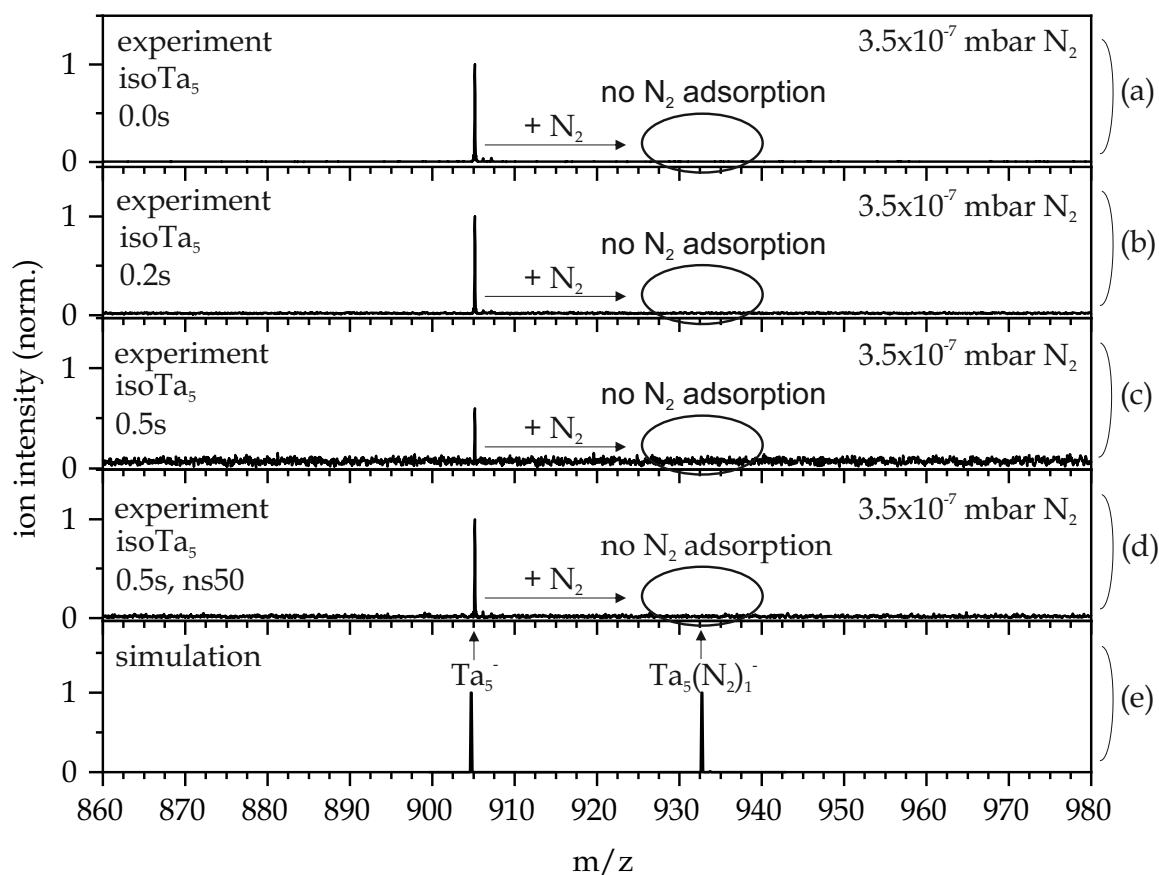


Figure 3: (a)-(c) Mass spectra of the size-selected Ta_5^- cluster (“iso Ta_5^- ”) exposed to 3.5×10^{-7} mbar of nitrogen at 26 K for storage times up to 0.5 s. (d) Summed mass spectrum of Ta_5^- with 3.5×10^{-7} mbar nitrogen at 26 K from 50 individual spectra (“ns50”). (e) The simulated masses of the bare tantalum cluster Ta_5^- and of the first nitrogen adsorbate species $[Ta_5(N_2)_1]^-$.

In a next step we size-selected the anionic tantalum cluster Ta_5^- in the quadrupole and introduced 3.5×10^{-7} mbar N_2 into the hexapole ion trap. Instead of choosing a quite high N_2 pressure, we now stored the cluster ions in the hexapole ion trap. A storage time of 0.5 s turned out to be the maximum storage time. For higher storage times the cluster signal disappears in the noise. We observe no nitrogen adsorption to the Ta_5^- cluster as shown in Figure 3(a)-(c). To obtain a sufficiently informative mass spectrum, we summed the intensity of 50 individual spectra (indicated in the spectrum by “ns50”). The resulting summed up spectrum in Figure 3(d) still reveals no further cluster signal but the bare Ta_5^- signal. We conclude that the adsorption of N_2 onto anionic Ta_5^- clusters and the stabilisation of the resulting cluster adsorbate complexes $[Ta_5(N_2)_m]^-$ does not seem possible.

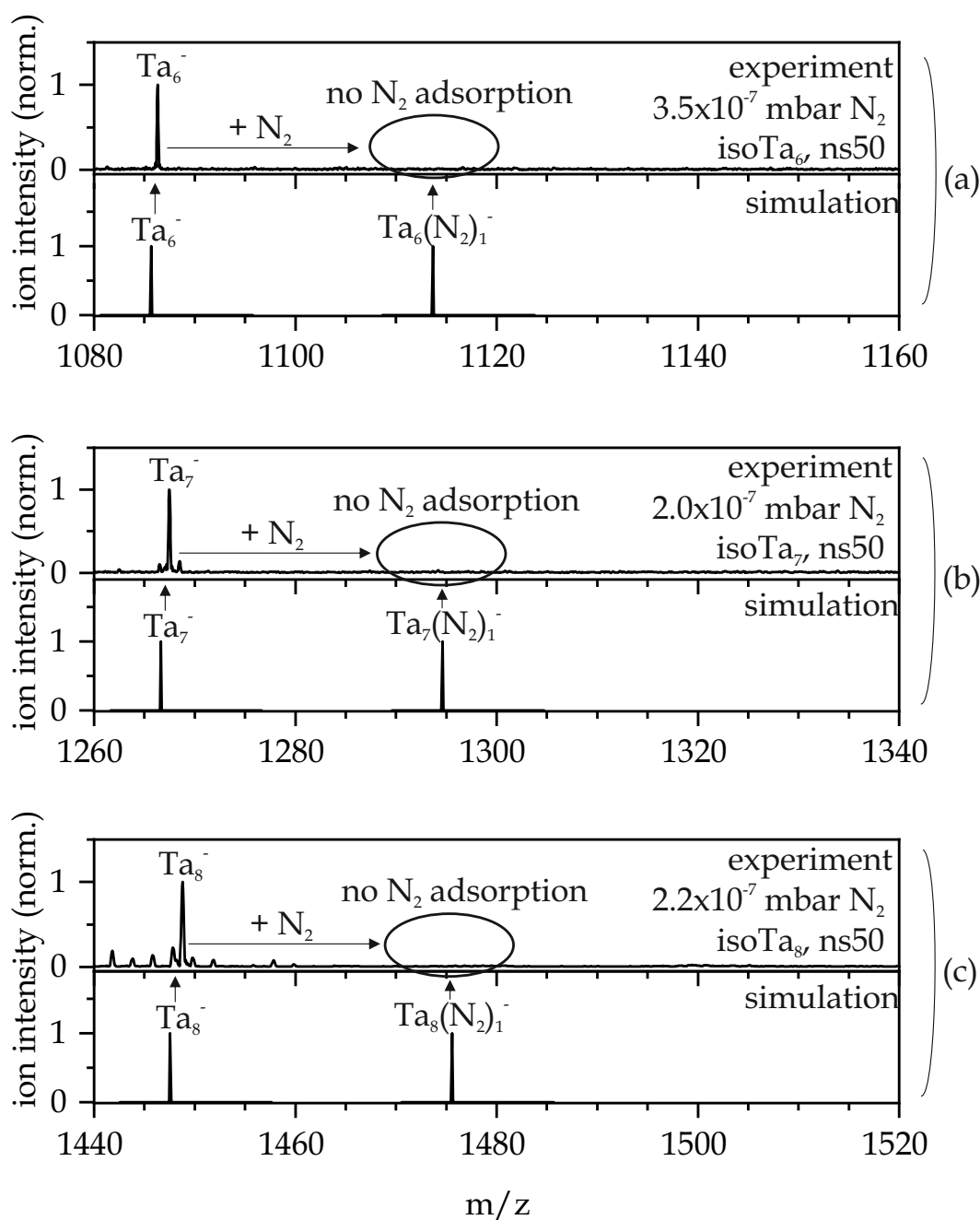


Figure 4: Experimental summed up mass spectra of the size-selected Ta_6^- (a), Ta_7^- (b) and Ta_8^- (c) cluster exposed to $2.0\text{--}3.5 \times 10^{-7}$ mbar of nitrogen at 26 K from 50 individual spectra (“ns50”). The simulated masses of the bare tantalum clusters Ta_6^- , Ta_7^- and Ta_8^- are shown below for assignment of the experimental cluster signals. The theoretical mass of the first nitrogen adsorbate species $[\text{Ta}_6(\text{N}_2)_1]^-$, $[\text{Ta}_7(\text{N}_2)_1]^-$ and $[\text{Ta}_8(\text{N}_2)_1]^-$ are also given there.

8. Size Dependence of N_2 Adsorption onto Ta_{4-10}^- Cluster Anions

After we could not observe nitrogen adsorption for either Ta_4^- or Ta_5^- , we also wanted to investigate larger tantalum clusters with respect to their nitrogen adsorption capability. Therefore, we recorded mass spectra of the size-selected clusters Ta_6^- , Ta_7^- and Ta_8^- with $2.0-3.5 \times 10^{-7}$ mbar nitrogen (Figure 4). Due to low signal intensities we again summed up 50 individual spectra to obtain proper spectra for each cluster species. We simulated the theoretical masses for $[Ta_6(N_2)_1]^-$, $[Ta_7(N_2)_1]^-$ and $[Ta_8(N_2)_1]^-$ for comparison at which masses the first nitrogen adsorbate species would be expected. This reveals no mass signals for nitrogen adsorption for Ta_6^- , Ta_7^- and Ta_8^- .

When we isolated the cluster Ta_9^- and summed up 50 individual spectra we obtained a mass spectrum (Figure 5(a)) which gave us a first indication of minimal nitrogen adsorption although we have not introduced nitrogen into the hexapole ion trap at this time. This is presumably due to the fact that residual nitrogen is still present in the trap from the previous experiments. In a next step we introduced 2.2×10^{-7} mbar nitrogen into the hexapole and summed up again 50 individual spectra. The resulting spectrum shows a slightly higher relative intensity for the nitrogen adsorbate species $[Ta_9(N_2)_1]^-$. So, the introduction of nitrogen into the hexapole ion trap has actually increased nitrogen adsorption onto the Ta_9^- cluster. This finding also continues in the study of the Ta_{10}^- cluster (Figure 5(b)). The summed-up spectrum without introduced nitrogen in the hexapole indeed shows a mass signal for the first nitrogen adsorbate species. The intensity of this signal strongly increases with injection of nitrogen into the hexapole. In addition, mass signals of further nitrogen adsorbate species are now also appearing. While the effect of nitrogen adsorption was still comparatively small for Ta_9^- , the nitrogen adsorption ability on Ta_{10}^- is significant. The comparison between the experimental mass spectrum and the simulated theoretical masses of the nitrogen adsorbate species $[Ta_{10}(N_2)_{1-4}]^-$, proves that Ta_{10}^- adsorbs up to four nitrogen molecules onto the cluster surface under our reaction conditions. We conclude that the nitrogen adsorption capacity to anionic tantalum clusters is size dependent. It is only above a cluster size of nine cluster atoms that the adsorption of N_2 onto the anionic tantalum clusters yields stable and detectable cluster adsorbate species $[Ta_n(N_2)_m]^-$. Due to the low intensities of the cluster species further investigations about the nitrogen adsorption capabilities are challenging. However, the recorded mass spectra already show a strong size dependence of the nitrogen adsorption capacity on anionic tantalum clusters.

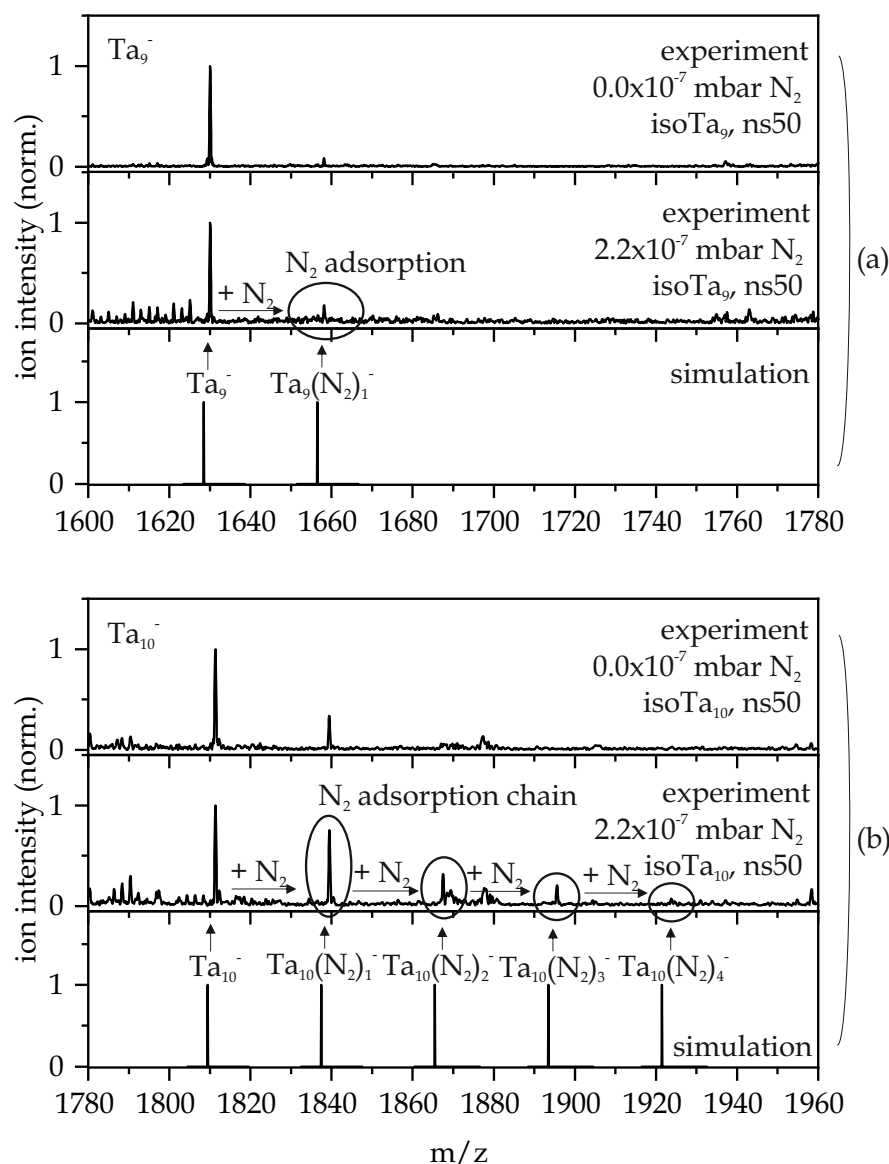


Figure 5: (a) Summed up mass spectrum of size-selected Ta_9^- cluster from 50 individual spectra (“ns50”) without and with introduced nitrogen (2.2×10^{-7} mbar). The simulated mass of the bare tantalum cluster Ta_9^- is shown below for assignment of the experimental cluster signal. The simulated mass spectrum of the first nitrogen adsorbate species $[\text{Ta}_9(\text{N}_2)_1]^-$ are also given there. (b) Summed up mass spectrum of size-selected Ta_{10}^- cluster from 50 individual spectra (“ns50”) without and with introduced nitrogen (2.2×10^{-7} mbar). The simulated mass of the bare tantalum cluster Ta_{10}^- is shown below for assignment of the experimental cluster signal. The simulated masses of the nitrogen adsorbate species $[\text{Ta}_{10}(\text{N}_2)_{1-4}]^-$ are also given there.

At this point we want to compare these findings of N₂ adsorption to tantalum cluster anions to the findings of our prior studies on tantalum cluster cations. It is noticeable that for the cationic clusters we could not find a seeming limit for the cluster size above which N₂ is adsorbed. Starting from Ta₂⁺ up to Ta₈⁺, the cluster cations of all sizes adsorb N₂. We recognize that the larger the cluster size, the more N₂ can be adsorbed to the cluster. [27–29] In contrast, we found n = 9 proved to be the minimum cluster size for N₂ adsorption and stabilization of the resulting cluster adsorbate complexes [Ta_n(N₂)_m]⁻. Ta₉⁻ is the smallest cluster that gives mass signals for N₂ adsorbate species in the present study. This finding is in line with literature [11]. In this publication the authors observe a significantly shifted threshold for anion cluster reactivity towards CO adsorption to much larger cluster sizes when compared to cationic cluster reactivity. Above n ~ 7 - 18 there is very little difference between the reactivity on anions and cations.

8.2.5 Conclusion

In this work, we studied the adsorption of N₂ onto small tantalum cluster anions Ta_n⁻, n = 4 - 10, under cryogenic conditions using a FT-ICR mass spectrometer. The signal intensities of the anionic clusters are significantly lower than those of the corresponding positively charged clusters. Nevertheless, the recorded mass spectra show that the ability of the anionic tantalum clusters to adsorb N₂ is strongly dependent on the cluster size n. We found n = 9 to be the minimum cluster size for N₂ adsorption onto Ta_n⁻ clusters to yield stable and detectable cluster adsorbate species [Ta_n(N₂)_m]⁻. The smaller clusters Ta₄⁻ to Ta₈⁻ are either chemically inert towards nitrogen or the cluster adsorbate species formation is accompanied by reactive detachment hampering any further experimental detection. However, the adsorption of N₂ onto these small anionic clusters and the stabilisation of the resulting cluster adsorbate complexes [Ta₄₋₈(N₂)_m]⁻ does not seem possible. Further investigation of the nitrogen adsorption processes and the species involved is prevented by the low intensities of the cluster species.

8.2.6 Acknowledgements

This work was supported by the German research foundation DFG within the trans-regional collaborative research center SFB/TRR 88 “Cooperative effects in homo and heterometallic complexes” (3met.de) and by the state research center OPTIMAS. We thank Thomas Kolling for technical assistance and valuable discussion.

8.2.7 References

- [1] E. L. Muetterties, *Science* **1977**, *196*, 839–848.
- [2] M. B. Knickelbein, *Annual Reviews* **1999**, *50*, 79–115.
- [3] P. B. Armentrout, *Annual Reviews* **2001**, *52*, 423–461.
- [4] R. A. J. O’Hair, G. N. Khairallah, *Journal of Cluster Science* **2004**, *15*, 331–363.
- [5] D. K. Böhme, H. Schwarz, *Angewandte Chemie International Edition* **2005**, *44*, 2336–2354.
- [6] S. M. Lang, T. M. Bernhardt, *Physical Chemistry Chemical Physics* **2012**, *14*, 9255–9269.
- [7] P. B. Armentrout, *Catalysis Science & Technology* **2014**, *4*, 2741–2755.
- [8] M. L. Anderson, M. S. Ford, P. J. Derrick, T. Drewello, D. P. Woodruff, S. R. Mackenzie, *The Journal of Physical Chemistry A* **2006**, *110*, 10992–11000.
- [9] J. Mwakapumba, K. M. Ervin, *International Journal of Mass Spectrometry and Ion Processes* **1997**, *161*, 161–174.
- [10] P. A. Hintz, K. M. Ervin, *The Journal of Chemical Physics* **1995**, *103*, 7897–7906.
- [11] I. Balteanu, U. Achatz, O. P. Balaj, B. S. Fox, M. K. Beyer, V. E. Bondybey, *International Journal of Mass Spectrometry* **2003**, *229*, 61–65.
- [12] L.-H. Mou, Q.-Y. Liu, T. Zhang, Z.-Y. Li, S.-G. He, *The Journal of Physical Chemistry A* **2018**, *122*, 3489–3495.
- [13] L.-H. Mou, Y. Li, Z.-Y. Li, Q.-Y. Liu, H. Chen, S.-G. He, *Journal of the American Chemical Society* **2021**, *143*, 19224–19231.
- [14] L.-H. Mou, Y. Li, G.-P. Wei, Z.-Y. Li, Q.-Y. Liu, H. Chen, S.-G. He, *Chemical Science* **2022**, *13*, 9366–9372.
- [15] J.-C. Hu, L.-L. Xu, H.-F. Li, D. Y. Valdivielso, A. Fielicke, S.-G. He, J.-B. Ma, *Physical Chemistry Chemical Physics* **2017**, *19*, 3136–3142.
- [16] Y. Zhao, J.-T. Cui, M. Wang, D. Y. Valdivielso, A. Fielicke, L.-R. Hu, X. Cheng, Q.-Y. Liu, Z.-Y. Li, S.-G. He, J.-B. Ma, *Journal of the American Chemical Society* **2019**, *141*, 12592–12600.

8. Size Dependence of N₂ Adsorption onto Ta_{4–10}[−] Cluster Anions

- [17] Z.-Y. Li, L.-H. Mou, G.-D. Jiang, Q.-Y. Liu, S.-G. He, *Chinese Journal of Chemical Physics* **2022**, *35*, 77–85.
- [18] X. Sun, X. Huang, *ACS Omega* **2022**, *7*, 22682–22688.
- [19] B. Huang, H. Zhang, L. Geng, Z. Luo, *The Journal of Physical Chemistry Letters* **2022**, *13*, 9711–9717.
- [20] J. Mohrbach, S. Dillinger, G. Niedner-Schatteburg, *The Journal of Physical Chemistry C* **2017**, *121*, 10907–10918.
- [21] S. Dillinger, J. Mohrbach, G. Niedner-Schatteburg, *The Journal of Chemical Physics* **2017**, *147*, 184305.
- [22] A. A. Ehrhard, M. P. Klein, J. Mohrbach, S. Dillinger, G. Niedner-Schatteburg, *Molecular Physics* **2021**, *119*, e1953172.
- [23] A. A. Ehrhard, M. P. Klein, J. Mohrbach, S. Dillinger, G. Niedner-Schatteburg, *The Journal of Chemical Physics* **2022**, *0*, 054308.
- [24] A. Straßner, M. P. Klein, D. V. Fries, C. Wiehn, M. E. Huber, J. Mohrbach, S. Dillinger, D. Spelsberg, P. B. Armentrout, G. Niedner-Schatteburg, *The Journal of Chemical Physics* **2021**, *155*, 244306.
- [25] A. Straßner, C. Wiehn, M. P. Klein, D. V. Fries, S. Dillinger, J. Mohrbach, M. H. Prosenc, P. B. Armentrout, G. Niedner-Schatteburg, *The Journal of Chemical Physics* **2021**, *155*, 244305.
- [26] J. Mohrbach, S. Dillinger, G. Niedner-Schatteburg, *The Journal of Chemical Physics* **2017**, *147*, 184304.
- [27] D. V. Fries, M. P. Klein, A. Steiner, M. H. Prosenc, G. Niedner-Schatteburg, *Physical Chemistry Chemical Physics* **2021**, *23*, 11345–11354.
- [28] D. V. Fries, M. P. Klein, A. Straßner, M. E. Huber, M. Luczak, C. Wiehn, G. Niedner-Schatteburg, *The Journal of Chemical Physics* **2023**, *159*, 164303.
- [29] D. V. Fries, M. P. Klein, A. Straßner, M. E. Huber, G. Niedner-Schatteburg, *The Journal of Chemical Physics* **2023**, *159*, 164306.
- [30] C. Berg, T. Schindler, G. Niedner-Schatteburg, B. V. E., *The Journal of Chemical Physics* **1995**, *102*, 4870–4884.

- [31] V. Bondybey, J. English, *The Journal of Chemical Physics* **1981**, 74, 6978–6979.
- [32] D. Proch, T. Trickl, *Review of Scientific Instruments* **1989**, 60, 713–716.
- [33] P. Caravatti, M. Allemann, *Organic Mass Spectrometry* **1991**, 26, 514–518.

8.3 Supplementary Information

SIZE DEPENDENCE OF N_2 ADSORPTION ONTO Ta_{4-10}^- CLUSTER ANIONS

Daniela V. FRIES, Maximilian LUCZAK, Christopher WIEHN, and Gereon NIEDNER-SCHATTEBURG

Department of Chemistry and State Research Center OPTIMAS,
Rheinland-Pfälzische Technische Universität (RPTU) Kaiserslautern-Landau,
67663 Kaiserslautern, Germany

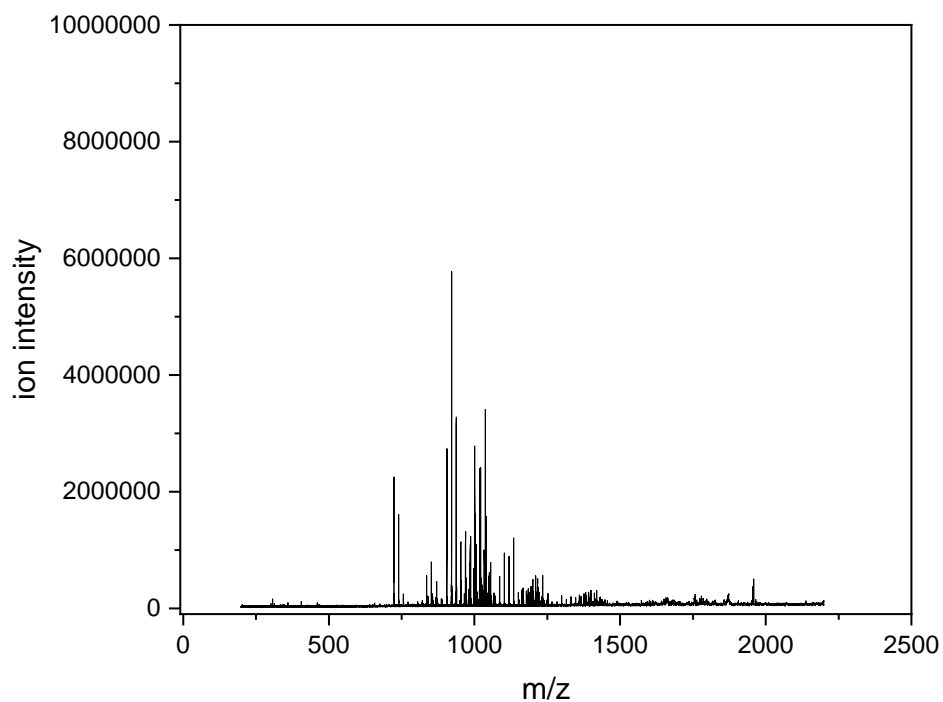


Figure S1: Overview mass spectrum of raw measured data of anionic tantalum clusters optimized for small cluster sizes.

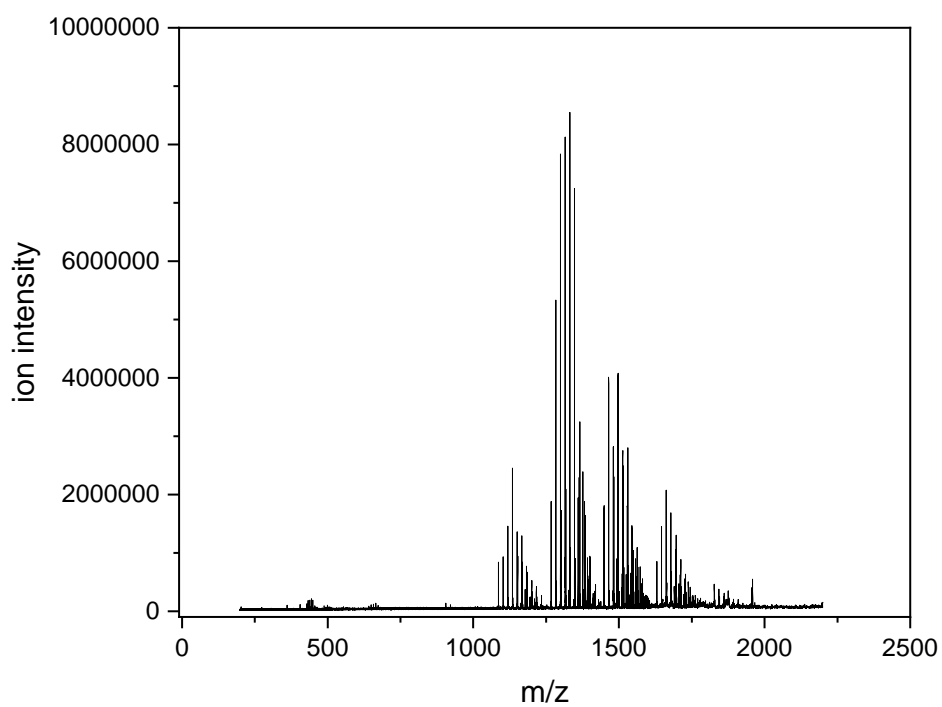


Figure S2: Overview mass spectrum of raw measured data of anionic tantalum clusters optimized for larger cluster sizes.

9 SUMMARY AND OUTLOOK

The present thesis reports on studies of atomically precise, size-selected tantalum cluster ions Ta_n^\pm under cryogenic conditions with respect to surface adsorbate interactions at the fundamental level, with emphasis on N_2 and H_2 adsorption and activation. A Fourier transform ion cyclotron resonance mass spectrometer (FT-ICR MS) setup, equipped with a laser vaporization (LVAP) source, a quadrupole mass filter and two cryogenically cooled ion traps, is used to generate cluster ions, select them by size, coordinate them with diatomic molecules such as N_2 or H_2 , and study both bare cluster ions and cluster adsorbate complexes under well-defined isothermal conditions. In addition, a tunable infrared (IR) OPO/OPA laser system can be coupled into the FT-IR MS setup, allowing comprehensive mass spectrometric studies in the form of adsorption kinetics as well as photodissociation measurements. The interpretation of the experimental results is complemented by quantum chemical simulations at the density functional theory (DFT) level. The wealth of results presented here is the result of systematic studies that have revealed valuable kinetic, spectroscopic, and quantum chemical information, which together paint a comprehensive picture of the elementary adsorption steps and mechanisms in detail.

N_2 Adsorption on Cationic Ta_{2-8}^+ Clusters

The stepwise N_2 adsorption on size-selected Ta_n^+ clusters, $n=2-8$, yielding $[Ta_n(N_2)_m]^+$, abbreviated (n,m) , reaches a limit $m_{(max)}$, which depends on cluster size n . Cryo adsorption kinetics allowed kinetic fits of consecutive N_2 adsorption steps, and the fits revealed significant N_2 desorption rates at higher adsorbate loads, up to discernible equilibrium. The variations in absolute rates find reasonable interpretation in terms of simple thermodynamic arguments, and provide some evidence for N_2 activation. The lack of IR-PD bands for the first adsorbate species and DFT modeling for conceivable activation pathways add to the evidence for the activation

9. Summary and Outlook

of N₂ and the cleavage ability of Ta₂⁺, Ta₃⁺, and Ta₄⁺. Spontaneous N₂ activation and cleavage by Ta_n⁺, n = 5-8, seems to be suppressed. The addition of one more tantalum core atom removes the ability of a small Ta_n⁺ cluster to activate N₂. The IR-PD spectra of the cluster adsorbate species (n,m), n = 5-8, start with some single and distinguishable N₂ end-on bands of the less occupied adsorbate complexes. At certain points of the N₂ charge, the IR-PD band pattern shows a general increase in spectral complexity and an inhomogeneous broadening of the bands, mainly towards red. This is most likely due to an increasing amount of double and triple N₂ coordination of Ta sites, eventually at all sites. The more N₂ ligands coordinate to single Ta sites, the more the vibrational frequencies shift to the red.

[Ta₂(N₂)_m]⁺ Adsorption kinetics, IR-PD experiments, and DFT modeling of Ta₂⁺ with N₂ confirm and extend a previous study under ambient conditions [1] and reveal an additional submerged entry channel barrier. Thus, spontaneous N₂ bond activation and cleavage by Ta₂⁺ is well confirmed.

[Ta₃(N₂)_m]⁺ For the tantalum cluster trimer Ta₃⁺, cryo studies and DFT simulations indicate sequential activation of up to three N₂ molecules across submerged barriers and along highly involved multidimensional reaction pathways. The cleavage path of the first N₂ molecule on Ta₃⁺ proceeds very much in line with the identified across edge above surface (AEAS) mechanism of Ta₄⁺. The second N₂ molecule undergoes similar activation steps until an unsurmountable barrier that prevents any final N₂ bond cleavage. In contrast, the N₂ activation reaction pathway for the adsorption of the third N₂ molecule onto the Ta₃⁺ cluster proceeds via a μ₂-χN,N:χN,N double side-on N₂ motif similar to that of (2,1). From (3,4), there is a sequential adsorption of additional N₂ molecules towards the end-on N₂ motifs.

[Ta₄(N₂)_m]⁺ The present study comprising IR-PD experiments and DFT modeling of N₂ adsorbate complexes of Ta₄⁺ confirms double activation and nitride formation, succeeded by single side-on N₂ coordination. Significant red shifts of IR-PD bands from side-on coordinated μ₂-χN,N:χN,N N₂ ligands correlate with the degree of tilting towards the second coordinating Ta center. IR-PD spectra and complementary DFT modeling provide evidence for the co-existence of end-on coordination isomers. This is consistent with measured adsorption kinetics indicating adsorption isomers and/or adsorbate shell rearrangement for species with higher adsorbate loading along the adsorption chain.

[Ta₅(N₂)_m]⁺ The N₂ adsorption kinetics of Ta₅⁺ are ambiguous. However, the initial short time kinetics allow standard fits in terms of consecutive adsorption and early desorption. Long time kinetics assume counter-intuitive courses, and these are much beyond an unequivocal interpretation. The current hypothesis includes a possible co-existence of isomeric cluster adsorbate complexes and spin quenching as indicated by modeled spin valley curves. IR-PD spectra of all species (5,m), m = 1 - 13, revealed IR-PD signals corresponding to end-on and/or side-on μ₂-χN:χN,N N₂ ligands. The IR-PD spectrum of the initial adsorbate species (5,1) provides clear evidence that spontaneous N₂ activation is suppressed.

[Ta₆(N₂)_m]⁺ The recorded kinetics of the cluster species (6,m) proof typical stepwise adsorption of up to 16 N₂ molecules. The recorded IR-PD spectra of the N₂ adsorption species (6,m) show numerous IR-PD signals in two spectral regions, for end-on and side-on coordinated N₂ oscillators, respectively. For the adsorbed N₂ molecules, DFT modeling predicts a sequence of initial N₂ end-on coordination and subsequent mixing with side-on N₂ coordination.

[Ta₇(N₂)_m]⁺ For Ta₇⁺ the adsorption kinetics reveal typical stepwise adsorption of up to 16 N₂ molecules as well. The (7,m) complexes, however, undergo significant N₂ desorption much before final equilibrium. This finding suggests an ongoing reorganization of the adsorbate shell. The recorded IR-PD spectra reveal numerous bands indicative of N₂ oscillators binding end-on to single Ta centers prior to N₂ oscillators coordinating in a side-on μ₂-χN:χN,N motif from (7,4) on and beyond.

[Ta₈(N₂)_m]⁺ The recorded kinetics of (8,m) are ambiguous, as is that of (5,m). While the initial short time kinetics allow for standard fits in terms of consecutive adsorption and early desorption, the long time kinetics assume counter-intuitive courses which are beyond an unequivocal interpretation. However, the observed IR-PD bands of (8,m) likely stem from end-on μ₁ coordinated N₂ ligands.

The current state of understanding of the ambiguous kinetics of (5,m) and (8,m) requires further investigation. The application of alternative modeling schemes beyond the simple stepwise adsorption model has been successful in the past for the Fe₁₇⁺ and Fe₁₈⁺ cases. [2] The application of similar scenarios to the current Ta₅⁺ and

Ta₈⁺ cases could be a promising approach for a conclusive interpretation of their adsorption kinetics. Future studies should include comprehensive DFT modeling of the (higher) loaded cluster adsorbate complexes (n,m), n = 5 - 8. Interpreting the corresponding measured IR-PD would benefit in terms of assigning cluster adsorbate complex geometries. The IR-PD studies performed so far provide strong but only indirect evidence for the activation and cleavage of N₂ by Ta₂₋₄⁺ clusters. Direct evidence could be obtained by spectroscopic examination of Ta-N fingerprints. This would require a different light source. Two-color IR experiments, in which one laser is used to overcome the activation barrier and a second laser is used to study the activated species, can also provide a means of studying the activated species.

H₂ Adsorption on Cationic Ta₂₋₈⁺ Clusters

The study of stepwise H₂ adsorption on size-selected tantalum cluster cations Ta_n⁺, n = 2 - 8, reveals an increasing trend in the adsorption limits m_{max} with increasing cluster size n at a stoichiometry close to 1:2. The overall picture from adsorption kinetics, IR-PD measurements and complementary DFT modeling show that the H₂ adsorption processes to Ta_n⁺ cluster exhibit dependencies on cluster size n and on adsorbate load m. The smallest tantalum cluster cation, Ta₂⁺, proves to be inert toward H₂ under the conditions of the experiments.

[Ta₃₋₅(H₂)_m]⁺ and [Ta₇(H₂)_m]⁺ The adsorption kinetics and the associated IR-PD study and some DFT modeling for conceivable (n,m) geometries find a convincing justification in the assumption that Ta_n⁺ clusters, n = 3 - 5, exhibit two distinct H₂ adsorption processes that follow each other: The first type is a dissociative H₂ adsorption reaction. It proceeds very fast and without competitive desorption reactions. The second type of process is characteristic of slow molecular adsorption reactions with multiple desorption reactions. The threshold is the completion of the first adsorbate shell up to (n,m = n). The molecularly adsorbed H₂ molecules are less strongly bound to the cluster core than the dissociatively adsorbed ones and are thus able to undergo desorption reactions. In the very special case of the (5,12) cluster, the last two H₂ ligands even coordinate in a formal third adsorbate shell. The predicted cluster geometry, whose assignment is complemented by measured IR-PD signals, and rate constants from kinetic measurements indicate that H₂ activation seems possible even late in the adsorption chain. The overall picture of the processes along the H₂

adsorption chain of Ta_7^+ reveals a less significant decrease in the adsorption rates beyond the formal first adsorption shell than observed for Ta_3^+ , Ta_4^+ and Ta_5^+ . The significant desorption rates appearing before $m = n$ is reached indicates premature completion of the first adsorbate shell. However, the recorded IR-PD spectra show evidence of dissociative adsorption of H_2 molecules up to $m = n$. The photon energy from the IR laser could induce a reorganisation of the cluster nucleus, paving the way for further dissociation of the originally molecularly adsorbed H_2 molecules. Finally, all H_2 molecules beyond $m = n$ are bound to the Ta_7^+ cluster in a molecular motif.

$[Ta_6(H_2)_m]^+$ and $[Ta_8(H_2)_m]^+$ The characteristics of H_2 adsorption on Ta_6^+ and Ta_8^+ are significantly different from those observed for Ta_{3-5}^+ and Ta_7^+ : In the case of $(6,m)$, the slow initial adsorption processes delay the entire adsorption chain. However, as the adsorption chain progresses, there are reaction processes that are again too fast to allow all $(6,m)$ species to be observed in the kinetics. Ta_8^+ shows an exceptional behavior, as the recorded ion intensities first reveal the stepwise adsorption of H_2 molecules, yielding species $(8,5)$ as an intermittent adsorption limit, which in turn adsorbs additional H_2 molecules in a delayed manner. The ion intensities of the species $(8,7)$ lead to the speculation of adsorbate shell reorganization and/or adsorbate induced cluster relaxation processes. IR-PD studies of the two cluster adsorbate species $(6,m)$ and $(8,m)$ indicate that the first H_2 molecules are adsorbed to the clusters in a dissociative manner. For the further course of the H_2 adsorption chain, it can be speculated that the formal first adsorbate shell might be completed before $m = n$ is reached. In these clusters there may be some Ta core atoms that are prevented from accepting hydrides due to their high neighborhood coordination to other Ta centres. Without predicting the DFT, these reasonable, but speculative, interpretations are the most conclusive currently available.

The current understanding of H_2 adsorption on Ta_n^+ clusters may benefit from further investigation, either to support the conclusions of the present studies or to expand the overall picture. Future studies could include comprehensive DFT modeling of other cluster adsorbate complexes (n,m) than those of $(4,m)$ and $(5,m)$. Interpreting the corresponding measured IR-PD would benefit in terms of assigning cluster adsorbate complex geometries. The IR-PD studies performed so far provide strong evidence for the activation and cleavage of H_2 by Ta_{3-8}^+ clusters as the used IR laser system provides IR radiation to probe Ta-H bonds. Spectral evidence of

molecular adsorbed H₂ could be obtained by spectroscopic examination of H-H fingerprints. This would require a different light source. Two-color IR experiments can also provide a means to study the activated species. The ambiguous kinetics of (8,m) might serve as starting point for further investigation such as an alternative modeling scheme as successfully applied in the past for Fe₁₇⁺ and Fe₁₈⁺[2].

N₂ Adsorption on Anionic Ta₄₋₁₀⁻ Clusters

The N₂ adsorption study of small tantalum cluster anions Ta_n⁻, n = 4 - 10, reveals that the signal intensities of the anionic clusters are significantly lower than those of the corresponding positively charged clusters. However, the recorded mass spectra show that the ability of anionic tantalum clusters to absorb N₂ depends strongly on cluster size n. The cluster size n = 9 is the minimum size for N₂ adsorption onto Ta_n⁻ clusters to yield stable and detectable cluster adsorbate species [Ta_n(N₂)_m]⁻. The adsorption of N₂ onto smaller anionic clusters Ta₄₋₈⁻ and the stabilisation of the resulting cluster adsorbate complexes [Ta₄₋₈(N₂)_m]⁻ does not seem possible. Further investigation of N₂ adsorption processes and species involved has been hampered by the low ion intensities of cluster species.

Beyond the present thesis, the logical next step would be a study of N₂/H₂ co-adsorption. The above summarized results for the adsorption of N₂ and H₂ on tantalum cluster ions Ta_n[±], giving a comprehensive picture of the elemental adsorption steps and mechanisms, provide an ideal basis for such co-adsorption studies.

References

- [1] C. Geng, J. Li, T. Weiske, H. Schwarz, *Proceedings of the National Academy of Sciences* **2018**, *115*, 11680–11687.
- [2] A. Straßner, M. P. Klein, D. V. Fries, C. Wiehn, M. E. Huber, J. Mohrbach, S. Dillinger, D. Spelsberg, P. B. Armentrout, G. Niedner-Schatteburg, *The Journal of Chemical Physics* **2021**, *155*, 244306.

10 ZUSAMMENFASSUNG UND AUSBLICK

Die vorliegende Arbeit beschäftigt sich mit Untersuchungen an gröÙenselektierten Tantalclusterionen Ta_n^\pm unter kryogenen Bedingungen. Der Studienschwerpunkt liegt auf Adsorption und Aktivierung von N_2 und H_2 durch diese Tantalcluster.

Ein Fourier Transform Ion Cyclotron Resonance Massenspektrometer (FT-ICR MS) Aufbau, mit einer Laserverdampfungsquelle (LVAP), einem Quadrupolmassenfilter und zwei kryogenen Ionenfallen, wird zur Erzeugung der Clustererionen, deren Größenselektierung und Koordinierung mit zweiatomigen Molekülen wie N_2 oder H_2 sowie der Untersuchung der nackten Clusterionen und Clusteradsorbatkomplexen unter genau definierten isothermen Bedingungen verwendet. Darüber hinaus besteht die Möglichkeit ein durchstimmbares Infrarot (IR) OPO/OPA Lasersystem in diesen FT-ICR MS Aufbau einzukoppeln. Dies ermöglicht umfassende massenspektrometrische Studien in Form von Adsorptionskinetiken und Photodissoziationsmessungen. Die Interpretation der experimentellen Ergebnisse wird durch quantenchemische Simulationen auf Dichtefunktionaltheorie (DFT) Level ergänzt. Die Fülle der in dieser Arbeit vorgestellten Ergebnisse stammt aus systematischen Untersuchungen, die in diesem Zusammenhang ausführliche kinetische, spektroskopische und quantenchemische Informationen lieferten. Es ergibt sich ein umfassendes und detailliertes Bild der elementaren Adsorptionsschritte und -mechanismen von N_2 und H_2 an gröÙenselektierten Tantalclusterionen Ta_n^\pm .

N_2 Adsorption an kationische Ta_{2-8}^+ Cluster

Die schrittweise Adsorption von N_2 an gröÙenselektierte Ta_n^+ Cluster, $n = 2-8$, welche zu den Clusteradsorbaten $[Ta_n(N_2)_m]^+$, abgekürzt als (n,m) , führen, erreicht

ein von der Clustergröße n abgängiges Adsorptionslimit $m_{(\max)}$. Die Kryoadsorptionskinetiken ermöglichen kinetische Fits der aufeinanderfolgenden N_2 Adsorptionsschritte. Für hohe N_2 Anlagerungen ergeben diese Fits signifikante Desorptionsreaktionen. Am Ende der Adsorptionskette wird ein Gleichgewicht aus Adsorptions- und Desorptionsreaktionen erreicht. Die Schwankungen der absoluten Geschwindigkeitskonstanten für die Adsorption des ersten N_2 Moleküls als Funktion der Clustergröße n lassen sich mit einfachen thermodynamischen Argumenten interpretieren und geben erste Hinweise auf N_2 Aktivierung. Das Fehlen von IR-PD Banden für die ersten Adsorbatspezies und DFT Modellierungen zu möglichen Aktivierungspfaden untermauern die Hinweise auf N_2 Aktivierung und Spaltung durch Ta_2^+ , Ta_3^+ und Ta_4^+ Cluster. Für Ta_n^+ Cluster, $n=5-8$, scheint dies nicht möglich. Die Fähigkeit der kleinen Ta_n^+ Clusters, N_2 zu aktivieren, geht durch das Hinzufügen des fünften Tantalatoms zum Clusterkern verloren. Die IR-PD Spektren der Clusteradsorbatspezies (n,m) , $n=5-8$, zeigen bereits für die ersten Adsorbatspezies $(n,1)$ signifikante N_2 end-on Banden. Mit zunehmender N_2 Anlagerung nimmt die Komplexität des IR-PD Bandenmusters der Clusteradsorbatspezies zu. Die entsprechenden Spektren zeigen eine inhomogene Verbreiterung des IR-PD Bandenbereichs, hauptsächlich in Richtung geringerer Wellenzahlen. Dies ist sehr wahrscheinlich auf einen zunehmenden Anteil an doppelt und dreifach koordinierten Tantalatomen zurückzuführen. Je mehr N_2 Adsorbate an die einzelnen Tantalatome des Clusterkerns koordinieren, desto größer die Rotverschiebung der Schwingungsfrequenzen dieser Adsorbate.

[$Ta_2(N_2)_m$] $^+$ Die Adsorptionskinetiken, IR-PD Experimente und DFT Modellierungen von Ta_2^+ mit N_2 bestätigen und erweitern eine frühere Studie unter Umgebungstemperaturbedingungen [1] und decken eine zusätzliche Barriere für den Eingangskanal der N_2 Adsorption auf. Das Ergebnis, dass Ta_2^+ Cluster spontan N_2 adsorbierten, aktivieren und spalten können, wird bestätigt und untermauert.

[$Ta_3(N_2)_m$] $^+$ Für Cluster des Tantaltrimers Ta_3^+ , zeigen Kryostudien und DFT Simulationen eine schrittweise Aktivierung von bis zu drei N_2 Molekülen über überwindbare Barrieren und entlang mehrdimensionaler Reaktionswege. Der Pfad der Spaltung des ersten N_2 Moleküls auf Ta_3^+ verläuft analog zum AEAS (above edge across surface) Mechanismus, welcher auch die Grundlage für die Adsorption und Spaltung von N_2 auf Ta_4^+ Clustern darstellt. Das zweite N_2 Molekül durchläuft ähnliche Aktivierungsschritte, bis die Reorganisation des Clusteradsorbatkomplexes

an eine unüberwindbare Barriere stößt, die eine finale Spaltung der N₂ Bindung verhindert. Der N₂ Aktivierungspfad des dritten N₂ Moleküls auf Ta₃⁺ Clustern verläuft schließlich über ein μ_2 - λ N₂: λ N₂ (doppelt side-on) Koordinationsmotiv, welches analog zu einem Zwischenprodukt im Aktivierungspfad von (2,1) ist. Ab (3,4) werden alle weiteren N₂ Moleküle molekular (end-on) adsorbiert.

[Ta₄(N₂)_m]⁺ Aus den Ergebnissen der IR-PD Experimenten und DFT Modellierungen von (4,m) Adsorbatkomplexen ergibt sich für die Reaktion von Ta₄⁺ Clustern mit drei N₂ Molekülen eine zweifache Aktivierung und Nitridbildung, gefolgt von einer side-on N₂ Koordinierung. Die signifikante Rotverschiebung der IR-PD Banden des side-on koordinierten μ_2 - λ N₂: λ N₂ N₂ Liganden korreliert mit dem Neigungsgrad des Liganden relativ zu den koordinierten Metallzentren. Die gemessenen IR-PD Spektren und DFT Modellierung der größeren Adsorbatspezies liefern Hinweise für die Koexistenz von Koordinationsisomeren. Auch die Ergebnisse der gemessenen Adsorptionskinetik deuten auf Adsorptionsisomere und/oder eine Reorganisation der Adsorbatschale bei Spezies mit hoher Adsorbatladung im Verlauf der Adsorptionskette hin.

[Ta₅(N₂)_m]⁺ Die Kinetik der N₂ Adsorption an Ta₅⁺ erlaubt bei kurzen Kinetikmesszeiten Fits in Form von sukzessiver Adsorption und frühen Desorptionsreaktionen. Bei langen Kinetikmesszeiten zeigen die Ionenintensitäten der Cluster und Clusteradsorbate kontraintuitive Verläufe, die eine eindeutige Interpretation erschweren. Die derzeitige Hypothese beinhaltet eine mögliche Koexistenz von verschiedenen Clusteradsorbatisomeren und ein mögliches Spinquenching, wie durch die modellierten Spin-Valley Kurven angezeigt. Die IR-PD Spektren aller Spezies (5,m), m = 1 - 13, zeigen IR-PD-Signale, die end-on und/oder side-on μ_2 - λ N₂: λ N₂ Liganden entsprechen. Das IR-PD Spektrum der ersten Adsorbatspezies, (5,1), zeigt deutlich, dass eine spontane N₂ Aktivierung verhindert ist.

[Ta₆(N₂)_m]⁺ Die aufgezeichnete Kinetik der Clusterspezies (6,m) zeigt eine typische stufenweise Adsorption von bis zu 16 N₂ Molekülen. Die gemessenen IR-PD Spektren der N₂ Adsorptionsspezies (6,m) zeigen zahlreiche IR-PD Signale in den Spektralbereichen für end-on und side-on koordinierte N₂ Liganden. DFT Modellierungen prognostizieren für die adsorbierten N₂ Moleküle eine Abfolge von zunächst end-on koordinierten N₂ Molekülen und für den weiteren Verlauf der Adsorptionskette eine Mischung aus end-on und side-on koordinierten N₂ Molekülen.

[Ta₇(N₂)_m]⁺ Für Ta₇⁺ zeigt die Adsorptionskinetik ebenfalls eine typische schrittweise Adsorption von bis zu 16 N₂ Molekülen. Die (7,m) Adsorbatkomplexe erfahren jedoch signifikante N₂ Desorptionsreaktionen lange vor Erreichen des endgültigen Gleichgewichts. Dies deutet auf eine kontinuierliche Reorganisation der Adsorbatschale hin. Die aufgenommenen IR-PD Spektren zeigen zahlreiche Banden, welche auf N₂ Liganden hindeuten, die end-on an einzelne Tantalzentren binden. Ab (7,4) koordinieren weitere N₂ Liganden in einem side-on μ₂-N₂-Motiv an die Ta₇⁺ cluster.

[Ta₈(N₂)_m]⁺ Die aufgezeichnete Kinetik von (8,m) erlaubt ebenso wie die von (5,m) für kurze Kinetikmesszeiten Fits in Form von sukzessiver Adsorption und frühen Desorptionsreaktionen. Allerdings zeigen die Ionenintensitäten bei langen Kinetikmesszeiten kontraintuitive Verläufe, die eine eindeutige Interpretation erschweren. Die beobachteten IR-PD-Banden von (8,m) stammen wahrscheinlich von end-on μ₁ koordinierten N₂ Liganden.

Das derzeitige Verständnis der Kinetiken von (5,m) und (8,m) bietet einen Ausgangspunkt für weitere Untersuchungen. Die Anwendung alternativer Modellierungsschemata, die über das im Rahmen dieser Arbeit angewendete, einfache schrittweise Adsorptionsmodell hinausgehen, konnten in der Vergangenheit für andere Metallclusterspezies (Fe₁₇⁺ und Fe₁₈⁺) erfolgreich angewendet werden [2]. Die Anwendung ähnlicher Szenarien auf die aktuellen Fälle Ta₅⁺ und Ta₈⁺ könnte ein vielversprechender Ansatz für eine tiefergehende Interpretation der Adsorptionskinetik sein. Zukünftige Studien könnten weiterhin umfassende DFT-Modellierungen der (höher) geladenen Clusteradsorbatkomplexe (n,m), n = 5 - 8, beinhalten. Eine erfolgreiche Identifizierung der Geometrien der Clusteradsorbatkomplexe könnten weitreichende Interpretationen der gemessenen IR-PD Spektren erlauben. Die bisher durchgeführten IR-PD Studien liefern einen starken, aber nur indirekten Beweis für die Aktivierung und Spaltung von N₂ durch Ta₂₋₄⁺ Cluster. Ein direkter Nachweis könnte durch die spektroskopische Untersuchung von Ta-N Fingerprintschwingungen erbracht werden. Dazu wäre eine andere Strahlungsquelle erforderlich. Zweifarben IR Experimente, bei denen ein Laser zur Überwindung der Aktivierungsbarriere und ein zweiter Laser zur Untersuchung der aktivierten Spezies verwendet wird, können ebenfalls ein Mittel zur weitergehenden Untersuchung der aktivierten Spezies sein.

H₂ Adsorption an kationische Ta₂₋₈⁺ Cluster

Für die schrittweise H₂ Adsorption an gröÙenselektierte Tantalclusterkationen Ta_n⁺, n = 2-8, ergibt sich, dass die Adsorptionsgrenzen m_{max} der Zunahme der ClustergröÙe n annähernd mit einer Stöchiometrie von 1:2 folgen. Das Gesamtbild aus Adsorptionskinetiken, IR-PD Messungen und DFT Modellierungen ergibt, dass die H₂ Adsorptionsprozesse und die daraus resultierenden Clusteradsorbatkomplexe von der ClustergröÙe n und der Adsorbatbeladung m der Cluster abhängen. Das kleinste Tantalclusterkation, Ta₂⁺, erweist sich unter den Bedingungen des Experimente als chemisch inert gegenüber H₂.

[Ta₃₋₅(H₂)_m]⁺ und [Ta₇(H₂)_m]⁺ Adsorptionskinetiken und IR-PD Messungen sowie DTF-Modellierungen zu möglichen (n,m) Clustergeometrien begründen die Hypothese, dass Ta_n⁺ Cluster, n = 3-5, zwei unterschiedliche nacheinander ablaufende H₂ Adsorptionsprozessen unterlaufen: Beim ersten Typ handelt es sich um dissoziative H₂ Adsorptionsreaktionen. Diese laufen sehr schnell und ohne konkurrierende Desorptionsreaktionen ab. Der zweite Typ ist charakteristisch für langsame molekulare Adsorptionsreaktionen, begleitet von Desorptionsreaktionen. Der Schwellenwert ist die Vollendung der ersten Adsorbatschale bis (n,m = n). Die molekular adsorbierten H₂ Moleküle sind weniger stark an den Clusterkern gebunden als die dissoziativ adsorbierten H₂ Liganden und können daher desorbieren. Im speziellen Fall des (5,12) Clusters koordinieren die letzten beiden H₂ Liganden sogar in einer formalen dritten Adsorbathülle. Die vorhergesagte Clustergeometrie, deren Zuordnung durch gemessene IR-PD Signale und Geschwindigkeitskonstanten aus kinetischen Messungen getroffen werden kann, deutet darauf hin, dass auch eine späte H₂ Aktivierung in der Adsorptionskette möglich ist. Das Gesamtbild der Prozesse entlang der H₂ Adsorptionskette von Ta₇⁺ zeigt eine weniger signifikante Abnahme der Adsorptionsraten jenseits der formalen ersten Adsorptionsschale als für Ta₃⁺, Ta₄⁺ und Ta₅⁺ beobachtet. Die signifikanten Desorptionsraten, welche auftreten bevor m = n erreicht ist, deuten auf eine vorzeitige Fertigstellung der ersten Adsorbatschale hin. Die aufgezeichneten IR-PD-Spektren geben jedoch Hinweise auf eine dissoziative Adsorption von H₂ Molekülen innerhalb der formalen ersten Adsorbathülle um den Ta₇⁺ cluster. Die Photonenenergie des IR Lasers könnte eine Reorganisation des Clusterkerns bewirken, was schließlich den Weg für die Dissoziation der ursprünglich molekular adsorbierten H₂ Moleküle ebnet. Darüber hinaus

sind alle H₂ Moleküle jenseits von $m = n$ an den Ta₇⁺ Cluster sehr wahrscheinlich molekular an den Cluster koordiniert.

[Ta₆(H₂)_m]⁺ und [Ta₈(H₂)_m]⁺ Die Charakteristiken der H₂ Adsorption an Ta₆⁺ und Ta₈⁺ unterscheiden sich deutlich von der H₂ Adsorptionscharakteristik an Ta₃₋₅⁺ und Ta₇⁺: Im Fall von (6,m) verzögern die langsamen ersten Adsorptionsprozesse die gesamte Adsorptionskette. Im weiteren Verlauf dieser Adsorptionskette treten jedoch Reaktionsprozesse auf, welche wiederum zu schnell sind, um alle (6,m) Spezies massenspektrometrisch beobachten zu können. Ta₈⁺ zeigt ebenfalls ein außergewöhnliches H₂ Adsorptionsverhalten. Die aufgezeichneten Ionenintensitäten zeigen zunächst die schrittweise Adsorption von H₂ Molekülen, wodurch die Spezies (8,5) als Adsorptionszwischenmaximum entsteht. Dieses Zwischenmaximum adsorbiert wiederum verzögert weitere H₂ Moleküle. Die Ionenintensitäten der Spezies (8,7) deuten auf eine Reorganisation der Adsorbathülle und/oder auf Clusteradsorbat-induzierte Relaxationsprozesse hin. IR-PD Untersuchungen der Clusteradsorbat-spezies (6,m) und (8,m) geben Hinweise darauf, dass die ersten H₂ Moleküle dissoziativ an die Cluster adsorbiert werden. Für den weiteren Verlauf der H₂ Adsorptionskette lässt sich schließen, dass die formale erste Adsorbathülle abgeschlossen sein könnte noch bevor $m = n$ erreicht ist. Es wäre denkbar, dass manche Ta Kernatome in diesen Clustern eine hohe Nachbarschaftskoordination mit anderen Ta Zentren aufweisen und dadurch an der Koordinierung von Hydriden gehindert werden.

Das derzeitige Verständnis der H₂ Adsorption an Ta_n⁺ Cluster könnte von weiteren Untersuchungen profitieren, entweder um die Schlussfolgerungen der vorliegenden Studien zu untermauern oder um das bestehende Gesamtbild zu erweitern. Zukünftige Studien könnten umfassende DFT Modellierungen weiterer Clusteradsorbatkomplexe (n,m) umfassen. Eine erfolgreiche Identifizierung der Geometrien der Clusteradsorbatkomplexe könnten weitergehende Interpretationen der gemessenen IR-PD Spektren erlauben. Die bisher durchgeführten IR-PD Untersuchungen liefern deutliche Hinweise auf die Aktivierung und Spaltung von H₂ durch Ta₃₋₈⁺ Cluster. Der direkte Nachweis von molekular adsorbiertem H₂ könnte durch die spektroskopische Untersuchung der H-H Schwingungen erfolgen. Dazu wäre eine andere Strahlungsquelle erforderlich. Zweifarben IR Experimente, bei denen

ein Laser zur Überwindung der Aktivierungsbarriere und ein zweiter Laser zur Untersuchung der aktivierten Spezies verwendet wird, können ebenfalls eine Möglichkeit zur weitergehenden Untersuchung der aktivierten Spezies bieten. Die Kinetik von (8,m) könnte den Ausgangspunkt für weitere Untersuchungen, wie z.B. ein alternatives Modellierungsschema, darstellen. In der Vergangenheit wurden solche alternativen Ansätze, die über ein einfaches schrittweises Adsorptionsschema hinaus gehen, bereits erfolgreich für Fe_{17}^+ und Fe_{18}^+ angewendet. [2]

N_2 Adsorption an anionische Ta_{4-10}^- Cluster

Die Untersuchung der N_2 Adsorption an kleine Tantalclusteranionen Ta_n^- , $n = 4-10$, ergibt, dass die Signalintensitäten der anionischen Cluster deutlich geringer sind als die der entsprechenden positiv geladenen Cluster. Die aufgenommenen Massenspektren zeigen jedoch, dass die Fähigkeit der anionischen Tantalcluster N_2 zu absorbieren stark von der Clustergröße n abhängt. Die Clustergröße $n=9$ ist die Mindestgröße zur Bildung stabiler und nachweisbarer Clusteradsorbatspezies $[\text{Ta}_n(\text{N}_2)_m]^-$. Eine Adsorption von N_2 an kleinere anionische Cluster Ta_{4-8}^- und die Stabilisierung der entsprechenden Clusteradsorbatkomplexe $[\text{Ta}_{4-8}(\text{N}_2)_m]^-$ scheint nicht möglich zu sein. Weitergehende Untersuchungen der N_2 Adsorptionsprozesse und der beteiligten Spezies wurden durch die geringen Ionenintensitäten der Clusterspezies erschwert.

Jenseits der vorliegenden Dissertation wäre die Untersuchung einer möglichen N_2/H_2 Co-Adsorption ein logischer nächster Schritt. Die in dieser Arbeit dargestellten und zusammengetragenen Ergebnisse zur Adsorption von N_2 und H_2 an Tantalclusterionen Ta_n^\pm ergeben ein umfassendes Bild der elementaren Adsorptionsschritte und -mechanismen und bieten eine ideale Grundlage für solche Co-Adsorptionsstudien.

References

- [1] C. Geng, J. Li, T. Weiske, H. Schwarz, *Proceedings of the National Academy of Sciences* **2018**, *115*, 11680–11687.
- [2] A. Straßner, M. P. Klein, D. V. Fries, C. Wiehn, M. E. Huber, J. Mohrbach, S. Dillinger, D. Spelsberg, P. B. Armentrout, G. Niedner-Schatteburg, *The Journal of Chemical Physics* **2021**, *155*, 244306.

APPENDIX: SELECTED JOINED PUBLICATIONS

A.1 Kinetics of Stepwise Nitrogen Adsorption by Size- Selected Iron Cluster Cations: Evidence for Size- Dependent Nitrogen Phobia

A.1.1 Preamble

The following chapter is a reprint of a publication in the journal “*The Journal of Chemical Physics*”

A. Straßner, M. P. Klein, M. E. Huber, J. Mohrbach, S. Dillinger, G. Niedner-Schatteburg and myself conducted the experiments. A. Straßner and C. Wiehn conducted the quantum chemical calculations. A. Straßner, G. Niedner-Schatteburg and myself conducted the kinetic fits algorithms. A. Straßner, P. B. Armentrout and G. Niedner-Schatteburg evaluated all data and wrote the manuscript, which all authors agreed to.

Full Reference

Kinetics of Stepwise Nitrogen Adsorption by Size- Selected Iron Cluster Cations: Evidence for Size-Depen- dent Nitrogen Phobia

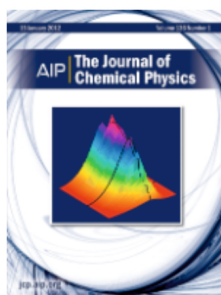
A. Straßner, M. P. Klein, **D. V. Fries**, C. Wiehn, M. E. Huber, J. Mohrbach, S. Dillinger, D. Spelzberg, P. B. Armentrout, G. Niedner-Schatteburg, *The Journal of Chemical Physics* **2021**, 155, 244306.

<https://doi.org/10.1063/5.0064965>

A.1.2 Reprint

Reprint permission

Reproduced with permission of AIP Publishing.



Kinetics of stepwise nitrogen adsorption by size-selected iron cluster cations: Evidence for size-dependent nitrogen phobia

Author: Straßner, Annika; Klein, Matthias P.

Publication: Journal of Chemical Physics

Publisher: AIP Publishing

Date: Dec 29, 2021

Rights managed by AIP Publishing.

Creative Commons

This is an open access article distributed under the terms of the [Creative Commons CC BY](https://creativecommons.org/licenses/by/4.0/) license, which permits unrestricted use, distribution, and reproduction in any medium, provided the original work is properly cited.

You are not required to obtain permission to reuse this article.

Kinetics of stepwise nitrogen adsorption by size-selected iron cluster cations: Evidence for size-dependent nitrogen phobia

Cite as: J. Chem. Phys. 155, 244306 (2021); doi: 10.1063/5.0064965

Submitted: 28 July 2021 • Accepted: 2 December 2021 •

Published Online: 29 December 2021



Annika Straßner,¹ Matthias P. Klein,¹ Daniela V. Fries,¹ Christopher Wiehn,¹ Maximilian E. Huber,¹ Jennifer Mohrbach,¹ Sebastian Dillinger,¹ Dirk Spelsberg,¹ P. B. Armentrout,² and Gereon Niedner-Schatteburg^{1,a)}

AFFILIATIONS

¹Fachbereich Chemie and Forschungszentrum OPTIMAS, Technische Universität Kaiserslautern, 67663 Kaiserslautern, Germany

²Department of Chemistry, University of Utah, Salt Lake City, Utah 84112, USA

^{a)}Author to whom correspondence should be addressed: gns@chemie.uni-kl.de

ABSTRACT

We present a study of stepwise cryogenic N₂ adsorption on size-selected Fe_n⁺ ($n = 8-20$) clusters within a hexapole collision cell held at $T = 21-28$ K. The stoichiometries of the observed adsorption limits and the kinetic fits of stepwise N₂ uptake reveal cluster size-dependent variations that characterize four structural regions. Exploratory density functional theory studies support tentative structural assignment in terms of icosahedral, hexagonal antiprismatic, and closely packed structural motifs. There are three particularly noteworthy cases, Fe₁₃⁺ with a peculiar metastable adsorption limit, Fe₁₇⁺ with unprecedented nitrogen phobia (inefficient N₂ adsorption), and Fe₁₈⁺ with an isomeric mixture that undergoes relaxation upon considerable N₂ uptake.

© 2021 Author(s). All article content, except where otherwise noted, is licensed under a Creative Commons Attribution (CC BY) license (<http://creativecommons.org/licenses/by/4.0/>). <https://doi.org/10.1063/5.0064965>

I. INTRODUCTION

The investigation of transition metal (TM) clusters and their ligation is a field of significant importance. The structural similarities of such clusters to catalytically active surfaces justify a quest for enhanced knowledge of cluster structure and properties.¹⁻⁵ Such knowledge might enable the rational design of improved catalysts for industrial use. Gas phase clusters serve as model systems for active sites on surfaces, and they provide for a cluster-size dependent tuning of metal mediated chemistry.^{2,6}

Early cluster studies reveal significant changes with the cluster size in their chemical and physical properties, which level off toward the bulk limit according to scaling laws.⁷⁻¹⁴ Particularly, iron clusters show a strong size effect in their reactions with small molecules; numerous experimental and theoretical studies document the gas-phase reactivity of negatively charged, neutral, and positively charged Fe_n clusters with small diatomic molecules, such

as H₂,^{8,9,15-17} D₂,^{18,19} N₂,²⁰ O₂,^{21,22} and CO,^{23,24} as well as the reactivity with larger molecules, such as ammonia,^{8,25-29} water,^{8,30,31} carbon dioxide,³² ethene,³³ and benzene.³⁴⁻³⁶

Although often obedient to scaling laws, iron clusters allow themselves singular exceptions, which are often coined “magic numbers” that tentatively relate to particular structural motifs. For example, the mass spectra of Fe_n⁺ reveal a sequence of magic numbers $n = 7$ (pentagonal bipyramid), 13 (icosahedron), 15 (bcc motif), and 19, 23 (polyicosahedron).³⁷ Neither assumptions regarding electronic shell closures³⁸ nor packing of hard spheres³⁹ help to explain these magic numbers. In remarkable contrast, collision-induced dissociation (CID) experiments do verify enhanced stabilities of the listed “magic numbers,” $n = 7, 13, 15,$ and 19 for ionic and neutral iron clusters.⁴⁰ Spin-polarized density functional theory (DFT) calculates high stabilities of small iron clusters with 7, 13, and 15 atoms and indicates the important role of magnetism in determining stabilities and magic numbers.⁴¹

A. Magnetism

The magnetism of small iron clusters is of interest by itself. The average magnetic moments per atom of neutral iron clusters as determined by Stern–Gerlach experiments are enhanced with respect to those of bulk iron.^{42,43} Small cluster ferromagnetism below 30 atoms is atom-like. The magnetic moments of large clusters approach the bulk limit, whereas some oscillations might relate to surface-induced spin-density waves, likely indicating some spin relaxation.^{42,44} Cryogenic homonuclear iron clusters Fe_n exist in two states with distinct magnetic moments μ , indicating distinct valences and metastability. The interpretation concluded there was Heisenberg-like ferromagnetism with a ground state configuration $3d_t^5 3d_l^2 4s^1$ ($S = 3/2$) yielding a magnetic moment of $3 \mu_B$ /atom and an excited state with $3d_t^4 3d_l^3 4s^1$ ($S = 1/2$) yielding a magnetic moment of $1 \mu_B$ /atom. A Falicov–Kimball model serves to explain metastability and near degeneracy of both states. Of course, non-scalable cluster size effects are much beyond such a simplified approach.⁴⁵

The Fe_{13}^+ cluster has drawn special attention because of its anomalously low magnetic moment that arises from antiferromagnetic coupling of the central atom to the atoms in the surrounding shell.⁴⁶ There is some controversy whether the low magnetic moment manifests a symmetry-driven quenching of the local spin moments of all cluster atoms with some larger quenching of the central atom.⁴⁷ Another DFT study found a magnetic transition upon ionization, namely, from a ferromagnetic-like configuration to an antiferromagnetic one with some T_h -deformation.⁴⁸ Other icosahedral metal clusters M_{13} received considerable attention in various contexts.^{49–53}

B. Further quantum chemical modeling

The inseparable structure–magnetism–stability relationship imposes a significant challenge for the quantum chemical modeling of Fe_n clusters. Early on, such studies revealed the tendency of Fe clusters toward extended bond lengths, narrower d-band widths, and maximum pairs of nearest-neighbor bonds, all of which maximize ferromagnetic stability.⁵⁴ In contrast, the most stable small Fe_n structures evaluated with DFT and molecular dynamics simulations in other studies are compact with short bond lengths below bulk values—but agree on high magnetic moments $\approx 3 \mu_B$ /atom,^{55,56} as confirmed elsewhere.⁵⁷ Some structural magnetic discontinuities are predicted for Fe_n at $n = 6$ and $n = 10$.⁵⁸

A more recent systematic DFT survey of Fe_n , Fe_n^- , and Fe_n^+ ($n = 7–20$) obtained ionization energies, vertical electron detachment energies, binding energies, and total magnetic moments that nicely reproduce the published experimental findings. Charge states and sizes modulate the obtained icosahedral structural motifs with indications of distorted hexagonal antiprismatic structures for $n = 14$ and beyond, coming back to capped icosahedral structures at $n = 19$.⁵⁹ Further studies confirm this geometrical evolution, and they manage to predict further experimental values, such as magnetic moments, ionization energies, electron affinities, fragment energies, and polarizabilities.^{24,60,61} Further advanced modeling deals with noncollinear magnetism, which is beyond the scope of the current study.^{62–64}

C. Catalytic N_2 activation

The physisorption and chemisorption of N_2 on metal surfaces have been a topic of considerable interest⁶⁵ because of its intimate connection with many catalytic processes, notably the Haber–Bosch process for ammonia production. Extensive investigations on TM clusters have been conducted to enable N_2 fixation under mild conditions and to elucidate efficient processes of N_2 activation and transformation.^{66–68} It is assumed that the rate-determining step in the industrial ammonia synthesis is the dissociation of N_2 using iron as a catalyst.^{69,70} The equivalent bottleneck in enzymatic N_2 activation is its fixation by the nitrogenase enzyme at room temperature.⁷¹

D. N_2 adsorption on Fe surfaces

In the context of industrial N_2 activation and enzymatic activation, it is the initial adsorption that precedes and likely directs the activation. Iron catalyzes the breaking of the strong N–N triple bond. It has been shown experimentally that N_2 adsorption on the Fe(111) surface takes place either in an α - N_2 motif (strongly inclined to the surface) or in a γ - N_2 motif (perpendicular to the surface), as elucidated by angle resolved photoelectron spectra and *ab initio* generalized valence bond calculations.⁷² Further spectroscopic studies of N_2 adsorbed on the Fe(111) surface refined these findings and revealed three characteristic α -, β -, and γ -states, which refer to side-on chemisorption (α), head-on chemisorption (γ), and dissociative chemisorption (β) to the metal surface atoms.^{65,73} Calculations identified two dissociation channels, one with a low energy barrier but a high entropy barrier and one highly activated “direct channel” with a completely new precursor state.⁷⁴ A subsequent DFT study predicted that the most favorable N_2 adsorption occurs on a quadruple hollow site, such as that on a Fe(110) surface.⁷⁵ Early combined matrix isolation and DFT studies of $\text{Fe}_{1,2,3}(\text{N}_2)_n$ complexes concluded that there was a strong preference for N_2 end-on coordination in the ground state species.^{76,77} Recent DFT calculations have modeled iron nitride cluster coalescence and concomitant total spin reduction.⁷⁸

E. IR spectroscopy of iron cluster adsorbate complexes

Exclusively dissociative H_2 adsorption to Fe_n^+ clusters yields hydride clusters, and their IR spectroscopic characterization reveals twofold or threefold coordinated hydrides, whereas extended metal surfaces prefer exclusively high coordination, threefold or higher, when migrating into the bulk.⁷⁹ Somewhat surprisingly, water hydrolysis by cationic Fe clusters increases with cluster size.⁸⁰

F. Our previous work of relevance

The University of Utah laboratory has examined the chemistry of iron cluster cations using guided ion beam tandem mass spectrometry (GIBMS) instrumentation. These include a determination of the cluster binding energies by collision-induced dissociation (CID) with Xe.^{40,81} Further studies examined reactions of Fe_n^+ with D_2 ($n = 2–15$),¹⁹ O_2 ($n = 2–18$),²² CO_2 ($n = 1–18$),³² and CO ($n = 1–17$).²³ CID studies of Fe_mO_n^+ ($m = 1–3$, $n = 1–6$)

A.1. Kinetics of Stepwise Nitrogen Adsorption by Size-Selected Iron Cluster Cations: Evidence for Size-Dependent Nitrogen Phobia

provided additional thermochemistry for these small iron oxide cluster cations.²¹ Of direct relevance to the present work, reactions of Fe_n^+ ($n = 1-19$) with N_2 were examined and Fe_n^+-N and Fe_n^+-2N bond energies were measured.²⁰ An activation barrier of 0.48 ± 0.03 eV was determined for activation of N_2 by the larger clusters ($n = 12, 15-19$). Fe_n^+-N bond energies were also determined in reactions with ND_3 ($n = 2-10, 14$).²⁹

G. TUK studies

In complement to these GIBMS studies at the University of Utah, the Technische Universität Kaiserslautern (TUK) laboratory utilizes a tandem cryo ion trap instrument,^{32,83} which allows the study of the adsorption and reaction kinetics of clusters under single collision conditions at temperatures down to 11 K as well as Infrared Photon Dissociation (IR-PD) spectroscopy. Prior studies of cationic nickel clusters established a concept of rough and smooth cluster surfaces,⁸⁴ and the combination of N_2 adsorption kinetics and IR spectroscopy allowed for systematic refinement of cluster size dependencies and structural changes.⁸⁵ The concept proved transferable by application to cationic rhodium clusters⁸⁶ and cationic cobalt clusters.⁸² N_2 and H_2 coadsorption on cationic ruthenium clusters yielded distinguishable IR fingerprints when changing the sequence of adsorptions.⁸⁷ Most recently, cationic tantalum clusters were investigated for their potential for N_2 activation, and a multidimensional path for N_2 cleavage was identified as an *across edge-above surface* (AEAS) mechanism.⁸⁸ Complementary investigations by gas phase X-ray Magnetic Circular Dichroism (XMCD) have characterized the spin and orbital contributions to the magnetic moments of Fe, Co, and Ni cluster cations.^{14,89}

In this work, N_2 adsorption onto cationic iron clusters $[\text{Fe}_n(\text{N}_2)_m]^+$ ($n = 8-20$) is elucidated by kinetics investigation under single collision conditions. Strong support of the present findings are obtained through our complementary cryogenic infrared spectroscopy study,⁹⁰ which we will refer to in the following as [IRS]. The combined studies provide insight into the metal-adsorbate bonding and unravel structure-reactivity relationships and their variations with cluster sizes.

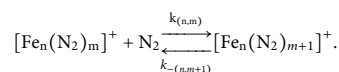
II. EXPERIMENTAL AND COMPUTATIONAL METHODS

A customized Fourier Transform Ion Cyclotron Resonance (FT-ICR) mass spectrometer (Apex Ultra Bruker Daltonics) was used to perform all the experiments. The Fe clusters were generated by a home-built laser vaporization cluster ion source (LVAP), as described before.^{91,92} The iron atoms were evaporated from a rotating 0.4 mm thick isotopically enriched ⁵⁶Fe foil (99.93%, Oak Ridge National Laboratories) using the second harmonic of a pulsed Nd:YAG laser (Innolas *Spotlight 300*, 20 Hz). The resulting hot plasma was captured by a He gas pulse (40 μs , 15 bars) created by a homebuilt piezoelectric valve.⁹³ The atoms and ions in the plasma cooled down and aggregated to clusters in the subsequent jet expansion through a 69 mm long channel (\varnothing 2 mm) into vacuum (10^{-7} mbar). The cluster beam was skimmed, and after passing a 90° ion beam bender, the clusters were mass selected using a quadrupole mass filter and injected into a cryogenic hexapole ion trap. The ion trap was cooled to 26 K by a closed cycle He cryostat. To achieve sufficient nitrogen attachment, the pressure in the

ion trap was increased from 1.2×10^{-7} mbar up to a maximum of 5.0×10^{-7} mbar. To accomplish efficient trapping and cooling of the ions, additional helium was introduced and the pressure increased to 4.0×10^{-6} mbar. The buffer and the reaction gas were introduced continuously. After storing the mass-selected ions for various times (0–15 s), the cluster adsorbate complexes of the form $[\text{Fe}_n(\text{N}_2)_m]^+$ (n, m) were guided by electrostatic lenses into the FT-ICR cell. The ICR uses a so-called “infinity” type⁸⁸ cell, which was held at temperatures below 10 K with a closed cycle He cryostat to prevent heating of the clusters by black-body radiation. The ICR cell was used to isolate and detect the formed $[\text{Fe}_n(\text{N}_2)_m]^+$ (n, m) cluster adsorbate complexes.

To investigate the cationic iron clusters and their nitrogen adducts, we used adsorption kinetics originating from reaction delay scans. Each recorded mass spectrum consists of an average of 40 mass spectra with fixed hexapole collision cell delays of 0–15 000 ms. We stored the generated $[\text{Fe}_n(\text{N}_2)_m]^+$ (n, m) cluster adsorbate complexes in the cryogenic hexapole under isothermal conditions at 26 K. N_2 addition to the Fe cluster cations takes place in bimolecular collisions, where the clusters initially act as their own heat bath. Helium buffer gas collisions start to re-thermalize the cluster adsorbate complexes on a millisecond time scale, while subsequent N_2 collisions and additions take place on a much longer kinetics time scale. Also any radiative stabilization would be much slower. Note that the kinetic energy dependence of $\text{Fe}_n^+ + \text{CO}$ association reactions was determined before, and these data served to model the bimolecular association processes convincingly over a time scale of 0.1 ms.²³ In the ICR cell, the absence of He buffer gas means that any stabilization of the complexes observed probably occurs by additional collisions with the N_2 gas present, although the longer time scale might also permit some radiative stabilization. This is consistent with the failure to observe these limits for smaller cluster sizes in the ICR cell (see below).

In all the investigated cases ($n = 8-20$), stepwise N_2 uptake reached an adsorption limit m_{max} . Fitting the experimental data with a pseudo-first-order-kinetic (“evofit” program⁹⁴), we obtained the relative rate constants for N_2 adsorption $k_{(n,m)}$ for each step $m \rightarrow m+1$ and for N_2 desorption $k_{-(n,m)}$ for each step $m+1 \rightarrow m$,



In the following plots, the variation of the background signal (gray area) relates to normalization of varying species intensities. Although these measured data and their fits could be displayed in several ways (Fig. S19), for the following plots, we chose a semi-logarithmic scale.

The absolute rate constants $k_{(n,m)}^{\text{abs}}$ are calculated from the relative rate constants $k_{(n,m)}$ with the absolute N_2 gas number densities $\rho_{\text{N}_2}(T)$ as the conversion factor,

$$k_{(n,m)}^{\text{abs}} = k_{(n,m)} / \rho_{\text{N}_2}(T).$$

We obtain approximate values for $\rho_{\text{N}_2}(T)$ indirectly from the pressure in the surrounding chamber $p_c^{(300\text{ K})}$ and an effective geometry factor c_{app} ,

$$\rho_{\text{N}_2}(26\text{ K}) = \frac{c_{\text{app}} P c}{k_B T_{300\text{ K}}}.$$

The geometry factor, c_{app} , has a significant temperature dependence and has been evaluated as 1.8 ± 0.4 at 26 K with a net uncertainty of $\pm 50\%$ by numerous kinetic studies of transition metal cluster cations with neutral reactants at cryogenic temperatures.⁸⁵

The average dipole orientation theory (ADO)^{95,96} extends the classical Langevin collision rate constant of ions with neutrals⁹⁷ toward polar molecules and is based on a classical trajectory of a linear dipole in the field of a point charge. The collision rate constant k^{ADO} gives the theoretical limit of the absolute rate constants,

$$k^{\text{ADO}} = \frac{q}{2\epsilon_0\sqrt{\mu}} \left(\sqrt{\alpha} + c\mu_D \sqrt{\frac{2}{\pi k_B T}} \right),$$

where q is the charge of an electron, ϵ_0 is the permittivity of vacuum, μ is the reduced mass of the cluster adsorbate complex, α is the polarizability ($\text{C}^2\text{m}^2/\text{J}$), μ_D is the dipole moment (D), and k_B is Boltzmann's constant (J/K). The parameter c lies between 0 and 1 and can be expressed by the polarizability volume α' and μ_D .⁹⁸ Note that the vanishing dipole moment of N_2 makes k^{ADO} become identical to the Langevin rate constant.

The absolute reaction efficiency γ shows the probability of a reaction occurring after a collision between the cationic iron cluster and the N_2 . It is calculated by the quotient of the absolute rate constant (k^{abs}) and the collision rate constant (k^{ADO}).

Kummerlöwe and Beyer introduced two models for calculating the collision rate constants of ionic clusters with neutral molecules: the hard sphere average dipole orientation model (HSA) and the surface charge capture model (SCC).⁹⁹ In both models, the cluster and the neutral reaction partner are assumed as hard spheres, and the charge is assumed as point charge. The difference is in the location of the charge. For the HSA model (k^{HSA}), the charge is located in the center of the cluster, while in the SCC model (k^{SCC}), the charge is freely movable but changes to the cluster surface during the attractive interaction with the neutral, polarizable collision partner.

III. RESULTS AND DISCUSSION

A. Molecular nitrogen adsorption on iron cluster cations: Trends and limits of adsorption

We have investigated the trapped $[\text{Fe}_n(\text{N}_2)_m]^+ = (n, m)$ clusters in the cryogenic hexapole trap under isothermal conditions at 26 K. We find a successive stepwise gain of +28 m/z as the trapping time is increased. The recorded mass spectra of the exposed Fe_n^+ cluster ($n = 8\text{--}20$) species thus reveal stepwise adsorption of molecular nitrogen.

N_2 uptake seems to reach limits beyond which further increases of N_2 pressure (up to 5×10^{-7} mbar) and/or trapping–exposure time (beyond 20 s) do not lead to a further increase in N_2 uptake by the iron clusters. In order to quantify this phenomenon, we define an adsorption limit by the particular value m_{max} of the largest detectable complex (n, m) as obtained by our setup.

Of course, there is always a dynamic adsorption/desorption equilibrium $(n, m_{\text{max}}) \rightleftharpoons (n, m_{\text{max}+1})$. However, this equilibrium is clearly on the side of (n, m_{max}) , and $(n, m_{\text{max}+1})$ does not populate. The forward rate constant $k_{m_{\text{max}}}$ is slow, the backward rate constant $k_{-m_{\text{max}+1}}$ is fast, and their ratio is large, which means that the equilibrium constant is small, and thus, the Gibbs energy $\Delta_r G^0(n, m_{\text{max}})$ of adsorption diminishes. In the recorded data, we find cases where the $(n, m_{\text{max}-1}) \rightleftharpoons (n, m_{\text{max}})$ equilibrium is on the side of m_{max} [Fig. 1(a)], and we find cases where it is on the side of $m_{\text{max}-1}$ [Fig. 1(b)].

Beyond such adsorption limits m_{max} , we find some cases with retardation in the uptake of N_2 $(n, m^*) \rightleftharpoons (n, m^* + 1)$ at particular values m^* , which therefore become the most intense cluster adsorbate species. In four cases, $n = 11, 12, 18,$ and 19 , we observe $m^* = m_{\text{max}}$ [e.g., Fig. 1(a)]; in another four cases, $n = 8, 9, 10,$ and 20 , we find $m^* = m_{\text{max}-1}$ [e.g., Fig. 1(b)]; and there are three further cases, $n = 14, 15,$ and $16, (17)$, where $m^* = m_{\text{max}-2}$. The $n = 13$ cluster is a special case where $m^* = m_{\text{max}-6}$. In Table I, we list m^* only for those cases where it differs from m_{max} . Beyond these effects at or close to saturation of N_2 adsorption, we find additional kinetic retardation of N_2 uptake at much lower levels of N_2 coverage of Fe cluster species. We list such findings as metastable adsorption limits m_x .

The thus defined three types of particular adsorbate levels, m_{max} , m^* , and m_x , serve as guidelines for some elucidation of adsorbate bonding and cluster geometries. Notably, $m_{\text{max}} : n \leq 1$ in all investigated cases, $n = 7\text{--}20$ (Fig. 2). We recognize four characteristic regions of (n, m_{max}) stoichiometries: small clusters, $n = 7$ and 8 , reveal $m_{\text{max}} = n$; mid-size clusters, $n = 9\text{--}13$, reveal $m_{\text{max}} = n - 1$; and large clusters, $n = 18\text{--}20$, reveal $m_{\text{max}} = n - 2$. Beyond these seemingly clear cases, there is a somewhat strange region of intermediate clusters, $n = 15\text{--}17$, where $m_{\text{max}} = n - 8$. The sole case of $(14, 8)$, which is $m_{\text{max}} = n - 6$, falls in between the mid-size cluster $m_{\text{max}} = n - 1$ region and the intermediate cluster region of $m_{\text{max}} = n - 8$.

In order to verify the found anomalies, we repeated our cryo adsorption experiments within the FT-ICR MS analyzing and trapping cell. This allows for a controlled variation of conditions in multiple regards (cf. Table S1 in the supplementary material). We found identical m_{max} results for $n = 16\text{--}19$ (Fig. 2, gray dots) as in the experiments that took place within the RF hexapole trap. For smaller clusters, $n \leq 15$, adsorption was too slow to reach m_{max} , presumably because there are insufficient thermalizing collisions in the ICR cell.

Some structural speculation seems possible. Regarding N_2 adsorption as a molecular titration of atomic surface binding sites—the ground-paving Langmuir picture—the results of Fig. 2 suggest that the small clusters ($n = 7$ and 8) possess “surface only” type structures, void of inner Fe atoms. Thus, each surface atom adsorbs a single N_2 and $m_{\text{max}} = n$. Mid-size clusters ($n = 9\text{--}13$) appear to possess a single Fe atom that is not accessible for N_2 adsorption. Thus, $m_{\text{max}} = n - 1$. Candidate structures include an $n = 13$ icosahedron and structures of smaller clusters that derive from it. In such cases, e.g., $n = 11$ and 12 , the former “inside” Fe atom starts to obtain some exposure to the outside, albeit by a shallow concave pocket. Apparently, N_2 does not coordinate to this semi hidden atom. Computed candidate structures for $n = 9$ and 10^{95} do not reveal such a concave pocket. All Fe atoms are

A.1. Kinetics of Stepwise Nitrogen Adsorption by Size-Selected Iron Cluster Cations: Evidence for Size-Dependent Nitrogen Phobia

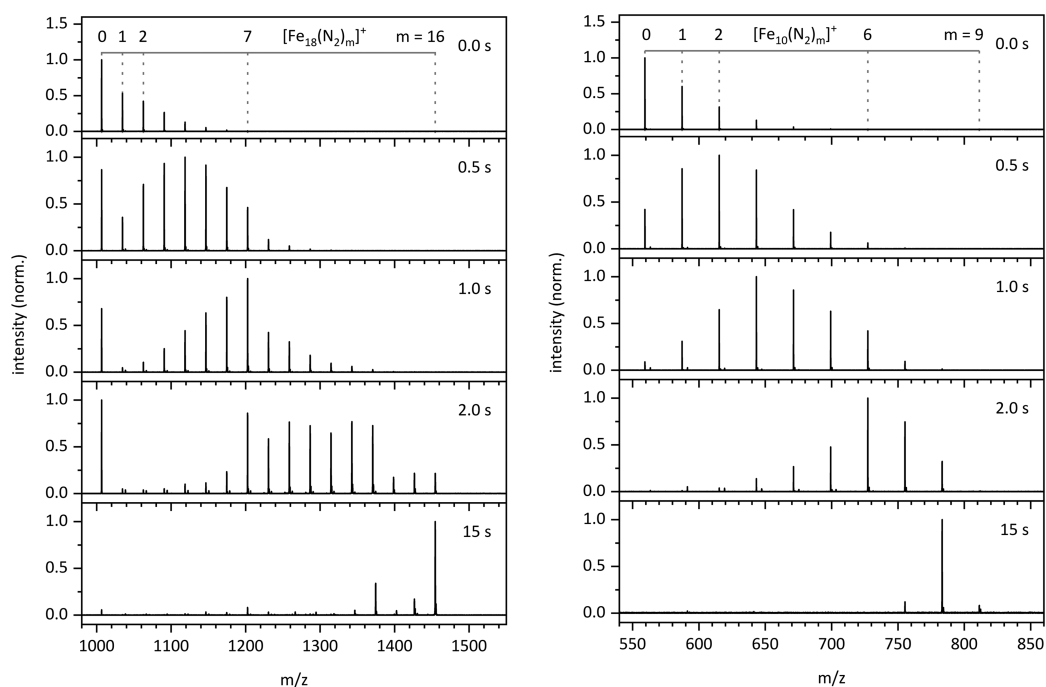


FIG. 1. Temporal evolution of the mass spectra of mass-selected $\text{Fe}_{18}^+ = (18, 0)$ clusters (the left stack) and of mass-selected $\text{Fe}_{10}^+ = (10, 0)$ clusters (the right stack). In both cases, the clusters are exposed to 2.1×10^{-7} mbar of N_2 in 3.8×10^{-6} mbar of He at 26 K for up to 15 s. Note the adsorption limits $m_{\text{max}} = 16$ and $m_{\text{max}} = 9$ and their relative intensities, the metastable adsorption limit $(n, m_x) = (18, 7)$, and the most intense cluster adsorbate complex $(n, m^*) = (10, 8)$. Minor peaks +4 amu beyond those of N_2 adsorbates signify single O_2 adsorbates which stem from residual O_2 background gas.

exposed and seem approachable from the outside by prospective adsorbates; however, both of these candidate structures possess a sole Fe atom that is eightfold coordinated to the next neighbor Fe atoms—with only fourfold to sixfold coordination of all the other Fe atoms.

Large clusters ($n = 18$ – 20) may continue with icosahedral binding motifs. A double icosahedron was predicted for $n = 19$.⁹⁵ Related structures may be derived by addition of a single capping atom or by removing a single atom, accompanied by some structural relaxation. In any case, we obtain candidate structures for $n = 18$ – 20 with two internal atoms that are not accessible to any adsorbates such that $m_{\text{max}} = n - 2$ behavior seems reasonable. Of course, it is conceivable—and in part likely—that a multitude of N_2 adsorbates could induce structural relaxation of the hosting surface.

In any case, the intermediate region, $n = 14$ – 17 , corresponds to none of these trends nor to the above structural arguments; its $m_{\text{max}} = n - 8$ behavior seems strange in terms of structural categories. This deems likely an alternative explanation in terms of electronic properties, and it is worthwhile to elucidate this phenomenon further.

B. Temperature dependence of the N_2 adsorption

We varied the cryo temperature of our RF hexapole trap within reasonable margins (21–28 K) in steps of 1 K and re-recorded adsorption limits for m_{max} of N_2 on Fe_n^+ clusters, $n = 8$ – 20 (Fig. 3). Note that in these experiments, we took care to stabilize the partial pressures within the RF hexapole trap to constant values, $p(\text{N}_2) = 2.4 \times 10^{-7}$ mbar and $p(\text{He}) = 3.6 \times 10^{-6}$ mbar, while we varied the N_2 pressure in the previous experiments (Fig. 2) as appropriate to achieve ultimate maxima of adsorption.

Besides the many details of these data, we find the general trend of high N_2 adsorbate loads at temperatures of 24 K and above and low N_2 loads below 24 K. This observation (from isothermal buffer gas experiments) is opposite to the expected equilibrium behavior of a rigid adsorber: Rising the temperature should ordinarily shift an adsorption/desorption equilibrium toward desorption. Instead, the higher temperature seems to assist in some kind of activation that allows for enhanced N_2 uptake—up to 26 K where we find the largest amounts of N_2 uptake. In the cases of some Fe_n^+ clusters, $n = 8$ – 10 and 15–17, the adsorption limit decreases somewhat in the 27 K and 28 K experiments. Note that we did take care in reproducing all of

TABLE I. Recorded adsorption limits m_{max} , most intense cluster adsorbate complexes m^* , and metastable adsorption limits m_x of N_2 adsorption on cationic Fe clusters Fe_n^+ , $n = 8-20$, in the RF hexapole trap at 26 K. For the corresponding graph, see Fig. S1 in the [supplementary material](#).

Cluster size n	Number of adsorbed N_2		
	m_x	m^*	m_{max}
8	4	7	8
9		7	8
10		8	9
11			10
12	7		11
13	4	6	12
14	4	6	8
15	2	5	7
16	3	6	8
17	4 ^a	7 ^a	9
18	7		16
19	9		17
20	11	17	18

^aWe extrapolate these numbers from experiments at two times higher N_2 partial pressure.

our findings by multiple independent runs of experiments throughout an extended period of time (of more than one year). We found full verification of these two trends with minor variations in absolute N_2 uptake counts.

Superimposed on these trends, there are interesting variations for particular size-selected Fe_n^+ clusters. Most remarkable, the Fe_{17}^+

cluster shows an extremely pronounced temperature dependence of N_2 uptake, which seemingly vanishes at 22 K and remains meager by amount and intensity at 21 and 23 K. We provide extended plots of temperature dependences in the [supplementary material](#) (Figs. S6–S18).

C. Isothermal kinetics under cryogenic conditions

We further investigated the stepwise N_2 adsorption on Fe_n^+ , $n = 8-20$, clusters by recording their reaction kinetics in more detail, and we performed pseudo-first-order kinetic fits by our genetic algorithm routine.⁹⁴ The kinetic fits confirm consecutive N_2 adsorption steps. The signals for all but one Fe_n^+ cluster reactant decay mono exponentially without any indication of a second isomeric component. This result allows us to fit each consecutive adsorption step by a single rate constant. In some cases—to be discussed below—the recorded data require fitting with inclusion of significant desorption reactions in order to achieve converged fits. The N_2 adsorption to Fe_{18}^+ is the single exception, which exhibits a clear biexponential decay in the initial adsorption step and thus reveals a more involved scheme of N_2 interactions.

1. $Fe_8^+ + N_2$ —An all surface Langmuir type $m_{max} = n$ case

In the case of (8, m), we had observed a metastable adsorption limit m_x at (8, 4), a most intense cluster adsorbate complex m^* at (8, 7), and the adsorption limit m_{max} at (8, 8). There are a few published DFT studies of cationic Fe_3^+ that have predicted a bisdisphenoid structure.^{59,61} One may expect that the next neighbor coordination of each of the Fe atoms modulates their functionality to

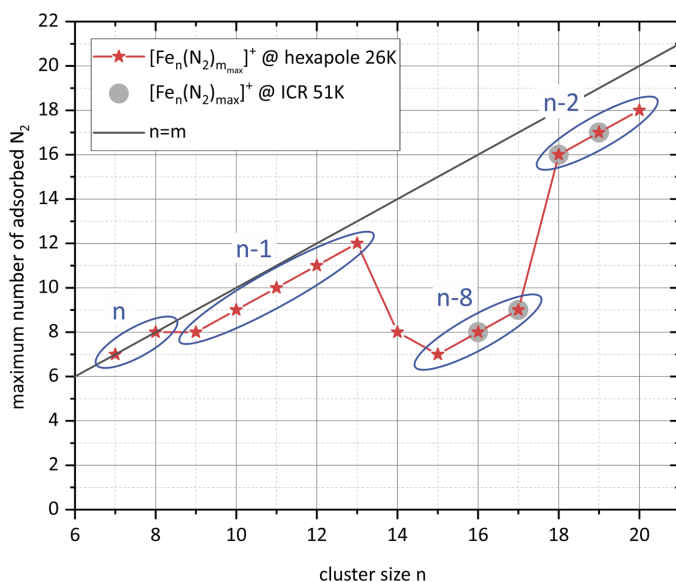


FIG. 2. Adsorption limits m_{max} of N_2 adsorption on cationic Fe clusters Fe_n^+ , $n = 6-20$, as recorded in the RF hexapole trap at 26 K in 3.6×10^{-6} mbar He buffer gas (red stars) and as recorded in the ICR cell at 51 K (gray dots). The black line stands for a 1:1 stoichiometry of N_2 and Fe ($n = m_{max}$). Mass-selected Fe_n^+ clusters were stored for up to 20 s and under exposure of up to 5×10^{-7} mbar N_2 at maximum, with saturation typically being reached at lower pressures. Note the indicated regions of different stoichiometries.

A.1. Kinetics of Stepwise Nitrogen Adsorption by Size-Selected Iron Cluster Cations: Evidence for Size-Dependent Nitrogen Phobia

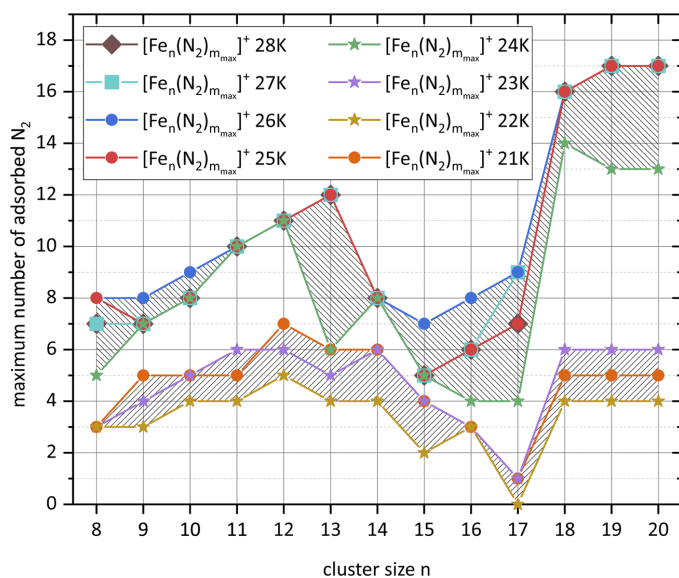


FIG. 3. Recorded N₂ adsorption limits m_{\max} on Fe_n^+ , $n = 8-20$, at 21–28 K when exposed for 15 s to 2.4×10^{-7} mbar of N₂ in 3.6×10^{-6} mbar He buffer gas. In general, the extent of N₂ adsorption decreases by lowering the temperature, and it shows a remarkably strong dependence on the cluster size. Note the diminished N₂ uptake of Fe_{17}^+ at the lowest temperatures. In general, we identify a “high T” regime of high N₂ uptake and a “low T” regime of low N₂ uptake, as emphasized by the shaded areas. These results are reproduced even when doubling the N₂ partial pressure (cf. Fig. S4 of the supplementary material).

act as binding sites for N₂ adsorbates. If so, then a Fe_8^+ cluster with a bisdisphenoid structure—comprising four fourfold and four fivefold coordinated Fe atoms—would lead to changes in consecutive N₂ adsorption at stoichiometries of (8, 4) and (8, 8). Our

recorded kinetic data are not in line with these predictions. DFT modeling of neutral Fe_8 clusters find either a capped pentagonal bipyramid^{24,60,64,100} or a bisdisphenoid structure.^{57–59,64} A capped pentagonal bipyramid Fe_8^+ would provide for one threefold, three

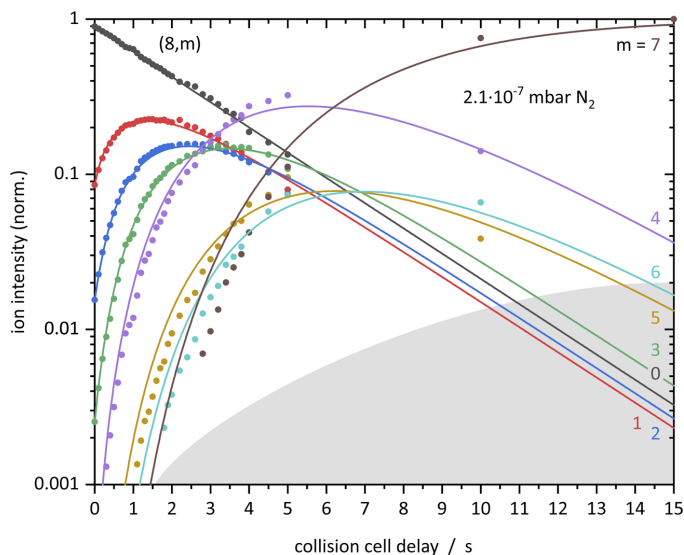


FIG. 4. Isothermal kinetics of the stepwise N₂ adsorption by the isolated Fe_8^+ cluster within 4.0×10^{-6} mbar He buffer gas and 2.1×10^{-7} mbar of N₂ (solid dots) at 26 K. The pseudo-first-order kinetic fits (solid lines) reveal reaction chains of up to seven consecutive steps.

fourfold, three fivefold, and one sixfold coordinated Fe atoms, all of which are located at the cluster surface and are accessible for adsorbates. Initial N_2 adsorption to the threefold and fourfold coordinated Fe sites and additional adsorption to the fivefold coordinated Fe atoms would result in changes in consecutive N_2 adsorption at stoichiometries (8, 4) and (8, 7). Such an assumption does indeed correlate well with the observed m_x and m^* values. The last adsorption step k_7 (cf. Fig. S34 and Table S15)—yielding the (8, 8) complex—might occur to the sixfold coordinated Fe site. We observe this step being very slow and leading to a very low intensity of the (8, 8) product complex (Fig. 4). Both of our findings appear to relate well to the high next neighbor coordination of this last Fe adsorption site.

2. $Fe_9^+ - Fe_{13}^+ + N_2$ —the $m_{max} = n - 1$ cases reveal center atom inclusion

In the range of $n = 9$ –13, we see stepwise N_2 adsorption up to an adsorption limit m_{max} of $n - 1$ N_2 molecules. In particular, the case of (9, m) reveals an adsorption maximum m_{max} at (9, 8) and a most intense cluster adsorbate complex m^* at (9, 7). Likewise, the (10, m) case reveals m_{max} at (10, 9). The most intense cluster adsorbate complex m^* at (10, 8) is in equilibrium with m_{max} and (10, 7). The fitted rate constants of N_2 adsorption show little step-by-step variation with a slight decline that increases steeply toward m_{max} (Fig. 5). Their values are documented in the supplementary material (cf. Figs. S35 and S36 and Tables S16 and S17).

The reported most stable structures for neutral Fe_9 and Fe_{10} clusters correspond to capped square antiprisms or to capped trigonal or capped pentagonal bipyramid motifs.^{24,58,60,61,64,100} These geometries would lead upon further growth by stepwise addition of

Fe atoms to the predicted icosahedral structure of neutral Fe_{13} .^{24,60,64} Two DFT studies of cationic Fe_9^+ and Fe_{10}^+ clusters^{61,100} predict capped pentagonal bipyramidal motifs. The Fe_9^+ capped pentagonal bipyramidal structure consists of four fourfold, one fivefold, two sixfold, and one eightfold coordinated Fe atoms, and the cluster surface has an all convex shape. The Fe_{10}^+ tricapped pentagonal bipyramidal structure consists of three four-, five-, and sixfold and one ninefold coordinated Fe atoms, and the cluster surface is all convex except for a shallow concave pocket at the ninefold coordinated Fe atom. In both cases, the single high-coordinated Fe atom might possess a lower N_2 adsorption enthalpy than all of the lower coordinated Fe atoms. If so, this might induce adsorption maxima $m_{max} = n - 1$ as observed.

In addition, the adsorption maximum m_{max} at (10, 9) reveals a dynamic adsorption/desorption equilibrium with the $m^* = n - 2$ complex (10, 8) and with (10, 7)—with the (10, 9) kinetic curve barely above the noise level. Similar behavior occurs for the $n = 9$ case at elevated pressures. This behavior is beyond an interpretation in merely structural terms. Instead enthalpic and entropic reasoning seems operational. It might be that the three sixfold Fe sites do not adsorb strongly.

The (11, m) case reveals an adsorption limit m_{max} at (11, 10) in equilibrium with its precursor (Fig. 6 left). The rate constants of stepwise N_2 adsorption are similar to the (9, m) and (10, m) cases, and they show little variation up to $m = 7$. In line with our previous studies of N_2 adsorption on Ni_n^+ clusters,⁸⁴ we identify this as an indication for a smooth cluster surface of many equivalent adsorption sites. The rate constant $k_{(11,8)}$ for the ninth adsorption step significantly diminishes by more than a factor of two. The final, ninth step reveals further reduced adsorption in equilibrium with desorption (cf. Fig. S37 and Table S18).

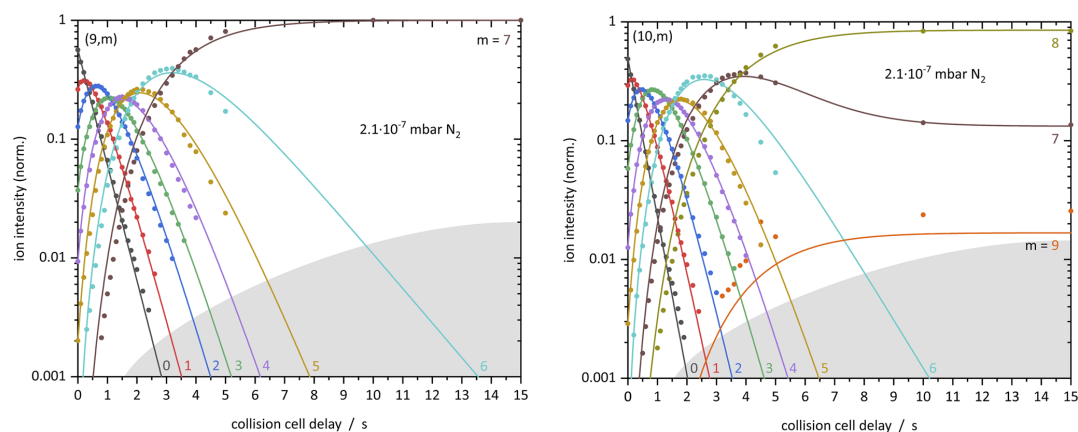


FIG. 5. Isothermal kinetics of the stepwise N_2 adsorption by isolated Fe_9^+ (left) and Fe_{10}^+ (right) clusters within 4.0×10^{-6} mbar He buffer gas and 2.1×10^{-7} mbar of N_2 (solid dots) at 26 K. The pseudo-first-order kinetic fits (solid lines) reveal reaction chains of up to seven and nine consecutive steps.

A.1. Kinetics of Stepwise Nitrogen Adsorption by Size-Selected Iron Cluster Cations: Evidence for Size-Dependent Nitrogen Phobia

In the case of (12, m), we find stepwise N_2 adsorption with roughly equal rate constants $k_{(12,m)}$ up to the adsorption limit m_{max} at (12, 11) (Fig. 6 right). In particular, there is no decline of adsorption rate constants toward saturation, and there is no indication for any desorption (cf. Fig. S38 and Table S19). Superimposed, we find somewhat retarded N_2 uptake in the eighth and tenth step, $k_{(12,7)}$ and $k_{(12,9)}$, and somewhat enhanced uptake at the ninth step, $k_{(12,8)}$. This behavior leads to a metastable adsorption limit m_x at (12, 7). This observation seems unlikely to find an interpretation in terms of purely structural arguments. Instead, we suggest the possibility of an adsorbate-induced reorganization of the Fe cluster core and/or of the adsorbate layer close to saturation.

Predicted structures of neutral and cationic clusters $n = 11, 12$ are four- and fivefold capped pentagonal bipyramids, which correspond to incomplete icosahedra.^{24,58,61,100} Such a Fe_{11}^+ structure would consist of two fourfold, three fivefold, five sixfold, and one tenfold Fe atoms. The Fe_{12}^+ analog would contain five fivefold, six sixfold, and one elevenfold Fe atoms. In both cases, a single high-coordinated Fe atom would locate in the center of the clusters, shielded against N_2 adsorption. This nicely corresponds to the observed $m_{max} = n - 1$ behavior. Further kinetic details cannot be derived from these structures in an obvious way.

The case of (13, m) is significantly different from all smaller clusters. There is an adsorption limit m_{max} at (13, 12), which excellently points toward an icosahedral structure as predicted before.^{24,58,60,61,64,100} The initial adsorption up to $m = 6$ is fast and stalls at this point; (Fig. 7) the seventh uptake, $k_{(13,7)}$, is slower by two orders of magnitude (Fig. S39 and Table S20). Surprisingly, the next intense larger observable cluster adsorbate complex is (13, 12). We do find very low intensity indications of complexes in between (13, 7) through (13, 11). They may exist merely as adsorbate intermediates. In effect, (13, 6) becomes a metastable adsorption limit m^* . Furthermore, any kinetic fits inevitably need to involve high values of $k_{(13,7)}$ through $k_{(13,11)}$, which rise by a factor of two with respect to the

values of the initial adsorption steps. This significant rise of the adsorption rate constant may originate from some kind of reorganization of the cluster adsorbate complexes in terms of their coupled geometric and electronic parameters. At this point, we can only speculate about details. It is conceivable that the known antiferromagnetic coupling of the central Fe atom in a naked Fe_{13}^+ cluster⁴⁶ relaxes under the influence of more than six N_2 ligands. Alternatively, the highly symmetric icosahedral shell of a naked Fe_{13}^+ cluster, which maximizes the amount of next neighbor interactions, starts to break down upon addition of a seventh N_2 ligand, and in effect, there will be lower coordinated Fe centers at the cluster surface that attract further ligands swiftly. Further evidence for the actual mechanism can be found in the accompanying paper on IR spectroscopy and DFT modeling.⁹⁰

3. $Fe_{14}^+ - Fe_{17}^+$ —the $m_{max} = n - 8$ cases reveal adsorption reluctance

The range of Fe_n^+ $n = 14-17$ clusters has a special adsorption behavior, namely, the initial N_2 uptake is as fast as in all of the other cases—likely close to the collision rate constant and thus with unit efficiency (as discussed below); however, the total amount of uptake is much reduced with respect to the smaller and larger clusters (Fig. 8). This range is therefore labeled as “somewhat reluctant.” The $n = 15-17$ clusters accept $n - 8$ N_2 molecules at maximum, and the $n = 14$ cluster accepts $n - 6$ N_2 molecules at maximum.

We find that the rate constant variations up to $k_{(14,7)}$ are identical to that for the case of $n = 13$ up to $k_{(13,7)}$ (cf. Fig. S40 and Table S21). This is a strong indication that these clusters have similar structures. However, the kinetic fits of Fe_{14}^+ do necessitate a significant amount of desorption, $k_{-(14,7)}$ and $k_{-(14,8)}$, which are absent in the case of Fe_{13}^+ . The (14, m) cluster complexes cease to take up any N_2 adsorbates beyond the ninth adsorption step at $k_{(14,8)}$, in contrast to the (13, m) complexes, which adsorb up to $k_{(13,11)}$, $m_{max} = 12$.

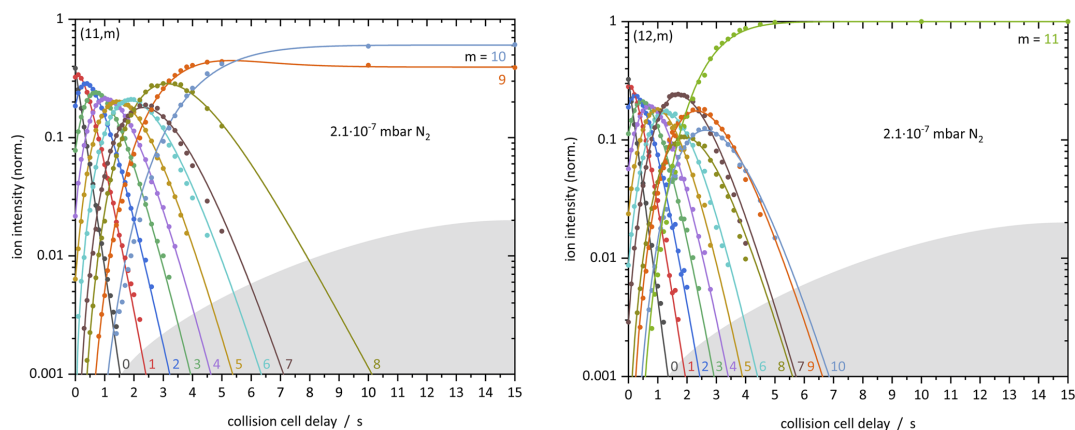


FIG. 6. Isothermal kinetics of the stepwise N_2 adsorption by isolated Fe_{11}^+ (left) and Fe_{12}^+ (right) clusters within 4.0×10^{-6} mbar He buffer gas and 2.1×10^{-7} mbar of N_2 (solid dots) at 26 K. The pseudo-first-order kinetic fits (solid lines) reveal reaction chains of up to 11 consecutive steps.

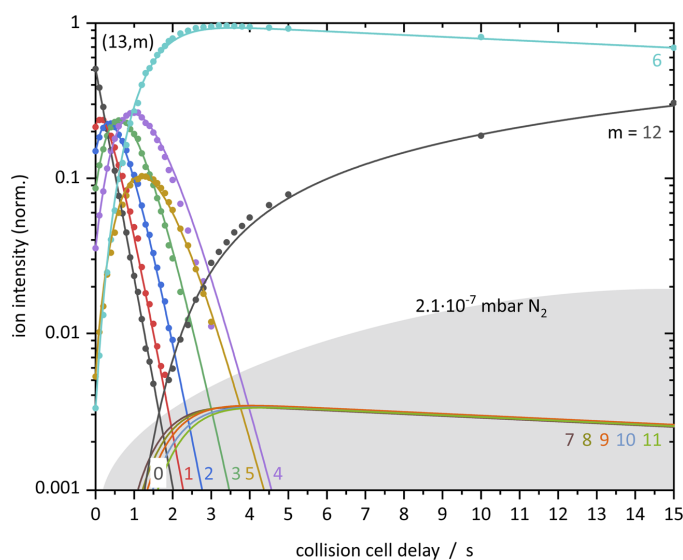


FIG. 7. Isothermal kinetics of the step-wise N_2 adsorption by the isolated Fe_{13}^+ cluster within 4.0×10^{-6} mbar He buffer gas and 2.1×10^{-7} mbar of N_2 (solid dots) at 26 K. The pseudo-first-order kinetic fits (solid lines) reveal reaction chains of up to 12 consecutive steps. We do not detect cluster adsorbate complexes $m = 7-11$. Modeling assumes that their intensities lie below our experimental noise level although some experiments did observe low levels of these species.

For Fe_n clusters with $n > 13$, there are just a few published DFT studies. The predicted most stable structures for neutral and cationic $Fe_{14}^{0/+}$ is the transformation from the icosahedron to a bicapped hexagonal antiprism.^{60,61,100} The $n = 13$ to $n = 14$ transition is of particular interest. Predictions are that the extra adatom integrates

at a bridging μ_2 position that may relax into a hexagonal ring upon further addition of adatoms.

There are similar N_2 uptake kinetics for clusters $n = 15$ and 16 (Fig. 9). Both reveal a most intense cluster adsorbate complex at $(n, m_{max-2}) = (15, 5)$ and a metastable adsorption

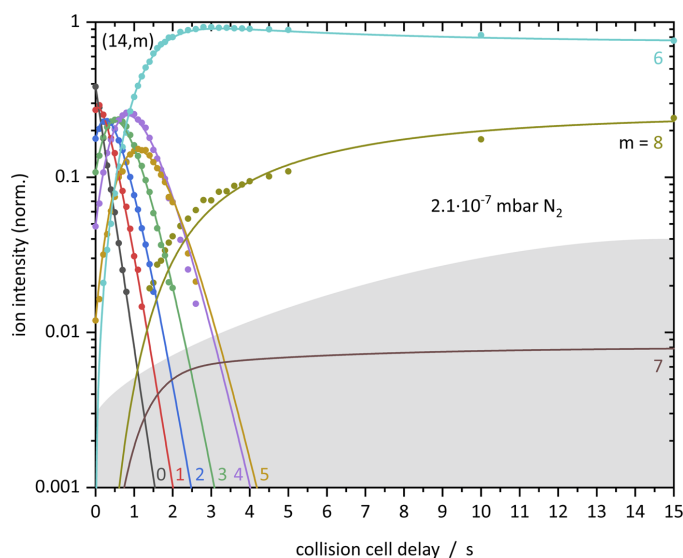


FIG. 8. Isothermal kinetics of the step-wise N_2 adsorption by the isolated Fe_{14}^+ cluster within 4.0×10^{-6} mbar He buffer gas and 2.1×10^{-7} mbar of N_2 (solid dots) at 26 K. The pseudo-first-order kinetic fits (solid lines) reveal N_2 uptake in up to eight consecutive steps and competing losses in the final two steps. Note the striking difference to the $n = 13$ case.

A.1. Kinetics of Stepwise Nitrogen Adsorption by Size-Selected Iron Cluster Cations: Evidence for Size-Dependent Nitrogen Phobia

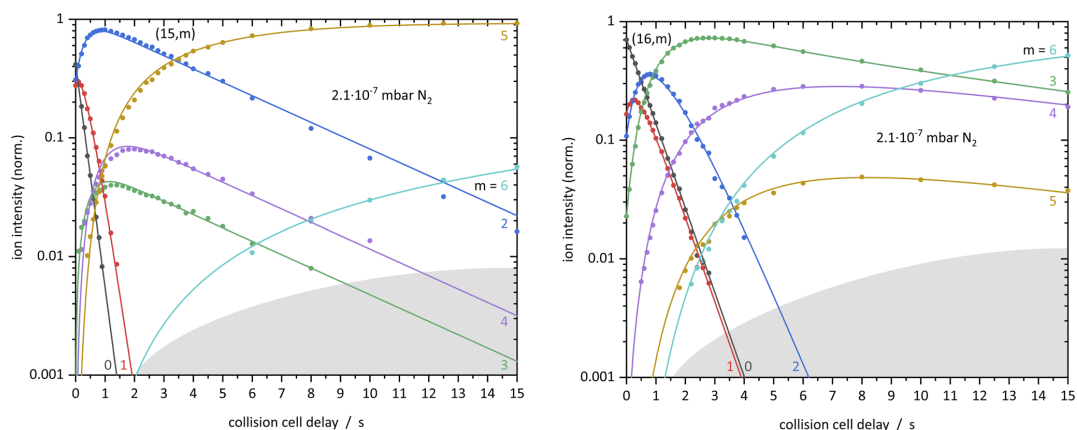


FIG. 9. Isothermal kinetics of the stepwise N_2 adsorption by the isolated Fe_{15}^+ (left) and Fe_{16}^+ (right) clusters within 4.0×10^{-6} mbar He buffer gas and 2.1×10^{-7} mbar of N_2 (solid dots) at 26 K. The pseudo-first-order kinetic fits (solid lines) reveal reaction chains of up to six consecutive steps in partial completion with desorption.

limit at $(n, m_{max-5}) = (15, 2)$. We note in passing that the Fe_{15}^+ cluster is more reluctant to take up N_2 under present conditions than any other cluster examined. This is documented by the observed saturation stoichiometry, $m_{max}/n = 0.47$, less than a one-to-two ratio, which is far away from a Langmuir type one-to-one behavior. It is another peculiar finding that both clusters, $n = 15$

and 16, experience considerable N_2 desorption at medium levels of coverage (cf. Figs. S41 and S42 and Tables S22 and S23).

All of the predicted most stable structures for neutral and cationic $Fe_{15}^{0/+}$ are bicapped hexagonal antiprisms.^{24,58,60,61,64,100} Both six membered-rings of the hexagonal antiprism are capped with a single Fe atom, and there is a single Fe atom in the center. The

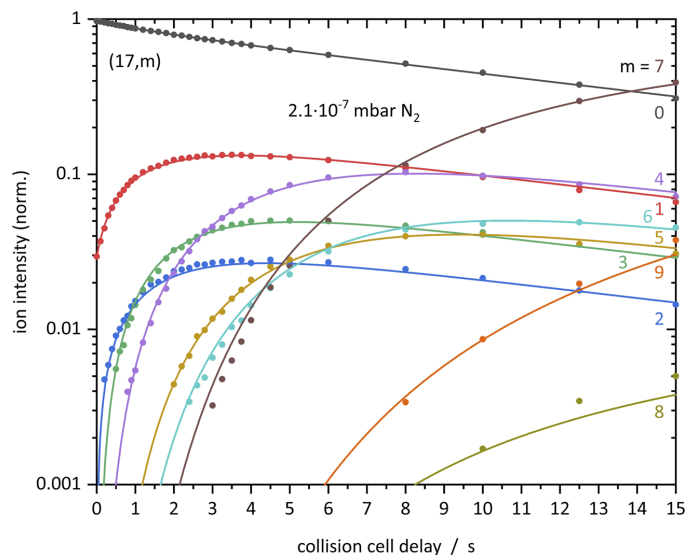


FIG. 10. Isothermal kinetics of the stepwise N_2 adsorption by the isolated Fe_{17}^+ cluster within 4.0×10^{-6} mbar He buffer gas and 2.1×10^{-7} mbar of N_2 (solid dots) at 26 K. The pseudo-first-order kinetic fits (solid lines) reveal reaction chains of up to nine consecutive steps.

neutral and cationic $\text{Fe}_{16}^{0/+}$ clusters are said to follow a “hexagonal-antiprism packing,” in which the extra Fe adatoms join on one of the two capped hexagons.^{60,61,100} The next neighbor coordination numbers of such a cluster geometry do not allow us to draw kinetic conclusions that would point toward our experimental observations. Further factors beyond the structures seem at play.

a. The special $n = 17$ case. Some of our early and preliminary experiments had revealed an absolute reluctance against N_2 uptake by the Fe_{17}^+ clusters. This finding had been reproducible throughout repetitive runs of experiments. By careful tuning of experimental conditions—in particular, minute adjustments of trapping and transfer potentials—we managed to observe some $[\text{Fe}_{17}(\text{N}_2)_m]^+$ complexes. Note that clusters of other sizes did not change their behavior in a noticeable way upon comparable adjustments. From this observation, we conclude there is very facile desorption in the case of $n = 17$.

Under the most “gentle” conditions achievable, we observe a significantly slower but noticeable N_2 adsorption to Fe_{17}^+ compared to all other clusters (Fig. 10). Note that 30% of the initially bare Fe_{17}^+ clusters remain naked even after storing them for 15 s in the presence of the N_2 environment and thermalizing He buffer gas within the RF hexapole trap. By inspection of the fitted rate constants, it becomes apparent that the desorption rate constants $k_{-(17,1)}$ and $k_{-(17,2)}$ are larger than the corresponding adsorption rate constants $k_{(17,0)}$ and $k_{(17,1)}$ (cf. Fig. S43 and Table S24). The resulting balance seems responsible for the delicate response to experimental conditions. Further desorption rate constants $k_{-(17,m)}$ are of significance in our fits for almost all steps m . This and the subsequent $n = 18$ case discussed below are the only clusters where there is appreciable N_2 desorption at all values of m .

In the case of $n = 17$, we undertook another set of kinetic investigations at elevated pressures of N_2 (4.7×10^{-7} mbar N_2) with identical conditions otherwise (Fig. S19). The N_2 uptake remains slow, but some of the N_2 desorption steps become significantly slower (Fig. S44 and Table S25). Therefore, the rapid N_2 desorption—special to $n = 17$ —appears to be quenched by N_2 collisions.

There are a few DFT predictions of $\text{Fe}_{17}^{0/+}$ cluster structures that find capped hexagon antiprisms for the neutral and cationic cases.^{60,61,100} The capping iron atoms are all on the same side of the hexagonal antiprism, and they gather in a triangle on this side of the cluster. It is not obvious how such a cluster geometry enables the observed special kinetic features.

Summarizing our kinetic findings in this $m_{\text{max}} = n - 8$ region, we do not find an obvious correspondence with the DFT predictions on cluster structures. It seems inevitable to interpret the kinetic findings in light of additional influential factors, such as the electronic structure and how it might change upon N_2 adsorption.

In this context, we envision the following three working hypotheses for the $m_{\text{max}} = n - 8$ behavior of Fe_{14-17}^+ :

- (1) The N_2 adsorbate reorganization might be hindered. The first N_2 molecules adsorb μ_1 end-on to the cluster complex with a slightly tilted motif over an edge or face. Subsequent to the adsorption of $n - 8$ N_2 molecules, a reorganization is needed to adsorb more N_2 . Compared to the Fe_{13}^+ case where an adsorbate reorganization must take place after the metastable

adsorption limit, a reorganization is not possible for these bigger cluster adsorbate complexes.

- (2) The Fe_{14-17}^+ cluster might possess capped hexagonal antiprism geometry, which would accept less N_2 adsorbates. The enthalpic arguments for such behavior—as opposed to largely icosahedral structural motifs otherwise—need to be elucidated by dedicated modeling beyond the present exploratory studies in the future.
- (3) If there is a connection between enhanced N_2 uptake and high-spin relaxation—as discussed further in the following and the adjoining [IRS]—then the hexagonal antiprismatic Fe_{14-17}^+ clusters may experience local spin pinning at some of their surface atoms, which would hinder stoichiometric N_2 uptake.

Orbital occupations of these clusters might be such that seven out of $n - 1$ surface atoms refuse to accept electron density from the N_2 lone-pair donor orbital, thus rendering their attachment unlikely. In contrast, the remaining Fe surface atoms readily do so. Thus, we speculate that there are two kinds of surface atoms in the Fe_{14-17}^+ cluster range.

4. $\text{Fe}_{18}^+ - \text{Fe}_{20}^+$ —the $m_{\text{max}} = n - 2$ behavior indicates a second interior atom

We find that the $n = 18-20$ clusters adsorb N_2 readily up to an $m_{\text{max}} = n - 2$ limit. These three clusters also reveal metastable adsorption limits that are larger than those of the $n = 15-17$ clusters. Up to these metastable limits of (18, 7), (19, 9), and (20, 11), the stepwise N_2 uptake points toward “smooth surface” behavior. Beyond this limit, the N_2 uptake becomes irregular and thus specific to the occupied adsorption sites—a “rough surface” behavior. Despite these analogies, the adsorption kinetic of Fe_{18}^+ is completely different compared to the adsorption kinetics of Fe_{19}^+ and Fe_{20}^+ .

a. The very special case of Fe_{18}^+ . The kinetics of N_2 uptake by Fe_{18}^+ , the (18, m) case, is the prominent instance of very involved adsorption behavior. The semi-logarithmic plot of the parent intensity Fe_{18}^+ upon N_2 uptake reveals a short-term steep decrease, an intermediate plateau, and a slow decline past 3.6 s reaction delay (Fig. 11 and emphasized in Fig. S22). Note that we have reproduced this behavior multiple times and under minute variations of reaction conditions (pressure, temperature, ion optics potentials, and ion source conditions). The behavior is completely reproducible. Figure S21 documents a nominal “best fit” of the recorded kinetic curves when assuming ordinary stepwise single N_2 adsorption and desorption only. Such a fit obviously fails.

The assumption of a mix of at least two isomers is strongly supported by the clear observation of the almost constant plateau of Fe_{18}^+ intensities at medium reaction delays ($t = 1-3$ s). It finds further support from the fact that N_2 reactant pressure variation does NOT change the relative intensity of this plateau. It thus stems from processes in the context of ion generation within the cluster ion source, namely, isomerism.

Two DFT studies of neutral and cationic $\text{Fe}_n^{0/+}$ clusters have predicted a “hexagonal-antiprism packing” for $\text{Fe}_{18}^{0/+}$.^{61,100} This implies a square cap on one side of the antiprism. Unfortunately, such structures do not lend obvious support to the kinetic N_2 adsorption maximum $m_{\text{max}} = n - 2$ nor to the elucidated coexistence

A.1. Kinetics of Stepwise Nitrogen Adsorption by Size-Selected Iron Cluster Cations: Evidence for Size-Dependent Nitrogen Phobia

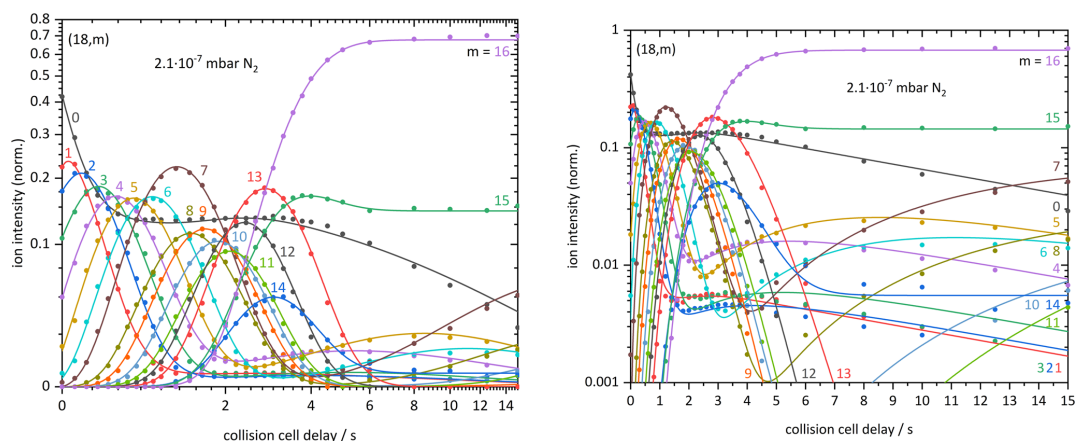


FIG. 11. Isothermal kinetics of the stepwise N_2 adsorption by the isolated Fe_{18}^+ cluster within 4.0×10^{-6} mbar He buffer gas and 2.1×10^{-7} mbar N_2 (solid dots) at 26 K. The pseudo-first-order kinetic fits (solid lines) reveal reaction chains up to 16 consecutive steps. Each fitting line comprises a sum of contributions from two isomer species, **A** and **B** (see text). This fit represents the minimum conversion scenario (MIC) between these two isomers. Note the different axis scaling: equidistant data points by nonlinear data transformation (left) and semi-logarithmic (right). A more detailed view of the initial area (0–4 s) can be found in Fig. S24. The corresponding fit of maximum conversion scenario (MAC) can be found in the [supplementary material](#). See the text for the definition of MIC and MAC scenarios.

of isomers **A** and **B**. A double icosahedral structure “minus one” of Fe_{18}^+ , similar to the predicted one of Fe_{19}^+ ,^{24,58,59,61} would provide for two Fe atoms inside an outer, largely *smooth* Fe shell. This would provide a feasible explanation for our observed adsorption maximum $m_{max} = n - 2$ (Fig. 2).

Our own DFT endeavors revealed conceivable candidate structures of Fe_{18}^+ , which are discussed at length, in the accompanying

[IRS] paper. Note that these calculations are exploratory and meant to prepare for more definitive studies in the future. It seems as if a largely icosahedral motif (**18ico**) might compete with a hexagonal antiprismatic motif (**18hex**). The cubic closely packed motif (**18cp**) seems less stable by more than 200 kJ/mol (Fig. 12). Most importantly, all of these motifs seem to comprise comparable high-spin states, multiplicities of $M = 56$ and 58. Thus, the exploratory DFT

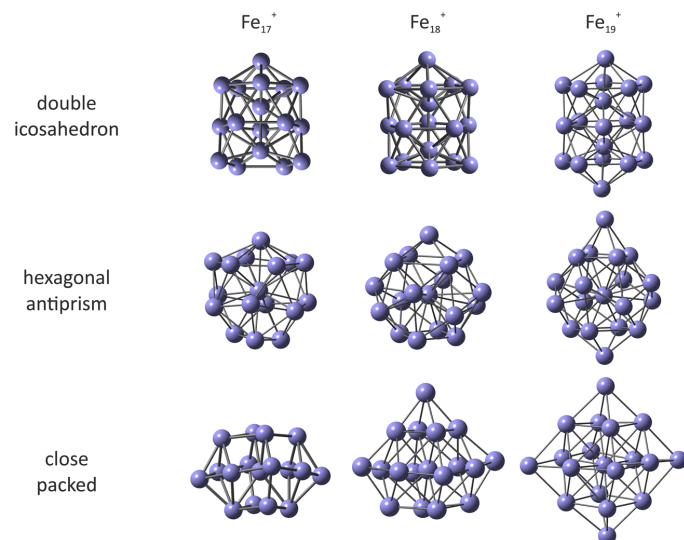


FIG. 12. Some DFT predicted geometries of Fe_{17}^+ (left), Fe_{18}^+ (center), and Fe_{19}^+ (right).

results point toward a purely geometric isomerism rather than to the coexistence of mere spin isomers. Note that the published XMCD studies conclude that there are high magnetic moments of almost constant $3.2\text{--}3.9 \mu_B/\text{Fe}$ atom throughout the size range of Fe_n^+ clusters, $n = 3\text{--}20$, which agrees perfectly with our exploratory DFT studies.^{14,46}

Because of the intrinsic complexity of the given task, our own DFT studies were conducted at the Perdew–Burke–Ernzerhof (PBE) level of theory without admixture of Hartree Fock exchange. In particular, our available computing resources did not allow for an equivalent survey at the enhanced level of hybrid exchange correlation functionals such as PBE0 or TPSSh. In this regard, we take the absolute values of computed stabilities with a grain of salt. In particular, two of the predicted isomers of Fe_{18}^+ come with comparable stabilities, and we take this as a qualitative finding. Beyond this, our computations do not allow for a quantitative prediction of energetic differences between the icosahedral motif (**18ico**) and the hexagonal antiprismatic motif (**18hex**). Moreover, it seems reasonable to rely on the prediction of lesser stability of the close packed motif (**18cp**) (Fig. 12).

Returning to the discussion of the recorded kinetics in terms of two (possibly three) participating isomers of Fe_{18}^+ , we need to find answers to at least three questions:

- Is it possible to obtain a unique fit of the coupled N_2 adsorption dynamics of both isomers?
- Does the second isomer originate exclusively from the cluster source, or is some interconversion by the stepwise N_2 adsorption conceivable?
- If interconversion of isomers occurs by N_2 adsorptions, does it occur upon low or high or any N_2 coverages?

After an extended survey of conceivable fitting schemes and after invoking at least three different fitting programs to model five independent kinetic datasets, the answer to question (a) is

negative. Ambiguities remain whatever approach is taken. Nevertheless, it became possible to extract significant findings from our concerted fitting attempts.

In particular, we found it possible to achieve kinetic fits of high quality (cf. Figs. S24, S26, and S30) for three limiting cases, which we label as *minimum conversion* (MIC), *maximum conversion* (MAC), and *delayed activation conversion* (DAC) scenarios. Of course, other conversion levels are conceivable, in particular, those that fall in between MIC and MAC. The highly speculative DAC scenario is elaborated in the [supplementary material](#) (cf. Text 6/Figs. S30–S33/Tables S10–S14) and does not yield further insight but shares the main finding with MIC and MAC, as discussed below. The MIC scenario implies coupling of as little isomeric adsorbate species as possible, and MAC implies coupling of as many such species as possible. Note that MIC sees complete N_2 desorption, whereas MAC sees some incomplete N_2 evaporation (cf. blue and red curves in Fig. 13).

Addressing question (b), we state that there is a likely admixture of about 10% up to at most 13% of a minor isomer of Fe_{18}^+ originating from the cluster ion source. Note that there is no such evidence for any other cluster size. We label the initially major isomer of Fe_{18}^+ , $I_0 \approx 0.42$, as $^A\text{Fe}_{18}^+$ and the minor isomer of Fe_{18}^+ , $I_0 \approx 0.10$, as $^B\text{Fe}_{18}^+$. The remaining initial intensities ($I_0 = 0.48$) are distributed among products with few N_2 adsorbates [see the [supplementary material](#) for further discussion of the procedure of ion admission to the hexapole trap and on starting points for kinetic recording and fitting procedures (cf. ESI Text 3.1)].

In order to address question (c), we examine the measured rate constants for adsorption and desorption of N_2 to and from Fe_{18}^+ as differentiated for isomers A and B and for the two limiting conversion cases, MIC and MAC (Figs. S25 and S27).

The N_2 uptake of isomer A is independent of the assumed conversion scheme. MIC and MAC scenarios yield identical rate

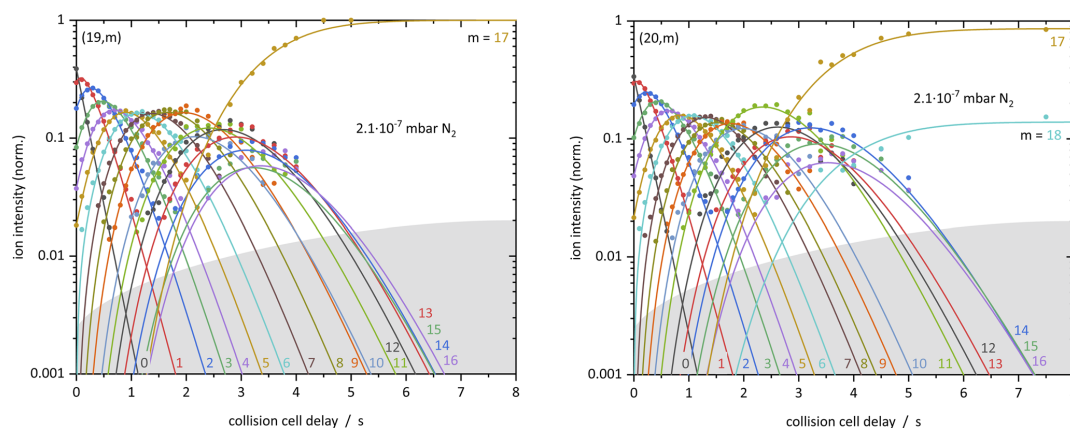


FIG. 13. Conversion rates of isomer A (loaded with $m_A \text{N}_2$ s) to isomer B (loaded with $m_B \text{N}_2$ s) for the MIC (green) and MAC scenarios (black, blue, and red). Note the presence of $m = 9$ conversion step in both cases, which leads to complete expulsion of all N_2 adsorbates.

A.1. Kinetics of Stepwise Nitrogen Adsorption by Size-Selected Iron Cluster Cations: Evidence for Size-Dependent Nitrogen Phobia

constants (cf. Figs. S25 and S27, black solid and open symbols). In particular, it is a robust finding that ${}^A\text{Fe}_{18}(\text{N}_2)_7^+$ and ${}^A\text{Fe}_{18}(\text{N}_2)_{13}^+$ —the $m = 7$ and 13 cases of isomer **A**—experience a reduced N_2 uptake as evidenced by the according dips in the fitted rate constants and the concomitant enhancement of intermediate product intensities in the recorded kinetic curves. Desorption is exclusive to $m > 13$ and thus points to the occurrence of weakly bound N_2 adsorbates upon high levels of coverages by 15 and 16 N_2 molecules. The significantly enhanced adsorption rate constant at ${}^A k_{(18,14)}$ is evident in MIC, MAC, and DAC scenarios but is void of an obvious interpretation. It is highly speculative but conceivable to consider an adsorbate shell reorganization (all tilted N_2 to all end-on N_2 in favor of adsorbate shell closure).

The N_2 uptake of isomer **B** is significantly more complicated (cf. Figs. S25 and S27, red solid and open symbols). In the cases of MIC and MAC scenarios, the first adsorption step ${}^B k_{(18,0)} = 0.1 \text{ s}^{-1}$ is significantly slower than the following adsorption steps. We see strong variations in adsorption and desorption rate constants. For both scenarios, the tenth adsorption step ${}^B k_{(18,9)}$ is fast, as are the $m = 1$ –3 adsorption steps. In both scenarios, several desorption rate constants are larger than the corresponding adsorption rate constants, e.g., ${}^B k_{-(18,8)} > {}^B k_{(18,7)}$ for the $m = 7$ step. That leads to a strong slowdown within the chain of consecutive adsorptions. It is common to the MIC and MAC scenarios that there are high levels of adsorption and desorption that are modulated strongly by the adsorbate level m . MIC stops at $m = 10$, whereas MAC reveals significant rate constants up to $m = 15$.

Most importantly, the conversion rate constants, which turn isomer **A** into isomer **B** (Fig. 13), are significant at or around $m = 9$ and include a concomitant expulsion of all of the accumulated

N_2 adsorbates. This holds for both MIC and MAC scenarios. Such an expulsion would be highly endothermic, estimated as almost 300 kJ/mol by our exploratory DFT calculations. A driving force for such expulsion would need to originate from another coupled process. Candidate processes are (a) geometric relaxation, (b) spin conversion, and (c) N_2 activation and any combination of these. Process (c) is in contradiction to the observation of complete N_2 expulsion—none of the adsorbed N_2 molecules is left behind upon isomeric conversion. Process (b) is not supported by our exploratory DFT modeling, i.e., spin relaxation seems stepwise, small and does not provide significant enthalpic gains. Finally, process (a) would need to be dramatic and much beyond the nearly isoenergetic candidate structures **18ico** and **18hex**, where the two most likely forms are almost degenerate (irrespective of spin state). Thus, the large driving force suggests consideration of the third conceivable isomer **18cp** because it qualitatively provides about 200 kJ/mol of excess enthalpy. In this regard, our exploratory DFT modeling does provide for some guidance toward an enthalpic interpretation of the kinetic findings. Upon uptake of seven or more N_2 adsorbates, the **18cp** structure might relax to **18ico** and/or **18hex**, while the excess relaxation enthalpy serves to evaporate all of the N_2 adsorbates.

Summarizing our present understanding of the prevailing N_2 adsorption kinetics of Fe_{18}^+ , we have depicted a generalized scheme of isomeric Fe_{18}^+ conversion through stepwise N_2 adsorption (Fig. S23). This scheme emphasizes the MIC scenario with complete adsorbate expulsion but interpolates somewhat toward the MAC scenario with some N_2 adsorbates remaining upon isomer conversion. The temporal evolution of isomers **A** and **B** in total and per species is provided elsewhere (Figs. S28 and S29).

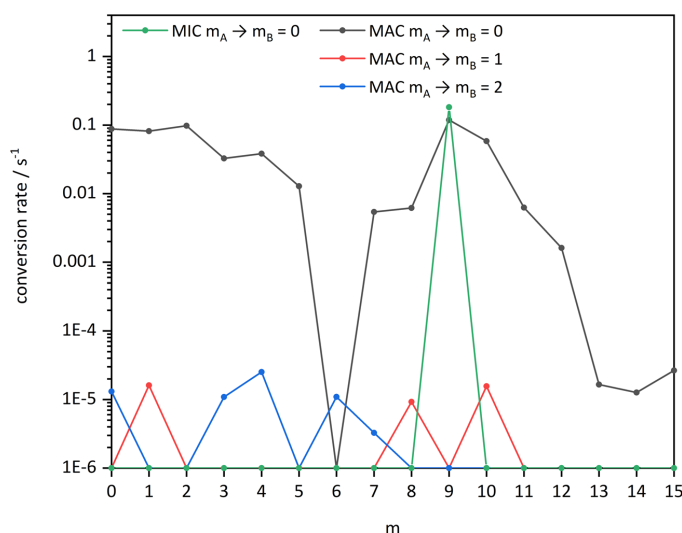


FIG. 14. Isothermal kinetics of the stepwise N_2 adsorption by isolated Fe_{18}^+ (left) and Fe_{20}^+ (right) clusters within 4.0×10^{-6} mbar He buffer gas and 2.1×10^{-7} mbar of N_2 (solid dots) at 26 K. The pseudo-first-order kinetic fits (solid lines) reveal reaction chains of up to 18 consecutive steps in a likely smooth surface adsorption fashion.

Beyond our tentative interpretation of the kinetic data and their fits, there is one robust finding from the MIC, MAC, and DAC fits. There must be an initial mixture of at least two isomers of naked Fe_{18}^+ generated in the cluster ion source. There is no evidence for more than one isomer in any other investigated case of Fe_n^+ ($n \neq 18$).

On the basis of insights gained from the adsorption kinetics and modeling, from our exploratory DFT studies and from published DFT studies by others, we now attempt to relate the isomers **A** and **B** to the calculated isomeric structures, **18ico**, **18hex**, and **18cp**. By enthalpic arguments, we find it necessary to relate major isomer **A** to **18cp**, as evidenced above. This leaves minor isomer **B** to interpret. Some guidance comes from the recorded adsorption limits (Fig. 2), which reveal values $m_{\text{max}} = n - 8$ in the range of $n > 13$, while $m_{\text{max}} = n - 1$ and $n - 2$ are observed at $n = 13$ and $n = 19$, respectively. Thus, Fe_{13}^+ and Fe_{19}^+ likely possess icosahedral structures. In line with this, we conclude that the minor isomer $^{\text{B}}\text{Fe}_{18}^+$ might coincide with some largely icosahedral structure close to the calculated isomer **18ico**, with small contributions of **18hex** possible. It is conceivable that smaller Fe_n^+ clusters that show “ $n - 8$ ” maximum absorption assume hexagonal structural

motifs. We take these assignments as our working hypothesis from here on.

b. Fe_{19}^+ and Fe_{20}^+ . It is much simpler to interpret the recorded N_2 adsorption kinetics of (19, m) and (20, m) (Fig. 14). We have observed adsorption limits m_{max} at (19, 17) and (20, 18) and metastable adsorption limits m_x at (19, 9) and (20, 11), and there is a most intense cluster adsorbate complex m^* at (20, 17).

Both clusters $n = 19$ and 20 undergo swift N_2 adsorption in a stepwise fashion at equal pace (cf. Figs. S45 and S46 and Tables S26 and S27). This indicates *smooth* surface behavior of equivalent adsorption sites. The genetic fitting algorithm insists on some contributions of slow N_2 desorption at $k_{-(20,8)}$, $k_{-(20,14)}$, and $k_{-(20,15)}$. These are of little significance in the overall kinetics. Past the metastable adsorption limit, the quality of fits diminishes. We attribute this effect to the transition from *smooth* to partially *rough* surface behavior at this point. *Rough* surfaces may experience parallel N_2 adsorption to distinguishable surface sites, which inherently presents difficulties in modeling by simple stepwise kinetics. In contrast, the last desorption step at $k_{-(20,18)}$ is significant. It leads to an N_2 adsorption/desorption equilibrium, which indicates that the 18th N_2

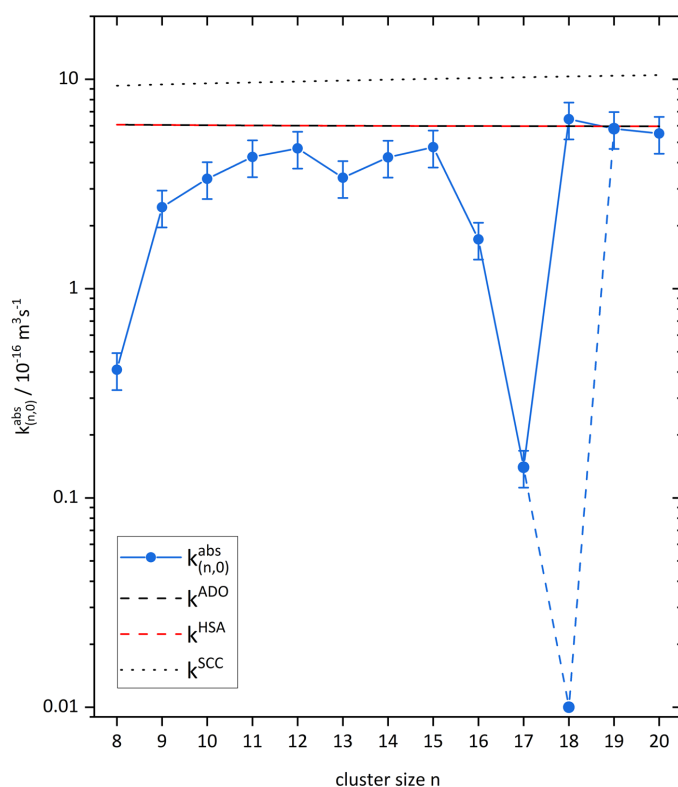


FIG. 15. Absolute rate constant $k_{(n,0)}^{abs}$ of the initial N_2 adsorption to Fe_n^+ clusters by experiment (blue dots, estimated error bars), according to classical average dipole orientation (ADO) theory (black dashed line), to the hard-sphere average (HSA) dipole orientation model (red dashed line), and to the surface charge capture model (dotted line). Note that the dashed blue line corresponds to the second unreactive Fe_{18}^+ isomer **B**. Also note that $10^{-16} \text{ m}^3 \text{ s}^{-1} = 10^{-10} \text{ cm}^3 \text{ s}^{-1}$. Numerical values are listed in Table II.

A.1. Kinetics of Stepwise Nitrogen Adsorption by Size-Selected Iron Cluster Cations: Evidence for Size-Dependent Nitrogen Phobia

TABLE II. Relative experimental and derived absolute N_2 adsorption rate constants for the initial N_2 adsorption to Fe_n^+ clusters in comparison to the calculated rate constants by classical ADO theory, the HSA model, and the SCC model. The experimental values, recorded at 4.0×10^{-6} mbar He buffer gas and 2.1×10^{-7} mbar of N_2 within the RF hexapole trap at 26 K, bear an estimated uncertainty of $\pm 20\%$. Note that $10^{-16} \text{ m}^3 \text{ s}^{-1} = 10^{-10} \text{ cm}^3 \text{ s}^{-1}$.

n	$k_{(n,0)}$ (s^{-1})	$k_{(n,0)}^{abs}$ ($10^{-16} \text{ m}^3 \text{ s}^{-1}$)	$k_{(n,0)}^{ADO}$ ($10^{-16} \text{ m}^3 \text{ s}^{-1}$)	$k_{(n,0)}^{HSA}$ ($10^{-16} \text{ m}^3 \text{ s}^{-1}$)	$k_{(n,0)}^{SCC}$ ($10^{-16} \text{ m}^3 \text{ s}^{-1}$)
8	0.38	0.41	6.07	6.07	9.33
9	2.2	2.45	6.05	6.05	9.44
10	3.1	3.35	6.03	6.03	9.55
11	3.9	4.26	6.02	6.02	9.66
12	4.3	4.68	6.01	6.01	9.76
13	3.1	3.39	6.00	6.00	9.86
14	3.9	4.24	5.99	5.99	9.96
15	4.3	4.74	5.99	5.99	10.05
16	1.6	1.72	5.98	5.98	10.14
17	0.13	0.14	5.98	5.98	10.23
18 A	5.9	6.45	5.97	5.97	10.32
18 B	0.01	0.01	5.97	5.97	10.32
19	5.3	5.81	5.97	5.97	10.40
20	5.0	0.55	5.96	5.96	10.48

adsorbate is loosely bound and (20,17) might correspond to a first adsorbate shell closure.

DFT modeling finds two conceivable structures for $m = 19$. First, there is a double icosahedron as determined mainly for the cationic Fe_{19}^+ cluster.^{24,58,59,61} Second, there is a capped hexagonal antiprism for the neutral Fe_{19} cluster.^{24,59,61,101} This hexagonal antiprism is capped on one side with a square pyramid. For the neutral and cationic $Fe_{20}^{0/+}$, modeling predicts a double icosahedron that is capped on one side with a Fe atom.^{24,59,61} The double icosahedron structure of Fe_{19}^+ would explain the $m_{max} = n - 2$ adsorption limit by its two inaccessible, inner atoms. Moreover, there is a conceivable interpretation of the metastable adsorption limit m_x at (20, 11) by adding the eleven N_2 to the one fourfold and ten sixfold coordinated Fe atoms. Up to the adsorption limit m_{max} at (20, 18), seven more N_2 molecules can add to the two sevenfold, three eightfold, and two ninefold coordinated Fe atoms.

5. Absolute rate constants of the initial N_2 adsorption

The absolute rate constants $k_{(n,m)}^{abs}$ were derived from the pseudo-first-order relative rate constants by normalization to the local N_2 reactant number density. We obtain such values for the initial uptake of the first N_2 adsorbate as a function of cluster size (Fig. 15, blue dots). Note that there are small uncertainties among the rate constants as a function of cluster size n , may be better than $\pm 5\%$, whereas all of the absolute values bear an estimated uncertainty of $\pm 20\%$.

For comparison, we calculated the collision rate constants according to the classical ADO theory, the HSA, and the SCC models (Table II). Within the given experimental uncertainties, the highest values of recorded rate constants agree favorably with the theoretical predictions. The small Fe_n^+ clusters $n = 8-10$ are somewhat reluctant to adsorb N_2 , which relates to limited heat baths (fewer vibrational

degrees of freedom) for dissipation of the heat of N_2 adsorption. The Fe_{13}^+ cluster reveals a small dip in N_2 adsorption rate constants that seemingly relates to its all *smooth* surface.

Most prominently, there is the remarkable dip toward reluctance of N_2 interaction at Fe_{17}^+ , and even more so at the **B** isomer of Fe_{18}^+ . The structural and/or electronic implications are unknown as of now and await high-level quantum chemical modeling much beyond our own exploratory low-level attempts.

IV. CONCLUSIONS

We present a study of stepwise N_2 adsorption on size-selected Fe_n^+ ($n = 8-20$) clusters. We have recorded their adsorption kinetics at 26 K in a hexapole collision cell and performed pseudo-first-order kinetic fits, which show stepwise N_2 adsorption. The N_2 uptake reaches an adsorption limit (m_{max}) with $m_{max} : n \leq 1$ in all investigated cases. In some cases, the adsorption limit m_{max} is not the most intense cluster adsorbate complex. This feature varies with cluster size.

We are able to identify four characteristic regions of (n, m_{max}) stoichiometries: Small clusters, $n = 7, 8$, reveal $m_{max} = n$, with a “surface only” type structure. The smaller medium-sized clusters, $n = 9-13$, reveal $m_{max} = n - 1$, with likely icosahedral structural motifs with a single inner Fe atom that is not accessible for N_2 adsorption. In particular, the Fe_{13}^+ cluster very likely assumes a highly symmetric icosahedral structure. The larger medium-sized clusters, $n = 14-17$, reveal an adsorption behavior of $m_{max} \approx n - 8$, and they likely assume “hexagonal antiprismatic” structural motifs. The large clusters, $n = 18-20$, reveal $m_{max} = n - 2$ adsorption limits that point toward capped icosahedral structures comprising two inner atoms. The Fe_{19}^+ cluster can be envisaged as a highly symmetric bi-icosahedron.

We find a strong temperature dependence of N_2 adsorption in the range of $T = 21-28$ K, and we identify two regions of low and

high adsorption loads above and below 24 K, respectively. The Fe_{17}^+ cluster shows the largest temperature dependence with N_2 adsorption vanishing at 22 K, which marks a remarkable case of nitrogen phobia that is unprecedented.

Our recorded adsorption kinetics reveals three cases with an especially conspicuous adsorption behavior. First, there is the Fe_{13}^+ cluster, which pauses at its metastable adsorption limit $m = 6$ but proceeds very rapidly by further stepwise adsorption up to $m_{\text{max}} = 12$. We speculate that there is a highly symmetric $\text{Fe}_{13}(\text{N}_2)_6^+$ complex with a maximum amount of Fe– N_2 -interaction hindering the seventh and further N_2 uptakes.

Second, there are the Fe_{17}^+ kinetics, located in the particularly noteworthy medium size region of $n = 14$ –17 with adsorption limits $m_{\text{max}} = n - 8$. Fe_{17}^+ has the slowest initial N_2 uptake among all recorded clusters. Our kinetic analysis points toward significant or even high kinetic rates of N_2 desorption in competition to the N_2 adsorption such that the net uptake becomes slow. We have not yet achieved a conclusive interpretation of the high desorption rates that occur for Fe_{17}^+ as opposed to all other clusters.

Third, there is the very special case of Fe_{18}^+ , which reveals the only N_2 uptake kinetics with a bi-exponential decay for the bare cluster ion, providing strong evidence for isomeric mixtures. By application of several conceivable fitting schemes, we identify three limiting cases of *minimum conversion* (MIC), *maximum conversion* (MAC), and *delayed activation conversion* (DAC), all of which unequivocally support the two-isomer hypothesis and which necessarily invoke the conversion of a major isomer into a minor one upon uptake of some 8 or 9 N_2 adsorbate molecules. With the help of our own exploratory DFT studies, we tentatively identify candidate structures for these isomers, namely, closely packed structure **18cp** as the major isomer **A**, which relax into the more favorable icosahedral/hexagonal antiprismatic structure **18ico/hex** by expulsion of the adsorbed N_2 layer.

In all of these cases, the net positive charge of the iron clusters enhances binding by charge-induced dipole interactions but also hampers π backdonation. These and other effects provide a subtle balance that might modulate under the influence of a net charge and of cluster geometry.^{100,101} We are investigating such charge effects by further experiments on anionic clusters, which will be reported in due time.

SUPPLEMENTARY MATERIAL

See the [supplementary material](#) for further adsorption limits; temperature dependent limits for different N_2 pressures; tabulated values for the rate constants, collision rates, and sticking probability; and the three different fitting possibilities (MIC, MAC, and DAC) with their unique characteristics.

ACKNOWLEDGMENTS

This work was supported by the German Research Foundation DFG within the Transregional Collaborative Research Center SFB/TRR 88 “Cooperative effects in homo and heterometallic complexes” (3MET.de) and by the State Research Center OPTIMAS. P.B.A. acknowledges support from the National Science Foundation (Grant No. CHE-1954142). The ^{56}Fe pure isotope

sample of this study was supplied by the United States Department of Energy Office of Science through the Isotope Program in the Office of Nuclear Physics. Quantum chemical modeling took place at the “Regionales Hochschulrechenzentrum Kaiserslautern” (RHRK). We thank Thomas Kolling for technical assistance and valuable discussions.

AUTHOR DECLARATIONS

Conflict of Interest

The authors have no conflicts to disclose.

Author Contributions

A.S., M.P.K., D.V.F., M.E.H., J.M., S.D., and G.N.-S. conducted the experiments. A.S. and C.W. conducted the quantum chemical calculations. A.S., D.S., and G.N.-S. conducted the kinetic fits algorithms. A.S., P.B.A., and G.N.-S. evaluated all data and wrote the manuscript, which all authors agreed to.

DATA AVAILABILITY

The data that support the findings of this study are available from the corresponding author upon reasonable request.

REFERENCES

- P. Boissel, *Astron. Astrophys.* **285**, L33 (1994).
- D. K. Böhme and H. Schwarz, *Angew. Chem., Int. Ed. Engl.* **44**, 2336 (2005).
- G. J. Kubas, *Chem. Rev.* **107**, 4152 (2007).
- P. B. Armentrout, *Catal. Sci. Technol.* **4**, 2741 (2014).
- N. Russo and D. R. Salahub, *Metal-Ligand Interactions: Structure and Reactivity* (Springer Science & Business Media, 2012), Vol. 474.
- R. A. J. O’Hair, *Chem. Commun.* **2006**, 1469.
- M. D. Morse, M. E. Geusic, J. R. Heath, and R. E. Smalley, *J. Chem. Phys.* **83**, 2293 (1985).
- E. K. Parks, B. H. Weiller, P. S. Bechthold, W. F. Hoffman, G. C. Nieman, L. G. Pobo, and S. J. Riley, *J. Chem. Phys.* **88**, 1622 (1988).
- R. L. Whetten, D. M. Cox, D. J. Trevor, and A. Kaldor, *Phys. Rev. Lett.* **54**, 1494 (1985).
- M. D. Morse, *Chem. Rev.* **86**, 1049 (1986).
- M. M. Kappes, *Chem. Rev.* **88**, 369 (1988).
- L.-S. Wang, X. Li, and H.-F. Zhang, *Chem. Phys.* **262**, 53 (2000).
- P. Armentrout, *Annu. Rev. Phys. Chem.* **52**, 423 (2001).
- J. Meyer, M. Tombers, C. van Wüllen, G. Niedner-Schatteburg, S. Peredkov, W. Eberhardt, M. Neeb, S. Palutke, M. Martins, and W. Wurth, *J. Chem. Phys.* **143**, 104302 (2015).
- S. C. Richtsmeier, E. K. Parks, K. Liu, L. G. Pobo, and S. J. Riley, *J. Chem. Phys.* **82**, 3659 (1985).
- E. K. Parks, K. Liu, S. C. Richtsmeier, L. G. Pobo, and S. J. Riley, *J. Chem. Phys.* **82**, 5470 (1985).
- N. O. Jones, M. R. Beltran, S. N. Khanna, T. Baruah, and M. R. Pederson, *Phys. Rev. B* **70**, 165406 (2004).
- M. R. Zakin, R. O. Brickman, D. M. Cox, and A. Kaldor, *J. Chem. Phys.* **88**, 6605 (1988).
- J. Conceição, S. K. Loh, L. Lian, and P. B. Armentrout, *J. Chem. Phys.* **104**, 3976 (1996).
- L. Tan, F. Liu, and P. B. Armentrout, *J. Chem. Phys.* **124**, 084302 (2006).
- M. Li, S.-R. Liu, and P. B. Armentrout, *J. Chem. Phys.* **131**, 144310 (2009).
- J. B. Griffin and P. B. Armentrout, *J. Chem. Phys.* **106**, 4448 (1997).

A.1. Kinetics of Stepwise Nitrogen Adsorption by Size-Selected Iron Cluster Cations: Evidence for Size-Dependent Nitrogen Phobia

- ²³C. P. McNary and P. B. Armentrout, *Phys. Chem. Chem. Phys.* **16**, 26467 (2014).
- ²⁴A. Jedidi, A. Markovits, C. Minot, M. Abderrabba, and M. A. Van Hove, *Phys. Chem. Chem. Phys.* **16**, 20703 (2014).
- ²⁵E. K. Parks, G. C. Nieman, L. G. Pobo, and S. J. Riley, *J. Chem. Phys.* **88**, 6260 (1988).
- ²⁶M. P. Irion and P. Schnabel, *J. Phys. Chem.* **95**, 10596 (1991).
- ²⁷K. O. Fossan and E. Uggerud, *Dalton Trans.* **2004**, 892.
- ²⁸K. A. Jackson, M. Knickelbein, G. Koretsky, and S. Srinivas, *Chem. Phys.* **262**, 41 (2000).
- ²⁹R. Liyanage, J. B. Griffin, and P. B. Armentrout, *J. Chem. Phys.* **119**, 8979 (2003).
- ³⁰G. L. Gutsev, M. D. Mochena, and C. W. Bauschlicher, *Chem. Phys.* **314**, 291 (2005).
- ³¹B. H. Weiller, P. S. Bechthold, E. K. Parks, L. G. Pobo, and S. J. Riley, *J. Chem. Phys.* **91**, 4714 (1989).
- ³²J. B. Griffin and P. B. Armentrout, *J. Chem. Phys.* **107**, 5345 (1997).
- ³³M. Ichihashi, T. Hanmura, and T. Kondow, *J. Chem. Phys.* **125**, 133404 (2006).
- ³⁴O. Gehret and M. P. Irion, *Chem. Phys. Lett.* **254**, 379 (1996).
- ³⁵I. Valencia, *Chem. Phys.* **476**, 46 (2016).
- ³⁶W. Zheng, S. N. Eustis, X. Li, J. M. Nilles, O. C. Thomas, K. H. Bowen, and A. K. Kandalam, *Chem. Phys. Lett.* **462**, 35 (2008).
- ³⁷M. Sakurai, K. Watanabe, K. Sumiyama, and K. Suzuki, *J. Chem. Phys.* **111**, 235 (1999).
- ³⁸W. D. Knight, K. Clemenger, W. A. de Heer, W. A. Saunders, M. Y. Chou, and M. L. Cohen, *Phys. Rev. Lett.* **52**, 2141 (1984).
- ³⁹W. Miehl, O. Kandler, T. Leisner, and O. Echt, *J. Chem. Phys.* **91**, 5940 (1989).
- ⁴⁰L. Lian, C. X. Su, and P. B. Armentrout, *J. Chem. Phys.* **97**, 4072 (1992).
- ⁴¹E. Kim, A. Mohrland, P. F. Weck, T. Pang, K. R. Czerwinski, and D. Tománek, *Chem. Phys. Lett.* **613**, 59 (2014).
- ⁴²I. M. L. Billas, A. Châtelain, and W. A. de Heer, *Science* **265**, 1682 (1994).
- ⁴³D. M. Cox, D. J. Trevor, R. L. Whetten, E. A. Rohlfing, and A. Kaldor, *Phys. Rev. B* **32**, 7290 (1985).
- ⁴⁴W. A. de Heer, P. Milani, and A. Chatelain, *Phys. Rev. Lett.* **65**, 488 (1990).
- ⁴⁵X. Xu, S. Yin, R. Moro, A. Liang, J. Bowlan, and W. A. de Heer, *Phys. Rev. Lett.* **107**, 057203 (2011).
- ⁴⁶M. Niemeyer, K. Hirsch, V. Zamudio-Bayer, A. Langenberg, M. Vogel, M. Kossick, C. Ebrecht, K. Egashira, A. Terasaki, T. Moeller, B. V. Issendorff, and J. T. Lau, *Phys. Rev. Lett.* **108**, 057201 (2012).
- ⁴⁷M. Wu, A. K. Kandalam, G. L. Gutsev, and P. Jena, *Phys. Rev. B* **86**, 174410 (2012).
- ⁴⁸P. G. Alvarado-Leyva, F. Aguilera-Granja, L. C. Balbás, and A. Vega, *Phys. Chem. Chem. Phys.* **15**, 14458 (2013).
- ⁴⁹D. E. Bergeron, A. W. Castleman, T. Morisato, and S. N. Khanna, *Science* **304**, 84 (2004).
- ⁵⁰R. Burgert, H. Schnöckel, M. Olzmann, and K. H. Bowen, Jr., *Angew. Chem., Int. Ed. Engl.* **45**, 1476 (2006).
- ⁵¹G. L. Gutsev, M. D. Mochena, C. W. Bauschlicher, Jr., W.-J. Zheng, O. C. Thomas, and K. H. Bowen, *J. Chem. Phys.* **129**, 044310 (2008).
- ⁵²Y. Jia and Z. Luo, *Coord. Chem. Rev.* **400**, 213053 (2019).
- ⁵³P. Felício-Sousa, K. F. Andriani, and J. L. F. Da Silva, *Phys. Chem. Chem. Phys.* **23**, 8739 (2021).
- ⁵⁴J. L. Chen, C. S. Wang, K. A. Jackson, and M. R. Pederson, *Phys. Rev. B* **44**, 6558 (1991).
- ⁵⁵M. Castro and D. R. Salahub, *Phys. Rev. B* **49**, 11842 (1994).
- ⁵⁶P. Ballone and R. O. Jones, *Chem. Phys. Lett.* **233**, 632 (1995).
- ⁵⁷S. Yu, S. Chen, W. Zhang, L. Yu, and Y. Yin, *Chem. Phys. Lett.* **446**, 217 (2007).
- ⁵⁸Q.-M. Ma, Z. Xie, J. Wang, Y. Liu, and Y.-C. Li, *Solid State Commun.* **142**, 114 (2007).
- ⁵⁹G. L. Gutsev, C. A. Weatherford, P. Jena, E. Johnson, and B. R. Ramachandran, *J. Phys. Chem. A* **116**, 10218 (2012).
- ⁶⁰O. Diéguez, M. Alemany, C. Rey, P. Ordejón, and L. Gallego, *Phys. Rev. B* **63**, 205407 (2001).
- ⁶¹H. K. Yuan, H. Chen, A. L. Kuang, C. L. Tian, and J. Z. Wang, *J. Chem. Phys.* **139**, 034314 (2013).
- ⁶²T. Oda, A. Pasquarello, and R. Car, *Phys. Rev. Lett.* **80**, 3622 (1998).
- ⁶³D. Hobbs, G. Kresse, and J. Hafner, *Phys. Rev. B* **62**, 11556 (2000).
- ⁶⁴G. Rollmann, P. Entel, and S. Sahoo, *Comput. Mater. Sci.* **35**, 275 (2006).
- ⁶⁵C. N. R. Rao and G. R. Rao, *Surf. Sci. Rep.* **13**, 223 (1991).
- ⁶⁶E. D. Pillai, T. D. Jaeger, and M. A. Duncan, *J. Phys. Chem. A* **109**, 3521 (2005).
- ⁶⁷S. Shetty, A. P. J. Jansen, and R. A. van Santen, *J. Phys. Chem. C* **112**, 17768 (2008).
- ⁶⁸C. Kerpál, D. J. Harding, J. T. Lyon, G. Meijer, and A. Fielicke, *J. Phys. Chem. C* **117**, 12153 (2013).
- ⁶⁹G. Ertl, *Angew. Chem., Int. Ed. Engl.* **47**, 3524 (2008).
- ⁷⁰J. R. Jennings, *Catalytic Ammonia Synthesis: Fundamentals and Practice* (Springer Science & Business Media, 2013).
- ⁷¹F. Bottomley and R. Burns, *A Treatise on Dinitrogen Fixation* (Wiley-Interscience, New York, 1979).
- ⁷²H.-J. Freund, B. Bartos, R. P. Messmer, H. Grunze, H. Kuhlbeck, and M. Neumann, *Surf. Sci.* **185**, 187 (1987).
- ⁷³M.-C. Tsai, U. Ship, I. C. Bassignana, J. Küppers, and G. Ertl, *Surf. Sci.* **155**, 387 (1985).
- ⁷⁴J. J. Mortensen, L. B. Hansen, B. Hammer, and J. K. Nørskov, *J. Catal.* **182**, 479 (1999).
- ⁷⁵J. J. Mortensen, M. V. Ganduglia-Pirovano, L. B. Hansen, B. Hammer, P. Stoltze, and J. K. Nørskov, *Surf. Sci.* **422**, 8 (1999).
- ⁷⁶H. A. Duarte, D. R. Salahub, T. Haslett, and M. Moskovits, *Inorg. Chem.* **38**, 3895 (1999).
- ⁷⁷T. L. Haslett, S. Fedrigo, K. Bosnick, M. Moskovits, H. A. Duarte, and D. Salahub, *J. Am. Chem. Soc.* **122**, 6039 (2000).
- ⁷⁸B. Chen, G. L. Gutsev, W. Sun, X. Kuang, C. Lu, L. G. Gutsev, S. M. Aldoshin, and B. R. Ramachandran, *Phys. Chem. Chem. Phys.* **23**, 2166 (2021).
- ⁷⁹I. Swart, F. M. F. de Groot, B. M. Weckhuysen, P. Gruene, G. Meijer, and A. Fielicke, *J. Phys. Chem. A* **112**, 1139 (2008).
- ⁸⁰D. M. Kiawi, V. Chernyy, J. Oomens, W. J. Buma, Z. Jamshidi, L. Visscher, L. B. F. M. Waters, and J. M. Bakker, *J. Phys. Chem. Lett.* **7**, 2381 (2016).
- ⁸¹S. K. Loh, D. A. Hales, L. Lian, and P. B. Armentrout, *J. Chem. Phys.* **90**, 5466 (1989).
- ⁸²S. Dillinger, J. Mohrbach, J. Hower, M. Gaffga, and G. Niedner-Schatteburg, *Phys. Chem. Chem. Phys.* **17**, 10358 (2015).
- ⁸³J. Mohrbach, J. Lang, S. Dillinger, M. Prosenec, P. Braunstein, and G. Niedner-Schatteburg, *J. Mol. Spectrosc.* **332**, 103 (2017).
- ⁸⁴J. Mohrbach, S. Dillinger, and G. Niedner-Schatteburg, *J. Phys. Chem. C* **121**, 10907 (2017).
- ⁸⁵S. Dillinger, J. Mohrbach, and G. Niedner-Schatteburg, *J. Chem. Phys.* **147**, 184305 (2017).
- ⁸⁶M. P. Klein, A. A. Ehrhard, J. Mohrbach, S. Dillinger, and G. Niedner-Schatteburg, *Top. Catal.* **61**, 106 (2018).
- ⁸⁷S. Dillinger, M. P. Klein, A. Steiner, D. C. McDonald, M. A. Duncan, M. M. Kappes, and G. Niedner-Schatteburg, *J. Phys. Chem. Lett.* **9**, 914 (2018).
- ⁸⁸D. V. Fries, M. P. Klein, A. Steiner, M. H. Prosenec, and G. Niedner-Schatteburg, *Phys. Chem. Chem. Phys.* **23**, 11345 (2021).
- ⁸⁹S. Peredkov, M. Neeb, W. Eberhardt, J. Meyer, M. Tombers, H. Kampschulte, and G. Niedner-Schatteburg, *Phys. Rev. Lett.* **107**, 233401 (2011).
- ⁹⁰A. Straßner, C. Wiehn, M. P. Klein, D. V. Fries, S. Dillinger, J. Mohrbach, and G. Niedner-Schatteburg, "Cryo spectroscopy of N₂ on cationic iron clusters," *155(23)* (in press) (2021).
- ⁹¹C. Berg, T. Schindler, G. Niedner-Schatteburg, and V. E. Bondybey, *J. Chem. Phys.* **102**, 4870 (1995).
- ⁹²S. Maruyama, L. R. Anderson, and R. E. Smalley, *Rev. Sci. Instrum.* **61**, 3686 (1990).

⁹⁵D. Proch and T. Trickl, *Rev. Sci. Instrum.* **60**, 713 (1989).

⁹⁶M. Graf, Diploma thesis, TU Kaiserslautern, 2006.

⁹⁵T. Su and M. T. Bowers, *J. Chem. Phys.* **58**, 3027 (1973).

⁹⁶T. Su and M. T. Bowers, *J. Am. Chem. Soc.* **95**, 1370 (1973).

⁹⁷P. Langevin, *Ann. Chim. Phys.* **5**, 245 (1905); available at (open access): <https://gallica.bnf.fr/ark:/12148/bpt6k34935p/f242.item>.

⁹⁸T. Su and M. T. Bowers, *Int. J. Mass Spectrom. Ion Phys.* **12**, 347 (1973).

⁹⁹G. Kummerlöwe and M. K. Beyer, *Int. J. Mass Spectrom.* **244**, 84 (2005).

¹⁰⁰D. Roy, R. Robles, and S. Khanna, *J. Chem. Phys.* **132**, 194305 (2010).

¹⁰¹P. Bobadova-Parvanova, K. A. Jackson, S. Srinivas, M. Horoi, C. Köhler, and G. Seifert, *J. Chem. Phys.* **116**, 3576 (2002).

A.2 Cryo Spectroscopy of N₂ on Cationic Iron Clusters

A.2.1 Preamble

The following chapter is a reprint of a publication in the journal *“The Journal of Chemical Physics”*

A. Straßner, M. P. Klein, S. Dillinger, J. Mohrbach, G. Niedner-Schatteburg and myself conceived and conducted the experiments. A. Straßner, C. Wiehn and M. H. Prosenc conducted the quantum chemical calculations. A. Straßner, P. B. Armentrout and G. Niedner-Schatteburg evaluated all data and wrote the manuscript, which all authors agreed to.

Full Reference

Cryo Spectroscopy of N₂ on Cationic Iron Clusters

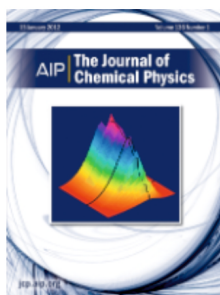
A. Straßner, C. Wiehn, M. P. Klein, D. V. Fries, S. Dillinger, J. Mohrbach, M. H. Prosenc, P. B. Armentrout, G. Niedner-Schatteburg, *The Journal of Chemical Physics* **2021**, 155, 244305.

<https://doi.org/10.1063/5.0064966>

A.2.2 Reprint

Reprint permission

Reproduced with permission of AIP Publishing.



Cryo spectroscopy of N₂ on cationic iron clusters

Author: Straßner, Annika; Wiehn, Christopher

Publication: Journal of Chemical Physics

Publisher: AIP Publishing

Date: Dec 28, 2021

Rights managed by AIP Publishing.

Creative Commons

This is an open access article distributed under the terms of the [Creative Commons CC BY](https://creativecommons.org/licenses/by/4.0/) license, which permits unrestricted use, distribution, and reproduction in any medium, provided the original work is properly cited.

You are not required to obtain permission to reuse this article.

Cryo spectroscopy of N₂ on cationic iron clusters

Cite as: J. Chem. Phys. 155, 244305 (2021); doi: 10.1063/5.0064966

Submitted: 28 July 2021 • Accepted: 25 October 2021 •

Published Online: 28 December 2021



View Online



Export Citation



CrossMark

Annika Straßner,¹ Christopher Wiehn,¹ Matthias P. Klein,¹ Daniela V. Fries,¹ Sebastian Dillinger,¹ Jennifer Mohrbach,¹ Marc H. Prosenč,¹ P. B. Armentrout,² and Gereon Niedner-Schatteburg^{1,a)}

AFFILIATIONS

¹Fachbereich Chemie and Forschungszentrum OPTIMAS, Technische Universität Kaiserslautern, 67663 Kaiserslautern, Germany²Department of Chemistry, University of Utah, Salt Lake City, Utah 84112, USA^{a)}Author to whom correspondence should be addressed: gns@chemie.uni-kl.de

TU Kaiserslautern, Fachbereich Chemie: Erwin-Schrödinger-Straße 52, 67663 Kaiserslautern, Germany

ABSTRACT

Infrared photodissociation (IR-PD) spectra of iron cluster dinitrogen adsorbate complexes $[\text{Fe}_n(\text{N}_2)_m]^+$ for $n = 8\text{--}20$ reveal slightly redshifted IR active bands in the region of $2200\text{--}2340\text{ cm}^{-1}$. These bands mostly relate to stretching vibrations of end-on coordinated N₂ chromophores, a $\mu_{1,\text{end}}$ end-on binding motif. Density Functional Theory (DFT) modeling and detailed analysis of $n = 13$ complexes are consistent with an icosahedral Fe_{13}^+ core structure. The first adsorbate shell closure at $(n, m) = (13, 12)$ —as recognized by the accompanying paper on the kinetics of N₂ uptake by cationic iron clusters—comes with extensive IR-PD band broadening resulting from enhanced couplings among adjacent N₂ adsorbates. DFT modeling predicts spin quenching by N₂ adsorption as evidenced by the shift of the computed spin minima among possible spin states (spin valleys). The IR-PD spectrum of (17,1) surprisingly reveals an absence of any structure but efficient non-resonant fragmentation, which might indicate some weakly bound (roaming) N₂ adsorbate. The multiple and broad bands of (17, m) for all other cases than (17,1) and (17,7) indicate a high degree of variation in N₂ binding motifs and couplings. In contrast, the (17,7) spectrum of six sharp bands suggests pairwise equivalent N₂ adsorbates. The IR-PD spectra of (18, m) reveal additional features in the $2120\text{--}2200\text{ cm}^{-1}$ region, which we associate with a $\mu_{1,\text{side}}$ side-on motif. Some additional features in the (18, m) spectra at high N₂ loads indicate a $\mu_{1,\text{tilt}}$ tilted end-on adsorption motif.

© 2021 Author(s). All article content, except where otherwise noted, is licensed under a Creative Commons Attribution (CC BY) license (<http://creativecommons.org/licenses/by/4.0/>). <https://doi.org/10.1063/5.0064966>

I. INTRODUCTION

The interaction of small molecules such as NO, N₂, and H₂ with transition metals (TMs) is an early elementary step in heterogeneous catalysis.^{1–6} TM cations^{7–9} and TM clusters^{10–14} have served as model systems to mimic such catalysts and related elementary processes. TM cluster studies offer the opportunity to study TM-adsorbate interactions in analogy to TM surface studies.^{15,16} These include an early mass spectral (MS) investigation of N₂ chemisorption to Fe and Co clusters.¹⁷

N₂ activation is an early elementary process in the course of ammonia synthesis, catalyzed under extreme conditions by the Haber–Bosch process using Fe, Ni, Ru, and other TMs.^{16,18–21} It is often identified as the rate-determining bottleneck of the overall reaction. Early surface science studies investigated N₂ adsorption on various Fe surfaces.^{22–25} A subsequent study of N₂ adsorbates on the Fe(111) surface by Low-Energy Electron Diffraction (LEED) in

conjunction with early *ab initio* modeling identified $\alpha\text{-N}_2$ and $\gamma\text{-N}_2$ binding motifs.²⁶ These observations may relate to variations in hapticities, namely, side-on (η^2) and end-on (η^1) coordination of N₂ to single metal centers, or variations in coordination, namely, on top of a single Fe center (μ_1), or bridging two centers (μ_2), or in the hollow of three centers (μ_3). A third $\beta\text{-N}_2$ motif was found by further spectroscopic investigations and describes a dissociative chemisorption of the N₂ molecule to the Fe(111) metal surface atoms.^{27,28} Further modeling identified various dissociation channels²⁹ and predicted the most favorable N₂ adsorption on a quadruple hollow site.³⁰ On a potassium promoted Fe(111) surface, Whitman *et al.* found ¹⁵N₂ vibrational frequencies of $\alpha\text{-N}_2$ (1415 cm^{-1}) and $\gamma\text{-N}_2$ (2100 cm^{-1}) in vibrational and thermal-desorption spectra.³¹

The Infrared Multiple Photon Dissociation (IRMPD) method is established to elucidate vibrational modes of adsorbates on TM clusters and TM coordination complexes as isolated ions.^{32–35} Its spectral range was extended by the advent of Free Electron Lasers (FELs)

in the IR.^{36–38} The brute force IRMPD method may turn into a more gentle single photon IR-PD method when ensuring a low fragmentation threshold, e.g., by the cryo mediated attachment of weakly bound chaperones that do not disturb other important features. Such an approach is labeled a tagging or messenger technique.^{39–43} Of course, molecular tags may turn into chromophores, and that is the case when utilizing N₂.⁴⁴

The tagging approach has proven successful and gained further insight into the adsorbate cluster interaction, for instance, in the case of Fe clusters with H₂ or water. IR spectroscopic characterization of Fe_n⁺ cluster H₂ adsorbate complexes has revealed the formation of twofold or threefold coordinated hydrides, whereas related studies of extended metal surfaces revealed a preference for exclusively high hydride coordination, threefold or higher, and migration into the bulk.⁴⁵ Somewhat surprisingly, the water hydrolysis by cationic Fe clusters increases with cluster size.⁴⁶ FEL studies of Fe cluster CO adsorbate complexes revealed systematic cluster size and charge effects.^{47–49}

At this point, it becomes beneficial to realize that the carbon monoxide molecule, CO, is one of the most widely studied ligands, and its composite binding mechanism is claimed to be well understood. The composite CO–TM binding is described in terms of a concerted σ -donation from CO to TM and a π -backdonation from TM to CO, as described for the case of TM surfaces⁵⁰ and for the cases of single TM centers in coordination compounds.^{51,52} In both cases, the CO–TM interactions lead to noticeable redshifts of CO vibrations with a diagnostic value. In strong analogy, all of these concepts transfer to the characterization of CO–TM cluster interactions^{53–56} and to N₂–TM interactions, N₂ being isoelectronic with CO and polarizing upon TM interaction.

Fundamentals of how nitrogen interacts with TM cations (TM = V, Nb, and Rh) were clarified by application of IRMPD spectroscopy in the Duncan group.^{57–59} The Fielicke group studied N₂ on neutral Ru clusters and identified exclusively end-on (η^1) coordination.⁶⁰ Discrete Fourier transform (DFT) modeling of N₂ on a Ru surface predicted activation barriers and active sites at the level of pure DFT functionals.⁶¹

It is a mandatory complement to augment spectroscopy by quantum chemical modeling of investigated systems whenever possible. Numerous theoretical studies dealt with the modeling of small, bare Fe clusters, investigating their structure, energetics, and magnetic moments.^{62–70} N₂ interactions with Fe clusters received attention in the course of further DFT modeling studies, all of which concluded in a strong preference of N₂ end-on coordination to single Fe centers.^{71,72} Most recent DFT modeling deals with the coalescence of iron nitride clusters and concomitant spin reduction, leaving open the question whether pure DFT functionals are applicable.⁷³

Iron cluster cation chemistry has been explored using guided ion beam tandem mass spectrometry (GIBMS) at the University of Utah. After initial measurements of the cluster binding energies by collision-induced dissociation (CID) with Xe,^{74,75} thermochemistry for reactions of Fe_n⁺ with D₂ ($n = 2–15$),⁷⁶ O₂ ($n = 2–18$),⁷⁷ CO₂ ($n = 1–18$),⁷⁷ and CO ($n = 1–17$)⁴⁹ was examined. Of direct relevance to the present work, reactions of Fe_n⁺ ($n = 1–19$) with N₂ and ND₃ were examined and Fe_n⁺–N and Fe_n⁺–2N bond energies were measured.^{78,79} An activation barrier of 0.48 ± 0.03 eV was determined for activation of N₂ by the larger clusters ($n = 12, 15–19$).

With the tandem cryo ion trap instrument^{44,80} at the Technische Universität Kaiserslautern (TUK) laboratory, we are able to conduct Infrared Photon Dissociation (IR-PD) spectroscopy experiments at temperatures down to 11 K, as well as adsorption and reaction kinetics studies. With this combination of methods, we were able to study the cluster-adsorbate-interaction of various TM clusters, e.g., for Ni_n⁺ clusters, we established a concept of size-dependent rough and smooth cluster surfaces.^{80–82} We transferred this concept to the N₂ adsorption on Rh_n⁺⁸³ and Co_n⁺⁴⁴ clusters. With the ability to introduce different reaction gases into two subsequent cryo ion traps, we were able to check the influence of one adsorbate on another and vice versa, applying (N₂, H₂) to Ru_s⁺ clusters.⁸⁴ Our recent IR-PD study of the N₂ activation by small Ta⁺ clusters revealed a multiple step activation pathway with submerged barriers.⁸⁵

The present study elucidates the vibrational spectroscopy of N₂ adsorbates onto cationic iron clusters [Fe_n(N₂)_m]⁺ ($n = 8–20$). It obtains strong support of its findings through our adjoined cryogenic kinetic study,⁸⁶ which we will refer to as CKS in the following. We gain insights into coordination motifs and interactions of N₂ adsorbates, and we receive some decisive support from our concomitant DFT modeling at the level of hybrid DFT functionals. These methods are not easily applied in the cases of larger clusters.

II. EXPERIMENTAL AND COMPUTATIONAL METHODS

All experiments were performed in a customized Fourier Transform Ion Cyclotron Resonance (FT-ICR) mass spectrometer (Apex Ultra Bruker Daltonics). It was used to perform the cluster production, isolation, N₂ condensation, IR-PD spectroscopy, and mass analysis. For a detailed description of the formation of the cluster adsorbate complexes, refer to CKS. As for those kinetic studies, the clusters and their adsorbate complexes were stored for spectroscopic interrogation within the RF hexapole ion trap in conjunction with a He buffer gas at 26 K. This ensures equilibrated cluster ion temperatures of below 40 K under any circumstances.

The IR-PD spectra were measured by coupling the FT-ICR cell to a tunable IR laser (spectral resolution: $\delta n = 0.9$ cm⁻¹ and pulse length $\delta t = 10$ ns). This laser is a KTP/KTA optical parametric oscillator/amplifier (OPO/A, LaserVision) system pumped by a pulsed 10 Hz injection seeded Nd:YAG laser (PL8000, Continuum). The following AgGaSe₂ crystal generates the difference frequency (DF) between the optical parametric amplifier (OPA) signal and idler waves and generates IR radiation in the range of 1000–2400 cm⁻¹. Each trapped and isolated ion packet is irradiated by 7–10 laser pulses (0.1–3.5 mJ/pulse) to create a sufficient amount of fragment ions. The IR-PD spectra were recorded as ion chromatograms while continuously scanning the IR wavelength. The IR-PD signal was evaluated as fragmentation efficiency = $\frac{\sum_i F_i}{\sum_i F_i + \sum_i P_i}$, where F_i and P_i indicate the fragment and the parent ion signals. An experimental IR-PD spectrum results from a plot of the fragmentation efficiency as a function of the laser frequency. The IR-PD spectra were recorded in the range of 1980–2340 cm⁻¹ on the [Fe_n(N₂)_m]⁺ = (n, m) species ($n = 8–20$). One or two photons provide sufficient energies to induce loss of a single N₂ adsorbate, which is predicted by our DFT modeling (see below) to be bound by about 30–50 kJ/mol (see, e.g., Fig. 11). For all complexes, the loss of single or multiple N₂ was the only observed fragmentation channels.

All density functional theory calculations, including geometry optimizations, and vibrational analysis, were performed using the Gaussian 09⁸⁷ and Gaussian 16⁸⁸ packages with the pure and hybrid exchange–correlation functionals Perdew–Burke–Ernzerhof (PBE),⁸⁹ PBE0,⁹⁰ and TPSSH^{91,92} for small clusters and the pure DFT functional PBE for the large ones. We utilized the Ahlrichs/Weigend effective core potential (ECP) basis set def2TZVP throughout.⁹³ We checked all obtained minimum structures for lack of imaginary frequencies. The computed IR spectra at the PBE0/def2TZVP level were scaled by a factor of 0.971 to account for prevailing anharmonicities, and they were convoluted by application of a Lorentz profile with FWHM = 5 cm⁻¹. All other obtained spectra are documented in the SI without scaling. We envisage our current DFT results as “exploratory,” and we rate them as a starting point for further and more elaborate calculations.

III. RESULTS AND DISCUSSION

A. First and second N₂ adsorption

In order to augment our kinetic findings (CKS), we recorded IR-PD spectra of the cluster adsorbate complexes [Fe_n(N₂)₁]⁺, abbreviated (*n*,1), and [Fe_n(N₂)₂]⁺, abbreviated (*n*,2), for *n* = 8–20. We recorded all of their spectra in the region of 1980–2340 cm⁻¹ (Fig. S1), and we recorded some further spectra of (18,16) and (13,6) in the region of 1150–2400 cm⁻¹ (Figs. S2 and S3). In summary, none of these spectra exhibited IR-PD bands below 2150 cm⁻¹. In the following, we focus on an analysis of the region from 2150 to 2340 cm⁻¹ (Fig. 1).

All species, except [Fe₁₇(N₂)₁]⁺, show at least one IR active band in the investigated region, and this band is most likely associated with stretching vibrations of end-on coordinated N₂ chromophores. The (*n*,1) and (*n*,2) species with *n* = 11, 12, 16, and 18 exhibit a slightly shifted second band each, and the (*n*,2) species with *n* = 8, 17, 19, and 20 reveal such a second band, while the corresponding (*n*,1) species do not. The appearance of a second band may originate from Fe_n⁺ cluster core isomers, from the presence of non-equivalent adsorption sites, or from different spin states of the cluster.

In general, these N₂ adsorbate bands are significantly redshifted with respect to the free N₂ stretching frequency (2330 cm⁻¹).⁹⁴ This redshift is a result of the σ -donor π -acceptor synergism that weakens the N–N bond. The Blyholder model⁵⁰ has established this concept for CO adsorbates on metal surfaces, and in our earlier studies, we have adapted it for N₂ adsorbates on Co, Ni, Ru, or Rh.^{44,80,81,83,84} As compared to the N₂ adsorption on cationic Co and Ni clusters,^{44,80,81} the present N₂ adsorbate bands are less redshifted with respect to the free N₂ stretching frequency.

Looking at the spectra in more detail, one can perceive several special features. The most conspicuous feature is the missing band in the (17,1) spectrum and—in contrast—the appearance of two bands in the (17,2) spectrum. Also noticeable is the shift of the narrow N₂ band of (13,1) to that of (13,2) by 12 cm⁻¹. The spectra of the (18,1) and (18,2) species are the only ones that exhibit additional but weak IR-PD signal below 2250 cm⁻¹. These broad bands are located around 2200 cm⁻¹, which is 90 cm⁻¹ to the red of the strong N₂ stretching band in (18,1) and (18,2). Note that the Fe₁₈⁺ cluster shows special behavior in the kinetic studies in the form of a less-reactive isomer (CKS). The 2200 cm⁻¹ bands in the IR-PD

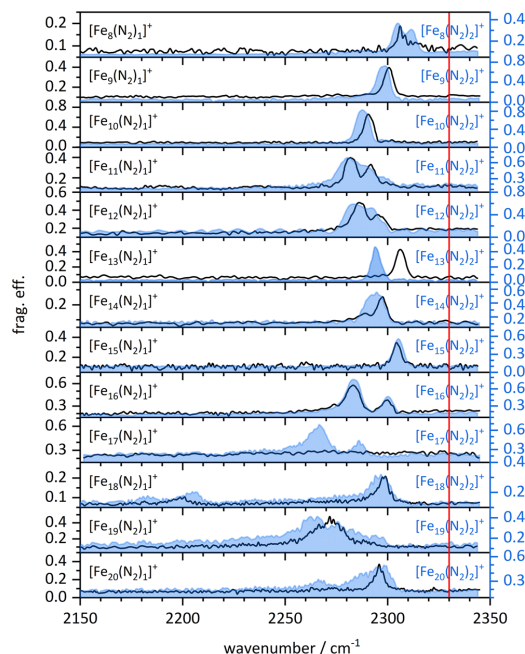


FIG. 1. IR-PD spectra of (*n*,1) (solid lines) and (*n*,2) (blue shaded areas) species for *n* = 8–20 at 26 K. All bands are significantly red-shifted with respect to the free N₂ stretch (red line). In most cases, there are only subtle differences between the spectra of first and second N₂ adsorbates. Only for [Fe₁₃(N₂)_{1,2}]⁺ and [Fe₁₇(N₂)_{1,2}]⁺ are there considerable differences upon adsorption of the second N₂ molecule. The [Fe₁₈(N₂)_{1,2}]⁺ cluster adsorbate complexes are the only species that come with some weak bands around 2200 cm⁻¹.

spectra of (18,1) and (18,2) might be an indicator for an enhanced or a further auxiliary interaction between cluster and nitrogen adsorbate, which might point toward a precursor of nitrogen activation.

The (19,1) spectrum reveals a significantly broadened band (FWHM > 20 cm⁻¹) around 2270 cm⁻¹. For *n* = 11 and 12, the second separated band for the (*n*,1) species transforms more to a shoulder in the spectra for the (*n*,2). The cluster with *n* = 14 reveals a shoulder in the case of (14,1), which has merged with the primary band in the (14,2) spectrum.

Thus, the recorded IR-PD spectra indicate preferential end-on coordination of N₂ adsorbates and some extraordinary enhanced interaction in the case of *n* = 18. Other more involved and activating types of N₂ binding, as known from surface studies, would lead to spectral features far below 2000 cm⁻¹.^{27,95} Our own calculations confirm that bridging motifs have IR absorptions in a much lower wavenumber range than investigated here (Fig. S14).

In summary, the observed peak positions of first and second N₂ adsorbates, likely end-on, reveal little to no systematic variation

(cf. Figs. 1 and 2), but for some solitary exceptions, that might result from specific adsorption sites and/or symmetric/antisymmetric couplings of adjacent N_2 chromophores. We take this finding as an indication for a largely equivalent bonding situation of the first and second N_2 on the Fe_n^+ cluster surface. The only exception is the Fe_{18}^+ cluster, which reveals some indication for an N_2 preactivating binding motif.

There are no clear trends of N_2 vibrational frequencies with cluster size, as observed in cationic Ni clusters and interpreted in terms of a charge dilution model (Fig. 2, dashed line).⁸⁰ One might conceive a weak trend among small iron clusters ($n = 8-11$) but not for bigger ones ($n \geq 12$). Overall, by comparing the present data with those of N_2 adsorption on cationic Ni clusters, it is noticeable that the Fe clusters show remarkably different behavior.

B. Fe_{13}^+

The spectra of $(13, m)$, $m = 1-6$ and 12, reveal several special features (Fig. 3). The intensities of cluster adsorbate complexes with $m = 7-11$ are very low (cf. Fe_{13}^+ kinetics in CKS), and thus, it is not possible to record their IR-PD spectra. The Fe_{13} cluster provides special features in x-ray magnetic circular dichroism (XMCD) investigations and computational studies.⁹⁶⁻⁹⁸ These studies show a significant dip of the magnetic moment per atom as compared to other sized clusters. Our own exploratory DFT calculations of the Fe_{13}^+ geometry and spin states were performed at three different levels of theory: PBE, PBE0, and TPSSh using the def2TZVP basis set throughout. The hybrid DFT functionals PBE0 and TPSSh predict high multiplicities, $2S + 1 = 46$ of the bare Fe_{13}^+ cluster with icosahedral structure (Figs. S8-10), whereas the pure DFT functional PBE, void of exact exchange, predicts a lower multiplicity, $2S + 1 = 36$

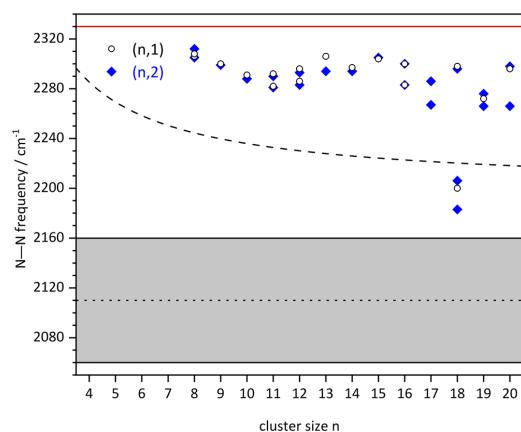


FIG. 2. N-N stretching frequency in $[Fe_n(N_2)_1]^+$ (black circles) and $[Fe_n(N_2)_2]^+$ (blue diamonds) for $n = 8-20$. The dashed line represents the trend of the N-N stretching frequency observed in cationic nickel clusters.⁸⁰ The red line is the stretching frequency of free N_2 . Also shown is the stretching frequency (black dotted line) with its FWHM (gray shaded area) of the so-called γ - N_2 on a clean iron surface, which is presumed to manifest some "on hollow" coordination, as revealed via vibrational EELS.⁹⁵

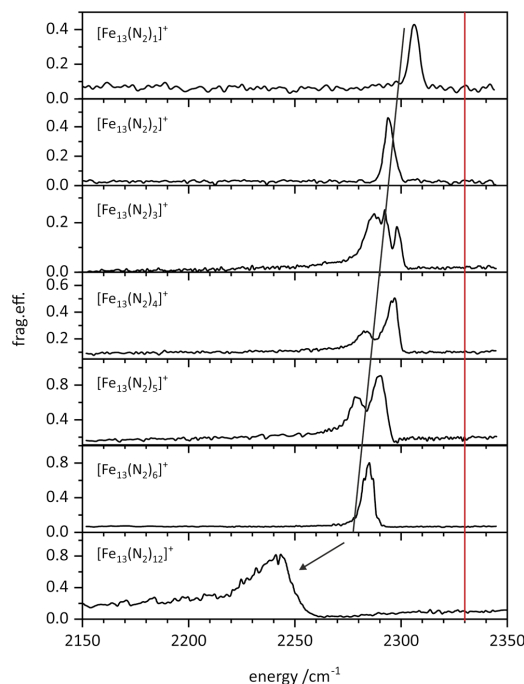


FIG. 3. IR-PD spectra of stepwise N_2 adsorption to the $(13, m)$ species at 26 K. From the narrow spectrum of the $[Fe_{13}(N_2)_6]^+$ cluster adsorbate complex, we deduce a highly symmetric geometry. There is a remarkable increase in the observed redshift from $(13, 6)$ to $(13, 12)$. The red vertical line indicates the stretching frequency of the free N_2 moiety.

(Figs. S8/S9). In the following, we primarily resort to results of the PBE0/def2TZVP level, which achieve the best agreement with the measured spectra using a scaling factor of 0.971. Results with the PBE functional (significantly smaller multiplicities and a scaling factor of significantly > 1) and with the TPSSh functional (at some points, different preferred structures and a scaling factor of ≈ 1) are included in the [supplementary material](#).

All of the measured IR active bands are redshifted with respect to the free N_2 stretching frequency (Fig. 3, red line). In a previous $Ta_4(N_2)_m$ study,⁸⁵ we identified a μ_2 - $\kappa N1:\kappa N1, N2$ across edge coordination motif and a μ_3 - $\kappa N1:\kappa N1, N2:\kappa N1, N2$ above surface motif, adopting the notation scheme of IUPAC and Salzer.⁹⁹ The latter does not apply in the current case of cryo N_2 spectra on Fe clusters; it would reveal much higher redshifts than observed. In any case, we utilize here the same nomenclature as in the tantalum case.

The $(13, 1)$ complex. We find a single sharp band at 2306 cm^{-1} (FWHM: 6 cm^{-1}). It seems reasonable at first sight that a highly symmetric icosahedron provides 12 equivalent adsorption sites, which leads to a single cluster adsorbate motif in the case of $(13, 1)$. This slightly redshifted band with respect to the free N_2 stretch

at 2330 cm⁻¹ indicates the presence of a μ_1 end-on adsorbed N₂ molecule, as confirmed by our own exploratory DFT calculations (Fig. S14). Some of the structures obtained—(13,1)A through (13,1)E—are archetypal (Fig. 4), and they deserve special attention, also in light of the upcoming discussion of larger clusters, $m = 17, 18$. There are small variations in stretching frequency if end-on coordinated N₂ is slightly tilted as in (13,1)A across an edge (μ_1 - κ N1(: κ N1), 46tet, ¹⁰²2304 cm⁻¹) or as in (13,1)B above a triangular facet (μ_1 - κ N1(: κ N1: κ N1), 46tet, 2316 cm⁻¹) of the icosahedron. Spin quenching, from 46tet to 44tet as in (13,1)C, comes with a tilt above facet (μ_1 - κ N1(: κ N1: κ N1), 44tet, 2285 cm⁻¹). We classify all of these three related motifs as N₂ end-on coordination, $\mu_{1,end}$. The energetic expense of the tilting is merely 2 kJ/mol; spin quenching adds an additional 15 kJ/mol.

There is another conceivable binding motif, (13,1)D, that comprises μ_2 bridging N₂ (μ_2 - κ N1: κ N1,N2, 44tet, 1883 cm⁻¹). This motif provides a significantly more redshifted IR fingerprint than that observed [cf. Fig. S2 (18,16) and Fig. S3 (13,6) for a survey of the low-frequency ranges] and an energetic expense of + 29 kJ/mol with respect to the most favorable $\mu_{1,end}$ motif.

At an even higher energy of + 43 kJ/mol, we find the (13,1)E structure, which provides an asymmetrically bound side-on N₂ ligand (μ_1 - κ N1,N2, 44tet, 2152 cm⁻¹) that reveals a medium amount of vibrational redshift. This $\mu_{1,side}$ motif finds no experimental support in the case of a smooth icosahedral surface, (13,1), but it shall become a focus of interest in the course of the $m = 18$ discussion.

The (13,2) complex. The observed single band of (13,2) jumps by 12 to 2294 cm⁻¹, with respect to the corresponding band in (13,1). The lack of any second band points toward the equivalence of both N₂ adsorbates, in accord with an icosahedral core structure.⁹⁷ For our DFT exploration, we chose three positions of the second N₂ adsorbate with respect to the first one: A directly adjacent arrangement (pseudo-ortho), an arrangement of both N₂ adsorbates with one Fe site in between (pseudo-meta), and an arrangement with opposite N₂ adsorbates, which corresponds to a distance of two vacant Fe sites (pseudo-para) (Fig. S17). The most stable structure with at most a single stretching frequency at 2298 cm⁻¹ is the 44tet with opposite N₂ adsorbates (Figs. S20/S21). This highly symmetric arrangement provides symmetrically and antisymmetrically coupled stretching vibrations of the two N₂s. The symmetrically coupled

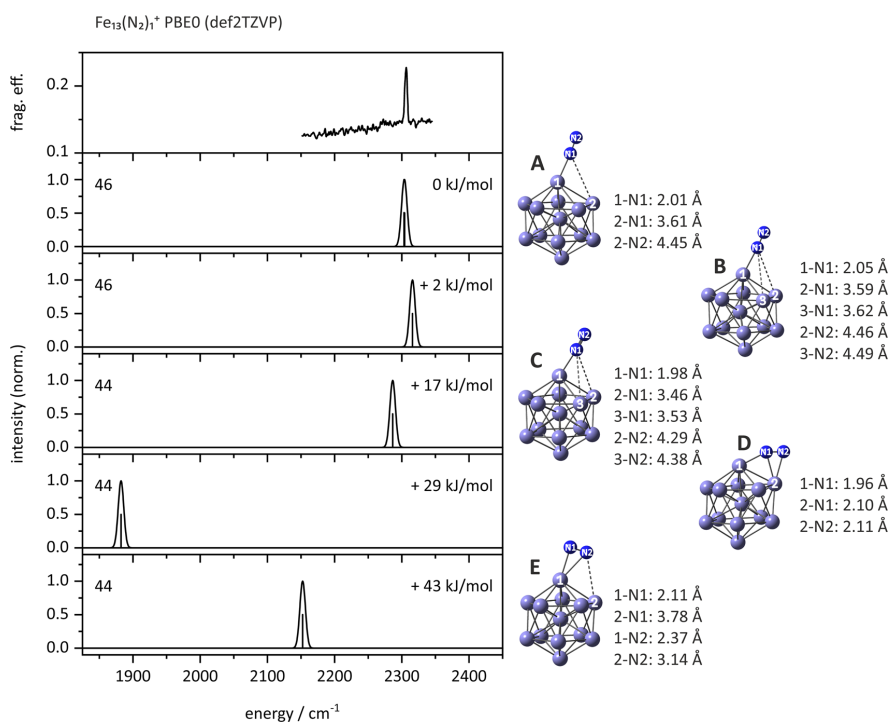


FIG. 4. Experimental IR-PD spectrum of (13,1) and DFT modeled spectra (PBE0/def2TZVP, scaling factor 0.971) with optimized cluster adsorbate structures and their Fe-N-bond lengths. End-on N₂ coordinations (A and B) match experiment the best. The asymmetric side-on coordination (E) is a motif that might become relevant at larger clusters (see the text).

stretching mode has very low IR intensity since no dipole moment changes by the vibration. The remaining antisymmetric stretching mode provides a single band. The calculated stretching frequency is 12 cm^{-1} shifted with respect to that of $[\text{Fe}_{13}(\text{N}_2)_1]^+ \text{A}$, in accord with the measured shift.

The (13,3) complex. In the spectrum of the (13,3) cluster adsorbate complex, we see three overlapping bands at 2287, 2292, and 2298 cm^{-1} . They indicate different adsorption sites, and they do not correspond exactly to any of the observed bands in (13,1) and (13,2). One might conceive a general shift by the amount of N_2 adsorption, as indicated by the diagonal line in Fig. 3. If so, then the 2294 cm^{-1} band in (3,2) corresponds to the 2287 cm^{-1} band in (13,3), and the 2306 cm^{-1} band in (13,1) corresponds to the 2298 cm^{-1} band in (13,3), making the 2292 cm^{-1} band in (13,3) a new feature. Of course, one has to keep in mind the known feature of symmetric and antisymmetric couplings of stretching modes in adjacent N_2 adsorbates.

By virtue of our DFT modeling, we identified five conceivable cluster adsorbate complexes of (13,3), with 3 N_2 molecules attached to the icosahedral surface (Fig. S25). A single structure includes the (13,2) adsorption motif [labeled (e) in Fig. S25], and this one turns out most favorable (by 15–21 kJ/mol) as compared to the other four structures (Fig. S28/S29). Third N_2 is added in the pseudo-ortho position to N_2 from the (13,2) motif, Fig. 5. Structure (e) assumes a 44tet, and it reveals three stretching frequencies at 2286, 2289, and 2303 cm^{-1} . The computed vibration at 2286 cm^{-1} originates from the antisymmetric stretching of the two adjacent N_2 molecules as in the (13,2) motif, and the symmetric combination appears at 2289 cm^{-1} . Both correspond well to the experimental bands at 2287 and 2292 cm^{-1} . The predicted vibration at 2303 cm^{-1} originates from the vibration of the sole distant N_2 molecule (Fig. 5), and it might correlate to the experimental band at 2298 cm^{-1} .

The (13,4) and (13,5) complexes. The IR-PD spectra of (13,4) and (13,5) reveal two bands each, which follow the general trend of shifts with the amount of N_2 adsorbates. Our exploratory quantum chemical modeling came close to interpret these bands but failed to obtain a close fit. We speculate that these bands might belong to vibrational motifs similar to (13,3), with the symmetric combination band being weak or blended.

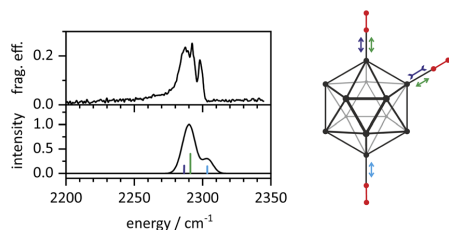


FIG. 5. Experimental IR-PD spectrum and DFT modeling of (13,3) vibrations. The computed structure is an icosahedron with a spin state of $2S + 1 = 44$. Three Fe centers adsorb an N_2 molecule each. The color-coding of the stick spectrum and the vibrational double arrow relate these to each other: the dark blue (antisymmetric) and green (symmetric), and the light blue represents stretching vibrations. The calculated spectrum is scaled for anharmonicity by 0.971. The central Fe atom and its coordination are omitted for clarity.

The (13,6) complex. The IR-PD spectrum of the (13,6) cluster adsorbate complex reveals a single, sharp band at 2285 cm^{-1} , with the same FWHM = 6 cm^{-1} as (13,1). We take both findings as strong evidence for high symmetry.

The anticipated icosahedral structure of naked Fe_{13}^+ provides a smooth cluster surface of 12 equivalent surface atoms. Seemingly, these 12 atoms might allow six equivalent adsorption sites. Our exploratory DFT modeling suggests the initial $\mu_{1,\text{end}}$ coordination of single N_2 adsorbates slightly tilted over an edge or face. Upon subsequent, multiple N_2 adsorptions of these slightly tilted end-on adsorbates result in a highly symmetric structure. Six of these motifs would fit on a single Fe_{13}^+ icosahedron. We find some evidence for such structures by our DFT modeling (Fig. 6), and the modeled vibrations come close to the experimental IR-PD spectrum (Fig. 7). Most noticeably, the single sharp band observed suggests that the vibrational couplings are weak, if present at all. This seems odd, given that all six N_2 adsorbates are adjacent to each other. In (13,2) and (13,3), such proximity leads to evident couplings and corresponding splittings. Their absence, or at least weakness, in (13,6) might indicate a considerable degree of N_2 tilting. As this coordinated, alternating tilting comes without vibrational coupling, the effect seems to relate to electronic coupling.

The (13,7) complex and beyond. As adsorption kinetics of the seventh N_2 is slow but speeds up considerably beyond, we failed to record IR-PD spectra of (13,7) through (13,11) because the ion intensities were extremely low. It looks as if the adsorption of seventh N_2 would be sterically hindered. Given a structure for (13,6) like that in Fig. 6, it seems conceivable that some reorganization of adsorbates needs to take place—in line with the observation of the low $k_{(13,6)}$ value (cf. CKS). After adsorption of seventh N_2 , a swift

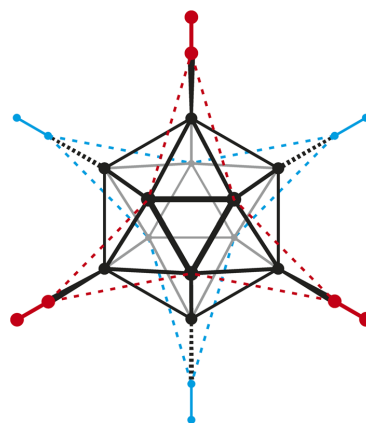


FIG. 6. A computed arrangement of six N_2 adsorbates with high symmetry in a $\text{Fe}_{13}(\text{N}_2)_6^+$ cluster adsorbate complex. The alternating tilting of N_2 ligands points out of plane to the front (red) and to the back (blue). The tilting of each end-on coordinated N_2 ligand occurs above a triangular facet toward a μ_3 -type coordination. We find N–N–Fe angles of 175° and N–Fe– $\text{Fe}_{\text{central}}$ angles of 150° , with minor variations for all six N_2 adsorbates. The central Fe atom and its coordination are omitted for clarity, and we apply Natta projection to Fe–N bonds only.

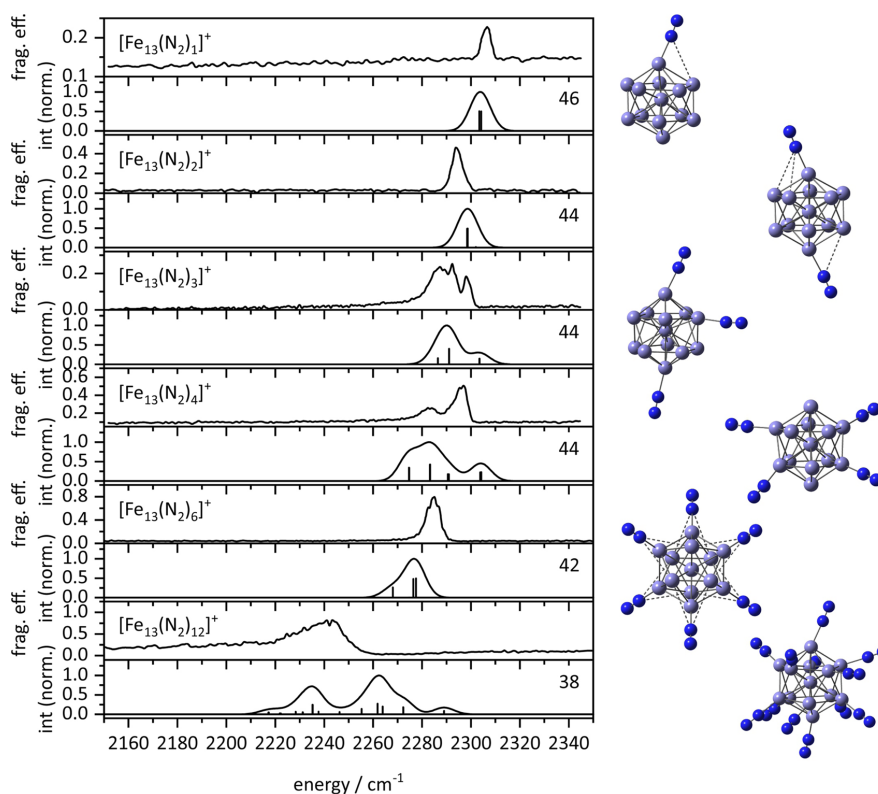


FIG. 7. Experimental IR-PD spectra and DFT modeled IR spectra of $(13,m)$, $m = 1-4, 6, 12$, at the PBE0/def2TZVP level (scaling factor: 0.971) and with most favorable multiplicity (as indicated); optimized structures are shown to the right of the DFT spectra. The modeling comes close to the observations, with differences in splittings and magnitudes. DFT modeling reaches its limits beyond $(13,12)$.

avalanche of further reorganization seems to occur such that adsorption to form $(13,12)$ is rapid. In **CKS**, we speculate about an adsorbate driven electronic reorganization of spin flips, which might act as the driving force. Further DFT modeling effort would be needed to come to more definite conclusions.

The $(13,12)$ complex. The IR-PD spectrum for the adsorption maximum, $m_{\max} = 12$, reveals a single broad, asymmetric band (FWHM = 18 cm^{-1}) with a long tail to the red. We speculate about two counteracting effects. A 1:1 stoichiometric, Langmuir-type end-on N₂ adsorption to each of 12 equivalent iron atoms on the icosahedron surface leads to a highly symmetric structure, and one might expect an IR-PD spectrum similar to that observed for $(13,6)$. On the other hand, the unavoidable proximity of the many N₂ molecules necessarily enables many mutual couplings that could lead to a significant broadening of otherwise equivalent IR stretching bands. In combination, a single shifted broad band might result. The observed magnitude of a $30\text{--}36 \text{ cm}^{-1}$ redshift going from $[\text{Fe}_{13}(\text{N}_2)_6]^+$ to

$[\text{Fe}_{13}(\text{N}_2)_{12}]^+$ is well in line with an observed redshift of $5\text{--}6 \text{ cm}^{-1}$ per additional N₂ ligand at smaller n . Our exploratory DFT calculations revealed multiple IR active N₂ stretching bands with many couplings that lead to a spreading out of bands across 100 cm^{-1} (Fig. 7).

The $(13, m)$ spin valleys by DFT. Although the IR-PD spectra do not provide information on the spin states of the cluster adsorbate complexes, the DFT calculations do. The results gain credibility through the favorable, yet qualitative modeling of the observed stretching vibrations. To verify this, however, we checked the relative stabilities of conceivable spin states of the studied cluster adsorbate complexes. Icosahedral Fe_{13}^+ geometries served as starting points, and we checked for full geometric relaxation of all nuclear degrees of freedom while maintaining full electronic convergence within the chosen quantum chemical model, the hybrid DFT functional PBE0, which comprises some admixture of Hartree-Fock-exchange and thus comes close to a valid

description of the actual electronics—excluding higher order effects such as spin–orbit coupling.

The total energies obtained are shown in Fig. 8 and correspond to the most stable adsorption isomers in all cases and form the basis for the following arguments. The results reveal an obvious so-called spin valley (as introduced before¹⁰⁰) with the highest stability of the naked Fe_{13}^+ at the spin multiplicity of $2S + 1 = 46$, a sextoquadragintet state. Notably, the adsorption of a single N_2 does not change this high-spin electronic arrangement, whereas the adsorption of two or more N_2 molecules does. In effect, there is a gradual spin quenching with progressive N_2 adsorption such that the (13,12) complex stabilizes at $2S + 1 = 38$. 12 N_2 adsorption events thus induce four instances of spin pairings. We have observed a similar spin-quenching phenomenon upon N_2 adsorption to Rh_5^+ clusters.¹⁰⁰

Although it is a challenge to interpret the observed spin quenching, it seems possible to speculate on the likely reasons. The naked Fe_{13}^+ cluster is superparamagnetic,^{96,98} and it is known to favor about three unpaired spins per atom on all of its surface atoms. These form a surface layer of singly occupied molecular orbitals (SOMOs) that exert Pauli repulsion to any closed-shell singlet state molecule (and N_2 is archetypical in this regard) that approaches. Thus, the molecule does not receive unpaired spin density. Donation of spin-paired electron density from the approaching N_2 to the cluster is thus hampered by the lack of accessible lowest unoccupied molecular orbitals (LUMOs), and the adsorption enthalpy will be small. This situation can change by turning pairs of cluster SOMOs into HOMO/LUMO pairs. The kinetic behavior provides some evidence that the concomitant promotion energy needed

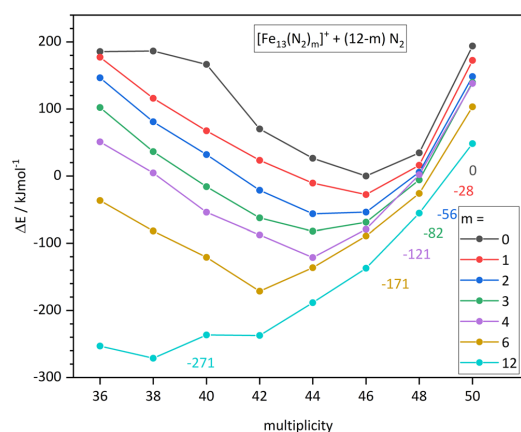


FIG. 8. Energetics of computed $[\text{Fe}_{13}(\text{N}_2)_m]^+$ cluster adsorbate complex structures as a function of the spin multiplicity $2S + 1$, normalized to the computed (13,0) spin isomer (icosahedron, 46tet) + 12 N_2 . The level of theory is PBE0/def2TZVP. Each depicted data point represents the optimized isomer of $[\text{Fe}_{13}(\text{N}_2)_m]^+$ in the given spin state. Connecting data of given m values yields the so-called spin valleys. The vertical offsets of adjacent curves indicate stepwise N_2 adsorption energies. Further spin-valley data at other levels of theory have similar shapes and are documented in the [supplementary material](#) (Figs. S4/S6).

for this conversion is overcompensated by the gain in adsorption enthalpy afforded by having an accessible LUMO for N_2 to bind. Thus, the rapid conversion of (13,6) to (13,12) is plausibly driven by this type of spin conversion. Accordingly, the spin valleys might be expected to shift stepwise toward lower multiplicities upon N_2 adsorption.

C. Fe_{17}^+

In the spectra of $(17,m)$, where $m = 1-7$ and 9, we observe broad bands in all cases of cluster adsorbate complexes, except for $(17,1)$, where no IR active band occurs, and $(17,7)$, which exhibits six narrow separate bands. All of the observed bands are redshifted with respect to the free N_2 stretching frequency (Fig. 9, red line). Note that the generally noisy spectra suffer from the weak ion intensities of all investigated $[\text{Fe}_{17}(\text{N}_2)_m]^+$ cluster adsorbate complexes. This is partially because of the very slow N_2 adsorption for Fe_{17}^+ (cf. Fe_{17}^+ kinetics in CKS). In addition, there is a high level of non-resonant fragmentation of about 20%–30% under present conditions, which is significantly less for all other cluster sizes n .

It is somewhat surprising to recognize the absence of any structure in the spectrum of $(17,1)$ but with reasonably efficient

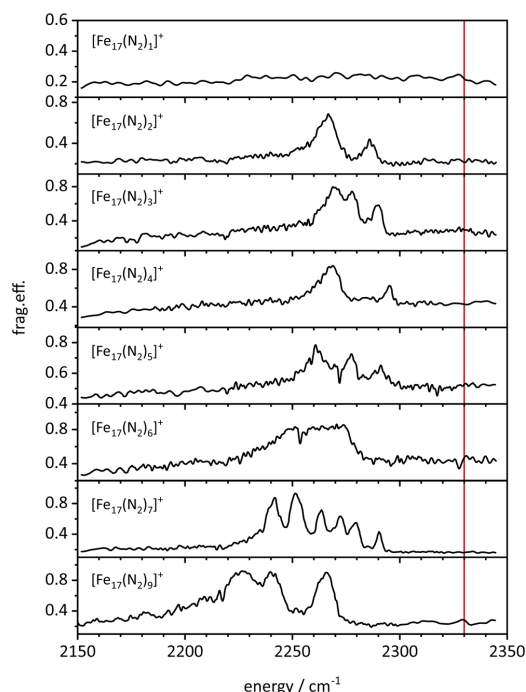


FIG. 9. IR-PD spectra of the $(17,m)$ species at 26 K. The spectrum of $(17,1)$ reveals no band but high non-resonant fragmentation, and the spectrum of $(17,7)$ reveals well resolved structures, while all other spectra experience significant broadening. The vertical red line indicates the stretching frequency of the free N_2 moiety.

non-resonant fragmentation. We speculate that there must be some kind of weakly bound, almost roaming N₂ adsorbate, which is volatile and susceptible to swift desorption (cf. Fe₁₇⁺ kinetics in CKS). This would imply a soft N₂ torsion, a broad distribution of N₂ orientations, and weak IR adsorption. The IR-PD spectra of “even” species (17,2) and (17,4) reveal two IR active bands at 2267 and 2286 cm⁻¹ and at 2269 and 2295 cm⁻¹, respectively, indicating the likely presence of two binding motifs of N₂. The “odd” species (17,3) and (17,5) reveal three bands at 2270, 2278, and 2290 cm⁻¹ and at 2261, 2277, and 2291 cm⁻¹, respectively. Part of the (17,3) spectrum with the splitting of 8 cm⁻¹ between the two most red-shifted bands is reminiscent of symmetric/antisymmetric couplings of N₂'s at adjacent equivalent adsorption sites, as observed and analyzed in the cases of [Ni_n(N₂)_m]⁺ investigated before.⁸⁰ The (17,5) spectrum is less well resolved and may allow for a similar interpretation but with high uncertainty. If so, the symmetric/asymmetric coupling of adjacent N₂ adsorbates would be significantly stronger as the coupling increased to about 20 cm⁻¹. The IR-PD spectrum of (17,6) is structureless with a single broad band (FWHM: 35 cm⁻¹) around 2265 cm⁻¹. This observation suggests that the adsorbate shell of six N₂'s on the surface of Fe₁₇⁺ is highly fluxional and strongly coupled. One might speculate about a “molten” adsorbate layer, which would be most surprising in view of the prevailing cryo conditions. Alternatively, the couplings among the seven N₂ ligands might increase with respect to those of mere six N₂ ligands such that the bands would spread further and become more easily discernible.

Even more surprising is the observation of a completely different spectrum for (17,7), which is well structured. This cluster adsorbate complex reveals six sharp, separate bands at 2242, 2251, 2264, 2272, 2280, 2290 cm⁻¹. As before, the splitting of 8–10 cm⁻¹ suggests the pairwise symmetric and antisymmetric coupling of N₂ adsorbates. It is remarkable to observe six resolved bands by seven N₂ chromophores, and it would take quantum chemical support to interpret this in detail (see below). In any case, we conclude that there can be little to no isomerism of (17,7) and suggest there must be a single distinct structure of the adsorbate layer. Thus, the (17,7) species is reminiscent of a “crystalline” adsorbate layer, which is in remarkable contrast to the suggested “molten” layer of (17,6).

The IR-PD spectrum of (17,9) reveals two broad and overlapping bands at 2227 and 2240 cm⁻¹ and a narrower isolated band at 2266 cm⁻¹. This result indicates a degree of symmetry and structural definition that is lower than (17,7) but higher than (17,6). The spectrum comes close to that of (17,3), which suggests a symmetric/asymmetric splitting of 13 cm⁻¹ for coupled N₂ oscillators, along with an interpretation of the 2266 cm⁻¹ band as corresponding to an isolated N₂ adsorbate.

It would be most desirable to check all of the above interpretations and assignments against appropriate high-level quantum chemical calculations. There are some DFT predictions of naked Fe₁₇ clusters published,^{66,68,69} which conclude that it has a capped hexagonal antiprism structure. Our own exploratory DFT studies at the PBE0 level find that the most stable structure has an icosahedral structural motif (cf. CKS, Fig. 14) with other structures conceivable. Unfortunately, it was impossible for us to conduct a systematic study of varying loads of N₂ adsorbates on these clusters. In this regard, as discussed below, the reduced level of theory (PBE) used to conduct

computational studies of a few (18, *m*) species did not provide useful spectroscopic information.

D. Fe₁₈⁺

As noted above (Fig. 1), the (18, *m*) case reveals a far red-shifted IR active region that is unique among all other investigated cluster sizes. Figure 10 shows spectra for *m* = 1–16. There are (multiple) bands in the region of 2120–2200 cm⁻¹ in addition to the end-on IR active region of 2200–2310 cm⁻¹. There are at least three facts that may—in principle—contribute to spectral complexity and need to be considered when interpreting the observed spectra: (1) the Fe₁₈⁺ structural isomerism as elucidated by kinetics (cf. CKS, Figs. 14 and S23), (2) the N₂ binding site isomerism, and (3) the N₂ coordination motif isomerism, where the binding motif might vary from on top (μ_1) via across edge (μ_2) to the above surface (μ_3). Our exploratory Fe₁₃(N₂)_{*m*}⁺ DFT studies at the appropriate PBE0 level of

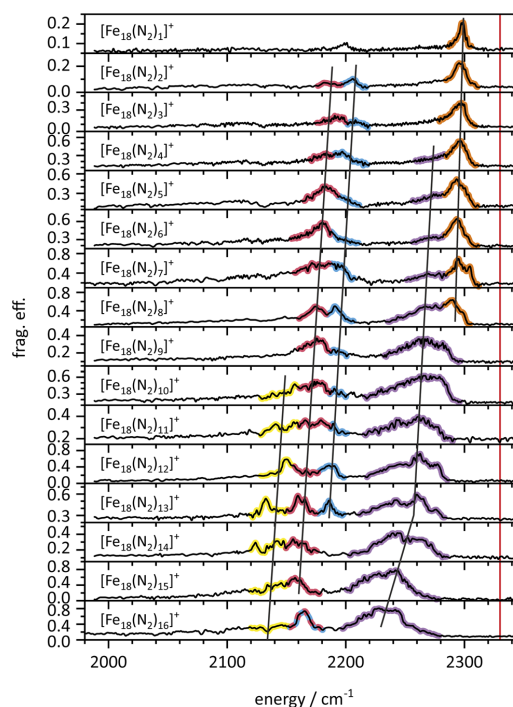


FIG. 10. Recorded IR-PD spectra of the (18, *m*) species at 26 K. All spectra reveal two IR active regions: from 2200 to 2320 cm⁻¹ and from 2100 to 2200 cm⁻¹. Tentative assignments associate the orange and violet features with a $\mu_{1,\text{end}}$ N₂ coordination, where the violet motif represents the more tilted end-on binding motif $\mu_{1,\text{tilt}}$. The more redshifted blue, red, and yellow features may relate to various $\mu_{1,\text{side}}$ N₂ coordination motifs (further details; see the text). All binding motifs shift to red with increasing N₂ adsorption. The red vertical line indicates the stretching frequency of free N₂.

theory (Fig. 4) revealed an unprecedented motif for (13,1)E, $\mu_{1,side}$, of an asymmetric bound side-on N_2 coordination μ_1 - $\kappa N_1, N_2$ with a stretching vibration at 2152 cm^{-1} , as well as a bridged μ_2 coordination motif (13,1)D, μ_2 - $\kappa N_1:\kappa N_1, N_2$, with a stretching vibration at 1883 cm^{-1} . The novel $\mu_{1,side}$ motif of (13,1)E exhibits a N_2 stretching mode that coincides with the range of the more redshifted region (2120 – 2200 cm^{-1}) in the spectra of (18, m). We speculate that the novel $\mu_{1,side}$ motif might appear in (18, m) as well. In contrast, the bridging μ_2 coordination motif of (13,1) is significantly more redshifted and thus does not serve to explain the (18, m) observations. As a matter of fact, none of our spectra reveal IR intensity in the predicted range of bridging μ_2 coordination. Note that the novel $\mu_{1,side}$ motif becomes IR active by virtue of an asymmetric coordination with Fe–N distances that were predicted to differ by about 0.2 \AA in the case of (13,1) (cf. Fig. 4).

The observed variations of the presumed $\mu_{1,side}$ IR fingerprint in (18, m), marked as yellow, red, and blue IR features in Fig. 10, may originate from non-equivalent N-binding Fe sites. The Fe_{18}^+ cluster has a rougher cluster surface, as compared to smooth, symmetric Fe_{13}^+ . This could be a reason for a diversity of N_2 binding motifs and the accessibility of the presumed $\mu_{1,side}$ motif.

The IR bands of (18, m) in the region of 2200 – 2310 cm^{-1} , marked as orange IR features, most likely correspond to the μ_1 end-on coordinated N_2 adsorbates, $\mu_{1,end}$. With higher N_2 coverage, mutual N_2 – N_2 interactions might set in and increase gradually. In effect, the average N_2 tilt with respect to the surface normal might increase, leading to band broadening and shifts to the red for $m \geq 9$. These effects provide a tentative assignment of the observed violet IR features as a $\mu_{1,tilt}$ adsorption motif.

All marked binding motifs in Fig. 10 shift to the red with increasing N_2 adsorption. The blue $\mu_{1,side}$ and orange $\mu_{1,end}$ motif vanish at high N_2 coverages, with the orange motif lost earlier than the blue motif. The difference $\Delta\nu(\text{blue} - \text{orange}) \approx 100\text{ cm}^{-1}$ remains constant throughout the variation of N_2 load ($m = 2$ – 8). The yellow $\mu_{1,side}$ motif sets in late at $m \geq 10$. The major red $\mu_{1,side}$ and violet $\mu_{1,end}$ motifs observed at almost all N_2 coverages provide a constant difference of $\Delta\nu(\text{red} - \text{violet}) \approx 90\text{ cm}^{-1}$ up to $m = 13$. The redshift of $\approx 2\text{ cm}^{-1}$ per additional N_2 adsorbate for the violet features increases at $m \geq 14$ up to $\approx 4.5\text{ cm}^{-1}$ per additional N_2 adsorbate. The band at 2200 cm^{-1} of (18,1) splits when adsorbing further N_2 's. In the cases of (18,2), (18,3), (18,8), and (18,13), the red and blue regions exhibit distinct bands that are separated by 15 – 20 cm^{-1} . This might indicate symmetric/antisymmetric N_2 stretching mode couplings with a slightly larger splitting than observed in the Ni– N_2 case.⁸⁰

Unfortunately, we cannot conduct a systematic DFT study of $Fe_{18}(N_2)_m^+$ complexes at the PBE0 because it would exceed our available computational resources. Our preliminary explorations at the reduced PBE level proved inappropriate and failed to predict any observed IR modes (Figs. S55/S59), as also observed in the cases of (13, m) and discussed above. Thus, the lack of explicit, high level DFT modeling precludes any definite assignments of the (18, m) IR-PD spectra. Nevertheless, the wealth of information from our kinetic studies, our IR experiments, and our exploratory DFT modeling of smaller clusters—most notably of (13,1)—allow for some valid speculation on the origin of the observed IR spectral features.

Despite our reluctance to utilize our DFT calculations at the PBE level for the interpretation of the IR-PD spectra, we, nevertheless, will examine the predicted structures, energetics, and spin couplings of some selected (18, m) species. We started our survey with three selected geometries of (18,0): icosahedral and hexagonal structural motifs, as documented in the literature,^{68–70,101} as well as a cubic-packed structure motif (Fig. S51). The computed stabilities of the icosahedral and the hexagonal structure are similar, whereas the cubic-packed motif is about 250 kJ/mol less stable (Fig. 11 and Fig. S51). In all three cases, we obtained clear preferences of high spin multiplicities: the icosahedral and hexagonal motifs get values of $2S + 1 = 56$ and 58 , respectively, and the less stable cubic packed motif gets $2S + 1 = 58$ as well. The addition of N_2 to any of the three Fe_{18}^+ structures, forming various $Fe_{18}(N_2)_m^+$ cluster adsorbate complexes, leads to a variety of different adsorbate geometries due to the variation of coordinating Fe centers as documented exhaustively in the supplementary material (Figs. S52–S59). Because our exploratory DFT calculations have reached their limits for these systems, we failed to obtain converged results in some cases. Nevertheless, it becomes discernible that stepwise N_2 adsorption induces stepwise spin quenching (Fig. 11)—a prediction that is well in line with the findings above for (13, m) clusters and recent findings in the case of Rhodium clusters: spin valleys shift lower upon higher adsorbate loads.¹⁰⁰

The kinetic studies of N_2 uptake by Fe_{18}^+ , cf. CKS, provide strong evidence for isomeric mixtures, tentatively assigned to a major component with a close packed structure (18cp) and a minor component with an icosahedral or hexagonal antiprismatic structure (18ico/18hex). The kinetics also suggest the conversion of a major isomer into a minor one upon uptake of some eight or nine N_2 adsorbate molecules. These kinetic findings correspond to the observation of the yellow feature and the disappearance of the orange ones in the IR spectra of (18, m) setting in around $m = 9$, the violet feature gradually setting in a little bit earlier.

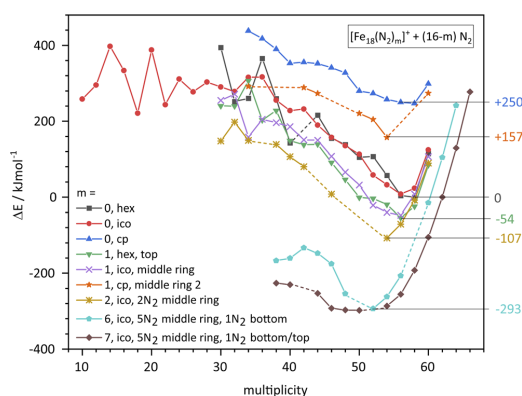


FIG. 11. Energetics of computed $[Fe_{18}(N_2)_m]^+$ cluster adsorbate structures (18, m) as a function of the spin multiplicity $2S + 1$, normalized to the most favorable (18,0) spin isomer (hexagonal, 58tet). The level of theory is PBE/def2TZVP.

IV. CONCLUSIONS

Our recorded IR-PD spectra of the cluster adsorbate complexes $[\text{Fe}_n(\text{N}_2)_1]^+$, abbreviated $(n,1)$, and $[\text{Fe}_n(\text{N}_2)_2]^+$, abbreviated $(n,2)$, for $n = 8-20$ revealed IR active bands in the region of 2150–2340 cm^{-1} . All investigated species, except $[\text{Fe}_{17}(\text{N}_2)_1]^+$, show at least one IR active band in the investigated region, and this band is most likely associated with stretching vibrations of end-on coordinated N₂ chromophores, the $\mu_{1,\text{end}}$ motif. These N₂ adsorbate bands are significantly redshifted with respect to the free N₂ stretching frequency (2330 cm^{-1}). In summary, the observed peak positions of first and second N₂ adsorbates, likely end-on, reveal little to no systematic variation. We take this finding as an indication for a largely equivalent bonding situation of the first and second N₂ adsorbate on the Fe_n^+ cluster surface. However, those complexes that exhibited special kinetic behavior are also special with respect to their IR spectra and vice versa.

The IR-PD spectra of $(13, m)$ reveal discernible couplings of proximate N₂ adsorbates setting in at $(13,3)$ and persisting up to $(13,5)$. On the basis of an icosahedral Fe_{13}^+ core structure, the observed $(13,6)$ sharp, single IR-PD band finds interpretation in terms of a high symmetry adsorbate arrangement, as also suggested by DFT modeling. The very fast kinetics of $(13,7-11)$ prevented any IR-PD spectra recordings for these clusters (cf. CKS). The first adsorbate shell closure at $(13,12)$ comes with extensive IR-PD band broadening resulting from more enhanced couplings, in line with the DFT modeling, which also predicts a spin quenching by N₂ adsorption as evidenced by the shift of the computed spin valleys (Fig. 8). Beyond these observations, the computed spectra provide the first hints of conceivable side-on and bridged coordination.

The IR-PD spectrum of $(17,1)$ surprisingly reveals an absence of any structure in the IR-PD spectrum but efficient non-resonant fragmentation. We speculate that there may be some kind of weakly bound, almost roaming, N₂ adsorbate, which is volatile and susceptible to swift desorption (cf. Fe_{17}^+ kinetics in CKS). The IR-PD spectra of $(17,m)$ show multiple and broad bands for all cases other than $(17,1)$ and $(17,7)$. We tentatively conclude that there is a high degree of variation in binding motifs and couplings of the N₂ adsorbates. In remarkable contrast, the six sharp and well separated bands in the IR-PD spectrum of $(17,7)$ suggest symmetric and antisymmetric couplings of pairwise equivalent N₂ adsorbates. An adsorbate load dependent reorganization among the N₂ adsorbates seems likely, and the concomitant structural volatility is consistent with the observed slow adsorption kinetics and high rates of desorption (cf. CKS).

The IR-PD spectra of $(18, m)$ reveal additional features in the 2120–2200 cm^{-1} region, which we associate with a side-on $\mu_{1,\text{side}}$ (μ_1 - κ -N₁,N₂) motif. We rule out a bridging μ_2 motif, which would come with a significantly larger redshift. The IR-PD bands of both the $\mu_{1,\text{end}}$ and $\mu_{1,\text{side}}$ motifs experience steady redshifts with increasing N₂ loadings. Interestingly, the $\mu_{1,\text{end}}$ associated IR-PD features are bimodal at medium N₂ loads, $(18,4)$ through $(18,8)$, and we conceive contributions of a $\mu_{1,\text{tilt}}$ adsorption motif at higher levels of N₂ loads. This phenomenon is possibly connected to structural relaxation of close-packed into icosahedral or antiprismatic hexagonal Fe_{18}^+ structures. Exploratory DFT modeling at the reduced PBE level proved inappropriate and failed to predict any observed IR modes, whereas more elaborate hybrid DFT modeling of the large cluster adsorbate complexes was computationally intractable.

Nevertheless, the exploratory PBE studies indicated some adsorbate-induced spin quenching as in the case of $(13,m)$ and as observed before in the case of $\text{Rh}_5^+(\text{N}_2)_m$.¹⁰⁰

SUPPLEMENTARY MATERIAL

See the [supplementary material](#) for spectra across extended frequency ranges, starting arrangements for DFT modeling, a comparison of computed cluster isomers with measured spectra, numerical values of spin isomers and spin contamination, and complementary levels of theory.

ACKNOWLEDGMENTS

This work was supported by the German Research Foundation DFG within the transregional collaborative research center SFB/TRR 88 “Cooperative effects in homo and heterometallic complexes” (3MET.de) and by the State Research Center OPTIMAS. P.B.A. acknowledges support from the National Science Foundation, Grant No. CHE-1954142. The ⁵⁶Fe pure isotope sample of this study was supplied by the United States Department of Energy Office of Science through the Isotope Program in the Office of Nuclear Physics. Quantum chemical modeling took place at the “Regionales Hochschulrechenzentrum Kaiserslautern” (RHRK). We thank Thomas Kolling for his technical assistance and valuable discussions. Finally, we would like to thank the reviewers for valuable comments.

AUTHOR DECLARATIONS

Conflict of Interest

A.S., M.P.K., D.V.F., S.D., J.M., and G.N.-S. conceived and conducted the experiments. A.S., C.W., and M.H.P. conducted the quantum chemical calculations. A.S., P.B.A., and G.N.-S. evaluated all data and wrote the manuscript, which all the authors revised and agreed to.

DATA AVAILABILITY

The data that support the findings of this study are available from the corresponding author upon reasonable request.

REFERENCES

- 1 T. Zambelli *et al.*, *Science* **273**, 1688 (1996).
- 2 J. K. Nørskov *et al.*, *J. Catal.* **209**, 275 (2002).
- 3 K. Honkala *et al.*, *Science* **307**, 555 (2005).
- 4 J. M. Thomas and W. J. Thomas, *Principles and Practice of Heterogeneous Catalysis* (John Wiley & Sons, 2014).
- 5 G. Ertl, H. Knözinger, and J. Weitkamp, *Handbook of Heterogeneous Catalysis* (CiteSeer, 1997), Vol. 2.
- 6 B. Cornils *et al.*, *Catalysis from A to Z: A Concise Encyclopedia* (John Wiley & Sons, 2020).
- 7 F. A. Khan, D. L. Steele, and P. B. Armentrout, *J. Chem. Phys.* **99**, 7819 (1995).
- 8 B. L. Tjelta and P. B. Armentrout, *J. Phys. Chem. A* **101**, 2064 (1997).
- 9 B. L. Tjelta, D. Walter, and P. B. Armentrout, *Int. J. Mass Spectrom.* **204**, 7 (2001).
- 10 C. Berg, G. Nieder-Schatteburg, and V. E. Bondybey, *Second International Conference on Low Temperature Chemistry* (BkMk Press, Kansas City, MO, 1996), Vol. 1.
- 11 R. Schlögl and S. B. Abd Hamid, *Angew. Chem., Int. Ed.* **43**, 1628 (2004).

- ¹²A. Nilsson, L. G. Pettersson, and J. Norskov, *Chemical Bonding at Surfaces and Interfaces* (Elsevier, 2011).
- ¹³S. M. Lang and T. M. Bernhardt, *Phys. Chem. Chem. Phys.* **14**, 9255 (2012).
- ¹⁴P. B. Armentrout, *Catal. Sci. Technol.* **4**, 2741 (2014).
- ¹⁵E. L. Muetterties and J. Stein, *Chem. Rev.* **79**, 479 (1979).
- ¹⁶G. Ertl, *Angew. Chem., Int. Ed. Engl.* **47**, 3524 (2008).
- ¹⁷M. D. Morse *et al.*, *J. Chem. Phys.* **83**, 2293 (1985).
- ¹⁸A. Mittasch and W. Frankenburg, in *Advances in Catalysis*, edited by W. G. Frankenburg, V. I. Komarewsky, and E. K. Rideal (Academic Press, 1950), p. 81.
- ¹⁹R. Schlögl, *Ammonia Synthesis in Handbook of Heterogeneous Catalysis* (Wiley-VCH Verlag GmbH & Co. KG, 2008), Vol. 2.
- ²⁰J. R. Jennings, *Catalytic Ammonia Synthesis: Fundamentals and Practice* (Springer Science & Business Media, 2013).
- ²¹H. Liu, *Ammonia Synthesis Catalysts: Innovation and Practice* (World Scientific, 2013).
- ²²F. Bozso *et al.*, *J. Catal.* **49**, 18 (1977).
- ²³F. Bozso, G. Ertl, and M. Weiss, *J. Catal.* **50**, 519 (1977).
- ²⁴G. Ertl, S. B. Lee, and M. Weiss, *Surf. Sci.* **114**, 515 (1982).
- ²⁵M. Grunze *et al.*, *Phys. Rev. Lett.* **53**, 850 (1984).
- ²⁶H.-J. Freund *et al.*, *Surf. Sci.* **185**, 187 (1987).
- ²⁷M. C. Tsai *et al.*, *Surf. Sci.* **155**, 387 (1985).
- ²⁸C. N. R. Rao and G. R. Rao, *Surf. Sci. Rep.* **13**, 223 (1991).
- ²⁹J. J. Mortensen *et al.*, *J. Catal.* **182**, 479 (1999).
- ³⁰J. J. Mortensen *et al.*, *Surf. Sci.* **422**, 8 (1999).
- ³¹L. J. Whitman *et al.*, *Phys. Rev. Lett.* **56**, 1984 (1986).
- ³²M. A. Duncan, *Annu. Rev. Phys. Chem.* **48**, 69 (1997).
- ³³M. A. Duncan, *Int. Rev. Phys. Chem.* **22**, 407 (2003).
- ³⁴N. R. Walker, R. S. Walters, and M. A. Duncan, *New J. Chem.* **29**, 1495 (2005).
- ³⁵J. Roithová, *Chem. Soc. Rev.* **41**, 547 (2012).
- ³⁶J. Oomens *et al.*, *Int. J. Mass Spectrom.* **254**, 1 (2006).
- ³⁷L. MacAleese and P. Maitre, *Mass Spectrom. Rev.* **26**, 583 (2007).
- ³⁸W. Schöllkopf *et al.*, in *Advances in X-Ray Free-Electron Lasers Instrumentation III* (International Society for Optics and Photonics, 2015), p. 95121L.
- ³⁹M. Okumura, L. I. Yeh, and Y. T. Lee, in *Laser Spectroscopy VII*, edited by T. W. Hänsch and Y. R. Shen (Springer, Berlin, Heidelberg, 1985), p. 122.
- ⁴⁰M. Okumura, L. I. Yeh, and Y. T. Lee, *J. Chem. Phys.* **88**, 79 (1988).
- ⁴¹L. Jiang *et al.*, *J. Am. Chem. Soc.* **132**, 7398 (2010).
- ⁴²M. Z. Kamrath *et al.*, *J. Am. Chem. Soc.* **133**, 6440 (2011).
- ⁴³A. B. Wolk *et al.*, *Acc. Chem. Res.* **47**, 202 (2014).
- ⁴⁴S. Dillinger *et al.*, *Phys. Chem. Chem. Phys.* **17**, 10358 (2015).
- ⁴⁵I. Swart *et al.*, *J. Phys. Chem. A* **112**, 1139 (2008).
- ⁴⁶D. M. Kiawi *et al.*, *J. Phys. Chem. Lett.* **7**, 2381 (2016).
- ⁴⁷A. Fielicke *et al.*, *Surf. Sci.* **603**, 1427 (2009).
- ⁴⁸J. T. Lyon *et al.*, *J. Chem. Phys.* **131**, 184706 (2009).
- ⁴⁹C. P. McNary and P. B. Armentrout, *Phys. Chem. Chem. Phys.* **16**, 26467 (2014).
- ⁵⁰G. Blyholder, *J. Chem. Phys.* **68**, 2772 (1964).
- ⁵¹J. Dewar, *Bull. Soc. Chim. Fr.* **18**, C71 (1951).
- ⁵²J. Chatt and L. A. Duncanson, *J. Chem. Soc.* **1953**, 2939.
- ⁵³G. L. Gutsev, M. D. Mochena, and C. W. Bauschlicher, Jr., *J. Phys. Chem. A* **108**, 11409 (2004).
- ⁵⁴A. Jedidi *et al.*, *Theor. Chem. Acc.* **133**, 1430 (2014).
- ⁵⁵A. Fielicke *et al.*, *J. Am. Chem. Soc.* **125**, 11184 (2003).
- ⁵⁶A. Fielicke *et al.*, *J. Chem. Phys.* **124**, 194305 (2006).
- ⁵⁷E. D. Pillai, T. D. Jaeger, and M. A. Duncan, *J. Phys. Chem. A* **109**, 3521 (2005).
- ⁵⁸E. D. Pillai, T. D. Jaeger, and M. A. Duncan, *J. Am. Chem. Soc.* **129**, 2297 (2007).
- ⁵⁹A. D. Brathwaite, H. L. Abbott-Lyon, and M. A. Duncan, *J. Phys. Chem. A* **120**, 7659 (2016).
- ⁶⁰C. Kerpál *et al.*, *J. Phys. Chem. C* **117**, 12153 (2013).
- ⁶¹S. Shetty, A. P. J. Jansen, and R. A. van Santen, *J. Phys. Chem. C* **112**, 17768 (2008).
- ⁶²M. Castro and D. R. Salahub, *Phys. Rev. B* **49**, 11842 (1994).
- ⁶³P. Ballone and R. O. Jones, *Chem. Phys. Lett.* **233**, 632 (1995).
- ⁶⁴T. Oda, A. Pasquarello, and R. Car, *Phys. Rev. Lett.* **80**, 3622 (1998).
- ⁶⁵D. Hobbs, G. Kresse, and J. Hafner, *Phys. Rev. B* **62**, 11556 (2000).
- ⁶⁶O. Diéguez *et al.*, *Phys. Rev. B* **63**, 205407 (2001).
- ⁶⁷G. Rollmann, P. Entel, and S. Sahoo, *Comput. Mater. Sci.* **35**, 275 (2006).
- ⁶⁸G. L. Gutsev *et al.*, *J. Phys. Chem. A* **116**, 10218 (2012).
- ⁶⁹H. K. Yuan *et al.*, *J. Chem. Phys.* **139**, 034314 (2013).
- ⁷⁰A. Jedidi *et al.*, *Phys. Chem. Chem. Phys.* **16**, 20703 (2014).
- ⁷¹H. A. Duarte *et al.*, *Inorg. Chem.* **38**, 3895 (1999).
- ⁷²T. L. Haslett *et al.*, *J. Am. Chem. Soc.* **122**, 6039 (2000).
- ⁷³B. Chen *et al.*, *Phys. Chem. Chem. Phys.* **23**, 2166 (2021).
- ⁷⁴S. K. Loh *et al.*, *J. Chem. Phys.* **90**, 5466 (1989).
- ⁷⁵L. Lian, C. X. Su, and P. B. Armentrout, *J. Chem. Phys.* **97**, 4072 (1992).
- ⁷⁶J. Conceição *et al.*, *J. Chem. Phys.* **104**, 3976 (1996).
- ⁷⁷J. B. Griffin and P. B. Armentrout, *J. Chem. Phys.* **106**, 4448 (1997).
- ⁷⁸L. Tan, F. Liu, and P. B. Armentrout, *J. Chem. Phys.* **124**, 084302 (2006).
- ⁷⁹R. Liyanage, J. B. Griffin, and P. B. Armentrout, *J. Chem. Phys.* **119**, 8979 (2003).
- ⁸⁰S. Dillinger, J. Mohrbach, and G. Niedner-Schatteburg, *J. Chem. Phys.* **147**, 184305 (2017).
- ⁸¹J. Mohrbach, S. Dillinger, and G. Niedner-Schatteburg, *J. Phys. Chem. C* **121**, 10907 (2017).
- ⁸²J. Mohrbach, S. Dillinger, and G. Niedner-Schatteburg, *J. Chem. Phys.* **147**, 184304 (2017).
- ⁸³M. P. Klein *et al.*, *Top. Catal.* **61**, 106 (2018).
- ⁸⁴S. Dillinger *et al.*, *J. Phys. Chem. Lett.* **9**, 914 (2018).
- ⁸⁵D. V. Fries *et al.*, *Phys. Chem. Chem. Phys.* **23**, 11345 (2021).
- ⁸⁶A. Straßner *et al.* "Kinetics of stepwise nitrogen adsorption by size-selected iron cluster cations: Evidence for size-dependent nitrogen phobia," (to be published).
- ⁸⁷M. Frisch *et al.*, *Gaussian 09* (Gaussian, Inc., Wallingford, CT, 2009).
- ⁸⁸M. J. Frisch *et al.*, *Gaussian 16* (Gaussian, Inc., Wallingford, CT, 2016).
- ⁸⁹J. P. Perdew, K. Burke, and M. Ernzerhof, *Phys. Rev. Lett.* **77**, 3865 (1996).
- ⁹⁰C. Adamo and V. Barone, *J. Chem. Phys.* **110**, 6158 (1999).
- ⁹¹J. Tao *et al.*, *Phys. Rev. Lett.* **91**, 146401 (2003).
- ⁹²V. N. Staroverov *et al.*, *J. Chem. Phys.* **119**, 12129 (2003).
- ⁹³F. Weigend and R. Ahlrichs, *Phys. Chem. Chem. Phys.* **7**, 3297 (2005).
- ⁹⁴W. M. Haynes, *CRC Handbook of Chemistry and Physics* (CRC Press/Taylor & Francis, Boca Raton, Florida, 2012), Vol. 93.
- ⁹⁵C. N. R. Rao, G. R. Rao, and K. Ppabhakaran, *Chem. Phys. Lett.* **134**, 47 (1987).
- ⁹⁶M. Niemeyer *et al.*, *Phys. Rev. Lett.* **108**, 057201 (2012).
- ⁹⁷M. Wu *et al.*, *Phys. Rev. B* **86**, 174410 (2012).
- ⁹⁸J. Meyer *et al.*, *J. Chem. Phys.* **143**, 104302 (2015).
- ⁹⁹A. Salzer, *Pure Appl. Chem.* **71**, 1557 (1999).
- ¹⁰⁰A. A. Ehrhard *et al.*, *Mol. Phys.* **119**, e1953172 (2021).
- ¹⁰¹Q.-M. Ma *et al.*, *Solid State Commun.* **142**, 114 (2007).
- ¹⁰²"tet" refers to the multiplicity as common for small spin values in singlet, doublet, etc. A 4tet thus refers to $2S + 1 = 46$, which implies 45 unpaired electrons with parallel spins.

A.3 Cryo Infrared Spectroscopy of N₂ Adsorption onto Bimetallic Rhodium-Iron Clusters in Isolation

A.3.1 Preamble

The following chapter is a reprint of a publication in the journal *“The Journal of Chemical Physics”*

M. P. Klein, A. A. Ehrhard, M. E. Huber, A. Straßner, D. V. Fries, S. Dillinger, and J. Mohrbach conducted the experiments. A. A. Ehrhard and M. P. Klein carried out quantum chemical calculations. M. P. Klein and G. Niedner-Schatteburg evaluated all data. M. P. Klein, S. Dillinger, and G. Niedner-Schatteburg wrote the manuscript, and all the authors revised and agreed.

Full Reference

Cryo Infrared Spectroscopy of N₂ Adsorption onto Bimetallic Rhodium-Iron Clusters in Isolation

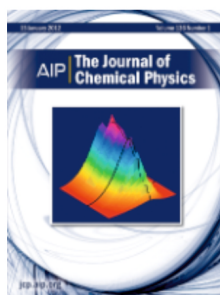
M. P. Klein, A. A. Ehrhard, M. E. Huber, A. Straßner, D. V. Fries, S. Dillinger, J. Mohrbach, G. Niedner-Schatteburg, *The Journal of Chemical Physics* **2022**, 156, 014302.

<https://doi.org/10.1063/5.0075289>

A.3.2 Reprint

Reprint permission

Reproduced with permission of AIP Publishing.



Cryo infrared spectroscopy of N₂ adsorption onto bimetallic rhodium–iron clusters in isolation

Author: Klein, Matthias P.; Ehrhard, Amelie A.

Publication: Journal of Chemical Physics

Publisher: AIP Publishing

Date: Jan 4, 2022

Rights managed by AIP Publishing.

Creative Commons

This is an open access article distributed under the terms of the [Creative Commons CC BY](#) license, which permits unrestricted use, distribution, and reproduction in any medium, provided the original work is properly cited.

You are not required to obtain permission to reuse this article.

Cryo infrared spectroscopy of N₂ adsorption onto bimetallic rhodium-iron clusters in isolation

Cite as: *J. Chem. Phys.* **156**, 014302 (2022); doi: [10.1063/5.0075289](https://doi.org/10.1063/5.0075289)

Submitted: 14 October 2021 • Accepted: 18 November 2021 •

Published Online: 4 January 2022



Matthias P. Klein,  Amelie A. Ehrhard,^{a)}  Maximilian E. Huber, Annika Straßner,  Daniela V. Fries, 
Sebastian Dillinger, Jennifer Mohrbach, and Gereon Niedner-Schatteburg^{b)} 

AFFILIATIONS

Fachbereich Chemie and Forschungszentrum OPTIMAS, Technische Universität Kaiserslautern, 67663 Kaiserslautern, Germany

^{a)} Present address: Max-Planck-Institut für Polymerforschung, 55128 Mainz, Germany.

^{b)} Author to whom correspondence should be addressed: gns@chemie.uni-kl.de.

Permanent address: Gereon Niedner-Schatteburg, Erwin-Schrödinger-Straße 52, 67663 Kaiserslautern.

ABSTRACT

We investigated the N₂ adsorption behavior of bimetallic rhodium-iron cluster cations [Rh_iFe_j(N₂)_m]⁺ by means of InfraRed MultiplePhotoDissociation (IR-MPD) spectroscopy in comparison with density functional theory (DFT) modeling. This approach allows us to refine our kinetic results [Ehrhard *et al.*, *J. Chem. Phys.* (in press)] to enhance our conclusions. We focus on a selection of cluster adsorbate complexes within the ranges of $i = j = 3-8$ and $m = 1-10$. For $i = j = 3, 4$, DFT suggests alloy structures in the case of $i = j = 4$ of high (D_{2d}) symmetry: Rh-Fe bonds are preferred instead of Fe-Fe bonds or Rh-Rh bonds. N₂ adsorption and IR-MPD studies reveal strong evidence for preferential adsorption to Rh sites and mere secondary adsorption to Fe. In some cases, we observe adsorption isomers. With the help of modeling the cluster adsorbate complex [Rh₃Fe₃(N₂)₇]⁺, we find clear evidence that the position of IR bands allows for an element specific assignment of an adsorption site. We transfer these findings to the [Rh₄Fe₄(N₂)_m]⁺ cluster adsorbate complex where the first four N₂ molecules are exclusively adsorbed to the Rh atoms. The spectra of the larger adsorbates reveal N₂ adsorption onto the Fe atoms. Thus, the spectroscopic findings are well interpreted for the smaller clusters in terms of computed structures, and both compare well to those of our accompanying kinetic study [Ehrhard *et al.*, *J. Chem. Phys.* (in press)]. In contrast to our previous studies of bare rhodium clusters, the present investigations do not provide any indication for a spin quench in [Rh_iFe_j(N₂)_m]⁺ upon stepwise N₂ adsorption.

© 2022 Author(s). All article content, except where otherwise noted, is licensed under a Creative Commons Attribution (CC BY) license (<http://creativecommons.org/licenses/by/4.0/>). <https://doi.org/10.1063/5.0075289>

I. INTRODUCTION

Transition metal clusters may serve as model systems for elemental processes that are of relevance in the context of heterogeneous catalysis.^{1,2} Such catalysts may consist of several metal components, either separated or as alloys, that contribute to the catalytic activity for various reactions.³ In the automobile three way catalyst, a combination of precious metals catalyzes oxidation of hydrocarbons and reduction of CO and nitrous oxides.⁴ The latter takes place on rhodium sites and effects the production of N₂ and CO₂.^{5,6} Iron is well known as a catalyst for dinitrogen activation, especially in the Haber-Bosch process. In this case, N₂ activation is considered as the rate limiting step. In the course of activation, physisorption of N₂ is the precursor state.⁷ Apart from this, the adsorption of N₂ onto surfaces to study the surface properties was an early research field.^{8,9}

Surface studies also provided information about the binding states of N₂ on Fe surfaces: α -N₂ (side-on) and γ -N₂

(end-on) adsorption motifs were identified.¹⁰ Upon adsorption onto rhodium surfaces, N₂ is polarized and the otherwise IR inactive N₂ stretching vibration becomes IR active.¹¹ Thus, chemisorbed and physisorbed N₂ species were identified where the physisorbed ones reveal no shift of the N₂ stretching vibration and are only very weakly bound (adsorption heat: 1.6 kcal/mol). The adsorption state and the adsorption site determine the stretching frequency. Recently, spectroscopic investigations of N₂ adsorption on zirconia supported Rh nanoparticles were used to investigate step-edge sites that are required to dissociate CO.¹² IR bands of N₂ adsorbed onto an oxidized or reduced Rh layer appear at 2293 or 2205 cm⁻¹, respectively. The π -backbonding effect could be instrumentalized to selectively adsorb N₂ onto exposed vanadium centers in a metal organic framework.¹³

Isolated transition metal clusters such as neutral Ru_n clusters also polarize and activate N₂ and make it accessible to infrared spectroscopy.¹⁴ The vibrational bands were observed red shifted

with respect to the free N_2 vibration. For cases of N_2 adsorbed onto cobalt cluster cations, we found similar red shifts of the N_2 stretching frequencies.¹⁵ The interaction between metal atoms at surfaces and adsorbates containing π -bonds can be explained in terms of the Blyholder model.¹⁶ This model refers to the same σ -donor, π -acceptor synergism as the Dewar–Chatt–Duncanson model for coordination compounds.^{17,18} The dependence of CO stretching frequencies on the number of metal atoms within the cluster can be explained by using the Fielickes charge dilution model.¹⁹

In addition, InfraRed MultiplePhotoDissociation (IR-MPD) spectra of CO and N_2 adsorbed onto a rhodium cation $[Rh(N_2/CO)_m]^+$ reveal a red shift of the N–N vibration and a blue shift of the CO vibration in the case of $m = 4$.²⁰ With the help of density functional theory (DFT) calculations, this result could be explained by a combination of σ -donation and electrostatic polarization of the ligand. The interaction of the non-polar N_2 -molecule with the metal atom is much weaker than that of the isoelectronic but polar CO. In N_2 , HOMO and LUMO are symmetrically shared by both atoms, and the HOMO–LUMO gap is considerable. In CO, HOMO and LUMO are mainly located on the carbon atom, which allows for a stronger bonding and back-bonding interaction with the metal atom. The HOMO–LUMO gap is significantly smaller than that of N_2 .

Until now, we published cryo-spectroscopic investigations of N_2 adsorption on Co,¹⁵ Ni,^{21,22} Ru,^{14,23} and Rh²⁴ clusters. A combination of IR studies with N_2 adsorption kinetics proved useful to investigate cluster surface morphologies and to discriminate *rough* and *smooth* cluster surfaces in the case of Ni.^{21,22,25} IR-MPD spectroscopy of $[Rh_i(N_2)_m]^+$ clusters revealed coexisting isomers and a spin quench upon N_2 adsorption.²⁴ It is necessary to support the experimental work with theoretical models, but in the case of clusters, these often reach their limits.²⁶

Rhodium–iron alloys were found to reveal interesting magnetic properties, such as transitions between antiferromagnetic and ferromagnetic states.^{27–40} In particular, theoretical studies have been performed to determine structures and magnetism of neutral $[Rh_iFe_j]$ clusters and they provide a set of initial structures for our own modeling and a basis of comparison with obtained data.⁴¹ In particular, for small clusters, Rh–Fe bonds are stronger than Fe–Fe and Rh–Rh bonds.⁴⁰ These differences diminish with an increase in the size of the cluster. The investigation of possible activation mediated by Fe atoms in mixed metal clusters is of interest for further catalyst development, and the N_2 stretching vibration may help to elucidate the cluster structure, in particular the distribution of metal atoms of the alloy or layered-type clusters.

Together with the accompanying kinetic paper [AAE],⁴² we present a combined spectroscopic and kinetic approach to investigate the N_2 adsorption steps and the cluster adsorbate complexes themselves. This approach has proven successful in the case of Ni clusters before.^{22,25} To facilitate readability, we use the short notation (i,j,m) for the cluster adsorbate complexes $[Rh_iFe_j(N_2)_m]^+$. The kinetic study presents extensive adsorption kinetic data for all cluster adsorbate complexes (i,j,m) with $i = j$, $i = j + 1$, and $i + 1 = j$ for $i = 3, \dots, 8$ and $j = 3, \dots, 8$ in the range of $(3,3,m), \dots, (8,8,m)$.

In our present study, we investigated a selection of cationic $[Rh_iFe_j(N_2)_m]^+$ cluster adsorbate complexes by means of infrared multiphotodissociation spectroscopy (IR-MPD). Single and maximum adsorption and special intermittent sizes are of special

interest. We interpret the obtained spectra in conjunction with corresponding DFT calculations. We chose to select for investigation the equiatomic $[Rh_iFe_j(N_2)_m]^+$ clusters with single N_2 adsorption ($m = 1$) and intermittent and high coverages, where the high load cases do not necessarily represent the maximum adsorption limit as defined in [AAE]. We compare our recorded IR-MPD spectra to those of pure rhodium and iron clusters.^{24,43} In the present study, we focused on N_2 adsorbates of the equiatomic (i,j,m) clusters, $i = j = 3, \dots, 8$.

For a description of the chosen (i,j,m) nomenclature and for a detailed discussion of the adsorption kinetics, refer to the accompanying kinetics paper [AAE]⁴² and to supplementary material S1 of Ref. 44.

II. EXPERIMENTAL METHODS AND COMPUTATIONAL APPROACH

In a customized 7 T Fourier Transform-Ion Cyclotron Resonance (FT-ICR)-mass spectrometer (Apex Ultra Bruker Daltonics), the metal clusters were produced and isolated. We let N_2 adsorb and performed InfraRed PhotoDissociation (IR-MPD) and mass analysis. The detailed construction and experimental procedure have been described elsewhere.^{15,22,42} In short, the $[Rh_iFe_j]^+$ clusters were generated by laser vaporization from a RhFe-target (¹⁰³Rh,⁵⁶Fe stoichiometry 1:1, *MaTecK*) and mass selected by using a quadrupole mass filter. The selected clusters are stored into a cryogenic hexapole ion trap, which is cooled to 26 K. The attachment of nitrogen is achieved by introducing N_2 , and we maintain the requested constant pressure of about $2.2\text{--}3.2 \times 10^{-7}$ mbar N_2 . We increase the pressure in the ion trap to roughly 3.0×10^{-6} mbar by adding helium gas to accomplish efficient trapping and cooling of the ions. The ions are stored for a variable time (0.0–3.0 s). Subsequently, the cluster ions are steered into the ICR-cell using various electrostatic ion lenses. Our ICR-cell of the so-called infinity-type⁴⁵ is cooled down to 10 K by using a closed cycle He cryostat to prevent heating of the clusters by black body radiation.

To study the N_2 adsorbates of the selected $[Rh_iFe_j]^+$ clusters within the ICR cell, we first isolate the metal cluster of interest in the quadrupole mass filter and afterward the cluster adsorbate complex of interest in the ICR cell and remove all other ions by correlated frequency sweeps and shots.

The number m of adsorbed N_2 on the cluster can be controlled by varying the storage time in the hexapole collision cell. The storage time can be increased until the number of N_2 adsorbed reaches a maximum limit, and at higher storage times, no further N_2 adsorption is observed, as is shown for $[Rh_3Fe_3]^+$ (Fig. 1). The $[Rh_3Fe_3]^+$ and $[Rh_4Fe_4]^+$ cluster can adsorb up to seven and eight N_2 molecules, respectively. We can observe an additional *intermittent adsorption limit* for some metal cluster cores, e.g., $[Rh_4Fe_4(N_2)_4]^+$. Here, the course of adsorption seems intermittent/interrupted, but it may continue with a lower adsorption rate. Detailed kinetic investigations have confirmed that this behavior correlates with a slower rate of additional N_2 adsorption above this intermittent limit [AAE].⁴² Upon closer inspection, the $[Rh_4Fe_4(N_2)_4]^+$ mass spectra further reveal but very weak adsorption peaks as discussed in the accompanying kinetic study. For the following spectroscopic investigations, we chose single N_2 adsorbed clusters and clusters at the *intermittent* and

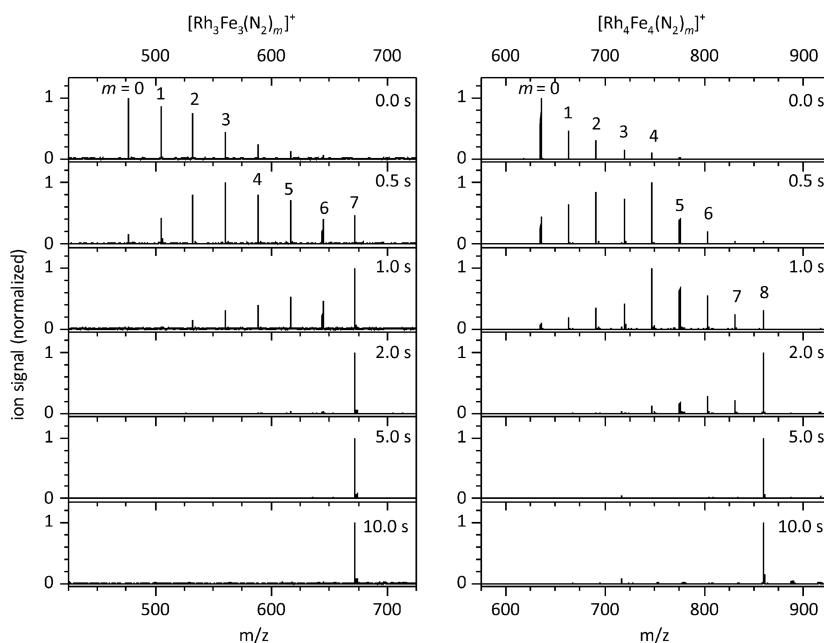


FIG. 1. FT-ICR mass spectra of $[\text{Rh}_3\text{Fe}_3(\text{N}_2)_m]^+$ and $[\text{Rh}_4\text{Fe}_4(\text{N}_2)_m]^+$ exposed to 2.8×10^{-7} mbar N_2 at a temperature of 26 K with various storage times in the cryogenic hexapole ion trap. $[\text{Rh}_3\text{Fe}_3]^+$ reveals a smooth adsorption behavior up to a limit of 7 N_2 , whereas measurements on the $[\text{Rh}_4\text{Fe}_4]^+$ cluster show, in addition to an adsorption limit of 8 N_2 , an intermittent limit of 4 N_2 , i.e., after a distinct number of N_2 is adsorbed, additional adsorption of N_2 happens with a slower rate (confirmed by detailed kinetic investigations done by [AAE]⁴²).

maximum adsorption limit. The adsorption limits are given in [AAE],⁴² Fig. 2.

A tunable IR laser system is coupled to the ICR cell to affect fragmentation of the stored ions. This laser is a

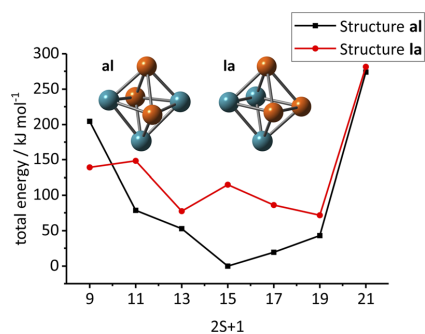


FIG. 2. Total energies of alloy-like $[\text{Rh}_3\text{Fe}_3]^+$ clusters (black squares) and of layered $[\text{Rh}_3\text{Fe}_3]^+$ clusters (red circles) as a function of spin multiplicity $2S + 1$ relative to the 15tet of structure (a1). The insets display the two possible isomers in a near octahedral geometry (see the text for details; Fe: orange and Rh: turquoise).

potassium titanyl phosphate/potassium titanyl phosphate/potassium titanyl arsenate (KTP/KTA) optical parametric oscillator/amplifier (OPO/A, *LaserVision*) system pumped by a pulsed 10 Hz injection seeded Nd:YAG laser (PL8000, *Continuum*) followed by an AgGaSe₂ crystal to generate the difference frequency (DF) between signal and idler waves.⁴⁶ This method can generate IR radiation in the range of 1200–2400 cm^{-1} . Each trapped and isolated package of ions is irradiated by 7–10 laser pulses to yield a sufficient number of fragment ions. A typical pulse energy spectrum is given in Fig. S1. The IR spectra were recorded as a series of mass spectra while continuously scanning the IR wavelength. We evaluated the IR-MPD signal as $\Sigma_n F_n / (\Sigma_n F_n + \Sigma_x P_x)$, where F_n and P_x indicate fragment and the parent ion signals, respectively. An IR-MPD spectrum as depicted in this work arises out of plot of the fragmentation efficiency as a function of laser frequency. We employed the IR-MPD spectroscopy in the 2140–2350 cm^{-1} range on the $[\text{Rh}_i\text{Fe}_j(\text{N}_2)_m]^+$ species ($i = j = 3, \dots, 8$ and $m = 1, \dots, 10$). In this range, we expected the end-on N_2 stretching frequencies of the species. We expanded this range to 1160–2400 cm^{-1} in selected cases to check for non-end-on N_2 ligands. The N–N stretching bands of side-on adsorbed N_2 on various metal surfaces have been reported in the range of 1220–1590 cm^{-1} before.^{47–52} We observed the band of side-on adsorbed N_2 on a Ta_4^+ cluster between 1443 and 1475 cm^{-1} .⁵³

For all complexes, the loss of the N_2 was the only observed fragmentation channel.

Geometry optimizations and vibrational analysis were performed by using the Gaussian 09 package⁵⁴ at the PBE0/ECP(Rh, Fe); cc-pVTZ(N) level of theory^{55,56} as proven suitable for cobalt, nickel, and rhodium clusters.^{15,21,22,24,44} We utilize Stuttgart RSC 1997 ECP(Rh) basis sets of double zeta quality.⁵⁷ We had to tolerate relaxed SCF convergence criteria of 10^{-5} (as compared to 10^{-8} in “standard” DFT calculations) to achieve SCF convergence.

III. RESULTS AND DISCUSSION

A. The computed structures and spin states of bare $[Rh_3Fe_3]^+$ and $[Rh_4Fe_4]^+$ clusters

We take as a starting point for our studies of bimetallic cluster adsorbate complexes $[Rh_iFe_j(N_2)_m]^+$, abbreviated as (i,j,m) , the modeling of the minimum structures of the bare (3,3,0) and (4,4,0) clusters. The optimization toward a minimum energy structure is more involved for bimetallic clusters than for monometallic clusters: One needs to take into account several mixing topologies, which imply various topologic isomers.

The Rh_3Fe_3 cluster was found to assume an octahedral structure.⁴¹ We took these findings as a basis for our calculations on the cationic $[Rh_3Fe_3]^+$ cluster. Within the octahedral geometry, there are exactly two possible distributions of 3 + 3 equivalent atoms: an intermixed “alloy” structure (**al**) and a segregated “layered” structure (**la**). Pairwise permutation of any two non-equivalent atoms would interconvert these two isomers into each other (cf. insets of Fig. 2). Within the two possible octahedral isomers, the rhodium and iron atoms find themselves to form two alternative triangular arrangements, respectively (Fig. 2). These triangles are perpendicularly oriented to each other in the alloy-like structure (**al**) (meridional) and are parallel to each other in the layered structure (**la**) (facial).

In order to model such conceivable isomers, we had to explore their possible spin multiplicities in parallel. It showed that both isomers are stable in all multiplicities explored ($2S + 1 = 9, \dots, 21$) and that their geometries do relax to a minor extent by some symmetry lowering. The alloy structure (**al**) is most stable when in a 15tet. This value fits well to the average spin moment per atom ($\bar{\mu}_N = 2.50\mu_B$ of the neutral cluster 16tet) calculated by Mokkath and Pastor for structure (**al**).⁴¹ All of (**al**)’s multiplet states are more stable than those of the layered structure (**la**)—but the 9tet. The most favorable layered multiplet, the 19tet of (**la**), is 72 kJ mol^{-1} less stable than the most favorable alloy multiplet, which is the 15tet of (**al**).

We compare the atomic distances to the next neighbors of each atom in the previously shown structures (**al**) and (**la**) with the bulk values and the previously calculated neutral cluster distances⁴¹ (Tables I, S1, and S2). Our calculated $[Rh_3Fe_3]^+$ cluster values come closer to the ones known from crystal data. The PW91 functional used by Mokkath *et al.*⁴¹ overbinds the Rh–Rh and the Rh–Fe distances in an (**la**)-type cluster and yields longer Fe–Fe contacts, compared to this work. The range of Rh–Fe bond length in structure (**la**) reflects that there are two different coordination geometries for each element, and thus, the symmetry is lower than in structure (**al**). Structure (**al**) provides eight Rh–Fe bonds, and structure (**la**) provides only six Rh–Fe bonds at the expense of additional Fe–Fe and Rh–Rh interaction.

TABLE I. Calculated atomic distances (in Å) of nearest neighbors within the two $[Rh_3Fe_3]^+$ cluster isomers (**al**) and (**la**) (15tet) in comparison with sums of atomic radii, with experimental data, and with calculations on an (**al**)-like structure.

Species	Sums of atomic radii		PW91 ^a	PBE0 ^b	PBE0 ^b
	Dimer	Bulk	(al)	(al)	(la)
Rh–Rh	Theo. 2.21 ^a	2.69 ^c	2.61	2.737	2.725
	Theo. 2.27 ^d				
	Exp. 2.3855 ^e				
	Exp. 2.28 ^f				
Rh–Fe		2.586 ^c	2.38	2.643–2.666	2.65
		2.581 ^h			
Fe–Fe	Exp. 2.198(2)	α Fe 2.482 ^c	2.62	2.580	2.584
		–2.2318(8) ^g			

^aReference 41.

^bThis work.

^cReference 62. Distance of the next neighbors in the fcc crystal; lattice parameter $a = 3.8032$ Å.

^dReference 58.

^eReference 59.

^fReference 60.

^gReference 61.

^hReference 63.

We started our survey for $[Rh_4Fe_4]^+$ minimum structures with bicapped octahedral structures (**b**),⁴¹ and we added cubic (**a**) and quadratic antiprismatic (**c**) and (**d**) structures, inspired by earlier investigations of pure Rh clusters by Harding *et al.*⁶⁴ In all these cases, we found a geometry relaxation toward a distorted bicapped octahedral structure (most stable when $2S + 1 = 22$), which consist of two Rh dimers that are separated by central four Fe atoms in a distorted tetrahedral conformation (Fig. 3, Tables S3–S6). The Rh–Fe–Rh coordination angles are obtuse (larger than 90°), and the Fe–Rh–Fe coordination angles are acute (smaller than 90°). Thus,

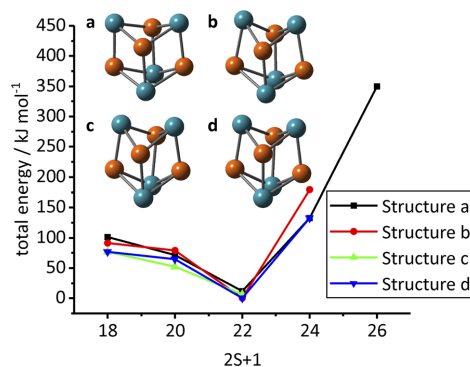


FIG. 3. Total energies of alloy-like $[Rh_4Fe_4]^+$ clusters as a function of the spin multiplicity $2S + 1$ relative to the 22tet of structure (**b**). Structures (**a**)–(**d**) originate from distinct starting geometries by relaxation in the course of optimization; they converge to a single structural type that comes close to D_{2d} symmetry. Note that only Rh–Fe bonds exist, and the Rh atoms are separated by the Fe atoms (for more details, see the text; Fe: orange and Rh: turquoise).

the rhodium atoms provide more space for adsorption of N₂. The PW91 functional predicts less Rh–Rh relaxation in distances relative to bulk values than our PBE0 modeling (Table II).

The computed Rh–Rh distances range between 2.706 and 2.737 Å, which is slightly but significantly larger than bond distances in the bulk. Besides likely electron delocalization, the bond length may provide some hints on strength of interaction between the atoms in the cluster. Our computed Rh–Rh and Fe–Fe distances are far off the ones from the dimer data. In the case of structure (a), one distance between neighbored Rh atoms (Rh2–Rh3; cf. Table S3) seems much too long to indicate a bond. For [Rh₄Fe₄]⁺, the Fe–Fe and Rh–Rh distances seem too long for a binding interaction. This would allow for large-scale flexibility at little enthalpic penalty. In contrast, all the computed Rh–Fe distances are short, indicating binding, for sure a stronger interaction than for Rh–Rh and Fe–Fe.

This implies that in the [Rh₄Fe₄]⁺ cluster, Rh–Fe bonds are dominant and each Rh atom is coordinated by three Fe atoms and vice versa. Moreover, within this [Rh₄Fe₄]⁺ cluster, the Fe–Fe and Rh–Rh interactions seem diminished in favor of dominant Fe–Rh bonding. This cluster is sufficiently large to maximize the favorable Rh–Fe interactions and to allow for considerable mixing. Structure (a) has relaxed to C_{2v}, and it is somewhat less stable (by ~6 kJ/mol) than (b)–(d), all of which resume almost perfect D_{2d} symmetry.

B. IR spectroscopy of N₂ adsorption onto [Rh_iFe_j]⁺ i = j = 3, ..., 8 clusters

We recorded IR-MPD spectra of N₂ adsorbed onto equiatomic rhodium–iron cluster cations (Figs. 4 and 5), and we found multitudes of bands, which are red shifted with respect to the free N₂ stretching vibration at 2330 cm⁻¹.⁶⁵ The obtained band positions range from 2175 to 2315 cm⁻¹. This is to compare to N₂ adsorbate spectra of cobalt clusters (2170–2290 cm⁻¹)¹⁵ and to those of nickel (2175–2280 cm⁻¹),^{21,22} tantalum (2180–2325 cm⁻¹),⁵³ iron (2270–2310 cm⁻¹),⁴³ and rhodium clusters (2180–2270 cm⁻¹).²⁴

The red and green shaded areas in the present spectra (Figs. 3 and 4) mark the previously found ranges of the band positions of single N₂ when adsorbed to pure rhodium and iron clusters, respectively.

In our present study, we took IR-MPD spectra of equiatomic [Rh_iFe_j(N₂)_m]⁺ clusters at three values of *m*: single N₂ adsorption *m* = 1 (black line in Figs. 4 and 5), intermittent coverage state (green shaded areas in Fig. 4), and high numbers of adsorbed N₂ (blue shaded areas in Figs. 4 and 5). For (3,3,*m*), we recorded IR-MPD spectra of *m* = 1 and 7, omitting the case of intermittent coverage. For exemplary measurements down to below 1200 cm⁻¹ and further recorded spectra of some more cluster adsorbate complexes (*i,j,m*), refer to the supplementary material.

1. The cases of single N₂ adsorption

In the cases of single and intermittent N₂ adsorption (Fig. 4) onto [Fe_iRh_j]⁺ clusters, we observe vibrational bands around 2250 ± 50 cm⁻¹, which coincides with the range of previously found vibrational bands of pure Rh cluster N₂ adsorbates.²⁴ This implies red shifts of about 30–130 cm⁻¹ with respect to the IR inactive stretching vibration of free N₂ (2330 cm⁻¹).⁶⁵ Encouraged by this coincidence, we assume that single N₂ preferentially adsorbs to a rhodium atom rather than to an iron atom. We find support for this assumption from previously calculated adsorption energy of N₂ on rhodium surfaces (54 kJ/mol), which is considerably higher than that on Fe surfaces (34 kJ/mol).¹ Our own calculations on [Rh₅(N₂)_m]⁺ cluster adsorbate complexes yielded an adsorption energy of 65 kJ/mol for the first adsorbate molecule.⁴⁴

a. [Rh₃Fe₃(N₂)₁]⁺ to [Rh₅Fe₅(N₂)₁]⁺. In all cases up to *i* = *j* = 5, there are single strong bands of single N₂ adsorbates (*m* = 1) at 2266, 2253, and 2237 cm⁻¹. These single bands gradually red shift by 29 cm⁻¹. Such a red shift was observed before in the case of N₂ adsorption to pure cobalt and rhodium cluster cations, and it was interpreted in terms of a cooperative polarization effect.^{15,24}

TABLE II. Calculated atomic distances (in Å) for nearest neighbors for the [Rh₄Fe₄]⁺ clusters (22tet) in comparison with the sum of atomic radii, experimental data, and calculations on a bicapped octahedral structure.

Species	Sums of atomic radii		PW91 ^a	PBE0 ^b	PBE0 ^b	PBE0 ^b	PBE0 ^b
	Dimer	Bulk					
Rh–Rh	Theo. 2.21 ^a	2.69 ^c	2.70	2.751–3.307	2.715–2.737	2.706–2.716	2.715–2.737
	Theo. 2.27 ^d						
	Exp. 2.3855 ^e						
	Exp. 2.28 ^f						
Rh–Fe		2.586 ^c	2.42	2.332–2.412	2.361–2.537	2.375–2.433	2.362–2.715
		2.581 ^h					
Fe–Fe	Exp. 2.198(2)	αFe 2.482 ^c	2.45	2.839–2.842	2.826–2.779	2.615–2.839	2.766–2.827
		–2.2318(8) ^g					

^aReference 41.

^bThis work.

^cReference 62. Distance of the next neighbors in the fcc crystal; lattice parameter *a* = 3.8032 Å.

^dReference 58.

^eReference 59.

^fReference 60.

^gReference 61.

^hReference 63.

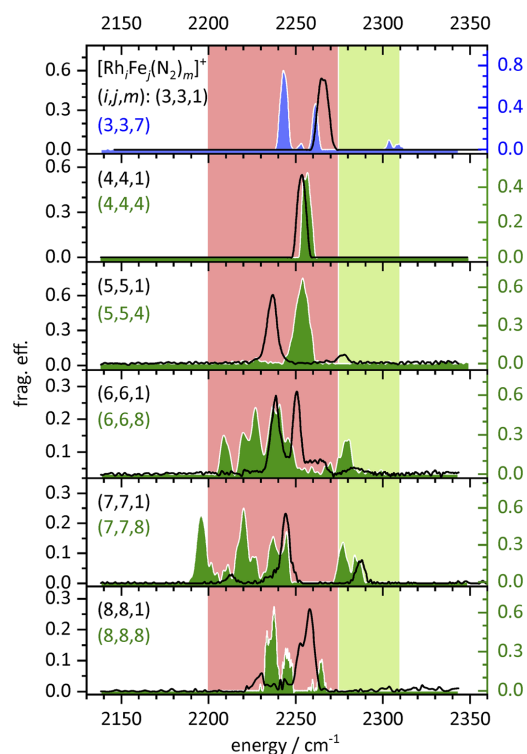


FIG. 4. IR-MPD spectra of single N_2 adsorption (black line) and of first intermittent N_2 adsorption (see the exptl. part; green shaded) on equiatomic alloy cluster cations $[Rh_iFe_j(N_2)_m]^+$ as a function of the size of the cluster core $i = j$. In the case of $i = j = 3$, the blue color denotes the absence of any intermittent adsorption limit. Instead, we provide the spectrum of the maximum N_2 adsorption limit at $m = 7$. The red and green shaded backgrounds indicate the known spectral ranges of the single N_2 vibrations on pure Rh and Fe cluster cations, respectively (for further details, see the text).

the (likely) metallic nature of the cluster cations allows for electron density back donation to molecular adsorbate acceptors (e.g., antibonding π^*). This would weaken the N–N bond and increase the red shift of the N_2 stretching frequency with the number of metal atoms. The further weak IR-MPD band of (5,5,1) at 2277 cm^{-1} likely stems from a combination band of N–N stretching plus Rh–N–N wagging character plus 40 cm^{-1} with respect to the pure N–N stretching band. We calculated an adsorption energy of the first N_2 onto the $Rh_3Fe_3^+$ cluster (cf. Table S7, Fig. S13) as high as 90 kJ/mol.

b. $[Rh_6Fe_6(N_2)_1]^+$. The $i = j = 6$ case is special in revealing two strong IR-MPD bands at 2239 and 2251 cm^{-1} by a mere single N_2 adsorbate, $m = 1$ (black line in Fig. 4). This may likely indicate two distinguishable N_2 binding sites, less likely two cluster isomers, and even less likely two spin state isomers. If, indeed, so, one may tentatively conclude on the presence of Rh atoms in two different

coordination geometries, which vary either by the number or by the nature of nearest neighbors. Of course, the presence of coexistence cluster isomers is conceivable as well. Elucidation remains to future DFT modeling. Above the second strong band, we find some more absorption around 2265 and 2285 cm^{-1} . Both may also originate from some combination band of N–N stretching plus Rh–N–N wagging character, the latter contributing by about 25 and 35 cm^{-1} , respectively.

c. $[Rh_7Fe_7(N_2)_1]^+$ and $[Rh_8Fe_8(N_2)_1]^+$. When inspecting the IR spectra of these larger clusters, the $m = 1$ cases reveal a remarkable blue shift of the observed single strong N_2 vibrational bands of 5 cm^{-1} from $i = j = 6$ to 7 (2244 cm^{-1}) and of 14 cm^{-1} from $i = j = 7$ to 8 (2258 cm^{-1}). This is surprising at first sight. If we assume an alloy-like structure, that is, only Rh–Fe bonds and no Rh–Rh or Fe–Fe bonds within these clusters, the number of iron atoms coordinating to each Rh atom will increase with the size of the cluster. Since Fe is more electronegative than Rh, more electron density is shifted from Rh to Fe and the vibrational frequency of Rh attached N_2 will decrease, which is due to less π -backbonding. The known charge dilution effect¹⁹ may also contribute to some extent, which would be minor for clusters of this size, however. The (8,8,1) cluster adsorbate complex has an additional shoulder on the red slope of the strong band at 2253 cm^{-1} that may indicate a second N_2 binding site. Both clusters, (7,7,1) and (8,8,1), show an additional band about 30 cm^{-1} to the red of the strong bands at 2213 and 2231 cm^{-1} , respectively. We observed these bands only upon exposure to high IR photon fluxes, and we assume these to represent hot bands. The spectrum (7,7,1) cluster adsorbate complex reveals an additional band red shifted with respect to the free N_2 stretching vibration by only 43 cm^{-1} at 2287 cm^{-1} , which may arise from a combination mode of N–N stretching and Rh–N–N wagging modes as assumed above for the cases of (5,5,1) and (6,6,1).

2. The cases of the “intermittent adsorption limits”

As outlined in Sec. II, we have defined those cluster adsorbate complexes as an intermittent adsorption limit where we find enhanced amounts of N_2 adsorption and delayed kinetics for further adsorption. Note that in all the investigated cases of $i = j = 4, \dots, 8$, there are such intermittent adsorption limits—but for the smallest cluster case, $i = j = 3$, where N_2 adsorption proceeds toward its maximum limit without any intermittent delay.

a. $[Rh_3Fe_3(N_2)_7]^+$. We observe two strong bands (at 2243 and 2261 cm^{-1}), one weak band (in between at 2253 cm^{-1}), and a couple of very weak near coinciding bands around 2305 cm^{-1} [blue spectrum, indicated as (3,3,7), in Fig. 4]. The former three of these bands fall within the red shaded area, and they likely stem from the stretching vibrations of those N_2 adsorbates, which adsorb onto Rh sites. The super-stoichiometric composition of a 6:7 metal:adsorbate ratio requires at least one metal site with geminal N_2 adsorption. We assume a monolayer with single adsorption of the first six N_2 molecules onto the $[Rh_3Fe_3]^+$ cluster, and the seventh N_2 adsorbs onto an already singly occupied site.

Symmetric/asymmetric couplings of those equivalent N_2 oscillators are expected to induce significant splittings. Further insights will arise from the DFT modeling of such vibrations (refer to chapter/section III C). The weak bands around 2305 cm^{-1} fall into the green shaded area of Fe– N_2 stretching vibrations, and they likely

arise from such N₂ adsorptions to iron sites. Note that this IR-MPD spectrum does not provide any discernible evidence for isomerization of any type, which well coincides with the swift adsorption kinetics up to the maximum adsorption limit as reported in [AAE].⁴²

b. [Rh₄Fe₄(N₂)₄]⁺. This cluster shows a single band at 2257 cm⁻¹, slightly blue shifted with respect to single N₂ adsorption by about 4 cm⁻¹, and well within the red shaded area of N₂ adsorption to Rh sites. This occurrence of a single band by numerous IR active N₂ oscillators is indicative of a high cluster symmetry. The computations of [Rh₄Fe₄]⁺ structures have suggested such a high symmetry in a D_{2d}-like structure (cf. inset of Fig. 5). All Rh atoms and all Fe atoms have the same coordination geometry, respectively; all Rh sites and all Fe sites are equivalent, respectively. An exclusive N₂ adsorption to Rh sites finds further support by structural and enthalpic reasons: The Rh atoms are coordinated by Fe with acute Fe–Rh–Fe angles, and they protrude from the cluster surface.

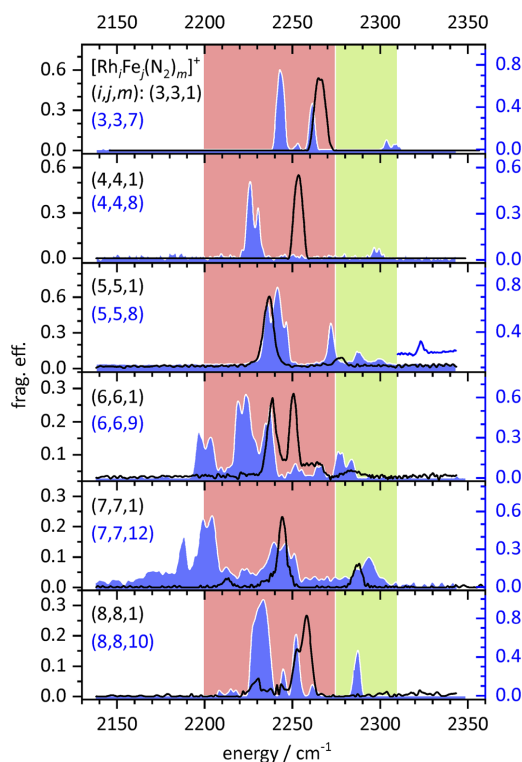


FIG. 5. IR-MPD spectra of single (black line) and high N₂ adsorption (blue shaded) on equiatomic cationic Rh–Fe alloy cluster cations as a function of the size of the cluster core $i = j$. The red and green shaded backgrounds indicate the known spectral ranges of the single N₂ vibrations on pure Rh and Fe cluster cations, respectively (for details, see the text).

This reduces steric hindrance by next neighbors and provides open space. For Fe sites, the opposite holds. Enthalpic reasoning arises from the computed N₂ adsorption enthalpies of pure Fe and Rh surfaces—which are stronger for Rh than for Fe.¹

c. [Rh₅Fe₅(N₂)₄]⁺. The IR-MPD spectrum of this cluster shows a single band at 2254 cm⁻¹, which falls into the red area, and it almost coincides with the single band of the [Rh₄Fe₄(N₂)₄]⁺ cluster adsorbate complex. Note the difference to the (4,4,1) and (5,5,1) cases, where the two single bands are displaced against each other by about 17 cm⁻¹. Once more, we take the occurrence of a single absorption band by multiple N₂ adsorbates as strong evidence for a cluster structure of high symmetry. However, its very nature is yet unexplored. A very weak band at 2227 cm⁻¹ might indicate either a hot band or a second isomer. Supporting DFT calculations are beyond the scope of the present study.

d. [Rh₆Fe₆(N₂)₈]⁺ and [Rh₇Fe₇(N₂)₈]⁺. In contrast to the IR-MPD spectra of the smaller clusters, these clusters provide spectra with numerous bands within the red shaded area of N₂ adsorption to Rh sites; they spread out over a range of up to 75 cm⁻¹. This likely points out that the Rh coordination sites are distinguishable and that these clusters are of low symmetry. There are bands at 2209, 2220, 2227, 2237, 2241, and 2245 cm⁻¹ of the (6,6,8) cluster adsorbate complex and at 2175, 2210, 2220, 2226, 2237, and 2244 cm⁻¹ of the (7,7,8) cluster adsorbate complex. There are some additional bands in the range of 2270–2290 cm⁻¹ that fall into the green shaded area of likely N₂ adsorption to Fe sites. Such adsorption is, indeed, conceivable in cases where the number of N₂ adsorbates exceeds the adsorbing Rh sites within the cluster. The excess of N₂ molecules may choose to accept the less favorable Fe sites. Of course, it is conceivable to adsorb multiple N₂ to single Rh, which might induce further splittings by symmetric/asymmetric coupling. Given the high total number of metal atoms in these clusters (12 and 14, respectively), it is likely that some atoms are not at the cluster surface. They may assume high coordination to the inside and form bulk-like bonding motifs. This remains to verify.

e. [Rh₈Fe₈(N₂)₈]⁺. In this intermittent adsorption limit case, the number of adsorbed N₂ molecules is the same as the number of Rh and Fe atoms, each. The IR-MPD spectrum reveals several bands within the red shaded area of preferential N₂ adsorption to Rh sites (at 2233, 2238, 2245, and 2265 cm⁻¹); there are no bands in the range of single Fe–N₂ adsorption. In view of the previous findings, all N₂ molecules seem to adsorb to Rh sites only—albeit to distinguishable ones. We observe two weak bands about +20 cm⁻¹ to blue, which we tentatively assign to stretch/wag combinations. All of this indicates a cluster structure of some symmetry that is slightly distorted. These findings may serve as a valuable starting point for further elucidation by future DFT modeling.

3. The cases of “maximum adsorption limits”

We recorded IR-MPD spectra of highly abundant clusters with high N₂ coverages, (4,4,8), (6,6,9), and (8,8,10), and of maximum adsorption limits (5,5,8) and (7,7,12). For all of these cluster adsorbate complexes, $m > i$. The (3,3,7) case is discussed above.

a. [Rh₄Fe₄(N₂)₈]⁺. Despite the high level of N₂ adsorption, $m = 8$, we observe a single band at 2226 cm⁻¹ with a shoulder at 2231 cm⁻¹. The center of this double band is red shifted by 25 cm⁻¹

with respect to single N_2 adsorption, $m = 1$, and by 28 cm^{-1} with respect to the intermittent N_2 adsorption, $m = 4$. By virtue of the red and green shaded areas, all the N_2 molecules likely adsorb onto Rh sites. This is conceivable based on the structural and enthalpic reasons discussed above. Closer inspection of the observed band reveals a small splitting of about 5 cm^{-1} . This likely results from the symmetric/antisymmetric coupling of stretching vibrations of two N_2 on the same Rh site. A weak band around 2297 cm^{-1} likely arises from some N_2 adsorption to Fe sites. Some splitting on the order of 4 cm^{-1} is discernible but close to the noise level. Note that higher levels of N_2 coverage up to $m_{\text{max}} = 11$ are in equilibrium, but their abundances are almost 2 orders of magnitude lower than that of $m = 8$.⁴² We find no indication of isomerization or swift adsorption/desorption equilibria in the recorded IR-MPD spectra of (4,4, m).

b. $[Rh_5Fe_5(N_2)_8]^+$. The strong band of the (5,5,8) cluster at 2241 cm^{-1} appears blue shifted by 4 cm^{-1} from the corresponding band of the (5,5,1) cluster at 2237 cm^{-1} and reveals some triple splitting by $4\text{--}6\text{ cm}^{-1}$. There is an additional set of three weaker bands to the blue at 2272 cm^{-1} and above. We tentatively assign these to other N_2 adsorption sites. The two bands at 2288 and 2299 cm^{-1} are in the green area of N_2 adsorbed likely to Fe clusters.

We may note in passing that in both cases of $i = j = 4$ and 5, the investigated levels of N_2 adsorption are $m = 4$ and $m = 8$. Both IR-MPD bands of $m = 4$ occur around $2254\text{--}2257\text{ cm}^{-1}$, and both IR-MPD bands of $m = 8$ shift considerably to red ($12\text{--}32\text{ cm}^{-1}$). Despite these similarities, the single N_2 adsorption cases (4,4,1) and (5,5,1) are remarkably different: The found single IR-MPD bands of $i = j = 4$ and 5 are shifted with respect to each other by 17 cm^{-1} .

There is an additional band at 2323 cm^{-1} that appears only upon application of maximum laser power (2.5 mJ/pulse as opposed to 1 mJ/pulse else). It likely originates from a merely bound and weakly polarized N_2 molecule, roaming around or locating close to other strongly bound N_2 adsorbates. The adsorption rates continuously decrease toward $m_{\text{max}} = 8$ (cf. [AAE]) and support such a weak interaction of the last N_2 ligand with the cluster.⁴² Thus, there may be, indeed, a loosely bound second shell N_2 adsorbate. For all of the least red shifted bands, 2299 cm^{-1} and above, we need to keep in mind the general possibility of stretching wagging combination modes.

c. $[Rh_6Fe_6(N_2)_9]^+$ and $[Rh_7Fe_7(N_2)_{12}]^+$ and $[Rh_8Fe_8(N_2)_{10}]^+$. In these three cases of $i = j = 6, 7$, and 8, we recorded the IR-MPD spectra of the cluster adsorbate complexes with $m = 9, 12$, and 10, respectively. We found bands for (6,6,9) at 2196, 2203, 2219, 2223, 2237, 2251, 2265, 2276, and 2284 cm^{-1} and for (8,8,10) at 2233, 2245, 2252, 2261, and 2287 cm^{-1} . The bands of the (7,7,12) spectrum separate into two sets: one in the red shaded Rh range at 2188, 2199, 2204, 2213, 2223, 2240, 2247, and 2251 cm^{-1} and one weaker set of overlapping bands in the green shaded Fe range around 2294 cm^{-1} . The spectra closely resemble to those of the lower coverage intermittent adsorption limits discussed above. All spectral features prevail, with some minor shifts and intensity variations occurring. There is one remarkable exception: In the $i = j = 8$ cases, there is an additional band at 2287 cm^{-1} in the $m = 10$ spectrum, which does not show in the $m = 8$ spectrum. This additional band is indicative of N_2 adsorption to Fe sites; it falls into the green shaded spectral area. Thus, we find evidence that the $i = j = 8$

cluster $[Rh_8Fe_8]^+$ adsorbs up to eight N_2 to Rh sites, and two more N_2 adsorbates onto Fe sites thereafter. In all three cases, we did not observe any bands around 2330 cm^{-1} .

With (7,7,12), we were able to record an IR-MPD spectrum of a maximum adsorption limit, despite an adsorption/desorption equilibrium between four species at long storage times.⁴² The spectrum shows broad bands, which are in line with a flexible adsorbate shell. The recorded bands exhibit narrow splittings of $4\text{--}10\text{ cm}^{-1}$, which indicate couplings as expected for double N_2 occupation of metal sites.

In addition, we recorded the spectrum of the (7,7,10) intermittent adsorption limit (cf. Fig. S11 of the supplementary material), which reveals remarkably sharp and widely spaced bands—void of the above-mentioned small couplings.

Upon closer inspection, some of the properties of the (6,6,9) and the (7,7,12) spectra warrant some more attention: First, for (6,6,9), the three strongest bands reveal a splitting up to 7 cm^{-1} , which does not show up to the first intermittent N_2 adsorption. Such splittings are likely indicative of symmetric/antisymmetric couplings of two N_2 at the same Rh site; see above. In this case, they show only at high N_2 loads. Even the weak bands in the green shaded area reveal a splitting. We conclude on some Rh and Fe atoms that are more exposed and others that are higher coordinated and thus do adsorb at most single N_2 . Second, the (6,6,9) and (7,7,12) spectra spread out over a range of up to 120 cm^{-1} . We assume that the most red shifted bands arise from N_2 adsorption onto a class of Rh atoms that provide a weak σ -acceptor and strong π -donor character. The less red shifted bands arise from N_2 adsorbed onto a class of Rh atoms with a strong σ -acceptor and weak π -donor character. In the case of the (8,8,10) cluster adsorbate complex, these separate classes seem to vanish.

The IR-MPD spectra of (6,6,9) and (8,8,10) document intermittent species, which are in equilibrium with the maximum adsorption limit and which constitute the most abundant species within these equilibria⁴² [AAE]. In both cases, the adsorption rate constants drop continuously with the increasing number of adsorbed N_2 molecules and the adsorption becomes slower, step by step. Investigation of their true maximum adsorption limits would also probably show weakly bound and weakly activated N_2 ligands as revealed for (5,5,8). However, the low abundance of these maximum adsorption limits (6,6,10) and (8,8,11) and their involvement in swift adsorption/desorption equilibria have impeded their spectroscopic investigation so far.

Quantum chemical modeling of all investigated species and their recorded spectra is far out of reach. Instead, we chose one case of limited complexity for exemplary DFT modeling in order to achieve some better understanding of the adsorption behavior and the structural properties of such an alloy cluster.

C. Modeling of the $[Rh_3Fe_3(N_2)_7]^+$ vibrational spectra

We chose the case of the maximum N_2 adsorption limit of $m_{\text{max}} = 7$ to the $i = j = 3$ alloy cluster as a test case for vibrational analysis by further DFT modeling. The most stable (3,3,7) isomers are based on a metal cluster core (3,3,0) of most stable type (al). Each of the Rh and Fe sites serves to adsorb single N_2 , and the seventh remaining N_2 serves to locate as a second adsorbate on one of the four optional and distinguishable sites (cf. Fig. 6 for atom labeling): at the Rh site

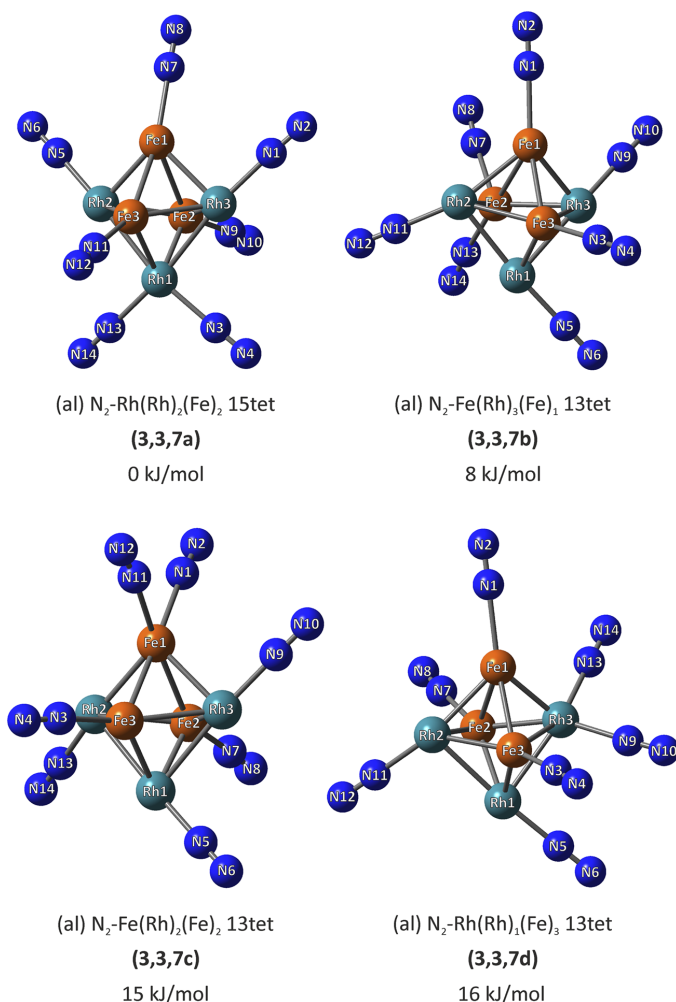


FIG. 6. DFT optimized structures of four most stable [Rh₃Fe₃(N₂)₇]⁺ clusters. All four isomers derive from the cluster core type (a). All N₂s chose to adsorb by μ₁-type end-on coordination. The most stable case (3,3,7a) reveals single N₂ adsorbates at each Rh and Fe site, but Rh₁ reveals two geminal N₂ adsorbates. This Rh site is unique by its two Rh next neighbors. Cases (3,3,7b) and (3,3,7c) reveal two geminal N₂ adsorbates at sites Fe₂ and Fe₁, respectively. Case (3,3,7d) reveals geminal N₂ adsorbates at site Rh₃. The xyz coordinates are provided in the [supplementary material](#) (Tables S9–S12).

(two Rh next neighbors, labeled Rh₁), at either of two equivalent Rh sites (one Rh next neighbor, labeled Rh₂ and Rh₃), at the Fe site (two Fe next neighbors, labeled Fe₁), or at either of the two equivalent Fe sites (one Fe next neighbor, labeled Fe₂ and Fe₃).

We compare the recorded IR-MPD spectra to our computed IR absorption spectra, where the computed spectra are scaled by 0.9385²⁴ to match experimental and calculated fundamentals of free N₂ (Fig. 7). It shows that the experimental IR-MPD spectrum matches best to the calculated absorption spectrum of the cluster in a 15tet with the seventh N₂ adsorbed to the sole Rh site with two Rh next neighbors (structures as displayed in Fig. 6; spectrum as

in Fig. 7, second to the top). We provide a compilation of assigned vibrational bands in Table III. Note that the calculated and observed bands are slightly shifted in their frequency against each other. However, the overall pattern and the IR intensities agree remarkably well when considering the most stable case of the DFT modeling. The other calculated isomers are at least 46 kJ/mol higher in energy, and their spectra are documented in Fig. S14.

The twofold occupation of a Rh site causes a symmetric/antisymmetric coupling and allows for an assignment of the recorded bands at 2253 cm⁻¹ (antisymmetric) and 2261 cm⁻¹ (symmetric) (N₃/N₄ and N₁₃/N₁₄). It is remarkable that there is a

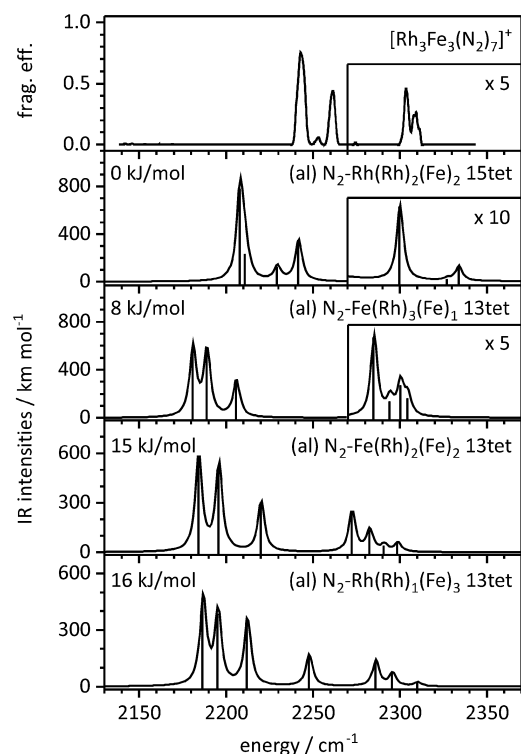


FIG. 7. Experimental IR-MPD spectrum (top trace) and calculated IR absorption spectra of some $[\text{Rh}_3\text{Fe}_3(\text{N}_2)_7]^+$ coordination and spin isomers. The calculated spectra (scaled by 0.9385) represent the four preferential coordination and spin isomers from Fig. 6. Note the slightly shifted and otherwise matching pattern of vibrational modes in the topmost computed spectrum of the most stable isomer (3,3,7a), which comes along in a 15tet spin state.

significant shift between the bands of N_2 adsorbed on Fe and on Rh. Indeed, all bands around 2250 cm^{-1} can be assigned to stretching vibrations of N_2 on rhodium—in line with our working hypothesis that spectral findings from pure Rh and pure Fe clusters may serve as a guide for a classification of spectral feature in the mixed alloy-type Rh–Fe clusters (visualized by the red and green shaded areas in Figs. 4 and 5).

The calculations indicate a symmetric/antisymmetric N_2 –Rh–Rh–Rh– N_2 coupling between the stretching vibrations of N_1/N_2 and N_5/N_6 . The coupling of these two distant but equivalent N_2 ligands is very weak (calculated as $3\text{--}4\text{ cm}^{-1}$) and does not necessarily manifest in separate bands. The weak recorded bands above 2300 cm^{-1} can be assigned to N_2 adsorbed to Fe. Calculations indicate no vibrational coupling between these Fe bound N_2 adsorbates. The calculated IR spectra of less stable coordination isomers (the two lower traces in Fig. 7) do not fit to the experimental IR-MPD spectrum. These results are in line with our kinetic measurements that exhibit swift adsorption to a single maximum adsorption limit without any equilibrium at the end of the adsorption chain.⁴²

In (3,3,7), the first six N_2 molecules adsorb onto a free metal site such that each metal site is singly occupied, independent of the metal (Rh or Fe). We observe a Langmuir type of stoichiometric adsorption. The seventh N_2 molecule has no choice but to adsorb onto an occupied site and finds itself as a geminal adsorbate, preferentially at a Rh site. The adsorption kinetics reveal a swift step-wise adsorption without any indication of an intermittent adsorption limit.⁴² The IR bands of the N_2 molecules adsorbed onto the Rh sites are in the range as observed for pure Rh clusters; those of N_2 adsorbed onto Fe sites are in the range as observed for pure Fe clusters, and these IR bands are by at least one order of magnitude less intense than the N_2 stretching IR bands at Rh sites. The polarization of N_2 by adsorption to Fe sites seems weaker than that by adsorption to Rh sites. Note that these results indicate a conservation of the 15tet spin state at the maximum adsorption limit (3,3,7) rather than a spin quench as observed for pure rhodium clusters before.^{24,44}

The modeling of the (3,3,7) cluster adsorbate complex, the thereby achieved assignment of recorded IR bands, and fur-

TABLE III. Vibrational data for the lowest lying $[\text{Rh}_3\text{Fe}_3(\text{N}_2)_7]^+$ structure. The scaling factor for the N_2 stretching frequencies is 0.9385. The low frequency modes are strongly coupling.

Mode	Type	Calc. freq. (cm^{-1})	Scaled freq. (cm^{-1})	IR intensity (km mol^{-1})	Measured $\bar{\nu}$ (cm^{-1})
1–18	Wagging modes	9.3–77	8.7–72	0.009–11	
19–32	Internal cluster vibrations	99–231	93–217	0.044–5.3	
33–47	Bending modes	249–343	234–322	0.39–32	
48	Asymm. stretch $\text{N}_1\text{--N}_2/\text{N}_5\text{--N}_6$	2352	2207	778	2243
49	Symm. stretch $\text{N}_1\text{--N}_2/\text{N}_5\text{--N}_6$	2356	2211	233	
50	Asymm. stretch $\text{N}_3\text{--N}_4/\text{N}_{13}\text{--N}_{14}$	2375	2229	124	2253
51	Symm. stretch $\text{N}_3\text{--N}_4/\text{N}_{13}\text{--N}_{14}$	2388	2241	351	2261
52	Stretch $\text{N}_7\text{--N}_8$	2450	2299	63	2304
53	Stretch $\text{N}_{11}\text{--N}_{14}$	2479	2327	2.3	2309
54	Stretch $\text{N}_9\text{--N}_{10}$	2487	2334	13	

ther insights above support in the interpretation of the (4,4,8) spectrum.

The IR-MPD spectrum of the (4,4,8) cluster adsorbate complex reveals a strong doublet band in the Rh range and a weak set of bands in the Fe range. Such a sparse spectrum by eight chromophores strongly suggests a single type of Rh adsorption sites and of Fe adsorption sites, which implies high symmetry. The recorded band in the Rh range is split by about 4 cm⁻¹, which likely indicates symmetric/antisymmetric coupling of a distant pair of N₂ molecules whose adsorption sites are separated by another metal atom, as revealed in the (3,3,7) case above. In the IR-MPD spectrum of (4,4,8), there is no indication of a splitting in the order of 12 cm⁻¹ and therefore no indication for double adsorption onto a single metal site. The IR-MPD spectrum thus indicates stoichiometric adsorption onto each of the eight metal sites. The IR-MPD spectrum of the (4,4,4) cluster adsorbate complex has not revealed any evidence for N₂ occupation of Fe sites, and the recorded single band indicates a highly symmetric cluster. The adsorption kinetics reveal an intermittent adsorption limit for this complex. We conclude on a highly symmetric cluster core that likely resembles the computed most stable D_{2d} structural type. The first four N₂ molecules likely adsorb onto the equivalent Rh atoms, whereas the remaining four adsorption steps yield at the equivalent Fe sites. The final product is a highly symmetric cluster adsorbate complex (4,4,8) with a Langmuir-type stoichiometric first adsorption shell.

IV. CONCLUSION

We have recorded IR-MPD spectra of size selected N₂ adsorbates on equiatomic Rh-Fe cluster cations. These spectra show a multitude of bands within ranges that coincide with spectra of N₂ adsorbates on Rh and Fe cluster cations recorded before. The sparse spectra of the cluster adsorbate complexes of [Rh₄Fe₄]⁺ and [Rh₅Fe₅]⁺ indicate high symmetries of these.

We have modeled geometries of [Rh₃Fe₃]⁺ and [Rh₄Fe₄]⁺ clusters and IR spectra of the [Rh₃Fe₃(N₂)₇]⁺ cluster, which confirm the propensity of the clusters to form as much Rh-Fe bonds as possible and which allow for high symmetry and an alloy-like character. A comparison with our adsorption kinetics yields a conclusive description of spectral phenomena, such as weakly adsorbed N₂ ligands. By the assignment of the blue shifted bands to Fe adsorption sites, we validate the sensitivity of the element of the N₂ stretching vibration with respect to adsorption to Fe or Rh sites. In the case of the [Rh₃Fe₃]⁺ cluster, we conclude on the formation of an N₂ monolayer on all metal atoms. The next N₂ molecule adsorbs onto a Rh atom in a geminal manner. The spectrum of the [Rh₄Fe₄]⁺ cluster indicates an adsorption of the first four N₂ molecules solely/exclusively onto the rhodium atoms. The spectrum of [Rh₄Fe₄(N₂)₈]⁺ indicates additional stoichiometric adsorption onto iron atoms. In contrast to bare rhodium clusters, our investigations do not provide any indication for a spin quench upon N₂ adsorption.

The present IR-MPD studies in conjunction with the DFT modeling relate recorded IR bands to element specific adsorption sites. We thereby find strong evidence for preferential adsorption to rhodium sites and merely secondary adsorption to iron.

SUPPLEMENTARY MATERIAL

See the [supplementary material](#) for spectral IR photon fluxes, for structural parameters and plots of computed cluster isomers, and for further IR-MPD spectra of further cluster adsorbate complexes.

ACKNOWLEDGMENTS

This work was supported by the German Research Foundation (DFG) within the Transregional Collaborative Research Center SFB/TRR 88 “Cooperative effects in homo- and heterometallic complexes” (3MET.de) and by the State Research Center OPTIMAS. We thank Thomas Kolling for assistance on technical questions of any kind. Finally, we thank the reviewers for most valuable comments, which are much appreciated.

AUTHOR DECLARATIONS

Conflict of Interest

The authors have no conflicts to disclose.

Author Contributions

M.P.K., A.A.E., M.E.H., A.S., D.V.F., S.D., and J.M. conducted the experiments. A.A.E. and M.P.K. carried out quantum chemical calculations. M.P.K. and G.N.-S. evaluated all data. M.P.K., S.D., and G.N.-S. wrote the manuscript, and all the authors revised and agreed.

DATA AVAILABILITY

The data that support the findings of this study are available from the corresponding author upon reasonable request.

REFERENCES

- 1 T. Bligaard and J. K. Nørskov, *Chemical Bonding at Surfaces and Interfaces* (Elsevier, Amsterdam, 2008), p. 255.
- 2 G. A. Somorjai, *Introduction to Surface Chemistry and Catalysis* (John Wiley & Sons, 1994).
- 3 O. Deutschmann *et al.*, *Ullmann's Encyclopedia of Industrial Chemistry* (Wiley-VCH Verlag GmbH & Co. KGaA, 2000).
- 4 M. Votsmeier *et al.*, *Ullmann's Encyclopedia of Industrial Chemistry* (Wiley-VCH Verlag GmbH & Co. KGaA, 2009).
- 5 G. Ertl, *Angew. Chem., Int. Ed.* **47**, 3524 (2008).
- 6 B. Harrison, B. J. Cooper, and A. J. J. Wilkins, *Platinum Met. Rev.* **25**, 14 (1981).
- 7 G. Ertl, *Catal. Rev.* **21**, 201 (1980).
- 8 S. Brunauer, P. H. Emmett, and E. Teller, *J. Am. Chem. Soc.* **60**, 309 (1938).
- 9 I. Langmuir, *J. Am. Chem. Soc.* **40**, 1361 (1918).
- 10 H.-J. Freund *et al.*, *Surf. Sci.* **185**, 187 (1987).
- 11 H. P. Wang and J. T. Yates, *J. Phys. Chem.* **88**, 852 (1984).
- 12 D. A. J. M. Ligthart *et al.*, *Catal. Commun.* **77**, 5 (2016).
- 13 D. E. Jaramillo *et al.*, *Nat. Mater.* **19**, 517 (2020).
- 14 C. Kerpál *et al.*, *J. Phys. Chem. C* **117**, 12153 (2013).
- 15 S. Dillinger *et al.*, *Phys. Chem. Chem. Phys.* **17**, 10358 (2015).
- 16 G. Blyholder, *J. Phys. Chem.* **68**, 2772 (1964).
- 17 J. Chatt and L. A. Duncanson, *J. Chem. Soc.* **1953**, 2939.
- 18 J. S. Dewar, *Bull. Soc. Chim. Fr.* **18**, C71 (1951).
- 19 A. Fielicke *et al.*, *J. Chem. Phys.* **124**, 194305 (2006).
- 20 A. D. Brathwaite, H. L. Abbott-Lyon, and M. A. Duncan, *J. Phys. Chem. A* **120**, 7659 (2016).

- ²¹J. Mohrbach, S. Dillinger, and G. Niedner-Schatteburg, *J. Phys. Chem. C* **121**, 10907 (2017).
- ²²S. Dillinger, J. Mohrbach, and G. Niedner-Schatteburg, *J. Chem. Phys.* **147**, 184305 (2017).
- ²³S. Dillinger *et al.*, *J. Phys. Chem. Lett.* **9**, 914 (2018).
- ²⁴M. P. Klein *et al.*, *Top. Catal.* **61**, 106 (2018).
- ²⁵J. Mohrbach, S. Dillinger, and G. Niedner-Schatteburg, *J. Chem. Phys.* **147**, 184304 (2017).
- ²⁶A. Nilsson, L. G. M. Pettersson, and J. K. Nørskov, *Chemical Bonding at Surfaces and Interfaces*, 1st ed. (Elsevier, Amsterdam; Boston, MA, 2008).
- ²⁷C. Paduani, *J. Appl. Phys.* **90**, 6251 (2001).
- ²⁸A. Hernando *et al.*, *Mater. Sci. Forum* **235–238**, 675 (1997).
- ²⁹A. Kashyap *et al.*, *J. Appl. Phys.* **95**, 7480 (2004).
- ³⁰R. Y. Gu and V. P. Antropov, *Phys. Rev. B* **72**, 012403 (2005).
- ³¹W. Lu *et al.*, *J. Mater. Sci.* **45**, 4919 (2010).
- ³²K. Ohtake *et al.*, *IEEE Trans. Magn.* **50**, 1 (2014).
- ³³X. Marti *et al.*, *Nat. Mater.* **13**, 367 (2014).
- ³⁴A. Heidarian *et al.*, *Nucl. Instrum. Methods Phys. Res., Sect. B* **358**, 251 (2015).
- ³⁵Y. Wakisaka *et al.*, *Phys. Rev. B* **92**, 184408 (2015).
- ³⁶J. Clarkson *et al.*, *Scientific Reports* **7**, 15460 (2017).
- ³⁷D. Odkhuu, *Phys. Rev. B* **93**, 064412 (2016).
- ³⁸R. Witte *et al.*, *Phys. Rev. B* **93**, 104416 (2016).
- ³⁹J. Chaboy *et al.*, *Phys. Rev. B* **59**, 3306 (1999).
- ⁴⁰J. H. Mokkath and G. M. Pastor, *Phys. Rev. B* **85**, 054407 (2012).
- ⁴¹J. H. Mokkath and G. M. Pastor, *J. Phys. Chem. C* **116**, 17228 (2012).
- ⁴²A. A. Ehrhard *et al.*, "Cryo Kinetics of N₂ Adsorption onto Bimetallic Rhodium-Iron Clusters in Isolation," *J. Chem. Phys.* (in press).
- ⁴³A. Straßner *et al.*, *J. Chem. Phys.* **155**, 244305 (2021).
- ⁴⁴A. A. Ehrhard *et al.*, *Mol. Phys.* **119**, e1953172 (2021).
- ⁴⁵P. Caravatti and M. Allemann, *Org. Mass Spectrom.* **26**, 514 (1991).
- ⁴⁶M. Gerhards, *Opt. Commun.* **241**, 493 (2004).
- ⁴⁷M. Grunze *et al.*, *Phys. Rev. Lett.* **53**, 850 (1984).
- ⁴⁸M. C. Tsai *et al.*, *Surf. Sci.* **155**, 387 (1985).
- ⁴⁹L. J. Whitman *et al.*, *Phys. Rev. Lett.* **56**, 1984 (1986).
- ⁵⁰L. J. Whitman, C. E. Bartosch, and W. Ho, *J. Chem. Phys.* **85**, 3688 (1986).
- ⁵¹C. N. R. Rao *et al.*, *Spectrochim. Acta, Part A* **43**, 1479 (1987).
- ⁵²P. Rochana, K. Lee, and J. Wilcox, *J. Phys. Chem. C* **118**, 4238 (2014).
- ⁵³D. V. Fries *et al.*, *Phys. Chem. Chem. Phys.* **23**, 11345 (2021).
- ⁵⁴M. J. Frisch *et al.*, Gaussian 09, Revision D.01 (Gaussian, Inc., Wallingford, CT, 2009).
- ⁵⁵C. Adamo and V. Barone, *J. Chem. Phys.* **110**, 6158 (1999).
- ⁵⁶T. H. Dunning, *J. Chem. Phys.* **90**, 1007 (1989).
- ⁵⁷D. Andrae *et al.*, *Theor. Chim. Acta* **77**, 123 (1990).
- ⁵⁸M. R. Beltran *et al.*, *Eur. Phys. J. D* **67**, 63 (2013).
- ⁵⁹F. A. Cotton *et al.*, *Acta Crystallogr., Sect. B: Struct. Sci., Cryst. Eng. Mater.* **27**, 1664 (1971).
- ⁶⁰K. A. Gingerich and D. L. Cocke, *J. Chem. Soc., Chem. Commun.* **1972**, 536.
- ⁶¹C. A. Murillo, *Angew. Chem., Int. Ed.* **48**, 5076 (2009).
- ⁶²D. R. Lide and D. M. Haynes *CRC Handbook of Chemistry and Physics*, 90th ed. (CRC Press, Boca Raton, 2010).
- ⁶³A. I. Zakharov *et al.*, *J. Exp. Theor. Phys.* **19**, 1348 (1964).
- ⁶⁴D. J. Harding *et al.*, *J. Chem. Phys.* **133**, 214304 (2010).
- ⁶⁵J. Bendsen, *J. Raman Spectrosc.* **2**, 133 (1974).

CURRICULUM VITAE

Daniela V. Fries

- 01/2020 - present **RPTU Kaiserslautern-Landau, Germany**
PHD, CHEMISTRY, Prof. G. Niedner-Schatteburg
Research topic: Kinetic and Spectroscopic Characterization of N₂ and H₂ activation by Transition Metal Clusters under Cryo Conditions
- 10/2016 - 12/2019 **TU Kaiserslautern, Germany**
MASTER OF SCIENCE, CHEMISTRY
Specialization modules: physical and inorganic chemistry
Master thesis: "Kinetische und IR-Spektroskopische Untersuchungen zur N₂ Adsorption an kationische Tantal Cluster unter Kryobedingungen"
- 05/2018 - 08/2018 **University of Liverpool, Materials Innovation Factory, UK**
STAY ABROAD, Prof. A. I. Cooper
Research topic: Synthesis of conjugated polymers containing coordination sites for metals for application in the area of photocatalysis
ERASMUS+ Stipendium: financial support for a stay abroad at University of Liverpool during master's studies
- 10/2013 - 09/2016 **TU Kaiserslautern, Germany**
BACHELOR OF SCIENCE, CHEMISTRY
Bachelor thesis: "Synthese und Gasphasencharakterisierung von trinuclearen, oxozentrierten Cobaltacetat-Komplexen"
- 09/2005 - 03/2013 **Carl-Bosch-Gymnasium, Ludwigshafen, Germany**
ABITUR

LIST OF PUBLICATIONS

The Journal of Chemical Physics (2023), 159, 164303

<https://doi.org/10.1063/5.0157217>

CRYO IR SPECTROSCOPY AND CRYO KINETICS OF DINITROGEN ACTIVATION AND CLEAVAGE BY SMALL TANTALUM CLUSTER CATIONS

Daniela V. Fries, Matthias P. Klein, Annika Straßner, Maximilian E. Huber, Maximilian Luczak, Christopher Wiehn, and Gereon Niedner-Schatteburg

The Journal of Chemical Physics (2023), 159, 164306

<https://doi.org/10.1063/5.0157218>

CRYO-IR SPECTROSCOPY AND CRYO-KINETICS OF CLUSTER N₂ ADSORBATE COMPLEXES OF TANTALUM CLUSTER CATIONS TA₅₋₈⁺

Daniela V. Fries, Matthias P. Klein, Annika Straßner, Maximilian E. Huber, and Gereon Niedner-Schatteburg

Journal of Organometallic Chemistry (2023), 987, 122618

<https://doi.org/10.1016/j.jorganchem.2023.122618>

A NOVEL CHELATING BIDENTATE NHC LIGAND BASED ON THE CATIONIC (H⁵-CYCLOPENTADIENYL)(H⁶-PHENYL)IRON(II) MOTIF

Christian Malchau, Nicole Ultes, Julia Ehrhard, Tobias R. Eger, Daniela V. Fries, Benjamin Oelkers, Sabine Becker, Gereon Niedner-Schatteburg, and Werner R. Thiel

European Journal of Inorganic Chemistry (2022), e202200106

<https://doi.org/10.1002/ejic.202200106>

TRANSITION METAL COMPLEXES OF NHC LIGANDS FUNCTIONALIZED WITH THE CATIONIC (H⁵-CYCLOPENTADIENYL)(H⁶-PHENYL)IRON(II) MOTIF

Christian Malchau, **Daniela V. Fries**, Yannick Mees, Marisa F. Jakobs, Yu Sun, Sabine Becker, Gereon Niedner-Schatteburg, and Werner R. Thiel

The Journal of Chemical Physics (2022), 156, 014302

<https://doi.org/10.1063/5.0075289>

CRYO INFRARED SPECTROSCOPY OF N₂ ADSORPTION ONTO BIMETALLIC RHODIUM-IRON CLUSTERS IN ISOLATION

Matthias P. Klein, Amelie A. Ehrhard, Maximilian E. Huber, Annika Straßner, **Daniela V. Fries**, Sebastian Dillinger, Jennifer Mohrbach, and Gereon Niedner-Schatteburg

The Journal of Chemical Physics (2021), 155, 244306

<https://doi.org/10.1063/5.0064965>

KINETICS OF STEPWISE NITROGEN ADSORPTION BY SIZE-SELECTED IRON CLUSTER CATIONS: EVIDENCE FOR SIZE-DEPENDENT NITROGEN PHOBIA

Annika Straßner, Matthias P. Klein, **Daniela V. Fries**, Christopher Wiehn, Maximilian E. Huber, Jennifer Mohrbach, Sebastian Dillinger, Dirk Spelsberg, Peter B. Armentrout, and Gereon Niedner-Schatteburg

The Journal of Chemical Physics (2021), 155, 244305

<https://doi.org/10.1063/5.0064966>

CRYO SPECTROSCOPY OF N₂ ON CATIONIC IRON CLUSTERS

Annika Straßner, Christopher Wiehn, Matthias P. Klein, **Daniela V. Fries**, Sebastian Dillinger, Jennifer Mohrbach, Marc H. Prosenc, Peter B. Armentrout, and Gereon Niedner-Schatteburg

Chemistry A European Journal (2021), 27, 15208-15216

<https://doi.org/10.1002/chem.202102520>

A CYCLOMETALATED NHC IRIDIUM COMPLEX BEARING A CATIONIC (H⁵-CYCLOPENTADENYL)(H⁶-PHENYL)IRON BACKBONE

Christian Malchau, Tom Milbert, Tobias Eger, **Daniela V. Fries**, Pascal J. Pape, Benjamin Oelkers, Yu Sun, Sabine Becker, Marc H. Prosenc, Gereon Niedner-Schatteburg, and Werner R. Thiel

Physical Chemistry Chemical Physics (2021), 23, 11345-11354

<https://doi.org/10.1039/D0CP06208A>, selected as **2021 HOT PCCP article**

OBSERVATION AND MECHANISM OF CRYO N₂ CLEAVEGE BY A TANTALUM CLUSTER

Daniela V. Fries, Matthias P. Klein, Annika Steiner, Marc H. Prosenc, and Gereon Niedner-Schatteburg

Zeitschrift für Physikalische Chemie (2018), 232, 649-669

<https://doi.org/10.1515/zpch-2017-1046>

CHARACTERIZATION OF TRINUCLEAR OXO BRIDGED COBALT COMPLEXES IN ISOLATION

Johannes Lang, **Daniela V. Fries**, and Gereon Niedner-Schatteburg

CONTRIBUTION TO CONFERENCES

ORAL PRESENTATIONS

121. Bunsentagung

Gießen (Germany), 07-09/09/2022

CRYO KINETICS AND IR SPECTROSCOPY OF N₂ ON TANTALUM-CLUSTER

Daniela V. Fries, Annika Straßner, Matthias P. Klein, Maximilian Huber, Maximilian Luczak, Christopher Wiehn, Marc H. Prosenc, and Gereon Niedner-Schatteburg

81st Workshop: international School of Solid State Physics ‘Dynamics of Electrons in Atomic and Molecular Nanoclusters’

Erice (Italy), 25-31/08/2022, selected as **hot topic talk**

CRYO IR SPECTROSCOPY AND KINETICS OF NITROGEN ON TANTALUM CLUSTERS TA₂₋₈⁺

Daniela V. Fries, Annika Straßner, Matthias P. Klein, Maximilian Huber, Maximilian Luczak, Christopher Wiehn, Marc H. Prosenc, and Gereon Niedner-Schatteburg

9. Promovierendenseminar Fachbereich Chemie

TU Kaiserslautern, 04/04/2022

OBSERVATION AND MECHANISM OF N₂ CLEAVAGE BY A TANTALUM CLUSTER UNDER CRYO CONDITIONS

Daniela V. Fries

DPG Frühjahrstagung SAMOP 2022

virtual event, 14 - 18/03/2022

CRYOKINETICS AND IR SPECTROSCOPY OF NITROGEN ON TANTALUM CLUSTERS

Daniela V. Fries, Annika Straßner, Matthias P. Klein, Maximilian Huber, Marc H. Prosenc, and Gereon Niedner-Schatteburg

DPG Frühjahrstagung SAMOP 2021

virtual event, 20 - 24/09/2021

N₂ CLEAVAGE BY TANTALUM CLUSTER UNDER CRYO CONDITIONS

Daniela V. Fries, Matthias P. Klein, Annika Straßner, Marc H. Prosenc, and Gereon Niedner-Schatteburg

120. Bunsentagung

virtual event, 10 - 12/05/2021

OBSERVATION AND MECHANISM OF N₂ CLEAVAGE BY A TANTALUM CLUSTER UNDER CRYO CONDITIONS

Daniela V. Fries, Matthias P. Klein, Annika Steiner, Marc H. Prosenc, and Gereon Niedner-Schatteburg

POSTER PRESENTATIONS

Gordon Research Conference: Gaseous Ions

Ventura (California, United States), 19 - 24/02/2023

N₂ CRYO ADSORPTION AND CLEAVGE ON TANTALUM CLUSTER

Daniela V. Fries, Lea Schneider, Annika Straßner, Matthias P. Klein, and Gereon Niedner-Schatteburg

Gordon Research Seminar: Gaseous Ions

Ventura (California, United States), 18 - 19/02/2023

N₂ CRYO ADSORPTION AND CLEAVGE ON TANTALUM CLUSTER

Daniela V. Fries, Lea Schneider, Annika Straßner, Matthias P. Klein, and Gereon Niedner-Schatteburg

Gordon Research Conference: Molecular and Ionic Clusters

Lucca (Barga, Italy), 07 - 12/08/2022

CRYO KINETICS AND IR SPECTROSCOPY OF N₂ ON TANTALUM-CLUSTER

Daniela V. Fries, Annika Straßner, Matthias P. Klein, Marc H. Prosenc, and Gereon Niedner-Schatteburg

Gordon Research Seminar: Molecular and Ionic Clusters

Lucca (Barga, Italy), 06 - 07/08/2022

CRYO KINETICS AND IR SPECTROSCOPY OF N₂ ON TANTALUM-CLUSTER

Daniela V. Fries, Annika Straßner, Matthias P. Klein, Marc H. Prosenc, and Gereon Niedner-Schatteburg

DANKSAGUNG

Nach fast zehn Jahren wissenschaftlicher Ausbildung in Kaiserslautern möchte ich mich an dieser Stelle bei allen bedanken, die mich in dieser spannenden und herausfordernden Zeit begleitet haben.

Zunächst möchte ich Prof. Dr. Gereon Niedner-Schatteburg für die Aufnahme in den Arbeitskreis, die Ausgabe des Promotions- und Forschungsthemas und die wissenschaftliche Betreuung in den letzten dreieinhalb Jahren bedanken. Ich bedanke mich für die konstruktiven Gespräche und Diskussionen insbesondere in den vielen Stunden des Paperschreibens. Außerdem wusste ich die mir eingeräumten Freiräume in der täglichen Labor- und Forschungstätigkeit und die stete Unterstützung mich sowohl wissenschaftlich, aber auch persönlich weiterzuentwickeln, immer sehr zu schätzen.

Vielen Dank, Jun.-Prof. Dr. Jennifer Meyer, für all die (nicht-) wissenschaftlichen Gespräche, Tipps und helfenden Hände seit du Teil des PC-Flurs bist. An so manchem späten Freitagabend war deine Anwesenheit und deine Hilfe Gold wert. Auch für die Übernahme meines Zweitgutachtens möchte ich dir sehr danken. Ich wünsche dir ganz viel Erfolg bei der weiteren Entwicklung deines Arbeitskreises und dem Vorrantreiben deiner Forschung.

Ich danke Herrn Prof. Dr. Werner Thiel für die Bereitschaft als dritter Prüfer Teil meiner Promotionskommission zu sein, die gute wissenschaftliche Zusammenarbeit mit seinem Arbeitskreis und die Unterstützung während meines Masterstudiums um einen Teil der Studienleistungen im Ausland erbringen zu können.

Ein Dankeschön geht auch in die Organische Chemie an Herrn Prof. Dr. Georg Manolikakes für die Übernahme des Prüfungsvorsitzes.

Danke auch an Herrn Prof. Dr. Markus Gerhards^d für die freundlichen Gespräche auf dem PC Flur und das wache Auge bis in die späten Abendstunden, wenn die Zeit mal schneller fortschritt als die zu erledigende Laborarbeit. Schade, dass dies nach meinem ersten Promotionsjahr nicht mehr möglich war.

Ich danke PD Dr. Christoph Rhien für die für die gute Zusammenarbeit bei den Anfängerpraktika und dem gemeinsamen Rätseln über das Eigenleben des Druckers.

Danke, Annika Straßner und Matthias Klein, dass ihr mich als Masterandin am FRITZ in euer Team aufgenommen habt. Annika, ein ganz großes Dankeschön geht an dich, dafür dass ich von dir lernen durfte - egal ob im wissenschaftlichen oder persönlichen Kontext. Ich erinnere mich sehr gerne an unsere Zusammenarbeit, die gemeinsame Messzeit und daran, dass wir immer versucht haben jeder Situation mit Humor zu begegnen. Danke, Matthias, dass ich dich zunächst bei der Tantalclusterforschung unterstützen durfte und ich das Thema in meiner Promotion schließlich komplett übernehmen und weiterführen konnte. Dankeschön auch für deine Unterstützung in den letzten Zügen meiner Promotion beim Durchdenken der Ergebnisse und Korrekturlesen meiner Arbeit.

Ich möchte auch dem Rest der Vorgängergeneration des AK GNS für die nette Aufnahme in den Arbeitskreis danken. Danke, Björn Kwasigroch, Mike Lembach und Yannick Mees, dass ich bei Fragen und Problemen immer auf offene Ohren gestoßen bin.

Danke an Maximilian Huber für die erste Zeit als "Next Generation" am FRITZ. Schade, dass daraus nichts wurde, aber ich freue mich sehr für dich, dass du deinen Platz im AK Meyer finden konntest und bin dir dankbar dafür, dass ich trotzdem stets auf deine Unterstützung im Labor zählen konnte.

Danke an meine aktuellen Doktorandenkollegen Maximilian Luczak und Christopher Wiehn für die wissenschaftliche Zusammenarbeit am FRITZ.

Ein Dank geht auch an alle Studierenden und Praktikanten, die ich bei ihren Abschlussarbeiten und Forschungspraktika (mit-)betreuen durfte. Ich danke euch für eure Fragen, bei denen ich selbst noch etwas lernen konnte, und eure Unterstützung bei meiner Forschung. Stellvertretend möchte ich hier insbesondere Katharina Rediger danken, für die gemeinsamen Erlebnisse, die vielen Gespräche über die Wissenschaft und weit darüber hinaus. Deine Gesellschaft im Büro war in jeder Hinsicht bereichernd.

Ein ganz großes Dankeschön geht auch an Thomas Kolling. Danke, dass du immer mit Rat und Tat am FRITZ zur Seite standest und dass ich dich in besonders herausfordernden Situationen auch nach Feierabend noch anrufen und auf einen hilfreichen Tipp hoffen konnte.

Ich danke Yevgeniy Nosenko für die vielen geduldigen Stunden Lasersupport und die vielen Dinge, die ich dabei lernen durfte.

Auch dem Sekretariatsteam um Sibylle Heideck, Birgit Harrison-Weber, Bärbel Stemmler und Petra Wetzl gilt ein Dankeschön für die Unterstützung bei jeglicher Bürokratie und dem gesamten nicht-wissenschaftlichem Arbeitsalltag angefangen bei meiner Einstellung bis hin zu meiner Aussprache.

Dankeschön an all die anderen Doktoranden und Gesichter auf dem PC Flur. Danke an Roumany Israil und Marcel Schmitt für die schöne Arbeitsatmosphäre und eure stete Hilfsbereitschaft. An vielen späten Abenden war eure Laserlampe das Licht am Ende des Tunnels und die Gewissheit nicht alleine auf dem Flur zu sein. Danke an Marcel Meta und Maurice Birk, stellvertretend für den gesamten AK Meyer, für die Adoption in euren Arbeitskreis zur Ablenkung und Unterhaltung abseits der Wissenschaft. Danke an die leider letzte Generation des AK Gerhards, stellvertretend an Sophie Steiger, Daniel Marhöfer und Patrick Strebert, für die gute Kollegialität über AK Grenzen hinaus. Die Achtminutenpausen im Hängemattenpark nach dem Mittagessen haben meine Tage bereichert.

Ich danke auch meinen Kommilitonen, die ich hier gar nicht alle namentlich erwähnen kann und von denen einige über die Jahre zu richtig guten Freunden geworden sind, dass wir uns gemeinsam dem Chemiestudium gestellt, es gemeistert und bis heute den Kontakt zueinander nicht verloren haben. Und danke an alle Personen, Freunde und Mitstreiter auch über den Fachbereich Chemie hinaus, dass ich mit euch gemeinsam über den Tellerand meines Fachgebiets hinausschauen durfte, und dass man mit euch immer eine Abwechslung vom Uni- und Forschungsalltag finden konnte.

Ein besonderer Dank geht an meine Familie, insbesondere an meine Eltern und meine Schwester. Danke für eure Unterstützung und euren Rückhalt. Du hattest recht, Mama, ich schaffe das!

Zu guter Letzt danke ich meinem Partner, für die Geduld, das Verständnis und die vielen motivierenden Worte in den letzten Jahren. Danke, dass du Teil meines Lebens bist und mich stärker machst.

Ich bitte alle, die ich in dieser Dankesliste übersehen oder nicht namentlich erwähnt habe, sich trotzdem angesprochen zu fühlen. Ihr wisst, dass ihr einen Teil dazu beigetragen habt, dass ich dieses Ziel erreichen konnte. Dafür bin ich euch sehr dankbar!

Eidesstattliche Erklärung

Hiermit bestätige ich, Daniela Veronika FRIES, dass die vorliegende Dissertation mit dem Titel

“Kinetic and Spectroscopic Characterization of N₂ and H₂ Activation by Tantalum Clusters under Cryo Conditions”

gemäß der Promotionsordnung des Fachbereichs Chemie der Technischen Universität Kaiserslautern (seit 01.01.2023 Rheinland-Pfälzische Technische Universität Kaiserslautern-Landau) selbstständig verfasst und mit keinen anderen, als den hier angegebenen, Quellen und Hilfsmitteln erstellt wurde.

Kooperationsprojekte innerhalb der eigenen Forschungsgruppe oder mit anderen Arbeitskreisen sowie die beteiligten Mitarbeiter sind zu Beginn der entsprechenden Arbeiten abgegrenzt.

Die vorliegende Arbeit wurde bei keiner anderen Hochschule als der Technischen Universität Kaiserslautern (seit 01.01.2023 Rheinland-Pfälzische Technische Universität Kaiserslautern-Landau) in ähnlicher oder gleicher Form eingereicht.

Kaiserslautern, Juli 2023

Daniela Veronika FRIES